

**PERFORMANCE ADVANTAGES AND RESONANCE ANALYSIS OF A
VARIABLE SPEED ROTOR USING GEOMETRICALLY EXACT BEAM
FORMULATIONS**

A Dissertation
Presented to
The Academic Faculty

By

Ruthvik Chandrasekaran

In Partial Fulfillment
of the Requirements for the Degree
Doctor of Philosophy in the
School of Aerospace Engineering

Georgia Institute of Technology

December 2021

Copyright © Ruthvik Chandrasekaran 2021

**PERFORMANCE ADVANTAGES AND RESONANCE ANALYSIS OF A
VARIABLE SPEED ROTOR USING GEOMETRICALLY EXACT BEAM
FORMULATIONS**

Approved by:

Prof. Dewey H. Hodges, Advisor
School of Aerospace Engineering
Georgia Institute of Technology

Assoc. Prof. Graeme J. Kennedy
School of Aerospace Engineering
Georgia Institute of Technology

Prof. David A. Peters
McKelvey School of Engineering
Washington University in St. Louis

Prof. George Kardomateas
School of Aerospace Engineering
Georgia Institute of Technology

Assoc. Prof. Julian J. Rimoli
School of Aerospace Engineering
Georgia Institute of Technology

Date Approved: November 23, 2021

Carpe diem, cum opus vitae statera

*To my mother, Padma,
My father, Chandrasekaran,
My great teachers,
My sister, Deepthi,
and
The rest of my family and friends...*

ACKNOWLEDGEMENTS

I would be nowhere close to where I am today without the help and guidance of a great many people I have met in my life. I will do my best to acknowledge them all, and by no means my gratitude is limited to the ones mentioned here.

First of all, I would like to express my sincerest gratitude to Prof. Dewey Hodges for providing me with this great opportunity to work with him and to be a part of his lab. I could not thank him enough for his extraordinary patience and support throughout my journey at Georgia Tech. I never imagined that I would be mentored by one of the greatest in the field of rotor blade mechanics and aeroelasticity. I am extremely grateful to be his student. He not only imparted his knowledge but also shared his wisdom and his great sense of humor, which kept me going during the tough times. If I could carry in my heart and mind an ounce of the humility he exhibits, I would be a better person on every occasion.

I would like to thank Prof. Graeme Kennedy, Prof. David Peters, Prof. George Kardomateas, and Prof. Julian Rimoli for being a part of my thesis committee and for their invaluable suggestions that have improved the quality of this work. I thank every one of them for giving me their time and energy in making this thesis more complete.

I would also like to thank Dr. Olivier Bauchau and his students for developing Dymore, which is at the core of this thesis. I am very grateful for his guidance in using Dymore. I cannot thank Dr. Hanif Hoseini and Dr. Seundo Heo enough for their tremendous help and support with Dymore during this study. If not for their help at critical points, I would have not been able to make any progress in my research.

I would be remiss if I didn't thank Prof. Jeff Jagoda for his tremendous moral and administrative support during my time at Georgia Tech. Without him, I can't even imagine being able to finish my Ph.D. program. He has been a pillar to lean on for many graduate students in the School of Aerospace Engineering.

I am deeply indebted to my teachers and mentors who prepared me for this journey. I

thank my undergrad advisor Dr. Vaitla Laxman at Amrita School of Engineering and my graduate advisor Dr. Venkatesan C., who was at IIT Kanpur, for shaping me as a researcher in the rotorcraft field. Without their guidance, I would have never been able to find my way.

I would like to thank my friends Hernan Logarzo and Siddarth for going through the thick and thin of a doctorate program side-by-side. I also thank my friends Kristen, Srishath, Kate, Raaghul, Mrudula, Prasoon, Farzaneh, Sriram, Sukruth, Vinodhini, Carolina, Sadegh, Anca and Nitansh who made my stay at Georgia Tech and Atlanta a memorable experience. I also thank my friends and lab-mates in the School of Aerospace Engineering, Donald, Julie, Nishant, Sampath, Komahan, Amir, Aqib, Hamza, Julia, Anusha, Eva, Nate, Archana, Caleb, Darshan, Harold, Jaechan, Yoobin, and Lee. I also thank Prof. Stephen Ruffin and Prof. Mitchell Walker for providing me with a GTA position whenever necessary. I am so thankful to Ms. Brittany Hodges and the entire Aerospace Department staff for their significant help during my Ph.D.

I would like to convey my special thanks to the GT Salsa club and GT Dance Association for adding music and dance to the Georgia Tech community. I will forever cherish the friendships I made on the dance floor.

Finally, I am so grateful to have a supportive family that showers me with love and provides me with emotional support despite being thousands of miles away. I thank them for all the sacrifices they've made to get me to this stage in life. I can never repay them for everything they have provided me. I owe them every aspect of my life.

TABLE OF CONTENTS

Acknowledgments	v
List of Tables	xi
List of Figures	xiii
Chapter 1: Introduction	1
1.1 Motivation	1
1.2 Literature Survey	7
1.2.1 Variable Speed Rotor (VSR)	7
1.2.2 Rotor Blade Modeling	13
1.2.3 Aerodynamics and Rotor Trimming	25
1.3 Objectives of the Present Study	29
Chapter 2: Rotor Blade Formulations	30
2.1 Geometrically Exact Beam Formulations	30
2.2 Aerodynamic Formulations	42
2.2.1 Unsteady Aerodynamics	45
2.2.2 ONERA Dynamic Stall	49
2.2.3 Inflow Model	50

2.2.4	Total Air Loads	52
Chapter 3: Rotor Modeling and Trim Method Validation		54
3.1	Blade Modeling	54
3.2	Rotor Trim	58
3.3	Model Validation	61
Chapter 4: VSR: Power Advantages and Resonance Studies		70
4.1	Rotor Properties	70
4.2	Baseline Conditions	72
4.3	Inflow States and Trim Angles	73
4.4	Power Advantages of a VSR	77
4.5	Resonance Points Identification	82
4.6	Resonance Transition Dynamics	85
4.6.1	Validation	85
4.6.2	Nominal Advance Ratio, $\mu_N = 0.3$	86
4.6.3	Nominal Advance Ratio, $\mu_N = 0.2$	100
4.6.4	Nominal Advance Ratio, $\mu_N = 0.1$	114
4.6.5	Nominal Advance Ratio, $\mu_N = 0$ (Hover)	133
4.6.6	Nominal Advance Ratio, $\mu_N = 0$: Perturbation Response	141
Chapter 5: Load Reduction During Resonance		155
5.1	Rotor Speed Transition Time	155
5.1.1	$\mu_N = 0.3$, 230 \rightarrow 180 RPM	155

5.1.2	$\mu_N = 0.3$, 180 \rightarrow 230 RPM	162
5.1.3	$\mu_N = 0.2$, 230 \rightarrow 150 RPM	167
5.1.4	$\mu_N = 0.2$, 150 \rightarrow 230 RPM	170
5.1.5	$\mu_N = 0.1$, 230 \rightarrow 130 RPM	172
5.1.6	$\mu_N = 0.1$, 130 \rightarrow 230 RPM	175
5.1.7	Transition Time: Summary	178
5.2	Structural Damping Impact	178
5.2.1	$\mu_N = 0.3$, 230 \rightarrow 180 RPM	179
5.2.2	$\mu_N = 0.3$, 180 \rightarrow 230 RPM	181
5.2.3	$\mu_N = 0.2$, 230 \rightarrow 150 RPM	182
5.2.4	$\mu_N = 0.2$, 150 \rightarrow 230 RPM	184
5.2.5	$\mu_N = 0.1$, 230 \rightarrow 130 RPM	186
5.2.6	$\mu_N = 0.1$, 130 \rightarrow 230 RPM	188
5.2.7	Structural Lag Damping (ζ): Summary	191
5.3	Rotor Blade Stiffness Impact	191
5.3.1	$\mu_N = 0.3$, 230 \rightarrow 180 RPM	193
5.3.2	$\mu_N = 0.3$, 180 \rightarrow 230 RPM	197
5.3.3	$\mu_N = 0.2$, 230 \rightarrow 150 RPM	199
5.3.4	$\mu_N = 0.2$, 150 \rightarrow 230 RPM	203
5.3.5	$\mu_N = 0.1$, 230 \rightarrow 130 RPM	204
5.3.6	$\mu_N = 0.1$, 130 \rightarrow 230 RPM	208
5.3.7	Impact of Lag Stiffness (EI_{Lag}): Summary	210
5.4	Combination Impact: Transition time (t_T) and ζ	211

5.4.1	$\mu_N = 0.3, 230 \rightarrow 180 \text{ RPM}$	211
5.4.2	$\mu_N = 0.3, 180 \rightarrow 230 \text{ RPM}$	213
5.4.3	$\mu_N = 0.2, 230 \rightarrow 150 \text{ RPM}$	215
5.4.4	$\mu_N = 0.2, 150 \rightarrow 230 \text{ RPM}$	217
5.4.5	$\mu_N = 0.1, 230 \rightarrow 130 \text{ RPM}$	219
5.4.6	$\mu_N = 0.1, 130 \rightarrow 230 \text{ RPM}$	220
5.4.7	Combined Impact (ζ & t_T): Summary	222
Chapter 6: Anti-Resonance System (ARS)		224
6.1	$\mu_N = 0.3, 230 \rightarrow 180 \text{ RPM}$	226
6.2	$\mu_N = 0.3, 180 \rightarrow 230 \text{ RPM}$	229
6.3	$\mu_N = 0.2, 230 \rightarrow 150 \text{ RPM}$	232
6.4	$\mu_N = 0.2, 150 \rightarrow 230 \text{ RPM}$	237
6.5	$\mu_N = 0.2, 230 \rightarrow 150 \text{ RPM}$ (Resonance Outside)	240
6.6	$\mu_N = 0.1, 230 \rightarrow 130 \text{ RPM}$	244
6.7	$\mu_N = 0.1, 130 \rightarrow 230 \text{ RPM}$	247
6.8	$\mu_N = 0.1, 230 \rightarrow 130 \text{ RPM}$ (Resonance Outside)	251
Chapter 7: Conclusions, Contributions and Future Work		255
7.1	Conclusions	255
7.2	Contributions	258
7.3	Future work	259
References		274

LIST OF TABLES

3.1	Rotor properties [155].	64
3.2	Nomenclature.	65
3.3	Blade stiffness properties and natural frequencies (DYMORE)	65
3.4	Rotor trim states at sea level.	66
4.1	Rotor properties [18].	70
4.2	Trim angles comparison for 3 state inflow.	72
4.3	Nominal advance ratio and free stream velocity.	72
4.4	Resonance points between 230 RPM and 180 RPM.	86
4.5	Resonance points between 230 RPM and 150 RPM.	100
4.6	Resonance points between 230 RPM and 130 RPM.	114
4.7	Trim angles comparison at $\mu_N = 0.1$	117
4.8	Resonance points between 230 RPM and 110 RPM.	133
4.9	Gust properties at $\mu_N = 0$	142
5.1	Transition time impact on high-to-low speed transition.	178
5.2	Transition time impact on low-to-high speed transition.	178
5.3	ζ impact on high-to-low speed transition.	191
5.4	ζ impact on low-to-high speed transition.	191

5.5	Lag stiffness for higher crossings ($\mu_N = 0.3$).	192
5.6	EI_{Lag} impact on high-to-low speed transition.	210
5.7	EI_{Lag} impact on low-to-high speed transition.	211
5.8	ζ and t_T impact on high-to-low speed transition.	222
5.9	ζ and t_T impact on low-to-high speed transition.	223
6.1	Mass properties: Baseline vs. ARS Blade.	225

LIST OF FIGURES

1.1	V-22 Osprey in helicopter mode.	2
1.2	V-22 Osprey in airplane mode.	2
1.3	XH-59 demonstrator aircraft built for the U.S army.	2
1.4	Sikorsky X2 demonstrator.	3
1.5	Lockheed's XH-51A compound helicopter.	4
1.6	Eurocopter X ³ in flight.	4
1.7	A-160T UAV helicopter with optimum speed rotor.	5
1.8	Carter PAV.	6
2.1	Beam in reference and deformed configuration.	31
2.2	Airfoil and airstation configuration.	42
2.3	Airfoil motion.	43
2.4	Velocity vectors on the airfoil.	44
2.5	Relative velocity with respect to the quarter-chord.	45
2.6	Airfoil with wind tunnel lift.	47
2.7	Airfoil with wind tunnel drag.	47
2.8	Data flow between structural, unsteady aerodynamics and inflow model.	52
3.1	Schematic of a hingeless rotor.	54

3.2	Hingeless rotor blade model in DYMORE.	55
3.3	Four-bladed rotor system.	55
3.4	Four-bladed rotor system.	56
3.5	Rotor model in DYMORE.	56
3.6	Hub plane tilt and free stream velocity.	56
3.7	Blade azimuth angle.	57
3.8	Airstation coordinates on a rotor blade.	57
3.9	Thrust force and pitching moment at the hub center.	58
3.10	Roll moment at the hub center.	59
3.11	Schematic of rotor and fuselage.	61
3.12	Forces and moments for propulsive trim.	62
3.13	Time history of rotor trimming at $\mu = 0$	66
3.14	Time history of rotor trimming at $\mu = 0.1$	67
3.15	Time history of rotor trimming at $\mu = 0.2$ (Pitch and roll moments).	67
3.16	Time history of rotor trimming at $\mu = 0.2$ (Thrust).	68
3.17	Time history of rotor trimming at $\mu = 0.3$	68
3.18	Trim angles comparison.	69
4.1	Rotor blade fan plot for $\zeta = 1\%$	71
4.2	Rotor blade fan plot showing nominal Ω	73
4.3	Trim angle convergence at $\mu_N = 0$	74
4.4	Trim angles convergence at $\mu_N = 0.1$	75
4.5	Trim angles convergence at $\mu_N = 0.2$ (Collective and lateral cyclic)	75

4.6	Trim angles convergence at $\mu_N = 0.2$ (Longitudinal cyclic)	76
4.7	Trim angles convergence at $\mu_N = 0.3$	76
4.8	Power savings at $\mu_N = 0$	78
4.9	Torque variation with rotor speed at $\mu_N = 0$	79
4.10	Power savings at $\mu_N = 0.1$	79
4.11	Torque variation with rotor speed at $\mu_N = 0.1$	80
4.12	Power savings at $\mu_N = 0.2$	80
4.13	Torque variation with rotor speed at $\mu_N = 0.2$	81
4.14	Power savings at $\mu_N = 0.3$	81
4.15	Torque variation with rotor speed at $\mu_N = 0.3$	82
4.16	Resonance points for $\mu_N = 0$	83
4.17	Resonance points for $\mu_N = 0.1$	83
4.18	Resonance points for $\mu_N = 0.2$	84
4.19	Resonance points for $\mu_N = 0.3$	84
4.20	Lag moment comparison for 2/rev lag resonance (180 \rightarrow 240 RPM)	85
4.21	Rotor torque comparison (180 \rightarrow 240 RPM)	86
4.22	Rotor speed change from 230 to 180 RPM (10 s)	87
4.23	Pitch angles for $\mu_N = 0.3$	88
4.24	Pitch angles variation with time for $\mu_N = 0.3$ (230 \rightarrow 180 RPM)	88
4.25	Time history of lag moment at blade root ($\mu_N = 0.3$; 230 \rightarrow 180 RPM)	89
4.26	FFT analysis of lag moment at resonance ($\mu_N = 0.3$; 230 \rightarrow 180 RPM)	89
4.27	Time history of lag force at blade root ($\mu_N = 0.3$; 230 \rightarrow 180 RPM)	90
4.28	FFT analysis of lag force at resonance ($\mu_N = 0.3$; 230 \rightarrow 180 RPM)	90

4.29	Time history of flap moment at blade root ($\mu_N = 0.3$; 230 \rightarrow 180 RPM)	91
4.30	FFT analysis of flap moment at resonance ($\mu_N = 0.3$; 230 \rightarrow 180 RPM)	91
4.31	Time history of torsional moment at blade root ($\mu_N = 0.3$; 230 \rightarrow 180 RPM)	92
4.32	FFT analysis of torsional moment at resonance ($\mu_N = 0.3$; 230 \rightarrow 180 RPM)	92
4.33	Time history of rotor torque ($\mu_N = 0.3$; 230 \rightarrow 180 RPM)	93
4.34	Rotor acceleration time history ($\Omega = 230$ to 180 RPM in 10 s)	93
4.35	FFT analysis of rotor torque at resonance ($\mu_N = 0.3$; 230 \rightarrow 180 RPM)	94
4.36	Rotor speed change from 180 to 230 RPM (10 s)	94
4.37	Rotor acceleration time history ($\Omega = 180$ to 230 RPM in 10 s)	95
4.38	Time history of lag moment at blade root ($\mu_N = 0.3$; 180 \rightarrow 230 RPM)	95
4.39	FFT analysis of lag moment at resonance ($\mu_N = 0.3$; 180 \rightarrow 230 RPM)	96
4.40	Time history of lag force at blade root ($\mu_N = 0.3$; 180 \rightarrow 230 RPM)	96
4.41	FFT analysis of lag force at resonance ($\mu_N = 0.3$; 180 \rightarrow 230 RPM)	97
4.42	Time history of flap moment at blade root ($\mu_N = 0.3$; 180 \rightarrow 230 RPM)	97
4.43	FFT analysis of flap moment at resonance ($\mu_N = 0.3$; 180 \rightarrow 230 RPM)	98
4.44	Time history of torsional moment at blade root ($\mu_N = 0.3$; 180 \rightarrow 230 RPM)	98
4.45	FFT analysis of torsional moment at resonance ($\mu_N = 0.3$; 180 \rightarrow 230 RPM)	99
4.46	Time history of rotor torque ($\mu_N = 0.3$; 180 \rightarrow 230 RPM)	99
4.47	FFT analysis of rotor torque at resonance ($\mu_N = 0.3$; 180 \rightarrow 230 RPM)	100
4.48	Rotor speed change from 230 to 150 RPM (16 s)	101
4.49	Rotor acceleration time history ($\Omega = 230$ to 150 RPM in 16 s)	101
4.50	Pitch angles for $\mu_N = 0.2$	102
4.51	Pitch angles variation with time for $\mu_N = 0.2$ (16 s, 230 \rightarrow 150 RPM)	102

4.52	Time history of lag moment at blade root ($\mu_N = 0.2$; 230 \rightarrow 150 RPM)	103
4.53	FFT analysis of lag moment at resonance ($\mu_N = 0.2$; 230 \rightarrow 150 RPM)	103
4.54	Pitch angles at 2/rev lag resonance (at 205.8 RPM)	104
4.55	Time history of lag force at blade root ($\mu_N = 0.2$; 230 \rightarrow 150 RPM)	104
4.56	FFT analysis of lag force at resonance ($\mu_N = 0.2$; 230 \rightarrow 150 RPM)	105
4.57	Time history of flap moment at blade root ($\mu_N = 0.2$; 230 \rightarrow 150 RPM) . . .	105
4.58	FFT analysis of flap moment at resonance ($\mu_N = 0.2$; 230 \rightarrow 150 RPM) . . .	106
4.59	Time history of torsional moment at blade root ($\mu_N = 0.2$; 230 \rightarrow 150 RPM) .	106
4.60	FFT analysis of torsional moment at resonance ($\mu_N = 0.2$; 230 \rightarrow 150 RPM) .	107
4.61	Time history of rotor torque ($\mu_N = 0.2$; 230 \rightarrow 150 RPM)	107
4.62	FFT analysis of rotor torque at resonance ($\mu_N = 0.2$; 230 \rightarrow 150 RPM)	108
4.63	Rotor speed change from 150 to 230 RPM (16 s)	108
4.64	Rotor acceleration time history ($\Omega = 150$ to 230 RPM in 16 s)	109
4.65	Time history of lag moment at blade root ($\mu_N = 0.2$; 150 \rightarrow 230 RPM)	109
4.66	FFT analysis of lag moment at resonance ($\mu_N = 0.2$; 150 \rightarrow 230 RPM)	110
4.67	Time history of lag force at blade root ($\mu_N = 0.2$; 150 \rightarrow 230 RPM)	110
4.68	FFT analysis of lag force at resonance ($\mu_N = 0.2$; 150 \rightarrow 230 RPM)	111
4.69	Time history of flap moment at blade root ($\mu_N = 0.2$; 150 \rightarrow 230 RPM) . . .	111
4.70	FFT analysis of flap moment at resonance ($\mu_N = 0.2$; 150 \rightarrow 230 RPM) . . .	112
4.71	Time history of torsional moment at blade root ($\mu_N = 0.2$; 150 \rightarrow 230 RPM) .	112
4.72	FFT analysis of torsional moment at resonance ($\mu_N = 0.2$; 150 \rightarrow 230 RPM) .	113
4.73	Time history of rotor torque ($\mu_N = 0.2$; 150 \rightarrow 230 RPM)	113
4.74	FFT analysis of rotor torque at resonance ($\mu_N = 0.2$; 150 \rightarrow 230 RPM)	114

4.75	Pitch angles for $\mu_N = 0.1$	115
4.76	Rotor speed change from 230 to 130 RPM (20 s)	115
4.77	Rotor acceleration time history ($\Omega = 230$ to 130 RPM in 20 s)	116
4.78	Time history of lag moment at blade root ($\mu_N = 0.1$; 230 \rightarrow 130 RPM)	117
4.79	FFT analysis of lag moment at first resonance ($\mu_N = 0.1$; 230 \rightarrow 130 RPM) .	117
4.80	FFT analysis of lag moment at second resonance ($\mu_N = 0.1$; 230 \rightarrow 130 RPM)	118
4.81	Time history of lag force at blade root ($\mu_N = 0.1$; 230 \rightarrow 130 RPM)	118
4.82	FFT analysis of lag force at first resonance ($\mu_N = 0.1$; 230 \rightarrow 130 RPM) . . .	119
4.83	FFT analysis of lag force at second resonance ($\mu_N = 0.1$; 230 \rightarrow 130 RPM) .	119
4.84	Time history of flap moment at blade root ($\mu_N = 0.1$; 230 \rightarrow 130 RPM) . . .	120
4.85	FFT analysis of flap moment at first resonance ($\mu_N = 0.1$; 230 \rightarrow 130 RPM) .	120
4.86	FFT analysis of flap moment at second resonance ($\mu_N = 0.1$; 230 \rightarrow 130 RPM)	121
4.87	Time history of torsional moment at blade root ($\mu_N = 0.1$; 230 \rightarrow 130 RPM) .	121
4.88	FFT analysis of torsional moment at first resonance ($\mu_N = 0.1$; 230 \rightarrow 130 RPM)	122
4.89	FFT analysis of torsional moment at second resonance ($\mu_N = 0.1$; 230 \rightarrow 130 RPM)	122
4.90	Time history of rotor torque ($\mu_N = 0.1$; 230 \rightarrow 130 RPM)	123
4.91	FFT analysis of rotor torque at first resonance ($\mu_N = 0.1$; 230 \rightarrow 130 RPM) .	123
4.92	FFT analysis of rotor torque at second resonance ($\mu_N = 0.1$; 230 \rightarrow 130 RPM) .	124
4.93	Rotor speed change from 130 to 230 RPM (20 s)	124
4.94	Rotor acceleration time history ($\Omega = 130$ to 230 RPM in 20 s)	125
4.95	Time history of lag moment at blade root ($\mu_N = 0.1$; 130 \rightarrow 230 RPM)	126

4.96	FFT analysis of lag moment at first resonance ($\mu_N = 0.1$; 130 \rightarrow 230 RPM)	126
4.97	FFT analysis of lag moment at second resonance ($\mu_N = 0.1$; 130 \rightarrow 230 RPM)	127
4.98	Time history of lag force at blade root ($\mu_N = 0.1$; 130 \rightarrow 230 RPM)	127
4.99	FFT analysis of lag force at first resonance ($\mu_N = 0.1$; 130 \rightarrow 230 RPM)	128
4.100	FFT analysis of lag force at second resonance ($\mu_N = 0.1$; 130 \rightarrow 230 RPM)	128
4.101	Time history of flap moment at blade root ($\mu_N = 0.1$; 130 \rightarrow 230 RPM)	129
4.102	FFT analysis of flap moment at first resonance ($\mu_N = 0.1$; 130 \rightarrow 230 RPM)	129
4.103	FFT analysis of flap moment at second resonance ($\mu_N = 0.1$; 130 \rightarrow 230 RPM)	130
4.104	Time history of torsional moment at blade root ($\mu_N = 0.1$; 130 \rightarrow 230 RPM)	130
4.105	FFT analysis of torsional moment at first resonance ($\mu_N = 0.1$; 130 \rightarrow 230 RPM)	131
4.106	FFT analysis of torsional moment at second resonance ($\mu_N = 0.1$; 130 \rightarrow 230 RPM)	131
4.107	Time history of rotor torque ($\mu_N = 0.1$; 130 \rightarrow 230 RPM)	132
4.108	FFT analysis of rotor torque at first resonance ($\mu_N = 0.1$; 130 \rightarrow 230 RPM)	132
4.109	Pitch angles for $\mu_N = 0$	133
4.110	Rotor speed change from 230 to 110 RPM (24 s)	134
4.111	Rotor acceleration time history ($\Omega = 230$ to 110 RPM in 24 s)	134
4.112	Time history of lag moment at blade root ($\mu_N = 0$; 230 \rightarrow 110 RPM)	135
4.113	Time history of lag force at blade root ($\mu_N = 0$; 230 \rightarrow 110 RPM)	135
4.114	Time history of flap moment at blade root ($\mu_N = 0$; 230 \rightarrow 110 RPM)	136
4.115	Time history of torsional moment at blade root ($\mu_N = 0$; 230 \rightarrow 110 RPM)	136
4.116	Time history of rotor torque ($\mu_N = 0$; 230 \rightarrow 110 RPM)	137

4.117	Rotor speed change from 110 to 230 RPM (24 s)	137
4.118	Rotor acceleration time history ($\Omega = 110$ to 230 RPM in 24 s)	138
4.119	Time history of lag moment at blade root ($\mu_N = 0$; 110 \rightarrow 230 RPM)	138
4.120	Time history of lag force at blade root ($\mu_N = 0$; 110 \rightarrow 230 RPM)	139
4.121	Time history of flap moment at blade root ($\mu_N = 0$; 110 \rightarrow 230 RPM)	139
4.122	Time history of torsional moment at blade root ($\mu_N = 0$; 110 \rightarrow 230 RPM)	140
4.123	Time history of rotor torque ($\mu_N = 0$; 110 \rightarrow 230 RPM)	140
4.124	Gust orientation with respect to the rotor disk	141
4.125	Time history of gust speed at $\mu_N = 0$	141
4.126	Time history of lag moment with gust ($\mu_N = 0$; 230 \rightarrow 110 RPM)	142
4.127	FFT analysis of lag moment after first perturbation ($\mu_N = 0$; 230 \rightarrow 110 RPM)	143
4.128	FFT analysis of lag moment after second perturbation ($\mu_N = 0$; 230 \rightarrow 110 RPM)	143
4.129	Time history of lag force with gust ($\mu_N = 0$; 230 \rightarrow 110 RPM)	144
4.130	Time history of flap moment with gust ($\mu_N = 0$; 230 \rightarrow 110 RPM)	144
4.131	FFT analysis of flap moment after first perturbation ($\mu_N = 0$; 230 \rightarrow 110 RPM)	145
4.132	FFT analysis of flap moment after second perturbation ($\mu_N = 0$; 230 \rightarrow 110 RPM)	145
4.133	Time history of torsional moment with gust ($\mu_N = 0$; 230 \rightarrow 110 RPM)	146
4.134	FFT analysis of torsional moment after first perturbation ($\mu_N = 0$; 230 \rightarrow 110 RPM)	146
4.135	FFT analysis of torsional moment after second perturbation ($\mu_N = 0$; 230 \rightarrow 110 RPM)	147
4.136	Time history of rotor torque with gust ($\mu_N = 0$; 230 \rightarrow 110 RPM)	147

4.137	FFT analysis of rotor torque after first perturbation ($\mu_N = 0$; 230 \rightarrow 110 RPM)	148
4.138	FFT analysis of rotor torque after second perturbation ($\mu_N = 0$; 230 \rightarrow 110 RPM)	148
4.139	Time history of lag moment with gust ($\mu_N = 0$; 110 \rightarrow 230 RPM)	149
4.140	FFT analysis of lag moment after first perturbation ($\mu_N = 0$; 110 \rightarrow 230 RPM)	149
4.141	FFT analysis of lag moment after second perturbation ($\mu_N = 0$; 110 \rightarrow 230 RPM)	150
4.142	Time history of lag force with gust ($\mu_N = 0$; 110 \rightarrow 230 RPM)	150
4.143	Time history of flap moment with gust ($\mu_N = 0$; 110 \rightarrow 230 RPM)	151
4.144	FFT analysis of flap moment after first perturbation ($\mu_N = 0$; 110 \rightarrow 230 RPM)	151
4.145	FFT analysis of flap moment after second perturbation ($\mu_N = 0$; 110 \rightarrow 230 RPM)	151
4.146	Time history of torsional moment with gust ($\mu_N = 0$; 110 \rightarrow 230 RPM) . . .	152
4.147	FFT analysis of torsional moment after first perturbation ($\mu_N = 0$; 110 \rightarrow 230 RPM)	152
4.148	FFT analysis of torsional moment after second perturbation ($\mu_N = 0$; 110 \rightarrow 230 RPM)	153
4.149	Time history of rotor torque with gust ($\mu_N = 0$; 110 \rightarrow 230 RPM)	153
4.150	FFT analysis of rotor torque after first perturbation ($\mu_N = 0$; 110 \rightarrow 230 RPM)	154
4.151	FFT analysis of rotor torque after second perturbation ($\mu_N = 0$; 110 \rightarrow 230 RPM)	154
5.1	Rotor speed transition time cases ($\mu_N = 0.3$; 230 \rightarrow 180 RPM)	156
5.2	Rotor speed transition time cases ($\mu_N = 0.3$; 230 \rightarrow 180 RPM)	156

5.3	Time history of lag moment at blade root ($\mu_N = 0.3$; 230 \rightarrow 180 RPM)	157
5.4	Lag moment's peak amplitude variation with transition time ($\mu_N = 0.3$; 230 \rightarrow 180 RPM)	158
5.5	Time history of flap moment at blade root ($\mu_N = 0.3$; 230 \rightarrow 180 RPM) . . .	159
5.6	Flap moment's peak amplitude variation with transition time ($\mu_N = 0.3$; 230 \rightarrow 180 RPM)	159
5.7	Time history of torsional moment at blade root ($\mu_N = 0.3$; 230 \rightarrow 180 RPM) .	160
5.8	Torsional moment's peak amplitude variation with transition time ($\mu_N = 0.3$; 230 \rightarrow 180 RPM)	160
5.9	Time history of rotor torque ($\mu_N = 0.3$; 230 \rightarrow 180 RPM)	161
5.10	Time history of rotor torque without 2 s and 5s transition ($\mu_N = 0.3$; 230 \rightarrow 180 RPM)	162
5.11	Rotor speed transition time cases ($\mu_N = 0.3$; 180 \rightarrow 230 RPM)	162
5.12	Rotor speed transition time cases ($\mu_N = 0.3$; 180 \rightarrow 230 RPM)	163
5.13	Time history of lag moment at blade root ($\mu_N = 0.3$; 180 \rightarrow 230 RPM)	163
5.14	Time history of rotor torque ($\mu_N = 0.3$; 180 \rightarrow 230 RPM)	164
5.15	Rotor speed with 3 s and 4 s transition times ($\mu_N = 0.3$; 180 \rightarrow 230 RPM) . .	165
5.16	Time history of rotor torque with 3 s and 4 s transition times ($\mu_N = 0.3$; 180 \rightarrow 230 RPM)	165
5.17	Time history of lag moment including 3 s and 4 s transition ($\mu_N = 0.3$; 180 \rightarrow 230 RPM)	166
5.18	Lag moment's peak amplitude variation with transition time ($\mu_N = 0.3$; 180 \rightarrow 230 RPM)	166
5.19	Rotor speed transition time cases ($\mu_N = 0.2$; 230 \rightarrow 150 RPM)	167
5.20	Rotor speed transition time cases ($\mu_N = 0.2$; 230 \rightarrow 150 RPM)	167
5.21	Time history of lag moment at blade root ($\mu_N = 0.2$; 230 \rightarrow 150 RPM)	168

5.22	Lag moment's peak amplitude variation with transition time ($\mu_N = 0.2$; 230 \rightarrow 150 RPM)	168
5.23	Time history of rotor torque ($\mu_N = 0.2$; 230 \rightarrow 150 RPM)	169
5.24	Time history of rotor torque from and above 14 s transition time ($\mu_N = 0.2$; 230 \rightarrow 150 RPM)	169
5.25	Rotor speed transition time cases ($\mu_N = 0.2$; 150 \rightarrow 230 RPM)	170
5.26	Rotor speed transition time cases ($\mu_N = 0.2$; 150 \rightarrow 230 RPM)	170
5.27	Time history of lag moment at blade root ($\mu_N = 0.2$; 150 \rightarrow 230 RPM)	171
5.28	Lag moment's peak amplitude variation with transition time ($\mu_N = 0.2$; 150 \rightarrow 230 RPM)	171
5.29	Time history of rotor torque ($\mu_N = 0.2$; 150 \rightarrow 230 RPM)	172
5.30	Rotor speed transition time cases ($\mu_N = 0.1$; 230 \rightarrow 130 RPM)	172
5.31	Rotor speed transition time cases ($\mu_N = 0.1$; 230 \rightarrow 130 RPM)	173
5.32	Time history of lag moment at blade root ($\mu_N = 0.1$; 230 \rightarrow 130 RPM)	173
5.33	Lag moment's peak amplitude at 3/rev resonance ($\mu_N = 0.1$; 230 \rightarrow 130 RPM)	174
5.34	Time history of rotor torque ($\mu_N = 0.1$; 230 \rightarrow 130 RPM)	174
5.35	Time history of rotor torque from and above 13 s transition time ($\mu_N = 0.1$; 230 \rightarrow 130 RPM)	175
5.36	Rotor speed transition time cases ($\mu_N = 0.1$; 230 \rightarrow 130 RPM)	175
5.37	Rotor speed transition time cases ($\mu_N = 0.1$; 230 \rightarrow 130 RPM)	176
5.38	Time history of lag moment at blade root ($\mu_N = 0.1$; 130 \rightarrow 230 RPM)	176
5.39	Lag moment's peak amplitude variation with transition time ($\mu_N = 0.1$; 130 \rightarrow 230 RPM)	177
5.40	Time history of rotor torque ($\mu_N = 0.1$; 130 \rightarrow 230 RPM)	177
5.41	Effect of structural damping on lag moment ($\mu_N = 0.3$; 230 \rightarrow 180 RPM) . .	179

5.42	Structural damping impact on lag moment peak amplitude ($\mu_N = 0.3$; 230 \rightarrow 180 RPM)	180
5.43	Effect of structural damping on rotor torque ($\mu_N = 0.3$; 230 \rightarrow 180 RPM) . .	180
5.44	Effect of structural damping on lag moment ($\mu_N = 0.3$; 180 \rightarrow 230 RPM) . .	181
5.45	Structural damping impact on lag moment peak amplitude ($\mu_N = 0.3$; 180 \rightarrow 230 RPM)	181
5.46	Effect of structural damping on rotor torque ($\mu_N = 0.3$; 180 \rightarrow 230 RPM) . .	182
5.47	Rotor torque peak value ($\mu_N = 0.3$; 180 \rightarrow 230 RPM)	182
5.48	Effect of structural damping on lag moment ($\mu_N = 0.2$; 230 \rightarrow 150 RPM) . .	183
5.49	Structural damping impact on lag moment peak amplitude ($\mu_N = 0.2$; 230 \rightarrow 150 RPM)	183
5.50	Effect of structural damping on rotor torque ($\mu_N = 0.2$; 230 \rightarrow 150 RPM) . .	184
5.51	Effect of structural damping on lag moment ($\mu_N = 0.2$; 150 \rightarrow 230 RPM) . .	184
5.52	Structural damping impact on lag moment peak amplitude ($\mu_N = 0.2$; 150 \rightarrow 230 RPM)	185
5.53	Effect of structural damping on rotor torque ($\mu_N = 0.2$; 230 \rightarrow 150 RPM) . .	185
5.54	Effect of structural damping on lag moment ($\mu_N = 0.1$; 230 \rightarrow 130 RPM) . .	186
5.55	Structural damping impact on first resonance amplitude ($\mu_N = 0.1$; 230 \rightarrow 130 RPM)	186
5.56	Structural damping impact on second resonance amplitude ($\mu_N = 0.1$; 230 \rightarrow 130 RPM)	187
5.57	Effect of structural damping on rotor torque ($\mu_N = 0.2$; 230 \rightarrow 150 RPM) . .	187
5.58	Effect of structural damping on lag moment ($\mu_N = 0.1$; 130 \rightarrow 230 RPM) . .	188
5.59	Structural damping impact on first resonance amplitude ($\mu_N = 0.1$; 130 \rightarrow 230 RPM)	189
5.60	Structural damping impact on second resonance amplitude ($\mu_N = 0.1$; 130 \rightarrow 230 RPM)	189

5.61	Effect of structural damping on rotor torque ($\mu_N = 0.1$; 130 \rightarrow 230 RPM)	190
5.62	Rotor torque peak value ($\mu_N = 0.1$; 130 \rightarrow 230 RPM)	190
5.63	Fan plot: Baseline Vs Case 1 ($\mu_N = 0.3$)	192
5.64	Fan plot: Baseline Vs Case 2 ($\mu_N = 0.3$)	193
5.65	Effect of lag stiffness on lag moment ($\mu_N = 0.3$; 230 \rightarrow 180 RPM)	194
5.66	Resonance amplitude variation with lag crossing ($\mu_N = 0.3$; 230 \rightarrow 180 RPM)	194
5.67	FFT on lag moment resonance amplitude ($\mu_N = 0.3$; 230 \rightarrow 180 RPM)	195
5.68	Effect of lag stiffness on rotor torque ($\mu_N = 0.3$; 230 \rightarrow 180 RPM)	195
5.69	Rotor torque peak value during resonance ($\mu_N = 0.3$; 230 \rightarrow 180 RPM)	196
5.70	FFT on rotor torque resonance amplitude ($\mu_N = 0.3$; 230 \rightarrow 180 RPM)	196
5.71	Effect of lag stiffness on lag moment ($\mu_N = 0.3$; 180 \rightarrow 230 RPM)	197
5.72	Resonance amplitude variation with lag crossing ($\mu_N = 0.3$; 180 \rightarrow 230 RPM)	198
5.73	Effect of lag stiffness on rotor torque ($\mu_N = 0.3$; 180 \rightarrow 230 RPM)	198
5.74	Rotor torque peak value during resonance ($\mu_N = 0.3$; 180 \rightarrow 230 RPM)	199
5.75	Fan plot: Baseline vs. Case 1 ($\mu_N = 0.2$)	200
5.76	Fan plot: Baseline vs. Case 2 ($\mu_N = 0.2$)	200
5.77	Effect of lag stiffness on lag moment ($\mu_N = 0.2$; 230 \rightarrow 150 RPM)	201
5.78	Resonance amplitude during first crossing ($\mu_N = 0.2$; 230 \rightarrow 150 RPM)	201
5.79	Resonance amplitude during second crossing ($\mu_N = 0.2$; 230 \rightarrow 150 RPM)	202
5.80	Effect of lag stiffness on rotor torque ($\mu_N = 0.2$; 230 \rightarrow 150 RPM)	203
5.81	Effect of lag stiffness on lag moment ($\mu_N = 0.2$; 150 \rightarrow 230 RPM)	203
5.82	Effect of lag stiffness on rotor torque ($\mu_N = 0.2$; 150 \rightarrow 230 RPM)	204

5.83	Fan plot: Baseline vs. Case 1 ($\mu_N = 0.1$)	204
5.84	Fan plot: Baseline vs. Case 2 ($\mu_N = 0.1$)	205
5.85	Effect of lag stiffness on lag moment ($\mu_N = 0.1$; 230 \rightarrow 130 RPM)	206
5.86	Resonance amplitude during first crossing ($\mu_N = 0.1$; 230 \rightarrow 130 RPM) . . .	206
5.87	Resonance amplitude during second crossing ($\mu_N = 0.1$; 230 \rightarrow 130 RPM) . .	207
5.88	Effect of lag stiffness on rotor torque ($\mu_N = 0.1$; 230 \rightarrow 130 RPM)	207
5.89	Effect of lag stiffness on lag moment ($\mu_N = 0.1$; 130 \rightarrow 230 RPM)	208
5.90	Resonance amplitude during first crossing ($\mu_N = 0.1$; 130 \rightarrow 230 RPM) . . .	208
5.91	Resonance amplitude during second crossing ($\mu_N = 0.1$; 130 \rightarrow 230 RPM) . .	209
5.92	Effect of lag stiffness on rotor torque ($\mu_N = 0.1$; 130 \rightarrow 230 RPM)	209
5.93	Rotor torque peak value during resonance ($\mu_N = 0.1$; 130 \rightarrow 230 RPM) . . .	210
5.94	Effect of ζ and t_T on lag moment ($\mu_N = 0.3$; 230 \rightarrow 180 RPM)	212
5.95	Resonance amplitude variation with ζ and t_T ($\mu_N = 0.3$; 230 \rightarrow 180 RPM) . .	212
5.96	Effect of ζ and t_T on rotor torque ($\mu_N = 0.3$; 230 \rightarrow 180 RPM)	213
5.97	Effect of ζ and t_T on lag moment ($\mu_N = 0.3$; 180 \rightarrow 230 RPM)	213
5.98	Resonance amplitude variation with ζ and t_T ($\mu_N = 0.3$; 180 \rightarrow 230 RPM) . .	214
5.99	Effect of ζ and t_T on rotor torque ($\mu_N = 0.3$; 180 \rightarrow 230 RPM)	214
5.100	Rotor torque peak value during resonance ($\mu_N = 0.3$; 180 \rightarrow 230 RPM) . . .	215
5.101	Effect of ζ and t_T on lag moment ($\mu_N = 0.2$; 230 \rightarrow 150 RPM)	215
5.102	Resonance amplitude variation with ζ and t_T ($\mu_N = 0.2$; 230 \rightarrow 150 RPM) . .	216
5.103	Effect of ζ and t_T on rotor torque ($\mu_N = 0.2$; 230 \rightarrow 150 RPM)	216
5.104	Effect of ζ and t_T on lag moment ($\mu_N = 0.2$; 150 \rightarrow 230 RPM)	217
5.105	Resonance amplitude variation with ζ and t_T ($\mu_N = 0.2$; 150 \rightarrow 230 RPM) . .	217

5.106	Effect of ζ and t_T on rotor torque ($\mu_N = 0.2$; $150 \rightarrow 230$ RPM)	218
5.107	Rotor torque peak value during resonance ($\mu_N = 0.2$; $150 \rightarrow 230$ RPM)	218
5.108	Effect of ζ and t_T on lag moment ($\mu_N = 0.1$; $230 \rightarrow 130$ RPM)	219
5.109	Resonance amplitude variation with ζ and t_T ($\mu_N = 0.1$; $230 \rightarrow 130$ RPM)	219
5.110	Effect of ζ and t_T on rotor torque ($\mu_N = 0.1$; $230 \rightarrow 130$ RPM)	220
5.111	Effect of ζ and t_T on lag moment ($\mu_N = 0.1$; $130 \rightarrow 230$ RPM)	220
5.112	Resonance amplitude variation with ζ and t_T ($\mu_N = 0.1$; $130 \rightarrow 230$ RPM)	221
5.113	Effect of ζ and t_T on rotor torque ($\mu_N = 0.1$; $130 \rightarrow 230$ RPM)	221
5.114	Rotor torque peak value during resonance ($\mu_N = 0.1$; $130 \rightarrow 230$ RPM)	222
6.1	Schematic of a hingeless blade with sliding mass.	224
6.2	Blade model in DYMORE with sliding point mass.	225
6.3	Fan plot: Baseline vs ARS Baseline ($\mu_N = 0.3$)	226
6.4	Location of sliding mass with time ($\mu_N = 0.3$; $230 \rightarrow 180$ RPM)	227
6.5	Fan plot: Baseline vs. ARS with mass at tip ($\mu_N = 0.3$)	227
6.6	Lag moment: Baseline vs. ARS ($\mu_N = 0.3$; $230 \rightarrow 180$ RPM)	228
6.7	Peak amplitude: Baseline vs. ARS ($\mu_N = 0.3$; $230 \rightarrow 180$ RPM)	228
6.8	Rotor torque: Baseline vs. ARS ($\mu_N = 0.3$; $230 \rightarrow 180$ RPM)	229
6.9	Location of sliding mass with time ($\mu_N = 0.3$; $180 \rightarrow 230$ RPM)	230
6.10	Fan plot: Baseline vs. ARS with mass at tip ($\mu_N = 0.3$)	230
6.11	Lag moment: Baseline vs. ARS ($\mu_N = 0.3$; $230 \rightarrow 180$ RPM)	231
6.12	Peak amplitude: Baseline vs. ARS ($\mu_N = 0.3$; $230 \rightarrow 180$ RPM)	231
6.13	Rotor torque: Baseline vs. ARS ($\mu_N = 0.3$; $230 \rightarrow 180$ RPM)	232

6.14	Fan plot: Baseline vs. ARS with mass at tip ($\mu_N = 0.2$)	233
6.15	Location of sliding mass with time ($\mu_N = 0.2$; $230 \rightarrow 150$ RPM)	233
6.16	Lag moment through resonance: Baseline vs. ARS ($\mu_N = 0.2$; $230 \rightarrow 150$ RPM)	234
6.17	Rotor torque through resonance: Baseline vs. ARS ($\mu_N = 0.2$; $230 \rightarrow 150$ RPM)	235
6.18	Fan plot: Baseline vs. ARS with 3% lag damping ($\mu_N = 0.2$)	235
6.19	Lag moment through resonance: Baseline vs. ARS with 3% lag damping ($\mu_N = 0.2$; $230 \rightarrow 150$ RPM)	236
6.20	Peak amplitude through resonance: Baseline vs. ARS with 3% lag damping ($\mu_N = 0.2$; $230 \rightarrow 150$ RPM)	236
6.21	Rotor torque through resonance: Baseline vs. ARS with 3% lag damping ($\mu_N = 0.2$; $230 \rightarrow 150$ RPM)	237
6.22	Fan plot: Baseline vs. ARS with mass at root ($\mu_N = 0.2$, $\zeta = 3\%$)	238
6.23	Location of sliding mass with time ($\mu_N = 0.2$; $150 \rightarrow 230$ RPM)	238
6.24	Lag moment: Baseline vs. ARS ($\mu_N = 0.2$; $230 \rightarrow 150$ RPM; $\zeta = 3\%$)	239
6.25	Peak amplitude: Baseline vs. ARS ($\mu_N = 0.2$; $230 \rightarrow 150$ RPM; $\zeta = 3\%$) . . .	239
6.26	Rotor torque: Baseline vs. ARS ($\mu_N = 0.2$; $150 \rightarrow 230$ RPM; $\zeta = 3\%$)	240
6.27	Fan plot: Baseline vs. ARS with mass back to baseline ($\mu_N = 0.2$, $\zeta = 3\%$)	241
6.28	Location of sliding mass with time ($\mu_N = 0.2$; $230 \rightarrow 150$ RPM)	241
6.29	Rotor speed change from 230 to 150 RPM (16 s)	242
6.30	Lag moment: Baseline vs. ARS ($\mu_N = 0.2$; $230 \rightarrow 150$ RPM; $\zeta = 3\%$)	242
6.31	Peak amplitude: Baseline vs. ARS ($\mu_N = 0.2$; $230 \rightarrow 150$ RPM; $\zeta = 3\%$) . . .	243
6.32	Rotor torque: Baseline vs. ARS ($\mu_N = 0.2$; $230 \rightarrow 150$ RPM; $\zeta = 3\%$)	243
6.33	Fan plot: Baseline vs. ARS with mass at tip ($\mu_N = 0.1$, $\zeta = 3\%$)	244

6.34	Location of sliding mass with time ($\mu_N = 0.1$; $230 \rightarrow 130$ RPM)	245
6.35	Rotor speed change from 230 to 130 RPM (20 s)	245
6.36	Lag moment: Baseline vs. ARS ($\mu_N = 0.1$; $230 \rightarrow 130$ RPM; $\zeta = 3\%$)	246
6.37	Second resonance amplitude: Baseline vs. ARS ($\mu_N = 0.1$; $230 \rightarrow 130$ RPM; $\zeta = 3\%$)	246
6.38	Rotor torque: Baseline vs. ARS ($\mu_N = 0.1$; $230 \rightarrow 130$ RPM; $\zeta = 3\%$)	247
6.39	Fan plot: ARS with mass at root vs. mass at tip ($\mu_N = 0.1$, $\zeta = 3\%$)	248
6.40	Location of sliding mass with time ($\mu_N = 0.1$; $130 \rightarrow 230$ RPM)	248
6.41	Rotor speed change from 130 to 230 RPM (20 s)	249
6.42	Lag moment: Baseline vs. ARS ($\mu_N = 0.1$; $130 \rightarrow 230$ RPM; $\zeta = 3\%$)	249
6.43	First resonance amplitude: Baseline vs. ARS ($\mu_N = 0.1$; $130 \rightarrow 230$ RPM; $\zeta = 3\%$)	250
6.44	Second resonance amplitude: Baseline vs. ARS ($\mu_N = 0.1$; $130 \rightarrow 230$ RPM; $\zeta = 3\%$)	250
6.45	Rotor torque: Baseline vs. ARS ($\mu_N = 0.1$; $130 \rightarrow 230$ RPM; $\zeta = 3\%$)	251
6.46	Fan plot: ARS resonance points movement ($\mu_N = 0.1$, $230 \rightarrow 130$ RPM, $\zeta = 3\%$)	252
6.47	Location of sliding mass with time ($\mu_N = 0.1$; $230 \rightarrow 130$ RPM)	252
6.48	Lag moment: Baseline vs. ARS ($\mu_N = 0.1$; $230 \rightarrow 130$ RPM; $\zeta = 3\%$)	253
6.49	Rotor torque: Baseline vs. ARS ($\mu_N = 0.1$; $230 \rightarrow 130$ RPM; $\zeta = 3\%$)	253

SUMMARY

The efficiency and operating envelope of rotorcraft are constrained by the speed of the rotor. Most helicopters operate at a constant rotor speed. Varying the speed of the rotor based on the operating condition could significantly improve the rotor's performance. In this study, a hingeless rotor model with elastic blades is built in Dymore to study various aspects of Variable Speed Rotor (VSR) technology. The rotor blades are modeled as one-dimensional beams using state of the art beam theory known as the geometrically exact beam theory (GEBT). An unsteady aerodynamics model with dynamic stall and finite-state dynamic inflow is used to obtain the aerodynamic loads acting on the rotor. The power savings that can be achieved at various advance ratios by varying the speed of the rotor is evaluated. Maximum power savings of 41.47% was achieved at $\mu_N = 0.2$. However, changing the rotor speed leads to vibration issues when a rotor passes through a resonance point. A methodology to identify the important resonance points for a given flight condition and rotor speed transition is also provided. The forces acting on the rotor blade during resonance crossings at different advance ratios is evaluated. It is found that the amplitude increase during resonance crossing is strongly dependent on the amplitude of the cyclic pitch angles during resonance.

Load reduction studies were carried out by varying the transition time, structural damping, and lag stiffness of the blade. The longer the rotor took to traverse a resonance region, the greater were the resonance loads. However, there were torque limitations on how quickly a rotor can pass through resonance. Increasing the structural damping was a very effective way of reducing the resonance loads. Increasing the lag stiffness of the rotor blade deteriorated the torque response due to 4/rev crossings. Combination studies were performed by combining the ideal transition times with 7% lag damping. A moving mass system called as the Anti-Resonance System (ARS) was conceptualized and modeled in Dymore. The ARS system was able to effectively move the resonance points out of the rotor operating range.

CHAPTER 1

INTRODUCTION

1.1 Motivation

Rotorcraft's efficiency and operating envelope is limited by constant speed of the main rotor. Most of the engine power is utilized in spinning the main rotor. Optimizing the rotor speed for different flight conditions could significantly reduce the power consumption. Changing the rotor speed during flight could lead to aerodynamic, control and predominantly vibration problems. Care should be taken while varying the rotor speed as it should not affect the aerodynamic performance profoundly otherwise it could lead to loss of altitude and speed. Stability of the helicopter should also be maintained and vibratory loads should be minimized during rotor speed change to increase the fatigue life of the blade and other helicopter components.

Historically, Variable Speed Rotor (VSR) technology has been implemented and tested in a few aircraft to achieve different performance goals. V-22 Osprey has a tilt rotor system which allows the aircraft to switch between helicopter mode and airplane mode, as shown in Figures 1.1 ¹ and 1.2 ², respectively. The rotor speed during airplane mode, 333 RPM, is about 19% lesser than in helicopter mode, 413 RPM.³ In the airplane mode the rotors are slowed down as lift is provided by wings and the rotors are only needed to overcome the drag force of the aircraft.

Sikorsky's XH-59, shown in Figure 1.3 ⁴, utilized the VSR technology to achieve high forward speeds. XH-59, which made its first flight in 1973, had two coaxial counter-rotating main rotors. This main rotor configuration primarily utilized the advancing sides to

¹https://en.wikipedia.org/wiki/Bell_Boeing_V-22_Osprey

²<https://www.youtube.com/watch?v=hUNJTaybCQQ>

³<https://www.globalsecurity.org/military/systems/aircraft/ostr.htm>

⁴https://en.wikipedia.org/wiki/Sikorsky_S-69



Figure 1.1: V-22 Osprey in helicopter mode. Figure 1.2: V-22 Osprey in airplane mode.

provide the necessary lift during high speeds, eliminating the limitations due to retreating blade stall that are common in conventional rotors. Hence, this was called the Advancing Blade Concept (ABC) rotor system. The aircraft had auxiliary turbojet engines to provide the required forward thrust so that the rotors can be used only for generating lift. The rotor could be slowed to a minimum of 78% of its nominal speed, 345 RPM, to prevent the air velocities from reaching transonic speeds on any part of the rotor. This combination of turbojets and slowed rotor allowed the aircraft to achieve high forward speeds. According to Ref. [1], slowing the rotor down further was not possible due to high loads on the rotor head.



Figure 1.3: XH-59 demonstrator aircraft built for the U.S army.

Another experimental VSR helicopter, which was based on the XH-59 design, was the Sikorsky X2 demonstrator [2]. X2, Figure 1.4 ⁵, used the same ABC rotor system concept from XH-59 while the turbojets were replaced by a single pusher propeller to provide thrust. Rotor speed was varied from 446 RPM to 360 RPM at speeds in excess of 200 knots. X2 was able to achieve a record speed of 250 knots (290 mph or 460 km/h) in level flight. The slowed rotor ensured that the rotor tip speed was maintained below a Mach number of 0.9.



Figure 1.4: Sikorsky X2 demonstrator.

Lockheed's XH-51A, which took its first flight almost seven years before XH-59, also varied the main rotor speed in modest quantity. XH-51A was also a compound helicopter with a single main rotor, a tail rotor, wings for additional lift and a jet engine for additional thrust. XH-51 is shown in Figure 1.5 ⁶. The rotor speed variation was limited between 90% and 100% of nominal rotor RPM [3]. With the slowed rotor, the helicopter was able to achieve a level flight speed of 223 knots (257 mph or 413 km/h).

Eurocopter, now known as Airbus Helicopters, also built a compound helicopter with variable speed rotor. This experimental helicopter was called X³. X³ has no tail rotor, the main rotor torque is countered by two tractor propellers with different pitch settings. The propellers are fitted at the end of small wings placed between the main rotor and passenger

⁵<http://www.blueskyrotor.com/performance/datasheet/Sikorsky/X2-X2>

⁶<https://alchetron.com/Lockheed-XH-51>



Figure 1.5: Lockheed's XH-51A compound helicopter.

cabin as shown in Figure 1.6. The rotor speed was reduced by 15% to achieve high speeds. This compound helicopter achieved a speed of 255 knots (293 mph or 472 km/h) in level flight, breaking the previous record set by X2.



Figure 1.6: Eurocopter X³ in flight.

Apart from achieving high speeds, VSR technology has also been used to reduce helicopter noise. Bell offers a 'quiet cruise' option for its modified 407 models. During this mode, the main rotor is slowed down to 92% ⁷ rotor rpm using a control system during cruise to keep the noise level down. This was done to mitigate the noise level while flying

⁷<https://www.ainonline.com/aviation-news/business-aviation/2012-10-30/bell-delivers-two-407gs-tourist-operations>

over urban areas, national parks and other noise restricted zones. Barlow et al. [4] describe an experimental OH-6A helicopter, predecessor of MD 500, which was shown to have reduced noise levels in hover and forward flight when the main rotor speed was reduced to 67%. Airbus H135, H145, H175 and H160 helicopters also have a control system that lowers the speed of the main rotor as they fly close to the ground.

Besides the above stated speed and noise advantages, significant power savings can also be achieved using VSR as mentioned at the beginning of this chapter. Very few technology demonstrators have been built as proof of concept. Of which, A-160T was the most significant and popular one, Figure 1.7⁸. A-160T was an autonomous unmanned aerial vehicle helicopter. A-160T uses Optimum Speed Rotor concept [5] where the rotor angular speed is varied until an optimum blade loading is achieved for a given flight condition. This optimum blade loading scenario minimizes the power required to operate the rotor and hence, improving the performance efficiency. The rotor speed could be varied from 140 RPM to 350 RPM using a two-speed transmission system. A-160T was able to hover out of ground effect at an altitude of 20,000 ft (3.78 miles or 6.09 km) and demonstrated long endurance flights up to 18.7 hours.



Figure 1.7: A-160T UAV helicopter with optimum speed rotor.

Carter PAV is a compound helicopter which has demonstrated the power advantages of

⁸https://en.wikipedia.org/wiki/Boeing_A160_Hummingbird

a slowed rotor [6, 7]. Carter PAV helicopter, shown in Figure 1.8, takes off with a powered rotor operating at 370 RPM until it attains enough forward speed. Once the helicopter reaches enough forward speed, the rotor is declutched from the engine, tilts back and operates as an autogyro at 100 RPM. Most of the lift is then produced by the wings. The company claims to have achieved considerable power savings by slowing the rotor. Carter PAV is set to be modified as an electric vehicle for urban air mobility.



Figure 1.8: Carter PAV.

Hence, variable speed rotors can be used to attain considerable noise, speed and power improvements in helicopters. However, varying the speed of the rotor comes with its own set of problems. Rotors are usually designed to operate far away from their structural resonance frequencies to ensure safe operation and long fatigue life. However, changing the speed of the rotor means that the rotor might be needed to operate through these resonance conditions. Significant vibration and stability problems could occur when a rotor natural frequency coincides with the rotating angular frequency (or an integer multiple of angular frequency) of the rotor leading to a resonance condition, which is usually associated with an increase in amplitude of deflections and forces. Understanding the characteristics of such resonances while varying the rotor speed is vital in mitigating their effects. Therefore, this study involves building a comprehensive rotor blade model that can capture the physics of a variable speed rotor accurately, carefully analyze the problems associated with varying the rotor speed and provide solutions to the identified problems.

1.2 Literature Survey

1.2.1 Variable Speed Rotor (VSR)

Literature survey showed that only a few studies have been done to show the advantages of a variable speed rotor. Patent by Karem [5] explains the concept of optimum speed rotor and power advantages it provides. This patent explains the construction of rotor blade that is suitable for wide rotor speed change without running into vibration issues. The patent claims that having a very stiff lightweight rotor removes any structural issues that could arise from operating at or close to rotor excitation frequencies. CAMRAD II was used to analyze the power benefits that could be obtained for two weight cases, 1400 lbs and 2600 lbs. A maximum of 70% and 45% power savings were evaluated at low speeds for low and heavy weight cases, respectively. However, the results of vibration analysis were not shared in this patent. Rotor speed was varied from 40% to 100% of maximum rotor speed in this study.

Prouty [8] discusses the benefits a VSR could provide with regards to hovering out of ground effect (HOG), maximizing endurance, maximizing range and attaining maximum speed using full engine power. A quantitative analysis was carried out for the example helicopter in his textbook [9] with VR-7 airfoil. Maximum Figure of Merit value, which is a measure of rotor efficiency in hover, was found to be located at different rotor RPM values for different altitudes. Specific endurance, hours per pound of fuel, was computed using the fuel flow rate for the engine at different forward speeds, rotor RPM and altitudes. Maximum specific range, nautical miles per pound of fuel, was computed and these rotor RPM values were found to be considerably higher than the maximum specific endurance rotor RPM values. Significant improvements in the maximum forward speed with the available power was also demonstrated by changing the rotor speed, especially at high altitudes. The author also discusses why a rotor dynamics engineer would be frustrated with the idea of changing the rotor speed. Rotors are typically tuned to operate at a safe distance from their

resonance frequencies. Varying the rotor speed would force them to operate through these resonance frequencies, which could lead to an increase of vibrations in the rotor and other helicopter components.

Steiner et al. [10, 11] have investigated the main rotor power reduction that could be obtained for a rotor similar to UH-60 Black Hawk helicopter from $\pm 15\%$ variation in rotor RPM. The study models a four-bladed fully articulated rotor system with rigid rotor blades having only flap degree of freedom. Rotor speed change was assumed to be achieved by changing the engine speed and not through transmission mechanism. Hence, the rotor speed variation was assumed to be only within $\pm 15\%$ from the baseline of 260 RPM. It is mentioned that large RPM variations could be achieved through a variable transmission mechanism.

Aerodynamic loads were evaluated from blade-element theory including Prandtl tip-loss correction. Three different gross weights, 16,000 lbs, 18,300 lbs and 22,000 lbs, and four different altitude conditions, sea level, 4000 ft, 8000 ft, and 12,000 ft, were considered. For a given gross weight and altitude, the vehicle was trimmed as a function of airspeed, altitude and rotor RPM using iterative procedure and power required was estimated. At sea level, changing the rotor speed to 220 RPM from base line of 260 RPM led to a maximum main rotor power reduction of 17% for 18,300 lbs gross weight. This maximum power reduction was achieved for a forward speed between 100 – 120 knots. Power reduction decreased with increase or decrease of forward speed and with increase in altitude. Only 5.5% maximum power reduction was achieved at an altitude of 12,000 ft. For a lower gross weight of 16,000 lbs, 18% reduction at sea level and 8.5% reduction at 12,000 ft was achieved. A higher gross weight of 22,000 lbs only had 8% reduction at sea level and 1% at 8000 ft. Low gross weight case was shown to have higher power reduction potential than high gross weight case. The power reduction also reduced with increase in altitude. High gross weight of 22,000 lbs did not have any power reduction at 12,000 ft, but an increase of rotor RPM from the baseline allowed flight at forward speeds which were not possible

with the baseline RPM. Hence, [10] also demonstrated the flight expansion capability of VSR.

Mistry and Gandhi [12] studied the effect of performance improvement that can be obtained from VSR and variable radius rotor combination. Earlier research on variable radius rotor technology is discussed in [13]. Linden et al.[13] examined a telescoping rotor with jack-screw mechanism, an in-plane folding rotor and a thin rolling rotor blade designs to achieve variable radius. The authors of [12] assume that the rotor radius could be varied by an actuated jack screw mechanism or through spring extension based on centrifugal force [14, 15]. A section of the rotor blade is stowed inside a fixed section which has a longer chord than the stowed section. The stowed section could slide out using one of the mechanisms described by the authors. The rotor radius and RPM are varied independently. The rotor RPM is varied $\pm 11\%$ from baseline RPM, and rotor radius is changed $+17\%$ to -16% from the baseline. The rotor used in this study is similar to UH-60A helicopter rotor model used in [10]. Power definitions used here are taken from [16]. Total power required is a combination of induced power, profile power and parasite power. Reducing the rotor RPM could increase the induced power, but it also reduces the profile power and hence, providing an overall decrease in total power. Parasite power plays a minimal role according to the authors.

The power reductions obtained through VSR alone are similar to the results obtained in [10] discussed previously. Varying the radius alone led to a maximum of about 8% power reduction for a gross weight of 16,000 lbs between 100 knots and 140 knots. This was achieved by reducing the rotor radius 10.5% below baseline at sea level. The power reduction for the same gross weight dropped to a maximum of 3% at 12,000 ft and the rotor radius was increased by 6% to achieve this. The power reductions were dropped further for a gross weight of 18,300 lbs. However, for a high gross weight of 24,000 lbs a maximum of 20% power reduction was obtained with 12% increase in rotor radius at 12,000 ft. Higher power reductions were achieved with a combination of variable speed

and variable radius rotor. A maximum power reduction of about 14%, 16% and 30% were achieved for 16,000 lbs, 18,300 lbs and 24,000 lbs, respectively, at various altitudes. This study showed that combining VSR with other technologies could prove to be beneficial in improving helicopter's performance.

DiOttavio and Friedmann [17] performed studies specific to A-160T to quantify the benefits of an optimal speed rotor. The rotor speed was varied from 100%, 395 RPM, to 56% in this study. Two vehicle weights, 5000 lbs and 3000 lbs were considered. Minimum RPM reduction of 56% was achieved for 3000 lbs vehicle at hover, which provided 30% reduction in power required. While a 5000 lbs vehicle only allowed for 70% reduction in RPM and 13% reduction in power at hover. Hence, lower weights allowed for greater power reduction, which was also seen in previous studies. Increasing the forward speed and altitude also limited the RPM change to ensure that the rotor doesn't stall completely. Improvement in specific range and endurance due to VSR was also shown in this paper. The specific range and endurance were increased by 20% and 32%, respectively, for the low weight vehicle. Optimum rotor speed also increased the HOGE ceiling. Both vehicles saw an increase in their maximum HOGE altitudes; 8% for 3000 lbs and 15% for 5000 lbs. However, this study doesn't include any comprehensive blade model or trim procedures.

As mentioned earlier, VSR system comes with its own set of challenges. Vibration problems being a major concern. One of the first comprehensive study on VSR vibration was carried out by Han and Smith [18]. In this paper, the authors analyzed the resonance crossing of a flexible rotor blade during angular speed change. The study considered a four-bladed hingeless rotor with uniform cross-sectional properties. Moderate deflection beam theory [19] with flap, lead-lag and torsional deformation was used for structural modeling of the rotor blade. Quasi-steady blade element theory with three-state dynamic inflow was used for aerodynamics modeling. In order to study the resonance crossing, the rotor speed was changed from 180 RPM to 240 RPM. During this speed change, the first lag frequency of the rotor coincides with the second multiple of rotor angular frequency, 2/rev resonance.

This led to a sharp increase in lead-lag bending moment amplitude at the rotor root. The rotor torque showed an increase in peak amplitude during resonance crossing. The study showed an increase of lead-lag moment with increase in flap deflection due to Coriolis effect. The time taken to cross this resonance region had a significant effect on blade forces and moments.

The authors showed that a dissimilar rotor blade, with mass distribution 5% less than the regular blade in a small segment of length, could drastically increase the peak torque of the rotor during resonance crossing. In an effort to reduce the loads during resonance crossing, the structural damping of the rotor blade was increased from 1% to 5%. The lead-lag peak to peak moment was decreased by 64.9% due to this increase. Even though this is a comprehensive study, there are several factors that the authors have not considered. The resonance crossing point and direction were chosen arbitrarily. The resonance loads study was performed only at an advance ratio of 0.3. The direction of resonance crossing, i.e., 180 to 240 RPM or 240 to 180 RPM, could have an effect on resonance loads according to Nayfeh and Mook [20] if non-linear resonances are involved, which was not investigated here.

Additional efforts were made by Han et al. [21] to reduce the loads during resonance crossing. A fluidlastic damper was used here to reduce the lead-lag moment of a stiff in-plane rotor. The damper was placed close to the tip of the rotor blade as stiff in-plane blades have low deformations at the root. The parameters of the fluidlastic damper, such as the tuning mass, tuning frequency, primary mass, tuning port area ratio, and loss factor, were chosen to reduce the lead-lag loads during the 2/rev resonance crossing. The damper was embedded chord-wise at the blade tip. Based on the assumptions made by the author, a maximum lag damping of 8% was obtained using this damper. Lead-lag moment loads were reduced by 65% by tuning the damper to 2/rev frequency. Han and Smith [22] also describe an embedded chord-wise damper to reduce lead-lag loads. However, the damper used in [22] was a simple mass-spring-dashpot system and no variable rotor speed was

taken into consideration. Most of the initial work by Han et al. on variable speed rotors is summarized in a technical report by DeSmidt et al. [23]. The report also talks about the design of a transmission system for variable speed rotors.

Han and Barakos [24] studied a variable speed tail rotor in association with a variable speed main rotor. Tail rotors were noted to consume 10 – 20% of total power historically. Previous studies have shown that varying the main rotor speed changes the rotor torque. An increase in rotor torque needs an increase in tail rotor thrust to trim the helicopter. If the tail rotor speed follows the main rotor speed, then the power savings obtained were found to be limited in this study. Lower tail rotor speeds were also found not to provide enough thrust needed to trim, especially in hover. Changing the tail rotor speed independently of the main rotor proved to be more effective. A maximum power saving of 30% over the baseline tail rotor power was evaluated in cruise condition.

Wind-tunnel testing of a variable speed rotor was performed by Berry and Chopra [25] to quantify the performance improvements and vibratory loads of a four-bladed rotor with 6 ft diameter. A maximum advance ratio of 0.64 was achieved by reducing the rotor speed by 35%. The vertical and longitudinal fixed-frame hub loads were measured. The 4/rev loads were found to be dominant and were seen to reduce with decrease in rotor speed. Bowen-Davies and Chopra [26] performed power, trim and load analysis of a UH-60A helicopter rotor system using UMARC, a rotorcraft comprehensive analysis code. The power savings obtained were similar to previous studies. The vertical hub loads were observed to decrease with reduction in rotor speed while the in-plane loads increased. The study claims that this is due to increase in stall region due to decrease in rotor speed.

Datta et al. [27] conducted a full-scale testing of a UH-60A rotor system. The tests were carried out in a 40 × 50 ft wind tunnel at 100%, 65% and 40% rotor speed. The tests revealed that the unsteady loads or dynamics loads acting on the rotor blades are significantly larger on the slowed rotor than on nominal speed rotor at high forward speeds. However, these load increases were not revealed by only looking at the hub loads. Nonetheless, the 4/rev

hub loads reduced by at least 50% for lower rotor speeds, which is consistent with previous studies.

In order to improve performance of VSR and reduce rotor loads, Han et al. [28] combine VSR with active twist blades. The twist of the blades was changed based on flight condition. This study was performed for a four blade articulated rotor similar to UH-60A and a rigid rotor blade model was used. The rotor speed was varied only 10% from baseline and blade twist was varied from 0 deg to -16 deg. Varying the rotor speed was shown to have higher power saving capabilities than varying the blade twist. However, combining these two technologies provided a maximum power saving of 20.9% at cruise speed as opposed to 17.8% using only variable speed rotor. Flap and lag loads at the blade root followed the subsequent trend. Reducing the rotor speed decreased the 1/rev and 4/rev loads while increasing the 2/rev and 3/rev loads. On the other hand, increasing the blade twist reduced the 2/rev and 3/rev loads while increasing the 1/rev and 4/rev loads. However, all torsional loads increased with decrease of rotor speed. Reducing the blade twist reduced the torsional loads in general. Hence, with the combination of variable rotor speed and twisted blades the authors believe that load reduction could be achieved. Resonance transition studies were not performed here.

In [29], an isolator was used to reduce the loads transferred to the pitch link. The 4/rev pitch link load was seen to increase with increase in forward speed and reduction in rotor speed. The author in this study describes a variable frequency fluidlastic isolator that can change its tuning frequency based on the rotor speed. Using this isolator the 4/rev pitch loads were reduced by 87.6% when the rotor speed was reduced by 16.7%.

1.2.2 Rotor Blade Modeling

Rotor blades are slender structures that have one dimension larger than the other two. Hence, they are usually treated as one-dimensional beams for modeling purposes. Beam models vary in complexity based on the kinematic and kinetic assumptions, which deter-

mine the accuracy of results.

Euler-Bernoulli beam theory [30] is a classical beam theory that dates back to 1750. This theory assumes that the cross-section remains perpendicular to the reference line upon deformation. Even though shear deformations are not taken into consideration, the theory provides good approximations to many engineering problems. Hence, it is widely used for preliminary calculations. However, Euler-Bernoulli beam theory over estimates the natural frequencies and the kinematic assumptions do not hold good for non-slender beams.

Rayleigh beam theory [31] builds on the Euler-Bernoulli assumptions by taking into account the rotation of the cross-section. The natural frequency prediction was greatly improved by including the rotary inertia effects. Timoshenko [32, 33] included shear deformation in addition to the rotary inertia effect in his beam theory. A significant improvement in accuracy was observed for non-slender beams and also for natural frequencies of higher modes. Formulations for all the above mentioned beam theories, their solution techniques and difference in results are discussed in detail in [34]. A detailed history of developments in beam theory is given by Love in his famous book on elasticity [35].

However, helicopter rotor blades undergo significant deformation in flight due to the aerodynamic loads. Rotor blade aeroelasticity is a well known non-linear problem and appropriate blade models should be used to capture the non-linearities. Hence, more sophisticated models are required than the simplistic beam models described above. Significant amount of work has been done since the 1950s on developing beam models that are suitable for both isotropic and composite rotor blades. The response of a helicopter rotor blade could also coupled between axial, bending and torsional deformations. Therefore, blade models should also permit such behavior in their formulations. The rotorcraft blade models developed over half a century also vary in their ability to capture large deformations accurately. If we were to classify popular rotor blade beam theories based on their ability to capture deformation, one could classify them into pre-moderate-deflection beam theories, moderate deflection beam theories and large deflection beam theories. These theories will

be introduced at appropriate locations in this section. Any theory introduced before moderate deflection theories should be considered under pre-moderate-deflection beam theories. Both the moderate deflection theories and large deflection theories were used to analyze isotropic and composite beams in various studies across literature.

In a NACA report published in 1957, Houbolt and Brooks [36] formulated the equations of motion for an initially twisted rotating beams under arbitrary air loads. The beams were assumed to be made of isotropic materials, in line with the propellers and helicopter blade designs of that time. The significance of this study was the consideration of coupling effects due to centrifugal forces. The neutral axis, mass center and elastic axis of the beam were not assumed to be coincident. Galerkin and Rayleigh-Ritz solution techniques were used here to demonstrate the significance of centrifugal coupling in this report. Importance of inertial coupling on the flap-lag stability of stability characteristics of a hingeless rotor was shown by Ormiston and Hodges [37]. The authors modeled the rotor as rigid blades with springs at the root. Effects of pre-cone, pitch-lag coupling, elastic coupling and aerodynamics coupling on stability were studied in detail. Similar stability and coupling studies were performed in [38] and [39]. Huber [38] uses a rigid blade model, whereas Hodges and Ormiston [39] use a torsionally rigid cantilever beam model.

Inclusion of geometric non-linearities in addition to inertial non-linearities, i.e., inertial coupling, was also found to be crucial for rotor blade aeroelasticity. Friedmann and Tong [40] derived the general non-linear equations of motion for an elastic hingeless rotor blade. The rotor blade was elastic for flap-lag motion throughout the blade and elastic in torsion only at the root. Third order non-linear terms were neglected in the flap-lag equations while they were retained in the torsion equations. These formulations were used to estimate the divergence and flutter stability boundaries of the blade in hover. Non-linear beam formulations are often accompanied with order reduction schemes where higher order terms are assumed to be small and neglected. These ordering schemes led to varying degree of non-linearities in the final formulations.

As mentioned earlier, helicopter rotor blades undergo considerable deformation due to aerodynamic and inertial loads. Hodges and Dowell [19] developed the first moderate deflection beam theory that mathematically treats the finite sectional rotations and moderately large deflections of a beam appropriately. In these formulations, a clear distinction was made between undeformed and deformed beam configurations. This distinction was not made in the pre-moderate deflection beam theories. Transformation relation between the triads of the undeformed and deformed co-ordinates were derived and non-linear strain-displacement relations were computed. However, strains were assumed to be small and the cross-section was still assumed to remain plane and perpendicular to the neutral axis. Hence, shear strains were neglected. The final formulations were obtained from both Hamilton's principle and Newton's approach in [19]. This theory was also an extension of the work carried out by Hodges [41]. These formulations are valid for twisted, non-uniform, isotropic beams under going moderate deflections.

Rosen and Friedmann [42] also developed a similar moderate deflection beam theory with lesser non-linear terms in the strain formulations. A version with additional non-linear terms was given in [43]. Non-linear fully elastic beam theories applicable to non-uniform twisted wind turbine blades and helicopter rotor blades were also developed by Kaza and Kvaternik [44, 45] contemporarily. Moderate deflection beam theories utilize an ordering scheme that decides the level of non-linearity present in the theory. Several non-linear terms in the final beam formulation affect the stability of a rotor blade. Effect of these non-linear terms on aeroelastic stability boundaries are discussed in [46, 47, 48].

The above mentioned theories may be sufficient for blades made of isotropic material. However, most of the modern rotor blades are made of composite materials. Some of the assumptions that were made for slender isotropic beams may not still hold good for composite beams. Out of plane deformation of the cross section, known as warping, and shear deformations of the blade might no longer be negligible. Elastic couplings that arise due to anisotropic material properties should also be taken into account in the beam formulations.

Rehfield and Atilgan discusses the high level of extension-twist and bending-shear coupling in a single-celled composite beam analyzed theoretically in [49]. Response of the beam to static lift, torsion and extension loads were determined. Torsional warping and shear deformations were also found to be significant for the composite beams used in this study. This analysis was further extended to multi-cell composite beams in [50]. The composite beam theories developed by Rehfield were validated using finite element results and experimental data. A single-celled beam was modeled using shell elements of NASTRAN by Hodges et al. [51] and a composite circular tube was tested by Nixon [52]. A good correlation was found between the theoretical, finite element and experimental results.

Usually, the three-dimensional beam analysis is divided into a 2-D cross-sectional analysis and a 1-D beam analysis [53]. The 2-D cross-sectional analysis was supposed to handle the warping behavior of a beam, which was then implicitly included in 1-D beam analysis. Several such cross-sectional studies will also be discussed here.

Worndle [54] derived the displacement formulations of a prismatic composite beam made of monoclinic materials. In addition to the torsional warping, warping deformation of the cross-section under bending loads were also considered in his formulations. A two-dimensional finite element analysis was performed to solve for the warping functions, which were then used to compute the shear center and stiffness properties of the beam. Formulations developed in this study were applicable to any arbitrarily shaped cross-section as long as they are made of monoclinic materials. Kosmatka and Friedmann [55, 56] further extended the composite beam formulations to fully anisotropic materials of any arbitrary cross-section. The beam was still assumed to be prismatic and the warping functions were solved using a 2-D finite element method. However, only torsional warping was considered in these analyses. The warping function was integrated into the strain terms of a moderate deflection beam theory to estimate the natural frequencies of a curved, pre-twisted propeller with swept tips.

Giavatto et al. [57] used a finite element method to compute the cross-sectional prop-

erties of an anisotropic prismatic beam with inhomogeneous cross-section. Absence of homogeneity in the cross-section was thought to increase the inter-laminar stresses. The formulations from this study were used to develop HANBA2, which is a computer program for cross-sectional analysis. Influence of boundary effects on the sectional properties were also taken into consideration. Unlike previous studies, warping functions for all three force and moment directions were computed in this study. The results were validated with analytical and experimental data. In [58], Bauchau analyzed transversely isotropic beams assuming that the cross-section remains rigid in its own plane but free to deform out of the plane. Warping displacements were evaluated in terms of orthonormal eigenwarpings expansions. Only thin-walled box beams were analyzed in this paper. A later study [59] expanded the analysis to general orthotropic materials.

The composite beam theories discussed above divide the beam analysis cross-sectional analysis and one-dimensional beam analysis. The sectional properties computed from 2-D analysis is fed to the 1-D beam model. This approach decouples the cross-sectional properties evaluation from beam analysis. However, formulations developed by Stemple and Lee [60] incorporated the warping displacements into the beam formulations and the entire problem was solved for warping displacements along with the beam response. Warping nodes were included in the finite element model in addition to the translation and rotation nodes of the beam. Static and free vibration analysis of composite beams undergoing large deflection were studied using the formulations developed [61]. However, this approach was found to be computationally more expensive than the decoupled approach.

Aeroelastic analysis of a composite rotor blade was carried out by Hong and Chopra using moderate deflection beam theory [62]. Material stress-strain coupling eventually leads to stiffness coupling in a beam. Hence, coupling terms that arise due to such material properties were found to have a significance influence on the aeroelastic stability of a hingeless rotor blade in hover. Sensitivity of aeroelastic stability to fiber orientation and layup sequence was also investigated by the authors. Hong and Chopra [63] extended this analysis

to bearingless rotor blades. Shear deformations were neglected in both of these references as moderate deflection beam theory [19] developed for isotropic materials were used. Also, rotor blade cross-section was treated as a box beam. A later study by Smith and Chopra [64] extended these formulations to include shear strain in the plane of the cross-section and torsional warping. Aeroelastic stability of composite blades in forward flight was also studied by Smith and Chopra in [65] and by Panda and Chopra in [66]. Song and Librescu [67] developed a moderate deflection theory for anisotropic beams including shear and warping deformation. The developed formulations were used to estimate the natural frequencies of thin-walled composite beams with closed cross-section.

As mentioned earlier, non-linear beam theories, such as moderate deflection beam theories use ordering schemes to neglect the higher order terms relative to lower order terms. The ordering scheme used for a particular formulation depends on the author's good engineering judgment, which introduces ad hoc assumptions into the formulations. It was also mentioned in Refs. [68] and [69] that moderate deflection theories with ordering schemes don't produce consistent formulations when stiffness in one direction is much smaller than the other directions. Also, moderate deflection theories don't correlate well with experimental results when beams undergo large deformations [70, 71]. Rosen and Friedmann [71] introduced correction terms into the formulation to match with experimental data. Hence, there was a need to develop new beam theories that accounts for large deflection, removes ad-hoc ordering schemes and provide mathematically elegant formulations. Such large deflection beam theories are discussed in the reminder of this section.

Hodges et al. [72, 69] developed a new beam theory in which the ordering scheme that limits the beam deformation to moderate rotations was no longer required. The transformation matrix between the undeformed and deformed beam triads was based on beam deformation quantities in moderate deflection beam theory. In this new method, Tait-Bryan orientation angles and Rodrigues parameters were used to describe the rotation. This approach allowed for the rotations to be captured exactly and allowed for large deforma-

tions to be captured accurately. Although shear deformations were not considered in [72], Hodges [69] provided the necessary material to incorporate shear into the final formulations. The strains were still assumed to be small in this theory.

Simo and Vu-Quoc [73] developed a three dimensional finite element formulation for beams undergoing large deformations. The transformation matrix here was based on Rodrigues formula as shown in [74]. The final formulations were found to be computationally simple. Borri and Merlini [75] also developed a similar theory using Lagrange technique to account for rotations. They extended the work on composite rotor blades in [57] to include large displacements and sectional rotations. The warping functions evaluated were included in a non-linear one dimensional beam analysis. Latter studies by Borri et al. [76] extended this theory to curved and twisted beams.

Large deflection beam theories were also developed by Bauchau and Hong [77, 78, 79] for initially curved and twisted composite beams. Isoparametric three-dimensional beam elements that can capture shear and warping deformations were used in the finite element formulations of [77]. Static and vibration analyses of composite blades were carried out and the results were found to be in good agreement with analytical and experimental data. Ref. [78] utilized one-dimensional finite element beam model based on Euler angles instead of 3-D finite element model and the computation time was reduced by a factor of 20. A slightly modified version of the original theory with a few modifications in the order of strain assumptions was provided in [79].

Minguet and Dugundhi [80] developed a composite beam theory based on Euler angles that accounts for large deformation without use of ordering scheme. Structural coupling that arise due to composite material properties were considered but the shear and warping deformations were ignored. The results were validated for thin cantilevered beams made of graphite and epoxy. Static and vibration experiments [81] were carried out to compare with the analytical data. Pai and Nayfeh [82] also developed a composite beam theory that takes into account the large sectional rotations and warping deformations. Three dimensional

beam formulations were developed to study small or large-amplitude vibrations, elastic and geometric couplings in anisotropic beams. An ordering scheme was utilized here to obtain a third order elastic non-linear equation of motion.

Danielson and Hodges [83] provided a generic beam formulations for initially curved and twisted beams based on mixed variation principle using rotation tensors. The theory accounted for large displacements and rotations while assuming that the strains are still small. The rotation tensor was decomposed into pure rotation tensor and stretch tensor, which simplified the beam's kinematic relations. The theory was applicable to both isotropic and composite beams. All the elastic couplings, shear and warping deformations were treated in this theory and was valid for both open and closed cross-section. A general version of this theory was presented in [84]. In this paper, two sets of formulations were presented. An explicit version with generalized displacements in its formulations and an intrinsic version without any displacements in its formulations. Only static formulations were obtained in both [83] and [84].

Hodges [85] provided an intrinsic beam formulations for dynamics of a twisted and curved beam in a moving frame. A finite element formulation based on mixed variational principles was also presented here. Fulton and Hodges [86] studied the stability characteristics of a composite hingeless rotor blade using the developed intrinsic formulations. Bending-shear coupling and extension-twist coupling were found to be important in analyzing the aeroelastic response of a composite rotor blade. The cross-sectional properties for the beam analyses were computed from the formulations developed by Borri et al.

In large deflection beam theories, the transformation between deformed and undeformed configuration is based on rotation parameters. Hence, these beam formulations are also called as 'geometrically exact' beam theories as the global rotations and displacements are captured exactly. Most of the geometrically exact large deflection theories discussed so far make a kinematic assumption in their formulations to include warping deformation. However, the warping deformations are not included explicitly in the one-dimensional

beam analysis. Warping is considered only for the cross-sectional properties evaluation, which is performed separately, and fed into the non-linear beam model as elastic laws. Usually, this evaluation is based on a different set of formulations i.e., it is not obtained from the global geometrically exact formulations framework.

Atilgan et al. [87, 88] provided a unified framework for analyzing composite beams. A three-dimensional geometrically non-linear theory of elasticity was used to obtain both the 2-D cross-sectional formulations and 1-D beam equations. The warping displacements were assumed to be small compared to the cross-section dimensions. Strains and local rotations, an additional degree of freedom in some large deformation theories, were assumed to be small compared to unity. Warping displacements were computed from 2-D analysis to evaluate the stiffness constants of the beam. The authors acknowledge that the stiffness values could change due to large deformation of the beam but the influence of large deformations on these constants were noted to be not significant. Hence, justifying splitting the beam analysis into 2-D and 1-D analysis. Large deformation intrinsic formulations were used to analyze isotropic and composite beams in this study. Results were found to be in good agreement with experimental data.

Another method that came into prominence for analyzing composite beams was the variational-asymptotic method (VAM) [53]. In this method, the three-dimensional strain energy of a beam was reduced to one-dimensional beam energy asymptotically. Hodges et al. [89] utilized the asymptotic method to derive the cross-sectional formulations for an anisotropic beam along with the one-dimensional geometrically exact beam theory from the same framework. An order approximation was performed on the strain energy which also provided the necessary conditions for the linear cross-sectional analysis to be valid. The stiffness properties were evaluated using a finite element computer code, which later developed into VABS (Variational Asymptotic Beam Section). Some of the stiffness values evaluated were found to be quite different from the values obtained from classical methods. The composite beam properties computed from this new method were found to agree

closely with experimental data. The formulations were extended to initially twisted and curved anisotropic beams by Cesnik and Hodges [90, 91]. The stiffnesses obtained from these formulations are extensively validated in [92]. A summary of the formulations that went into VABS and its capabilities are provided in [93]. The nonlinear geometrically exact beam formulations that are obtained through VAM framework have to be solved numerically. Static and free vibration analyses of curved composite beams based on mixed finite element method was carried out by Hodges et al. in [94]. Cross-sectional properties of a composite beam including obliqueness, where the reference line is not perpendicular to the cross-section, and trapeze effect, increase of torsional rigidity with axial force, were evaluated by Cesnik et al. in [95]. Popescu and Hodges [96] describe trapeze effect as a non-linear phenomenon and hence, it was treated using non-linear cross-sectional analysis as opposed to the usual linear cross-sectional analysis.

Volovoi et al. [97] developed formulations to include the Vlasov effect, also known as end effect, in anisotropic beam analysis using asymptotic method. Vlasov effect was found to be significant in open cross-section thin-walled beams. Later works by Yu et al. added shear deformation to 1-D beam models [98] and introduced Vlasov correction [99] to improve the accuracy of existing asymptotic models. Other composite beam theories based on ad-hoc assumptions were also developed simultaneously. Anisotropic beam theories were developed in [100], [101] and [102] to study the response and cross-sectional properties of thin-walled composite beams. A comprehensive ad-hoc beam theory was developed by Jung et al. [103], which had the capabilities to analyze both thick and thin-walled composite beams.

Bauchau and Kang [104] implemented a large deflection beam theory into a multi-body formulation to analyze helicopter rotor blades. In [104], a generic formulation was developed using rotation vectors that would allow for modeling complex multi-body configurations. The authors analyzed several rigid body problems and a ground resonance problem of a rotor system. The results were found to be in good agreement with analytical values.

These formulations became the precursor to DYMORE, a multi-body dynamics code [105]. [106] and [107] provide a discussion on the numerical techniques that were used to solve flexible multi-body problems.

Carrera et al. [108, 109, 110] developed a new approach to formulate beam equations using axiomatic method. The displacement field was assumed to be a polynomial series function with unknown coefficients, which were solved using a finite element approach. An order reduction was performed on the series to suit the desired level of accuracy. This method was known as Carrera's Unified Formulation (CUF). Yu and Blair [111] developed an analysis tool called GEBT (Geometrically Exact Beam Theory) based on the large deflection beam formulations developed by Hodges and his co-workers. GEBT uses a mixed formulation approach as opposed to a fully intrinsic or a fully displacement formulation. Yu et al. [112] and Gupta [113] also made improvements to VABS analysis tool.

Bauchau and Han used Hamiltonian formalism in [114] to obtain cross-sectional formulations for composite beams from three-dimensional elasticity. The authors claim that this new approach was more accurate as no truncation terms were involved. Han and Bauchau [115] also derived geometrically exact beam equations from this new approach. Response of highly curved composite beams was also presented in [115].

Rotor blade modeling in this study is carried out using a large deflection beam theory described in [116], which has been implemented in DYMORE by Bauchau and his co-workers. Large deflection beam theories are also known as geometrically exact beam theories for the reasons mentioned previously. The theory used in this study permits warping deformation and shear deformation. Strains and local rotations are assumed to be small. The formulations of this theory will be provided in the following chapter. Application of this beam theory to multi-body systems is discussed in [117] and [116]. A large deflection beam theory has never been applied to study the variable speed rotor problem before. However, non-linear large deflection theories have been applied to analyze other aeroelastic problems [118, 119, 120, 121, 122]. More information on rotorcraft beam theory

developments is provided in Refs. [123], [124], [125], and [126].

1.2.3 Aerodynamics and Rotor Trimming

In addition to blade structural modeling, aerodynamics modeling also has to be refined enough to appropriately treat the rotary wing aeroelasticity problem. The helicopter blade undergoes oscillatory motion due to harmonic pitch control input and also due to elastic nature of the blade. Hence, unsteady aerodynamic theories are required to accurately predict the air loads acting on the rotor system.

Theodorsen [127, 128] gave one of the first analytical expression to predict the loads acting on an oscillating airfoil. Theodorsen's theory assumes that the flow is two-dimensional, inviscid and incompressible. The airfoil is assumed to be thin and undergoing a simple harmonic oscillation with only pitch and heave motion. The terms in lift and moment are divided into 'apparent mass' terms (non-circulatory) and 'circulatory' terms. Circulatory terms account for the shed wake behind the airfoil using Theodorsen's function, $C(k)$. Theodorsen's theory assumes that the free stream velocity is constant, which makes the theory not applicable where lead-lag motion is involved. Greenberg [129] extended the theory to include pulsating free stream. The angle of attack was also assumed to vary harmonically about a mean value in Greenberg's theory similar to helicopter blade's pitch input. One of the important characteristics of helicopter aerodynamics is the presence of wake beneath the rotor disc, which is absent in fixed wing. The two theories mentioned so far do not consider the downward wake effects. Loewy included the downward wake to estimate the aerodynamic loads acting on an airfoil undergoing sinusoidal oscillation in a 2-D flow [130]. Formulations developed in this study were valid only for hover with low inflow. Loewy's theory was extended to forward flight by Shipman and Wood to study rotor blade flutter [131].

The theories discussed so far assume that the blade undergoes harmonic oscillations, and hence are in the frequency domain. However, blades close to stability boundaries

could undergo arbitrary motions. Therefore, it is necessary to obtain air loads in the time domain that can handle this arbitrary motion. Efforts were made to transform Theodorsen, Greenberg and Loewy theories from frequency domain to time domain [132, 133, 134].

One of the widely used time domain unsteady theory is the dynamic inflow model initially developed by Peters [135]. The inflow velocity was assumed to vary both radially and azimuthally across the rotor. Inflow was expressed in terms of a first order variation in radius, first harmonic variation along the azimuth and a steady portion. The formulation developed in [135] has been used widely to analyze helicopter rotor blades and become the basis for more advanced inflow models. Flap-lag stability and damping of a rotor blade in forward flight were studied using the developed formulations by Goankar and Peters in Refs. [136] and [137], respectively. The model was further improved by Pitt and Peters [138].

Peters et al. [139, 140] developed finite state unsteady induced flow models where the inflow expression was no longer limited to first order. The rotor was assumed to be a disc with a pressure jump across the disc. Pressure distribution and induced velocity across the rotor disc is assumed to be series expansion with Legendre functions. This generalized formulations allowed for the rotor disc to be at any angle of attack. Wake effects were also considered with a skewed cylindrical wake assumption for forward flight. Expressing these formulations in frequency and eigenvalue domain were also possible. However, convergence was noted to be a bit slow, and hence requiring several terms in the series assumption.

Another unsteady aerodynamics phenomenon that plays an important role in rotary wing aeroelasticity is the dynamic stall effect. As the rotor moves through the azimuth, the pitch angle varies to balance the loads from the advancing and retreating sides of the blade. The pitch angle is decreased in the advancing side and increased on the retreating side. At high speeds, the difference in pitch angle could be large and some sections of the blade could see a large change in angle of attack which could lead to flow separation and stalling

of the airfoil. This phenomenon is known as dynamic stall. The flow reattaches once the blade section crosses this region. The loads acting on the airfoil during this phenomenon has been studied by various researchers. One of the popular dynamic stall models is the ONERA model [141, 142]. The model has parameters that needs to be computed empirically to accurately predict the air loads acting on an airfoil before-stall, during-stall and post-stall regions. Application and comparison of this model to experimental results is discussed in [143]. ONERA model was further improved by Rogers [144] and Peters [145]. Some of the initial assumptions were modified to make the theory consistent with other unsteady theories such as Greenberg's for small angle of attack and Theodorsen's for steady free stream. Beddoes [146, 147] developed a more detailed version of dynamic stall model which was further extended by Leishman [148, 149]. Leishman-Beddoes model [150] is capable of calculating unsteady lift, pitch and also drag forces acting on an airfoil. Compressibility effects are also treated rigorously in this model. Further literature on rotary wing aerodynamics is provided in [151] and [152].

In order to perform any aeroelastic analysis of rotor blades, rotor needs to be trimmed to the given flight condition. Trim is described as the correct adjustment of aircraft controls, attitude and cargo in order to obtain a desired steady flight condition [153]. There are several types of trim procedures and several methods of performing rotor trim analysis. Peters and Barwey [153] provide a detailed account on types of trim and trim solution procedures. Moment trim, propulsive trim and six-degree-of-freedom trim are mentioned as some of the common trim types. In [153], moment trim is described as a type of trim in which a rotor with a fixed hub is trimmed to a specific thrust, pitching moment and rolling moment. The controls are provided by collective and cyclic pitch inputs. In propulsive trim the hub is allowed to tilt forward to provide a force equilibrium for the fuselage drag. Power requirement was also included in trim in some cases. Six-degree-of-freedom trim is trimming of the three forces and three moments by collective pitch, cyclic pitches, tail rotor pitch, body pitch and roll angles with yaw defined. Commonly used solution techniques,

such as harmonic balance, Newton-Raphson iteration, periodic shooting, finite elements in time and Auto-pilots are discussed in this study.

Friedmann and Shamie [154, 48] describe wind tunnel trim, also called as moment trim here, as a trim procedure in which the rotor is treated like it is placed in a wind tunnel. Fuselage drag forces are neglected in this trim procedure and as a result, horizontal and vertical force equilibrium is not considered. Rolling and pitching moments are enforced to be zero and hub is allowed to tilt here. Advance ratio, collective pitch and hub tilt angles are specified and thrust, cyclic cosine and sine angles are computed. Propulsive trim procedure was described as trimming the rotor like it is in actual forward flight. The weight of the aircraft is balanced by the thrust and force equilibrium is achieved in all directions. Roll and pitch moments are maintained to be zero. Advance ratio and weight is specified for an arbitrary hub tilt to compute collective and cyclic pitch angles iteratively from the force and moment balance equations. Friedmann et al. [155] provide a detailed set of trim results for a hingeless rotor in forward flight using harmonic balance technique, which is useful in validating numerical results.

Peters and Morillo solved a trim problem with unknown and unsteady rotor speed using harmonic balance [156]. Peters and Kim [157, 158] used an automatic feedback control system that monitors the hub loads continuously and corrects the control inputs to match the specified trim state. This technique was found to be superior to other trim techniques for systems with moderate damping. Peters and Li [159] discuss an auto-pilot controller which trims a rotor system during time marching of equations of motion. Auto-pilot controllers require a Jacobian matrix that is obtained from perturbing the initial control guesses. Control values are updated after one period based on the error, Jacobian and gain values.

In the present study, an auto-pilot controller will be used to trim the rotor system. Details about the auto-pilot controller and the Jacobian matrix computation will be provided in the subsequent chapters.

1.3 Objectives of the Present Study

Based on the literature review, it was found that the structural aspects of a variable speed rotor has not been addressed adequately. In this work, resonance behavior of a variable speed rotor blade will be treated elaborately. The objectives of the current study are stated below.

- Build a rotor blade aeroelasticity model using large deflection beam theory to analyze variable speed rotors.
- Trim the rotor using an auto-pilot controller to the desired flight conditions.
- Analyze the performance improvements that can be achieved by changing the rotor speed of a hingeless rotor blade.
- Identify the resonance crossing points of a hingeless rotor blade from performance studies.
- Analyze the loads acting on a rotor blade during resonance crossings. Examine the characteristics of resonance crossing at different flight conditions and explore any non-linear resonance behaviors described by Nayfeh and Mook [20].
- Explore methods of reducing additional vibratory loads on the rotor hub during resonance crossings. Influence of transition time and blade's structural properties on load reduction will be studied.

The rotor model used in this study is one of the most comprehensive models used to study variable speed rotors to date.

CHAPTER 2

ROTOR BLADE FORMULATIONS

Helicopter rotor blades are slender structures that could undergo large deformations in flight due to aerodynamic and inertial loads. Rotor blade aeroelasticity requires appropriate blade and unsteady aerodynamics modeling to accurately capture the blade response. Rotor blades are usually modeled as one-dimensional beam structures as discussed in the previous chapter. Aeroelastic response of the blade is also a non-linear problem and hence, the non-linear beam and aerodynamics formulations are used in the present work. A non-linear geometrically exact beam theory is used to model the rotor blade. The Peters et al. [139] unsteady aerodynamics model is used to obtain the aerodynamic loads along with the Pitt-He [140] finite state inflow model. The beam formulations and the aerodynamics formulation are presented in this chapter.

2.1 Geometrically Exact Beam Formulations

A curved beam in its reference and deformed configuration is shown in Figure 2.1 [116]. Reference configuration is the undeformed configuration of the beam. The beam is initially curved and twisted with a length of L and a cross-sectional area of \mathcal{A} . The dotted blue line in Figure 2.1 is the reference line of the undeformed configuration, which is perpendicular to the cross-section. A curvilinear coordinate α_1 is used to measure the length along the beam's reference line. The beam moves in an inertial reference frame \mathcal{I} with origin \mathbf{O} and an orthogonal Cartesian basis $(\bar{\mathbf{i}}_1, \bar{\mathbf{i}}_2, \bar{\mathbf{i}}_3)$. Point \mathbf{B} is at the intersection of the reference line and the cross-sectional plane. A frame \mathcal{B}_0 is defined in the reference configuration at point \mathbf{B} with orthogonal basis $(\bar{\mathbf{b}}_1, \bar{\mathbf{b}}_2, \bar{\mathbf{b}}_3)$. Basis vector $\bar{\mathbf{b}}_1$ is tangent to the reference line at point \mathbf{B} . Vectors $\bar{\mathbf{b}}_2$ and $\bar{\mathbf{b}}_3$ are in the plane of the cross-section. Basis vectors of \mathcal{I}

and \mathcal{B}_0 are related through a rotation tensor as $\bar{\mathbf{b}}_i = \underline{\underline{R}}_0(\alpha_1) \bar{\mathbf{i}}_i$, where $\underline{\underline{R}}_0$ is a rotation tensor resolved in \mathcal{I} basis and the subscript i takes the values 1, 2 and 3. The position vector of point B along the reference line is given as $\underline{x}_0(\alpha_1)$.

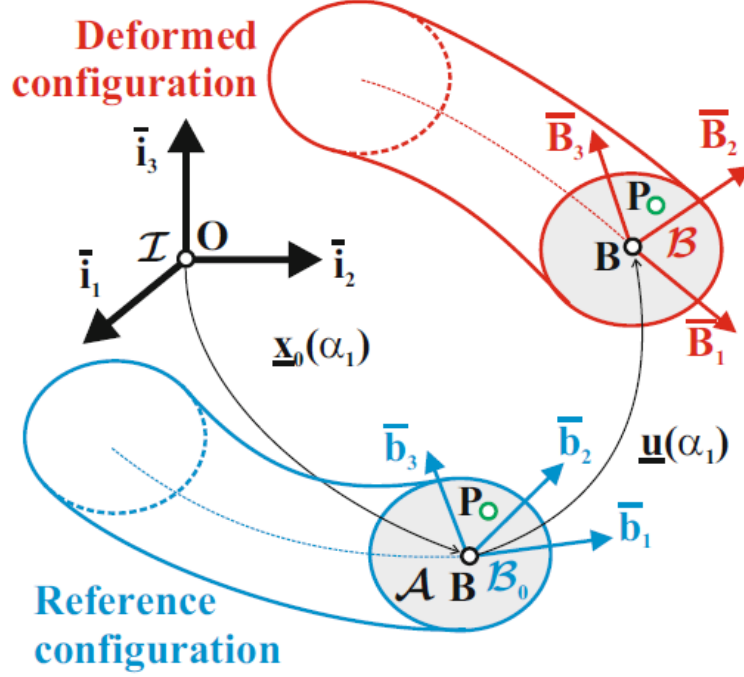


Figure 2.1: Beam in reference and deformed configuration.

Point P, which is a material point on the cross-section, has a position vector as given in equation (2.1).

$$\underline{x}(\alpha_1, \alpha_2, \alpha_3) = \underline{x}_0(\alpha_1) + \alpha_2 \bar{\mathbf{b}}_2 + \alpha_3 \bar{\mathbf{b}}_3 \quad (2.1)$$

where α_1 and α_2 are the coordinates of point P along $\bar{\mathbf{b}}_2$ and $\bar{\mathbf{b}}_3$ unit basis vectors, respectively.

When the beam deforms, all the points on the cross-section move to a new position. The motion of the beam can be divided into three parts. One, the rigid translation of the beam cross-section which is given by the displacement vector $\underline{u}(\alpha_1)$ of point B. Two, the rigid rotation of the beam cross-section defined by the rotation tensor $\underline{\underline{R}}$ which brings the \mathcal{B}_0 frame to the \mathcal{B} frame in the deformed configuration with basis $(\bar{\mathbf{B}}_1, \bar{\mathbf{B}}_2, \bar{\mathbf{B}}_3)$ i.e., $\bar{\mathbf{B}}_i = \underline{\underline{R}}(\alpha_1) \bar{\mathbf{b}}_i$. Three, the warping displacement of the cross-section $w(\alpha_1, \alpha_2, \alpha_3)$. The

warping displacement includes both in-plane and out-of-plane deformations of the cross-section and is given as

$$\underline{w}(\alpha_1, \alpha_2, \alpha_3) = w_1 \overline{\mathbf{B}}_1 + w_2 \overline{\mathbf{B}}_2 + w_3 \overline{\mathbf{B}}_3 \quad (2.2)$$

where w_1 , w_2 and w_3 are the magnitudes of warping displacement in $\overline{\mathbf{B}}_1$, $\overline{\mathbf{B}}_2$ and $\overline{\mathbf{B}}_3$ directions, respectively. The position vector of point P in the deformed configuration is now given as follows.

$$\underline{X}(\alpha_1, \alpha_2, \alpha_3) = \underline{x}_0(\alpha_1) + \underline{u}(\alpha_1) + \alpha_2 \overline{\mathbf{B}}_2 + \alpha_3 \overline{\mathbf{B}}_3 + w_1 \overline{\mathbf{B}}_1 + w_2 \overline{\mathbf{B}}_2 + w_3 \overline{\mathbf{B}}_3 \quad (2.3)$$

Since, $\overline{\mathbf{B}}_i = \underline{\underline{R}} \underline{\underline{R}}_0^T \bar{\mathbf{i}}_i$. The above equation becomes

$$\underline{X}(\alpha_1, \alpha_2, \alpha_3) = \underline{x}_0(\alpha_1) + \underline{u}(\alpha_1) + \underline{\underline{R}} \underline{\underline{R}}_0^T (\underline{w} + \alpha_2 \bar{\mathbf{i}}_2 + \alpha_3 \bar{\mathbf{i}}_3) \quad (2.4)$$

Warping displacements are usually computed from a two-dimensional finite element formulation and hence, only the resultant cross-sectional properties will be used for the one-dimensional beam analysis. Therefore, warping will not appear explicitly in rest of the formulations.

Sectional strains for a beam with shallow curvature are defined as follows.

$$\underline{e} = \begin{Bmatrix} \underline{\epsilon} \\ \underline{\kappa} \end{Bmatrix} = \begin{Bmatrix} \underline{x}'_0 + \underline{u}' - (\underline{\underline{R}} \underline{\underline{R}}_0^T) \bar{\mathbf{i}}_1 \\ \underline{k} + \underline{\underline{R}} \underline{k}_i \end{Bmatrix} \quad (2.5)$$

where $\underline{\epsilon}$ has the axial and shear strain terms and $\underline{\kappa}$ has the bending curvature and twist terms. $\underline{k} = axial(\underline{\underline{R}}' \underline{\underline{R}}^T)$ is the sectional curvature vector in \mathcal{I} basis and \underline{k}_i are the components of the curvature vector in the beam's reference configuration. A derivative with respect to α_1 is denoted using $(.)'$ notation. The operator *axial* is defined as $axial(\underline{\underline{A}}) = (\underline{\underline{A}} - \underline{\underline{A}}^T)/2$ for any second-order tensor $\underline{\underline{A}}$. The strain equation (2.5) is obtained by taking the difference

between the basis vectors of the reference and deformed configuration and their spatial derivatives. This technique is explained in detail in [116] and [126]. In the deformed configuration, \mathcal{B} , the strain can be expressed as

$$\underline{\underline{\epsilon}}^* = (\underline{\underline{R}} \underline{\underline{R}}_0)^T \underline{\underline{\epsilon}} \quad (2.6)$$

$$\underline{\underline{\kappa}}^* = (\underline{\underline{R}} \underline{\underline{R}}_0)^T \underline{\underline{\kappa}} \quad (2.7)$$

The notation $(.)^*$ denotes that the components of a vector or a tensor is in the \mathcal{B} basis.

If \underline{N}^* and \underline{M}^* are the beam's sectional forces and moments, respectively, then the sectional constitutive law can be written as

$$\begin{Bmatrix} \underline{N}^* \\ \underline{M}^* \end{Bmatrix} = \underline{\underline{\mathcal{C}}}^* \begin{Bmatrix} \underline{\underline{\epsilon}}^* \\ \underline{\underline{\kappa}}^* \end{Bmatrix} \quad (2.8)$$

where $\underline{\underline{\mathcal{C}}}^*$ is the 6×6 sectional stiffness matrix that is obtained from the beam's cross-sectional as discussed previously. Using the strain equations and the constitutive law, the principle of virtual work for the static case can be written as

$$\int_0^L (\delta \underline{\underline{\epsilon}}^{*T} \underline{N}^* + \delta \underline{\underline{\kappa}}^{*T} \underline{M}^*) d\alpha_1 = \delta W_{ext} \quad (2.9)$$

where δ is the variation operator. Taking variation of the strain in equation (2.6) we get

$$\delta \underline{\underline{\epsilon}}^* = \delta (\underline{\underline{R}} \underline{\underline{R}}_0)^T \underline{\underline{\epsilon}} + (\underline{\underline{R}} \underline{\underline{R}}_0)^T \delta \underline{\underline{\epsilon}} \quad (2.10)$$

$$\delta \underline{\underline{\epsilon}} = \delta (\underline{x}'_0 + \underline{u}'_0) - \delta (\underline{\underline{R}} \underline{\underline{R}}_0) \bar{\mathbf{i}}_1 \quad (2.11)$$

Variation of a vector between two frames has a relation that is similar to the time derivative relation between two frames. Here, the angular velocity term is replaced by the virtual rotation vector $\delta \underline{\psi}$. Let's consider two frames **A** and **B** as an example. The variation

relation [126] is given as

$$\delta(\underline{vector}) = \mathbf{A}\delta(\underline{vector}) = \mathbf{B}\delta(\underline{vector}) + \underline{\delta\psi} \times (\underline{vector}) \quad (2.12)$$

The above equation could also be written as

$$\delta(\underline{vector}) = \mathbf{A}\delta(\underline{vector}) = \mathbf{B}\delta(\underline{vector}) + \widetilde{\underline{\delta\psi}}(\underline{vector}) \quad (2.13)$$

where $\widetilde{(\quad)}$ represents a skew-symmetric matrix with the vector components. The virtual rotation vector is related to the rotation matrix $\underline{\underline{R}}$ by the following relation,

$$\underline{\underline{\delta\psi}} = axial(\delta\underline{\underline{R}}\underline{\underline{R}}^T) \quad (2.14)$$

or

$$\widetilde{\underline{\delta\psi}} = \delta\underline{\underline{R}}\underline{\underline{R}}^T \quad (2.15)$$

Using the relationships given in the equations (2.12 — 2.15) in equation (2.11) and simplifying the variation of strains we get the following relations

$$\delta\underline{\underline{\epsilon}}^* = (\underline{\underline{R}}\underline{\underline{R}}_0)^T [\delta\underline{u}' + (\widetilde{x}'_0 + \widetilde{u}')\underline{\underline{\delta\psi}}] \quad (2.16)$$

$$\delta\underline{\underline{\kappa}}^* = (\underline{\underline{R}}\underline{\underline{R}}_0)^T \underline{\underline{\delta\psi}}' \quad (2.17)$$

Hence, the virtual work relation (2.9) can now be written as

$$\int_0^L \left\{ \left[\delta\underline{u}'^T + \underline{\underline{\delta\psi}}^T (\widetilde{x}'_0 + \widetilde{u}')^T \right] (\underline{\underline{R}}\underline{\underline{R}}_0)\underline{\underline{N}}^* + \underline{\underline{\delta\psi}}'^T (\underline{\underline{R}}\underline{\underline{R}}_0)\underline{\underline{M}}^* \right\} d\alpha_1 = \delta W_{ext} \quad (2.18)$$

Now we define $\underline{\underline{N}} = (\underline{\underline{R}}\underline{\underline{R}}_0)\underline{\underline{N}}^*$, $\underline{\underline{M}} = (\underline{\underline{R}}\underline{\underline{R}}_0)\underline{\underline{M}}^*$ and $\delta W_{ext} = \int_0^L [\delta\underline{u}^T \underline{\underline{f}} + \underline{\underline{\delta\psi}}^T \underline{\underline{m}}] d\alpha_1$. $\underline{\underline{f}}$ and $\underline{\underline{m}}$ are the externally applied forces and moments, respectively, per unit span of the

beam. Substituting these definitions in the equation (2.18) we get

$$\int_0^L \left\{ \left[\delta \underline{u}'^T + \delta \underline{\psi}^T (\tilde{x}'_0 + \tilde{u}')^T \right] \underline{N} + \delta \underline{\psi}'^T \underline{M} \right\} d\alpha_1 = \int_0^L \left[\delta \underline{u}^T \underline{f} + \delta \underline{\psi}^T \underline{m} \right] d\alpha_1 \quad (2.19)$$

On integrating by parts and using the relation $(\tilde{x}'_0 + \tilde{u}')^T = -(\tilde{x}'_0 + \tilde{u}')$, the above equation can be simplified as

$$\begin{aligned} \int_0^L \delta \underline{u}^T [-\underline{N}' - \underline{f}] d\alpha_1 + \int_0^L \delta \underline{\psi}^T [-\underline{M}' - (\tilde{x}'_0 + \tilde{u}') \underline{N} - \underline{m}] d\alpha_1 \\ + \underline{N} \delta \underline{u}^T \Big|_0^L + \underline{M} \delta \underline{\psi}^T \Big|_0^L = 0 \end{aligned} \quad (2.20)$$

Hence, the governing equation of the beam for a static case is as follows.

$$\underline{N}' + \underline{f} = 0 \quad (2.21)$$

$$\underline{M}' + (\tilde{x}'_0 + \tilde{u}') \underline{N} + \underline{m} = 0 \quad (2.22)$$

Dynamic governing equations can be obtained by including the kinetic energy of a beam in the virtual work equation and taking a variation of the kinetic energy like the static case. Before we dive into it, some of the relations that would be needed for our derivation are provided below.

Velocity of the material point **P** can be obtained by taking the time derivative of equation (2.4) in inertial frame without the warping displacement.

$$\underline{v} = \dot{\underline{X}} = 0 + \dot{\underline{u}}(\alpha_1) + \dot{\underline{R}} \underline{R}_0 (\alpha_2 \bar{\mathbf{i}}_2 + \alpha_3 \bar{\mathbf{i}}_3) \quad (2.23)$$

where $\dot{(\cdot)}$ denotes derivative with respect to time. Let $\underline{s}^{*T} = \{0, \alpha_2, \alpha_3\}$. The relation between angular velocity, $\underline{\omega}$, and angular rotation tensor is given as $\tilde{\omega} = \dot{\underline{R}} \underline{R}^T$. Using these

equations in equation (2.23) we get

$$\underline{v} = \underline{\dot{u}} + (\underline{R} \underline{R}_0) \tilde{\omega}^* \underline{s}^* = \underline{\dot{u}} + (\underline{R} \underline{R}_0) \tilde{s}^{*T} \underline{\omega}^* \quad (2.24)$$

where $\underline{\omega}^* = (\underline{R} \underline{R}_0)^T \underline{\omega}$. Velocity in the material \mathcal{B}_0 frame is given as

$$\underline{v}^* = (\underline{R} \underline{R}_0)^T \underline{v} = (\underline{R} \underline{R}_0)^T \underline{\dot{u}} + \tilde{s}^{*T} \underline{\omega}^* \quad (2.25)$$

If ρ is the material density in the reference configuration, then the kinetic energy of the beam is

$$K = \frac{1}{2} \int_0^L \int_{\mathcal{A}} \rho \underline{v}^{*T} \underline{v}^* d\mathcal{A} d\alpha_1 \quad (2.26)$$

Substituting equation (2.25) in the above equation we get the following equation.

$$K = \frac{1}{2} \int_0^L \int_{\mathcal{A}} \rho \left[\underline{\dot{u}}^T (\underline{R} \underline{R}_0) + \underline{\omega}^{*T} \tilde{s}^* \right] \left[(\underline{R} \underline{R}_0)^T \underline{\dot{u}} + \tilde{s}^{*T} \underline{\omega}^* \right] d\mathcal{A} d\alpha_1 \quad (2.27)$$

Let's define $m = \int_{\mathcal{A}} \rho d\mathcal{A}$, $\underline{\eta}^* = \frac{1}{2} \int_{\mathcal{A}} \rho \underline{s}^* d\mathcal{A}$ and $\underline{\varrho}^* = \frac{1}{2} \int_{\mathcal{A}} \rho \tilde{s}^* \tilde{s}^{*T} d\mathcal{A}$. m is the mass per unit span of the beam, $\underline{\eta}^*$ is the position vector of the sectional center of mass with respect to point B and $\underline{\varrho}^*$ is the sectional tensor of inertia per unit span. Substituting these definitions in the kinetic energy equation and on simplifying we get a one-dimensional integral equation.

$$K = \frac{1}{2} \int_0^L \left[m \underline{\dot{u}}^T \underline{\dot{u}} + 2m \underline{\dot{u}}^T (\underline{R} \underline{R}_0) \tilde{\eta}^{*T} \underline{\omega}^* + \underline{\omega}^{*T} \underline{\varrho}^* \underline{\omega}^* \right] d\alpha_1 \quad (2.28)$$

To make the above equation compact, let us define the following variables.

$$\underline{\underline{\mathcal{M}}}^* = \begin{bmatrix} m \underline{I} & m \tilde{\eta}^{*T} \\ m \tilde{\eta}^* & \underline{\varrho}^* \end{bmatrix} \quad (2.29)$$

$$\underline{\mathcal{V}}^* = \begin{Bmatrix} (\underline{R}\underline{R}_0)^T \underline{\dot{u}} \\ \underline{\omega}^* \end{Bmatrix} = \begin{bmatrix} (\underline{R}\underline{R}_0)^T & \underline{0} \\ \underline{0} & (\underline{R}\underline{R}_0)^T \end{bmatrix} \begin{Bmatrix} \underline{\dot{u}} \\ \underline{\omega} \end{Bmatrix} = (\underline{R}\underline{R}_0)^T \underline{\mathcal{V}} \quad (2.30)$$

where \underline{I} is an identity matrix and

$$\underline{\mathcal{V}} = \begin{Bmatrix} \underline{\dot{u}} \\ \underline{\omega} \end{Bmatrix}, \quad \underline{R}\underline{R}_0 = \begin{bmatrix} (\underline{R}\underline{R}_0) & \underline{0} \\ \underline{0} & (\underline{R}\underline{R}_0) \end{bmatrix} \quad (2.31)$$

If \underline{h}^* and \underline{g}^* are the sectional linear and angular momentum, respectively, in the material frame, then the momentum vector $\underline{\mathcal{P}}^*$ is

$$\underline{\mathcal{P}}^* = \begin{Bmatrix} \underline{h}^* \\ \underline{g}^* \end{Bmatrix} = \underline{\mathcal{M}}^* \underline{\mathcal{V}}^* \quad (2.32)$$

The kinetic energy can now be written in a compact form as

$$K = \frac{1}{2} \int_0^L \underline{\mathcal{V}}^{*T} \underline{\mathcal{M}}^* \underline{\mathcal{V}}^* d\alpha_1 \quad (2.33)$$

Variation of kinetic energy is

$$\delta K = \int_0^L \delta \underline{\mathcal{V}}^{*T} \underline{\mathcal{M}}^* \underline{\mathcal{V}}^* d\alpha_1 \quad (2.34)$$

where $\delta \underline{\mathcal{V}}^{*T} = \begin{bmatrix} \delta(\underline{\dot{u}}^T(\underline{R}\underline{R}_0)) & \delta \underline{\omega}^{*T} \end{bmatrix}$. Using the relationships between the rotation tensor, virtual rotation vector and angular velocities, it can be shown that $\delta(\underline{\dot{u}}^T(\underline{R}\underline{R}_0)) = (\delta \underline{\dot{u}}^T + \delta \underline{\psi}^T \underline{\dot{u}}^T)(\underline{R}\underline{R}_0)$ and $\delta \underline{\omega}^{*T} = \delta \underline{\dot{\psi}}^T(\underline{R}\underline{R}_0)$. Hence, using these relations and equation (2.32) the variation of K becomes

$$\delta K = \int_0^L \left[(\delta \underline{\dot{u}}^T + \delta \underline{\psi}^T \underline{\dot{u}}^T)(\underline{R}\underline{R}_0) \quad \delta \underline{\dot{\psi}}^T(\underline{R}\underline{R}_0) \right] \begin{Bmatrix} \underline{h}^* \\ \underline{g}^* \end{Bmatrix} d\alpha_1 \quad (2.35)$$

If $\underline{h} = (\underline{R} \underline{R}_0) \underline{h}^*$ and $\underline{g} = (\underline{R} \underline{R}_0) \underline{g}^*$, then the above equation becomes

$$\delta K = \int_0^L \left[\delta \underline{u}^T \underline{h} + \delta \underline{\psi}^T \dot{\underline{u}}^T \underline{h} + \delta \dot{\underline{\psi}}^T \underline{g} \right] d\alpha_1 \quad (2.36)$$

Using Hamilton's principle and equation (2.9) we get

$$\int_{t_i}^{t_f} \left[\delta K - \int_0^L (\delta \underline{\epsilon}^{*T} \underline{N}^* + \delta \underline{\kappa}^{*T} \underline{M}^*) d\alpha_1 + \delta W_{ext} \right] dt = 0 \quad (2.37)$$

On performing integration by parts on the term $\int_{t_i}^{t_f} \delta K dt$, we obtain the following form.

$$\int_{t_i}^{t_f} \delta K = \int_{t_i}^{t_f} \int_0^L \left[-\delta \underline{u}^T \dot{\underline{h}} + \delta \underline{\psi}^T \dot{\underline{u}}^T \underline{h} - \delta \underline{\psi}^T \dot{\underline{g}} \right] d\alpha_1 dt \quad (2.38)$$

Combining the above equation with equation (2.20), we get the governing equations of motion of a beam.

$$\dot{\underline{h}} - \underline{N}' = \underline{f} \quad (2.39)$$

$$\dot{\underline{g}} + \dot{\underline{u}}^T \underline{h} - \underline{M}' - (\tilde{x}'_0 + \tilde{u}') \underline{N} = \underline{m} \quad (2.40)$$

Based on the obtained force equilibrium equations, a finite element formulation will be derived with the linearized force terms. Now, let us define the following terms to build a compact form of the beam equation.

$$\underline{\mathcal{P}} = \begin{Bmatrix} \underline{h} \\ \underline{g} \end{Bmatrix}, \quad \underline{\mathcal{F}}^I = \dot{\underline{\mathcal{P}}} + \begin{bmatrix} \underline{0} & \underline{0} \\ \dot{\underline{u}} & \underline{0} \end{bmatrix} \underline{\mathcal{P}}, \quad \underline{\mathcal{F}}^C = \begin{Bmatrix} \underline{N} \\ \underline{M} \end{Bmatrix} \quad (2.41)$$

$$\underline{\mathcal{F}}^D = \begin{bmatrix} \underline{0} & \underline{0} \\ (\tilde{x}'_0 + \tilde{u}')^T & \underline{0} \end{bmatrix} \begin{Bmatrix} \underline{N} \\ \underline{M} \end{Bmatrix} = \begin{Bmatrix} \underline{0} \\ (\tilde{x}'_0 + \tilde{u}')^T \underline{N} \end{Bmatrix}, \quad \underline{\mathcal{F}}^{ext} = \begin{Bmatrix} \underline{f} \\ \underline{m} \end{Bmatrix} \quad (2.42)$$

Hence, the equations (2.39) and (2.40) of the beam becomes

$$\underline{\mathcal{F}}^I - \underline{\mathcal{F}}^{C'} + \underline{\mathcal{F}}^D = \underline{\mathcal{F}}^{\text{ext}} \quad (2.43)$$

Dissipative forces are sometimes required in the beam analysis. Let us define the dissipative forces in the inertial frame as $\underline{f}^d = \mu \underline{\underline{C}} \dot{\underline{e}}$, where μ is the damping coefficient with unit $1/s$ and $\underline{\underline{C}} = (\underline{\underline{\mathcal{R}}} \underline{\underline{\mathcal{R}}}_0) \underline{\underline{C}}^* (\underline{\underline{\mathcal{R}}} \underline{\underline{\mathcal{R}}}_0)^T$. Time derivative of strain is

$$\dot{\underline{e}} = \begin{Bmatrix} \dot{\underline{u}} + \tilde{E}_1 \underline{\omega} \\ \underline{\omega}' \end{Bmatrix} \quad (2.44)$$

where $\tilde{E}_1 = \tilde{x}'_0 + \tilde{u}'$. Let $\underline{f}^{dT} = \left\{ \underline{N}^{dT} \quad \underline{M}^{dT} \right\}$, where \underline{N}^d and \underline{M}^d are the sectional dissipative force and moment vectors, respectively, in the frame \mathcal{I} . Including the dissipative forces as non-conservative forces in the Hamilton's principle leads to two distinct dissipative force terms as shown below.

$$\underline{\mathcal{F}}^{dC} = \underline{f}^d = \begin{Bmatrix} \underline{N}^d \\ \underline{M}^d \end{Bmatrix}, \quad \underline{\mathcal{F}}^{dD} = \begin{bmatrix} \underline{\underline{0}} & \underline{\underline{0}} \\ \tilde{E}_1^T & \underline{\underline{0}} \end{bmatrix} \underline{f}^d = \begin{Bmatrix} \underline{\underline{0}} \\ \tilde{E}_1^T \underline{N}^d \end{Bmatrix} \quad (2.45)$$

Including the dissipative terms, the beam equation (2.43) becomes

$$\underline{\mathcal{F}}^I - (\underline{\mathcal{F}}^C + \underline{\mathcal{F}}^{dC})' + (\underline{\mathcal{F}}^D + \underline{\mathcal{F}}^{dD}) = \underline{\mathcal{F}}^{\text{ext}} \quad (2.46)$$

Finite element formulation for the beam is obtained from a weighted residual method. The weak form of the beam governing equation can be written as follows.

$$\int_0^l \underline{\underline{N}}^T \left[\underline{\mathcal{F}}^I - (\underline{\mathcal{F}}^C + \underline{\mathcal{F}}^{dC})' + (\underline{\mathcal{F}}^D + \underline{\mathcal{F}}^{dD}) - \underline{\mathcal{F}}^{\text{ext}} \right] d\alpha_1 = 0 \quad (2.47)$$

where l is the length of the beam element and $\underline{\underline{N}}$ is the displacement interpolation matrix

containing the shape functions, $\underline{\underline{N}} = [h_1(s)\underline{\underline{I}}, h_2(s)\underline{\underline{I}}, h_3(s)\underline{\underline{I}}]$. h_1, h_2 and h_3 are the shape functions and s is a non-dimensional quantity defined along the span of a finite element. Lagrange polynomials are used as shape functions in this study. On integrating by parts, equation (2.47) becomes

$$\int_0^l \left[\underline{\underline{N}}^T \underline{\underline{F}}^I + \underline{\underline{N}}'^T (\underline{\underline{F}}^C + \underline{\underline{F}}^{dC}) + \underline{\underline{N}}^T (\underline{\underline{F}}^D + \underline{\underline{F}}^{dD}) \right] d\alpha_1 = \int_0^l \underline{\underline{N}}^T \underline{\underline{F}}^{\text{ext}} d\alpha_1 \quad (2.48)$$

However, this is a non-linear set of equations. Hence, a linearization process is required for solving the system of equations. Linearization is carried out by computing the increments, $\Delta()$, of the force terms and its components. All the increments of the force terms are listed as below.

$$\Delta \underline{\underline{F}}^I = \underline{\underline{K}}^I \Delta \underline{\underline{q}} + \underline{\underline{G}}^I \Delta \dot{\underline{\underline{q}}} + \underline{\underline{M}} \Delta \ddot{\underline{\underline{q}}} \quad (2.49)$$

$$\Delta \underline{\underline{F}}^C = \underline{\underline{S}} \Delta \underline{\underline{q}}' + \underline{\underline{O}} \Delta \underline{\underline{q}} \quad (2.50)$$

$$\Delta \underline{\underline{F}}^D = \underline{\underline{P}} \Delta \underline{\underline{q}}' + \underline{\underline{Q}} \Delta \underline{\underline{q}} \quad (2.51)$$

$$\Delta \underline{\underline{F}}^{dC} = \underline{\underline{S}}^d \Delta \underline{\underline{q}}' + \underline{\underline{O}}^d \Delta \underline{\underline{q}} + \underline{\underline{G}}^d \Delta \dot{\underline{\underline{q}}} + \underline{\underline{E}}^d \Delta \dot{\underline{\underline{q}}}' \quad (2.52)$$

$$\Delta \underline{\underline{F}}^{dD} = \underline{\underline{P}}^d \Delta \underline{\underline{q}}' + \underline{\underline{Q}}^d \Delta \underline{\underline{q}} + \underline{\underline{X}}^d \Delta \dot{\underline{\underline{q}}} + \underline{\underline{Y}}^d \Delta \dot{\underline{\underline{q}}}' \quad (2.53)$$

where $\Delta \underline{\underline{q}}^T = \{\Delta \underline{\underline{u}}^T, \Delta \underline{\underline{p}}^T\}$, $\Delta \dot{\underline{\underline{q}}}^T = \{\Delta \dot{\underline{\underline{u}}}^T, \Delta \dot{\underline{\underline{p}}}^T\}$ and $\Delta \ddot{\underline{\underline{q}}}^T = \{\Delta \ddot{\underline{\underline{u}}}^T, \Delta \ddot{\underline{\underline{p}}}^T\}$. Vector $\underline{\underline{p}}$ is the rotation parameter vector. Rotation is parameterized using Wiener-Milenković parameters. Rotation parameters have the relations $\underline{\underline{\omega}} = \underline{\underline{H}}(\underline{\underline{p}}) \dot{\underline{\underline{p}}}$ and $\underline{\underline{\kappa}} = \underline{\underline{H}}(\underline{\underline{p}}) \underline{\underline{p}}'$. $\underline{\underline{H}}$ is the tangent tensor as defined in [116]. The linearization process for the forces is mathematically involved and is presented in detail in [116]. Expressions for the coefficient matrices $\underline{\underline{K}}^I, \underline{\underline{G}}^I, \underline{\underline{M}}, \underline{\underline{S}}, \underline{\underline{O}}, \underline{\underline{P}}, \underline{\underline{Q}}, \underline{\underline{S}}^d, \underline{\underline{O}}^d, \underline{\underline{G}}^d, \underline{\underline{E}}^d, \underline{\underline{P}}^d, \underline{\underline{Q}}^d, \underline{\underline{X}}^d$ and $\underline{\underline{Y}}^d$ in the linearization equations is given

in [116]. Now, let us include all the increment of the force terms in equation (2.48).

$$\int_0^l \left[\underline{\underline{N}}^T (\underline{\mathcal{F}}^I + \Delta \underline{\mathcal{F}}^I) + \underline{\underline{N}}'^T (\underline{\mathcal{F}}^C + \Delta \underline{\mathcal{F}}^C + \underline{\mathcal{F}}^{dC} + \Delta \underline{\mathcal{F}}^{dC}) + \underline{\underline{N}}^T (\underline{\mathcal{F}}^D + \underline{\mathcal{F}}^{dD}) \right] d\alpha_1 = \int_0^l \underline{\underline{N}}^T \underline{\mathcal{F}}^{\text{ext}} d\alpha_1 \quad (2.54)$$

Now, let us make the following relations using the displacement interpolation matrix.

$$\underline{q}(\alpha_1) = \underline{\underline{N}} \hat{q}, \quad \underline{q}'(\alpha_1) = \underline{\underline{N}}' \hat{q}, \quad \dot{\underline{q}}(\alpha_1) = \underline{v}(\alpha_1) = \underline{\underline{N}} \dot{\hat{q}} = \underline{\underline{N}} \hat{v} \quad (2.55)$$

$$\ddot{\underline{q}}(\alpha_1) = \underline{a}(\alpha_1) = \underline{\underline{N}} \ddot{\hat{q}} = \underline{\underline{N}} \hat{a} \quad (2.56)$$

where \hat{q} , \hat{v} and \hat{a} are the nodal displacements, velocities and accelerations, respectively. Substituting equations (2.49—2.53) and the above relations in equation (2.54) we get the following form of the dynamic equilibrium equation.

$$\hat{\underline{\underline{M}}} \Delta \hat{a} + \hat{\underline{\underline{G}}} \Delta \hat{v} + \hat{\underline{\underline{K}}} \Delta \hat{q} = \hat{\underline{\underline{F}}}^{\text{ext}} - \hat{\underline{\underline{F}}} \quad (2.57)$$

where

$$\hat{\underline{\underline{M}}} = \int_0^l \underline{\underline{N}}^T \underline{\underline{\mathcal{M}}} \underline{\underline{N}} d\alpha_1 \quad (2.58)$$

$$\hat{\underline{\underline{G}}} = \int_0^l \left[\underline{\underline{N}}^T (\underline{\underline{\mathcal{G}}}^I + \underline{\underline{\mathcal{X}}}^d) \underline{\underline{N}} + \underline{\underline{N}}'^T \underline{\underline{\mathcal{G}}}^d \underline{\underline{N}} + \underline{\underline{N}}'^T \underline{\underline{\mathcal{E}}}^d \underline{\underline{N}}' + \underline{\underline{N}}^T \underline{\underline{\mathcal{Y}}}^d \underline{\underline{N}}' \right] d\alpha_1 \quad (2.59)$$

$$\hat{\underline{\underline{K}}} = \int_0^l \left[\underline{\underline{N}}^T (\underline{\underline{\mathcal{K}}}^I + \underline{\underline{\mathcal{Q}}} + \underline{\underline{\mathcal{Q}}}^d) \underline{\underline{N}} + \underline{\underline{N}}'^T (\underline{\underline{\mathcal{S}}} + \underline{\underline{\mathcal{S}}}^d) \underline{\underline{N}}' \right. \quad (2.60)$$

$$\left. + \underline{\underline{N}}'^T (\underline{\underline{\mathcal{Q}}} + \underline{\underline{\mathcal{Q}}}^d) \underline{\underline{N}} + \underline{\underline{N}}^T (\underline{\underline{\mathcal{P}}} + \underline{\underline{\mathcal{P}}}^d) \underline{\underline{N}}' \right] d\alpha_1 \quad (2.61)$$

$$\hat{\underline{\underline{F}}} = \int_0^l \left[\underline{\underline{N}}^T \underline{\mathcal{F}}^I + \underline{\underline{N}}'^T (\underline{\mathcal{F}}^C + \underline{\mathcal{F}}^{dC}) + \underline{\underline{N}}^T (\underline{\mathcal{F}}^D + \underline{\mathcal{F}}^{dD}) \right] d\alpha_1 \quad (2.62)$$

$$\hat{\underline{\underline{F}}}^{\text{ext}} = \int_0^l \underline{\underline{N}}^T \underline{\mathcal{F}}^{\text{ext}} d\alpha_1 \quad (2.63)$$

The aerodynamics forces and moments that will be acting on the rotor blade are formulated

in the following section. These external loads are included in the beam formulation through the $\hat{\underline{F}}^{\text{ext}}$ term.

2.2 Aerodynamic Formulations

An unsteady aerodynamics theory developed by Peters et al. [139] will be used in this study to obtain the aerodynamic loads acting on the beam. The aerodynamic loads will be computed at distinct locations along the beam. Airfoils are assumed to be rigidly attached to the beam elements. Figure 2.2 shows an airfoil attached to the beam element at point S along the curvilinear coordinate location s_i . The motion of the airfoil is determined by the motion of the beam. Each airfoil has an airstation, A, as shown in Figure 2.2, where the aerodynamic loads are computed. An orthonormal basis $\mathcal{A}_o = (\bar{a}_1, \bar{a}_2, \bar{a}_3)$ defines the orientation of the airfoil. The airfoil lies in a plane passing through the point A and perpendicular to \bar{a}_1 . \bar{a}_2 is along the airfoil leading edge and \bar{a}_3 is along the positive lift direction. An orthonormal basis $\mathcal{E} = (\bar{e}_1, \bar{e}_2, \bar{e}_3)$ is defined at point S, which defines the orientation of the beam's cross-sectional plane. Orientation of \mathcal{A}_o and \mathcal{E} need not coincide. The cross-sectional plane passes through the point S and perpendicular to \bar{e}_1 . \bar{e}_1 is tangent to the curvilinear line. The aerodynamic properties of the airfoil are assumed to be unaffected by the warping of the cross-section. Also, the airfoil is rigid and does not contribute any additional inertial properties to the beam.

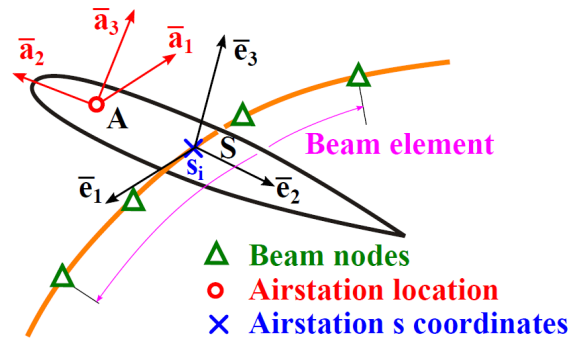


Figure 2.2: Airfoil and airstation configuration.

Airstation is typically located at quarter-chord of the airfoil. The kinematics of the airfoil is obtained by assuming a rigid body motion in the inertial frame as shown in Figure 2.3.

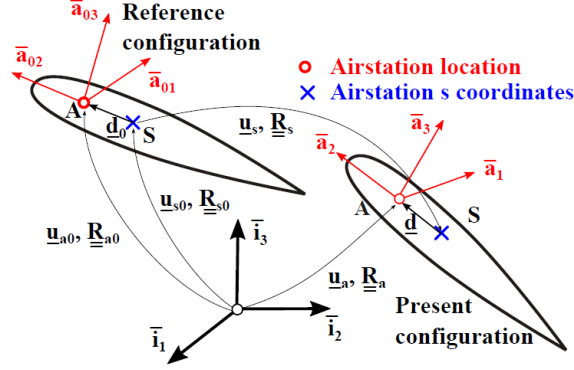


Figure 2.3: Airfoil motion.

The position vector of S and A in the reference configuration is given as \underline{u}_{s0} and \underline{u}_{a0} , respectively. In the reference configuration, the inertial orientation of the cross-section is given by \underline{R}_{s0} and the airfoil orientation is given by \underline{R}_{a0} . The position vector of the airstation in reference configuration is

$$\underline{u}_{a0} = \underline{u}_{s0} + \underline{d}_0 \quad (2.64)$$

If the point S translates and rotates as specified by \underline{u}_s and \underline{R}_s , respectively, then the new position of A is given by

$$\underline{u}_a = \underline{u}_{s0} + \underline{u}_s + \underline{d} = \underline{u}_{s0} + \underline{u}_s + \underline{R}_s \underline{d}_0 \quad (2.65)$$

The orientation of \mathcal{A}_o basis is given by $\underline{R}_a = \underline{R}_s \underline{R}_{a0}$. Since the airfoil is rigid, the angular velocity of A and S are identical, and so are the angular accelerations. Hence, $\underline{\omega} = \underline{\omega}_a = \underline{\omega}_s$ and $\underline{\dot{\omega}} = \underline{\dot{\omega}}_a = \underline{\dot{\omega}}_s$. Therefore, the velocity and acceleration of point A is given as

$$\underline{v}_a = \underline{v}_s + \underline{\tilde{\omega}}_s \underline{d}, \quad \underline{\dot{v}}_a = \underline{\dot{v}}_s + (\underline{\dot{\tilde{\omega}}}_s + \underline{\tilde{\omega}}_s \underline{\tilde{\omega}}_s) \underline{d} \quad (2.66)$$

In order to comply with the aerodynamic convention, the airstation is assumed to be located at the quarter-chord, coinciding with the aerodynamic center. Relative flow velocity is usually required for the formulation of unsteady aerodynamic theories. Hence, the relative velocity of the flow with respect to the airfoil's quarter chord and mid-chord is given, respectively, as

$$\hat{\underline{v}}_a^{qc} = \underline{V}_\infty + \underline{\lambda} - \underline{v}_a \quad (2.67)$$

$$\hat{\underline{v}}_a^{mc} = \hat{\underline{v}}_a^{qc} - \tilde{\omega}_a \underline{\eta} = (\underline{V}_\infty + \underline{\lambda} - \underline{v}_a) - \tilde{\omega}_a \underline{\eta} \quad (2.68)$$

where \underline{V}_∞ is the far field flow velocity, which is of constant magnitude and direction, and $\underline{\lambda}$ is the average inflow velocity over the airfoil. $\underline{\eta}$ is the quarter-chord position vector with respect to the mid-chord as shown in Figure 2.4.

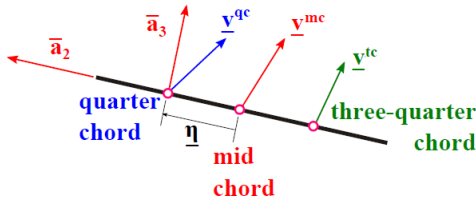


Figure 2.4: Velocity vectors on the airfoil.

The quarter-chord and mid-chord relative velocities in the airfoil basis \mathcal{A}_o can be written as

$$\hat{\underline{v}}_a^{qc**} = \underline{\underline{R}}_a^T (\underline{V}_\infty + \underline{\lambda} - \underline{v}_a) \quad (2.69)$$

$$\hat{\underline{v}}_a^{mc**} = \underline{\underline{R}}_a^T [(\underline{V}_\infty + \underline{\lambda} - \underline{v}_a) - \tilde{\omega}_a \underline{\eta}] \quad (2.70)$$

where $()^{**}$ denotes that the components of a vector or a tensor is in the \mathcal{A}_o basis. The components of the relative velocity in equation (2.69) can be defined as

$$\hat{\underline{v}}_a^{qc**} = \underline{\underline{R}}_a^T \hat{\underline{v}}_a^{qc} = \begin{Bmatrix} U_1 \\ -U_2 \\ U_3 \end{Bmatrix} \quad (2.71)$$

where U_1 is the radial velocity component i.e., the velocity along \bar{a}_1 . U_2 and U_3 are shown in Figure 2.5. The negative sign of U_2 is to be consistent with the sign convention used in aerodynamic theories.

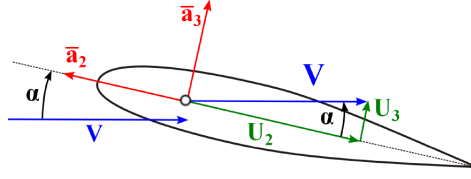


Figure 2.5: Relative velocity with respect to the quarter-chord.

The relative flow acceleration at the quarter chord is obtained by taking the time derivative of equation (2.71). Therefore, $\hat{\underline{a}}_a^{qc**} = \dot{\underline{v}}_a^{qc**} = \underline{R}_a^T \tilde{\omega}^T \hat{\underline{v}}_a^{qc} + \underline{R}_a^T \dot{\underline{v}}_a^{qc} = \tilde{\omega}^{**T} \hat{\underline{v}}_a^{qc**} - \underline{R}_a^T \dot{\underline{v}}_a^{qc}$. It is assumed that $\dot{\underline{v}}_a^{qc} \approx -\underline{v}_a^{qc}$ as far field velocity and average inflow are assumed not to change significantly. The components of acceleration vector in \mathcal{A}_o basis is given as $(\hat{\underline{a}}_a^{qc**})^T = \{A_1, -A_2, A_3\}$. Also, the radial velocity is ignored as the unsteady theory used here focuses on the flow components in the airfoil plane. Hence, the acceleration component A_3 is given as $A_3 = \omega_2^{**} U_1 + \omega_1^{**} U_2 - \dot{v}_{a3}^{**} \approx \omega_1^{**} U_2 - \dot{v}_{a3}^{**}$. Therefore, the magnitude of the resultant velocity is given as

$$V = \sqrt{U_2^2 + U_3^2} \quad (2.72)$$

The angle of attack α shown in Figure 2.5 is defined by the equations

$$U_2 = V \cos(\alpha), \quad U_3 = V \sin(\alpha) \quad (2.73)$$

2.2.1 Unsteady Aerodynamics

Once the velocities over the airfoil are defined, the loads are computed from the unsteady aerodynamics theory developed by Peters et al. [139]. The expressions for circulation over the airfoil and the pressure drop across the airfoil is given in detail in [139] and [105]. The final expressions for loads acting on the airfoil will be provided here. Since we are analyzing a rotor, the inflow is computed from the finite state three-dimensional induced inflow model developed in [140]. This inflow model will be discussed in the later part of this chapter. For a thin rigid airfoil in a two-dimensional inviscid and incompressible flow,

the steady loads are given as

$$L^s = a_0 \rho_a b U_2 U_3 \quad (2.74)$$

$$D^s = a_0 \rho_a b U_3^2 \quad (2.75)$$

$$M^s = a_0 \rho_a \frac{b^2}{2} U_2 U_3 - \frac{b}{2} L^s = 0 \quad (2.76)$$

where L^s , D^s and M^s are the steady lift, drag and moment about the quarter chord, respectively. L^s is along \bar{a}_3 , D^s is along \bar{a}_2 and nose-up moment is positive. a_0 is the slope of the lift curve, ρ_a is the density of air and b is half the chord length. The unsteady components of load are given as

$$L^{us} = a_0 \rho_a b^2 U_2 \omega_1 - a_0 \rho_a \frac{b^2}{2} \dot{v}_{a3} \quad (2.77)$$

$$D^{us} = 0 \quad (2.78)$$

$$M^{us} = -a_0 \rho_a \frac{b^4}{16} \dot{\omega}_1 - \frac{b}{2} L^{us} \quad (2.79)$$

where ω_1 is the pitch rate of the airfoil about \bar{a}_1 axis, nose-up rotation is assumed to be positive. Since the Peters et al. unsteady aerodynamic theory is obtained for a thin airfoil in an inviscid, incompressible flow, the results are approximate in nature. Hence, these results could be improved by introducing correction terms from wind-tunnel experiments (or CFD results). An airfoil test set-up to obtain steady loads in a wind tunnel is shown in Figure 2.6. L^{wt} is the force normal to the flow direction, which has the expression

$$L^{wt} = c_\ell(\alpha, M) \rho_a b V^2 \quad (2.80)$$

where c_ℓ is the experimental lift coefficient, which is a function of angle of attack α and Mach number M . The steady lift and drag loads from the unsteady theory can be rewritten

as follows.

$$L^s = a_0 \rho_a b U_2 U_3 = \rho_a b V^2 a_0 \frac{U_3}{V} \frac{U_2}{V} = \rho_a b V^2 (a_0 \sin(\alpha)) \cos(\alpha) \quad (2.81)$$

$$D^s = a_0 \rho_a b U_3 U_3 = \rho_a b V^2 a_0 \frac{U_3}{V} \frac{U_3}{V} = \rho_a b V^2 (a_0 \sin(\alpha)) \sin(\alpha) \quad (2.82)$$

From the Figure 2.6, it is seen that

$$L^s = L^{wt} \cos(\alpha) \quad (2.83)$$

$$D^s = L^{wt} \sin(\alpha) \quad (2.84)$$

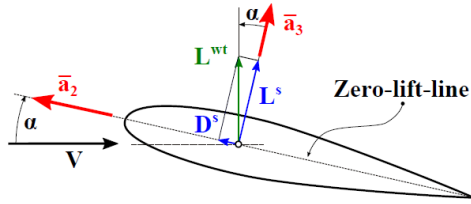


Figure 2.6: Airfoil with wind tunnel lift.

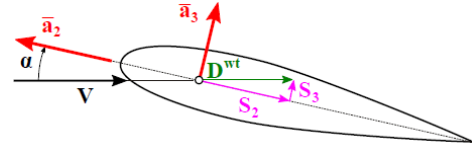


Figure 2.7: Airfoil with wind tunnel drag.

If $c_\ell(\alpha, M) = a_0 \sin \alpha$, then the theoretical value and experimental measurement are one and the same. If a table of c_ℓ is given for an airfoil, then the corrected lift and drag loads can be computed. If the steady state moment about the quarter-chord is measured, then

$$M^{wt} = c_m(\alpha, M) 2\rho_a b^2 V^2 \quad (2.85)$$

where c_m is the experimental moment coefficient. Therefore, including the correction terms equations 2.81, 2.82 and moment can be written as

$$\hat{L}^s = c_\ell(\alpha, M) \rho_a b V U_2 \quad (2.86)$$

$$\hat{D}^s = c_\ell(\alpha, M) \rho_a b V U_3 \quad (2.87)$$

$$\hat{M}^s = c_m(\alpha, M) 2\rho_a b^2 V^2 \quad (2.88)$$

Peters unsteady theory assumes that the flow is inviscid and hence, viscous drag forces are neglected. Once again, wind tunnel test data is used to include drag correction terms into the formulation. If D^{wt} is the drag force measured in the wind tunnel as shown in Figure 2.7, then

$$D^{wt} = c_d(\alpha, M) \rho_a b V^2 \quad (2.89)$$

where c_d is the experimental drag coefficient. The components of the drag force S_2 and S_3 , also shown in Figure 2.7, can be written as

$$S_2 = c_d(\alpha, M) \rho_a b V^2 \cos(\alpha) = c_d(\alpha, M) \rho_a b V U_2 \quad (2.90)$$

$$S_3 = c_d(\alpha, M) \rho_a b V^2 \sin(\alpha) = c_d(\alpha, M) \rho_a b V U_3 \quad (2.91)$$

Next, we try to estimate the skin friction drag acting on the airfoil. If there is flow along the blade in \bar{a}_1 direction, then the magnitude of the resultant velocity of U_1 and U_2 components is defined as $V_R = \sqrt{U_1^2 + U_2^2}$. Contribution to skin friction drag from U_3 component is assumed to be small, and therefore neglected. Let c_{d0} be the skin friction drag coefficient, which is estimated to be equal to the c_d value at zero lift condition. Skin friction drag force is defined as

$$D^{sf} = c_{d0}(M) \rho_a b V_R^2 \quad (2.92)$$

The components of skin friction drag are $S_1^{sf} = c_{d0} \rho_a b V_R U_1$ and $S_2^{sf} = c_{d0} \rho_a b V_R U_2$. On carefully adding these terms to equations (2.90) and (2.91), we get the total drag expressions as

$$S_1 = S_1^{sf} = c_{d0}(M) \rho_a b V_R U_1 \quad (2.93)$$

$$S_2 = c_d(\alpha, M) \rho_a b V U_2 - c_{d0}(M) \rho_a b U_2^2 + c_{d0}(M) \rho_a b V_R U_2 \quad (2.94)$$

$$S_3 = c_d(\alpha, M) \rho_a b V U_3 \quad (2.95)$$

The second term in equation (2.94) is to ensure that the skin friction drag is not double counted from the other two terms in the equation.

2.2.2 ONERA Dynamic Stall

Another aerodynamic phenomenon that needs to be accounted for analysis of helicopter rotor blades is the dynamic stall effect. Dynamic stall affects the loads acting on the airfoil. ONERA dynamic stall model will be used in the current work. This model is based on the delayed dynamic stall and the second-order linear differential equation to compute circulation Γ , the circulation per unit span of the blade.

$$\frac{d^2\Gamma}{dt^2} + \eta\bar{V}\frac{d\Gamma}{dt} + \omega^2\bar{V}^2\Gamma = -V\omega^2(\bar{V}^2\Delta C + e\bar{V}\frac{d\Delta C}{dt}) \quad (2.96)$$

The differential equation for lift, drag and moment is obtained by replacing Γ by Γ_L , Γ_D and Γ_M , respectively. ΔC is the difference in aerodynamic coefficient between its linear static value extrapolated in the stalled region and its actual value at the angle of attack considered [105]. ΔC is replaced by ΔC_L , ΔC_D and ΔC_M based on the equation being solved and $\bar{V} = V/b$. More details of the derivation are provided in [141, 142]. The parameters ω , η and e are defined as

$$\omega = \omega_0 + \omega_1\Delta C_L^2, \quad \eta = \eta_0 + \eta_1\Delta C_L^2, \quad e = e_0 + e_1\Delta C_L^2 \quad (2.97)$$

The parameters ω_0 , ω_1 , η_0 , η_1 , e and e_1 are specific to a given airfoil and depend on the Mach number of the flow. The range of values for these parameters is provided in [105]. On solving the governing differential equation, the dynamic stall loads are given as

$$L^{DS} = \rho_a V b \Gamma_L \quad (2.98)$$

$$D^{DS} = \rho_a V b \Gamma_D \quad (2.99)$$

$$M^{DS} = 2\rho_a V b^2 \Gamma_M \quad (2.100)$$

2.2.3 Inflow Model

The inflow model used in this study was developed by Peters and He [140]. It is a finite-state three-dimensional generalized dynamic wake theory. The formulations are based on quasi-steady potential flow with small perturbations. Starting with the continuity and momentum equations, a general solution for pressure potential is obtained. The potential, Φ , written as a Fourier expansion is

$$\Phi(\nu, \eta, \psi, \bar{t}) = \sum_{m=0}^{\infty} \sum_{n=m+1, m+3}^{\infty} P_n^m Q_n^m(i\eta) [C_n^m(\bar{t}) \cos(m\psi) + D_n^m(\bar{t}) \sin(m\psi)] \quad (2.101)$$

where P_n^m and Q_n^m are the Legendre functions of the first and second kind, respectively, and C_n^m and D_n^m are the unknown coefficients. ν , η and ψ are the ellipsoidal coordinates and \bar{t} is the non-dimensional time variable, time variable multiplied with rotor speed. The rotor is assumed to be disk with a pressure jump across the disk. The rotor lift can be expressed as the pressure difference between the upper and lower surface of the disk. The above equation can be written at $\eta = 0$ in terms of the azimuth angle ψ and non-dimensional radial location \bar{r} as

$$P(\bar{r}, \psi, \bar{t}) = \sum_{m=0}^{\infty} \sum_{n=m+1, m+3}^{\infty} \bar{P}_n^m(\nu) [\tau_n^{mc}(\bar{t}) \cos(m\psi) + \tau_n^{ms}(\bar{t}) \sin(m\psi)] \quad (2.102)$$

\bar{r} is non-dimensionalized with respect to rotor radius. Also,

$$\nu = \sqrt{1 - \bar{r}^2} \quad (2.103)$$

$$\bar{P}_n^m(\nu) = (-1)^m \frac{P_n^m}{\rho_n^m} \quad (2.104)$$

$$(\rho_n^m)^2 = \frac{(n+m)!}{(2n+1)(j-m)!} \quad (2.105)$$

$$\tau_n^{mc}(\bar{t}) = (-1)^{m+1} 2Q_n^m(i0)\rho_n^m C_n^m \quad (2.106)$$

$$\tau_n^{ms}(\bar{t}) = (-1)^{m+1} 2Q_n^m(i0)\rho_n^m D_n^m \quad (2.107)$$

Analogously, the induced inflow velocity normal to the disk, w , is also assumed to have a Fourier series form. The series is also in terms of the azimuth angle ψ and non-dimensional radial location \bar{r} .

$$w(\bar{r}, \psi, \bar{t}) = \sum_{r=0}^{\infty} \sum_{j=r+1, r+3}^{\infty} \Psi_j^r(\bar{r}) [\alpha_j^r(\bar{t}) \cos(r\psi) + \beta_j^r(\bar{t}) \sin(r\psi)] \quad (2.108)$$

Ψ_j^r should be a complete set of linearly independent functions in terms of \bar{r} . Ψ_j^r is assumed to be

$$\Psi_j^r = \phi_j^r(\bar{r}) = \frac{1}{\nu} \bar{P}_j^r(\nu) \quad (2.109)$$

The function ϕ_j^r is given as

$$\phi_j^r(\bar{r}) = \sqrt{(2j+1)H_j^r} \sum_{q=r, r+2}^{j-1} \bar{r}^q \frac{(-1)^{(q-r)/2} (j+q)!!}{(q-r)!! (q+r)!! (j-q-1)!!} \quad (2.110)$$

where

$$H_j^r = \frac{(j+r-1)!! (j-r-1)!!}{(j+r)!! (j-r)!!} \quad (2.111)$$

Now, we have to make the connection between the inflow velocity and pressure potential to solve for the unknown coefficients. The induced inflow velocity (w) and the pressure potential (Φ) are related as follows [140].

$$w = -\frac{1}{V_{\infty}} \int_0^{\infty} \frac{\partial \Phi^V}{\partial z} d\xi \quad (2.112)$$

$$\frac{dw}{d\bar{t}} = -\frac{\partial \Phi^A}{\partial z} \Big|_{\eta=0} \quad (2.113)$$

ξ is the coordinate along the free stream, positive upstream. V_{∞} is the magnitude of far field flow velocity. Φ^V is the convection component of pressure and Φ^A is the perturbation component of pressure in the direction of the flow. Therefore, $\Phi = \Phi^V + \Phi^A$. Substituting

the expressions for w and Φ in the above equations, we obtain an algebraic set of equations with α_j^r and β_j^r as unknowns.

$$\frac{2}{\pi} H_n^m \alpha_j^{r+} + L_c^{-1} V_n^m \alpha_j^r = \frac{1}{2} \tau_n^{mc} \quad (2.114)$$

$$\frac{2}{\pi} H_n^m \beta_j^{r+} + L_s^{-1} V_n^m \beta_j^r = \frac{1}{2} \tau_n^{ms} \quad (2.115)$$

The expressions for L_c^{-1} , L_s^{-1} and V_n^m are provided in [140]. The average induced velocity is given by $\sqrt{3}\alpha_1^0$. The right hand side terms are the load terms which are obtained from the unsteady aerodynamics theory discussed previously. Hence, the system of equations are solved to obtain the inflow velocity w , which is then reinserted into the unsteady theory to update the loads. This feedback loop is shown in Figure 2.8.

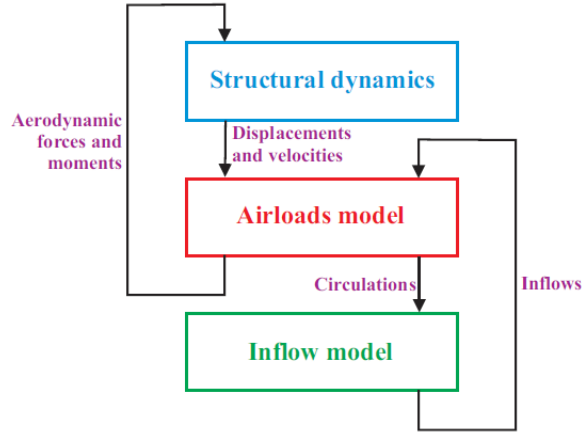


Figure 2.8: Data flow between structural, unsteady aerodynamics and inflow model.

2.2.4 Total Air Loads

The total loads that are acting on the airfoil can be written as a sum of steady loads with wind tunnel corrections, unsteady loads and dynamic stall loads. Inflow model goes into the load calculation as discussed in the previous section. Let F_1 , F_2 and F_3 be the forces acting in \bar{a}_1 , \bar{a}_2 and \bar{a}_3 directions, respectively. M_1 , M_2 and M_3 are the moments acting

about \bar{a}_1 , \bar{a}_2 and \bar{a}_3 axes, respectively. The total loads can be written as

$$F_1 = S_1 \quad (2.116)$$

$$F_2 = f_{tl}(\hat{D}^s + D^{us} + D^{DS}) - S_2 \quad (2.117)$$

$$F_3 = f_{tl}(\hat{L}^s + L^{us} + L^{DS}) + S_3 \quad (2.118)$$

$$M_1 = f_{tl}(\hat{M}^s + M^{us} + M^{DS}) \quad (2.119)$$

$$M_2 = 0 \quad (2.120)$$

$$M_3 = 0 \quad (2.121)$$

where f_{tl} is the tip loss factor, which ensures that the aerodynamic lift vanishes at the tip of the rotor blade.

Hence, the structural and aerodynamic formulations that will go into the analysis of the rotor blade is given in this chapter. In the next chapter, rotor blade modeling and rotor trimming using DYMORE will be discussed along with the other results pertaining to variable speed rotor analysis.

CHAPTER 3

ROTOR MODELING AND TRIM METHOD VALIDATION

3.1 Blade Modeling

The rotor blade model that will be used in this study will be built in DYMORE. The multi-body dynamics capabilities of DYMORE along with the inclusion of geometrically exact beam theory for blade analysis and sufficiently comprehensive aerodynamic models made DYMORE a good choice for studying variable speed rotors. The characteristics of the blade model built in DYMORE will be discussed in this section.

The analysis in the present work will be focused on hingeless rotor systems. A schematic diagram of a typical hingeless rotor assembly with the hub, the upper swash plate, a pitch-link and a rotor blade is shown in Figure 3.1.

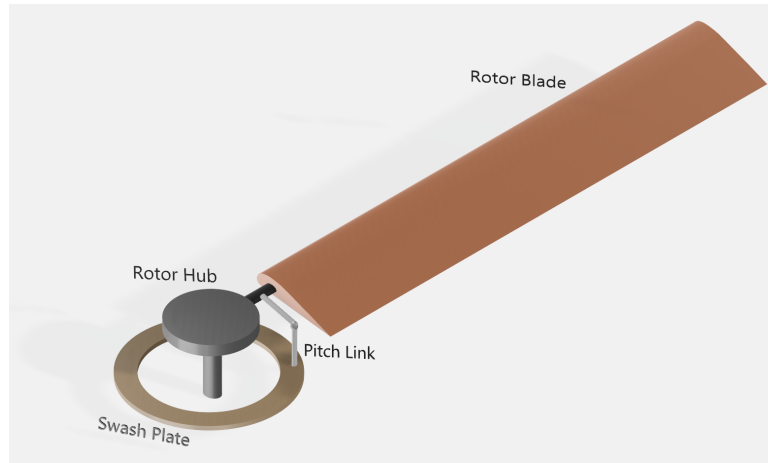


Figure 3.1: Schematic of a hingeless rotor.

The rotor model built in DYMORE will be a simplified version of the hingeless rotor system. The hub rotation about the mast axis and the pitching of the blade about the feathering axis will be modeled using revolute joints. The rotor blade will be modeled as a one-dimensional beam discretized into finite-elements. The distance between the hub

center and the rotor blade's root attachment point is assumed to be zero. A representation of this model is shown in Figure 3.2.

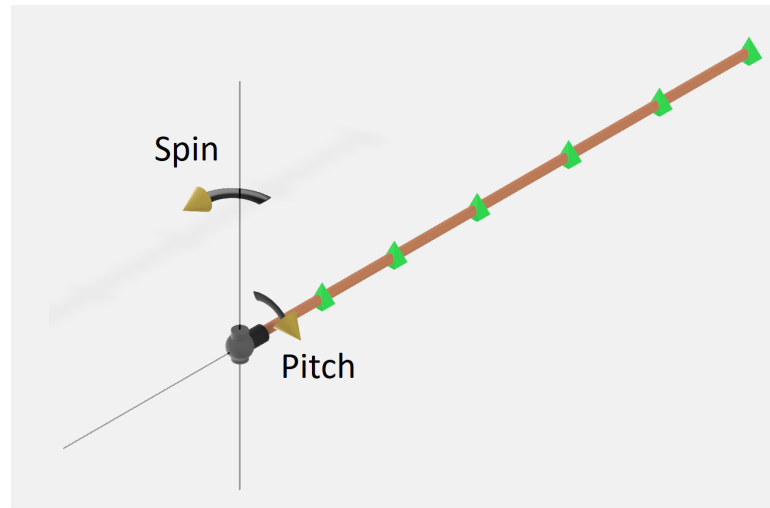


Figure 3.2: Hingeless rotor blade model in DYMORE.

The green triangles represent the end nodes of a finite element used to discretize the blade, as shown in Figure 3.3. The number of finite elements and the order of the finite element's shape function will be chosen such that the blade's response is converged.

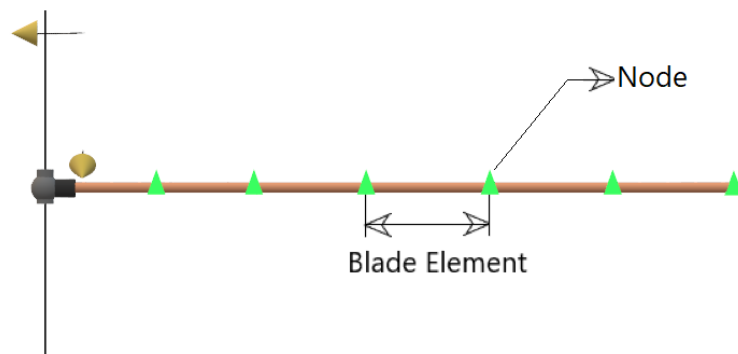


Figure 3.3: Four-bladed rotor system.

Hence, a four-bladed hingeless rotor system shown in Figure 3.4 can be modeled in DYMORE as beam elements as shown in Figure 3.5. This allows one to capture the physics of the rotor blade and the rotor system without inheriting the complexities of an actual rotor hub assembly.

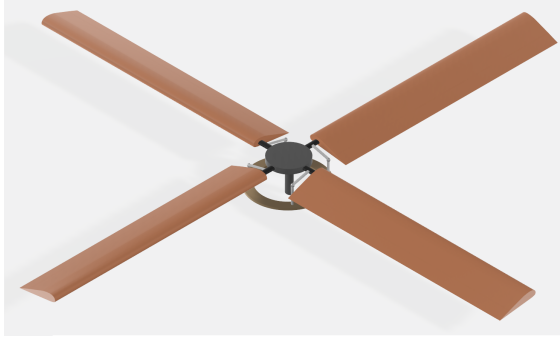


Figure 3.4: Four-bladed rotor system.

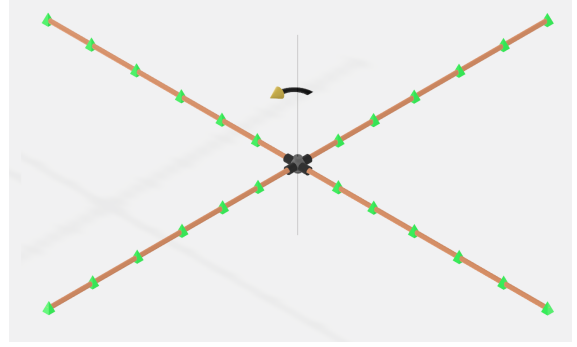


Figure 3.5: Rotor model in DYMORE.

At this point, let us define some important frames. Let \mathbf{I} be a frame that is located at the hub center with unit vectors $(\bar{\mathbf{i}}_1, \bar{\mathbf{i}}_2, \bar{\mathbf{i}}_3)$. The orientation of this frame doesn't change with time and is assumed to be aligned with the inertial frame. Let \mathbf{H} $(\bar{\mathbf{h}}_1, \bar{\mathbf{h}}_2, \bar{\mathbf{h}}_3)$ be the hub frame which is attached to the hub center and tilts with the mast but doesn't spin. The unit vector $\bar{\mathbf{h}}_3$ is along the mast axis. The plane containing $\bar{\mathbf{h}}_1$ and $\bar{\mathbf{h}}_2$ will be known as the hub plane. The angle the hub plane makes with the free stream flow is given as α as shown in Figure 3.6.

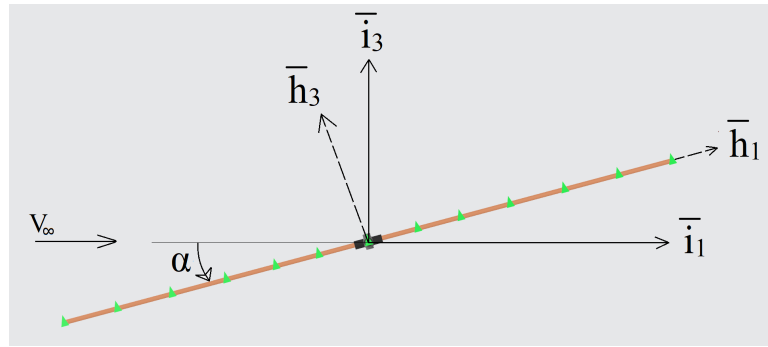


Figure 3.6: Hub plane tilt and free stream velocity.

Let \mathbf{r} $(\bar{\mathbf{r}}_1, \bar{\mathbf{r}}_2, \bar{\mathbf{r}}_3)$ be a frame with origin at the hub center which tilts with the hub plane and also moves with the blade as the blade spins. $\bar{\mathbf{r}}_3$ and $\bar{\mathbf{h}}_3$ are always aligned in the same direction. $\bar{\mathbf{r}}_1$ is initially along $\bar{\mathbf{h}}_1$ and makes an angle ψ with $\bar{\mathbf{h}}_1$ as the rotor spins about $\bar{\mathbf{h}}_3$ as shown in Figure 3.7. ψ is the azimuthal displacement of the blade.

As the blade travels in the azimuthal direction, the pitch of the blade is varied to counter the differential lift that arises from the advancing and retreating sides of the blade. The

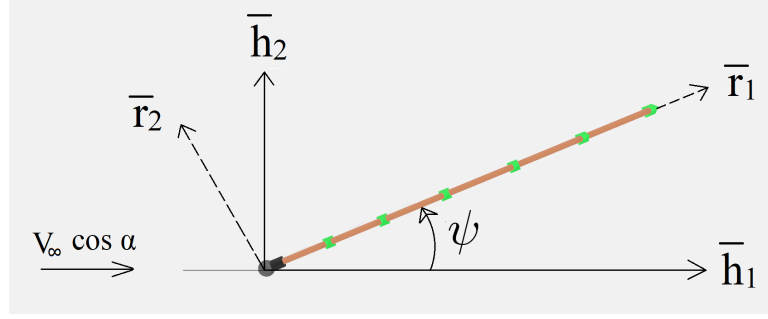


Figure 3.7: Blade azimuth angle.

pitching motion is considered to be a first harmonic function of azimuth as

$$\theta(\psi) = \theta_0 + \theta_{1s} \sin(\psi) + \theta_{1c} \cos(\psi) \quad (3.1)$$

where θ_0 is the collective pitch angle, θ_{1s} is the longitudinal cyclic pitch angle and θ_{1c} is the lateral cyclic pitch angle. Trimming the rotor involves finding these coefficients for a given flight condition. This will be discussed in detail in the next section.

In order to compute the aerodynamic loads, it is necessary to define the airstation locations on the rotor blade. The airstation location is determined by airstation coordinate as discussed in the previous chapter. The location of the airstation coordinate need not coincide with the beam's finite element nodal locations, as shown in Figure 3.8. In this study, the airstation coordinates are usually assumed to be located at the Gaussian points along the beam, unless otherwise specified.

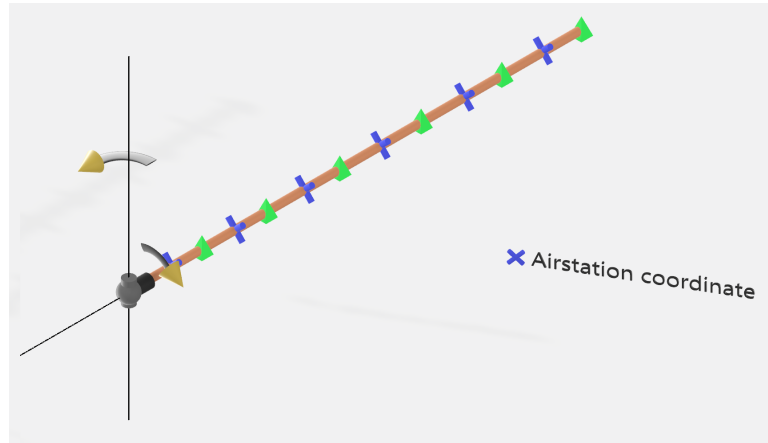


Figure 3.8: Airstation coordinates on a rotor blade.

The dynamic response of the rotor blade will be obtained by solving the equation of motion of the beam using time integration schemes. The generalized- α time marching scheme will be used in the present work [116]. Generalized- α scheme is proven to be a great tool for solving structural dynamics and multi-body problems with large number of degrees of freedom.

3.2 Rotor Trim

As discussed in the first chapter, it is important to trim the rotor in order to perform any sort of aeroelastic analysis. The trim procedure used in the present work will be an amalgamation of wind tunnel trim and propulsive trim described in [48]. Since our rotor doesn't have a fuselage attached to it, the procedure will be very similar to wind tunnel trim. However, instead of specifying collective pitch as described in [48], thrust will be specified to obtain vertical force balance.

The thrust force and moments acting on the hub is shown in Figures 3.9 and 3.10. T is the thrust resultant, which is a sum of all the thrust forces generated by each blade, acting at the hub center and along \bar{h}_3 . M_P is the pitching moment about the hub center, measured positively along \bar{h}_2 . M_R is the roll moment about the hub center, measured positively along \bar{h}_1 .

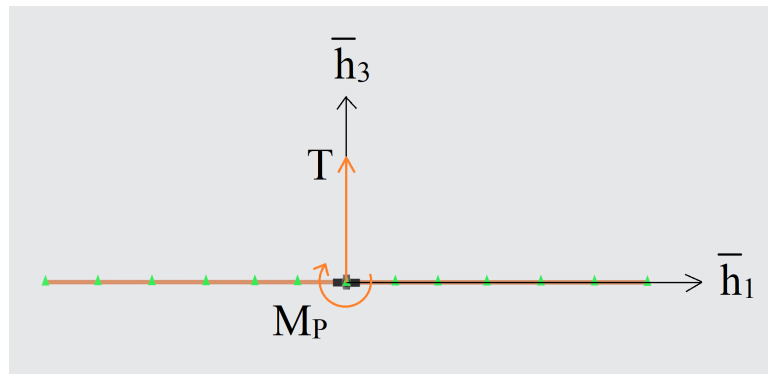


Figure 3.9: Thrust force and pitching moment at the hub center.

Since a time marching scheme is used to determine the blade response, an auto-pilot

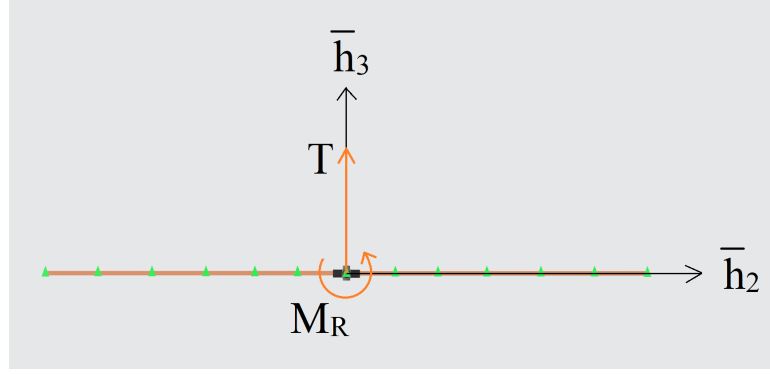


Figure 3.10: Roll moment at the hub center.

controller can be used to trim the rotor. The auto-pilot controller monitors the hub loads continuously and corrects the control inputs to reach the specified state. The hub loads that are averaged over a complete rotation will be used for rotor trimming. In our case, the pitch angles θ_0 , θ_{1s} and θ_{1c} will be the control inputs which will be corrected continuously. The hub loads that will be monitored and specified are T , M_P and M_R . A Butterworth filter will be used to obtain an average value of these quantities. It is necessary to specify initial guess values for the pitch angles, which will determine the hub loads for a given flight condition. Let us call this to be the reference state of the rotor. The controller then drives the pitch angles so that the specified or target value of hub loads are achieved. When the specified hub loads are achieved, the rotor is said to be in a trimmed state. The auto-pilot control law used is as follows

$$\begin{bmatrix} \theta_0 \\ \theta_{1s} \\ \theta_{1c} \end{bmatrix}_f = \begin{bmatrix} \theta_0 \\ \theta_{1s} \\ \theta_{1c} \end{bmatrix}_i + \Delta t [J]^{-1} \begin{bmatrix} g_1 & 0 & 0 \\ 0 & g_2 & 0 \\ 0 & 0 & g_3 \end{bmatrix} \left\{ \begin{bmatrix} T \\ M_P \\ M_R \end{bmatrix}_{Target} - \begin{bmatrix} T \\ M_P \\ M_R \end{bmatrix}_i \right\} \quad (3.2)$$

where Δt is the time step size, given as $\Delta t = t_f - t_i$. t_f and t_i are the final and initial times of the time step, respectively. Subscripts f and i represent the quantities at final and initial time, respectively. J is the Jacobian matrix, which is evaluated as shown in equation (3.3). g_1 , g_2 and g_3 are the gain values that ensure that the pitch angles are changed incrementally.

Sharp change in the pitch angles could destabilize the time integration scheme.

$$J = \begin{bmatrix} \frac{\partial T}{\partial \theta_0} & \frac{\partial T}{\partial \theta_{1s}} & \frac{\partial T}{\partial \theta_{1c}} \\ \frac{\partial M_P}{\partial \theta_0} & \frac{\partial M_P}{\partial \theta_{1s}} & \frac{\partial M_P}{\partial \theta_{1c}} \\ \frac{\partial M_R}{\partial \theta_0} & \frac{\partial M_R}{\partial \theta_{1s}} & \frac{\partial M_R}{\partial \theta_{1c}} \end{bmatrix} \quad (3.3)$$

The ability of the controller to trim the rotor depends significantly on the Jacobian matrix. In order to compute the Jacobian, consider the rotor in its reference state. In this state, the initial pitch angles are perturbed by a small quantity one after the other. When a pitch angle is perturbed, the rotor is allowed to spin until it reaches a steady load state. These new hub loads obtained at the end are used to compute the unknown first order derivatives in equation (3.3) using a finite difference process. Hence, perturbing θ_0 by $\Delta\theta_0$ allows one to compute the first column of the Jacobian matrix. Similarly, the second and third column can be computed by perturbing θ_{1s} and θ_{1c} , respectively. The Jacobian matrix can be written in the finite difference form as

$$J = \begin{bmatrix} \frac{T_{pert} - T_{ref}}{\Delta\theta_0} & \frac{T_{pert} - T_{ref}}{\Delta\theta_{1s}} & \frac{T_{pert} - T_{ref}}{\Delta\theta_{1c}} \\ \frac{(M_P)_{pert} - (M_P)_{ref}}{\Delta\theta_0} & \frac{(M_P)_{pert} - (M_P)_{ref}}{\Delta\theta_{1s}} & \frac{(M_P)_{pert} - (M_P)_{ref}}{\Delta\theta_{1c}} \\ \frac{(M_R)_{pert} - (M_R)_{ref}}{\Delta\theta_0} & \frac{(M_R)_{pert} - (M_R)_{ref}}{\Delta\theta_{1s}} & \frac{(M_R)_{pert} - (M_R)_{ref}}{\Delta\theta_{1c}} \end{bmatrix} \quad (3.4)$$

where the notation $(\)_{pert}$ refers to the steady state quantity in the perturbed state with respect to the perturbation quantity in the denominator. The notation $(\)_{ref}$ refers to the reference state of the rotor. The Jacobian needs to be computed only once for a given reference state and it can be used to trim the rotor to different trim states. The Jacobian computed for a specific reference state was also found to work well in the neighboring reference states. Now, let us validate our model and trim procedure with a few results from literature.

3.3 Model Validation

In order to validate the trim procedure and the rotor model, we will be using the results from [155]. In [155], a hingeless rotor and fuselage system was trimmed using a propulsive trim procedure. The schematic of the rotor-fuselage system is shown in Figure 3.11. The fuselage was represented as a flat plate in [155] to compute the drag force acting on the fuselage. The resultant drag force acts through the drag center. Center of gravity, C.G., of the rotorcraft is located below the drag center as shown in the schematic diagram.

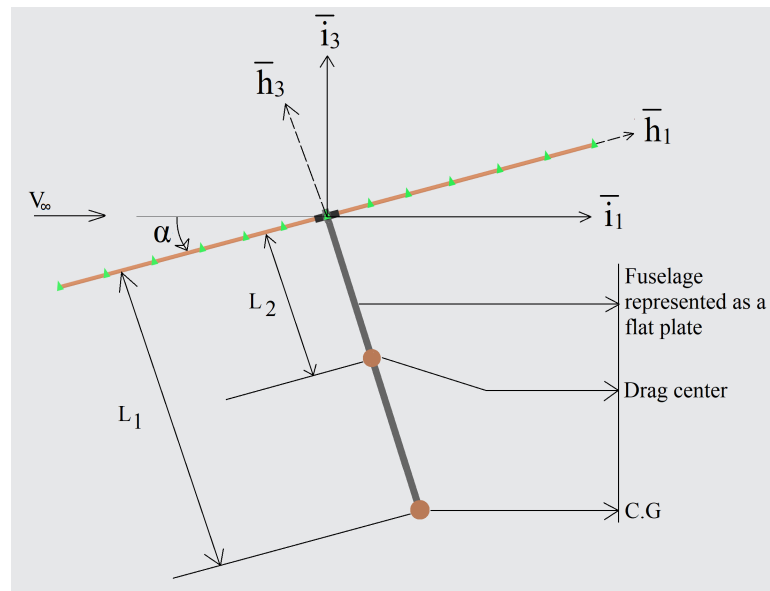


Figure 3.11: Schematic of rotor and fuselage.

Since we have our trim formulation setup only for wind tunnel trim, the propulsive trim problem needs to be transformed into a wind tunnel trim problem. In order to do this, let us consider the forces and moments acting on the rotor and fuselage as shown in Figure 3.12. F_L is the longitudinal rotor force along the hub plane. F_d is the resultant drag force acting along the free stream and W is the weight of the rotorcraft. Lateral forces were neglected during the trim procedure in [155].

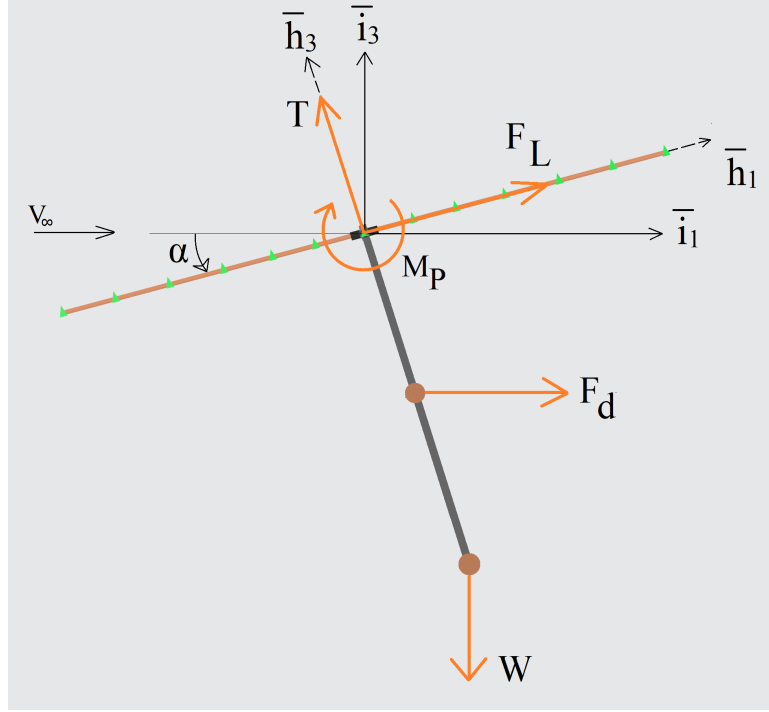


Figure 3.12: Forces and moments for propulsive trim.

The force and moment balance equations are as follows

$$\Sigma F_{\bar{\mathbf{i}}_1} = 0$$

$$-T \sin(\alpha) + F_L \cos(\alpha) + F_d = 0 \quad (3.5)$$

$$\frac{T \sin(\alpha) - F_d}{\cos(\alpha)} = F_L \quad (3.6)$$

$$\Sigma F_{\bar{\mathbf{i}}_3} = 0$$

$$T \cos(\alpha) + F_L \sin \alpha - W = 0 \quad (3.7)$$

$$T \cos(\alpha) + F_L \sin \alpha = W \quad (3.8)$$

Using the expression for F_L from equation (3.6), we get

$$T \cos(\alpha) + \frac{T \sin(\alpha) - F_d}{\cos(\alpha)} \sin \alpha = W \quad (3.9)$$

$$\frac{T \cos^2(\alpha) + T \sin^2(\alpha)}{\cos(\alpha)} - \frac{F_d}{\cos(\alpha)} = W \quad (3.10)$$

$$\frac{T}{\cos(\alpha)} - F_d \frac{\sin \alpha}{\cos \alpha} = W \quad (3.11)$$

$$W \cos(\alpha) + F_d \sin(\alpha) = T \quad (3.12)$$

$$\Sigma M_{C.G.} \bar{\mathbf{i}}_2 = 0$$

$$M_P + F_d(L_1 - L_2) \cos(\alpha) + F_L L_1 = 0 \quad (3.13)$$

$$-F_d(L_1 - L_2) \cos \alpha - F_L L_1 = M_P \quad (3.14)$$

$$-F_d(L_1 - L_2) \cos \alpha - \frac{T \sin(\alpha) - F_d}{\cos(\alpha)} L_1 = M_P \quad (3.15)$$

The drag force is given by the following expression

$$F_d = \frac{1}{2} \rho C_{df} A \cos(\alpha) V_\infty^2 \quad (3.16)$$

where C_{df} is the coefficient of drag for a flat plate and A is the flat plate area. For a flat plate $C_{df} = 1.28$.

Hence, for a given value of α , thrust and pitching moment can be computed from equation (3.12) and (3.15) for a given free stream velocity. On enforcing the roll moment to be zero, we have converted the propulsive trim problem in [155] into a wind tunnel trim problem. The auto pilot control law discussed in the previous section will be used to trim the rotor provided in [155]. The trim angles computed from our formulations will be compared with the trim angles provided in [155] as a validation exercise. The properties of a soft-in-plane rotor given in [155] is provided in Table 3.1. The nomenclature for the symbols used in Table 3.1 is provided in Table 3.2

The rotating non-dimensional first flap, lag and torsion frequencies of the blade used in [155] are given as

$$\omega_{F1} = 1.125 \quad \omega_{L1} = 0.732 \quad \omega_{T1} = 3.263 \quad (3.17)$$

Table 3.1: Rotor properties [155].

$m = 5.51 \text{ kg/m}$	$R = 4.91 \text{ m}$	$\Omega = 425 \text{ RPM}$
$EI_{Flap} = 6.7235 \times 10^4 \text{ Nm}^2$	$EI_{Lag} = 1.9092 \times 10^5 \text{ Nm}^2$	$GJ = 9.3430 \times 10^3 \text{ Nm}^2$
$EA = 5.1605 \times 10^7 \text{ N}$	$W = 2.1935 \times 10^4 \text{ N}$	$a = 2\pi$
$A = 0.75 \text{ m}^2$	$c = 0.27 \text{ m}$	$c_d = 0.01$
$B = 4$	$\tau = 0^\circ$	$L_1 = 2.45 \text{ m}$
$L_2 = 1.22 \text{ m}$	$mI_{Flap} = 0.00 \text{ kg m}$	$mI_{Lag} = 5.32 \times 10^{-2} \text{ kg m}$

These frequencies are non-dimensionalized using the rotor speed. A moderate deflection beam theory was used in [155]. In order to match these natural frequencies, a slightly different set of stiffness properties are used in our model. These properties are given in Table 3.3.

The torsional stiffness is same as in [155] while the flap and lag stiffnesses are slightly different. This could be because of the differences in beam formulations and a small amount of structural damping included in our model to ensure numerical stability. Rest of the rotor properties are same as shown in Table 3.1. The rotor blade was discretized into 10 finite elements. Third order finite elements were used in the discretization. This was sufficient to obtain converged results.

Quasi-steady Greenberg's aerodynamic theory was used in [155]. Stall effects were neglected and the inflow was assumed to be uniform. Hence, we will be using a quasi-steady version of Peter's aerodynamics model, which neglects the unsteady terms. The uniform inflow is achieved by using a single inflow state in the dynamic inflow model. The dynamic stall effects will be neglected as well to bring our aerodynamics model close to the aerodynamics model in [155] for the validation exercise.

The rotor angle, α , variation with the advanced ratio, μ , is taken from [155] as shown in

Table 3.2: Nomenclature.

Symbol		Symbol	
m	Mass per unit length (kg/m)	R	Rotor radius (m)
EI_{Flap}	Flapwise stiffness (Nm ²)	EI_{Lag}	Lagwise stiffness (Nm ²)
GJ	Torsional stiffness (Nm ²)	EA	Axial Stiffness (N)
W	Weight of helicopter (N)	a	Airfoil's lift curve slope
A	Fuselage plate area (m ²)	c	Airfoil chord length (m)
B	Number of blades	mI_{Flap}	Flapwise moment of inertia of the cross-section (kg m)
mI_{Lag}	Lagwise moment of inertia of the cross-section (kg m)	τ	Blade pre-twist angle (deg)

Table 3.3: Blade stiffness properties and natural frequencies (DYMORE)

$EI_{Flap} = 6.8350 \times 10^4 \text{ Nm}^2$	$EI_{Lag} = 1.9236 \times 10^5 \text{ Nm}^2$	$GJ = 9.3430 \times 10^3 \text{ Nm}^2$
$\omega_{F1} = 1.125$	$\omega_{L1} = 0.732$	$\omega_{T1} = 3.263$

Table 3.4. The corresponding thrust and pitching moment values computed from equation (3.12) and (3.15), respectively, are also presented in Table 3.4. Advance ratio is defined as $\mu = V_\infty/(\Omega R)$ in our study. The Jacobian matrix is computed for initial guess value of pitch angles and the rotor is trimmed for the states mentioned in Table 3.4. The time history of rotor trimming is shown in Figures 3.13 — 3.17.

Table 3.4: Rotor trim states at sea level.

μ	α (rad)	T (N)	M_P (Nm)	M_R (Nm)
0	0	2.1935×10^4	0	0
0.1	0.0105	2.1937×10^4	-2.2469×10^2	0
0.2	0.0383	2.1962×10^4	-6.9191×10^2	0
0.3	0.0825	2.2066×10^4	-1.3723×10^3	0

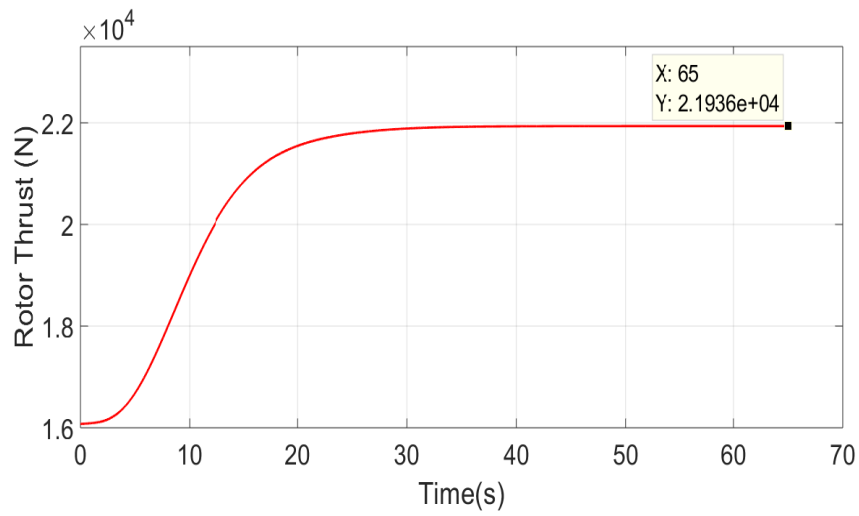
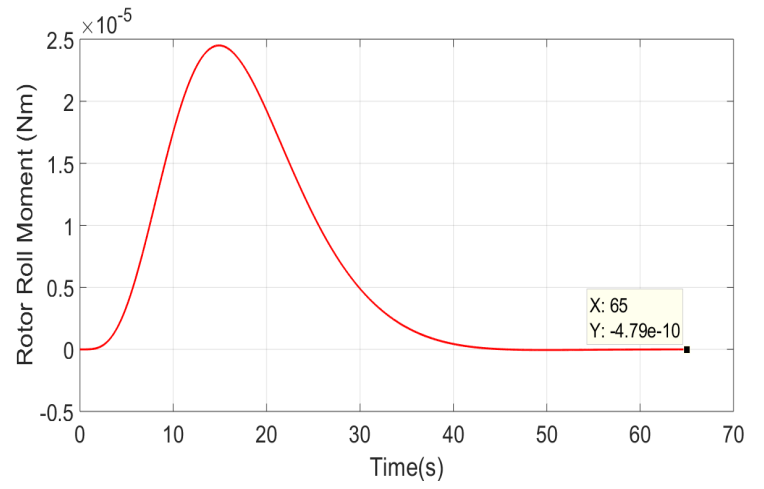
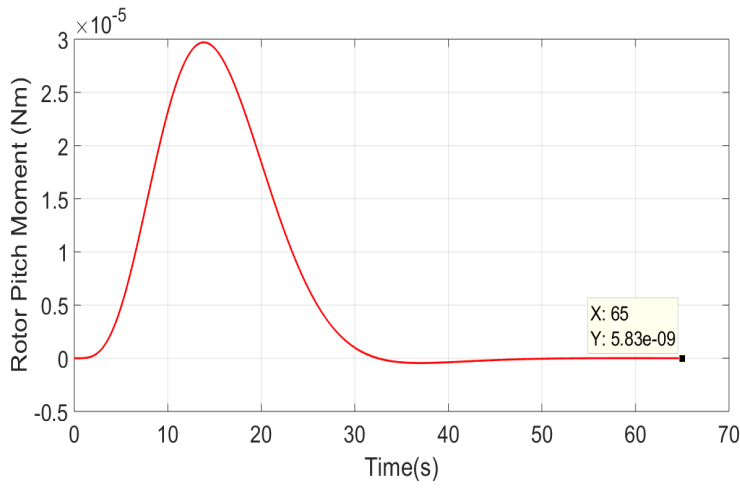


Figure 3.13: Time history of rotor trimming at $\mu = 0$.

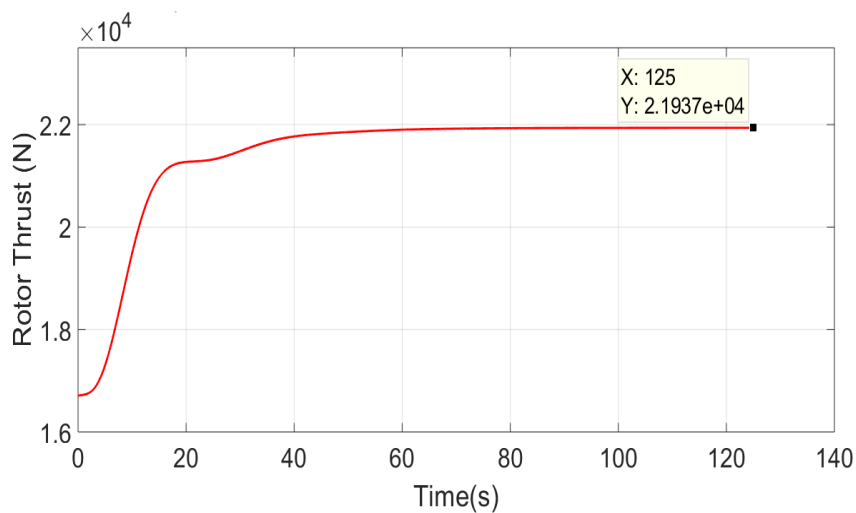
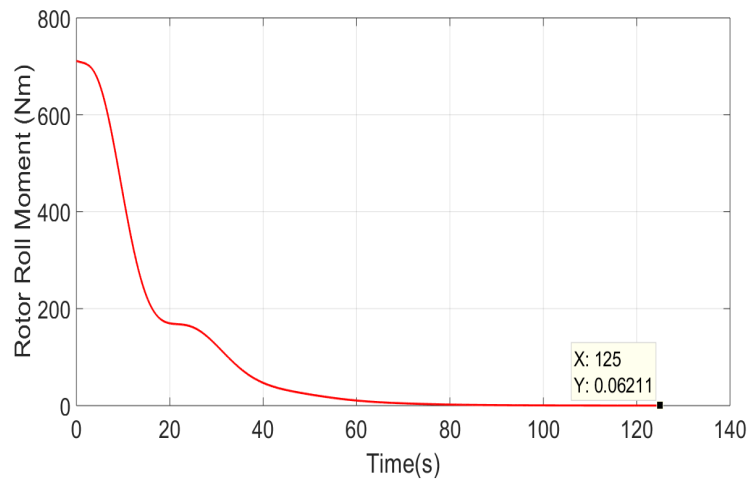
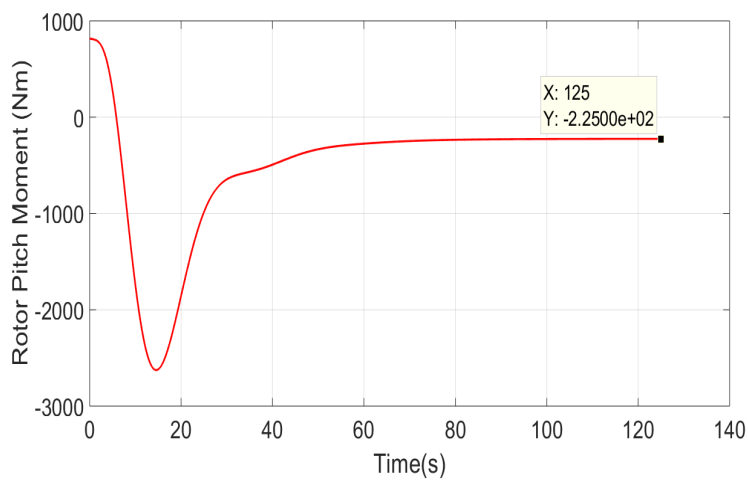


Figure 3.14: Time history of rotor trimming at $\mu = 0.1$.

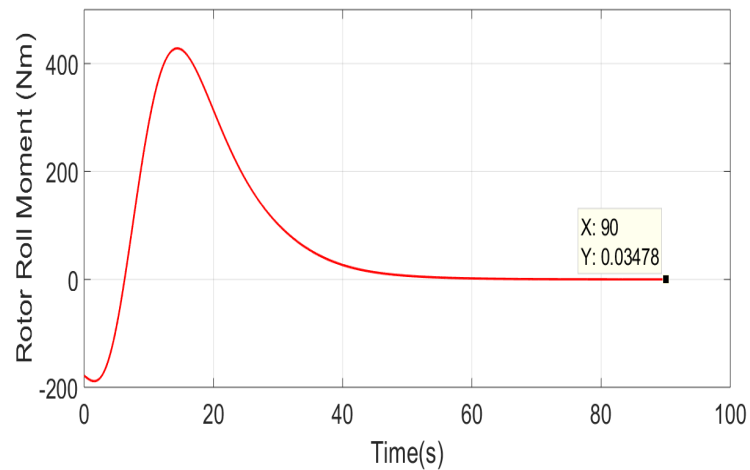
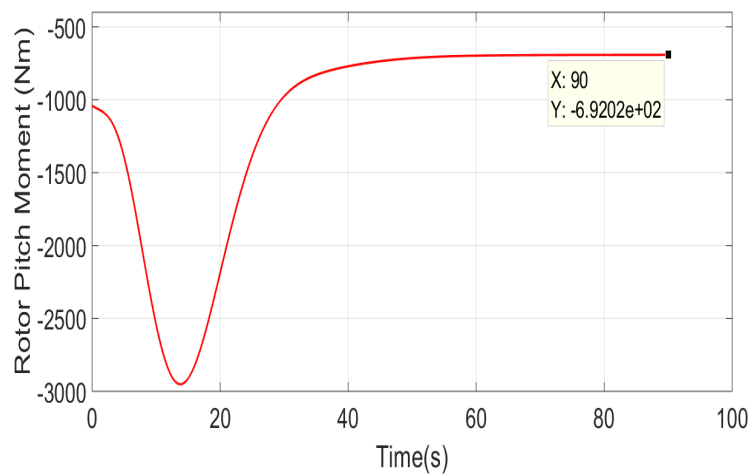


Figure 3.15: Time history of rotor trimming at $\mu = 0.2$ (Pitch and roll moments).

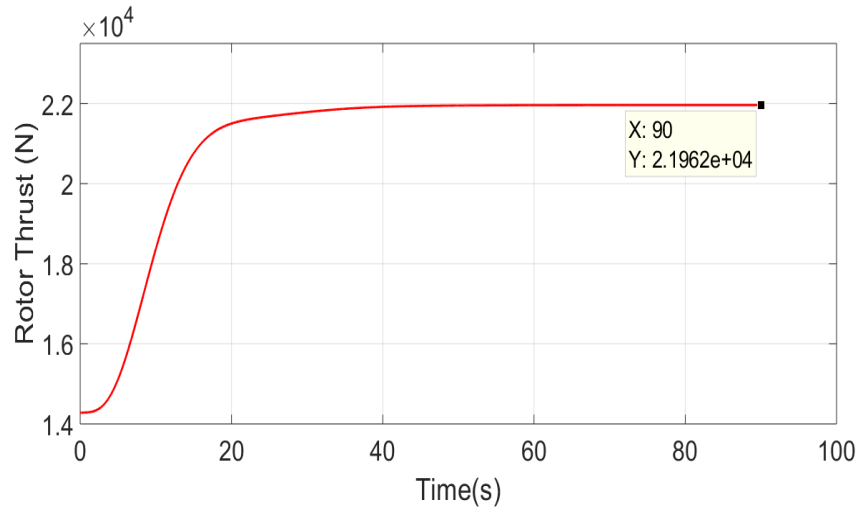


Figure 3.16: Time history of rotor trimming at $\mu = 0.2$ (Thrust).

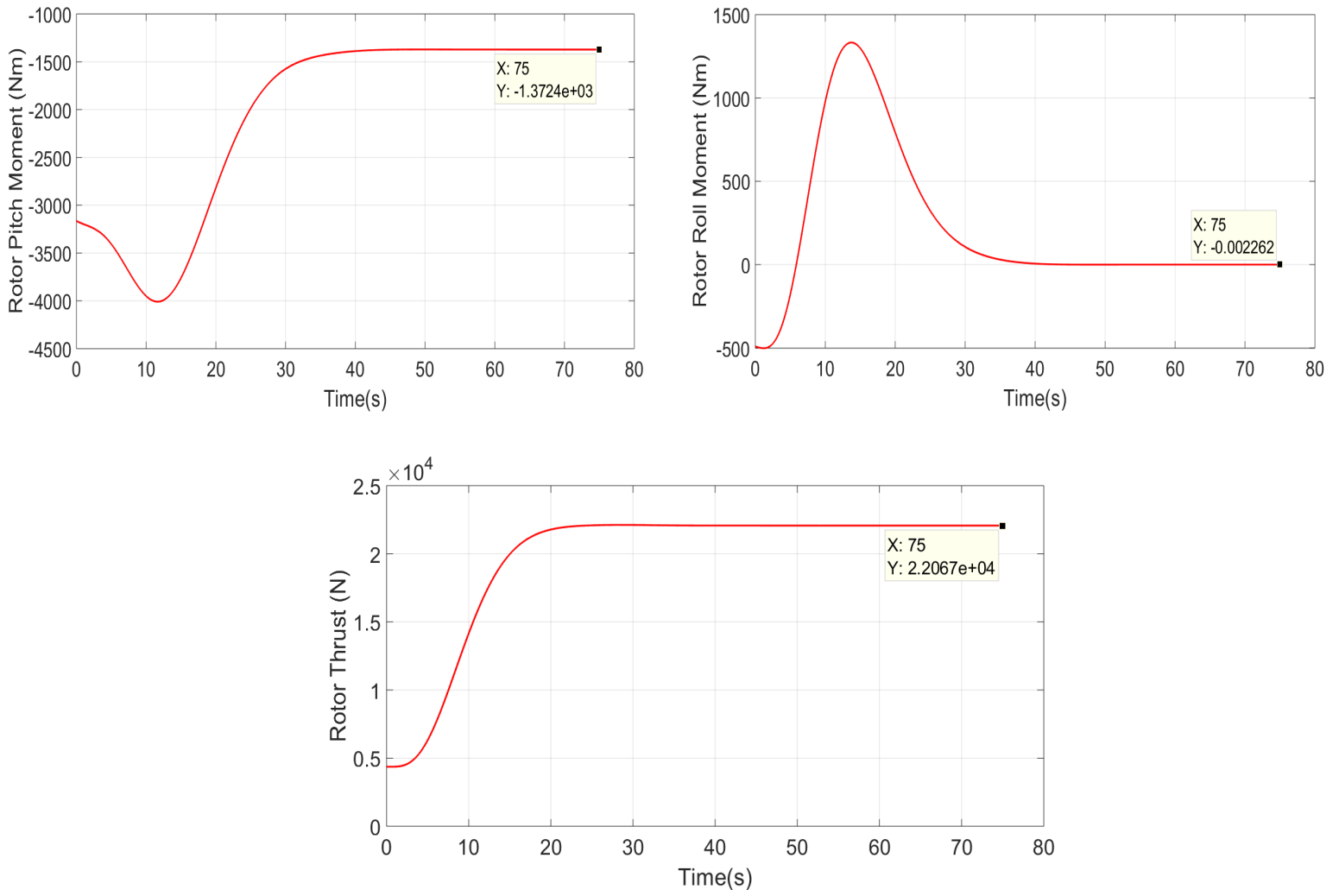


Figure 3.17: Time history of rotor trimming at $\mu = 0.3$.

A comparison of the trim angles show that the pitch angles obtained in the present study are close to the pitch angles provided in [155]. There results are shown in Figure 3.18. The collective pitch angle obtained is slightly greater than the collective pitch provided in [155]. This could be because of the difference in the beam formulations and aerodynamic models between the two studies. However, the cyclic pitch angles are in very good agreement.

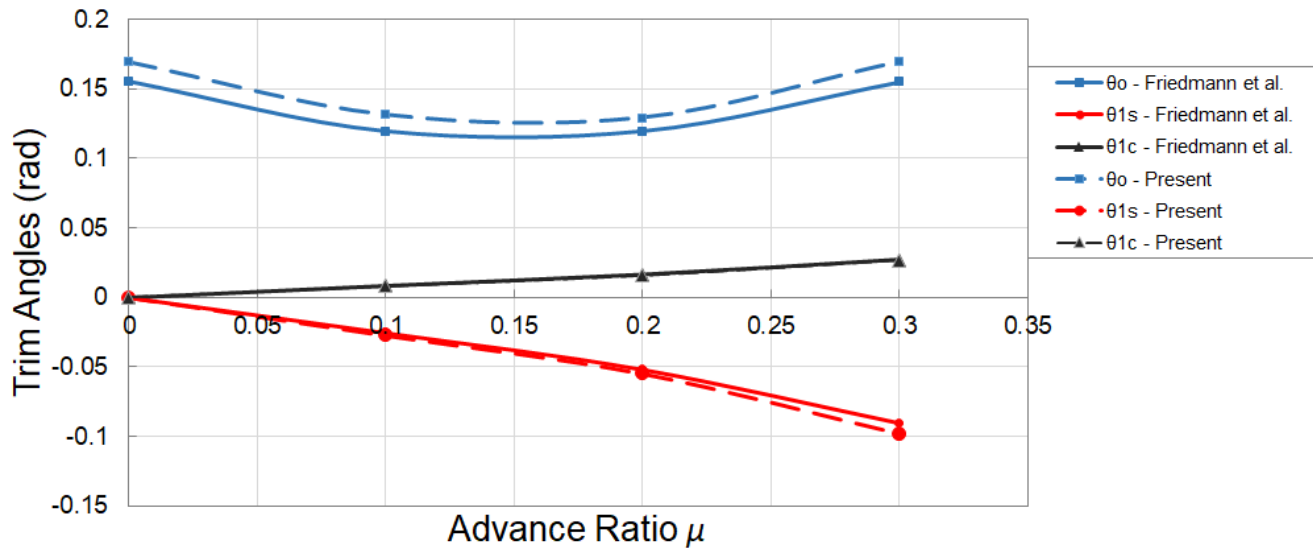


Figure 3.18: Trim angles comparison.

CHAPTER 4

VSR: POWER ADVANTAGES AND RESONANCE STUDIES

After validating the rotor model we built in DYMORE in the previous chapter, we will be analyzing a variable speed rotor in this chapter. The rotor used for this study will be described in the initial sections of this chapter. The later sections provide a proper framework to analyze a variable speed rotor.

4.1 Rotor Properties

For variable speed rotor studies, we will be using the rotor provided in [18] which is similar to the rotor studied in [22]. In [18], the authors studied the lead-lag resonance crossing using a moderate deflection beam theory and quasi-steady aerodynamics. The properties of the hingeless rotor that will be used in this study is provided in Table 4.1.

Table 4.1: Rotor properties [18].

$m = 10 \text{ kg/m}$	$R = 6 \text{ m}$	$B = 4$
$EI_{Flap} = 1.8340 \times 10^5 \text{ Nm}^2$	$EI_{Lag} = 1.8640 \times 10^6 \text{ Nm}^2$	$GJ = 8.16 \times 10^4 \text{ Nm}^2$
$EA = 1.0 \times 10^8 \text{ N}$	$W = 1.2096 \times 10^4 \text{ N}$	Airfoil: NACA 0012
Center of mass offset = 0 m	$c = 0.6 \text{ m}$	Lag damping, $\zeta = 1\%$
Flap damping, $\eta = 0.3\%$	$\tau = 0^\circ$	Shear center offset = 0 m
Centroid offset = 0 m	$mI_{Flap} = 0.052 \text{ kg m}$	$mI_{Lag} = 0.2 \text{ kg m}$

The first flap, second flap, first lag and first torsional non-rotating frequencies of our blade are matching with the frequencies provided in [22]. The fan plot with 1% structural

damping in lag is shown in Figure 4.1. The fan plot will provide important guidance in resonance crossing studies.

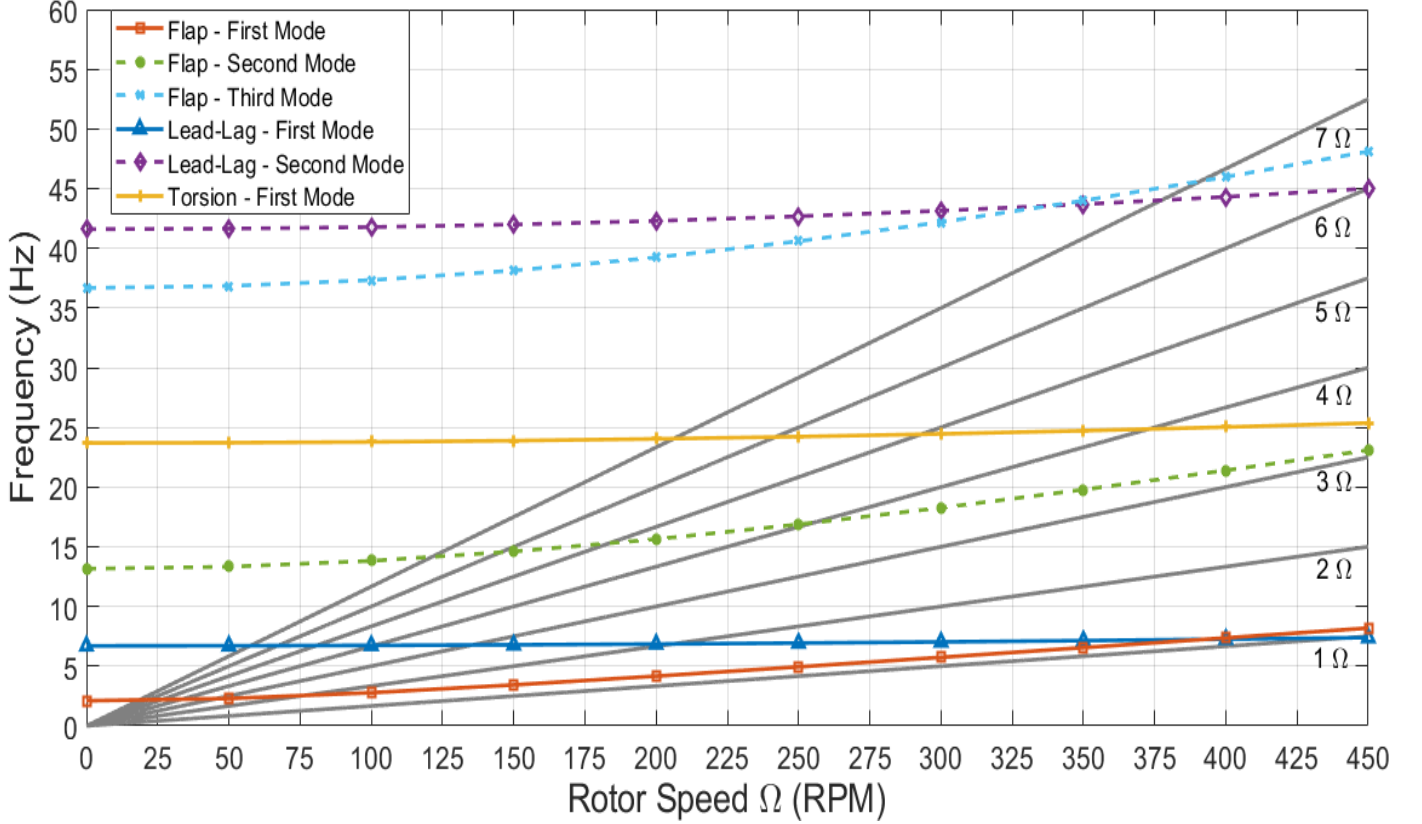


Figure 4.1: Rotor blade fan plot for $\zeta = 1\%$.

The trim results from [18] are compared with the trim results from our model. Wind tunnel trim procedure was followed in [18], but the rotor was trimmed for longitudinal and lateral tip-path-plane angles instead of roll and pitch moment. The authors also used a quasi-steady aerodynamics model, whereas unsteady aerodynamic terms are included in our model. However, a three-state dynamic inflow was used to match with the inflow states used in [18]. The results are shown in Table 4.2. The collective (θ_0) and lateral cyclic (θ_{1c}) angles are very close to the literature values. The longitudinal cyclic angle θ_{1s} deviates noticeably from literature values. This could be because of differences in the trim procedure and rotor model. This serves as another validation of our rotor model and trimming technique.

Table 4.2: Trim angles comparison for 3 state inflow.

$\Omega = 180 \text{ RPM}$ $V_\infty = 28.27 \text{ m/s}$		
Pitch Angles	Han and Smith [18]	Present Study
θ_0	5.2025°	5.2057°
θ_{1s}	-3.5063°	-2.70°
θ_{1c}	2.8354°	2.7786°

4.2 Baseline Conditions

The nominal angular speed for our rotor is chosen to be 230 RPM. It can be seen from the fan plot that the natural frequencies of the rotor blade cross the multiples of rotor speed (1Ω , 2Ω and so on) at several locations. These crossing locations are known as resonance points. At these resonance points, the blade's response amplifies as the operating frequency overlaps with the blade's natural frequency. Hence, the nominal rotor speed, Ω_N is chosen to be sufficiently far away from the resonance points as shown in Figure 4.2.

For $\Omega_N = 230 \text{ RPM}$, the advance ratio and the corresponding free stream velocity is provided in Table 4.3. The nominal advance ratio μ_N is defined as $V_\infty/(\Omega_N R)$.

Table 4.3: Nominal advance ratio and free stream velocity.

$\Omega_N = 230 \text{ RPM}, T = 1.2096 \times 10^4 \text{ N}$				
μ_N	0.0	0.1	0.2	0.3
$V_\infty \text{ (m/s)}$	0.00	14.45	28.90	43.35

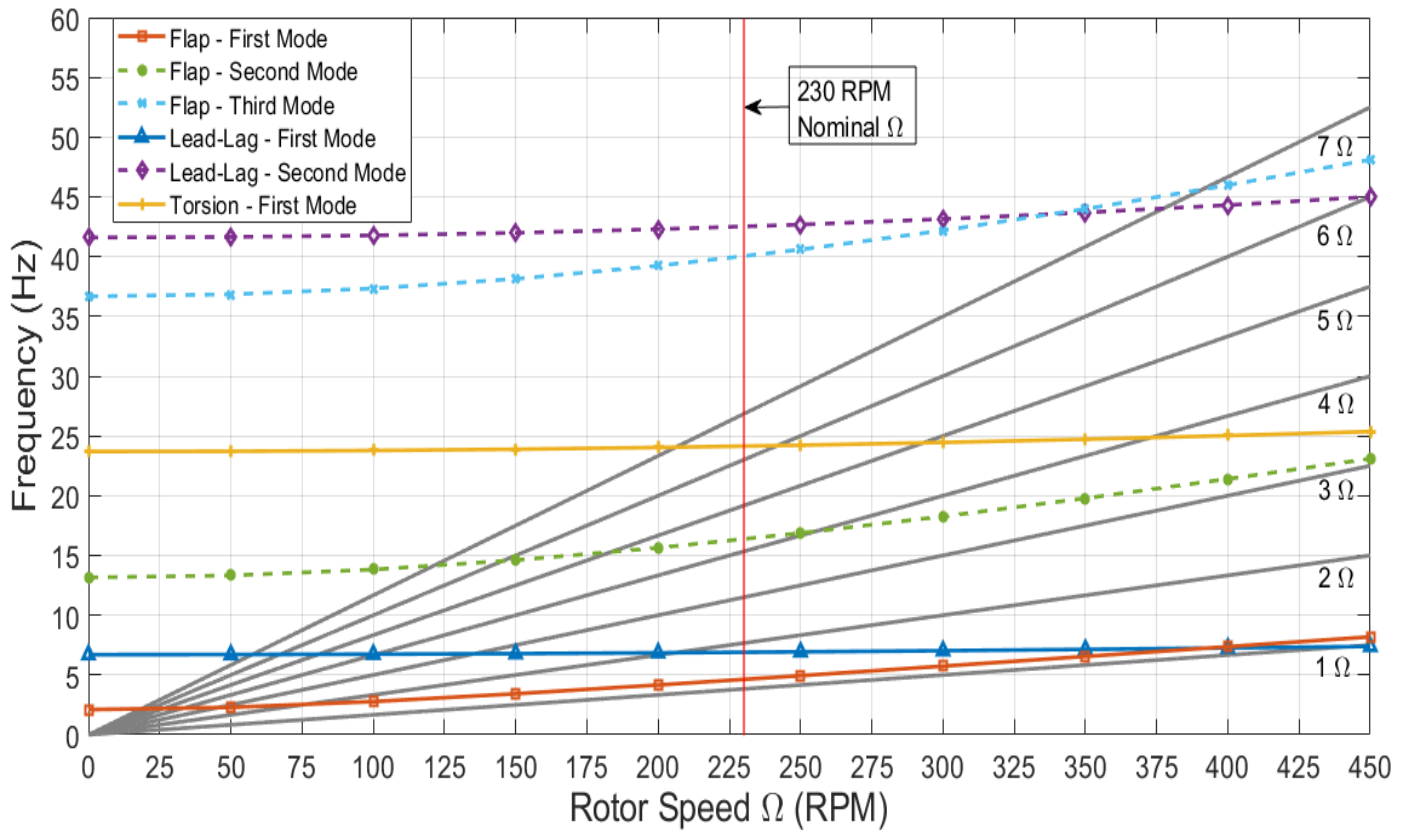


Figure 4.2: Rotor blade fan plot showing nominal Ω .

4.3 Inflow States and Trim Angles

An important parameter that affects the load distribution across the rotor is the inflow velocity. The inflow doesn't tend to be uniform across the rotor blade. In order to capture the inflow accurately, the number of inflow states has to be increased. In this section, we will be studying the effect of inflow states on trim angles. The number of inflow states in our aerodynamics model is increased and the behavior of trim angles is observed.

In the hovering flight condition, $\mu_N = 0$, the collective pitch angle shows a converged behavior for inflow states greater than 10 as shown in Figure 4.3. Beyond 10 states, there appears to be no significant changes to the trimmed θ_0 value. The lateral and longitudinal cyclic values are zero for hover.

In the forward flight condition, the lateral cyclic angle is affected greatly by the number

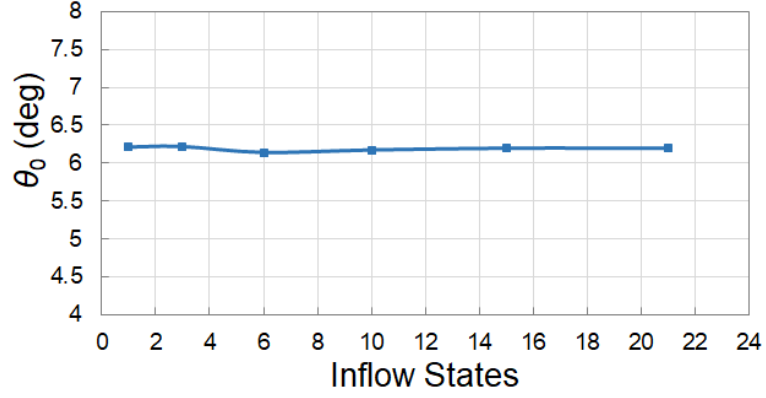


Figure 4.3: Trim angle convergence at $\mu_N = 0$

of inflow states. The results for $\mu_N = 0.1$ is shown in Figure 4.4. Lateral cyclic θ_{1c} shows convergence behavior only after 15 inflow states, whereas θ_0 and θ_{1s} show convergence after 10 inflow states with slight numerical deviation.

As the forward speed increases, more inflow states are required to capture the inflow accurately. The results for $\mu_N = 0.2$ and $\mu_N = 0.3$ are shown in Figures 4.5, 4.6 and 4.7. The lateral cyclic angle shows convergence behavior after 21 inflow states for an advance ratio of 0.2. For an advance ratio of 0.3, convergence is achieved after 55 inflow states. Hence, we will be using the necessary number of inflow states for a given advance ratio to ensure trim angles convergence in the consequent analysis.

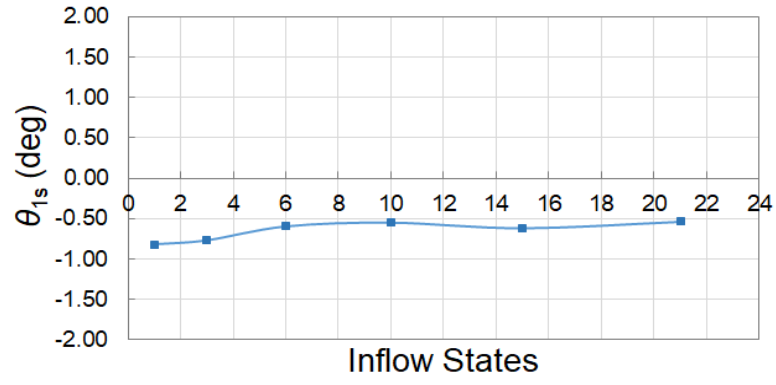
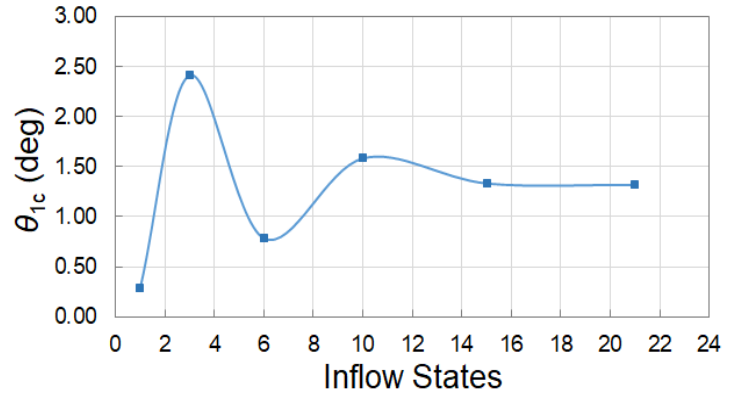
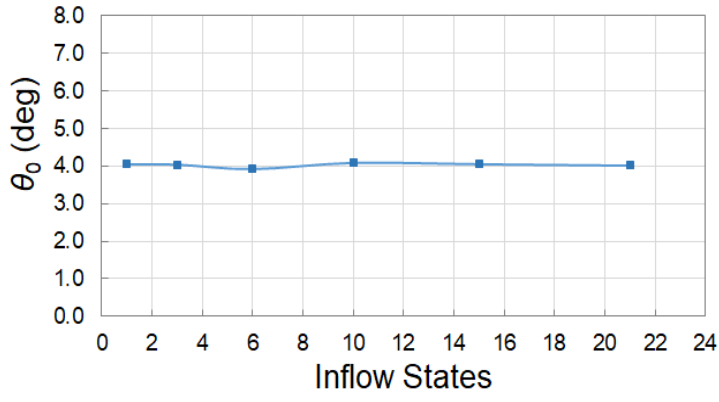


Figure 4.4: Trim angles convergence at $\mu_N = 0.1$

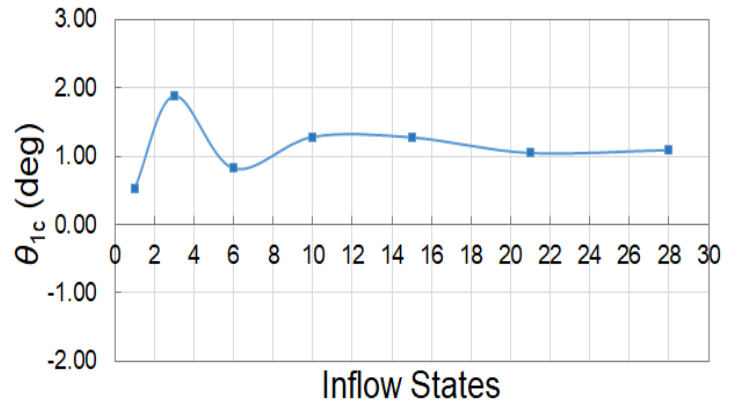
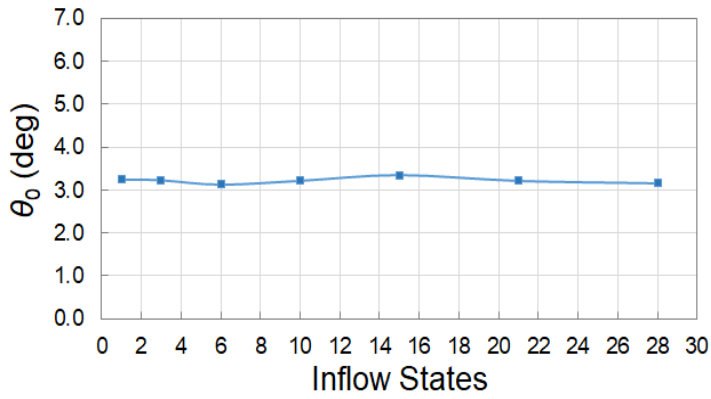


Figure 4.5: Trim angles convergence at $\mu_N = 0.2$ (Collective and lateral cyclic)

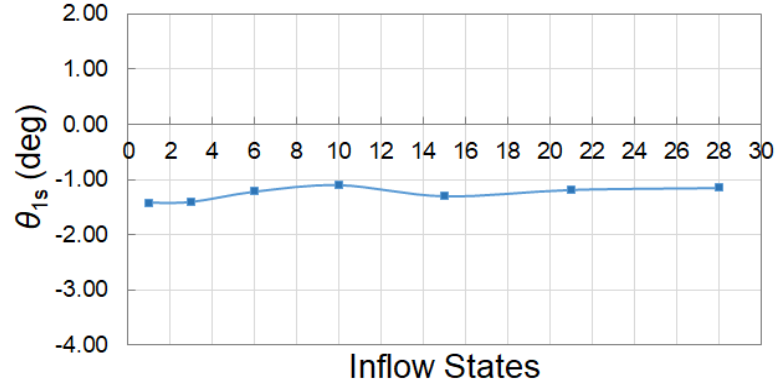


Figure 4.6: Trim angles convergence at $\mu_N = 0.2$ (Longitudinal cyclic)

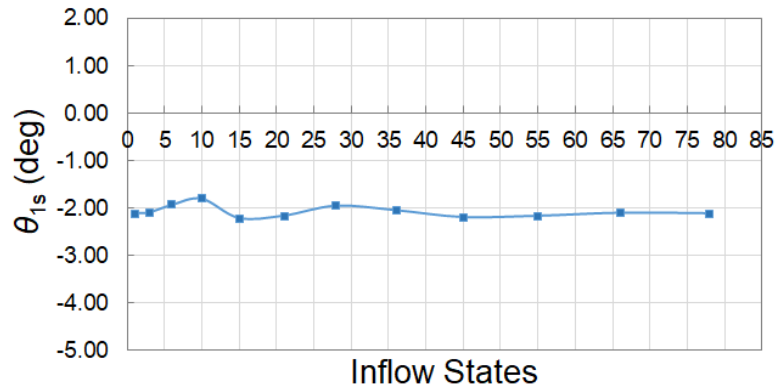
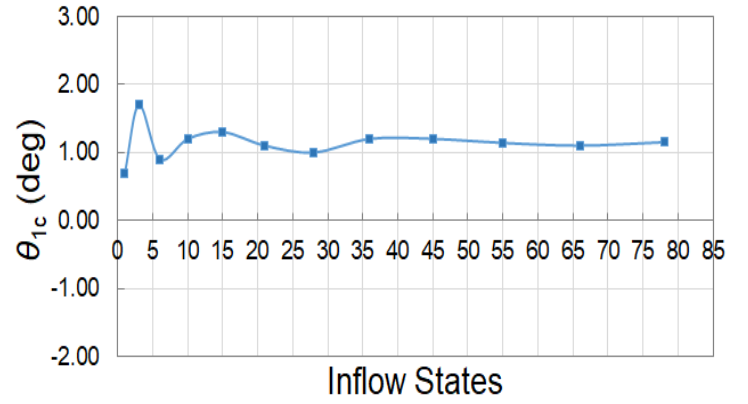
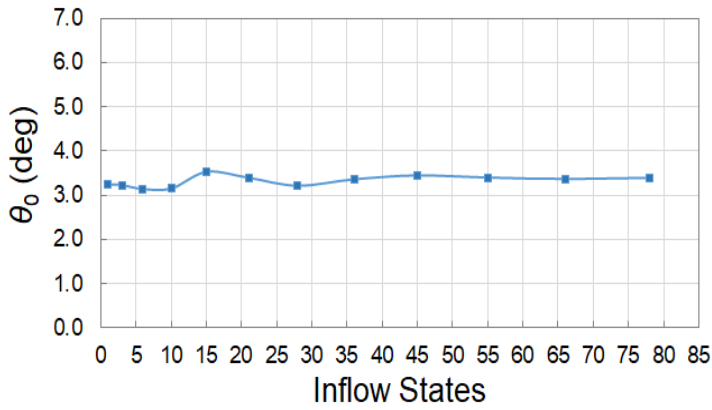


Figure 4.7: Trim angles convergence at $\mu_N = 0.3$

4.4 Power Advantages of a VSR

As discussed in the first chapter, varying the rotor speed can improve the performance of a rotor. However, such studies for a hingeless rotor are scarce in the literature. The detailed power studies by Steiner et al. [10] is limited to an articulated rotor with rigid blades having only flap degrees of freedom. Hence, in this section we will be using our comprehensive rotor model to quantify the power advantages that could be achieved by varying the rotor speed.

In this analysis, we assume that the rotor is fitted with a transmission system that allows unlimited speed change. A continuously variable transmission (CVT) system could provide a wide range of gear ratios unlike a fixed-ratio transmission system. CVT systems were shown to be advantageous for VSR in [160]. The rotor speed is changed from its baseline of 230 RPM and the power required to run the rotor at the new RPM is evaluated for sea level altitude ($\rho_a = 1.2041 \text{ kg/m}^3$ at 20°C). The thrust produced by the rotor and the forward speed of the rotorcraft remains unchanged for a given nominal advance ratio even though the rotor speed changes. Hence, the rotor needs to be trimmed for the new Ω to produce the same thrust and moment balance. In this section, we are only looking at the steady state values of a trimmed rotor and not the transition dynamics of changing rotor speed.

In hover, the rotor requires a power of 202 hp to balance the drag loads acting on the rotor at 230 RPM, as shown in Figure 4.8. The drag loads formulation is provided in section 2.2. The drag loads acting on the airfoil due to lift and dynamic stall will be referred to as induced drag in this study. The drag loads due to the profile of the airfoil along with the skin friction drag will be referred to as profile drag. This helps us in explaining the power behavior.

The total torque that is required to spin the rotor at a constant speed is shown in Figure 4.9. As the rotor speed decreases from 230 RPM, the power required to spin the rotor is decreased. As the rotor speed is decreased, the pitch angle needs to increase in amplitude

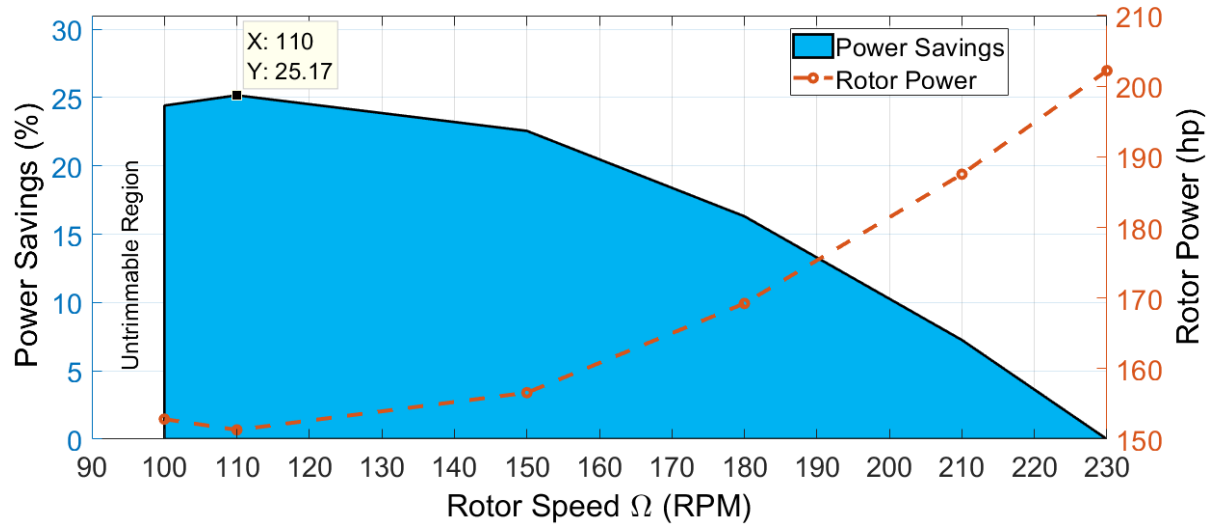


Figure 4.8: Power savings at $\mu_N = 0$

to produce the same amount of thrust. Due to the increase in pitch angle, the induced drag increases leading to an over all increase in rotor torque as shown in Figure 4.9. However, the profile drag decreases with reduction in rotor speed as the velocities seen by the airfoil sections are lower. Total torque is a summation of the torques required to balance the induced drag and profile drag. Power is defined as rotor torque multiplied by rotor speed. Even though the overall torque increases, reducing the rotor speed has a net effect of reducing the total power requirement. Hence, reducing the rotor speed from 230 RPM to 210 RPM provides about 7% power savings. Reducing the rotor speed further improves the rotor performance and a maximum power saving of 25% is achieved at 110 RPM for our rotor. Reducing the rotor speed beyond 110 RPM decreases the power savings to 24% as the torque curve gets steeper. Beyond this point the rotor is not trimmable. Any further increase in the pitch angle stalls the rotor and thus making the rotor unable to produce the required thrust. Power savings achieved due to reduced rotor speed comes with a 56% increase in rotor torque in hover but improves the hover endurance performance of a rotorcraft appreciably.

In forward flight, the rotor torque shows a different behavior than hover. The power savings also improve considerably. For $\mu_N = 0.1$, reducing the rotor speed improves the

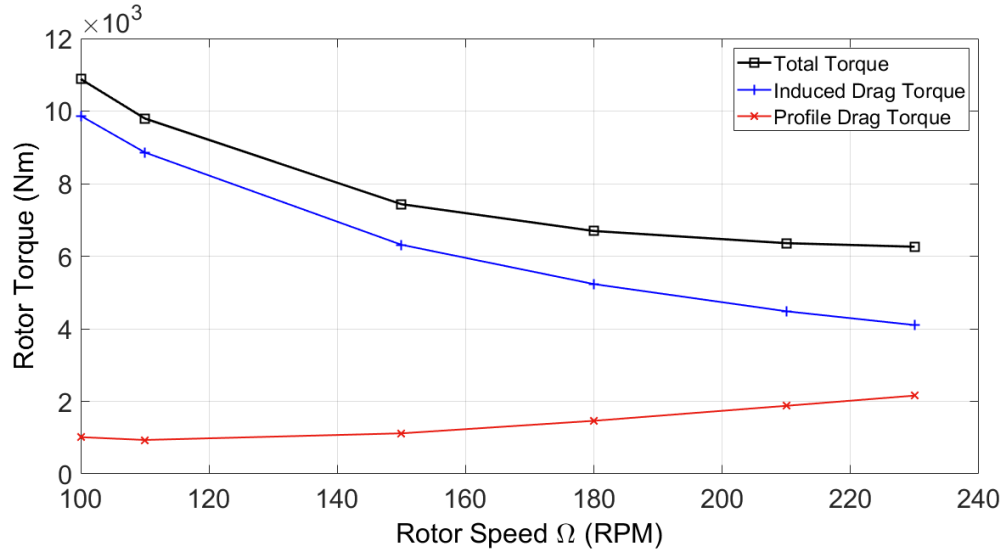


Figure 4.9: Torque variation with rotor speed at $\mu_N = 0$

power ratings of the rotor by a maximum of 37.7%. The minimum power is achieved at a rotor speed of 130 RPM as shown in Figure 4.10. It is to be noted that the trim boundary of the rotor is increased to 130 RPM in this case as compared to 100 RPM in hover. Hence, the percentage of rotor speed change that can be achieved or required reduces with increase of forward speed. In hover, 52% change from Ω_N is required to attain minimum power, whereas at $\mu_N = 0.1$ minimum power can be achieved by 43% change from Ω_N .

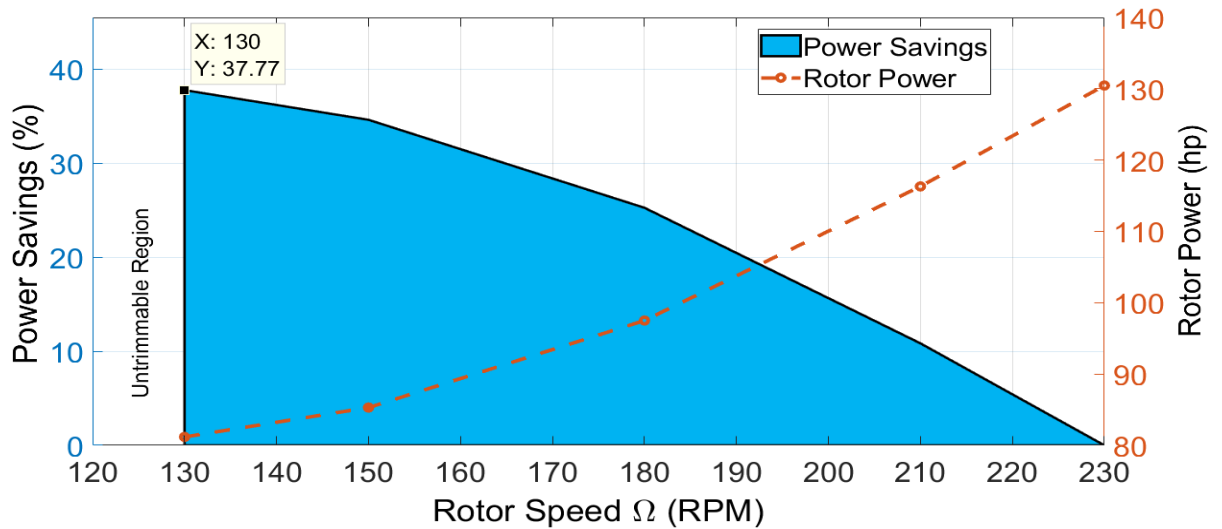


Figure 4.10: Power savings at $\mu_N = 0.1$

The rotor torque decreases as the rotor speed is reduced from 230 RPM to 180 RPM,

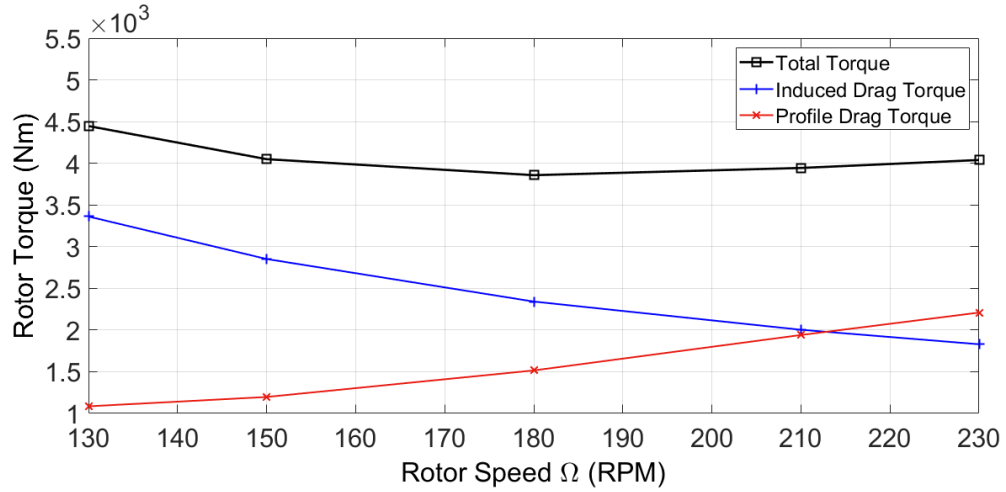


Figure 4.11: Torque variation with rotor speed at $\mu_N = 0.1$

shown in Figure 4.11. This is because the profile drag decrease is greater than the increase of induced drag with reduction in rotor speed. Hence, an overall decrease in rotor torque is observed till 180 RPM. Beyond this Ω , the induced drag starts to increase greatly leading to an increase in total torque. However, only 10% increase in rotor torque is observed from the baseline value at minimum power point.

At $\mu_N = 0.2$, the power savings show a considerable improvement reaching a maximum of 41% at 150 RPM, shown in Figure 4.12. The significant power reduction is a result of profile drag being greatly dominant at this forward speed.

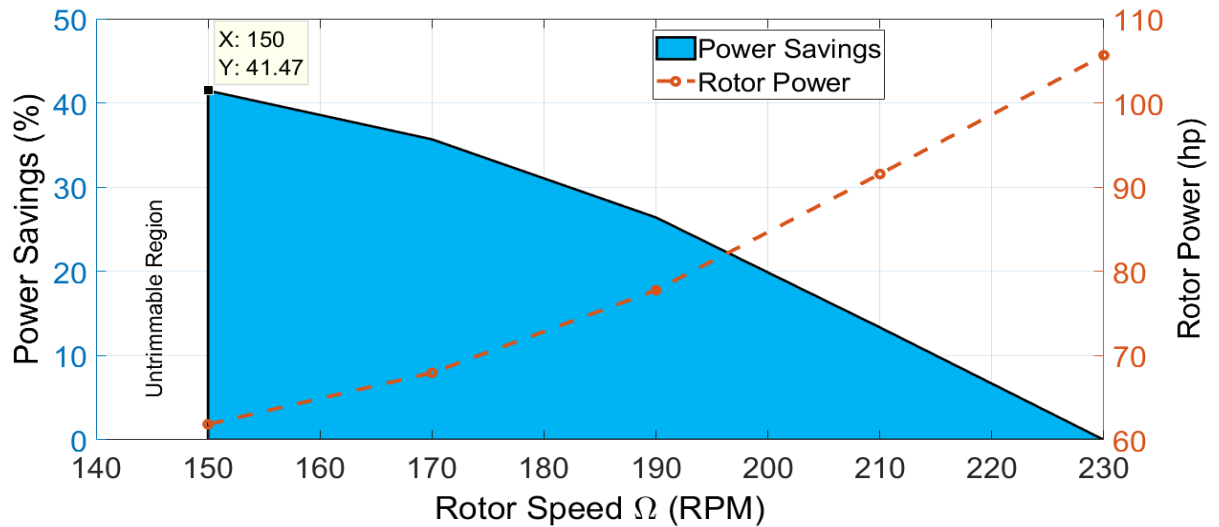


Figure 4.12: Power savings at $\mu_N = 0.2$

Reducing the rotor speed caused the profile drag to decrease as expected and there was also an absence of significant increase in induced drag. This can be seen in the rotor torque curve shown in Figure 4.13, leading to a notable power reduction. The total torque has also reduced by 10% from the baseline at 150 RPM.

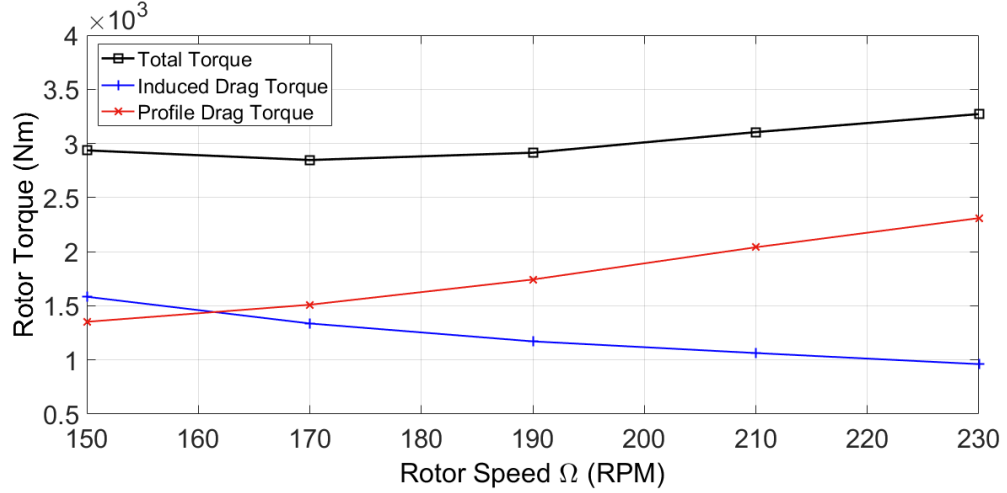


Figure 4.13: Torque variation with rotor speed at $\mu_N = 0.2$

For $\mu_N = 0.3$, the power saving reduces. Even though the rotor is trimmable until 170 RPM, the maximum power saving of 24% is attained at 180 RPM. The power curve is shown in Figure 4.14.

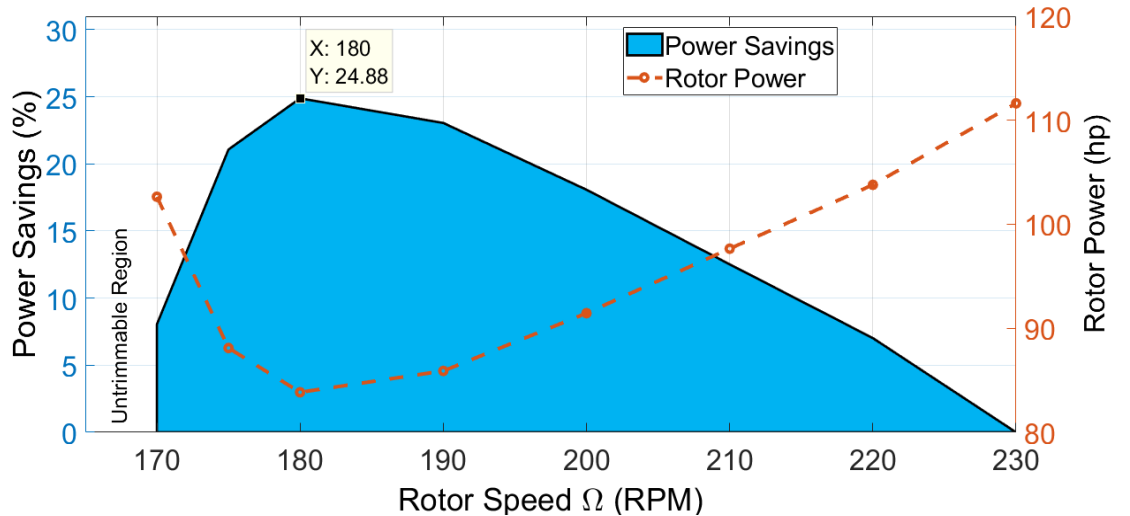


Figure 4.14: Power savings at $\mu_N = 0.3$

For reduction beyond 180 RPM, the power saving reduces sharply to 8% at 170 RPM before reaching the untrimmable region. This sharp decrease in power saving is associated

with a sharp increase in rotor torque as shown in Figure 4.15. This sudden increase of torque is due to a rapid increase in profile drag and continuous increase of induced drag at high angles of attack.

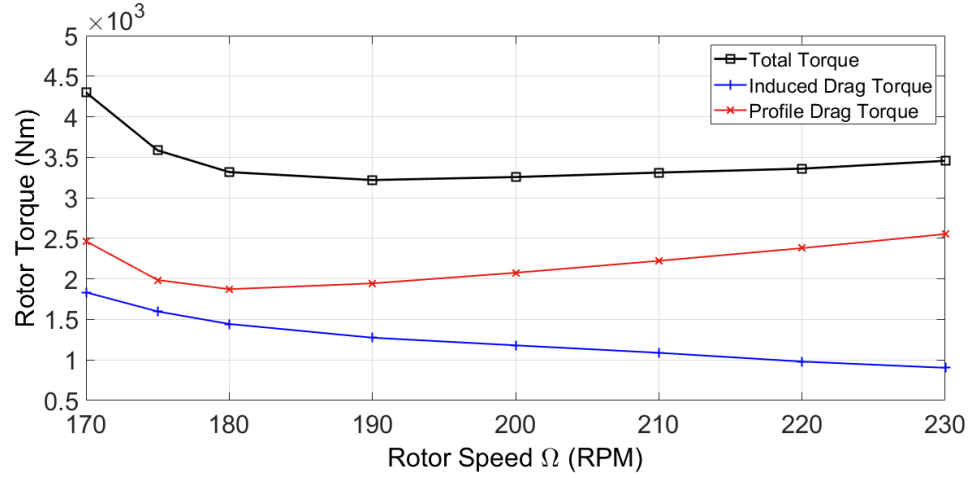


Figure 4.15: Torque variation with rotor speed at $\mu_N = 0.3$

4.5 Resonance Points Identification

Performing a power advantage study such as the one discussed in the previous section makes a strong case to consider variable speed rotors. More importantly, it also serves as a guide to identify the resonance crossing points that needs to be studied from the fan plot. The resonance crossing points are identified for different advance ratios in Figures 4.16, 4.17, 4.18 and 4.19.

The resonance crossing points up to 7Ω are identified in this exercise. Whether these higher frequency resonance crossing points are important or not is something that needs to be studied.

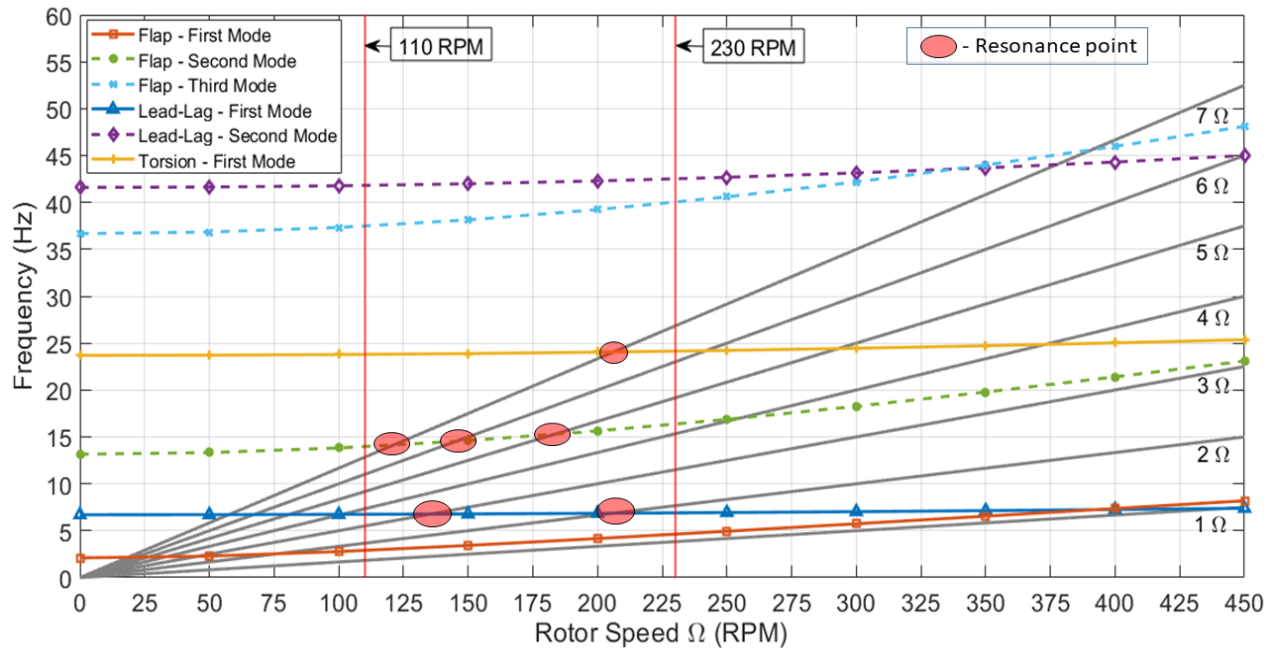


Figure 4.16: Resonance points for $\mu_N = 0$

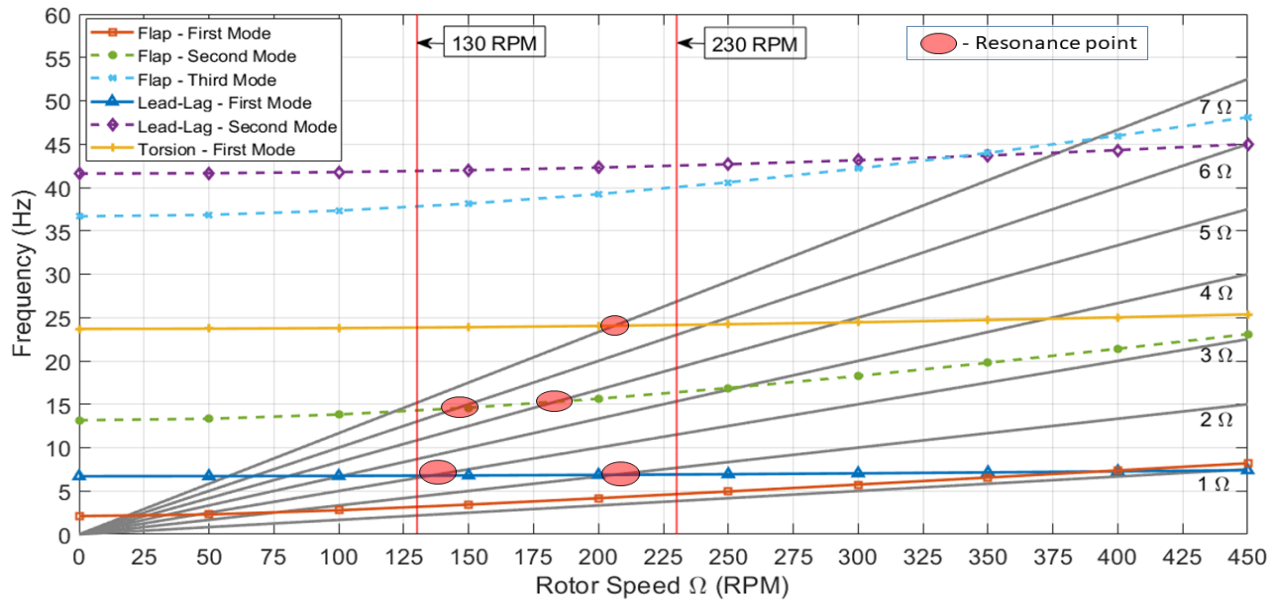


Figure 4.17: Resonance points for $\mu_N = 0.1$

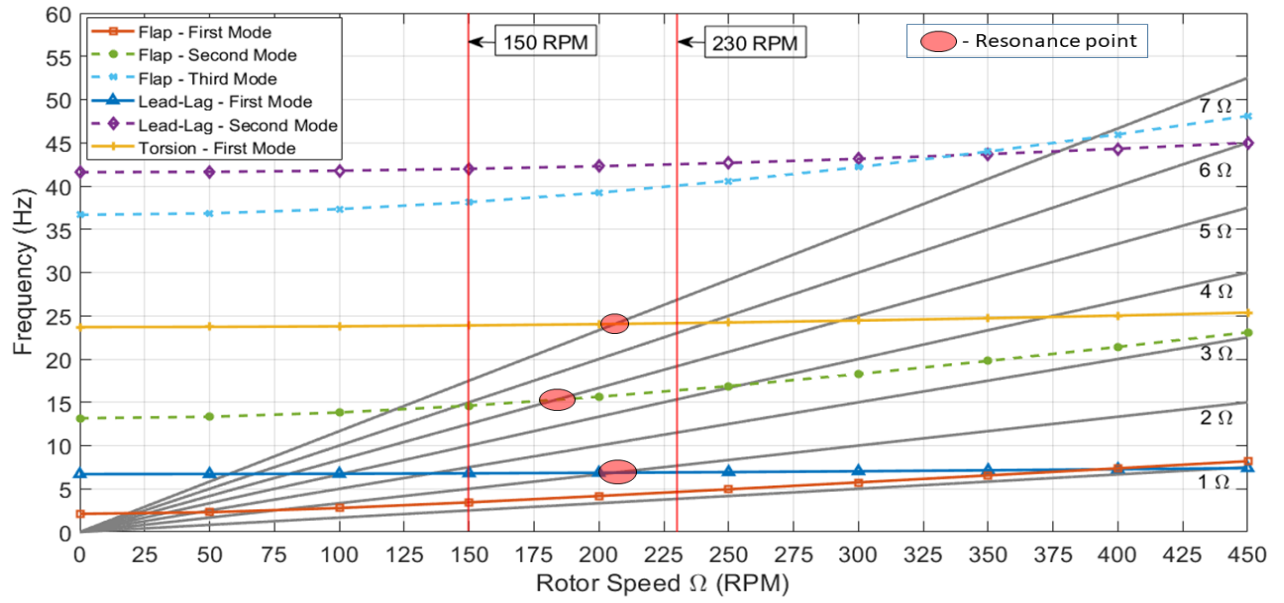


Figure 4.18: Resonance points for $\mu_N = 0.2$

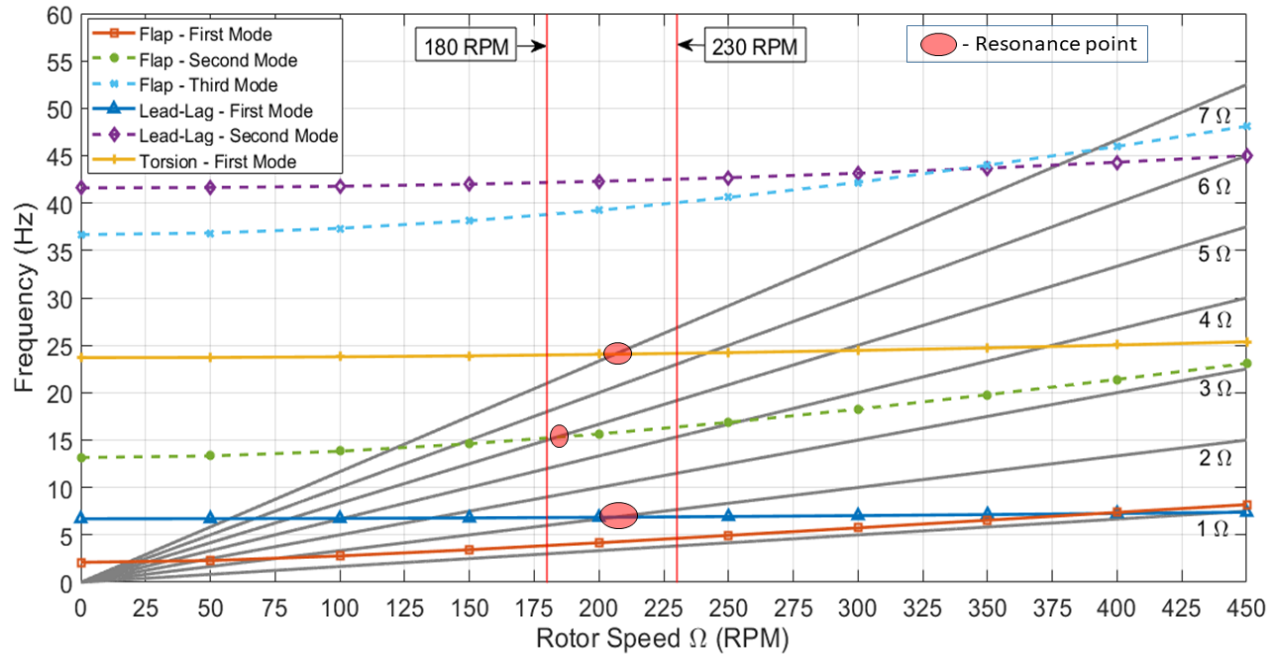


Figure 4.19: Resonance points for $\mu_N = 0.3$

4.6 Resonance Transition Dynamics

In this section, we will be focusing on the response of the rotor blade as it passes through the resonance points. Before we dive into our results, our model needs to be validated for resonance study.

4.6.1 Validation

The resonance results from [18] are used to validate our model. In [18], the rotor speed was changed from 180 RPM to 240 RPM in 10 seconds. The lag moment and rotor torque are compared in Figures 4.20 and 4.21, respectively.

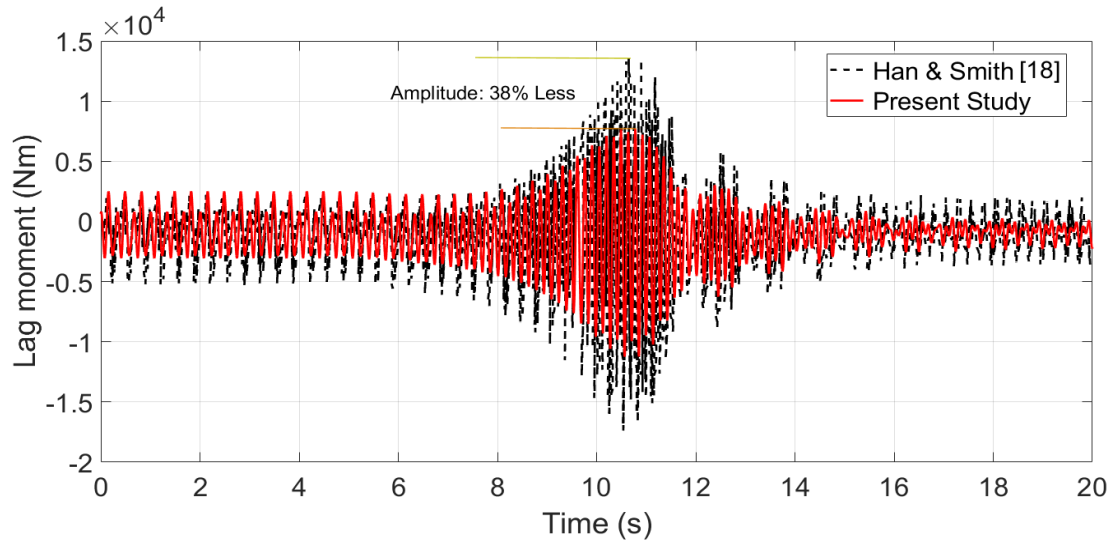


Figure 4.20: Lag moment comparison for 2/rev lag resonance (180 → 240 RPM)

The lag moment amplitude differs by 38% for the 2/rev lag resonance crossing as shown in Figure 4.20. This deviation could be a result of differences in the aerodynamics model, trim procedure and beam model. Twenty one inflow states were used in our model to ensure θ_{1c} convergence, which in turn affects the trim angles. It will be shown later that trim angles play a significant role in resonance response. The authors in [18] trimmed the rotor for flap angles instead of rotor moments. The rotor torque comparison, Figure 4.21, shows that the present model predicts higher amplitude oscillations than published data. This could

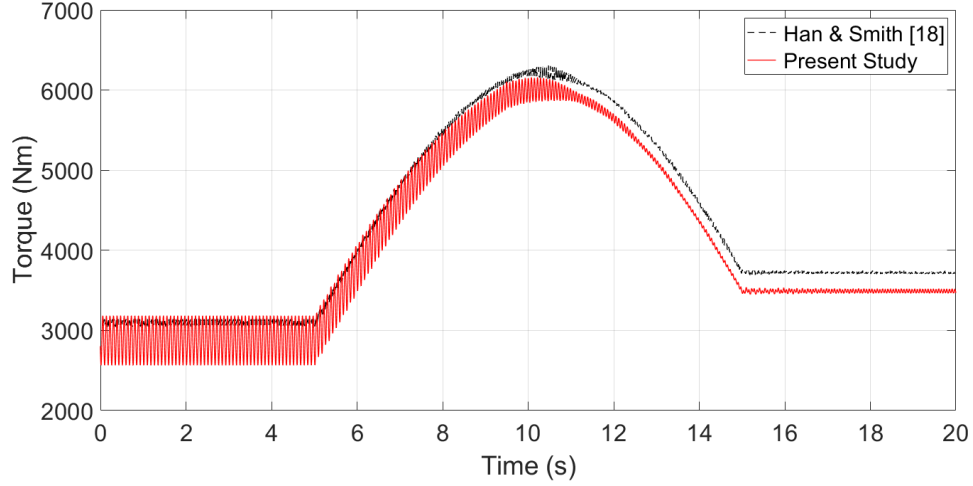


Figure 4.21: Rotor torque comparison (180 → 240 RPM)

be because of the quasi-steady assumptions and use of blade-element theory in [18]. The resonance results for the conditions in our study are given in the subsequent sections.

4.6.2 Nominal Advance Ratio, $\mu_N = 0.3$

Now, let us consider the resonance crossing points between 230 RPM and 180 RPM at $\mu_N = 0.3$, shown in Figure 4.19. There are three resonance crossing points in this region as provided in Table 4.4. The unit per rev (/rev) denotes that the frequency is non-dimensionalized with respect to rotor speed Ω .

Table 4.4: Resonance points between 230 RPM and 180 RPM.

Blade Frequency Mode	Crossing Point (/rev)	Crossing Frequency (Hz)
1 st Lag	2	6.863
2 nd Flap	5	15.299
1 st Torsion	7	24.056

Transition: 230 to 180 RPM

The rotor speed is changed smoothly from 230 RPM to 180 RPM as shown in Figure 4.22.

The rotor speed function is as follows

$$\Omega(t) = \Omega_1 + (\Omega_2 - \Omega_1) \left[1 - \cos^2 \left(\frac{\pi}{2} \times \frac{t - t_1}{t_2 - t_1} \right) \right] \quad (4.1)$$

where Ω_1 is the initial speed, Ω_2 is the final speed, t_1 is the time at the start of transition and t_2 is the time at the end of transition. The rotor pitch angles are obtained by trimming the rotor for every 10 RPM between the two rotor speeds and curve fitted to obtain continuous data. This data is provided in Figure 4.23. Once the rotor speed is known as a function of time, pitch angles can be computed as a function of time as shown in Figure 4.24.

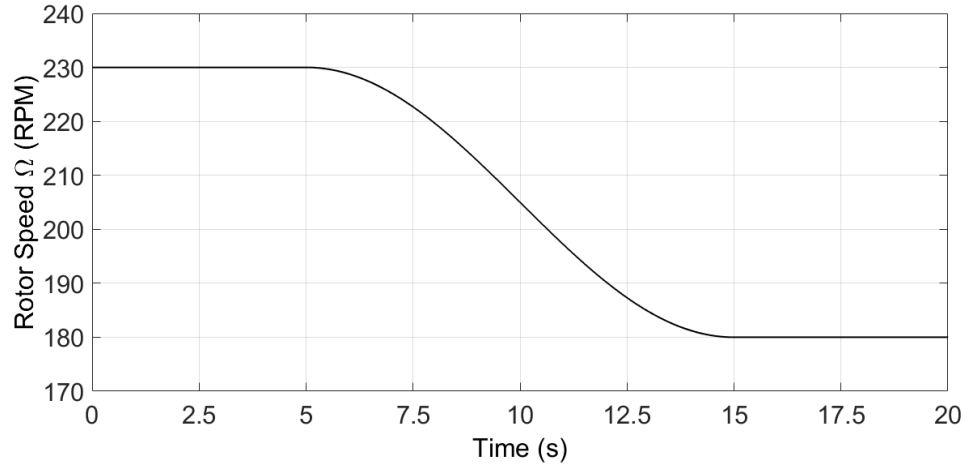


Figure 4.22: Rotor speed change from 230 to 180 RPM (10 s)

As the rotor speed is varied smoothly, the lag moment, flap moment and torsion moment at the blade root are obtained as a function of time in the blade frame. This allows us to observe the change in moment amplitudes due to resonance. Performing an FFT analysis on the signal would reveal which of the three resonance crossings has a dominant effect on the blade response.

The time history of the lag moment is shown in Figure 4.25. It can be seen that the lag moment at the blade root increases significantly around 10 to 12 seconds. During this

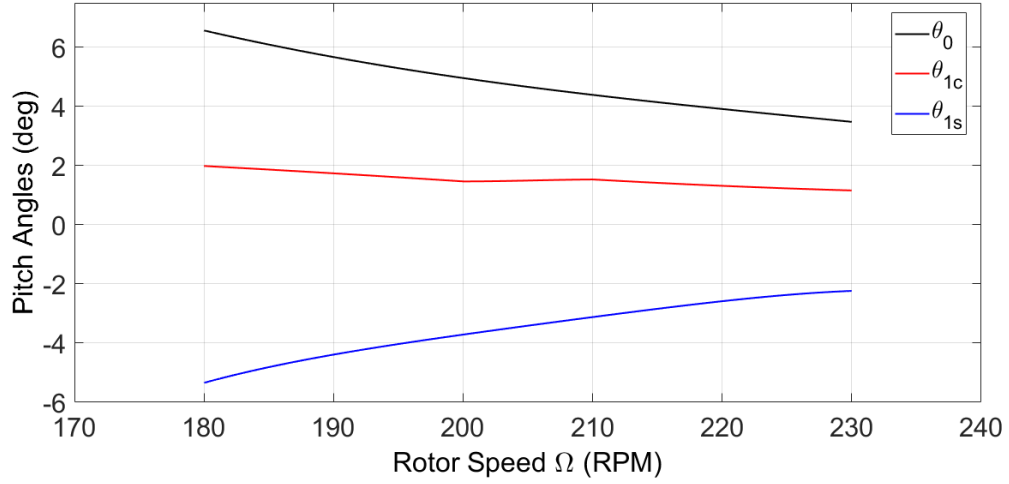


Figure 4.23: Pitch angles for $\mu_N = 0.3$

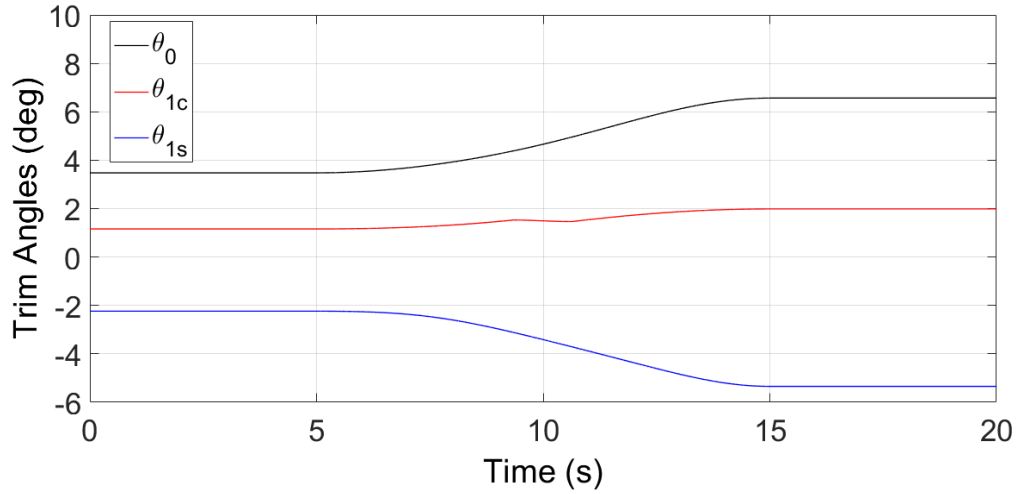


Figure 4.24: Pitch angles variation with time for $\mu_N = 0.3$ (230 → 180 RPM)

period the rotor crosses through the 2/rev lag resonance and 7/rev torsion resonance. The lag moment amplitude increases 10 times the nominal amplitude.

An FFT analysis of the lag moment in the high amplitude time frame shows that the dominant frequencies are 3.33 Hz and 6.66 Hz, Figure 4.26. The rotor operating frequency 1/rev and the lag resonance frequency 2/rev seem to be the driving factors for amplitude increase. The amplitude of the 2/rev signal is almost 10 times the 1/rev signal. Hence, the increase in amplitude is primarily because of the lag resonance. The 7/rev torsional resonance doesn't seem to have any effect on the lag moment response as no peaks are

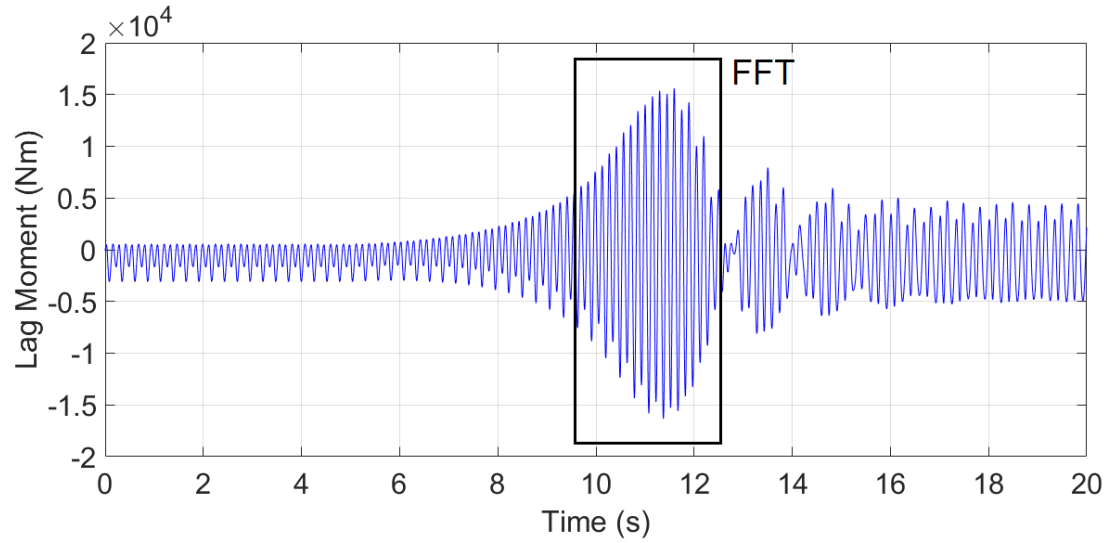


Figure 4.25: Time history of lag moment at blade root ($\mu_N = 0.3$; 230 \rightarrow 180 RPM)

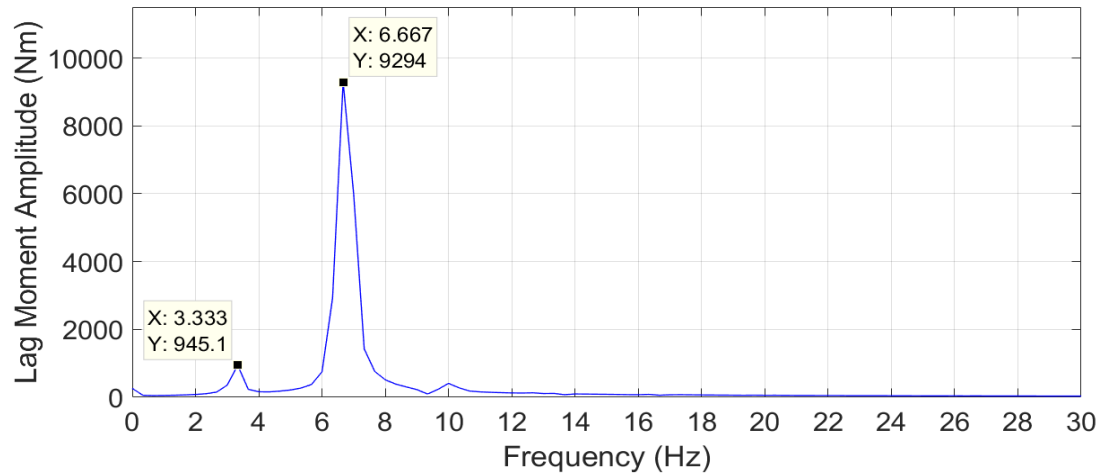


Figure 4.26: FFT analysis of lag moment at resonance ($\mu_N = 0.3$; 230 \rightarrow 180 RPM)

observed at higher frequencies in the FFT analysis.

The lag force behavior is shown in Figure 4.27. The dominating frequency is still 2/rev as seen in the FFT analysis, Figure 4.28.

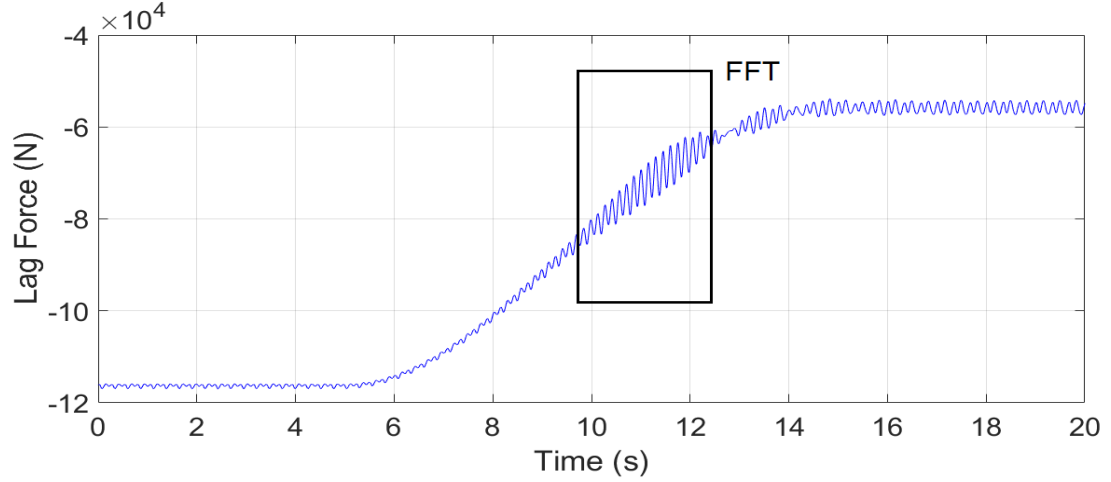


Figure 4.27: Time history of lag force at blade root ($\mu_N = 0.3$; 230 \rightarrow 180 RPM)

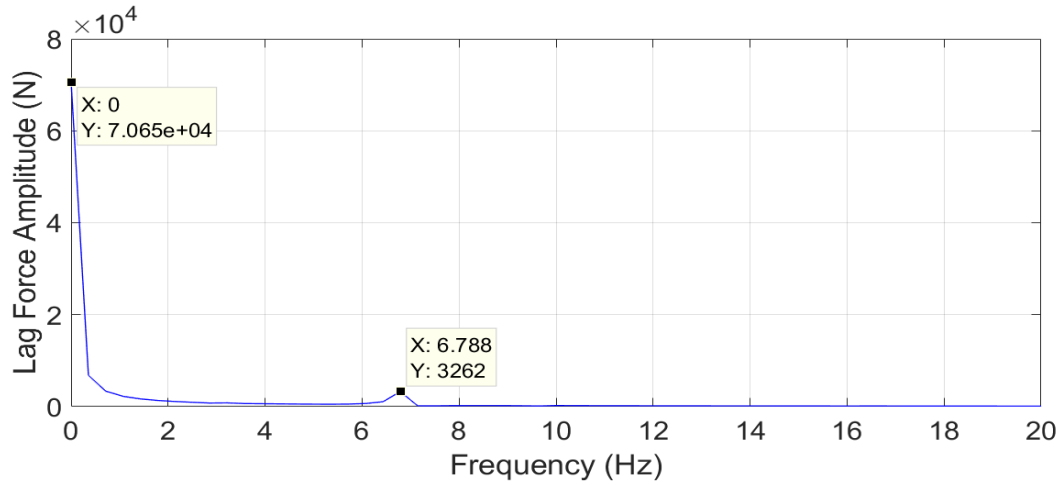


Figure 4.28: FFT analysis of lag force at resonance ($\mu_N = 0.3$; 230 \rightarrow 180 RPM)

Flap moment time history is provided in Figure 4.29. The flap moment amplitude does not increase significantly like lag moment, even though the second flap frequency crosses 5Ω . However, there is a noticeable increase in the flap moment amplitude. An FFT analysis of the data, Figure 4.30, shows that the flap moment increase is arriving from the 2/rev excitation. Hence, lag resonance is responsible for the flap moment increase as well. Even so, the increase is small compared to the mean flap moment value.

The variation of torsional moment with time shows that the resonance crossing increases the torsional moment amplitude considerably. The time history plot is given in Figure 4.31. The first torsional frequency crosses the 7/rev frequency line around 206

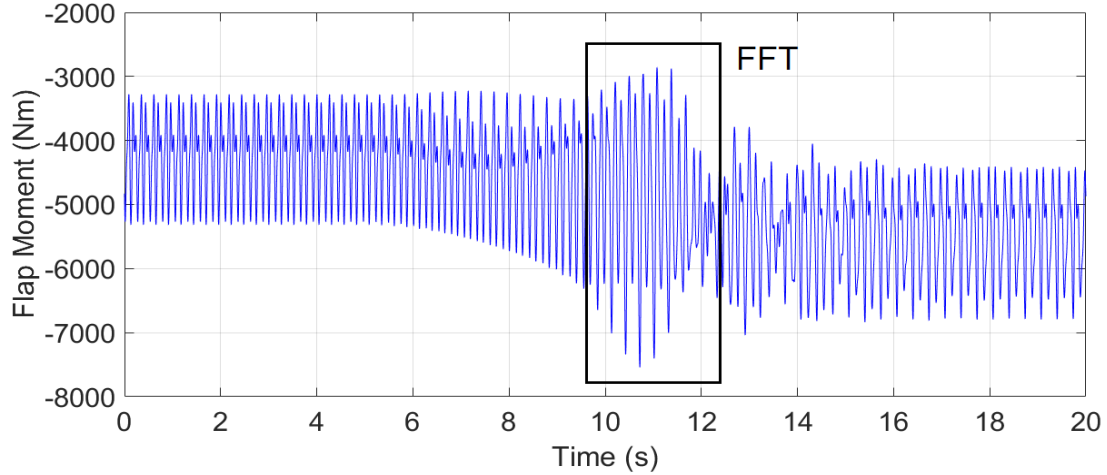


Figure 4.29: Time history of flap moment at blade root ($\mu_N = 0.3$; 230 \rightarrow 180 RPM)

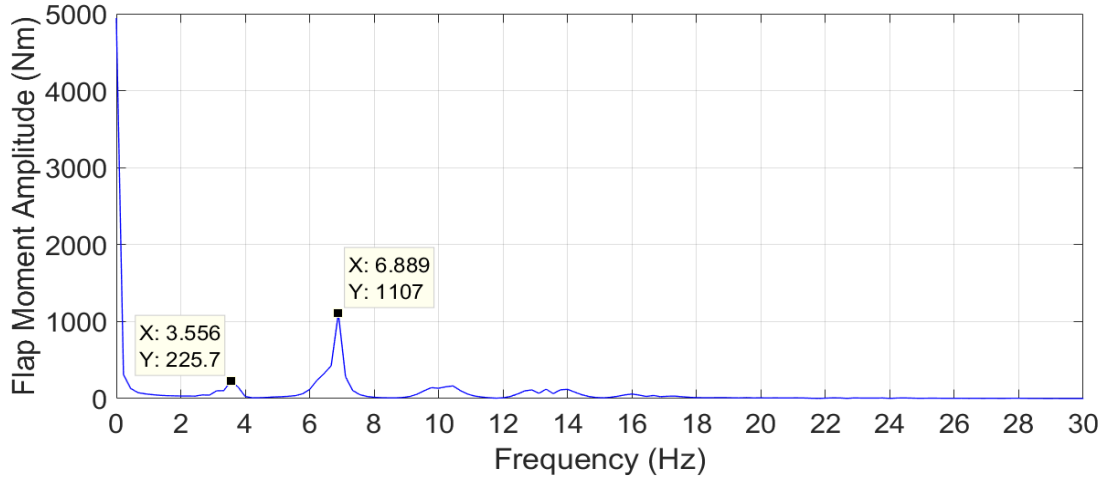


Figure 4.30: FFT analysis of flap moment at resonance ($\mu_N = 0.3$; 230 \rightarrow 180 RPM)

RPM. However, the FFT data shows that the dominating frequency is still 2/rev coming from the lag resonance. Hence, the higher frequency resonance crossing does not seem to have any noticeable impact on torsional response. This can be seen in the FFT Figure 4.32 as no visible peak exists beyond 16 Hz. Apart from the expected 1/rev peak, there are two additional low amplitude peaks close to 3/rev and 4/rev frequencies. These higher frequencies also contribute modestly to the torsional response during the steady state.

Another important rotor parameter that needs to be studied is the rotor torque. As we have seen before, rotor torque is a function of rotor speed. The rotor torque variation during the rotor speed change from 230 RPM to 180 RPM in the hub frame is shown in Figure

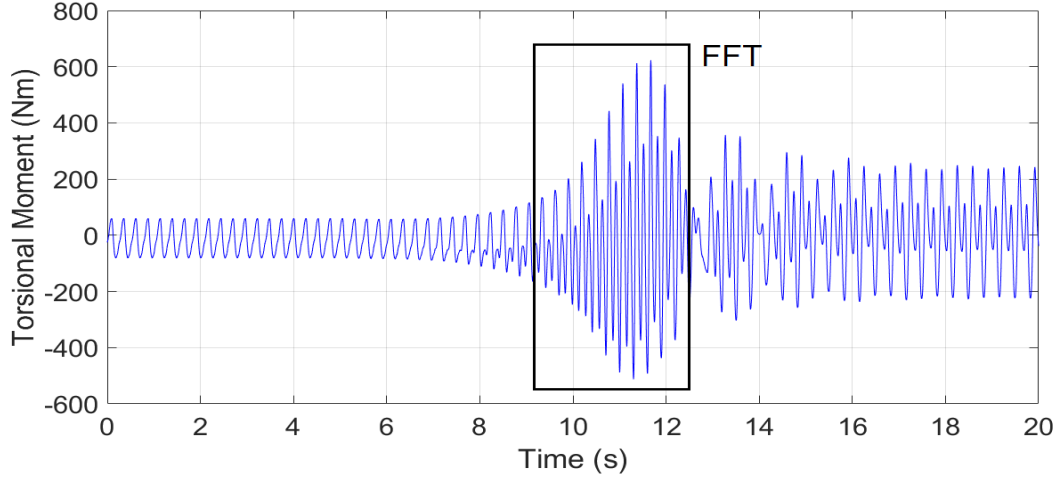


Figure 4.31: Time history of torsional moment at blade root ($\mu_N = 0.3$; 230 \rightarrow 180 RPM)

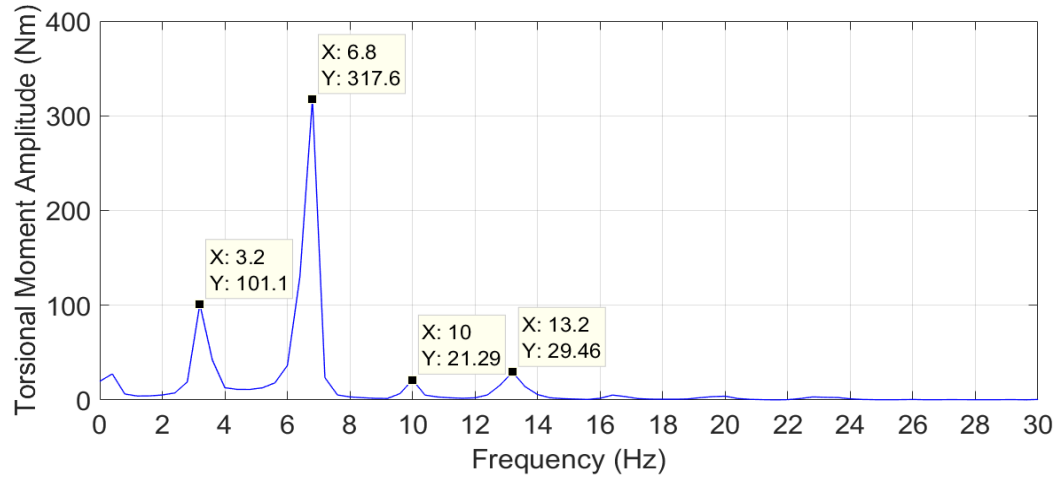


Figure 4.32: FFT analysis of torsional moment at resonance ($\mu_N = 0.3$; 230 \rightarrow 180 RPM)

4.33. The rotor torque decreases significantly with the decrease in rotor speed initially. However, as the rotor speed decrease rate starts to slow down, the torque slowly increases and reaches a steady state value. Therefore, the rotor torque follows the rotor's angular acceleration trend. The angular acceleration is shown in Figure 4.34. The rotor torque settles at the new steady state mean value, which is below the initial steady state mean value in this case, once the angular acceleration reaches zero.

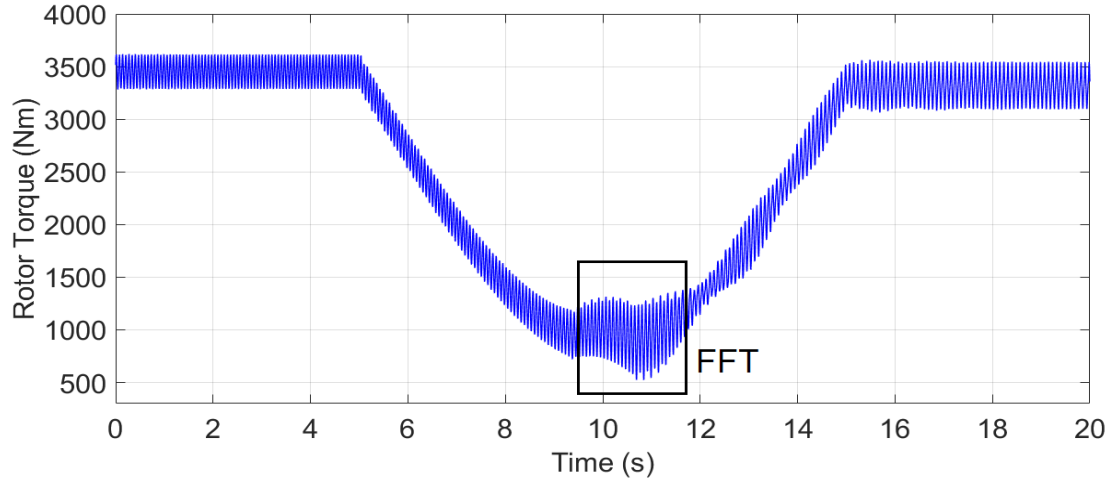


Figure 4.33: Time history of rotor torque ($\mu_N = 0.3$; 230 \rightarrow 180 RPM)

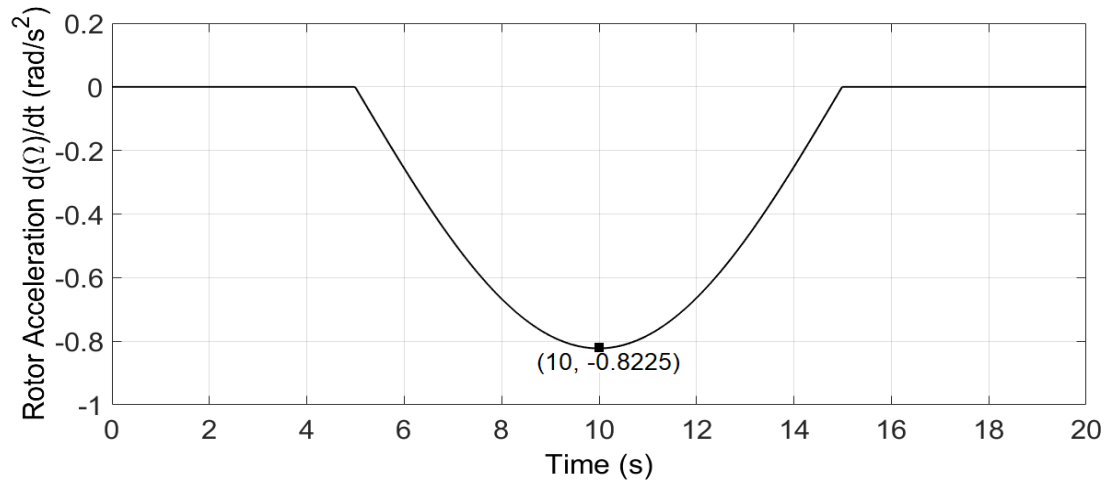


Figure 4.34: Rotor acceleration time history ($\Omega = 230$ to 180 RPM in 10 s)

The torque response curve also shows that there is an increase in rotor torque amplitude near the resonance crossing point in comparison to its neighborhood. A Fourier analysis in this region shows that a 4/rev excitation is causing this bump along with a lower amplitude 2/rev excitation. The hub acts as a filter that lets the 4/rev frequencies from the moving frame to the fixed frame for a four-bladed rotor system. This increased magnitude of torque in the fixed frame seems to be arriving from the 2/rev lag excitation in the moving frame.

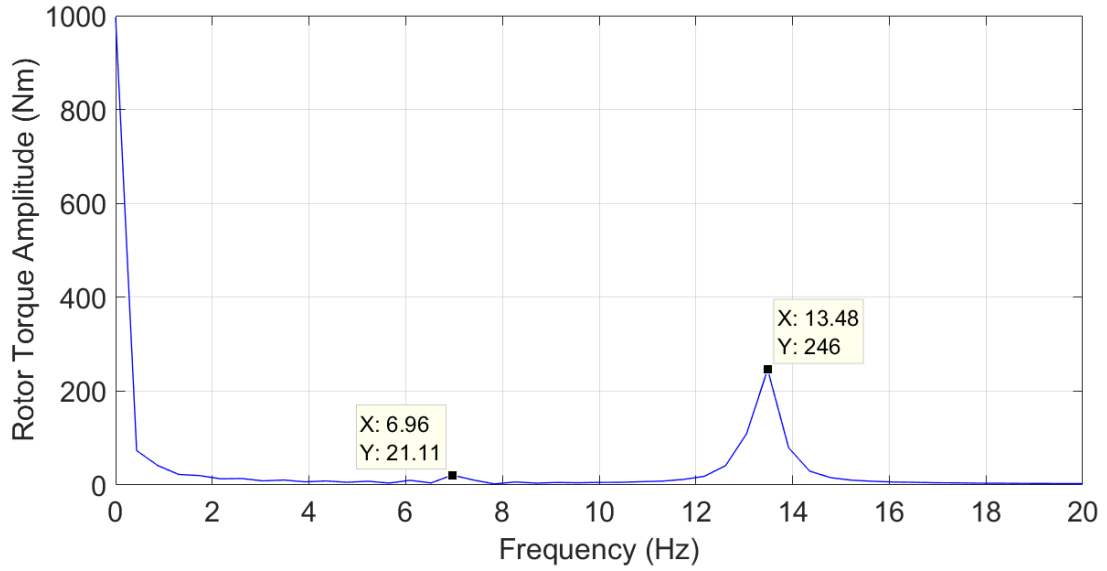


Figure 4.35: FFT analysis of rotor torque at resonance ($\mu_N = 0.3$; 230 \rightarrow 180 RPM)

Transition: 180 to 230 RPM

Once the rotor speed is reduced to 180 RPM, the rotor is operating at an increased efficiency. However, the maneuverability of the helicopter decreases as the rotor sections operate at high angles of attack. If the pilot decides to go back to nominal RPM for an increased maneuverability, the rotor speed needs to be changed smoothly from 180 to 230 RPM. The rotor speed and acceleration for 10 seconds transition are shown in Figures 4.36 and 4.37, respectively.

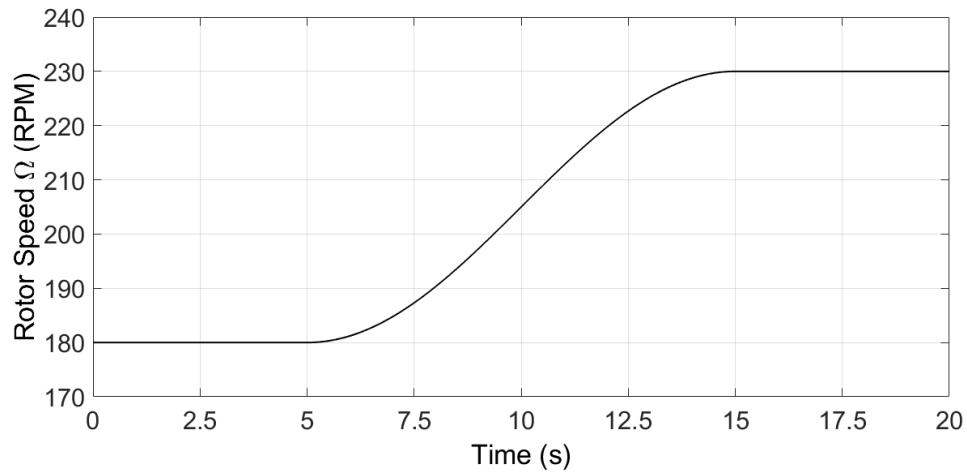


Figure 4.36: Rotor speed change from 180 to 230 RPM (10 s)

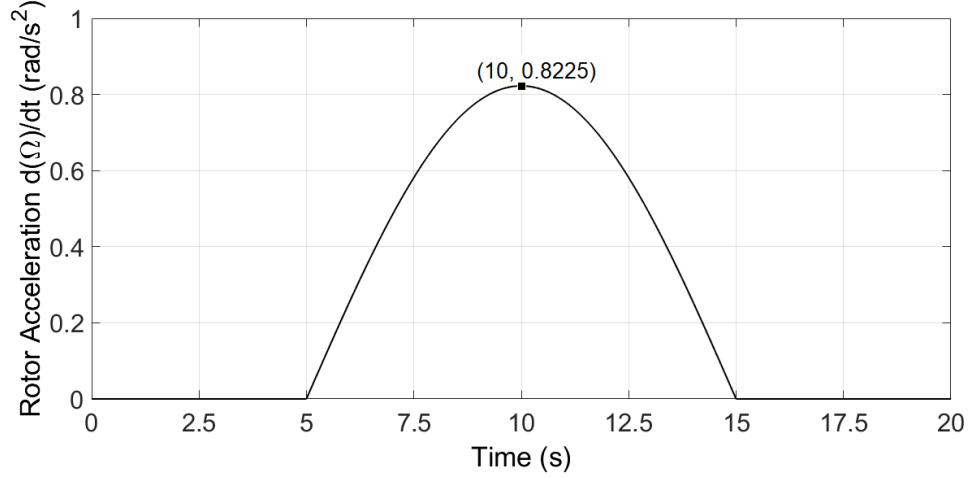


Figure 4.37: Rotor acceleration time history ($\Omega = 180$ to 230 RPM in 10 s)

The lag moment during this transition shows a similar behavior as the transition from 230 to 180 RPM. However, the magnitude of the lag moment increase has reduced, shown in Figure 4.38, comparatively. The amplitude and frequencies of the lag moment in the resonance region is shown in Figure 4.39. It can be seen that the frequency close to $2/\text{rev}$ is still dominating, but the amplitude is close to 8×10^3 Nm as compared to 9×10^3 Nm in the reverse transition, Figure 4.28. Hence, crossing the same resonance point in two different directions displays a non-linear resonance type behavior as discussed in [20].

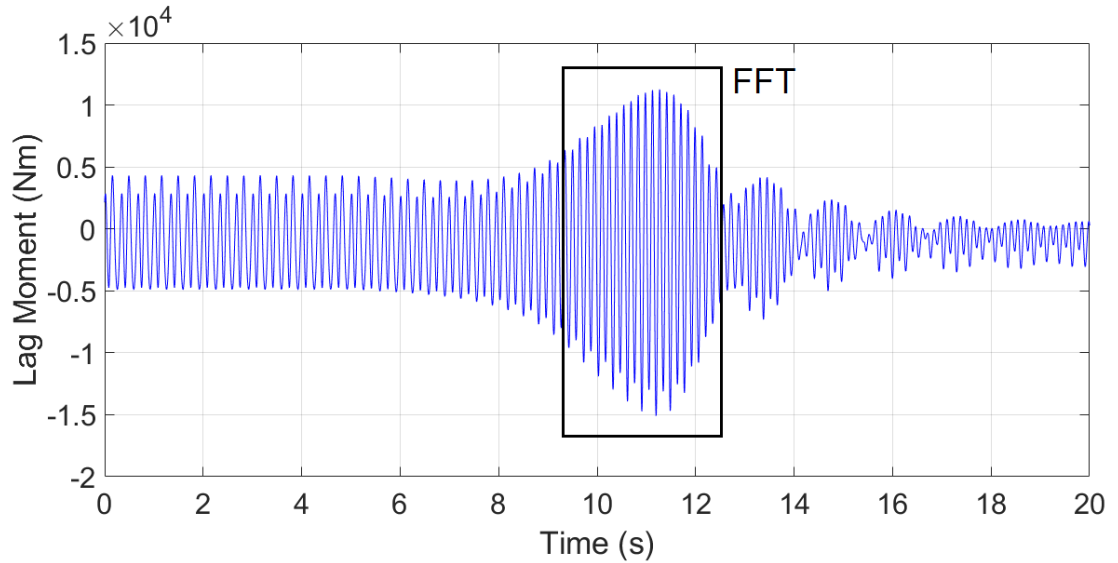


Figure 4.38: Time history of lag moment at blade root ($\mu_N = 0.3$; 180 \rightarrow 230 RPM)

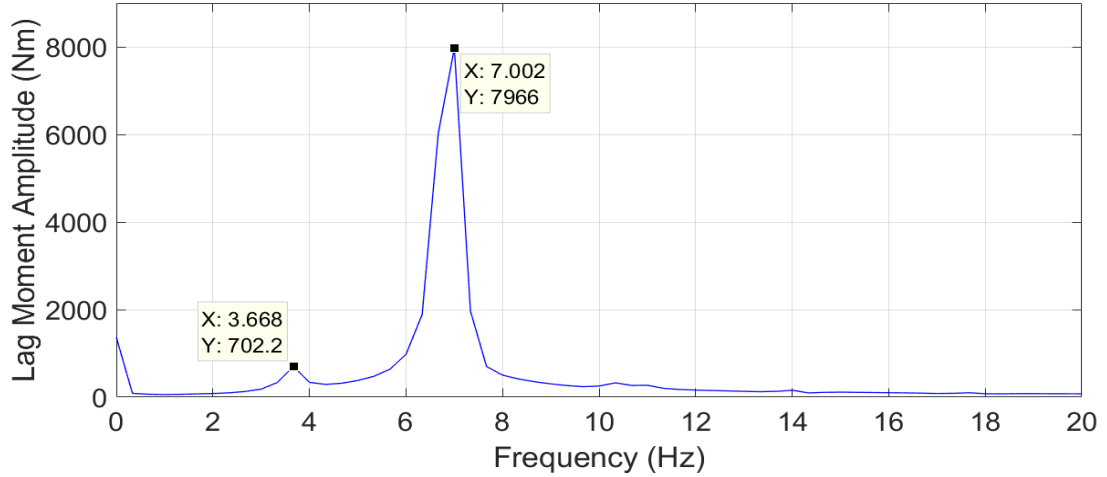


Figure 4.39: FFT analysis of lag moment at resonance ($\mu_N = 0.3$; 180 \rightarrow 230 RPM)

The lag force follows a trend similar to the rotor speed as shown in Figure 4.40. As the rotor speed increases, the lag force increases in the negative \bar{r}_2 direction. Lag force also shows an increased amplitude during the 2/rev resonance crossing. However, the amplitude of the increased lag force is small compared to the mean value as shown in Figure 4.41. This value is also lower compared to the 2/rev peak value for transition in the opposite direction, 4.28.

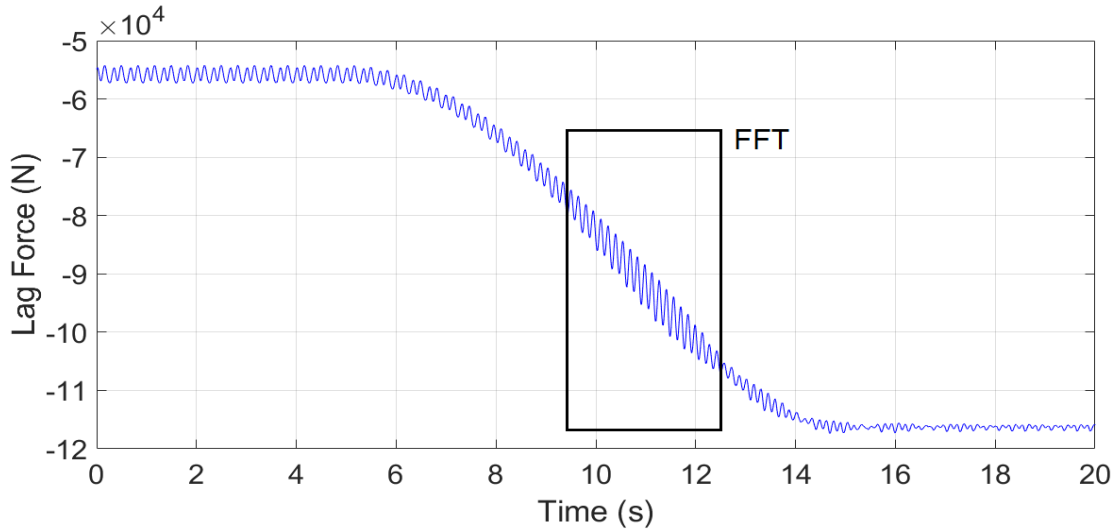


Figure 4.40: Time history of lag force at blade root ($\mu_N = 0.3$; 180 \rightarrow 230 RPM)

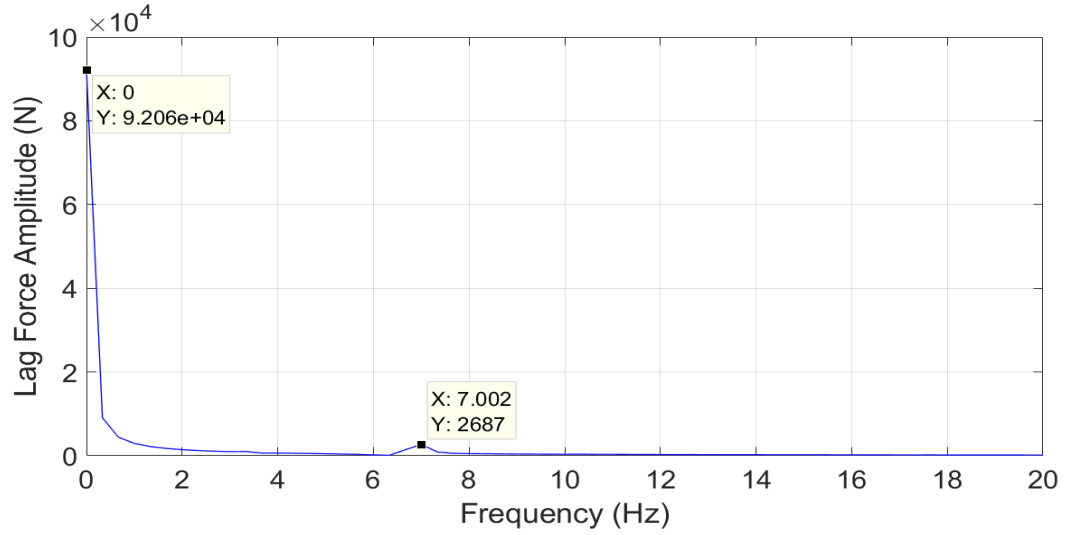


Figure 4.41: FFT analysis of lag force at resonance ($\mu_N = 0.3$; $180 \rightarrow 230$ RPM)

Flap moment response and the FFT plot of the resonance region are shown in Figures 4.42 and 4.43, respectively. The 2/rev frequency is still dominating with frequencies close to 1/rev, 3/rev and 4/rev contributing in meager quantities to the total amplitude. However, the peak at 2/rev is slightly greater than the corresponding peak for the reverse transition, Figure 4.30.

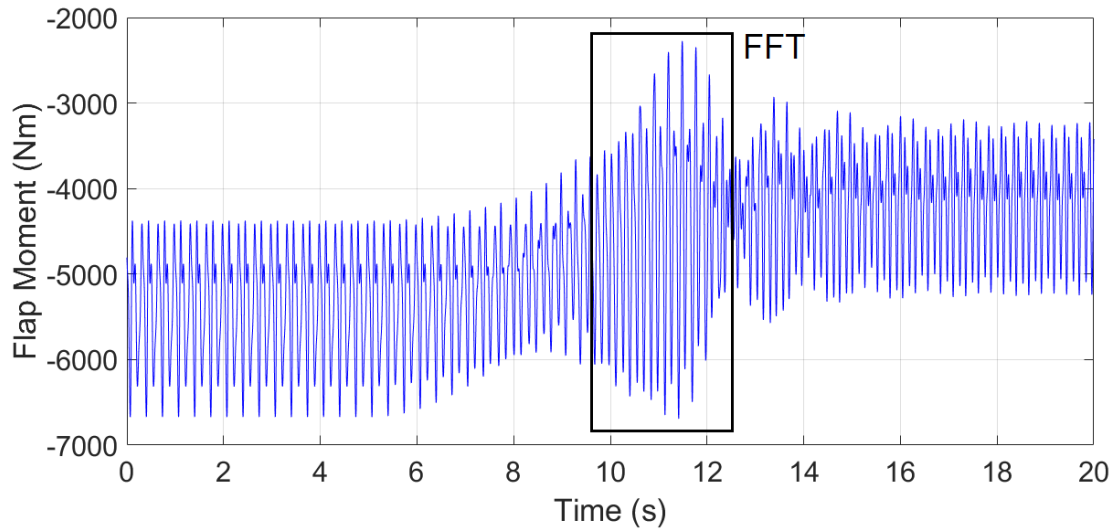


Figure 4.42: Time history of flap moment at blade root ($\mu_N = 0.3$; $180 \rightarrow 230$ RPM)

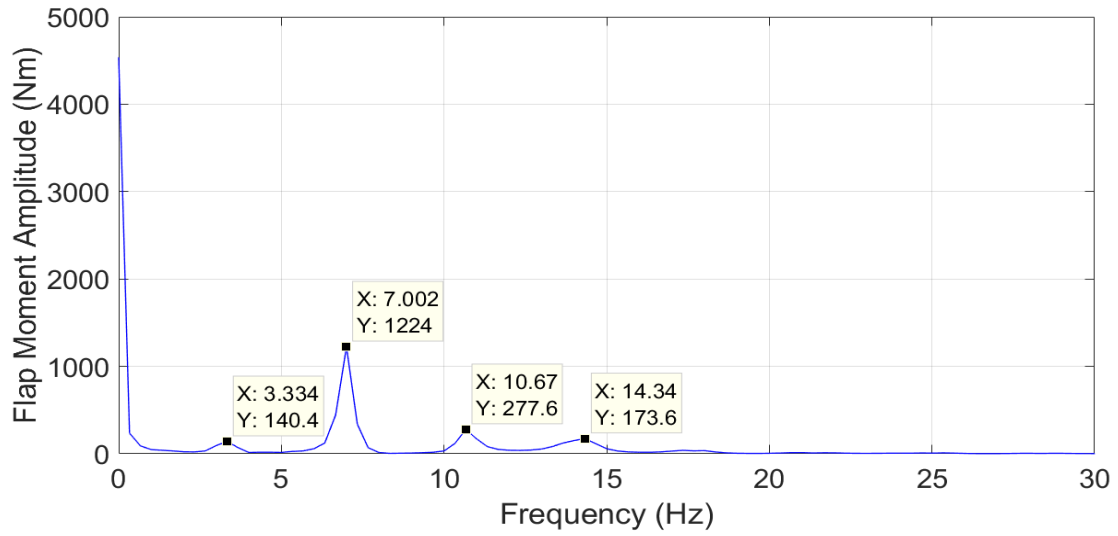


Figure 4.43: FFT analysis of flap moment at resonance ($\mu_N = 0.3$; 180 \rightarrow 230 RPM)

Torsional moment response is shown in Figure 4.44. The FFT of the resonance region signal is given in Figure 4.45. The dominating frequency is 2/rev with 1/rev being the second dominant frequency. The amplitudes are noticeably lower than the amplitudes in Figure 4.32.

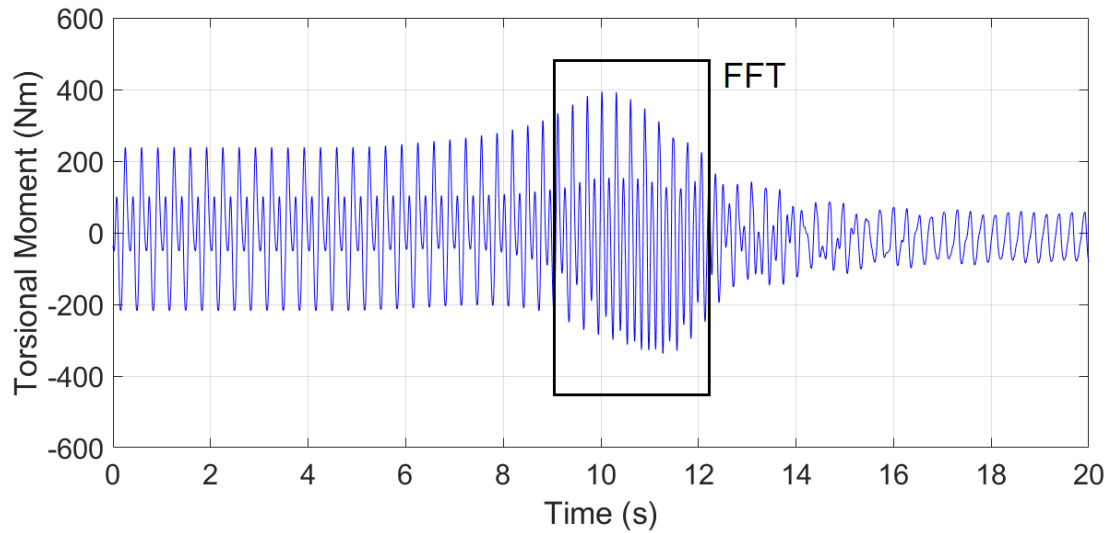


Figure 4.44: Time history of torsional moment at blade root ($\mu_N = 0.3$; 180 \rightarrow 230 RPM)

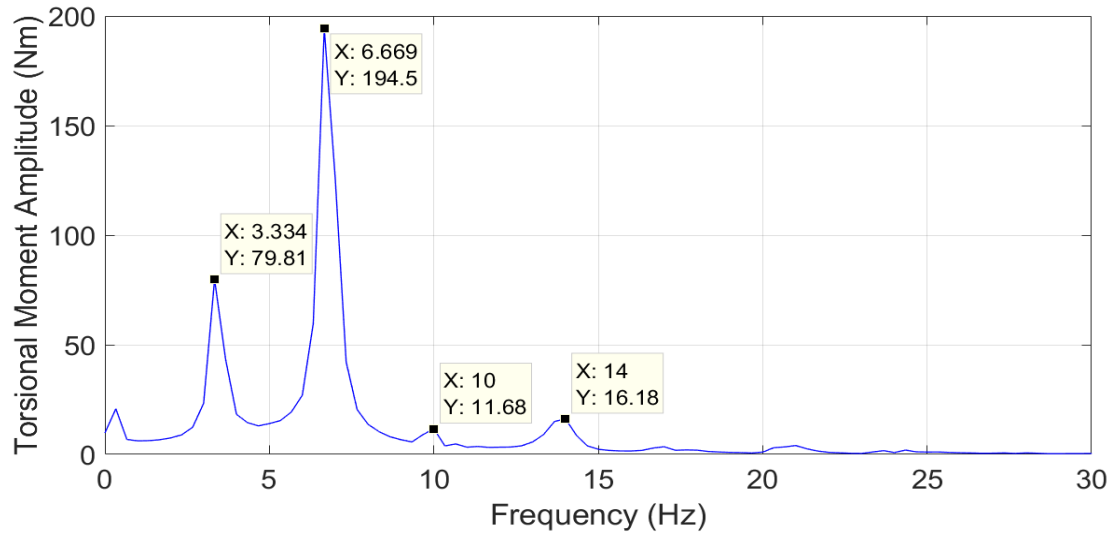


Figure 4.45: FFT analysis of torsional moment at resonance ($\mu_N = 0.3$; 180 \rightarrow 230 RPM)

The rotor torque increases during the transition from 180 to 230 RPM and follows the rotor acceleration trend. The rotor torque is shown in Figure 4.46. The rotor torque reaches a peak close to 6000 Nm during resonance crossing. This is significantly higher than the torque response during the opposite transition, where the torque reduces in comparison to the steady state value. The FFT analysis shows that the 4/rev response is dominating compared to the 2/rev response in the fixed frame, Figure 4.47. The peak amplitudes are comparable to the amplitudes in Figure 4.35 except for the mean value.

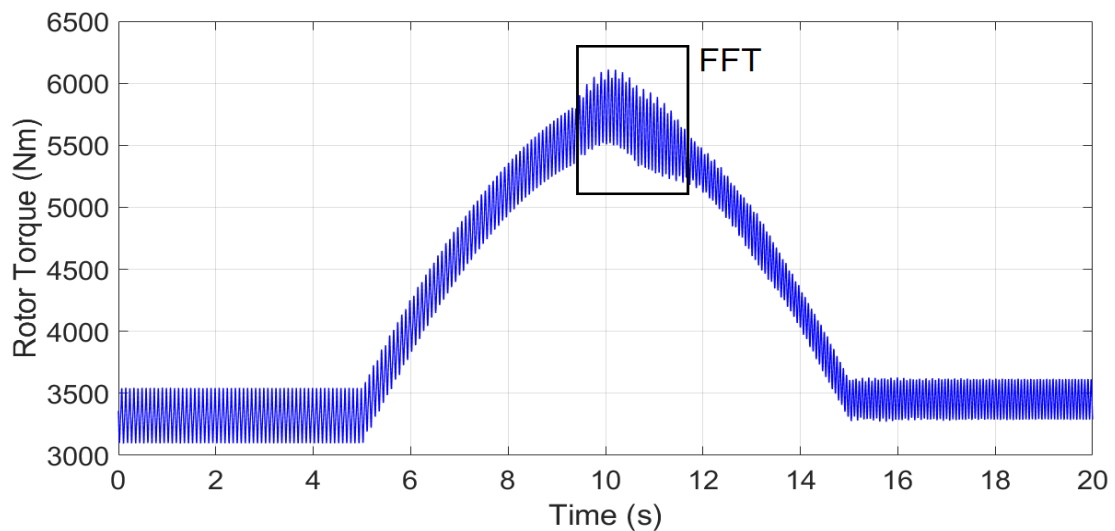


Figure 4.46: Time history of rotor torque ($\mu_N = 0.3$; 180 \rightarrow 230 RPM)

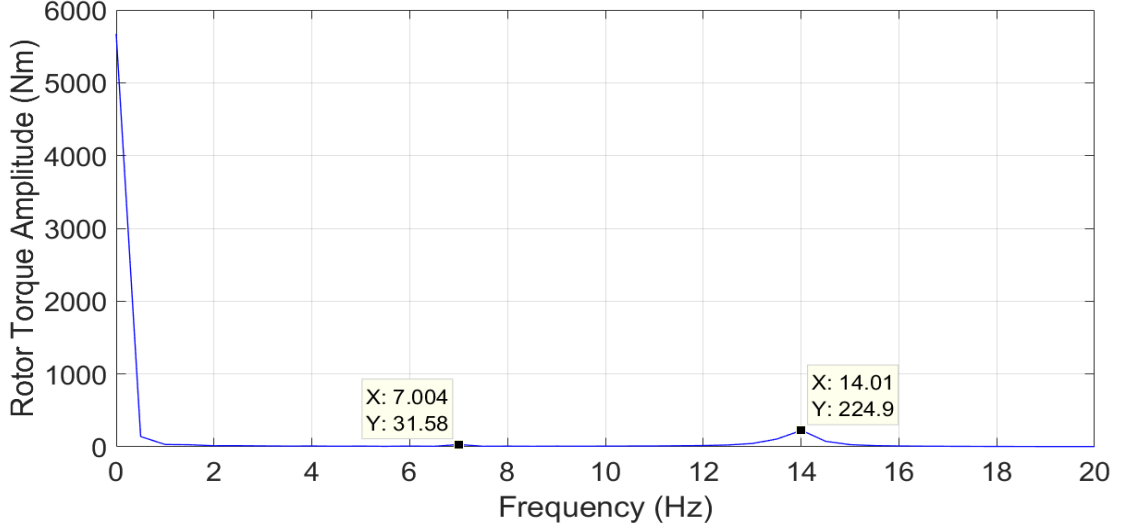


Figure 4.47: FFT analysis of rotor torque at resonance ($\mu_N = 0.3$; $180 \rightarrow 230$ RPM)

4.6.3 Nominal Advance Ratio, $\mu_N = 0.2$

After analyzing the transition for $\mu_N = 0.3$, let us consider the resonance crossing points for the nominal advance ratio of 0.2. It can be seen from Figure 4.18 that the resonance crossing points for $\mu_N = 0.2$ are same as $\mu_N = 0.3$. As the rotor speed is reduced to 150 RPM from the nominal speed, no additional resonance points get added. However, as the rotor is operating at a different forward speed, the response of the blade is expected to be different for the same resonance crossings. The resonance points are given in Table 4.5.

Table 4.5: Resonance points between 230 RPM and 150 RPM.

Blade Frequency Mode	Crossing Point (/rev)	Crossing Frequency (Hz)
1 st Lag	2	6.863
2 nd Flap	5	15.299
1 st Torsion	7	24.056

The response of the blades during transition is given in the following sections.

Transition: 230 to 150 RPM

In order to have a reasonable comparison across the advance ratios, the rotor speed is changed in such a way that the amplitude of the peak or valley of the rotor acceleration curve remains the same across all μ_N values during transition. The rotor speed is changed from 230 to 180 RPM in 10 seconds for $\mu_N = 0.3$. Therefore, the rotor speed is changed from 230 to 150 RPM in 16 seconds for $\mu_N = 0.2$. This leads to the rotor acceleration curve shown in Figure 4.49, which has the same valley as Figure 4.34 but stretched in time. The rotor speed and trim angles are shown in Figures 4.48 and 4.50, respectively.

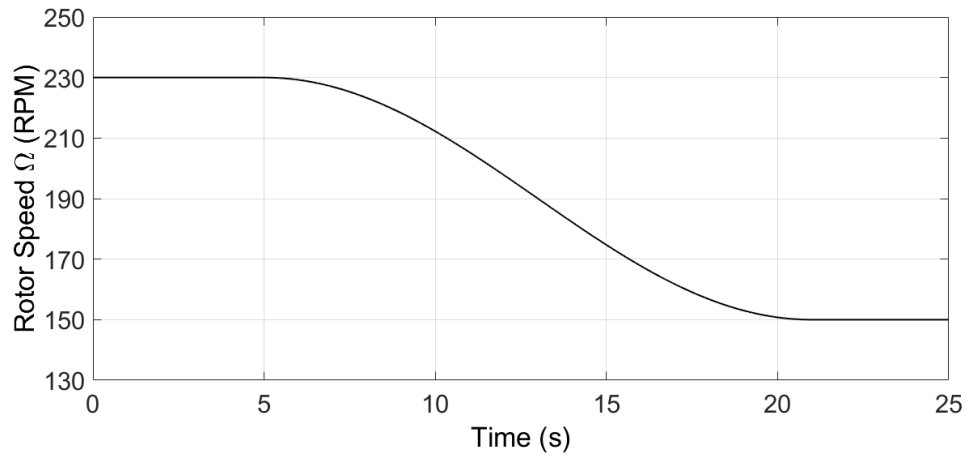


Figure 4.48: Rotor speed change from 230 to 150 RPM (16 s)

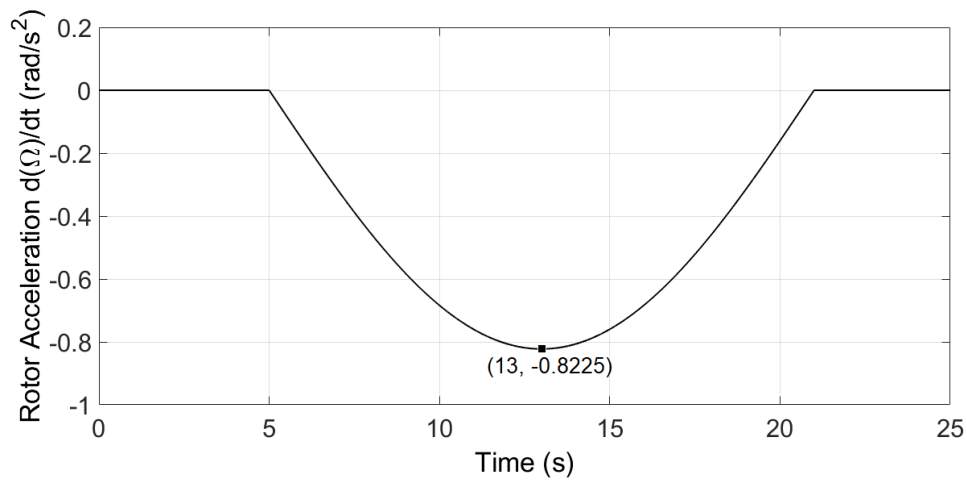


Figure 4.49: Rotor acceleration time history ($\Omega = 230$ to 150 RPM in 16 s)

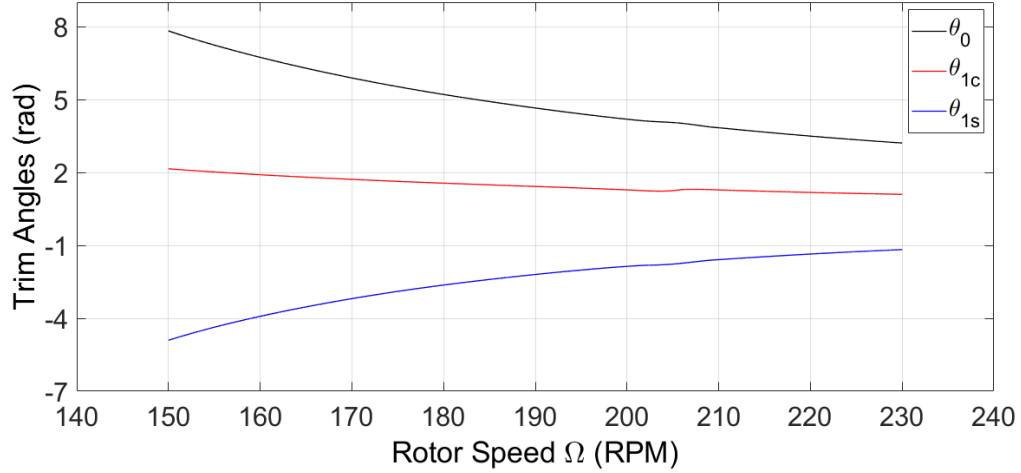


Figure 4.50: Pitch angles for $\mu_N = 0.2$

For readers who are once again curious about how the pitch angles vary with time, it is shown in Figure 4.51. This graph will not be provided for the subsequent sections as it becomes redundant once the pitch angles are given as a function of rotor speed.

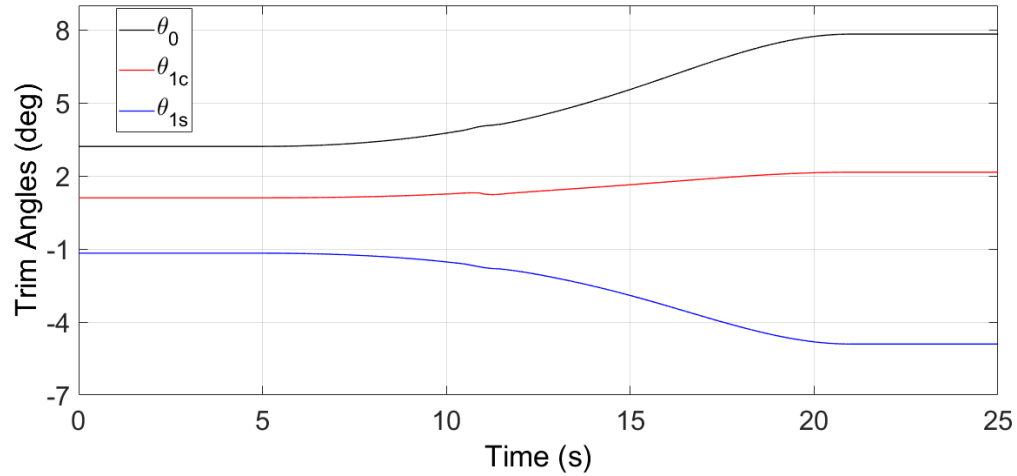


Figure 4.51: Pitch angles variation with time for $\mu_N = 0.2$ (16 s, 230 \rightarrow 150 RPM)

Lag moment time history is shown in Figure 4.52. The amplitude during resonance is lower compared to the $\mu_N = 0.3$ case. This can also be seen in the FFT analysis of the resonance region, Figure 4.53. The reason for this lower amplitude increase, despite having a relatively close $\dot{\Omega}$ during resonance, can be explained by observing the pitch angles. Figure 4.54 gives the trim angles at 2/rev lag crossing for $\mu_N = 0$ to 0.3. θ_{1c} does not vary significantly in forward speed but the θ_{1s} value decreases in magnitude with decrease

in μ_N . Having a lower cyclic pitch angle means that the blade's response is less harmonic than the previous case. This reduced harmonic behavior of the blade leads to a lower amplitude increase during resonance. However, the increase in amplitude during resonance is still approximately 7 times the steady state amplitude at 230 RPM. As expected, the dominating frequency is still 2/rev with 1/rev and 3/rev making small contributions.

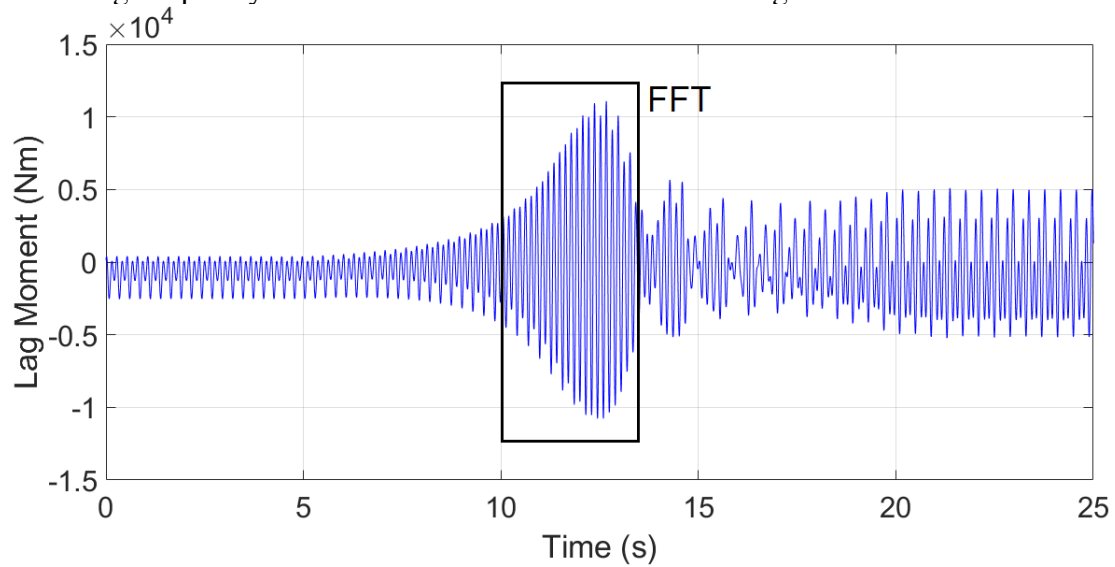


Figure 4.52: Time history of lag moment at blade root ($\mu_N = 0.2$; 230 \rightarrow 150 RPM)

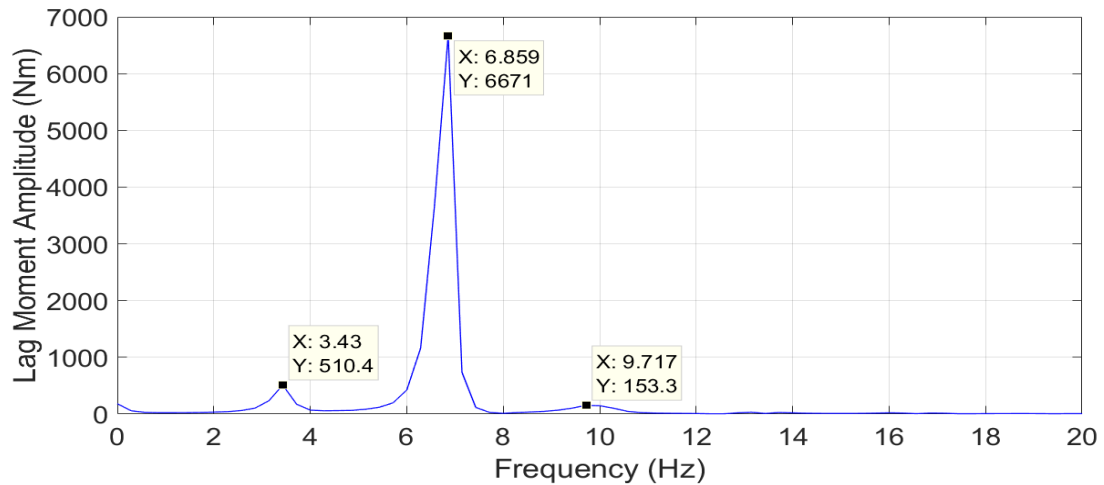


Figure 4.53: FFT analysis of lag moment at resonance ($\mu_N = 0.2$; 230 \rightarrow 150 RPM)

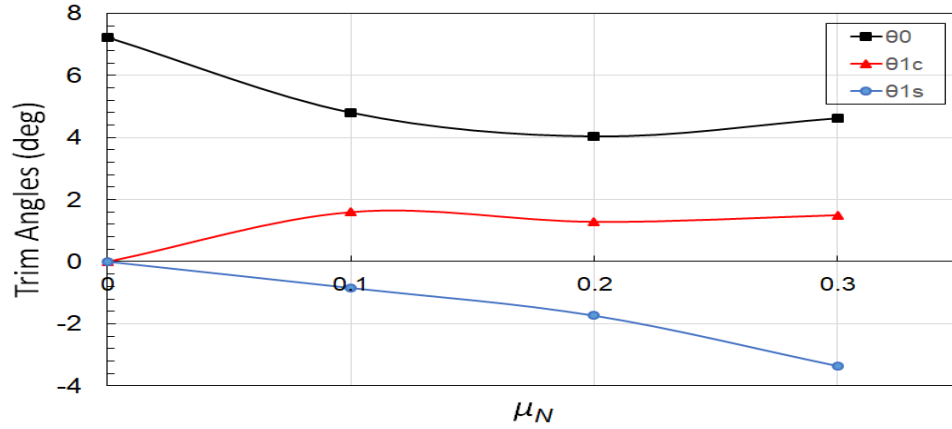


Figure 4.54: Pitch angles at 2/rev lag resonance (at 205.8 RPM)

The lag force decreases in magnitude with reduction in rotor speed, Figure 4.55. The resonance crossing causes a noticeable increase in the lag force during transition. FFT of this signal is shown in Figure 4.56.

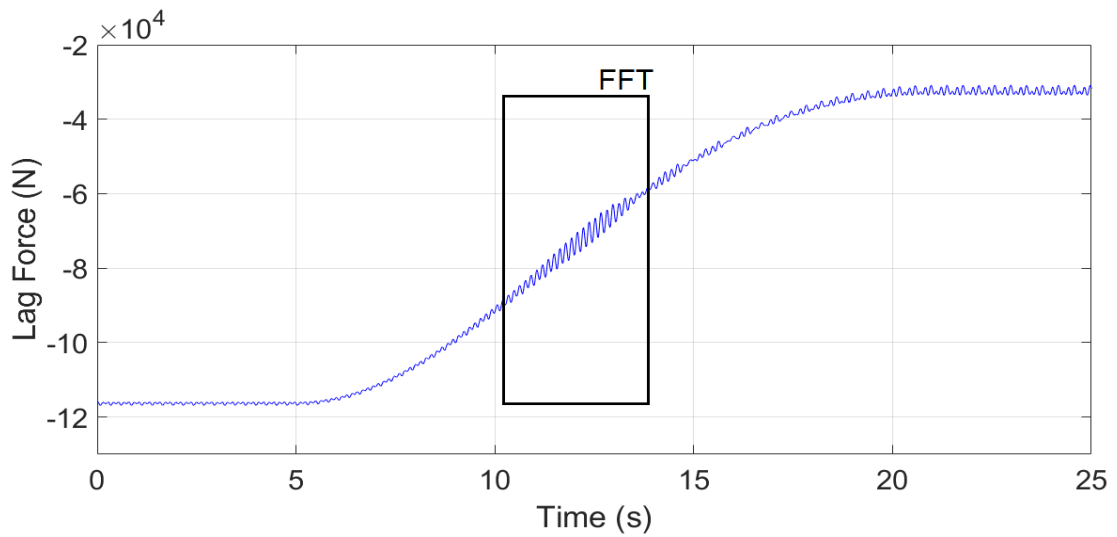


Figure 4.55: Time history of lag force at blade root ($\mu_N = 0.2$; 230 → 150 RPM)

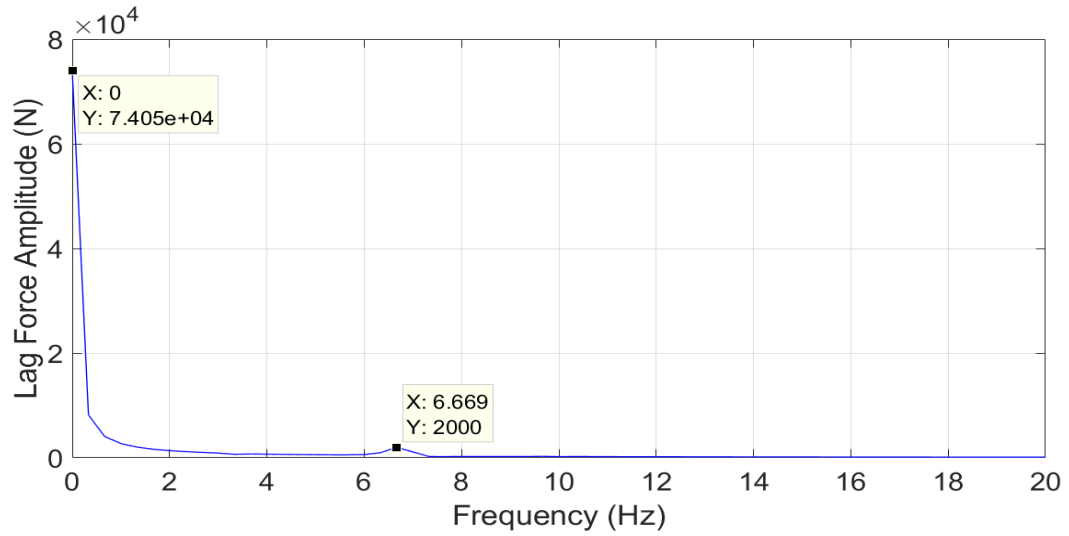


Figure 4.56: FFT analysis of lag force at resonance ($\mu_N = 0.2$; 230 \rightarrow 150 RPM)

Flap moment resonance also has a lower amplitude compared to the corresponding value at higher forward speed, Figure 4.57. Even though the 2/rev frequency is dominating, Figure 4.58, the frequencies close to 3/rev and 5/rev also make small contributions to the resonance. It should be noted that the rotor's second flap frequency crosses 5/rev during this transition.

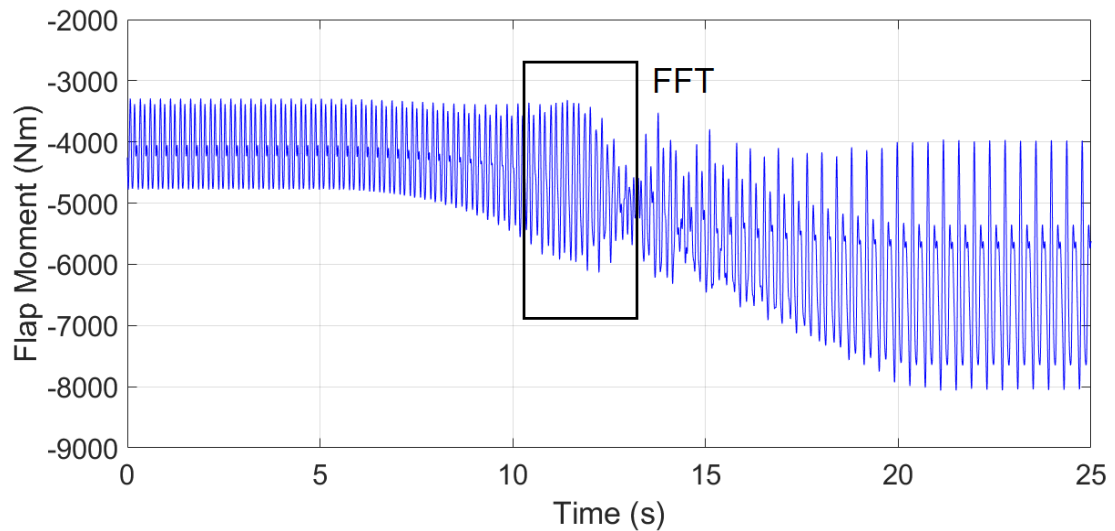


Figure 4.57: Time history of flap moment at blade root ($\mu_N = 0.2$; 230 \rightarrow 150 RPM)

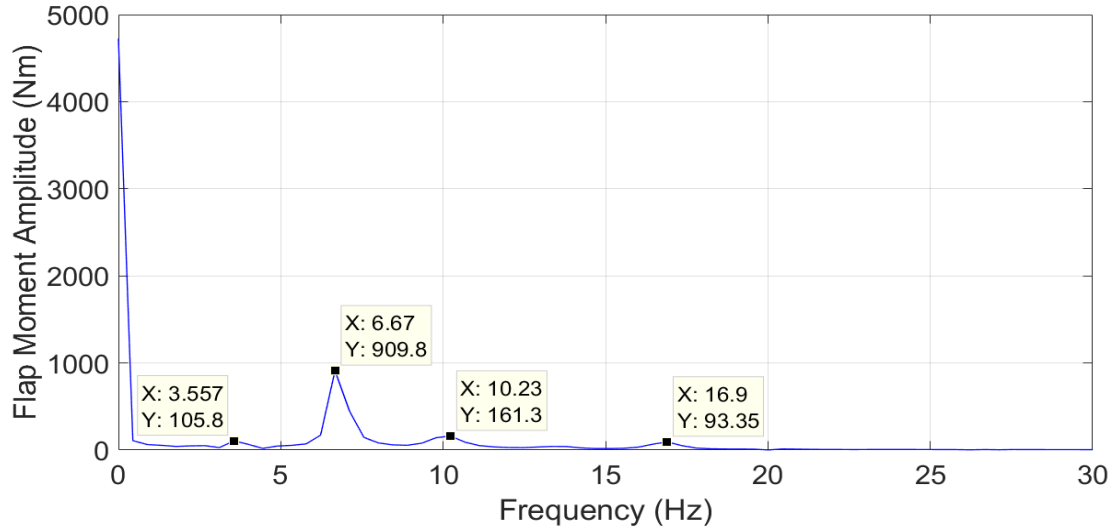


Figure 4.58: FFT analysis of flap moment at resonance ($\mu_N = 0.2$; 230 \rightarrow 150 RPM)

The frequencies that are dominating the torsional moment response are similar to the previous cases, Figures 4.59 and 4.60. The amplitude of the dominating frequency is lower in comparison. The 7/rev first torsion crossing doesn't seem to have any noticeable impact on the blade response.

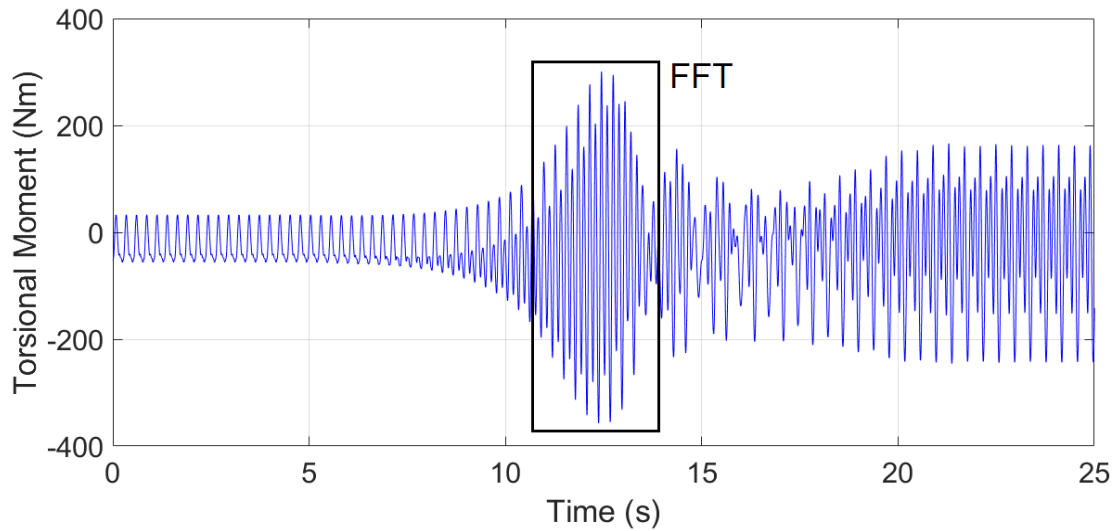


Figure 4.59: Time history of torsional moment at blade root ($\mu_N = 0.2$; 230 \rightarrow 150 RPM)

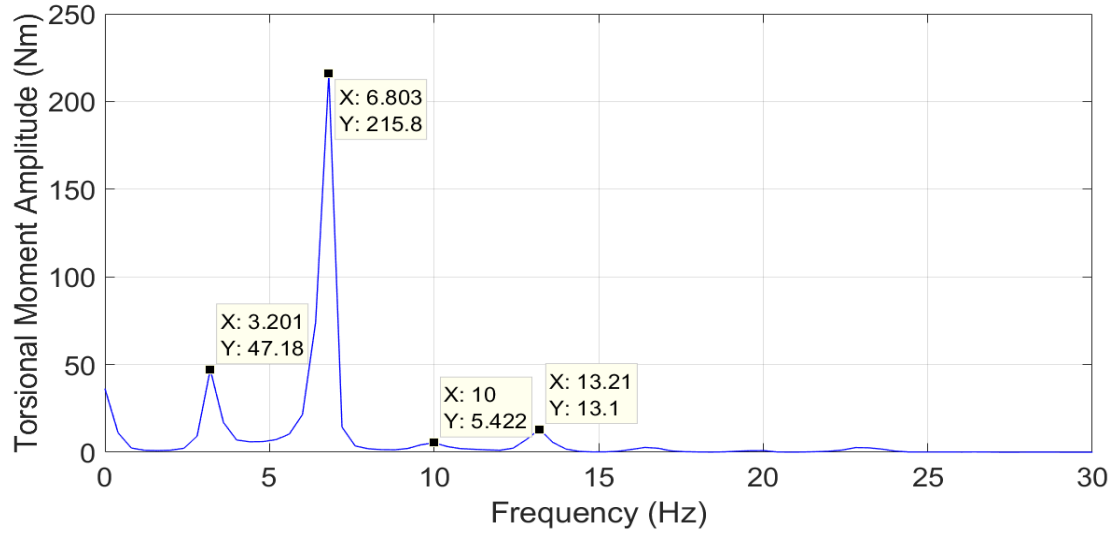


Figure 4.60: FFT analysis of torsional moment at resonance ($\mu_N = 0.2$; 230 \rightarrow 150 RPM)

The rotor torque response is different compared to the previous case, as seen in Figure 4.61. The amplitude starts growing around 10 seconds and seems to have multiple frequencies contributing to the resonance behavior. FFT analysis of this signal reveals that the frequencies between 12 and 14 Hz, which are close to 4/rev, are playing a role in this peculiar behavior, Figure 4.62.

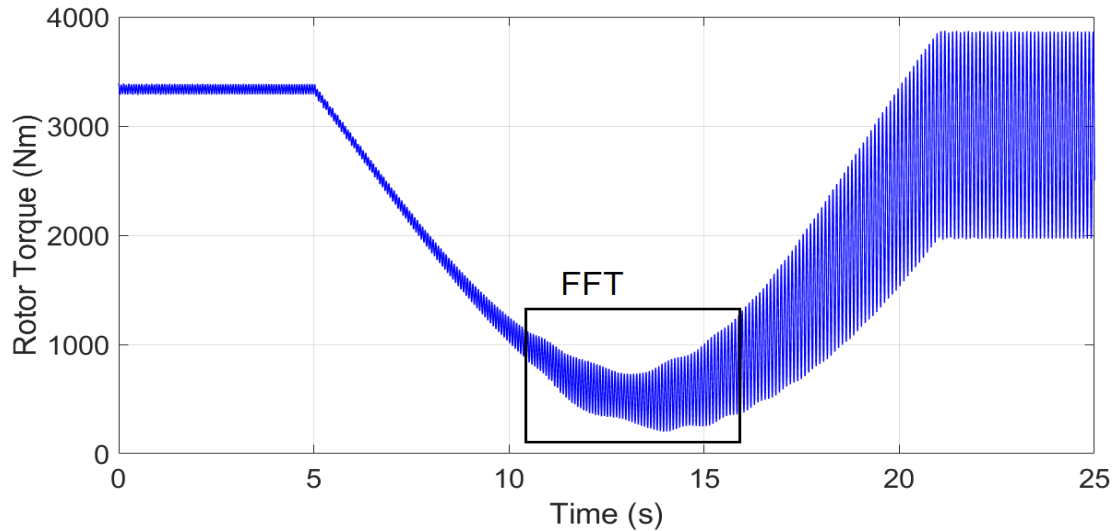


Figure 4.61: Time history of rotor torque ($\mu_N = 0.2$; 230 \rightarrow 150 RPM)

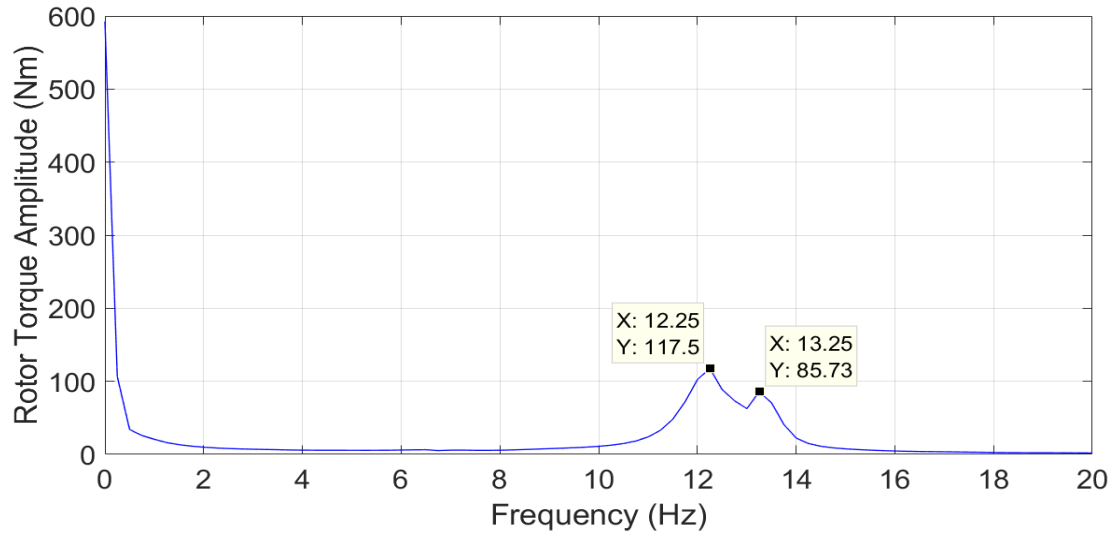


Figure 4.62: FFT analysis of rotor torque at resonance ($\mu_N = 0.2$; 230 \rightarrow 150 RPM)

Transition: 150 to 230 RPM

The reverse transition from 150 to 230 RPM will be dealt with in this section. The rotor speed is increased from lower RPM to higher RPM in 16 seconds. The rotor speed is shown in Figure 4.63 and the acceleration curve is shown in Figure 4.64.

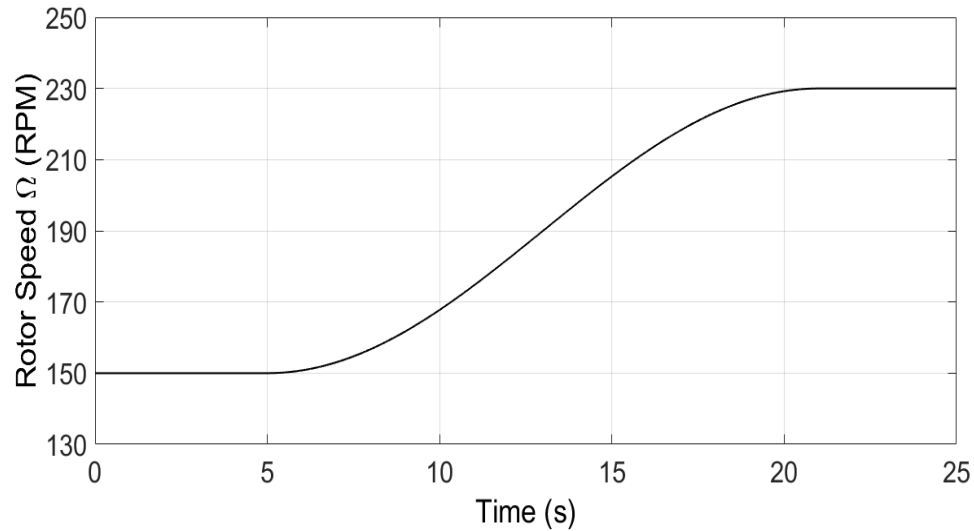


Figure 4.63: Rotor speed change from 150 to 230 RPM (16 s)

Lag moment time history, Figure 4.65, shows that the amplitude during resonance is slightly lower compared to the previous case at $\mu_N = 0.2$. Hence, the low-to-high speed

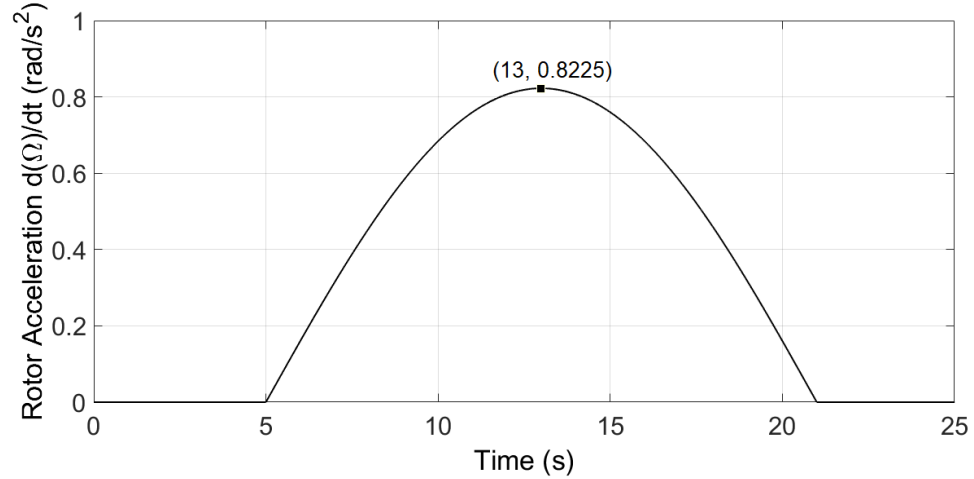


Figure 4.64: Rotor acceleration time history ($\Omega = 150$ to 230 RPM in 16 s)

transition cases are noticed to have lower lag moment amplitude increase during resonance than the high-to-low speed transitions. Similar trend has been observed for $\mu_N = 0.3$ cases. This could be because of the pitch angles having a decreasing trend in the low-to-high speed transition, Figure 4.50. FFT analysis of the resonance region, Figure 4.66, shows that even though the 2/rev and 1/rev signals have lower amplitudes, the mean value is higher in this case. This should be taken into account if one were to perform fatigue analysis. The dominating frequency is still 2/rev.

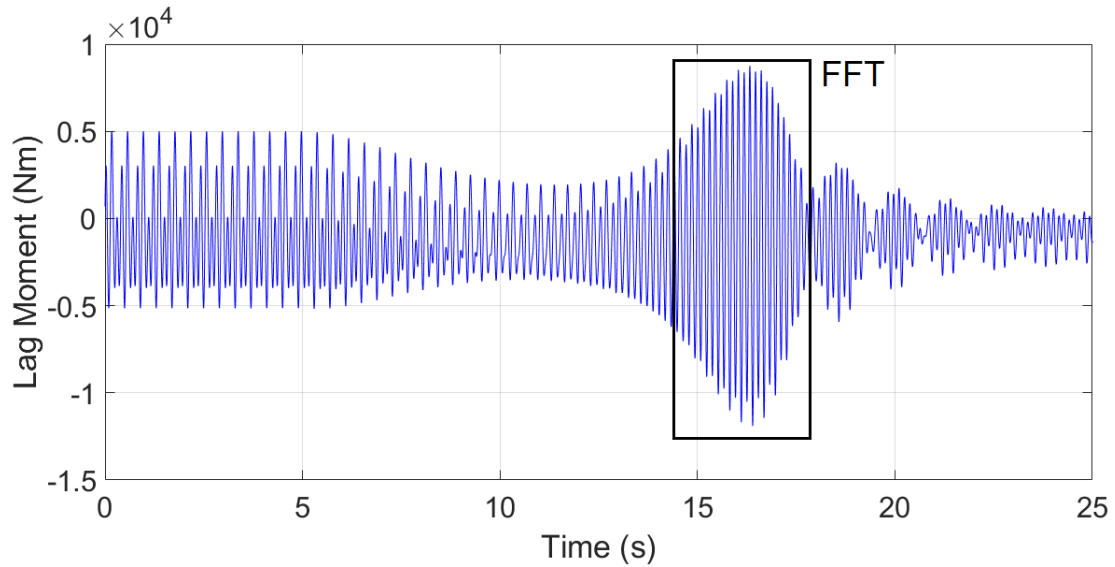


Figure 4.65: Time history of lag moment at blade root ($\mu_N = 0.2$; 150 \rightarrow 230 RPM)

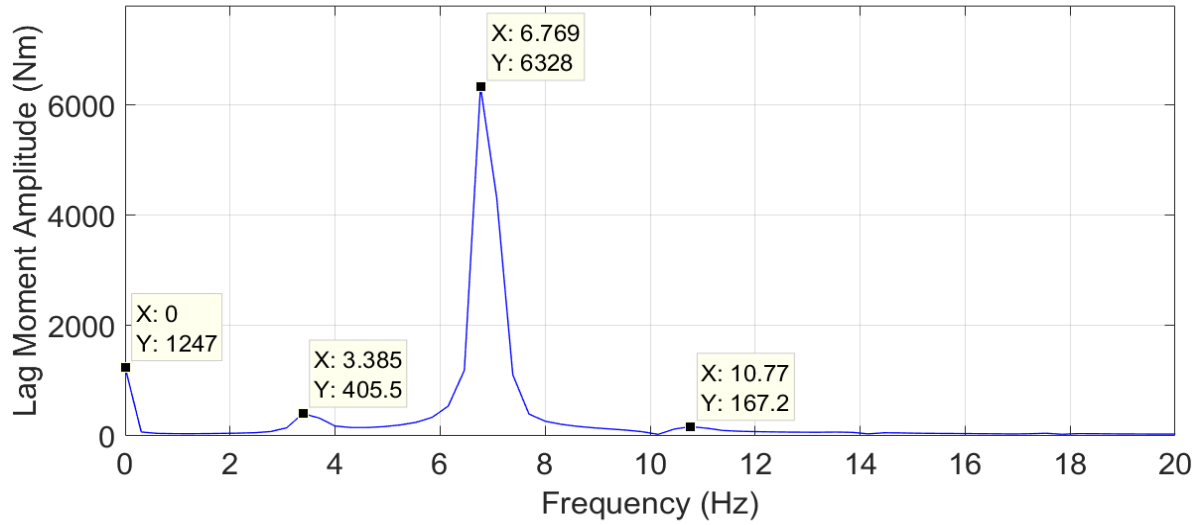


Figure 4.66: FFT analysis of lag moment at resonance ($\mu_N = 0.2$; 150 \rightarrow 230 RPM)

The lag force heads in the opposite direction, as expected, compared to the previous case as shown in Figure 4.67. However, the magnitude of 2/rev is slightly higher here, Figure 4.68. The mean value is also higher as the rotor speed is operating at a greater speed. It should be noted at this point that the lag force doesn't increase significantly like the lag moment during resonance crossing.

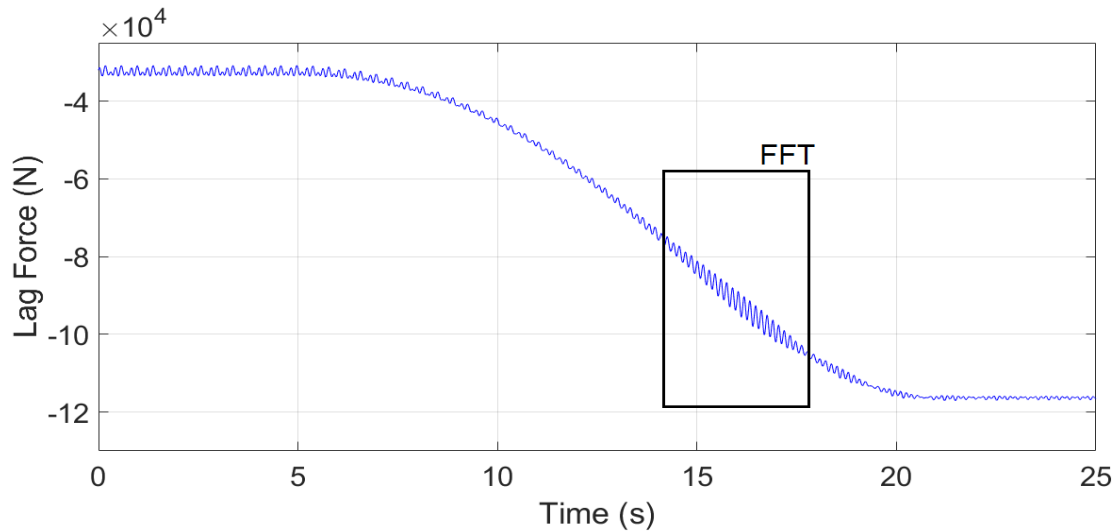


Figure 4.67: Time history of lag force at blade root ($\mu_N = 0.2$; 150 \rightarrow 230 RPM)

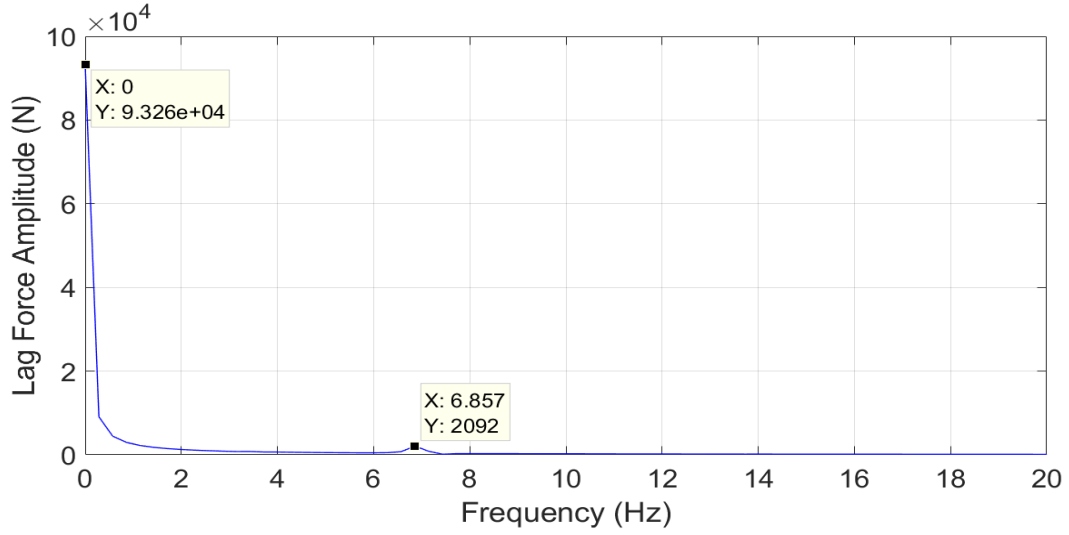


Figure 4.68: FFT analysis of lag force at resonance ($\mu_N = 0.2$; 150 \rightarrow 230 RPM)

Flap moment resonance has a behavior very similar to the reverse transition case. The dominating frequencies still remain the same, with mean value being the highest. The flap moment and the corresponding FFT plot of the resonance region are shown in Figures 4.69 and 4.70, respectively. The amplitudes of the FFT peaks are also comparable to the transition in the opposite direction.

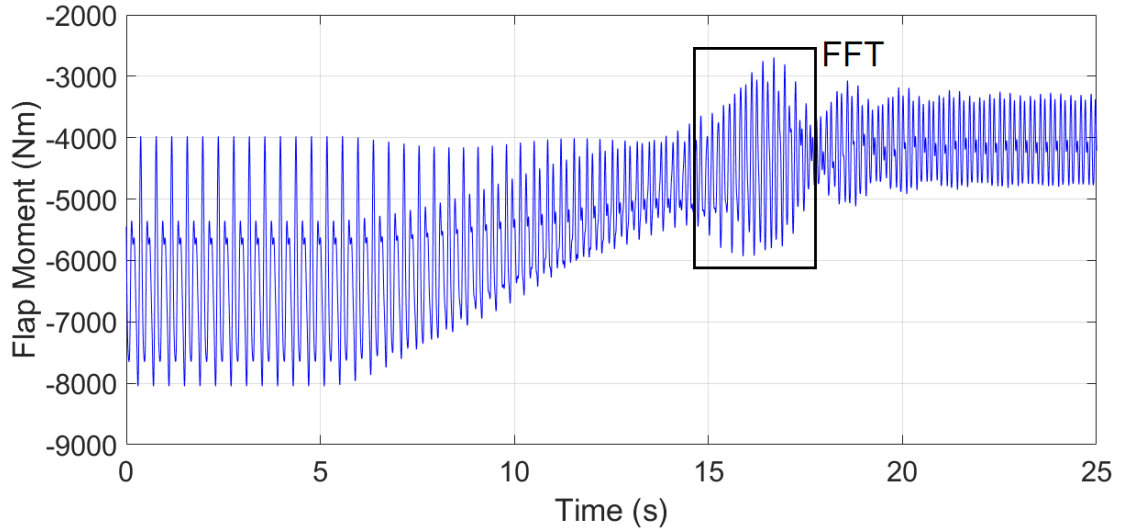


Figure 4.69: Time history of flap moment at blade root ($\mu_N = 0.2$; 150 \rightarrow 230 RPM)

The torsional moment's resonance response is smoother in comparison to the previous transition. The same frequencies are dominating with a moderately lower amplitude as

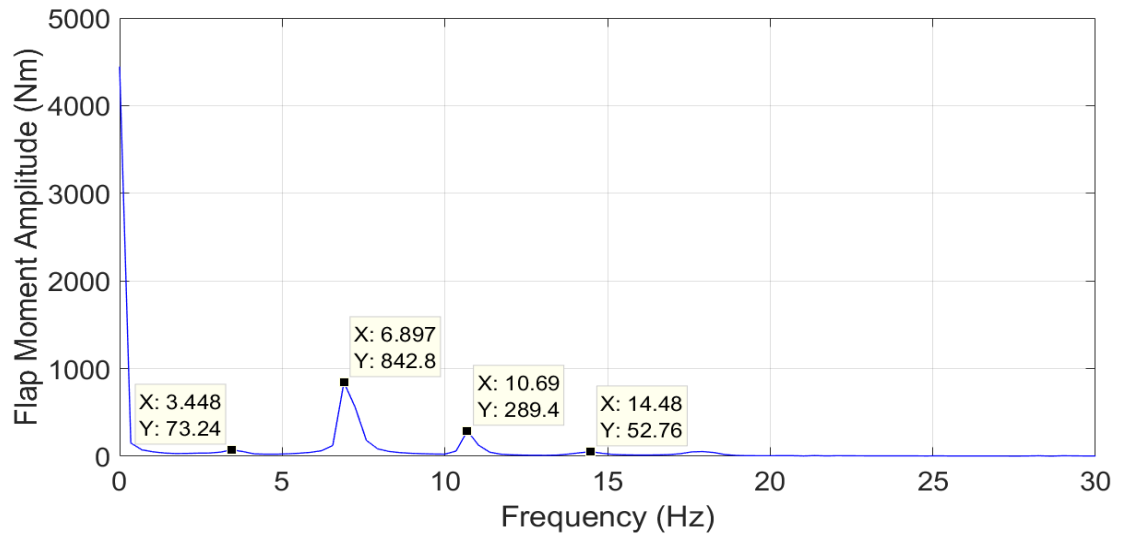


Figure 4.70: FFT analysis of flap moment at resonance ($\mu_N = 0.2$; 150 \rightarrow 230 RPM)

shown in Figure 4.72. The 2/rev crossing has a noticeable impact on the torsional moment response. Figure 4.71 gives the time history of torsional moment at the blade root.

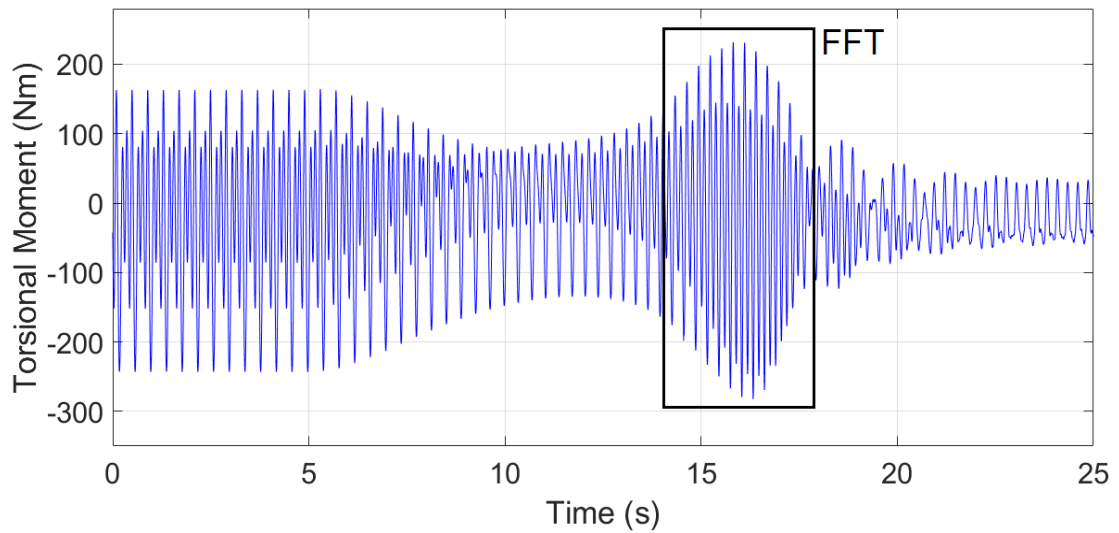


Figure 4.71: Time history of torsional moment at blade root ($\mu_N = 0.2$; 150 \rightarrow 230 RPM)

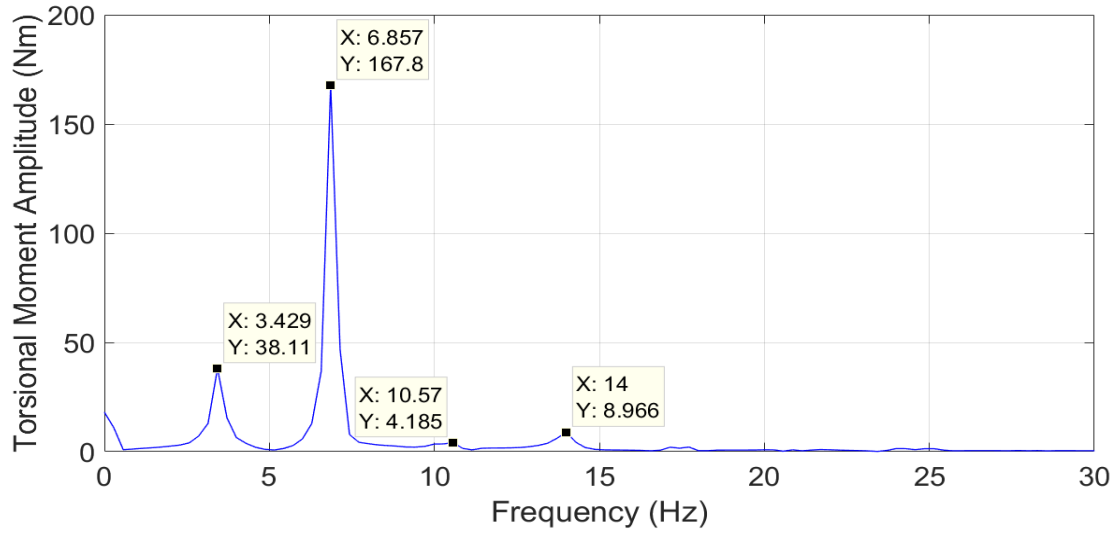


Figure 4.72: FFT analysis of torsional moment at resonance ($\mu_N = 0.2$; 150 \rightarrow 230 RPM)

The rotor torque response has a distinct bump due to resonance as shown in Figure 4.73 that was missing in the previous scenario. As expected, the mean amplitude is considerably higher during rotor speed increase, Figure 4.74. The FFT analysis shows that only a single peak close to 4/rev is contributing to the resonance response from the higher end of the spectrum. Contribution from a band of frequencies is not observed here.

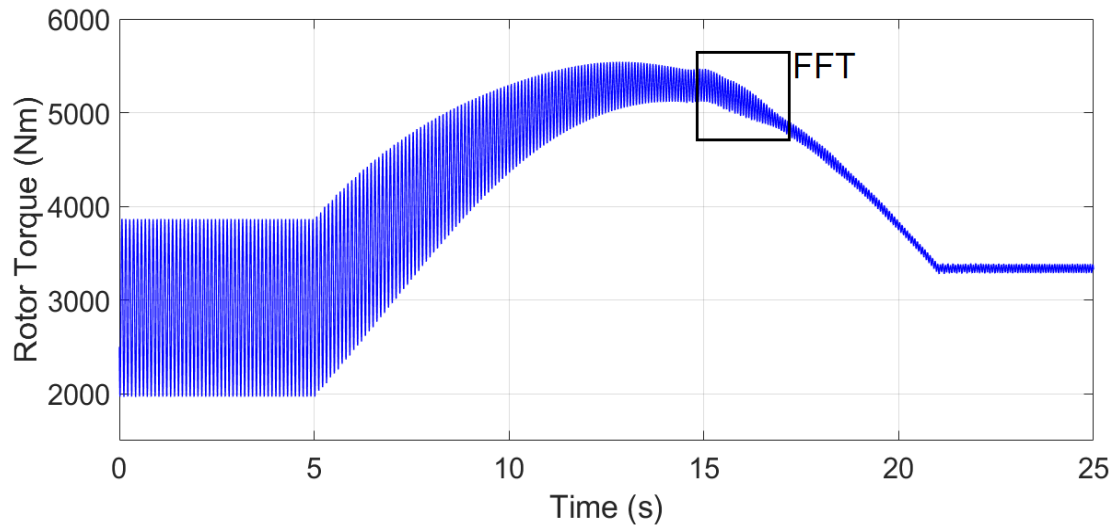


Figure 4.73: Time history of rotor torque ($\mu_N = 0.2$; 150 \rightarrow 230 RPM)

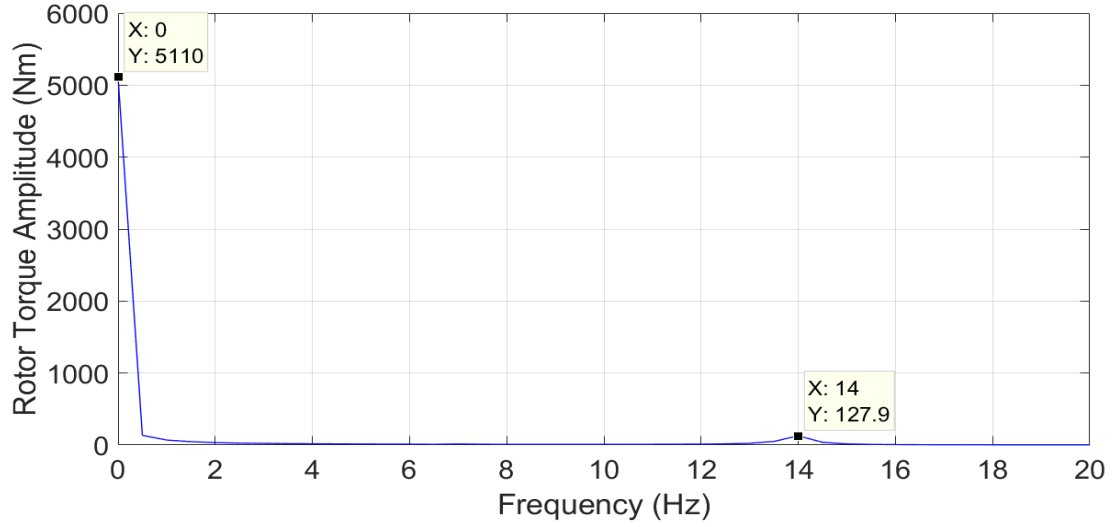


Figure 4.74: FFT analysis of rotor torque at resonance ($\mu_N = 0.2$; 150 \rightarrow 230 RPM)

4.6.4 Nominal Advance Ratio, $\mu_N = 0.1$

The resonance crossing points for $\mu_N = 0.1$ are shown in Figure 4.17. Two additional resonance crossing points come into the picture as the rotor speed is changed from 230 RPM to 130 RPM. First lag frequency crosses 3Ω and second flap frequency crosses 6Ω lines between 130 and 150 RPM. Hence, two lower frequency crossings, 2/rev and 3/rev, are involved during this transition. The relevant resonance frequencies are given in Table 4.6.

The trim angles for rotor speeds between 130 and 230 RPM are given in Figure 4.75.

Table 4.6: Resonance points between 230 RPM and 130 RPM.

Blade Frequency Mode	Crossing Point (/rev)	Crossing Frequency (Hz)
1 st Lag	2	6.863
2 nd Flap	5	15.299
1 st Torsion	7	24.056
1 st Lag	3	6.775
2 nd Flap	6	14.530

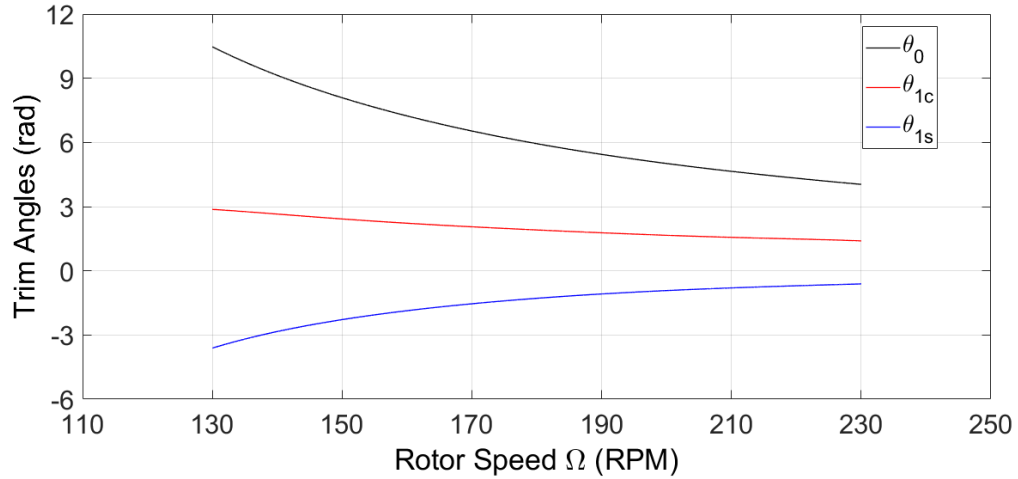


Figure 4.75: Pitch angles for $\mu_N = 0.1$

Transition: 230 to 130 RPM

The rotor speed is changed from 230 to 130 RPM in 20 seconds as shown in Figure 4.76. This allows the rotor acceleration to have the same valley, or peak, magnitude as the previous cases, Figure 4.77.

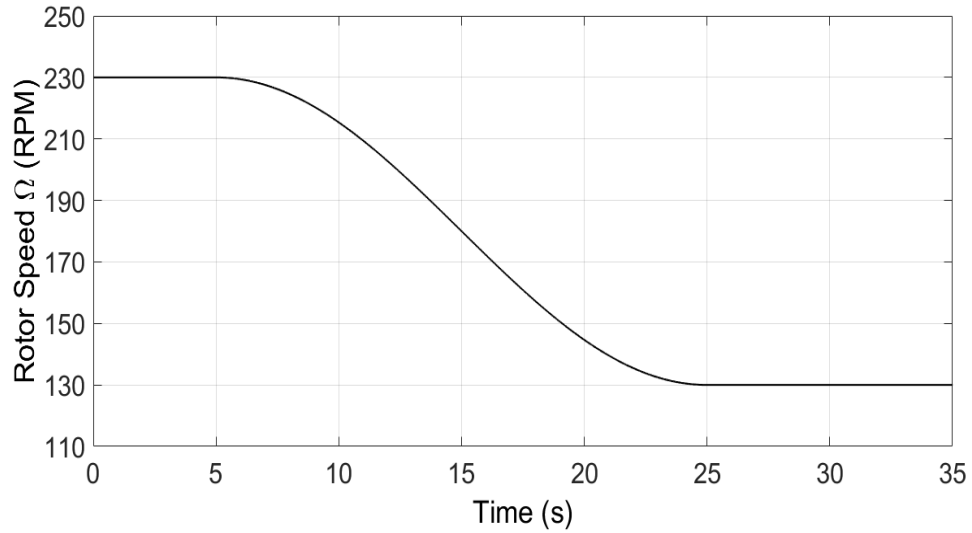


Figure 4.76: Rotor speed change from 230 to 130 RPM (20 s)

Lag moment response is shown in Figure 4.78. There are two resonance bumps during this transition, which was not observed in the previous transitions. The first bump is referred to as the first resonance crossing, and the second bump as the second resonance

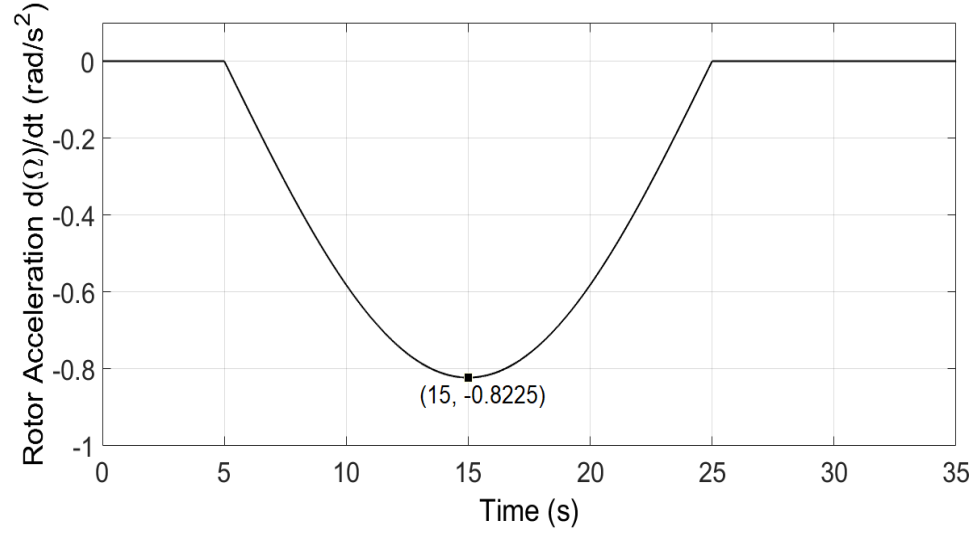


Figure 4.77: Rotor acceleration time history ($\Omega = 230$ to 130 RPM in 20 s)

crossing. FFT analysis reveals that the first resonance is due to the 2/rev crossing, Figure 4.79. The amplitude of this 2/rev lag resonance is lower than any other 2/rev resonance discussed before. The second resonance has an observably higher amplitude and the same is seen in the FFT results, Figure 4.80. The dominating frequency is close to 3/rev suggesting that the response is due to the first lag frequency crossing the 3/rev line. Both these behaviors can be explained based on the pitch angles during resonance. As discussed previously, the cyclic pitch angles decrease with decrease in forward speed, Figure 4.54. Hence, the lag moment amplitude increase during the 2/rev resonance decreases with decrease in forward speed. However, the pitch angles increase in magnitude as the rotor speed is reduced. The trim angles during 2/rev and 3/rev crossing is shown in Table 4.7 for comparison. The values during 3/rev crossing are greater in magnitude than those at the 2/rev crossing, which leads to a greater amplitude increase during resonance.

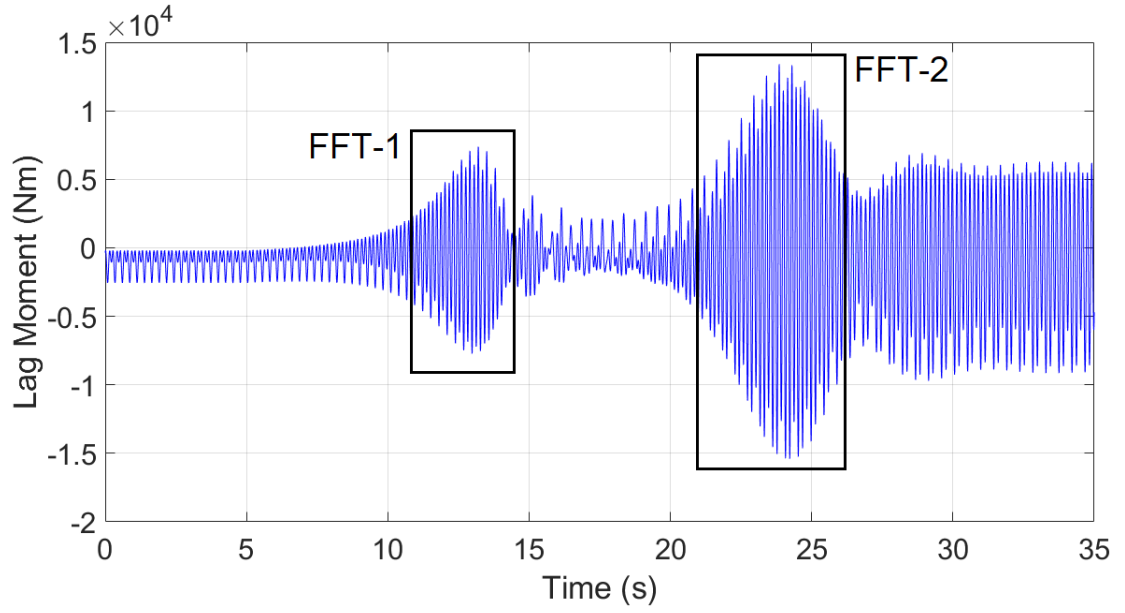


Figure 4.78: Time history of lag moment at blade root ($\mu_N = 0.1$; 230 \rightarrow 130 RPM)

Table 4.7: Trim angles comparison at $\mu_N = 0.1$

Trim Angles	2/rev Crossing (205.8 RPM)	3/rev Crossing (135.5 RPM)
	(deg)	(deg)
θ_0	4.795	9.693
θ_{1c}	1.601	2.754
θ_{1s}	-0.8477	-3.15

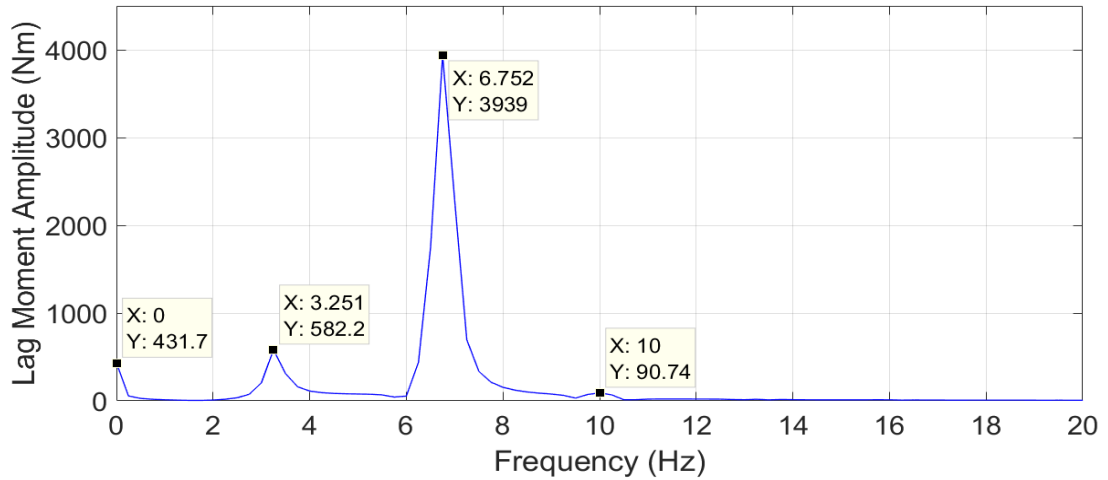


Figure 4.79: FFT analysis of lag moment at first resonance ($\mu_N = 0.1$; 230 \rightarrow 130 RPM)

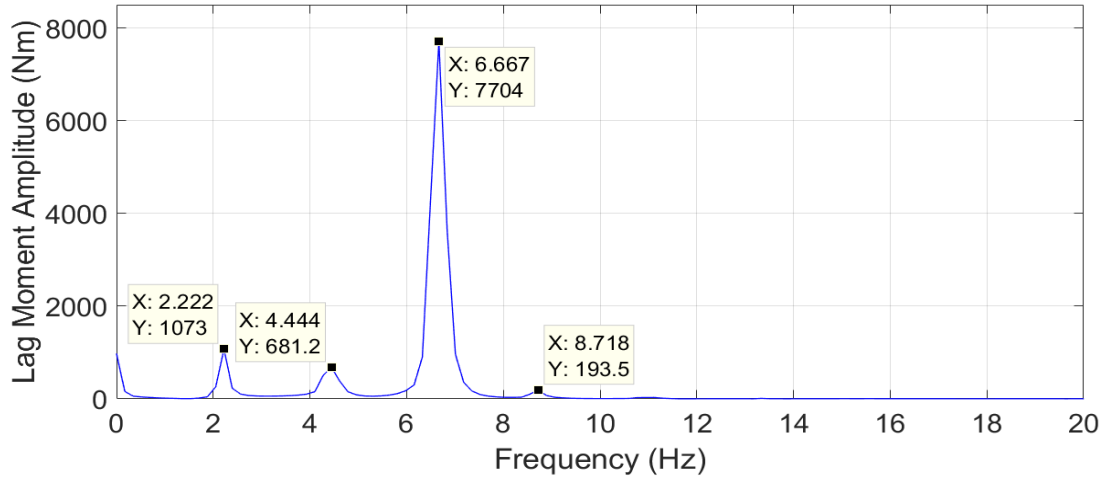


Figure 4.80: FFT analysis of lag moment at second resonance ($\mu_N = 0.1$; 230 \rightarrow 130 RPM)

The lag force also has two resonance regions as shown in Figure 4.81. Again, the second resonance has a greater relative increase in magnitude compared to the first resonance. The 2/rev peak, Figure 4.82, has a lower amplitude in comparison to the 3/rev peak shown in Figure 4.83.

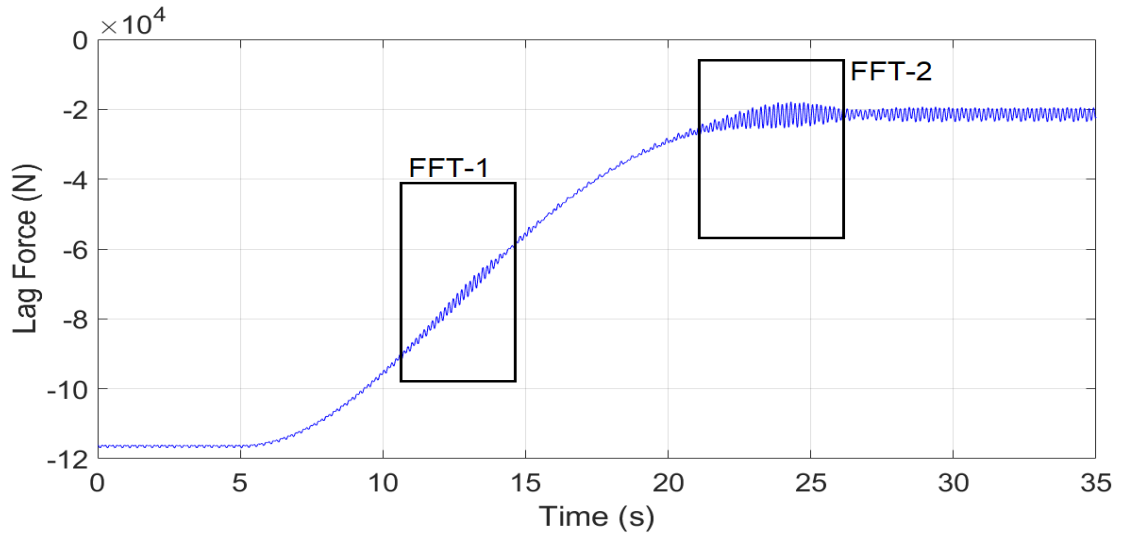


Figure 4.81: Time history of lag force at blade root ($\mu_N = 0.1$; 230 \rightarrow 130 RPM)

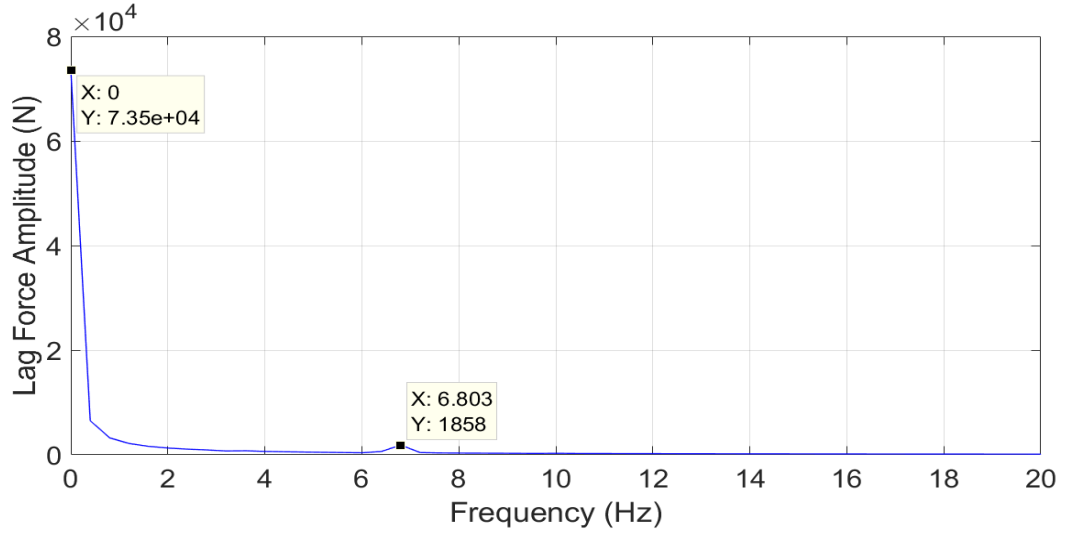


Figure 4.82: FFT analysis of lag force at first resonance ($\mu_N = 0.1$; 230 \rightarrow 130 RPM)

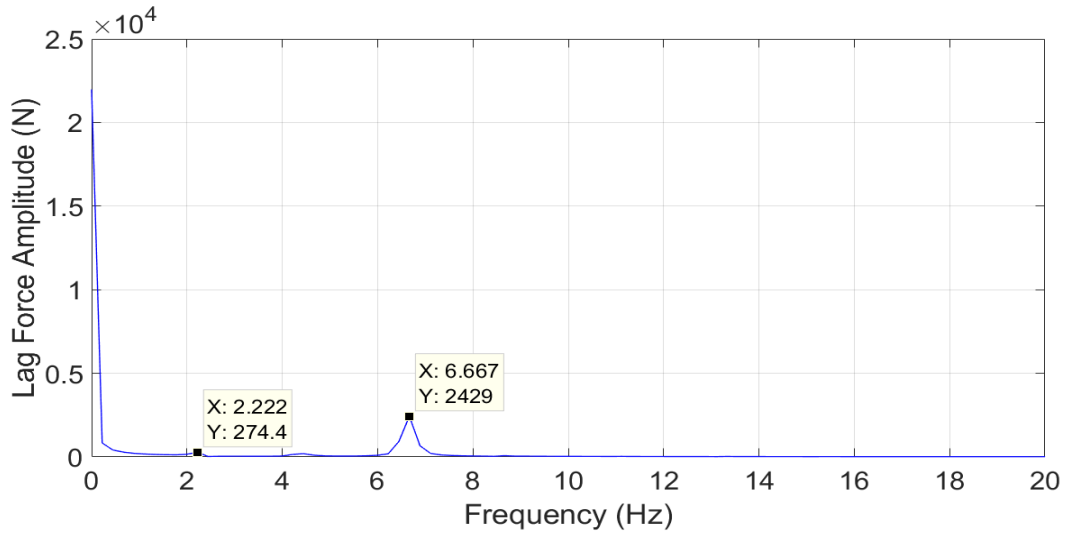


Figure 4.83: FFT analysis of lag force at second resonance ($\mu_N = 0.1$; 230 \rightarrow 130 RPM)

Flap moment also shows a similar resonance behavior as seen in Figure 4.84. The amplitude increase during the first resonance is not only less than half of the second resonance, it is also lower than the corresponding value at $\mu_N = 0.2$. The FFT analysis is given in Figures 4.85 and 4.86. The noticeable frequencies are 2/rev, 3/rev and 4/rev in both the resonances. The dominating frequency is 2/rev in the first crossing and 3/rev in the second crossing. The higher frequency flap crossings like 5/rev and 6/rev have little effect on the response.

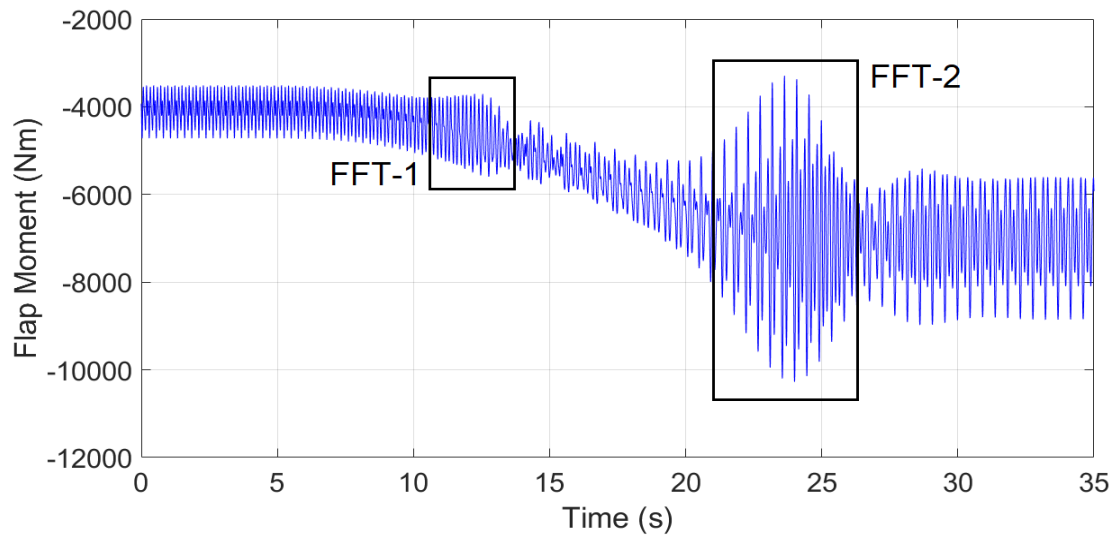


Figure 4.84: Time history of flap moment at blade root ($\mu_N = 0.1$; 230 \rightarrow 130 RPM)

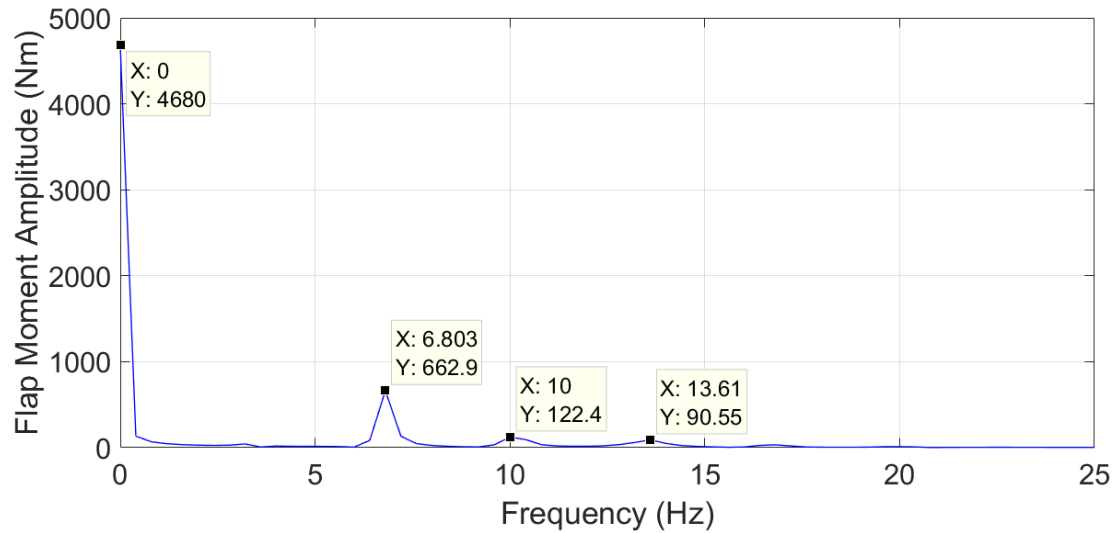


Figure 4.85: FFT analysis of flap moment at first resonance ($\mu_N = 0.1$; 230 \rightarrow 130 RPM)

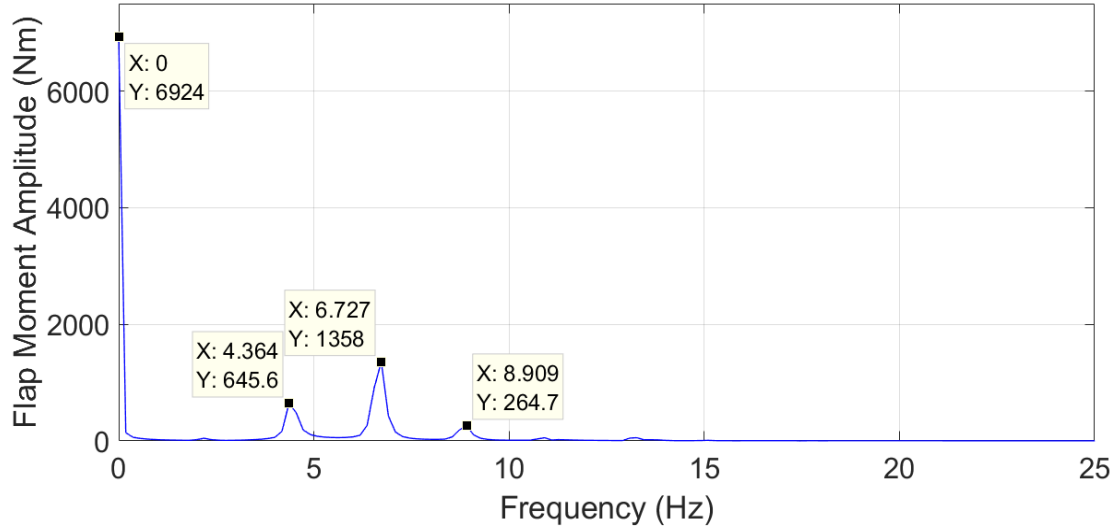


Figure 4.86: FFT analysis of flap moment at second resonance ($\mu_N = 0.1$; 230 \rightarrow 130 RPM)

The torsional moment response is shown in Figure 4.87. The amplitude of the second resonance is more than three times the amplitude of first resonance. The dominating frequencies are still 2/rev and 3/rev as shown in Figures 4.88 and 4.89. During the second resonance, 1/rev, 2/rev and 5/rev also make secondary contributions.

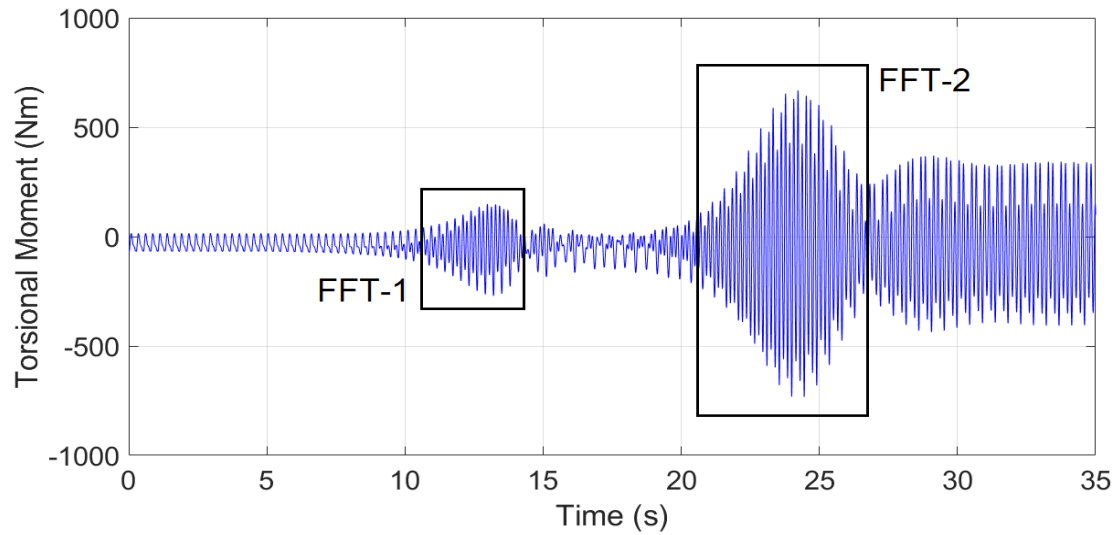


Figure 4.87: Time history of torsional moment at blade root ($\mu_N = 0.1$; 230 \rightarrow 130 RPM)

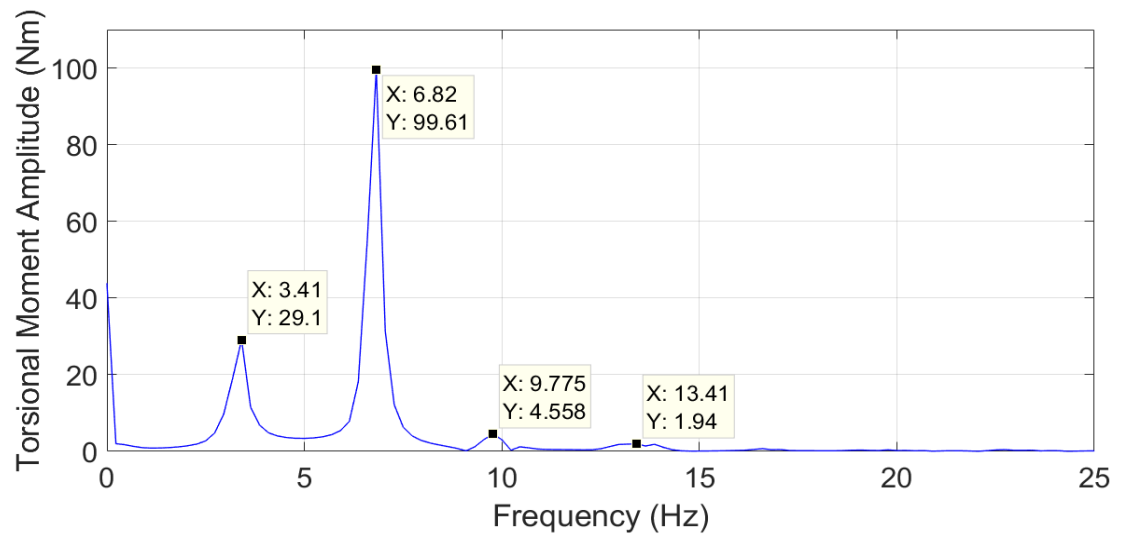


Figure 4.88: FFT analysis of torsional moment at first resonance ($\mu_N = 0.1$; 230 \rightarrow 130 RPM)

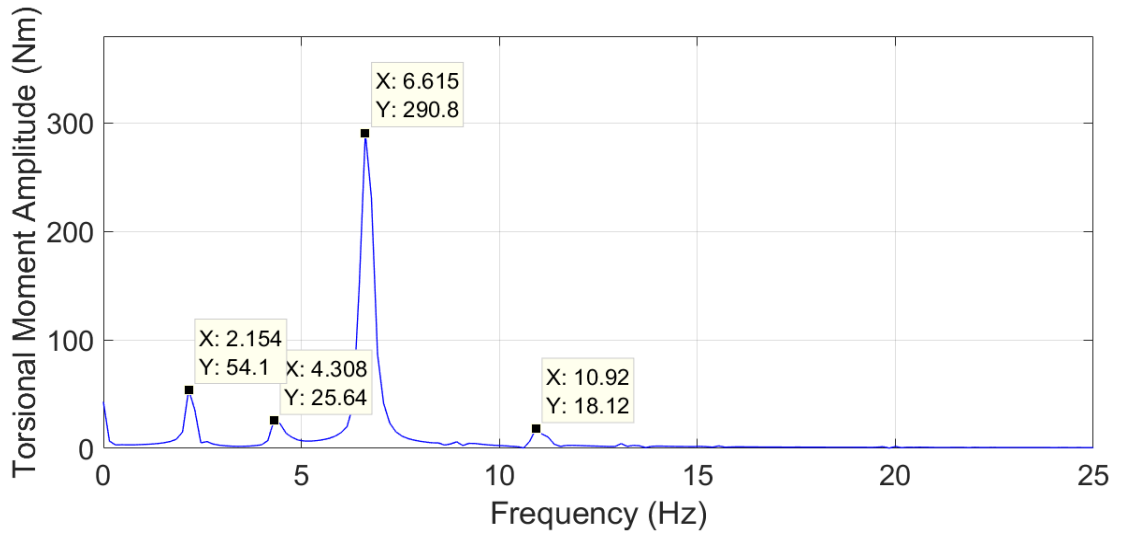


Figure 4.89: FFT analysis of torsional moment at second resonance ($\mu_N = 0.1$; 230 \rightarrow 130 RPM)

The rotor torque response increases in magnitude as the rotor reaches lower angular speeds, as seen in Figure 4.90. The amplitude increase due to resonance shows a gentle behavior in both the first and second resonances. The first resonance's amplitude increase is barely noticeable in comparison to the final torque amplitude. The FFT plot, Figure 4.91, shows that a 3.5/rev frequency makes a contribution less than ten times the mean value to the response. However, a 4/rev frequency makes a comparable contribution, slightly less than one fourth, to the torque response during the second crossing as shown in Figure 4.92.

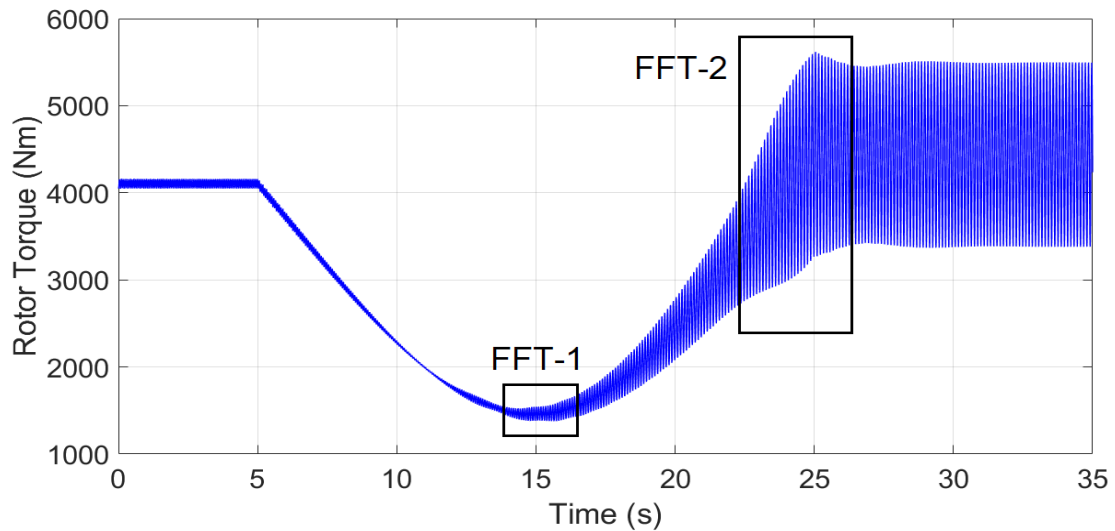


Figure 4.90: Time history of rotor torque ($\mu_N = 0.1$; 230 \rightarrow 130 RPM)

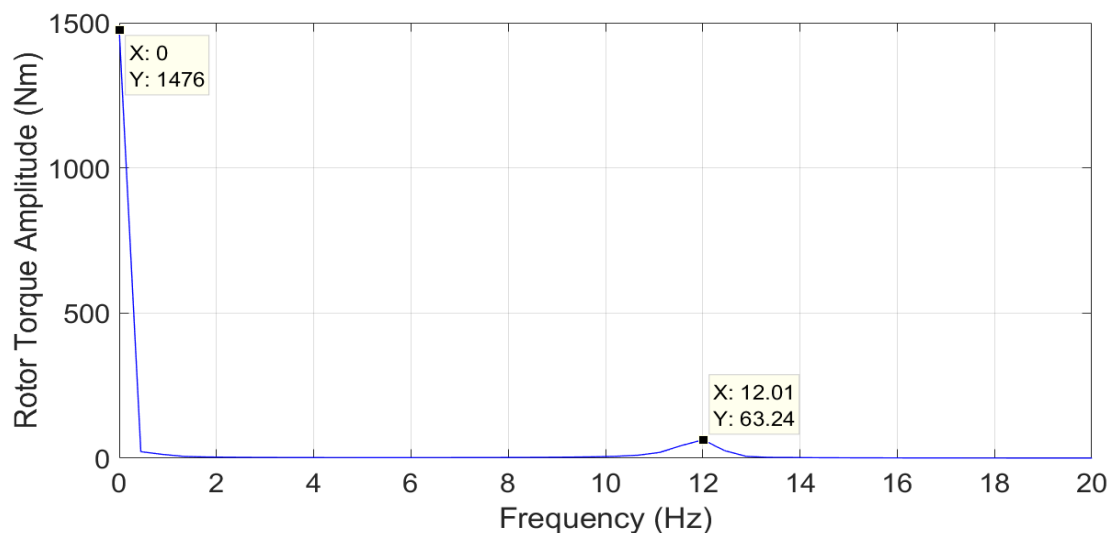


Figure 4.91: FFT analysis of rotor torque at first resonance ($\mu_N = 0.1$; 230 \rightarrow 130 RPM)

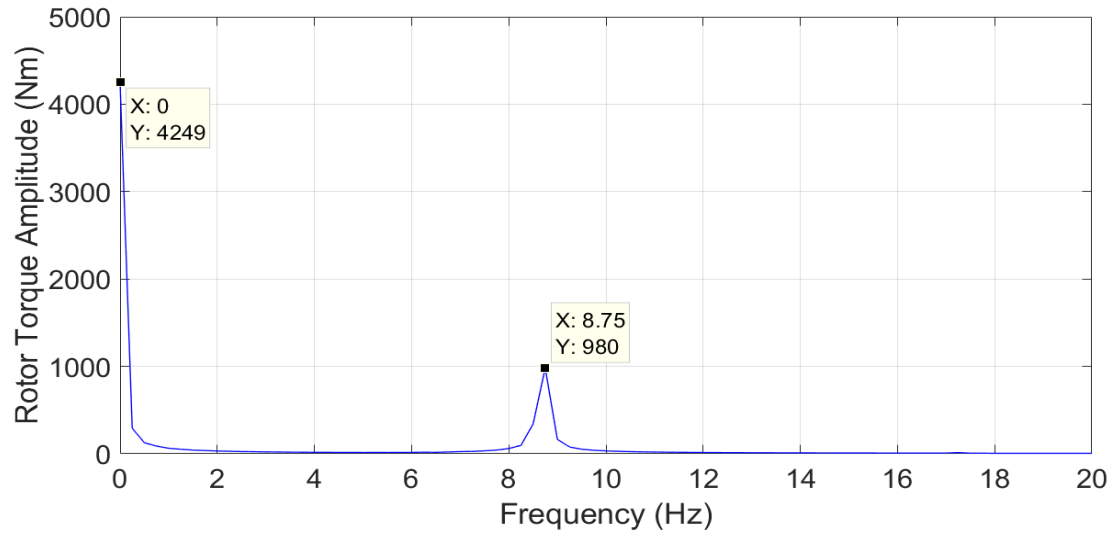


Figure 4.92: FFT analysis of rotor torque at second resonance ($\mu_N = 0.1$ 230 \rightarrow 130 RPM)

Transition: 130 to 230 RPM

The rotor speed and rotor acceleration for the reverse transition from 130 to 230 RPM are given in Figures 4.93 and 4.94, respectively.

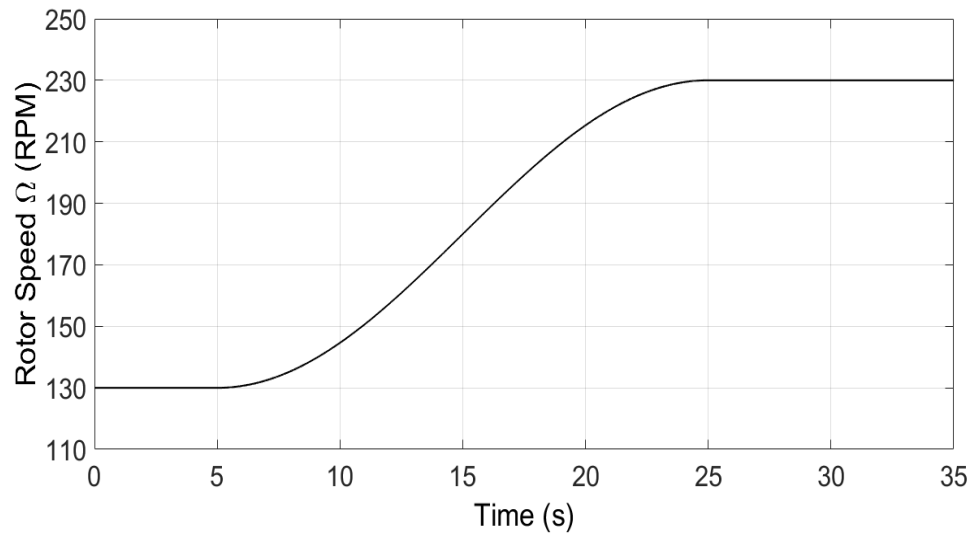


Figure 4.93: Rotor speed change from 130 to 230 RPM (20 s)

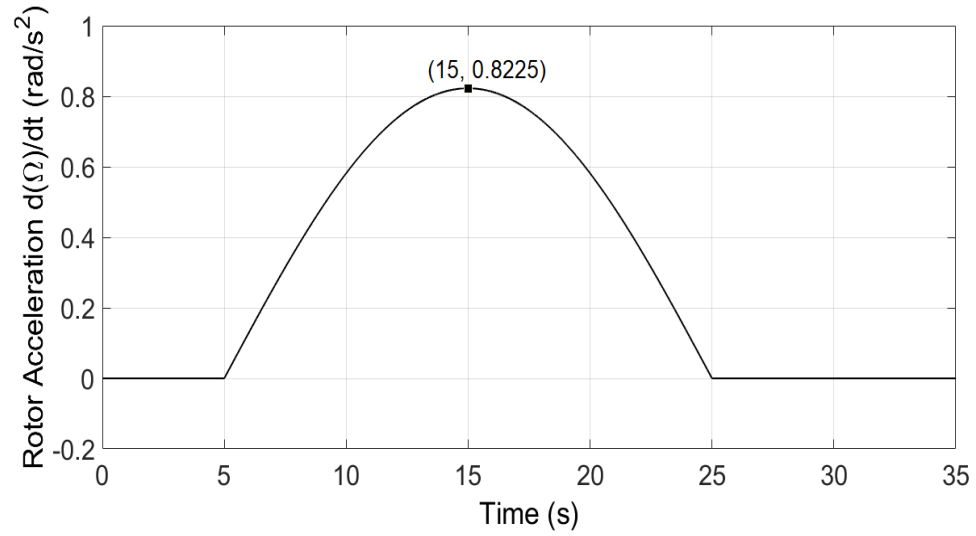


Figure 4.94: Rotor acceleration time history ($\Omega = 130$ to 230 RPM in 20 s)

Lag moment response shows a transposed behavior as the rotor sees the 3/rev lag resonance first and then the 2/rev lag resonance during this transition, Figure 4.95. Now, the first and second resonance of the previous transition switch places. The first resonance has a higher amplitude than the second resonance. The FFT analysis of the first and second resonance is given in Figures 4.96 and 4.97.

As expected, FFT analysis reveals that the first resonance is due to the 3/rev crossing, Figure 4.96. The amplitude of this 3/rev lag resonance is even higher than the previous 3/rev lag resonance for the reverse transition. The second resonance is due to 2/rev crossing and the amplitude is slightly higher than the previous case, Figure 4.97. It is interesting to note that the frequencies for the low to high rotor speed change are slightly offset to the right in the FFT plots.

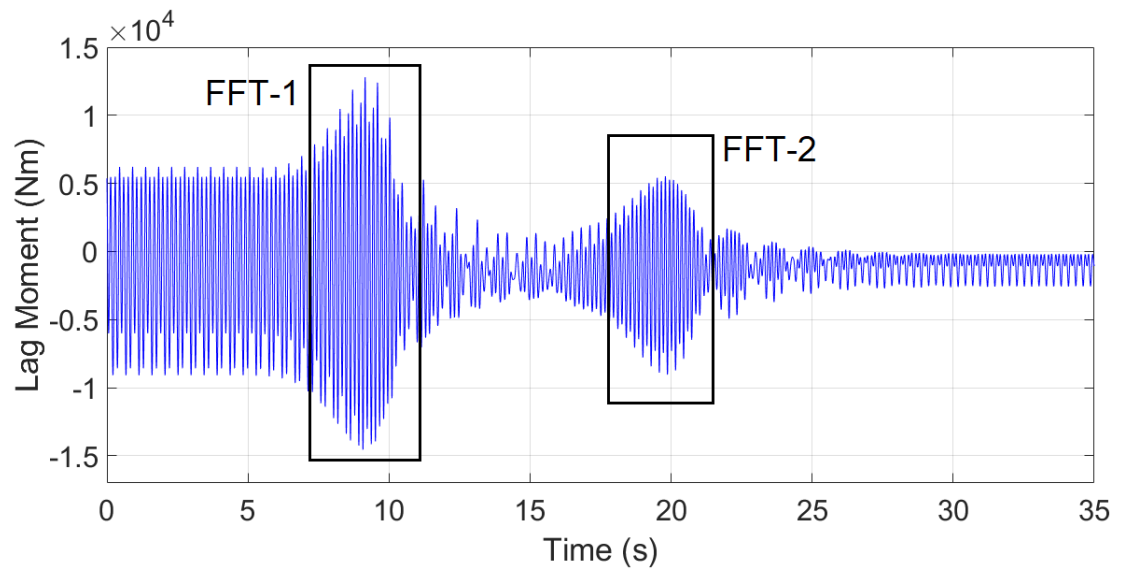


Figure 4.95: Time history of lag moment at blade root ($\mu_N = 0.1$; 130 \rightarrow 230 RPM)

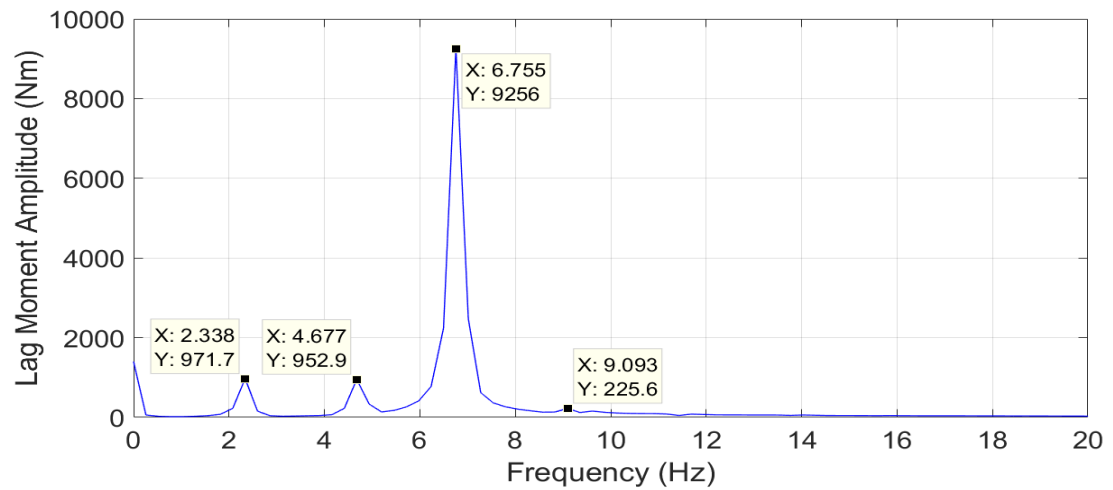


Figure 4.96: FFT analysis of lag moment at first resonance ($\mu_N = 0.1$; 130 \rightarrow 230 RPM)

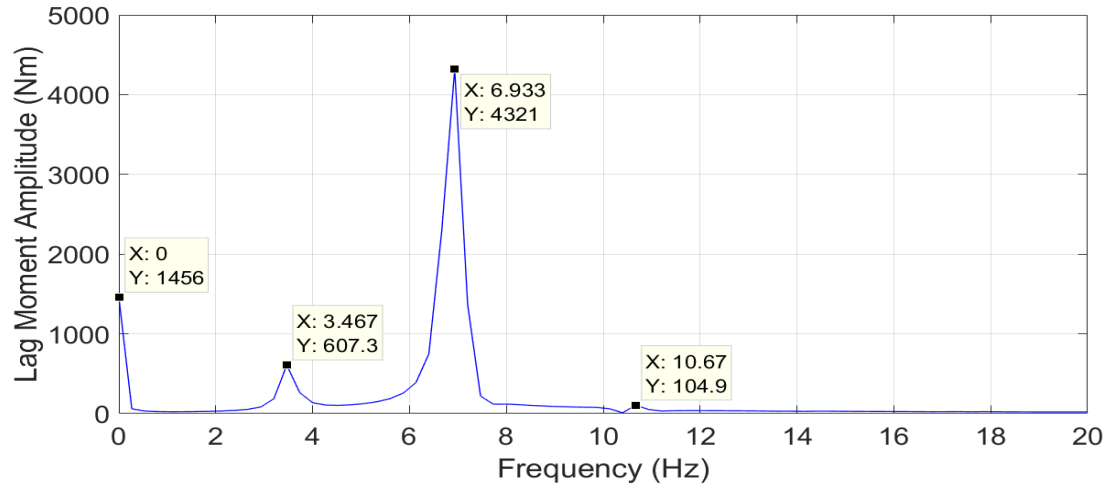


Figure 4.97: FFT analysis of lag moment at second resonance ($\mu_N = 0.1$; 130 \rightarrow 230 RPM)

The lag force's resonance regions are small in comparison to the mean value of the lag force, Figure 4.98. The FFT plots of the resonance regions are given in Figures 4.99 and 4.100.

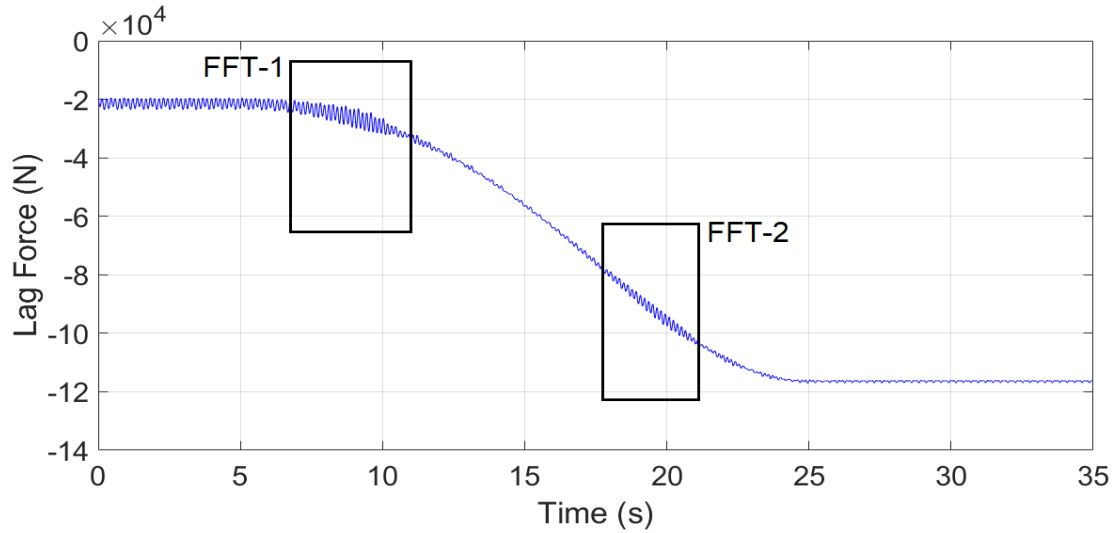


Figure 4.98: Time history of lag force at blade root ($\mu_N = 0.1$; 130 \rightarrow 230 RPM)

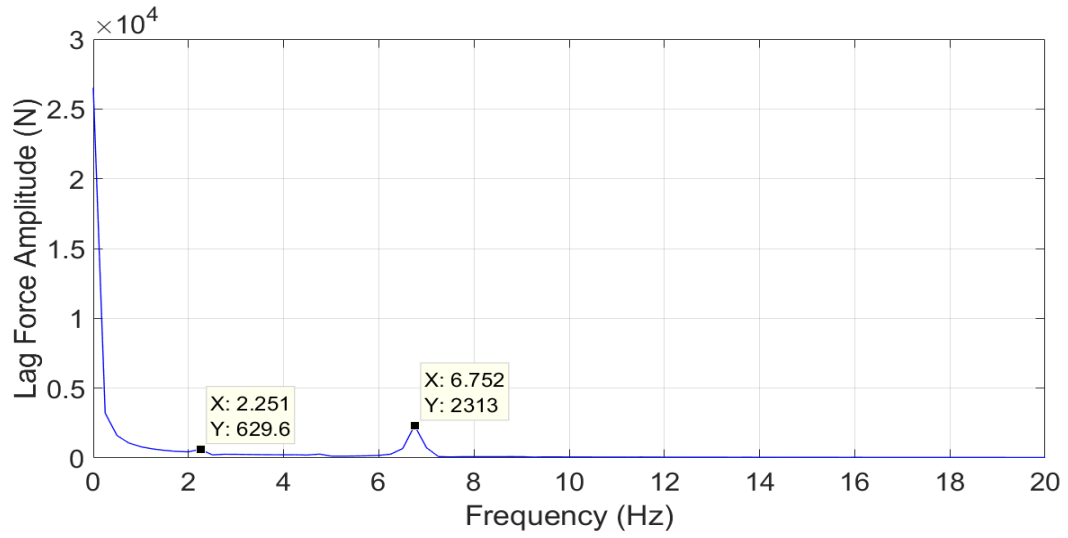


Figure 4.99: FFT analysis of lag force at first resonance ($\mu_N = 0.1$; 130 \rightarrow 230 RPM)

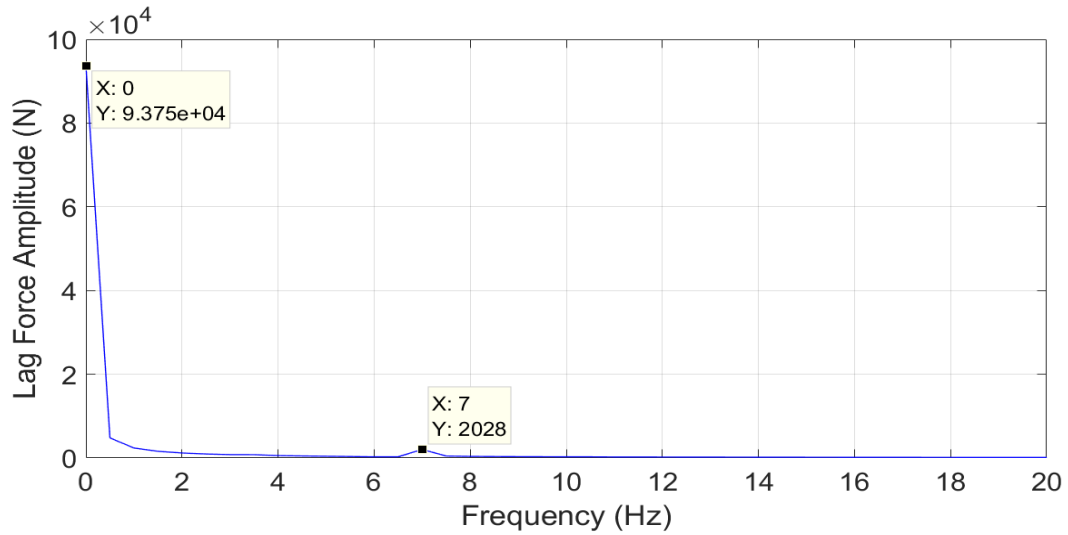


Figure 4.100: FFT analysis of lag force at second resonance ($\mu_N = 0.1$; 130 \rightarrow 230 RPM)

Flap moment's resonance behavior is shown in Figure 4.101. The 3/rev resonance amplitude is more than twice the 2/rev resonance amplitude. The FFT plots are given in Figures 4.102 and 4.103. The noticeable frequencies are still 2/rev and 3/rev for both the resonances.

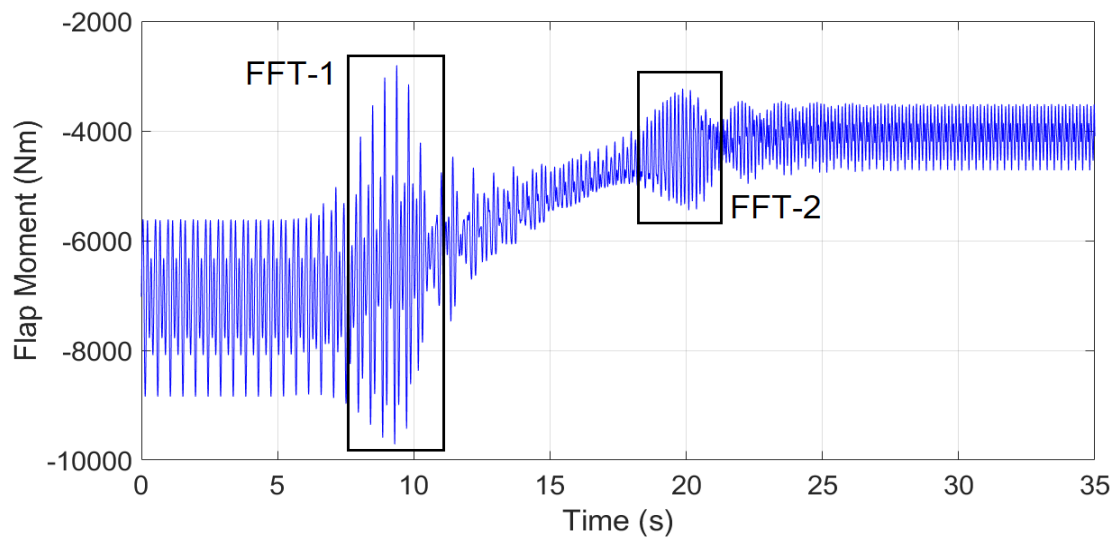


Figure 4.101: Time history of flap moment at blade root ($\mu_N = 0.1$; 130 \rightarrow 230 RPM)

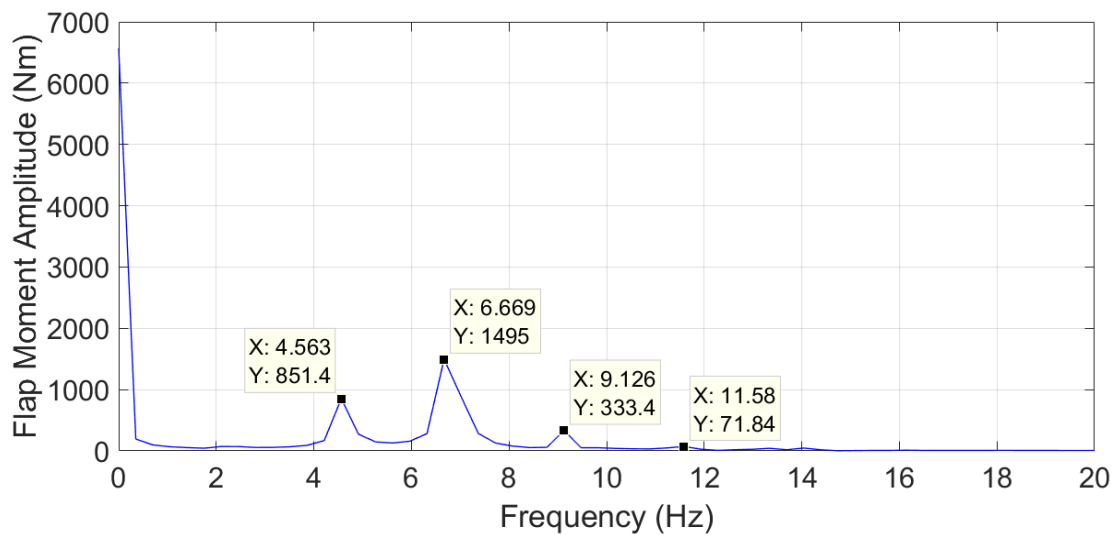


Figure 4.102: FFT analysis of flap moment at first resonance ($\mu_N = 0.1$; 130 \rightarrow 230 RPM)

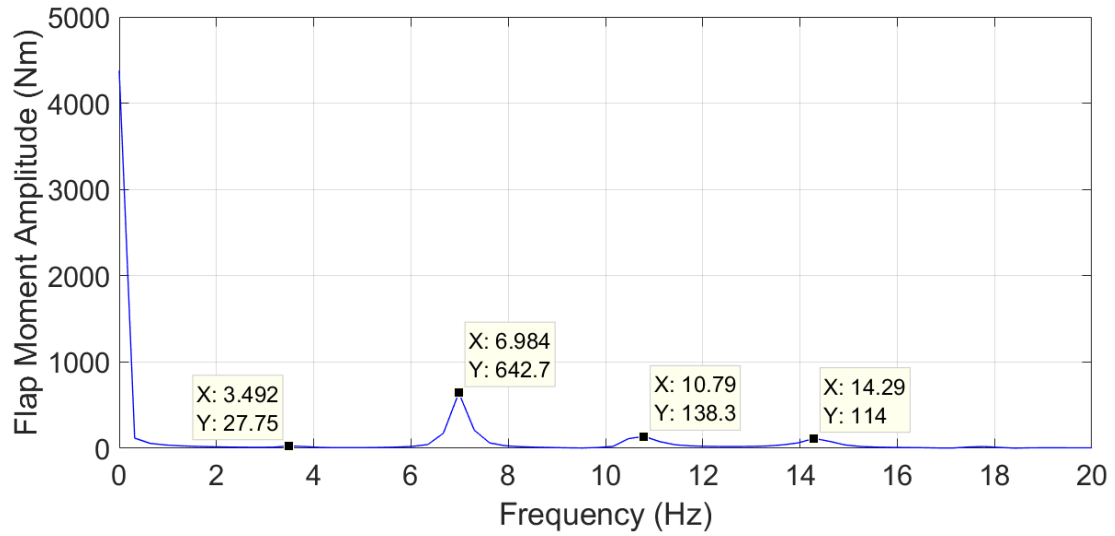


Figure 4.103: FFT analysis of flap moment at second resonance ($\mu_N = 0.1$; 130 \rightarrow 230 RPM)

The torsional moment response, shown in Figure 4.104, has a trend very similar to the lag moment response. The first resonance has a magnitude which is marginally greater than the previous 3/rev transition during the backward crossing, Figure 4.105. The second resonance is comparable in magnitude to the reverse 2/rev transition as shown in Figure 4.106.

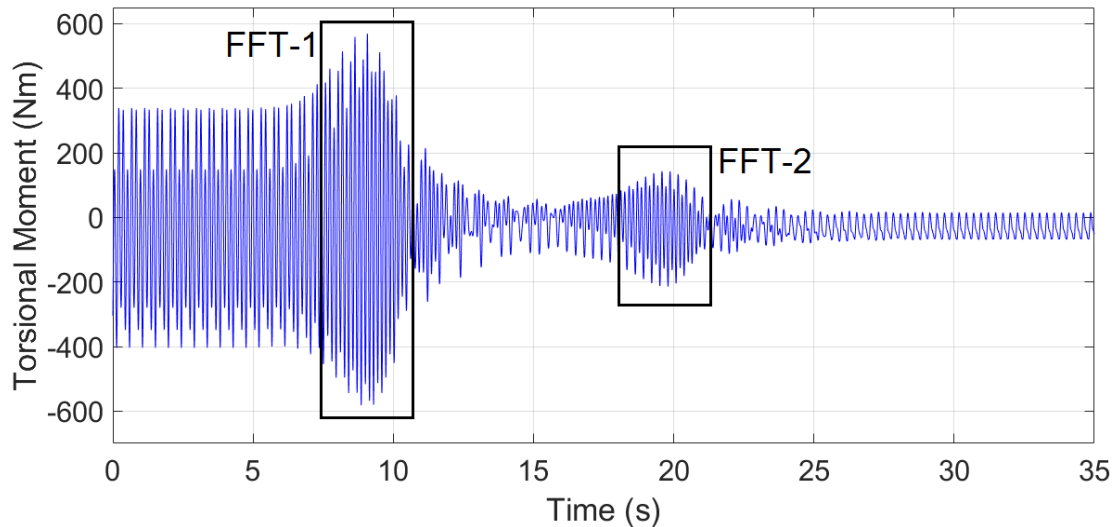


Figure 4.104: Time history of torsional moment at blade root ($\mu_N = 0.1$; 130 \rightarrow 230 RPM)

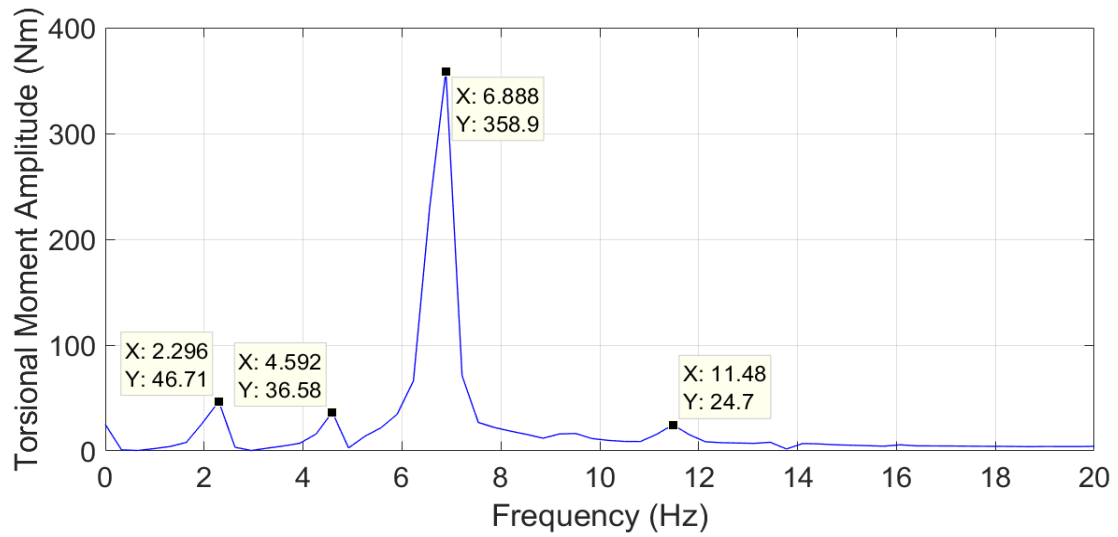


Figure 4.105: FFT analysis of torsional moment at first resonance ($\mu_N = 0.1$; 130 \rightarrow 230 RPM)

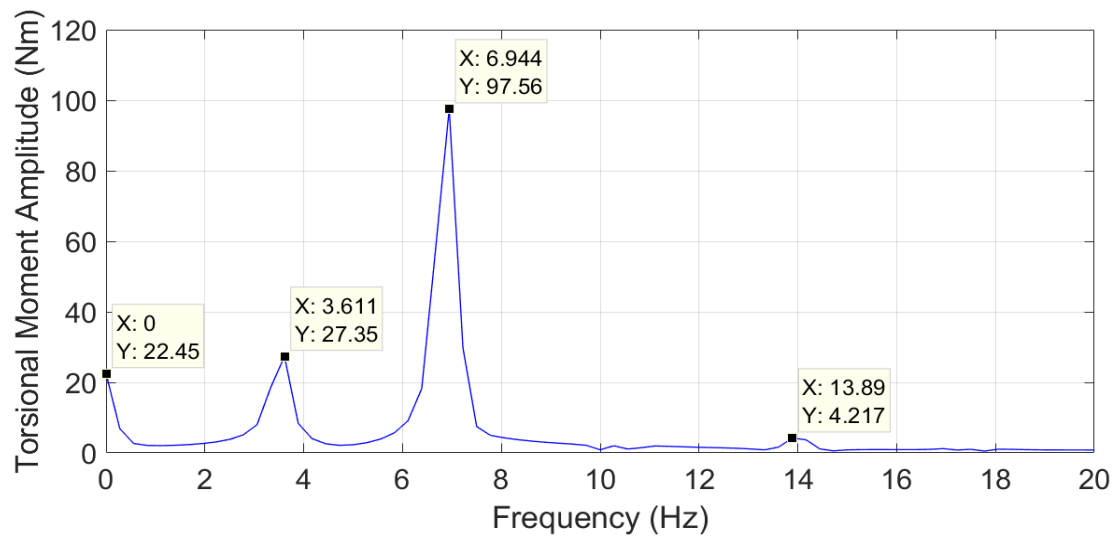


Figure 4.106: FFT analysis of torsional moment at second resonance ($\mu_N = 0.1$; 130 \rightarrow 230 RPM)

The rotor torque response seems to be affected only by the first resonance crossing. As seen in Figure 4.107, the torque increases initially due to increase of rotor acceleration. The increase is also associated with an oscillatory behavior. FFT analysis of this region shows that a band of frequencies close to 4/rev during the 3/rev crossing is causing such a behavior, Figure 4.108. The second crossing doesn't seem to have any effect on the rotor torque. However, the peak value of rotor torque during the transition almost reaches 6.5×10^3 Nm, which is the highest torque attained thus far in forward speeds.

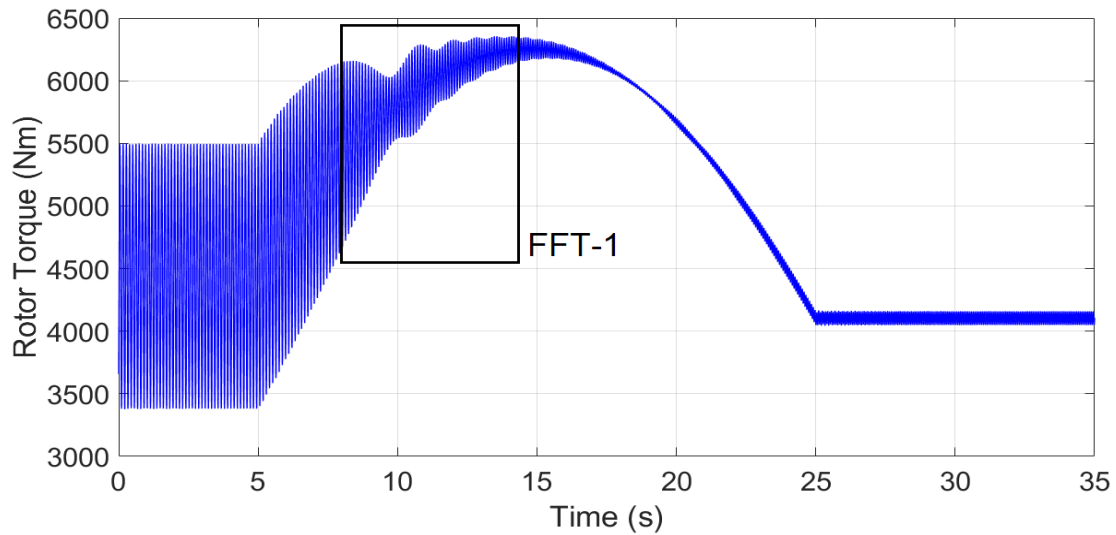


Figure 4.107: Time history of rotor torque ($\mu_N = 0.1$; 130 \rightarrow 230 RPM)

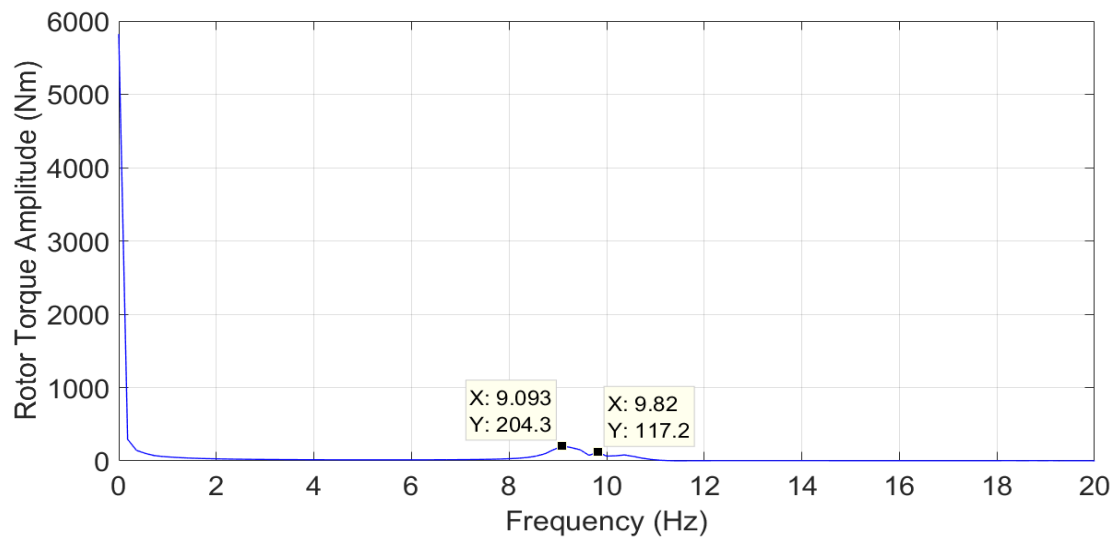


Figure 4.108: FFT analysis of rotor torque at first resonance ($\mu_N = 0.1$; 130 \rightarrow 230 RPM)

4.6.5 Nominal Advance Ratio, $\mu_N = 0$ (Hover)

The resonance crossing points for $\mu_N = 0.0$ are given in Figure 4.16. One additional resonance crossing point is added to the previous set to get a new set for $\mu_N = 0$. Second flap frequency crosses the 7Ω line at 121.30 RPM. The resonance frequencies are given in Table 4.8. The trim angles for rotor speeds between 110 and 230 RPM are given in Figure 4.109.

Table 4.8: Resonance points between 230 RPM and 110 RPM.

Blade Frequency Mode	Crossing Point (/rev)	Crossing Frequency (Hz)
1 st Lag	2	6.863
2 nd Flap	5	15.299
1 st Torsion	7	24.056
1 st Lag	3	6.775
2 nd Flap	6	14.530
2 nd Flap	7	14.151

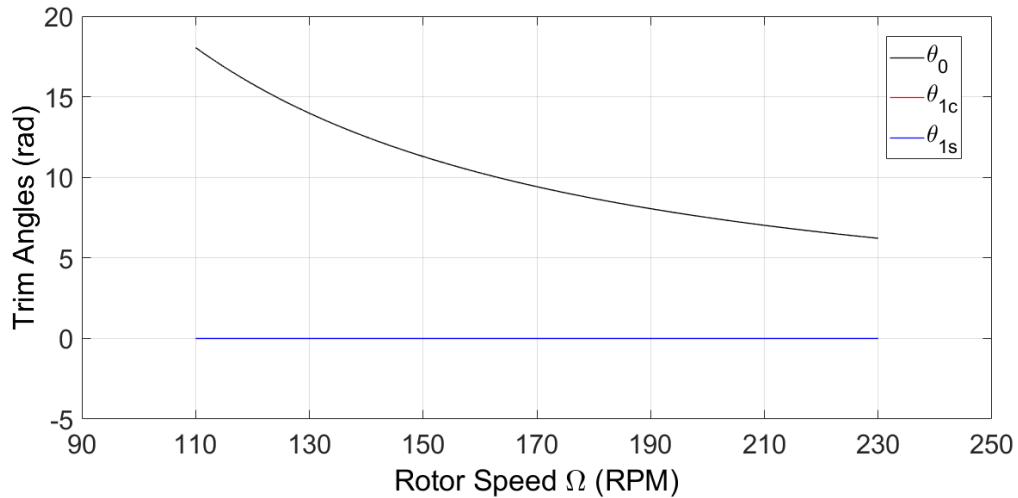


Figure 4.109: Pitch angles for $\mu_N = 0$

Transition: 230 to 110 RPM

The rotor speed is changed from 230 to 110 RPM in 24 seconds as shown in Figure 4.110. The rotor starts changing speed at 5 seconds and ends at 29 seconds mark. The rotor acceleration is given in Figure 4.111.

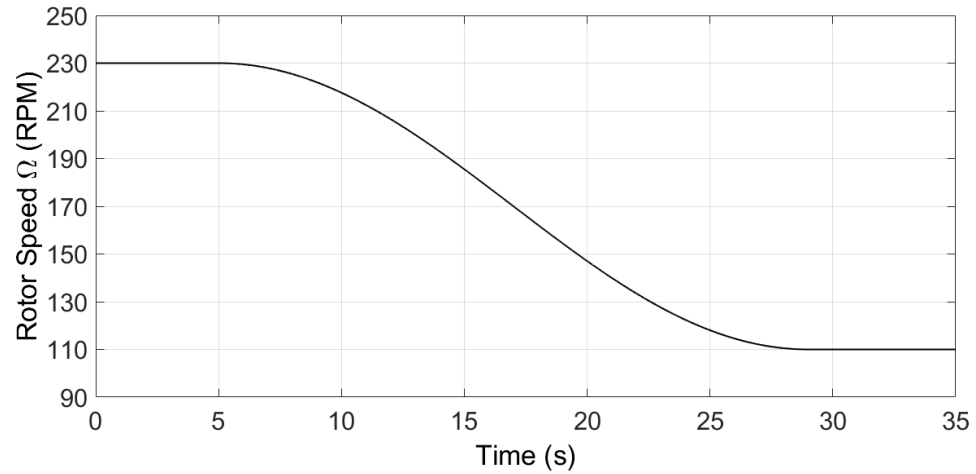


Figure 4.110: Rotor speed change from 230 to 110 RPM (24 s)

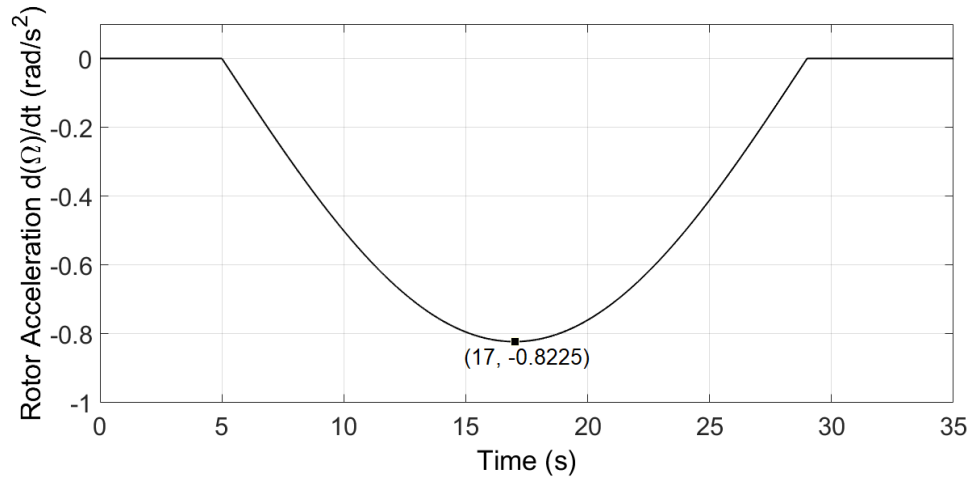


Figure 4.111: Rotor acceleration time history ($\Omega = 230$ to 110 RPM in 24 s)

Lag moment response is shown in Figure 4.112. It is interesting to see that the resonance crossings have no effect on the blade response in hover condition. The lag moment response is smooth during the entire transition. This is because of the zero cyclic pitch angles in hover, Figure 4.109. As mentioned previously, the cyclic pitch angles affect the

blade response during resonance crossing. The absence of cyclic pitch angles makes the blade response non-harmonic, and thus, the blade passes through resonances without any amplitude increase.

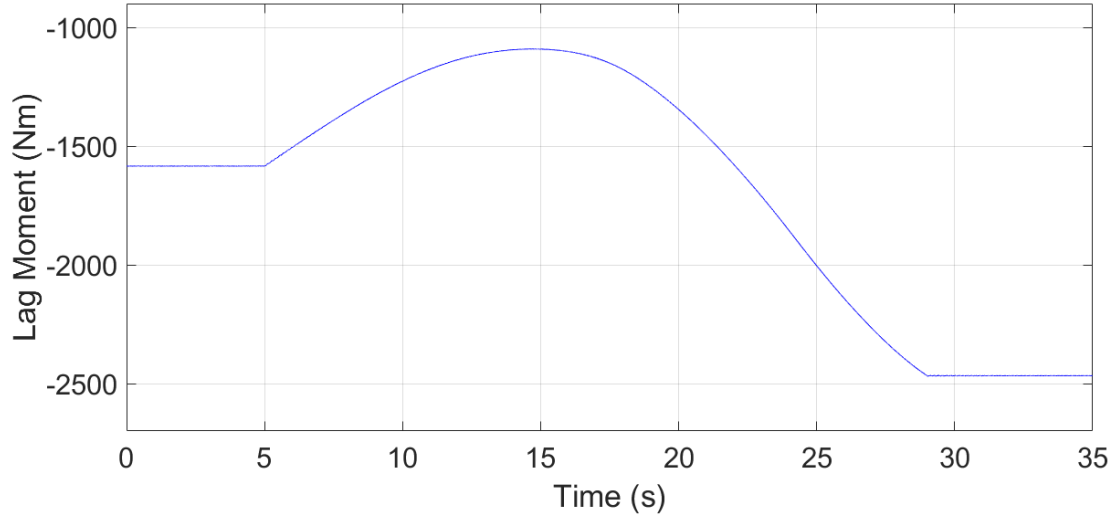


Figure 4.112: Time history of lag moment at blade root ($\mu_N = 0$; 230 \rightarrow 110 RPM)

Other blade parameters also show a similar behavior. The lag force, flap moment, torsional moment and rotor torque are given in Figures 4.113, 4.114, 4.115 and 4.116, respectively. Hence, none of the resonance crossings had any impact on the blade response during the hover transition.

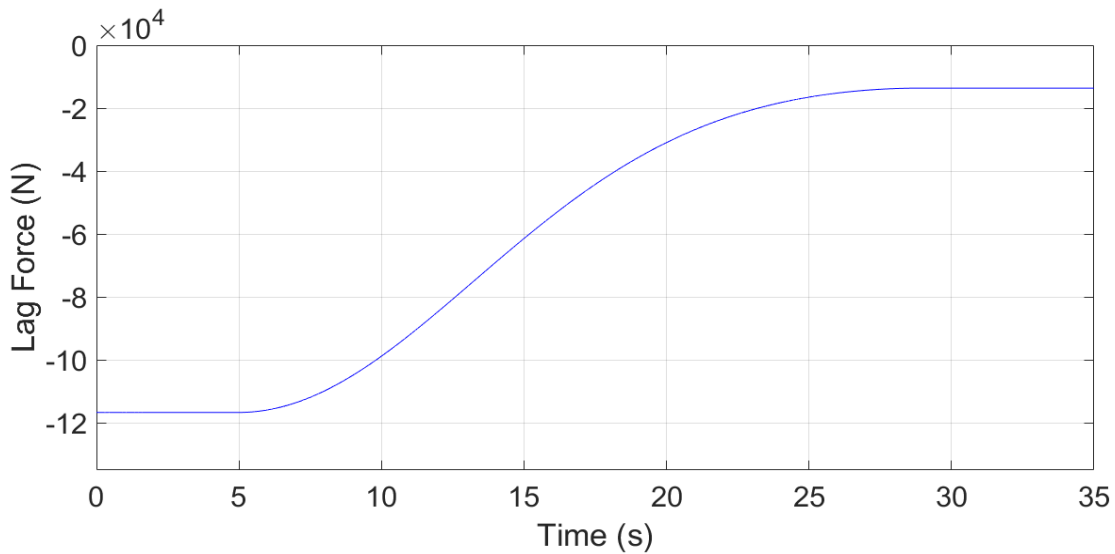


Figure 4.113: Time history of lag force at blade root ($\mu_N = 0$; 230 \rightarrow 110 RPM)

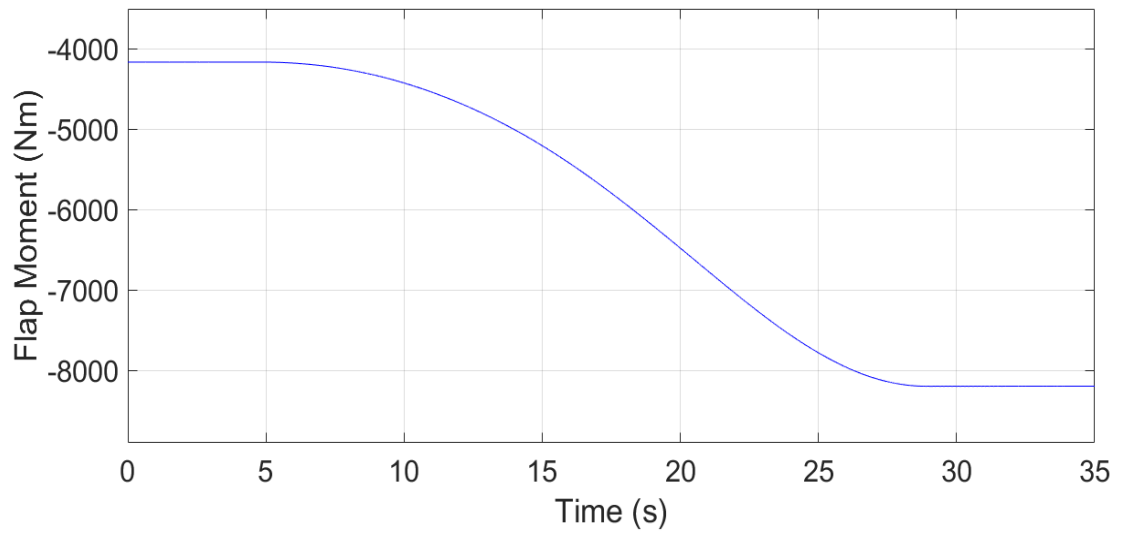


Figure 4.114: Time history of flap moment at blade root ($\mu_N = 0$; 230 \rightarrow 110 RPM)

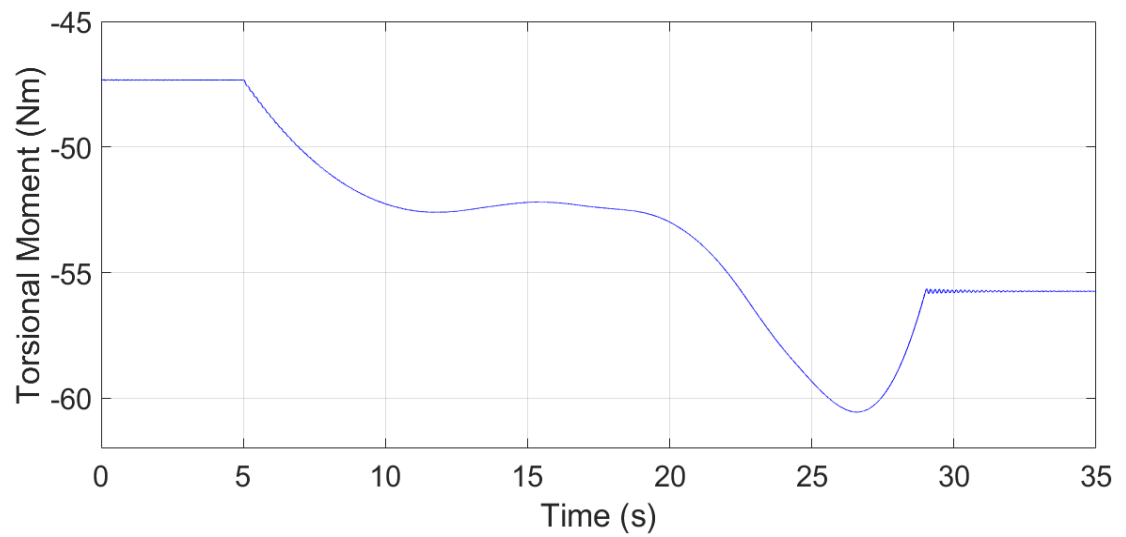


Figure 4.115: Time history of torsional moment at blade root ($\mu_N = 0$; 230 \rightarrow 110 RPM)

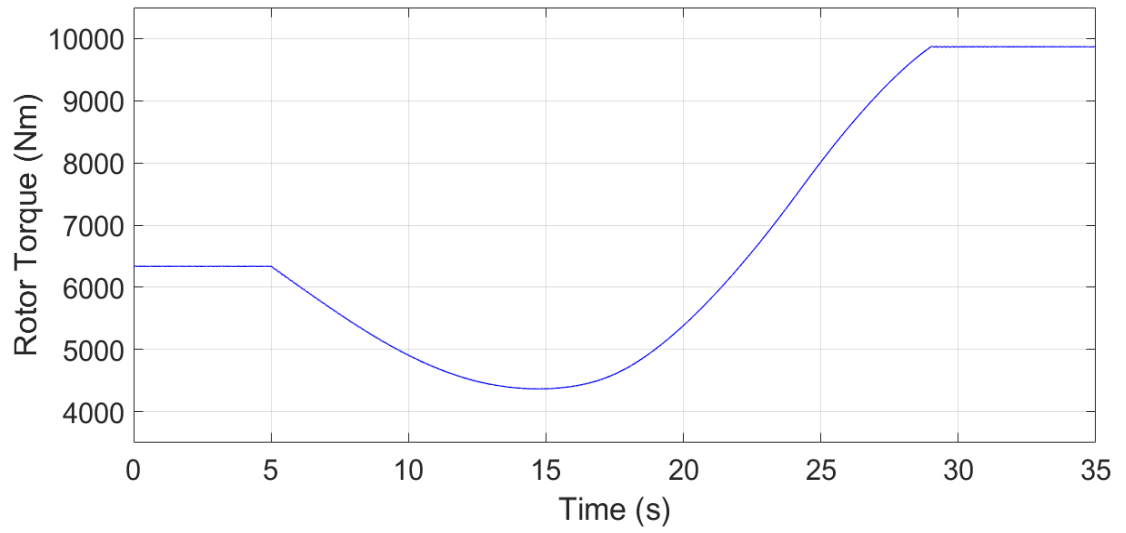


Figure 4.116: Time history of rotor torque ($\mu_N = 0$; 230 \rightarrow 110 RPM)

Transition: 110 to 230 RPM

The rotor speed variation is shown in Figure 4.117. The rotor acceleration is given in Figure 4.118.

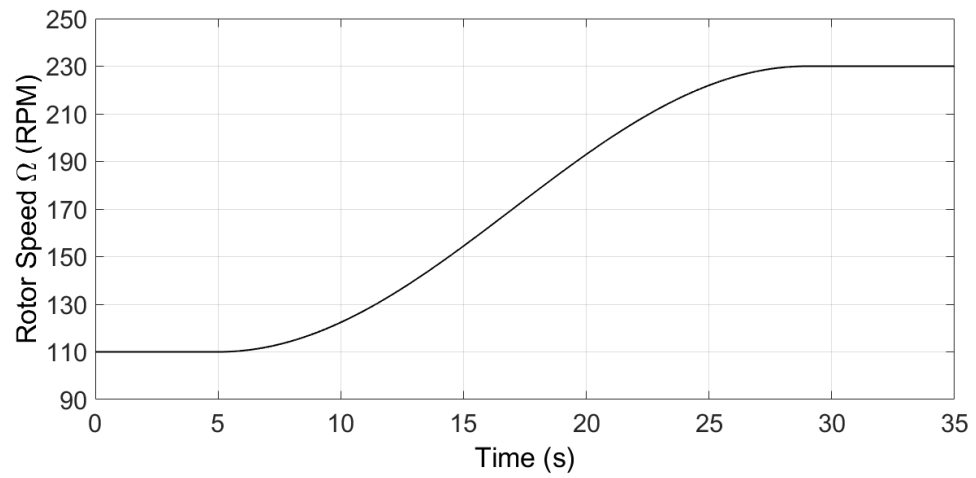


Figure 4.117: Rotor speed change from 110 to 230 RPM (24 s)

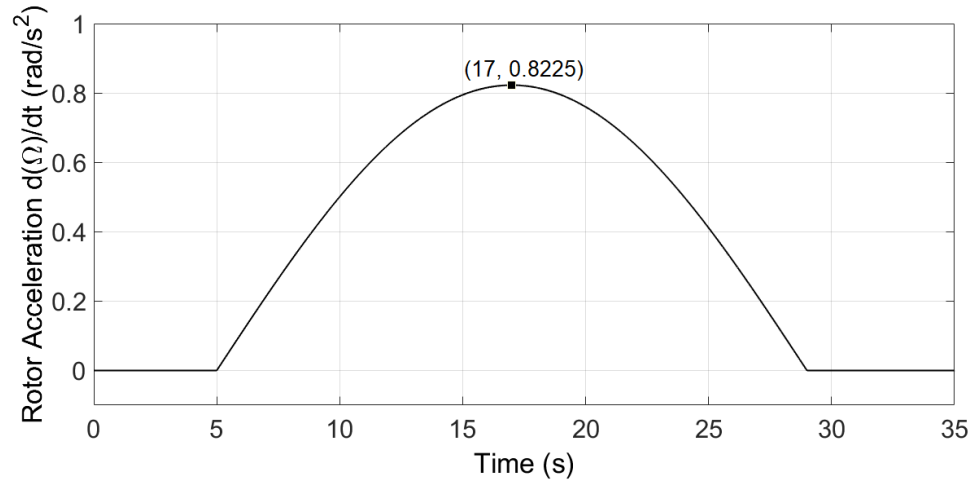


Figure 4.118: Rotor acceleration time history ($\Omega = 110$ to 230 RPM in 24 s)

The blade's transition response in this case is similar to the reverse transition response as seen in the previous section. Lag moment response is shown in Figure 4.119. Here again, resonance crossings have no effect on the blade response. The lag force, flap moment, torsional moment and rotor torque are given in Figures 4.120, 4.121, 4.122 and 4.123, respectively.

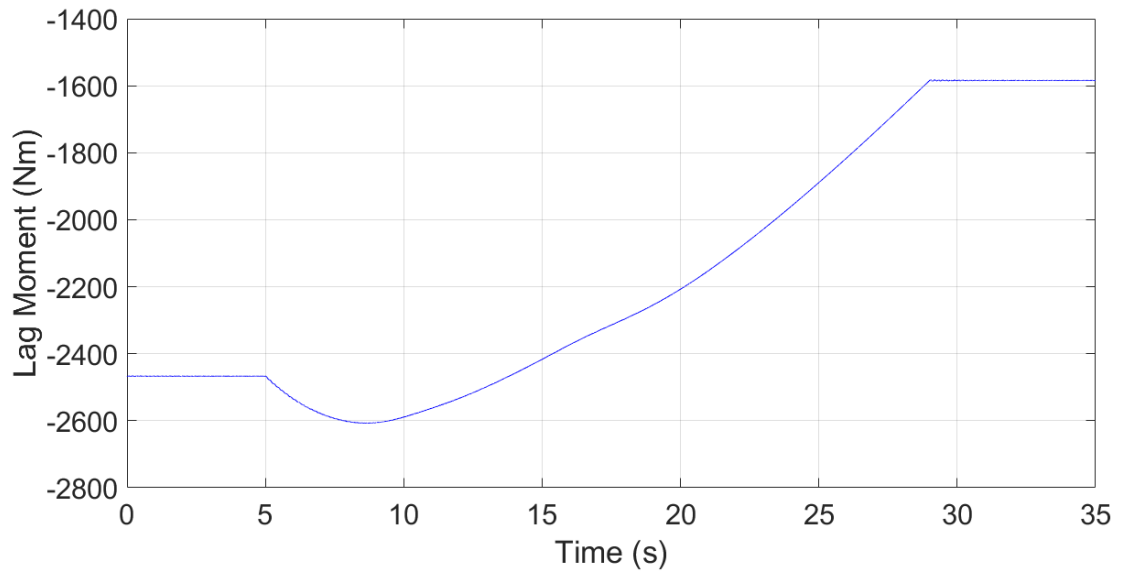


Figure 4.119: Time history of lag moment at blade root ($\mu_N = 0$; 110 \rightarrow 230 RPM)

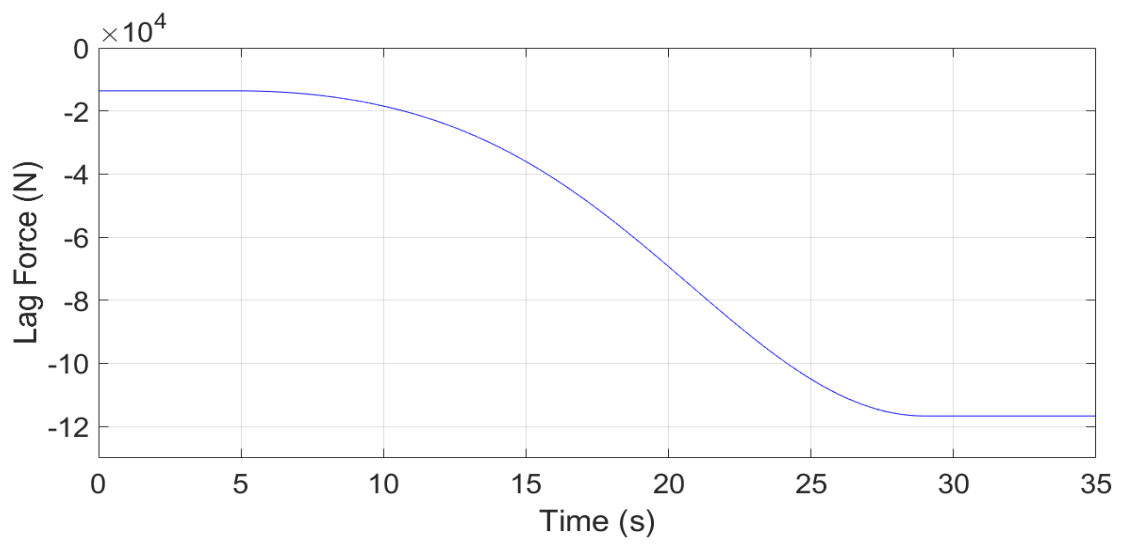


Figure 4.120: Time history of lag force at blade root ($\mu_N = 0$; 110 \rightarrow 230 RPM)

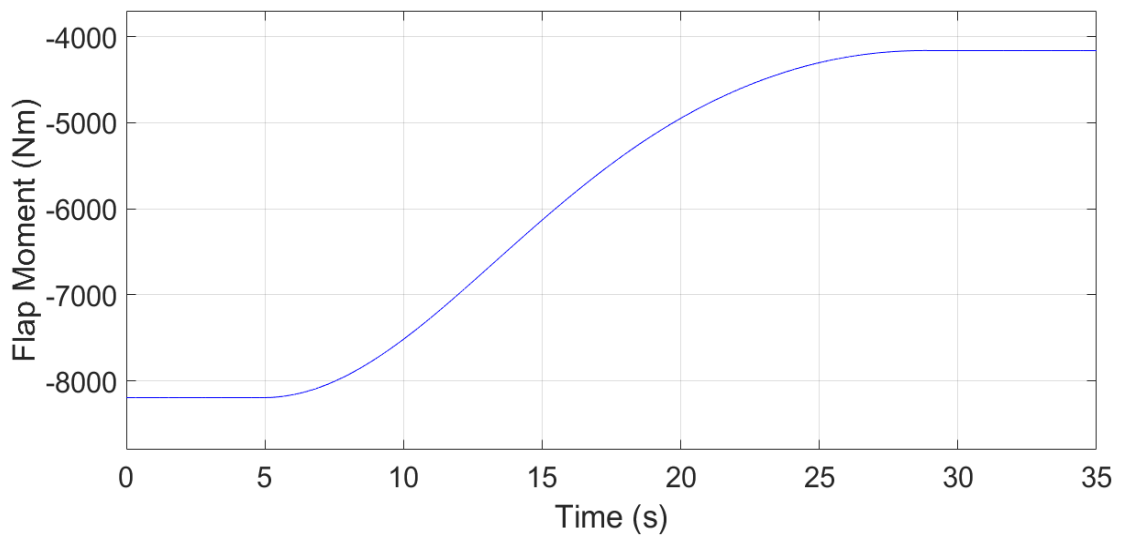


Figure 4.121: Time history of flap moment at blade root ($\mu_N = 0$; 110 \rightarrow 230 RPM)

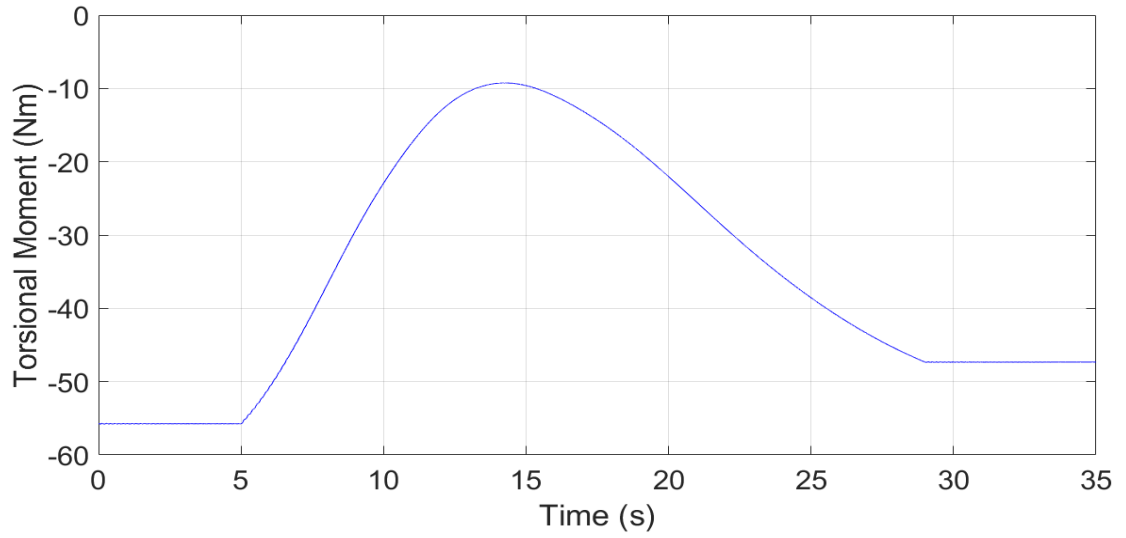


Figure 4.122: Time history of torsional moment at blade root ($\mu_N = 0$; 110 \rightarrow 230 RPM)

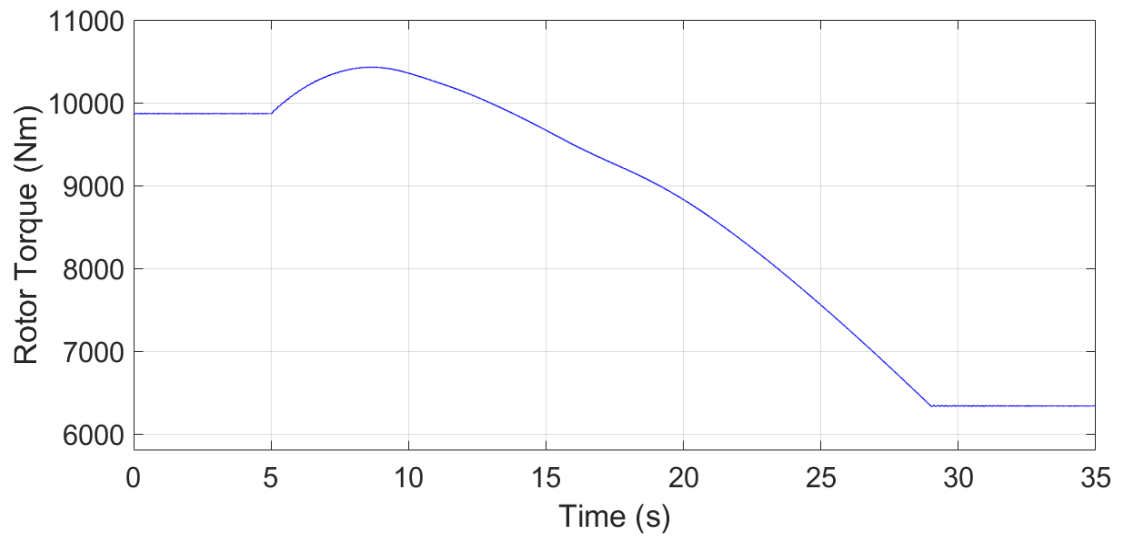


Figure 4.123: Time history of rotor torque ($\mu_N = 0$; 110 \rightarrow 230 RPM)

However, oscillations could be introduced into the blade response due to external disturbances. The disturbances can be in the form of a atmospheric breeze or pilot input. Hence, we will introduce some perturbations to the rotor and see how the blades behave during transition at hover.

4.6.6 Nominal Advance Ratio, $\mu_N = 0$: Perturbation Response

Let us introduce perturbations in the form a gust wind. The orientation of the gust velocity, V_g , is shown in Figure 4.124. α_g is the angle between the free stream and gust velocity. The gust velocity is chosen to be 6 knots (3.086 m/s), which is between a light and gentle breeze on a Beaufort wind scale. The properties of the gust are given in Table 4.9. We will be introducing two perturbations during transition. One close to the beginning of the transition and one close to the middle of the transition as shown in Figure 4.125. The response of the blade will be studied in the following sections. The transition occurs between 5 and 29 seconds.

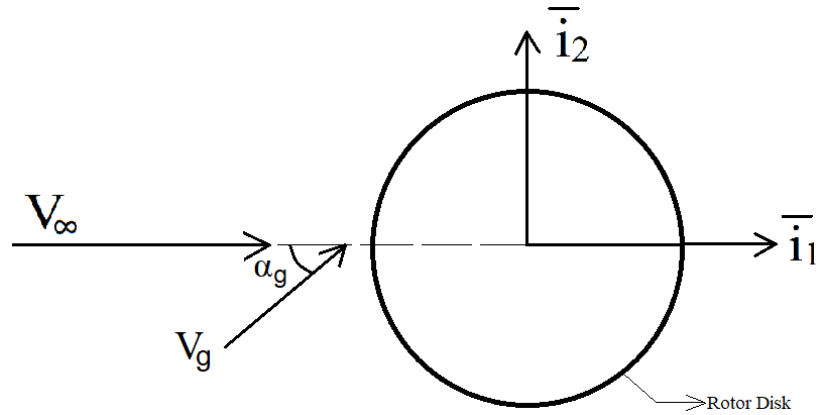


Figure 4.124: Gust orientation with respect to the rotor disk

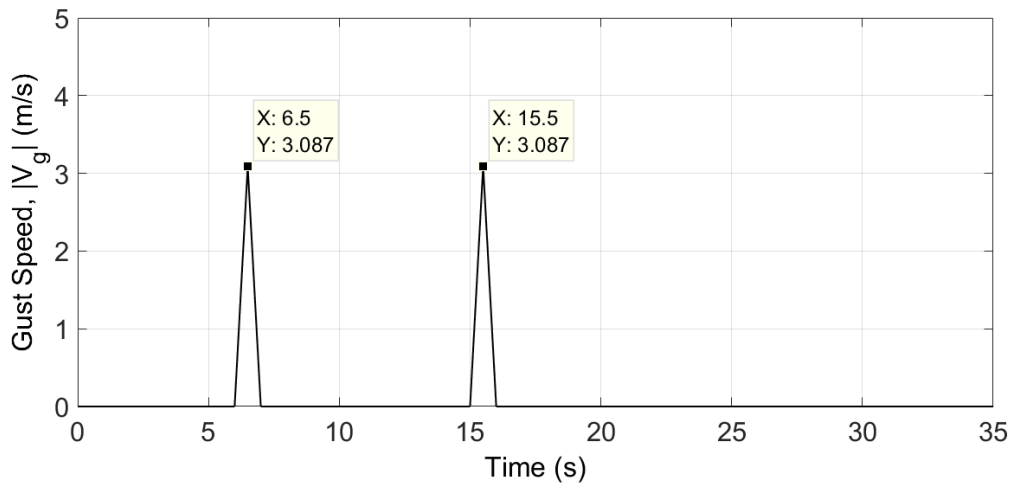


Figure 4.125: Time history of gust speed at $\mu_N = 0$

Table 4.9: Gust properties at $\mu_N = 0$.

$ V_g $	6 knots or 3.086 m/s
α_g	60°

Perturbed Transition: 230 to 110 RPM

The rotor speed, acceleration and pitch angle evolve in the same fashion as shown in the unperturbed section. Hence, the only addition is the gust wind to the free stream.

Lag moment response during the perturbed transition is shown in Figure 4.126. It can be seen that the perturbation increases the amplitude and introduces oscillatory behavior into the moment response. The oscillatory behavior, however, dies out with time and does not show any sudden increase due to resonance crossings. The FFT analyses of the regions after perturbations are given in Figures 4.127 and 4.128. The region after first perturbation seems to be influenced by the 2/rev crossing, which is in the vicinity, as the dominating frequency is 6.8 Hz. The region after second perturbation is influenced by the 3/rev crossing with 6.75 Hz being the dominating frequency.

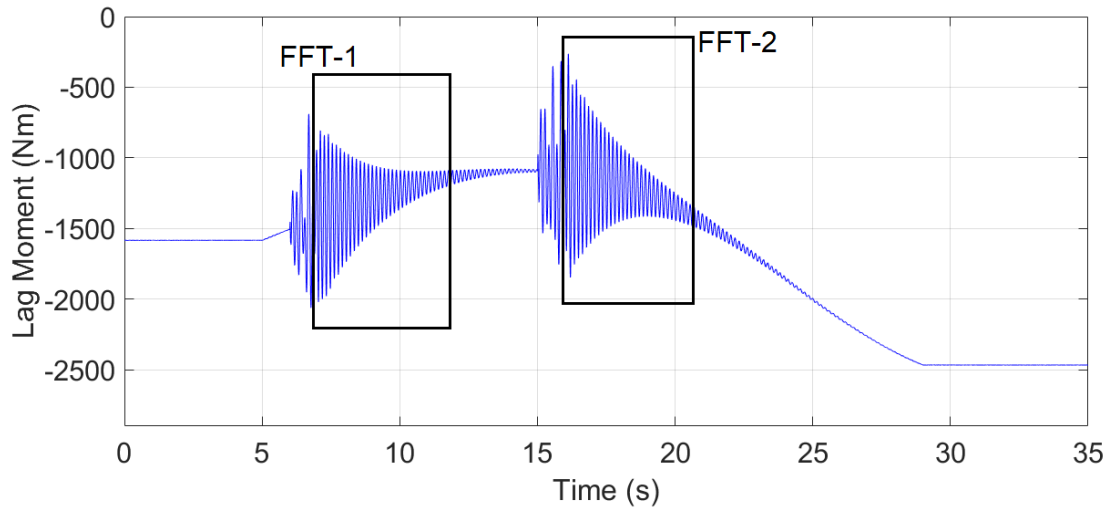


Figure 4.126: Time history of lag moment with gust ($\mu_N = 0$; 230 \rightarrow 110 RPM)

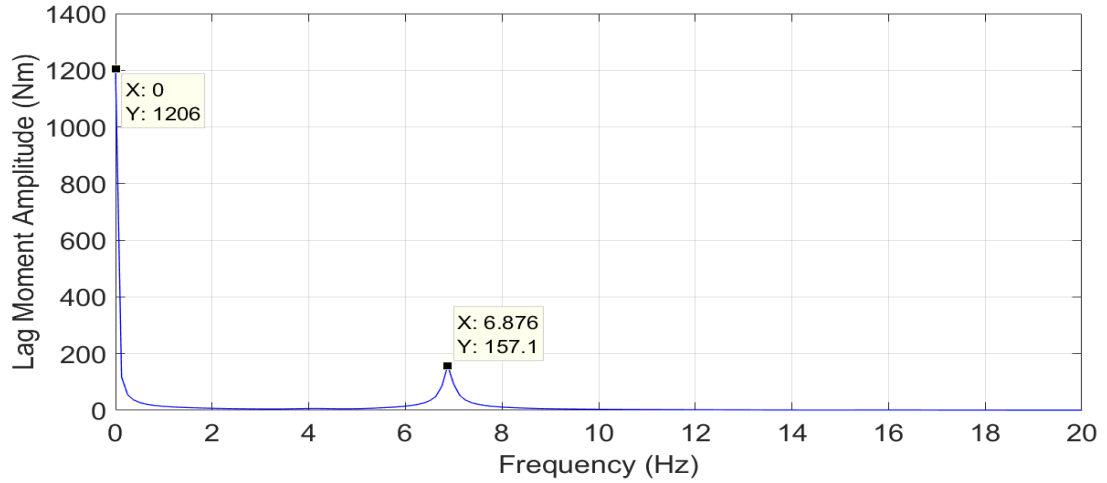


Figure 4.127: FFT analysis of lag moment after first perturbation ($\mu_N = 0$; 230 \rightarrow 110 RPM)

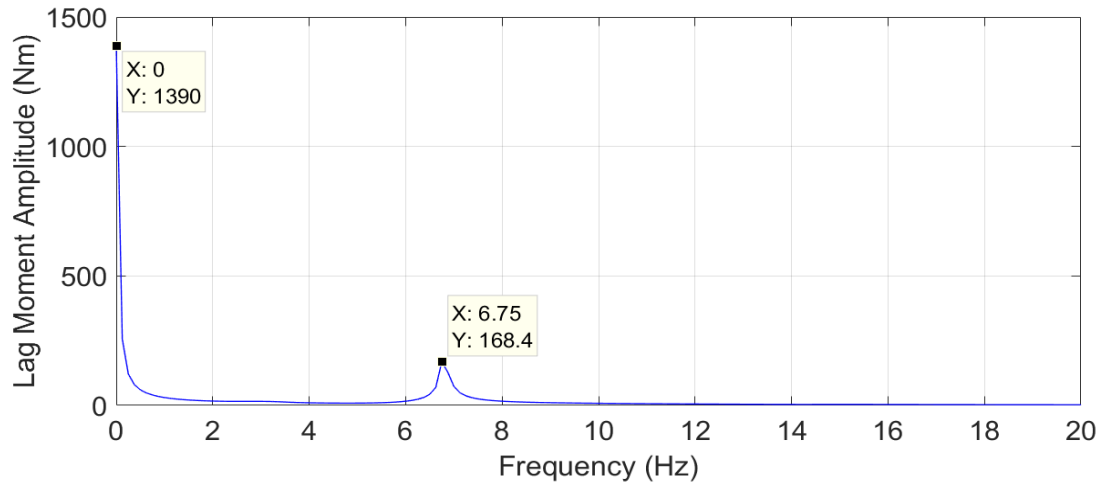


Figure 4.128: FFT analysis of lag moment after second perturbation ($\mu_N = 0$; 230 \rightarrow 110 RPM)

The lag force, on the other hand, is not affected greatly by the introduced perturbations. The lag force response is given in Figure 4.129. The FFT analysis of the post perturbed region did not reveal any frequencies. Hence, the FFT results are not shown here.

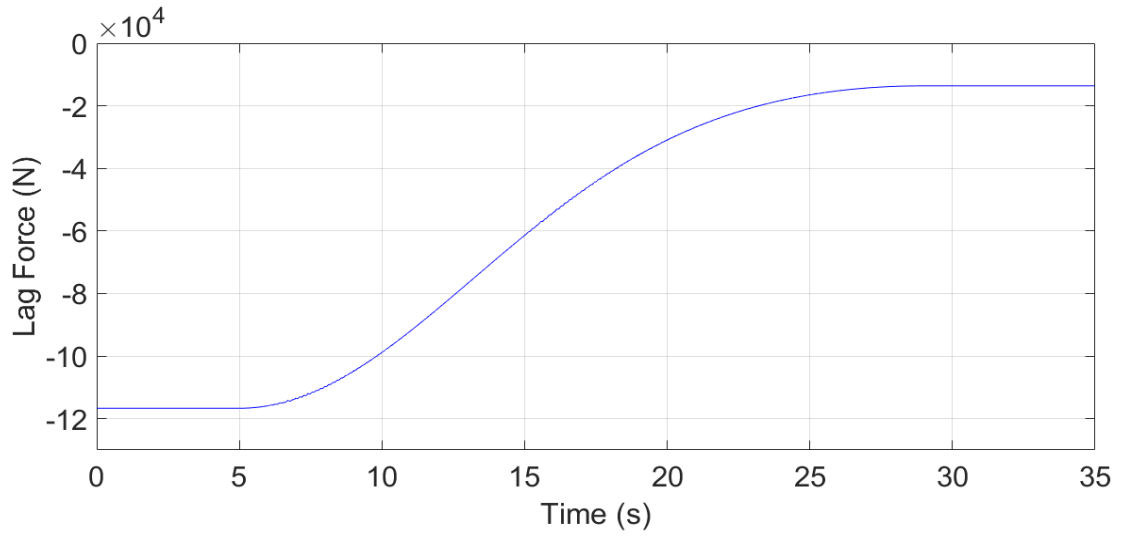


Figure 4.129: Time history of lag force with gust ($\mu_N = 0$; 230 \rightarrow 110 RPM)

Flap moment response is affected by the perturbations, Figure 4.130, but the resulting response after perturbations is not significant. This is unlike the lag moment response. This could be because of the flap damping of a rotor blade being usually higher than the lag damping. The FFT analysis of the post perturbed regions show a small bump around 6.8 Hz, Figures 4.131 and 4.132.

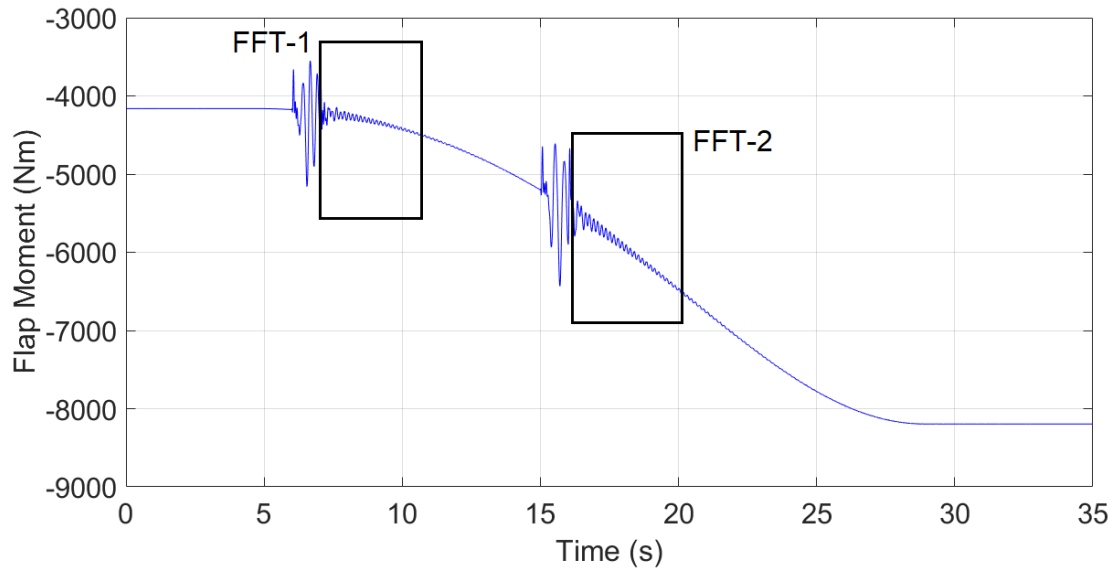


Figure 4.130: Time history of flap moment with gust ($\mu_N = 0$; 230 \rightarrow 110 RPM)

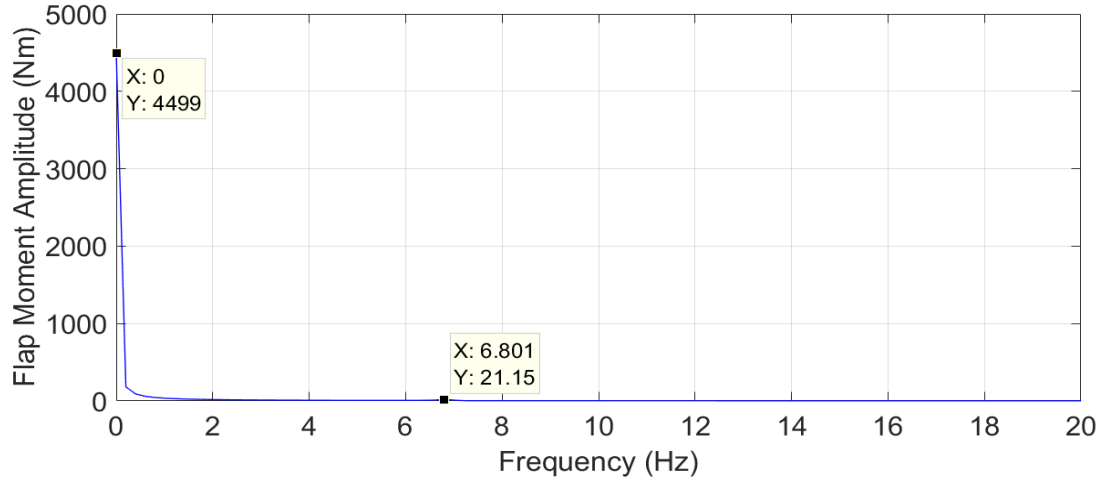


Figure 4.131: FFT analysis of flap moment after first perturbation ($\mu_N = 0$; 230 \rightarrow 110 RPM)

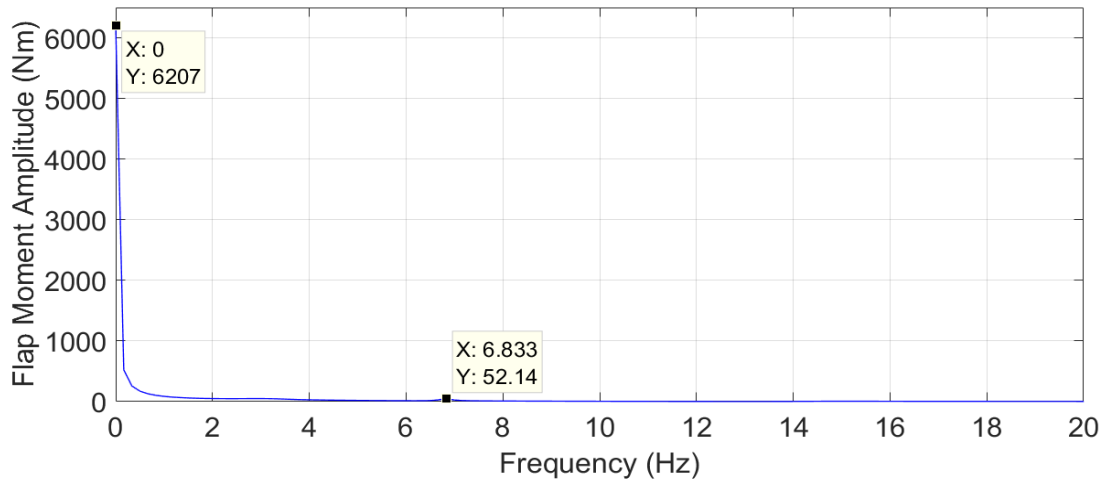


Figure 4.132: FFT analysis of flap moment after second perturbation ($\mu_N = 0$; 230 \rightarrow 110 RPM)

The torsional moment responds in a similar manner as the lag moment. The regions after perturbation have an oscillatory behavior that dampens out slowly as shown in Figure 4.133. The FFT analysis is done over a large region until the oscillations damp out. Hence, the magnitudes corresponding to the 2/rev and 3/rev frequencies are small compared to the initial oscillations. These are given in Figure 4.134 and Figure 4.135.

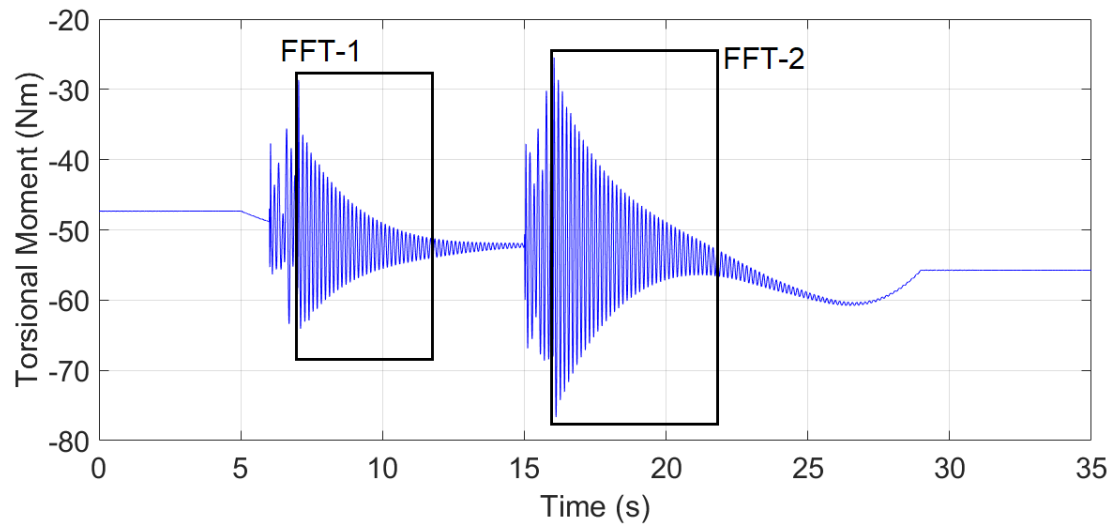


Figure 4.133: Time history of torsional moment with gust ($\mu_N = 0$; 230 \rightarrow 110 RPM)

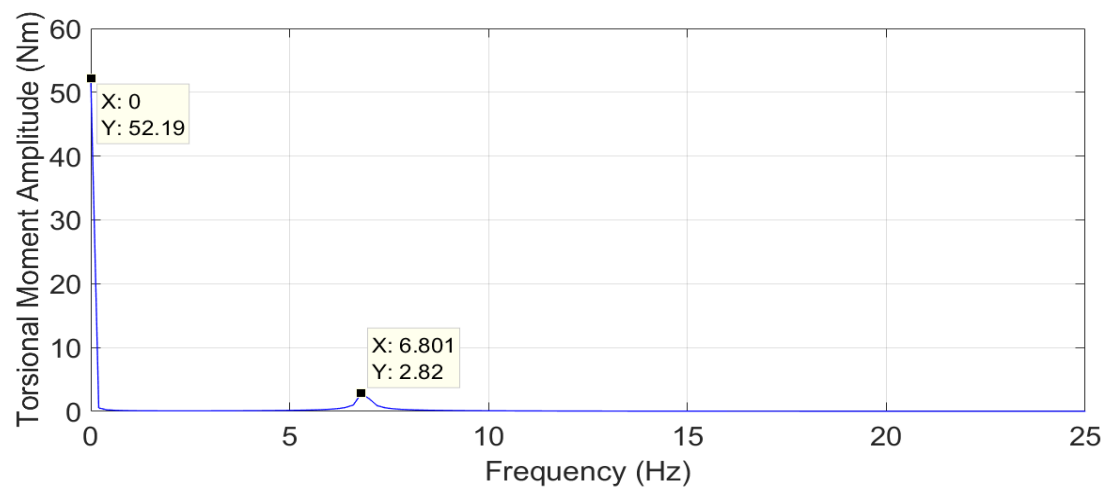


Figure 4.134: FFT analysis of torsional moment after first perturbation ($\mu_N = 0$; 230 \rightarrow 110 RPM)

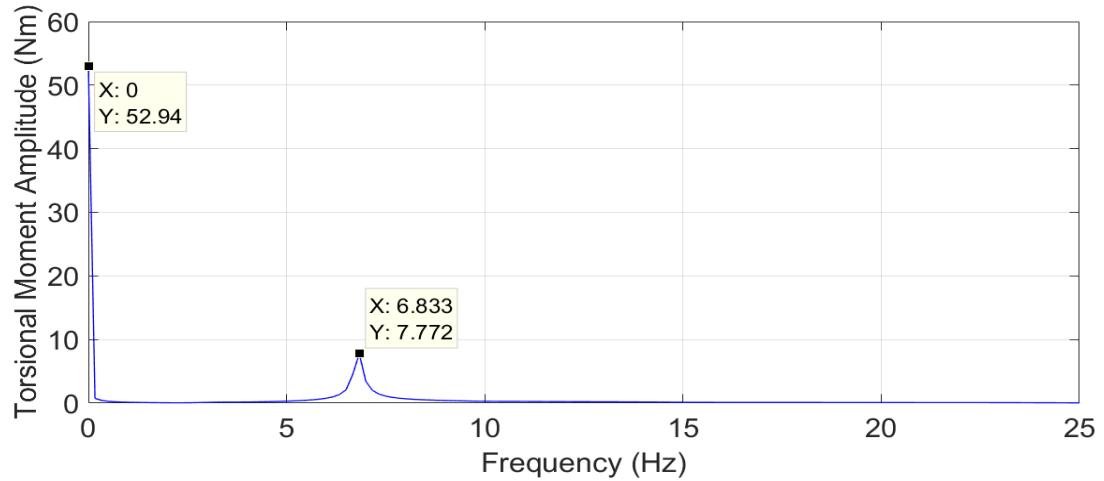


Figure 4.135: FFT analysis of torsional moment after second perturbation ($\mu_N = 0$; 230 \rightarrow 110 RPM)

The rotor torque's oscillation actually increases in amplitude noticeably right after the perturbation period before damping out, shown in Figure 4.136. This sort of behavior is also noticed for the torsional moment, but not as clearly as here. The FFT analysis shows that the second perturbation leads to greater amplitude oscillations compared to the first perturbation as shown in Figures 4.137 and 4.138. The dominating frequencies are still 2/rev, for the first perturbation, and 3/rev, for the second perturbation.

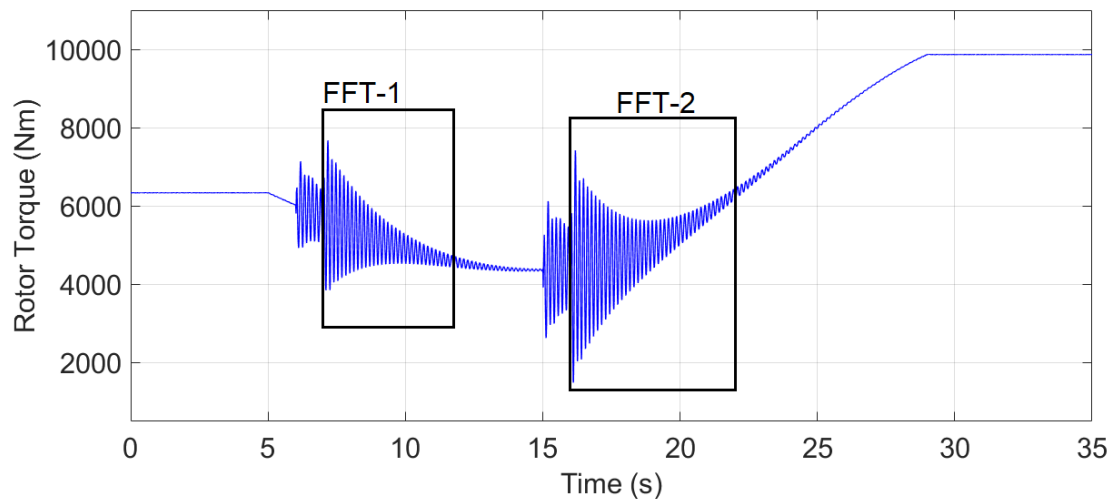


Figure 4.136: Time history of rotor torque with gust ($\mu_N = 0$; 230 \rightarrow 110 RPM)

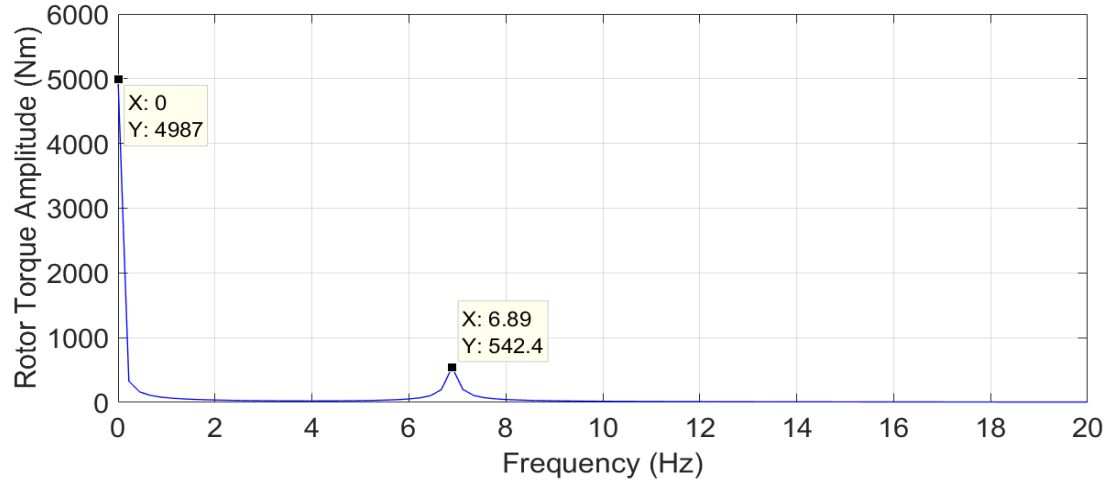


Figure 4.137: FFT analysis of rotor torque after first perturbation ($\mu_N = 0$; 230 \rightarrow 110 RPM)

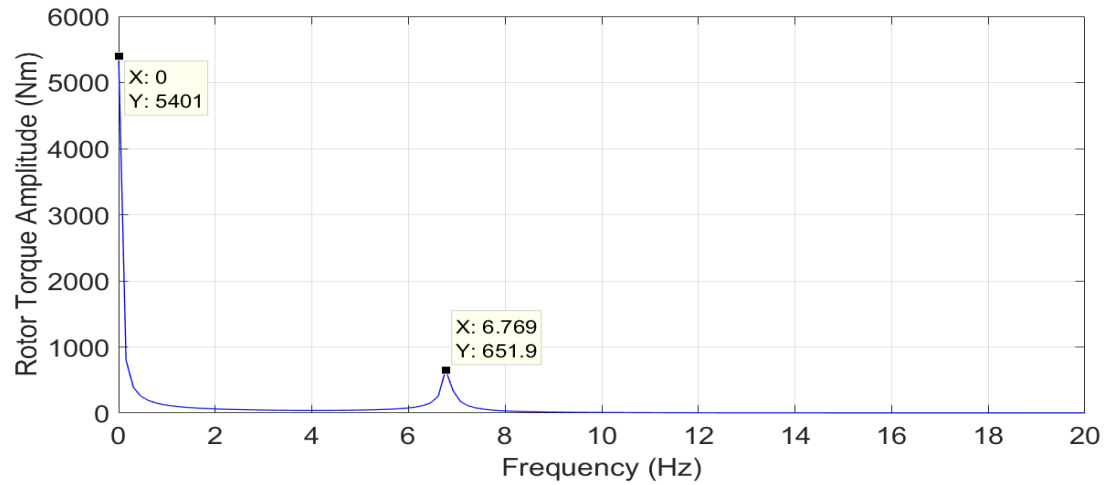


Figure 4.138: FFT analysis of rotor torque after second perturbation ($\mu_N = 0$; 230 \rightarrow 110 RPM)

Perturbed Transition: 110 to 230 RPM

The rotor transition takes place in the same manner as described in the second part of section 4.6.5 as far as rotor speed, acceleration and pitch angles are concerned.

Lag moment response shows that the first perturbation incites a higher magnitude response both during and after the perturbation in comparison to the second gust, Figure 4.139. The oscillatory behavior dies out with time like in the previous case and does not show any sudden increase due to resonance crossings. The region after the first perturbation is influenced by the 3/rev lag crossing as the dominating frequency is 6.72 Hz. The FFT analyses

are given in Figures 4.140 and 4.141. The region after second perturbation is influenced by 2/rev lag crossing.

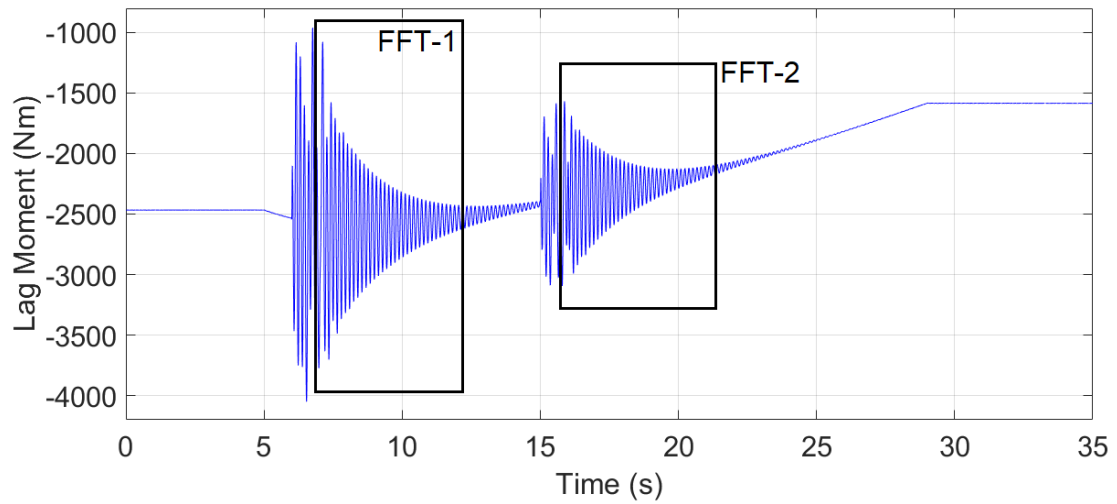


Figure 4.139: Time history of lag moment with gust ($\mu_N = 0$; 110 \rightarrow 230 RPM)

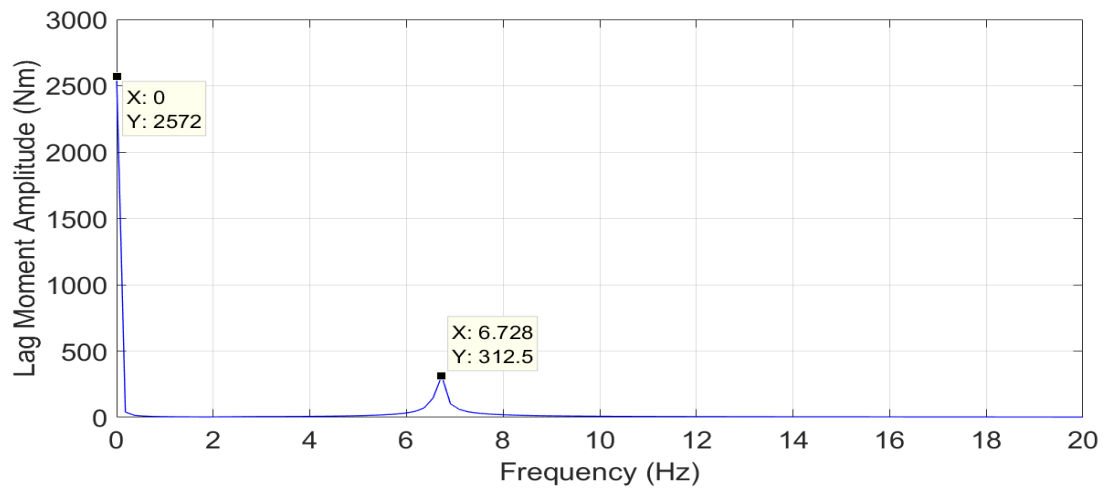


Figure 4.140: FFT analysis of lag moment after first perturbation ($\mu_N = 0$; 110 \rightarrow 230 RPM)

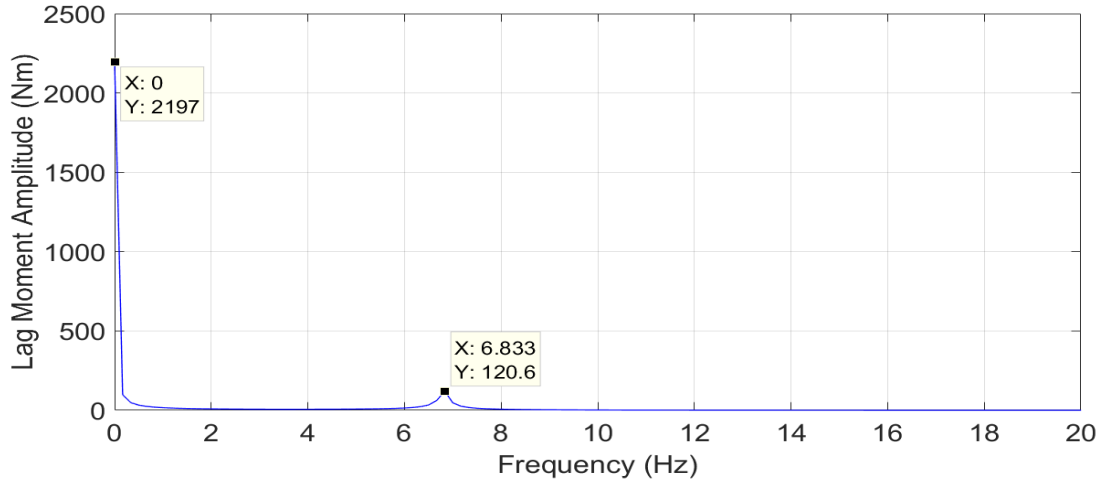


Figure 4.141: FFT analysis of lag moment after second perturbation ($\mu_N = 0$; 110 \rightarrow 230 RPM)

The lag force response is given in Figure 4.142. The lag force is not significantly influenced by the introduced wind gust.

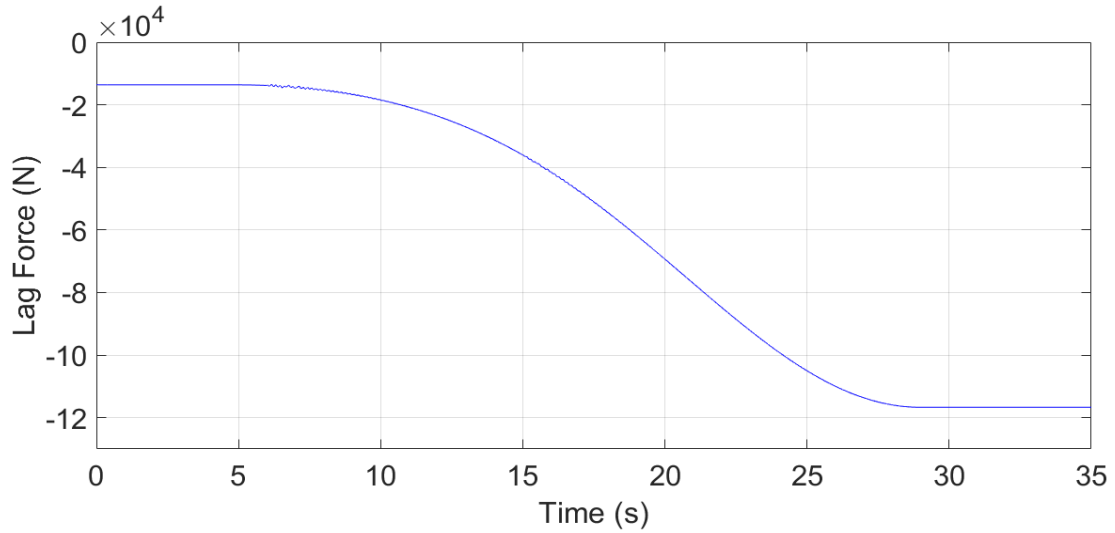


Figure 4.142: Time history of lag force with gust ($\mu_N = 0$; 110 \rightarrow 230 RPM)

The flap moment does not increase greatly after perturbations and the resulting oscillations dampen out quickly as shown in Figure 4.143. This is similar to the previous case. The FFT analysis of the post perturbed regions are shown in Figure 4.144 and 4.145. The second flap frequency crossings are not affecting the blade response during this transition.

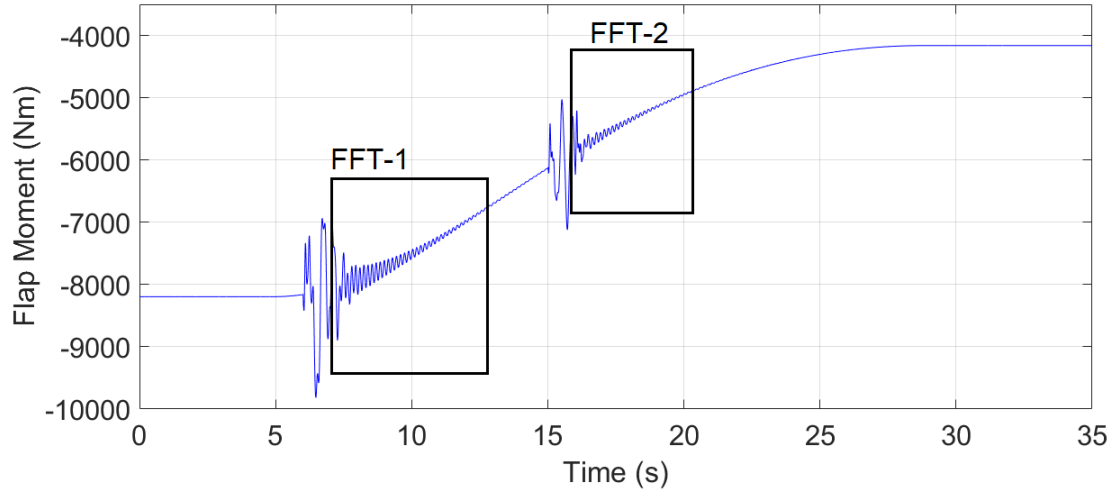


Figure 4.143: Time history of flap moment with gust ($\mu_N = 0$; 110 \rightarrow 230 RPM)

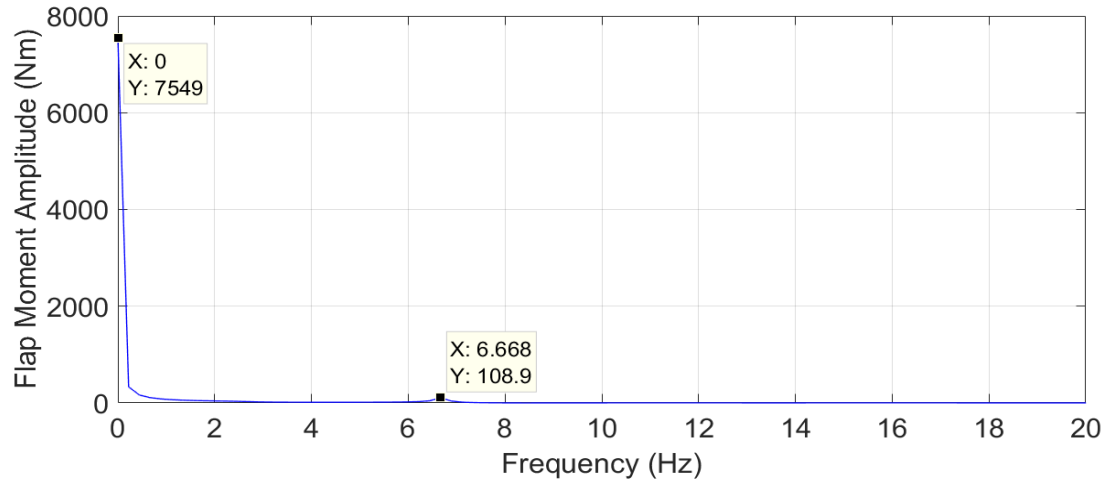


Figure 4.144: FFT analysis of flap moment after first perturbation ($\mu_N = 0$; 110 \rightarrow 230 RPM)

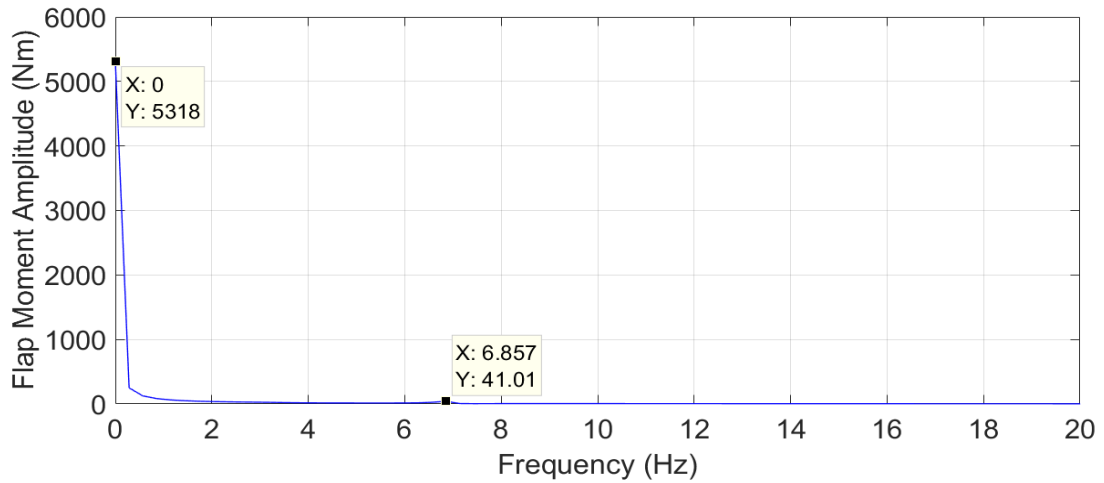


Figure 4.145: FFT analysis of flap moment after second perturbation ($\mu_N = 0$; 110 \rightarrow 230 RPM)

Torsional moment response is shown in Figure 4.146. Here again, the region after first perturbation have greater magnitude oscillations than the second perturbation. The FFT plots are given in Figures 4.147 and 4.148.

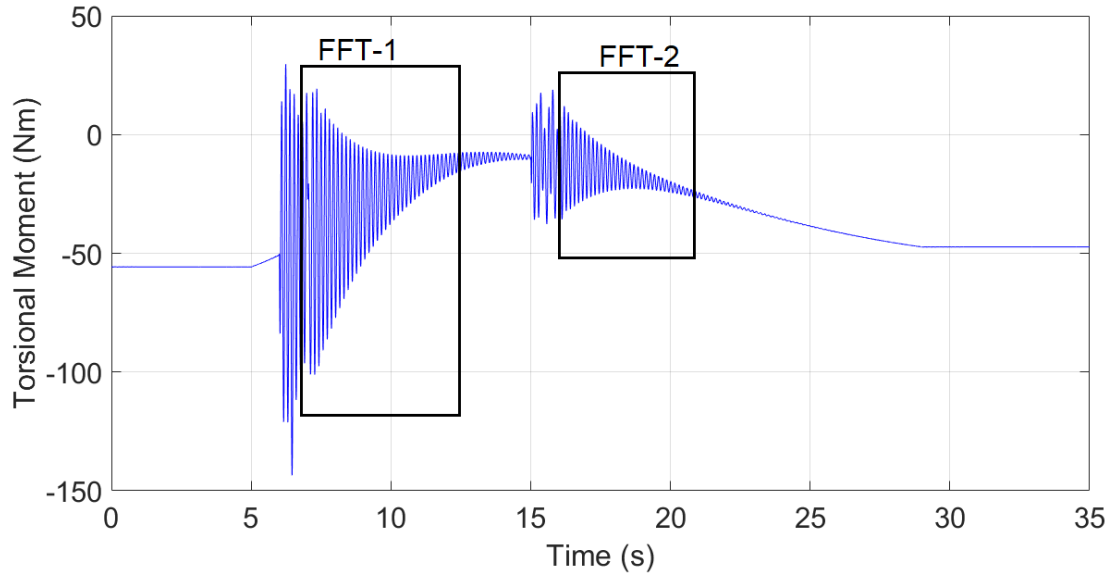


Figure 4.146: Time history of torsional moment with gust ($\mu_N = 0$; 110 \rightarrow 230 RPM)

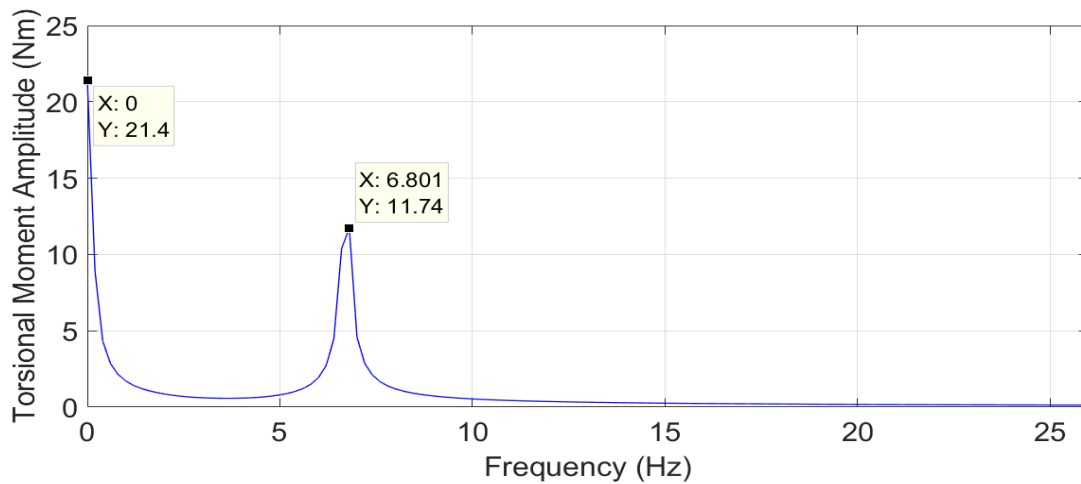


Figure 4.147: FFT analysis of torsional moment after first perturbation ($\mu_N = 0$; 110 \rightarrow 230 RPM)

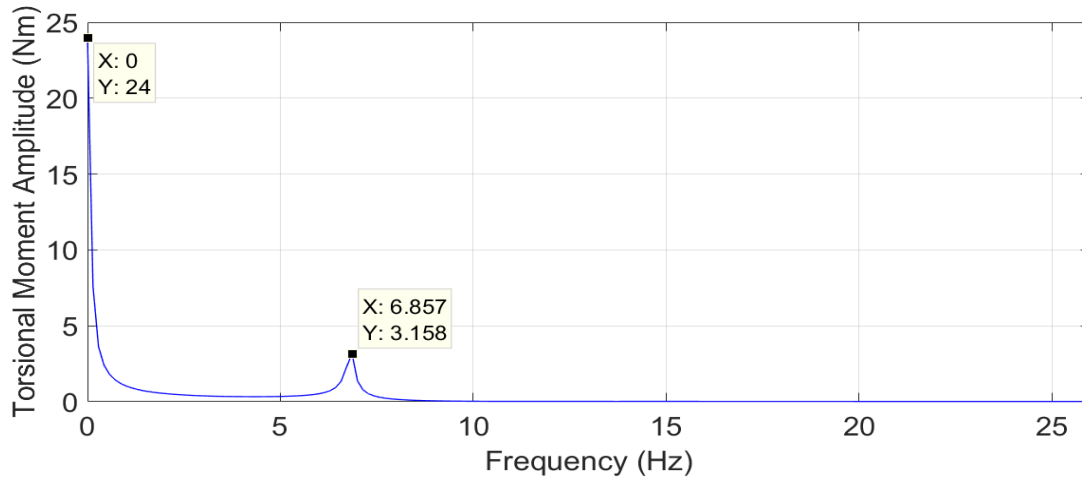


Figure 4.148: FFT analysis of torsional moment after second perturbation ($\mu_N = 0$; 110 \rightarrow 230 RPM)

The rotor torque response is shown in Figure 4.149. The FFT analysis shows that the dominating frequencies are still 3/rev and 2/rev as seen in Figures 4.150 and 4.151, respectively. The 4/rev frequency that was influencing the rotor torque response in forward flight is not playing a role in the hover flight condition.

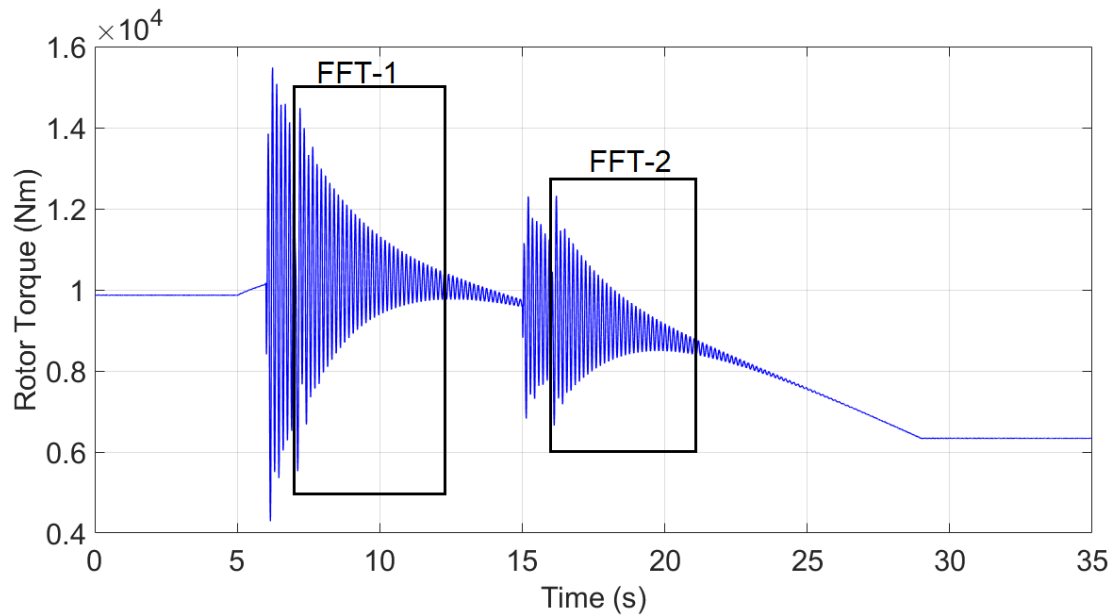


Figure 4.149: Time history of rotor torque with gust ($\mu_N = 0$; 110 \rightarrow 230 RPM)

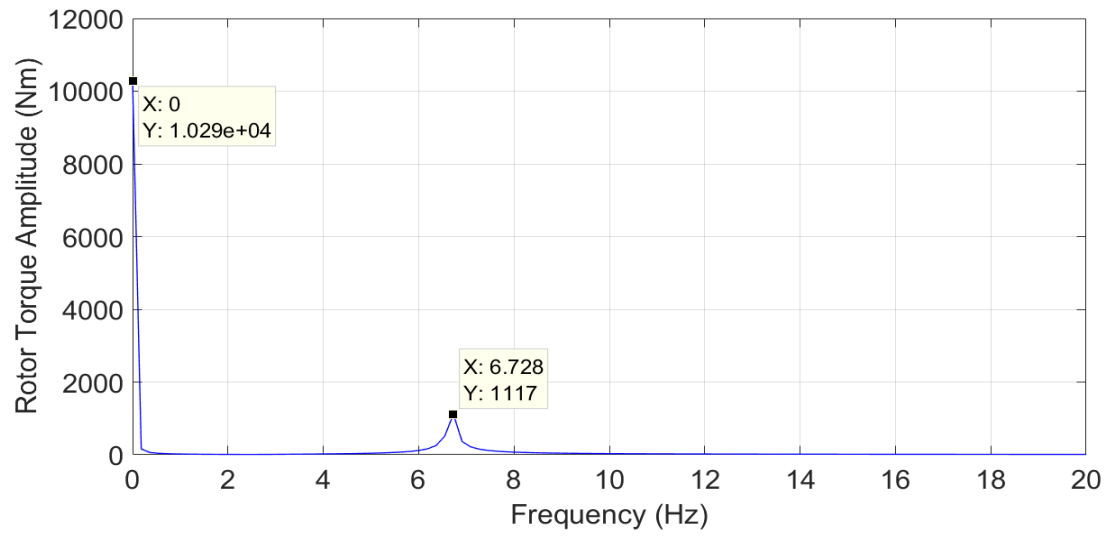


Figure 4.150: FFT analysis of rotor torque after first perturbation ($\mu_N = 0$; 110 \rightarrow 230 RPM)

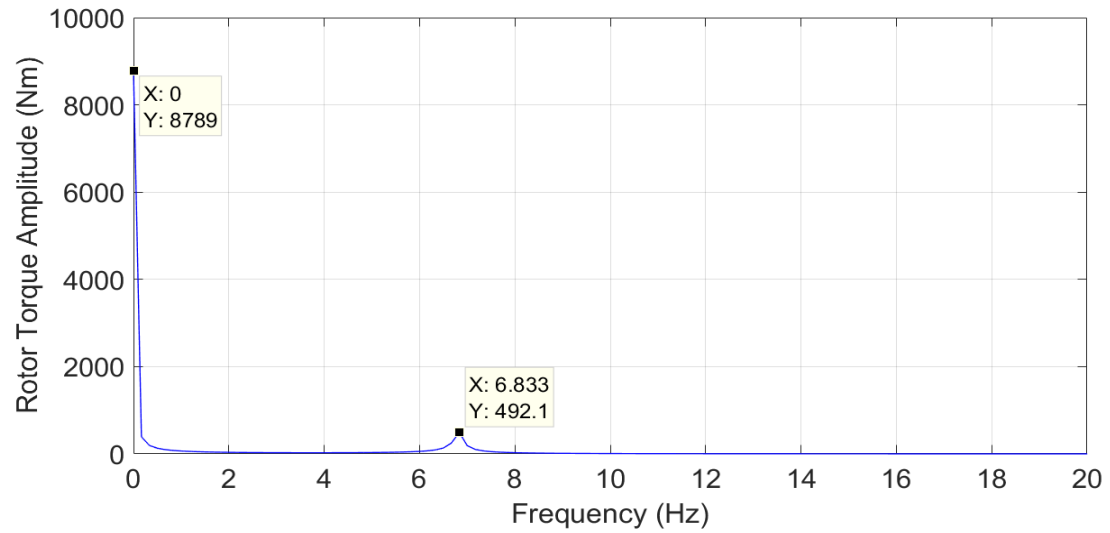


Figure 4.151: FFT analysis of rotor torque after second perturbation ($\mu_N = 0$; 110 \rightarrow 230 RPM)

CHAPTER 5

LOAD REDUCTION DURING RESONANCE

As seen in the previous chapter, the loads at the blade root increase significantly during resonance crossing. The increased loads lead to lower fatigue life of the blade, increased vibration of the hub, transmission system, and fuselage. This could result in several structural problems. Hence, it is vital to reduce the resonance loads. In this chapter, some of the important parameters of the resonance crossing and the blade are modified to study their impact on the blade response. The resonance crossing time, blade structural damping, and blade stiffness are chosen as the parameters of interest.

5.1 Rotor Speed Transition Time

The amount of time spent by the rotor close to the resonance region is expected to have a notable impact of the resonance loads. The rate at which the rotor passes through the resonance region, i.e. rotor acceleration, is both increased and decreased from the baseline value to study its effects.

5.1.1 $\mu_N = 0.3, 230 \rightarrow 180$ RPM

The baseline rotor speed transition time for $\mu_N = 0.3$ is 10 s. The transition time is varied from 2 s to 25 s as shown in Figure 5.1. The corresponding acceleration curves are shown in Figure 5.2. The blade response is captured for all these cases.

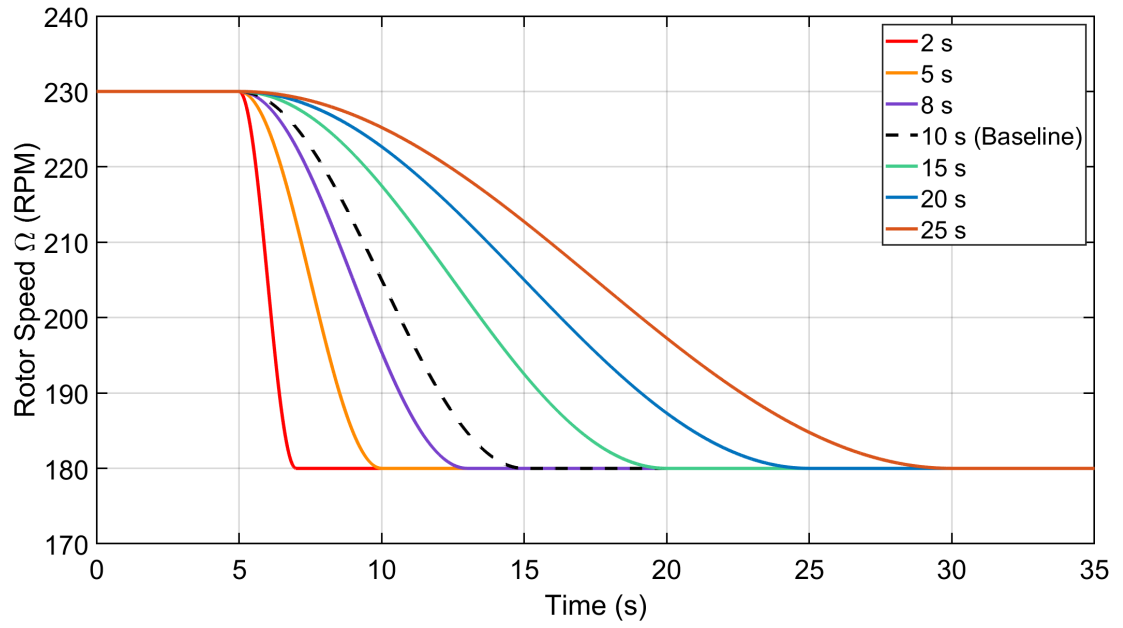


Figure 5.1: Rotor speed transition time cases ($\mu_N = 0.3$; $230 \rightarrow 180$ RPM)

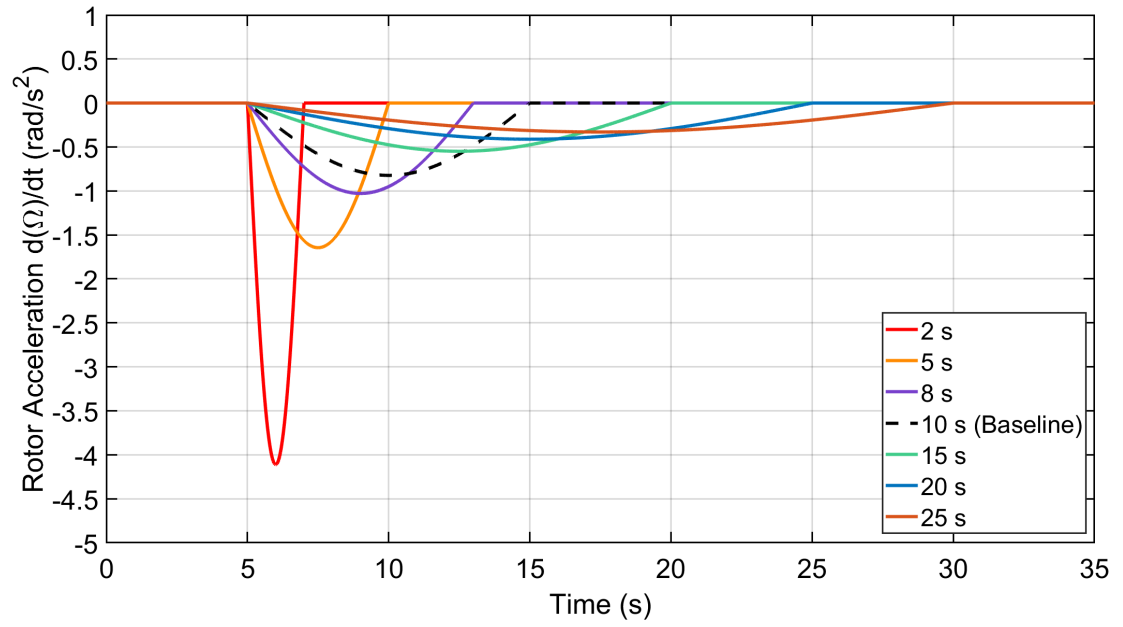


Figure 5.2: Rotor speed transition time cases ($\mu_N = 0.3$; $230 \rightarrow 180$ RPM)

The root lag moments for different transition times are compared as shown in Figure 5.3. The baseline response is shown in the black dashed lines. As the transition time is reduced from the baseline, the peak amplitude of the lag moment during resonance also decreases. The 2 s transition has the lowest amplitude. On the other hand, increasing the transition time from the base line also increases the lag moment amplitude during resonance. Hence, the quicker a rotor passes through the resonance the more desirable it is in terms of the lag moment response.

The resonance response shifts to the right as the resonance crossing is delayed with increase in transition time. The variation of the peak amplitudes with transition time is shown in Figure 5.4. A maximum of 37% reduction in the peak amplitude from the baseline is observed for 2 s transition, whereas, a 20% increase is noticed for 25 s transition. In Figure 5.4, the percentage changes with respect to the baseline amplitude are also specified.

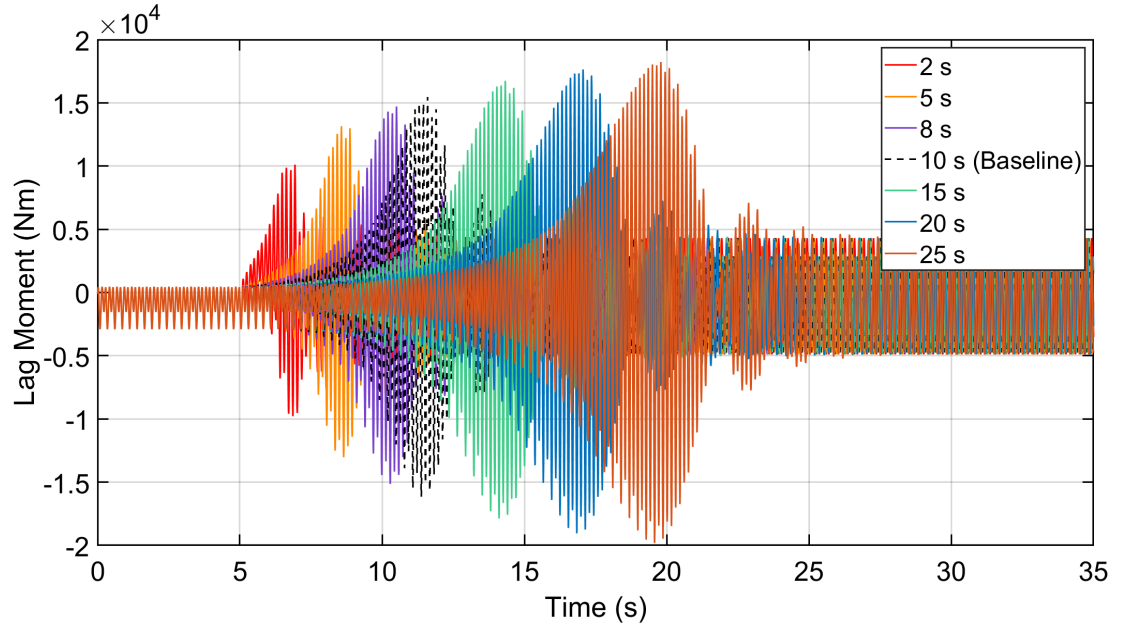


Figure 5.3: Time history of lag moment at blade root ($\mu_N = 0.3$; $230 \rightarrow 180$ RPM)

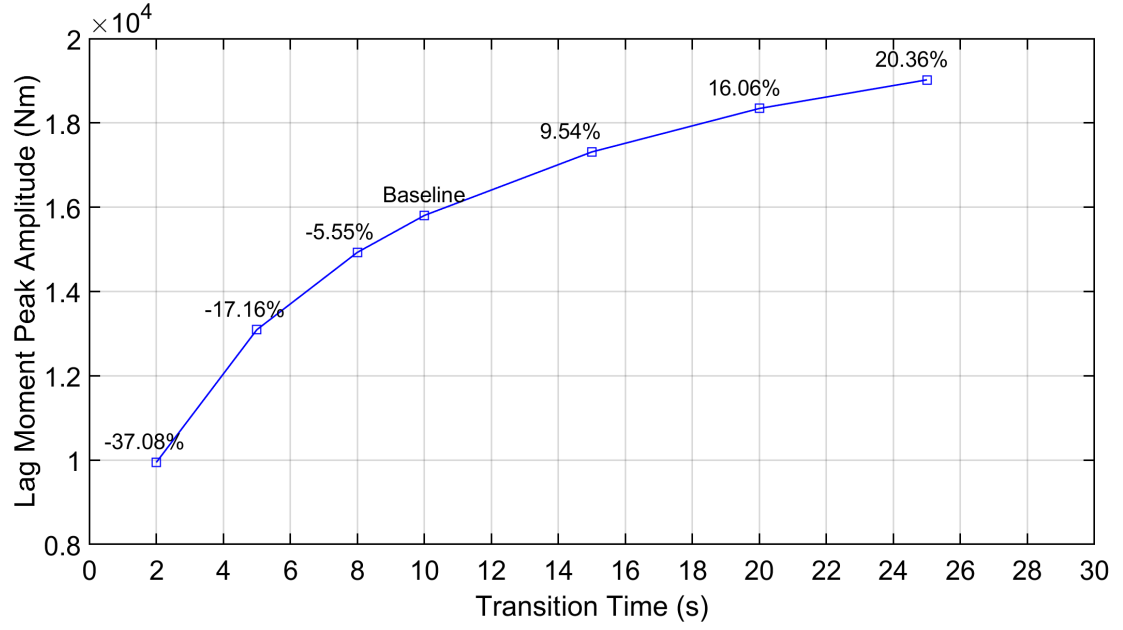


Figure 5.4: Lag moment's peak amplitude variation with transition time ($\mu_N = 0.3$; 230 \rightarrow 180 RPM)

Lag force response is not discussed in the rest of our analysis as no significant force increase was observed in the previous cases. Flap moments during resonance are compared in Figure 5.5. The peak amplitudes show a similar trend as the lag moment response. The dominating frequency is still 2/rev for all transition times. The variation of peak amplitudes is shown in Figure 5.6. Only a maximum of 18% reduction in amplitude was observed by changing the transition time from 10 s to 2 s.

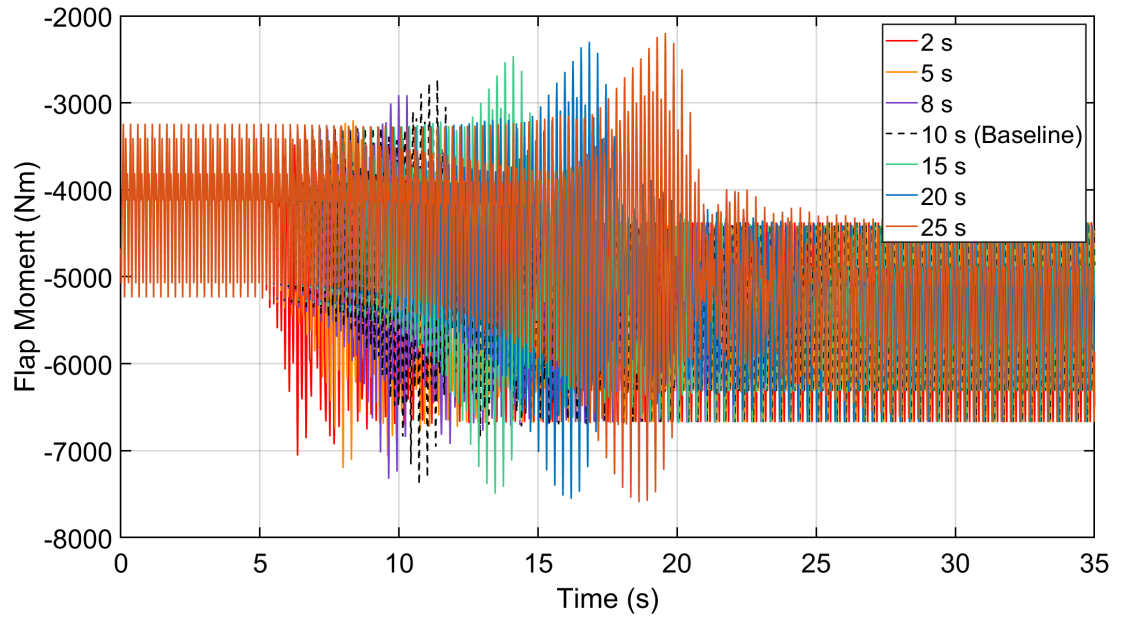


Figure 5.5: Time history of flap moment at blade root ($\mu_N = 0.3$; $230 \rightarrow 180$ RPM)

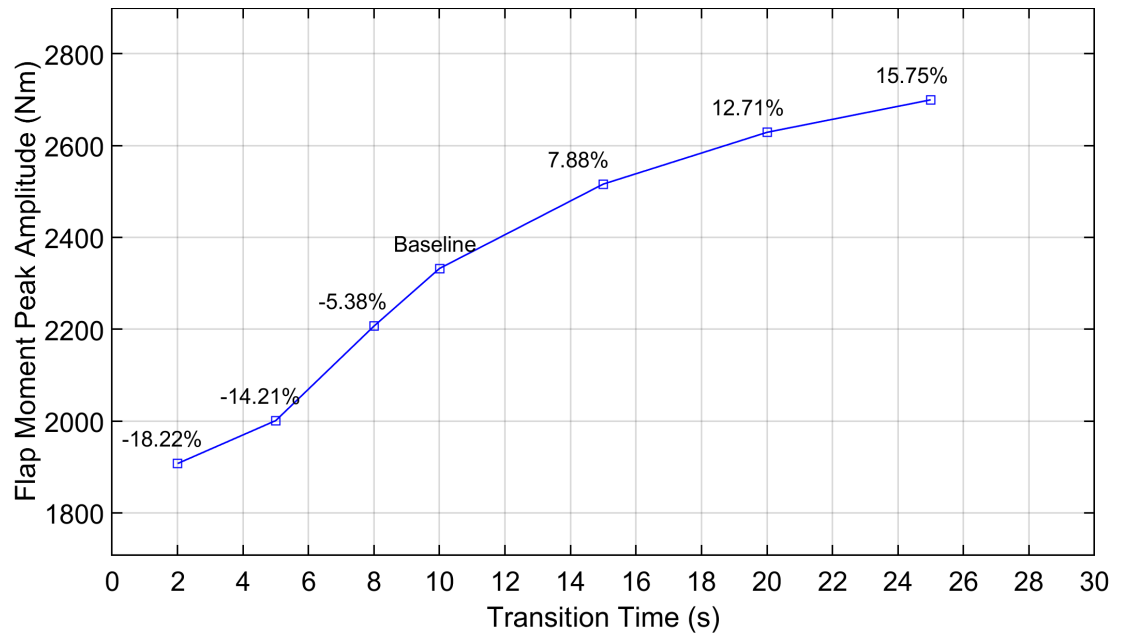


Figure 5.6: Flap moment's peak amplitude variation with transition time ($\mu_N = 0.3$; $230 \rightarrow 180$ RPM)

Torsional moment response is shown in Figure 5.7. It can be seen that the response is identical to the lag moment response, Figure 5.3, but lower in magnitudes. The peak amplitude variation is shown in Figure 5.8.

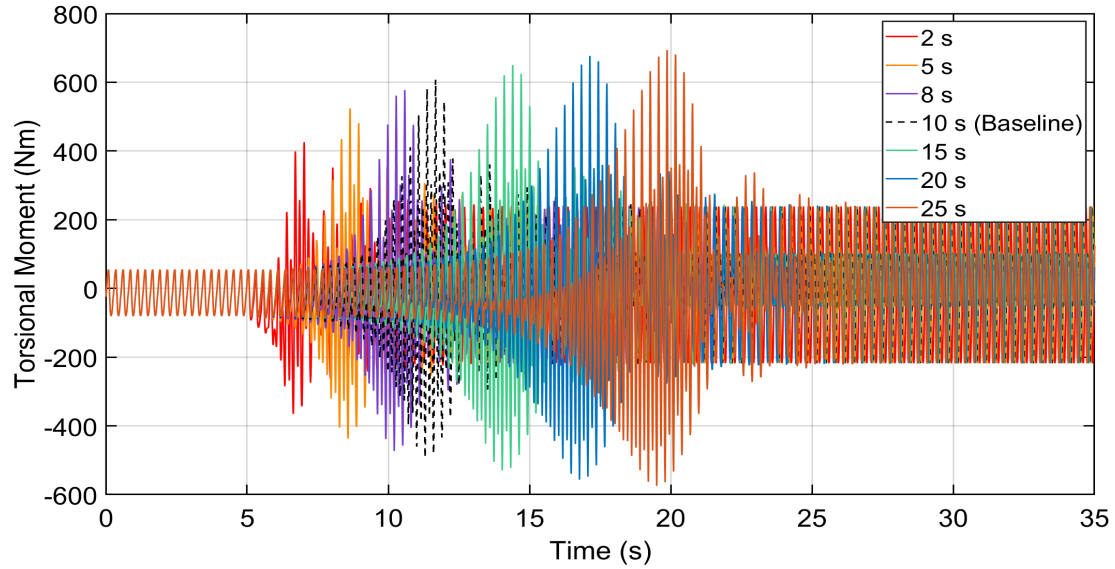


Figure 5.7: Time history of torsional moment at blade root ($\mu_N = 0.3$; $230 \rightarrow 180$ RPM)

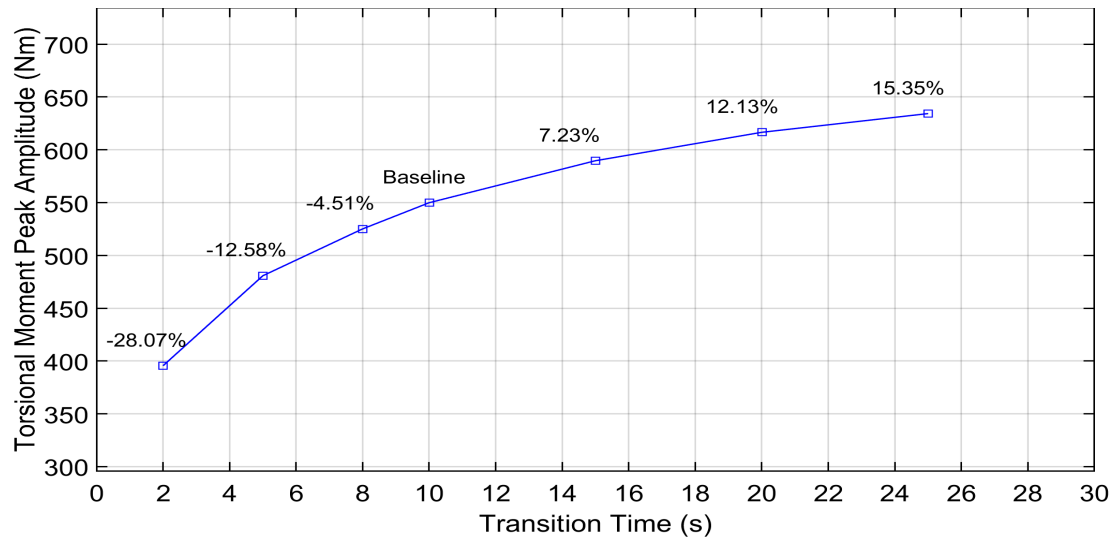


Figure 5.8: Torsional moment's peak amplitude variation with transition time ($\mu_N = 0.3$; $230 \rightarrow 180$ RPM)

Rotor torque required to achieve the rotor speed transition times described previously is shown in Figure 5.9. As expected, the rotor torque needs to decrease in amplitude to reduce

the rotor speed. However, for the 2 s and 5 s transitions the rotor torque becomes negative for a significant portion of the transition. This means that the torque not only needs to reduce in amplitude, but the transmission system should apply torque opposite to the spin direction to reduce the rotor speed quickly. This is analogous to applying brakes to the wheels of a moving vehicle. Building a transmission system that can achieve this will be quite an engineering task. If we assume that our transmission system can only reduce the torque but cannot apply torque in the opposite direction, the minimum possible transition time is 8 s, where the valley just touches the zero line as shown in Figure 5.10. The eight seconds transition only allows for a 5.5% reduction in peak amplitude of the lag moment as shown in Figure 5.4. The transitions above the baseline time require a lower change in torque from the baseline value but at a penalty of higher loads at the blade root.

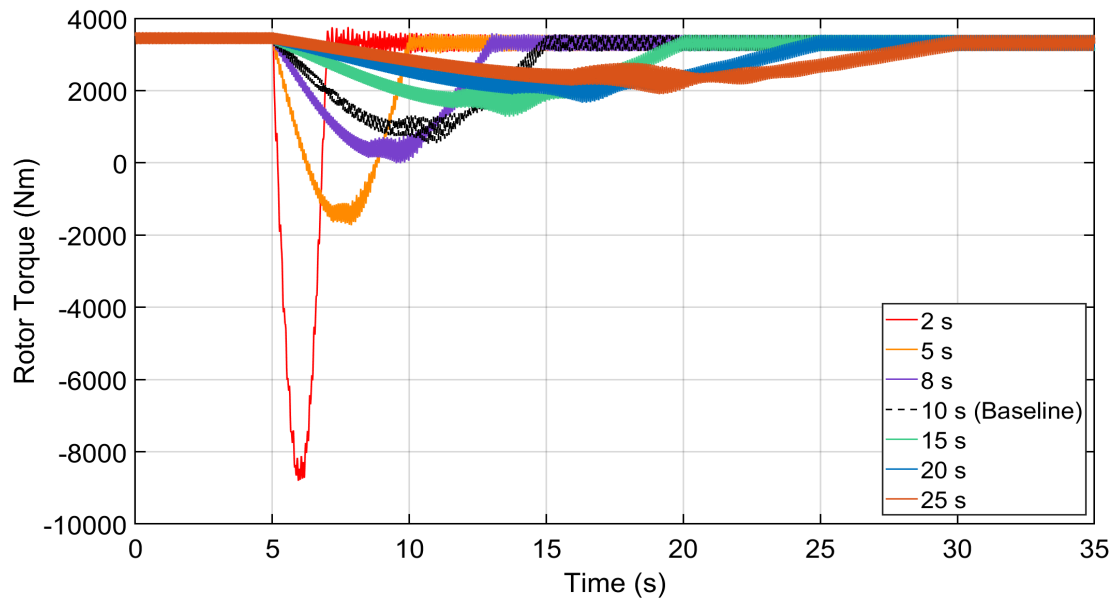


Figure 5.9: Time history of rotor torque ($\mu_N = 0.3$; 230 \rightarrow 180 RPM)

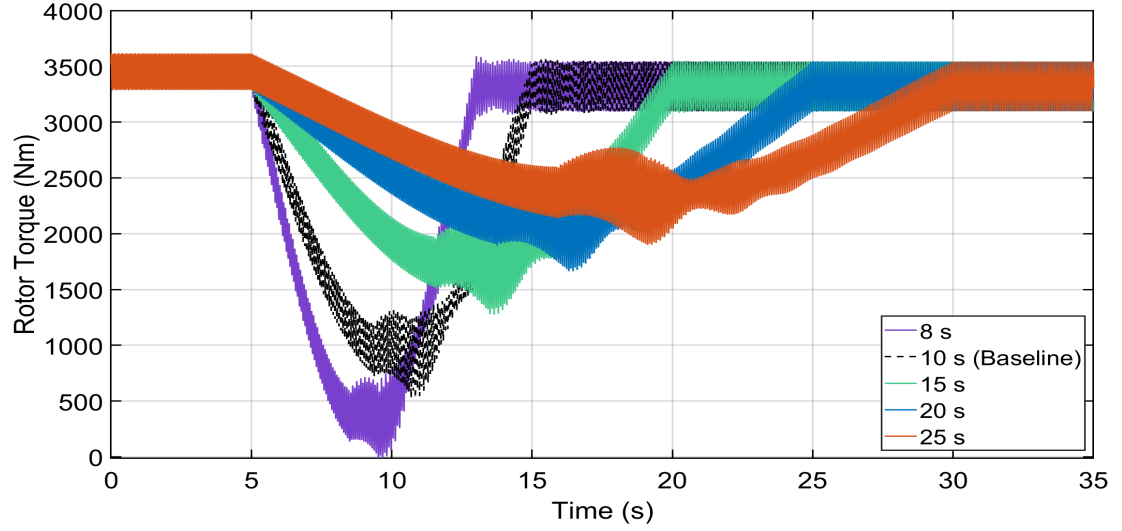


Figure 5.10: Time history of rotor torque without 2 s and 5s transition ($\mu_N = 0.3$; 230 \rightarrow 180 RPM)

5.1.2 $\mu_N = 0.3$, 180 \rightarrow 230 RPM

The transition times and rotor acceleration curves are shown in Figures 5.11 and 5.12, respectively. Since the resonance response of the flap moment and torsional moment are dependent on the lag resonance, only lag moment and rotor torque are discussed in the rest of our analysis unless necessary.

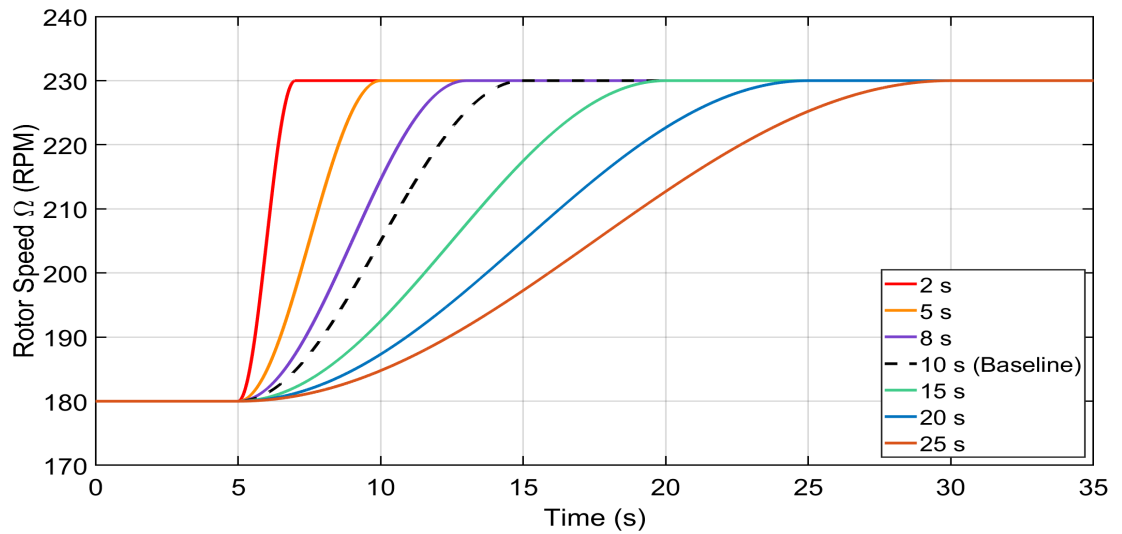


Figure 5.11: Rotor speed transition time cases ($\mu_N = 0.3$; 180 \rightarrow 230 RPM)

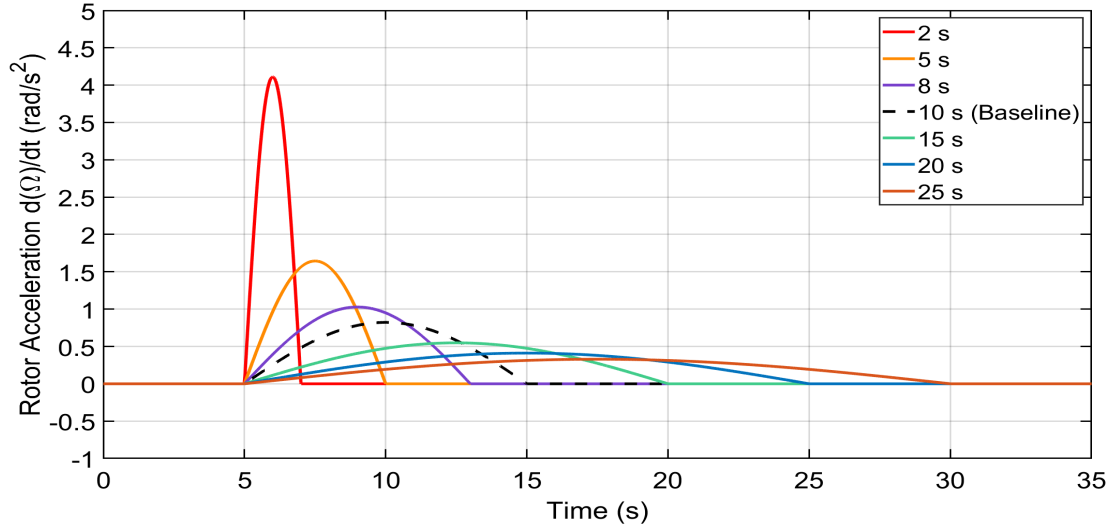


Figure 5.12: Rotor speed transition time cases ($\mu_N = 0.3$; $180 \rightarrow 230$ RPM)

For the transition times given in Figure 5.11, the lag moment response is shown in Figure 5.13. As discussed in the previous chapter, the lower-to-higher rotor speed transition has a lower amplitude increase during resonance. However, the increase of peak amplitude with increase in transition time is consistent with the previous case.

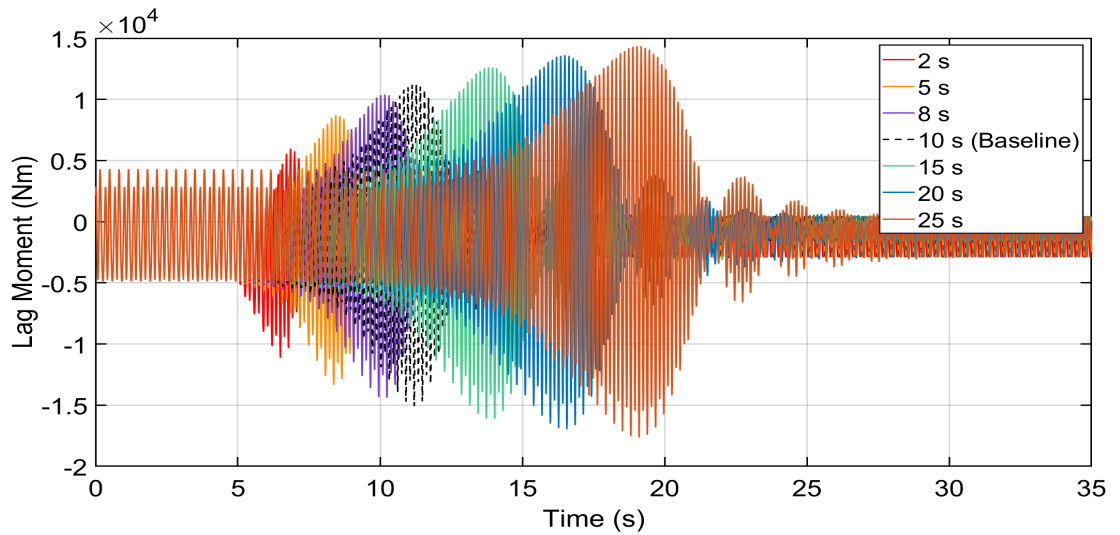


Figure 5.13: Time history of lag moment at blade root ($\mu_N = 0.3$; $180 \rightarrow 230$ RPM)

It is important to pay attention to the rotor torque behavior during this transition as it is expected to increase. The rotor torque responses are shown in Figure 5.14. It can be seen that the rotor torque increases drastically for shorter transition times. For the 2

s transition, the torque increases to almost 1.6×10^4 Nm. An upper bound on the torque needs to be imposed to have a reasonable allowable torque increase during transition. Based on our previous analysis, the maximum torque required during a no external disturbance transition was 1.04×10^4 Nm for the hover case, Figure 4.123. Hence, with some margin, we can assume that the transmission system can provide a torque up to 1.1×10^4 Nm during transition. With this assumption, the 2 s transition becomes unachievable. The 5 s transition has a peak only close to 8.5×10^4 Nm. Hence, there is some room to reduce the transition time from 5 s.

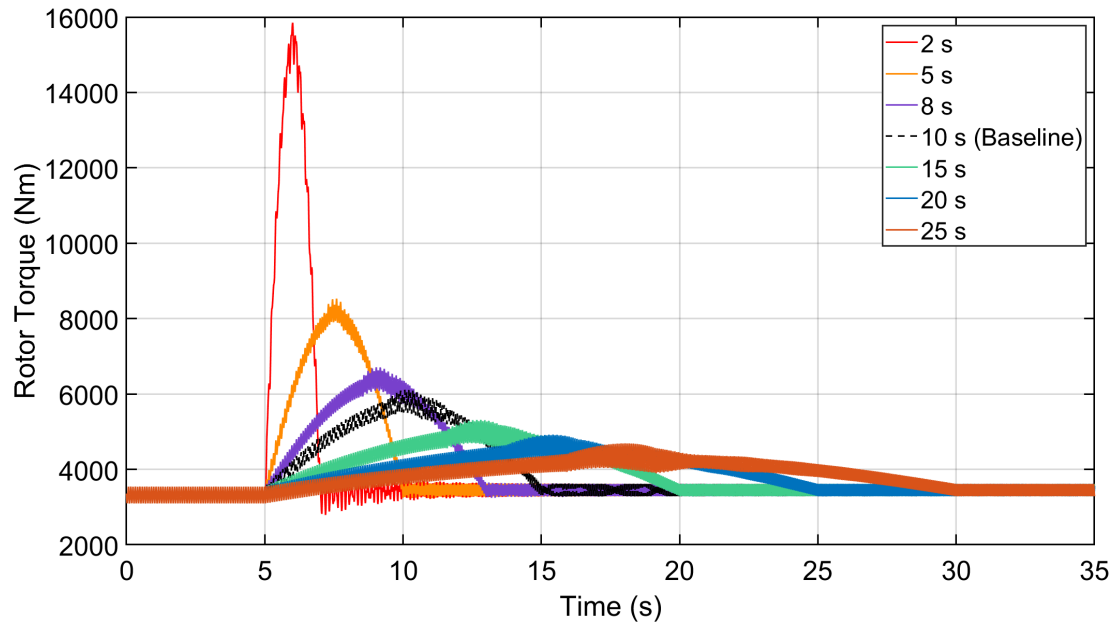


Figure 5.14: Time history of rotor torque ($\mu_N = 0.3$; $180 \rightarrow 230$ RPM)

The analysis was repeated for 3 and 4 s transition times, Figure 5.15. The corresponding rotor torques are shown in Figure 5.16. The 3 s transition is too short as the rotor torque crosses the 1.1×10^4 Nm limit. Hence, 4 s transition is the ideal case. The lag moment response for all the cases is shown in Figure 5.17. The corresponding peak amplitudes are shown in Figure 5.18. The peak amplitude is reduced by 21.5% from the baseline for the 4 s transition.

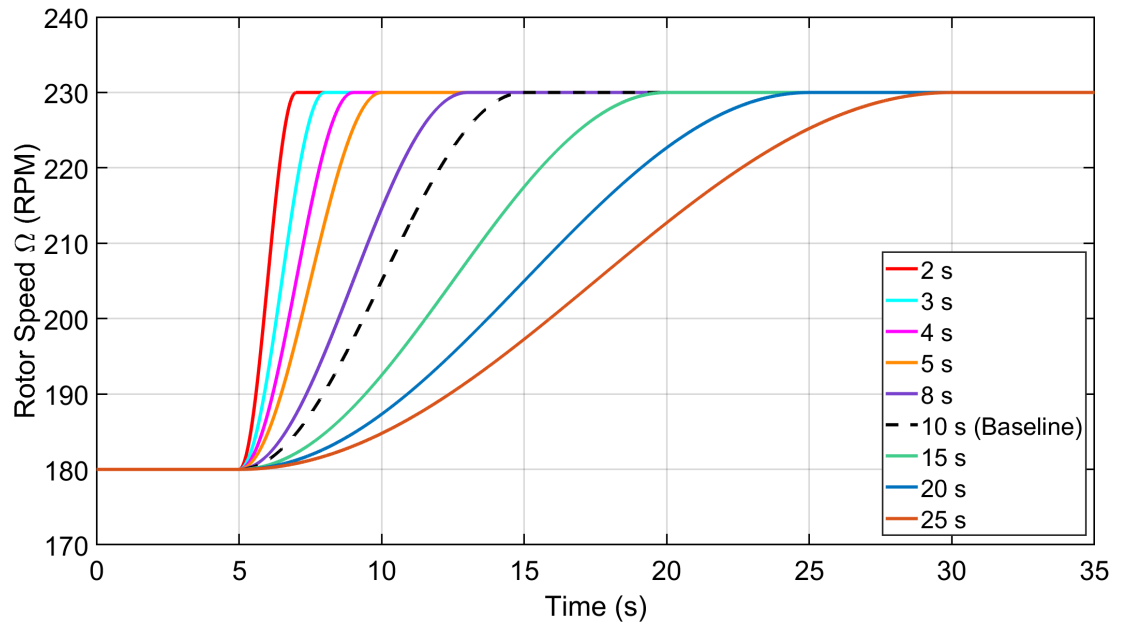


Figure 5.15: Rotor speed with 3 s and 4 s transition times ($\mu_N = 0.3$; 180 \rightarrow 230 RPM)

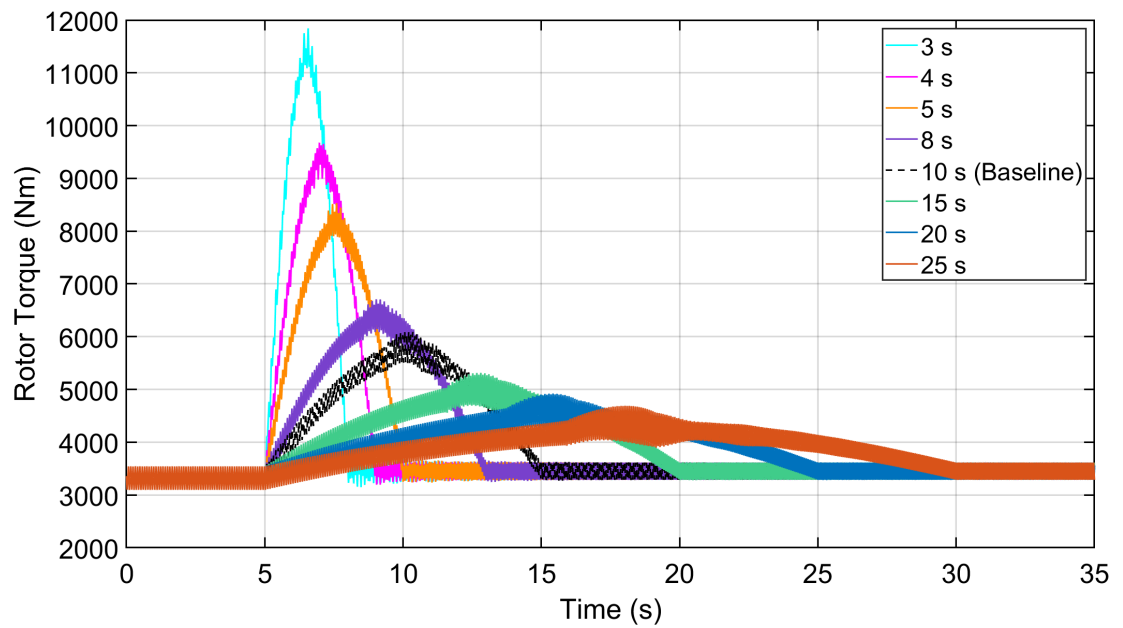


Figure 5.16: Time history of rotor torque with 3 s and 4 s transition times ($\mu_N = 0.3$; 180 \rightarrow 230 RPM)

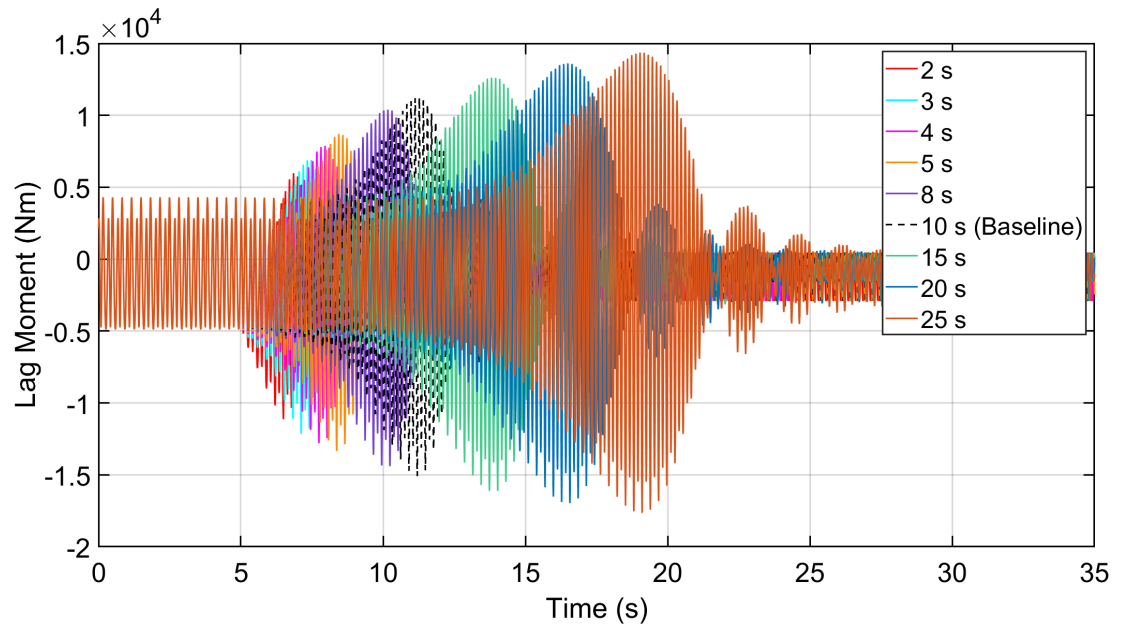


Figure 5.17: Time history of lag moment including 3 s and 4 s transition ($\mu_N = 0.3$; 180 \rightarrow 230 RPM)

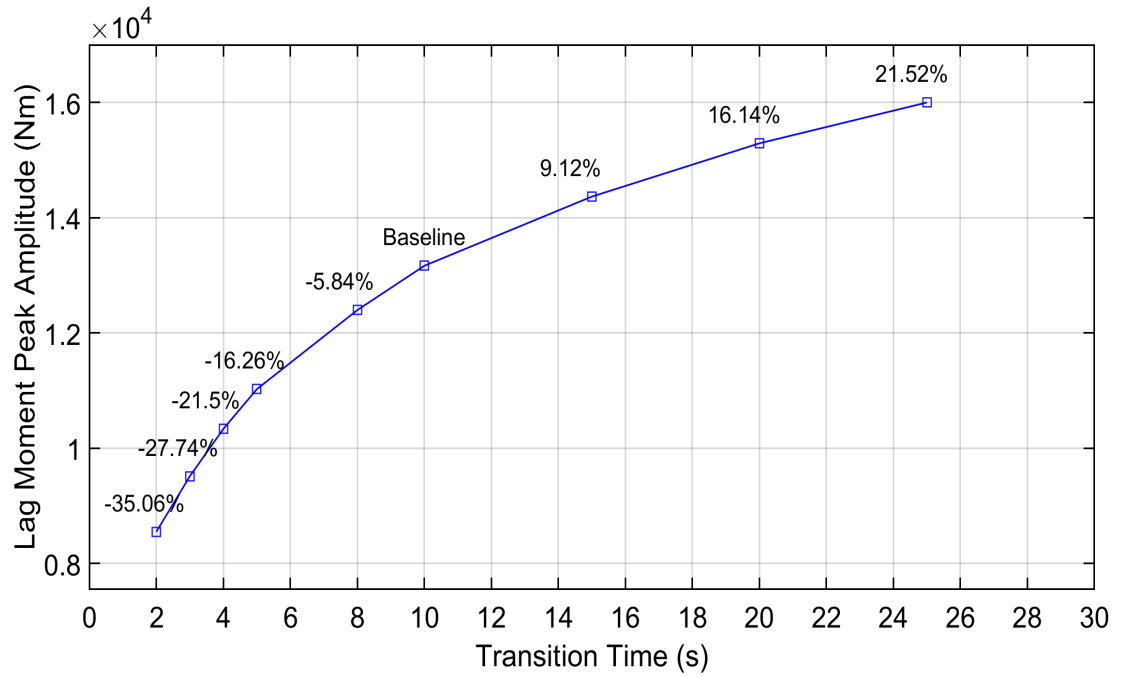


Figure 5.18: Lag moment's peak amplitude variation with transition time ($\mu_N = 0.3$; 180 \rightarrow 230 RPM)

5.1.3 $\mu_N = 0.2$, 230 \rightarrow 150 RPM

The baseline transition time for $\mu_N = 0.2$ is 16 s. The transition time is varied from 5 to 25 seconds as shown in Figure 5.19. The rotor acceleration curves are shown in Figure 5.20.

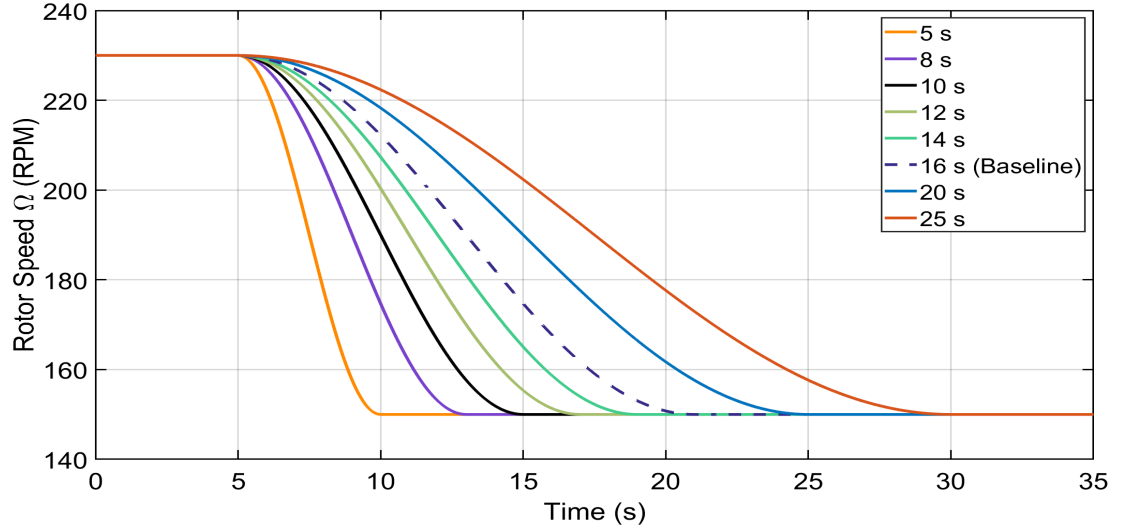


Figure 5.19: Rotor speed transition time cases ($\mu_N = 0.2$; 230 \rightarrow 150 RPM)

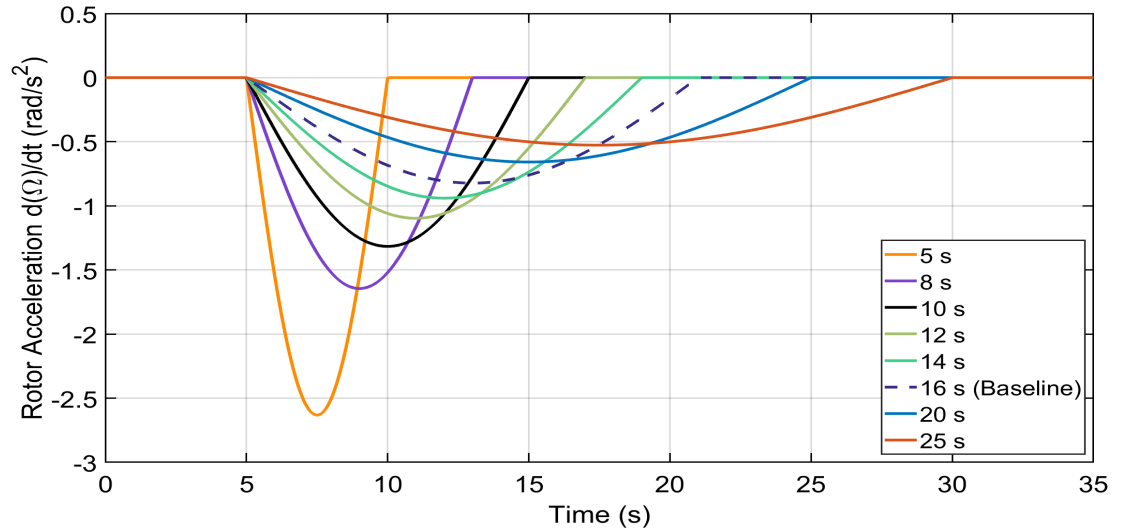


Figure 5.20: Rotor speed transition time cases ($\mu_N = 0.2$; 230 \rightarrow 150 RPM)

The lag moment response for these transition times is shown in Figure 5.21. The peak amplitude variation is shown in 5.22. In order to choose the ideal transition time, we need to look at the rotor torque response. The torque behavior is shown in Figure 5.23. It can be

seen that below 14 seconds transition time the torques enter the reverse torque region. The torque just touches the zero line for 14 s case, Figure 5.24. Hence, only a 3.5% reduction in peak amplitude from the baseline can be achieved for lag moment as seen in Figure 5.22. Therefore, obtaining a significant decrease in lag moment peak amplitude by reducing the transition time seems unlikely for the high-to-low rotor speed change scenario.

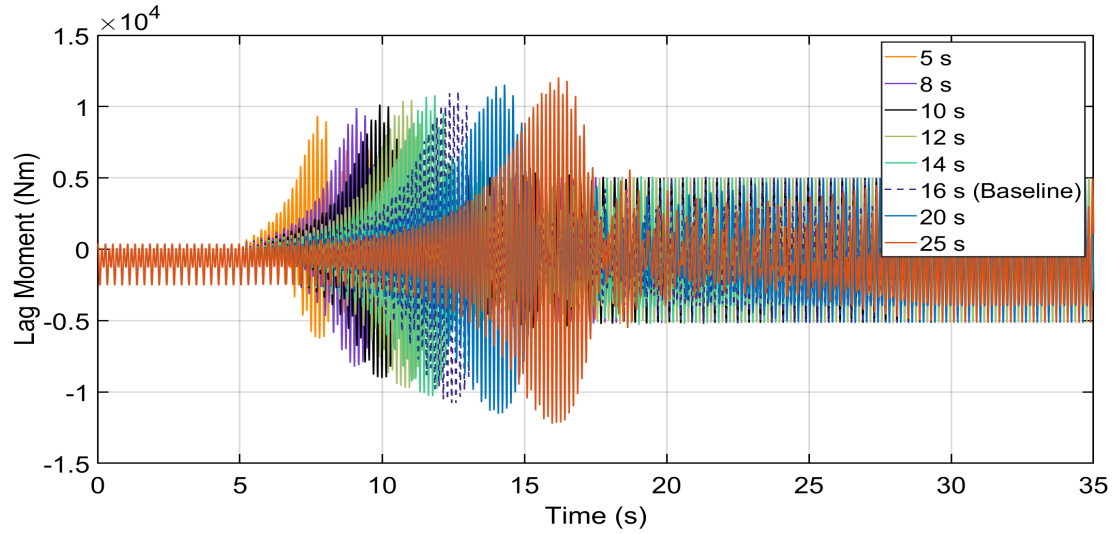


Figure 5.21: Time history of lag moment at blade root ($\mu_N = 0.2$; 230 \rightarrow 150 RPM)

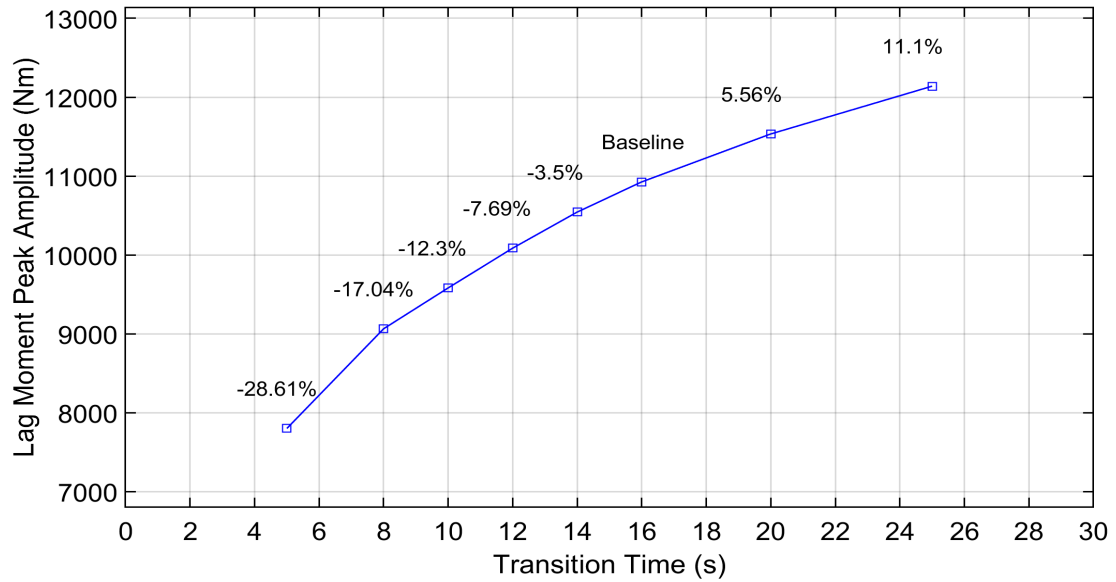


Figure 5.22: Lag moment's peak amplitude variation with transition time ($\mu_N = 0.2$; 230 \rightarrow 150 RPM)

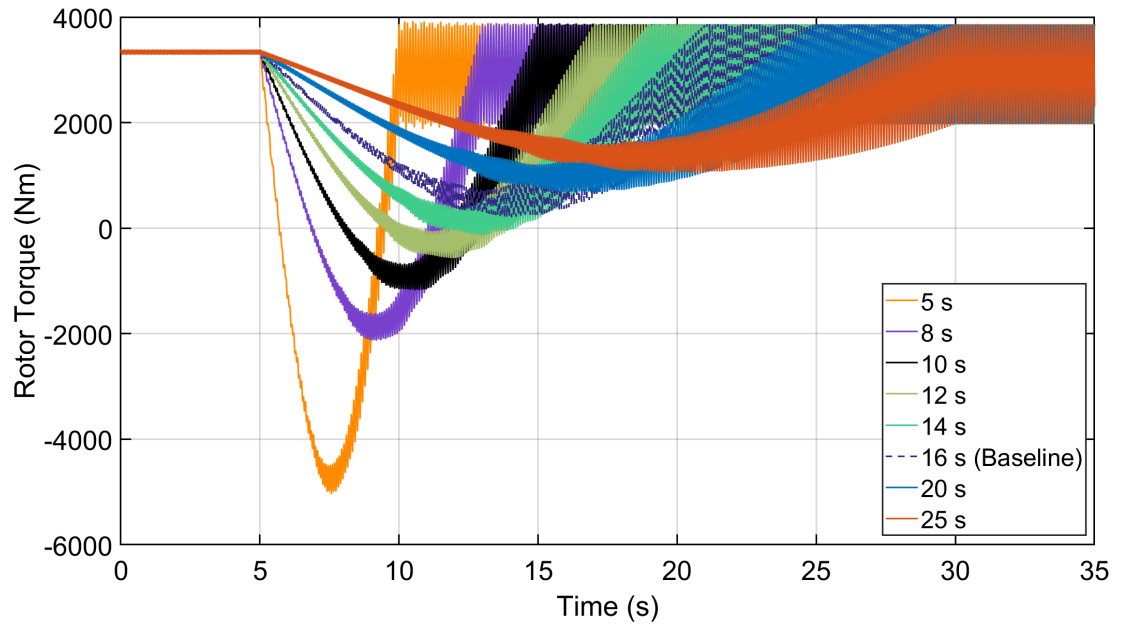


Figure 5.23: Time history of rotor torque ($\mu_N = 0.2$; $230 \rightarrow 150$ RPM)

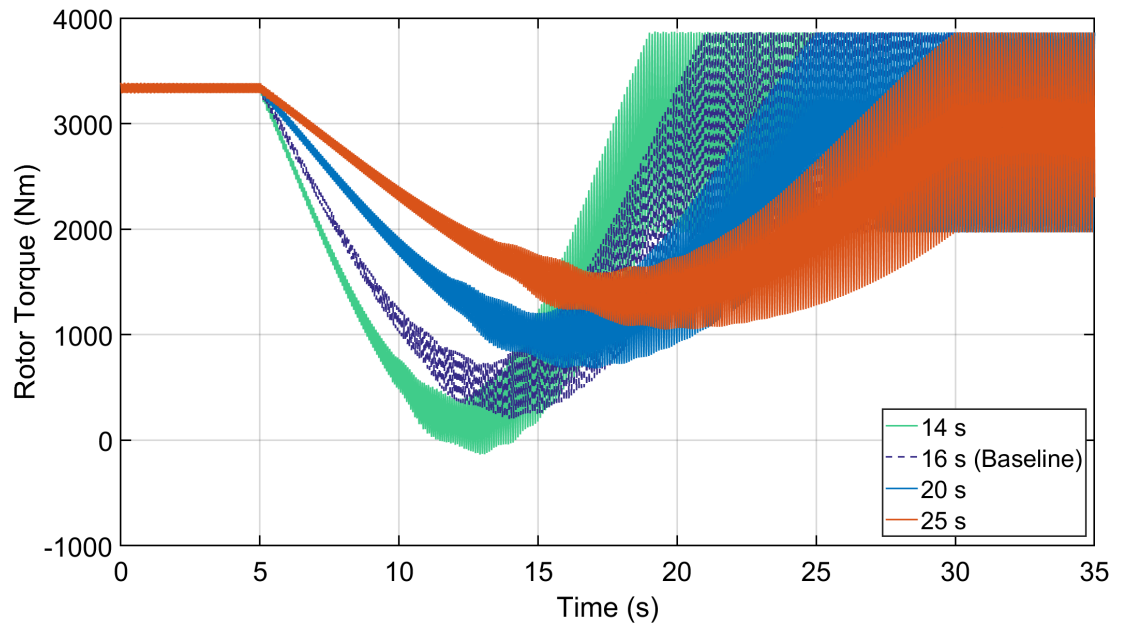


Figure 5.24: Time history of rotor torque from and above 14 s transition time ($\mu_N = 0.2$; $230 \rightarrow 150$ RPM)

5.1.4 $\mu_N = 0.2$, 150 \rightarrow 230 RPM

The rotor speed and acceleration for the low-to-high speed transition at $\mu_N = 0.2$ are shown in Figures 5.25 and 5.26, respectively.

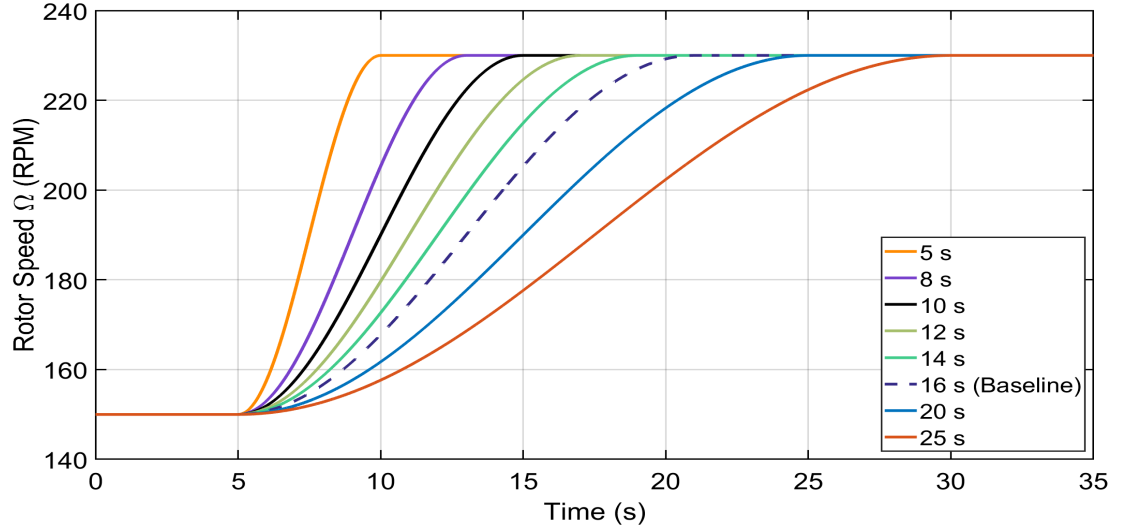


Figure 5.25: Rotor speed transition time cases ($\mu_N = 0.2$; 150 \rightarrow 230 RPM)

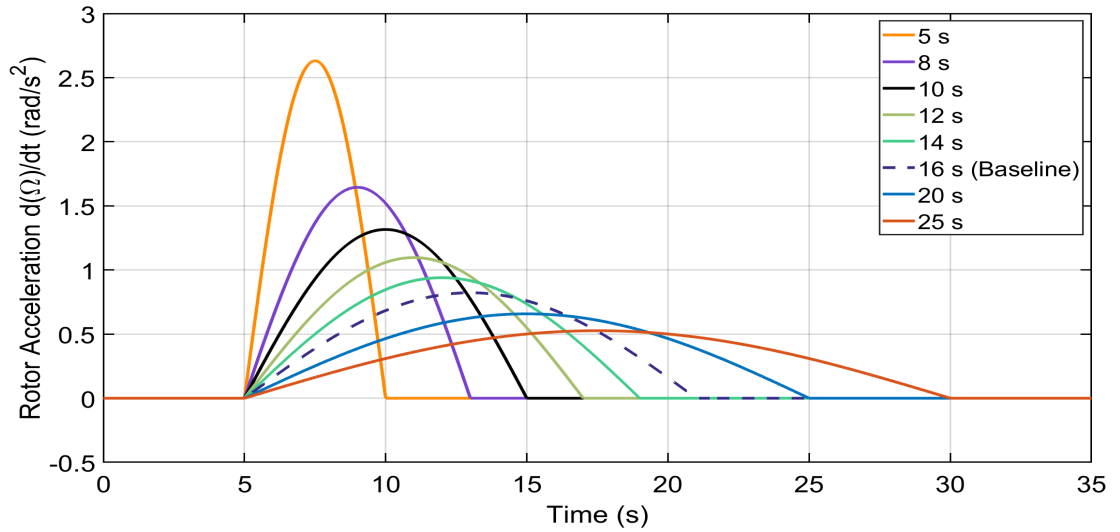


Figure 5.26: Rotor speed transition time cases ($\mu_N = 0.2$; 150 \rightarrow 230 RPM)

The lag moment responses are given in Figure 5.27. The variation of peak amplitude with transition time is shown in 5.28. The reduction in peak amplitude that can be achieved depends on whether the torque increase during transition is below the acceptable limit,

11000 Nm (1.1×10^4 Nm), or not. From Figure 5.29, it can be seen that the torque for 5 seconds transition is just below this limit. Reducing the transition time any further will increase the torque beyond the assumed limit. Therefore, almost 28% reduction in lag moment peak amplitude can be achieved, Figure 5.28, which is significantly higher compared to the 3.5% reduction in the previous case.

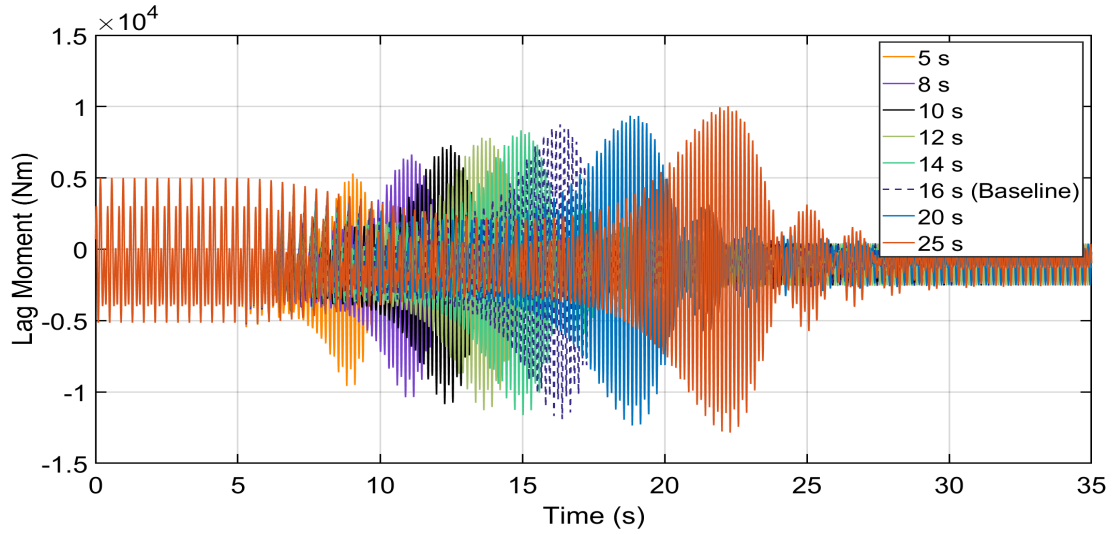


Figure 5.27: Time history of lag moment at blade root ($\mu_N = 0.2$; 150 \rightarrow 230 RPM)

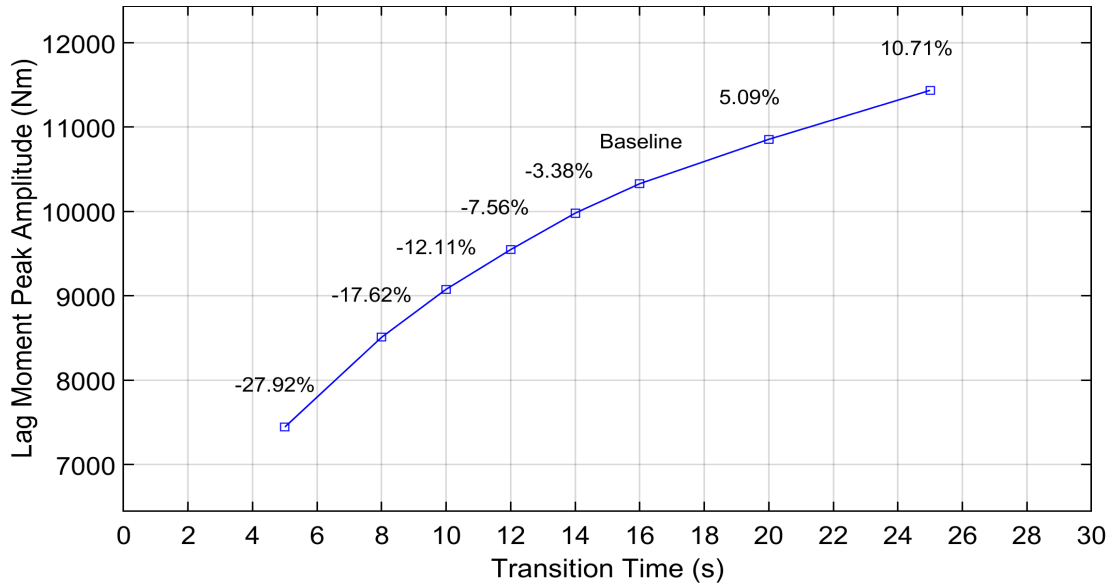


Figure 5.28: Lag moment's peak amplitude variation with transition time ($\mu_N = 0.2$; 150 \rightarrow 230 RPM)

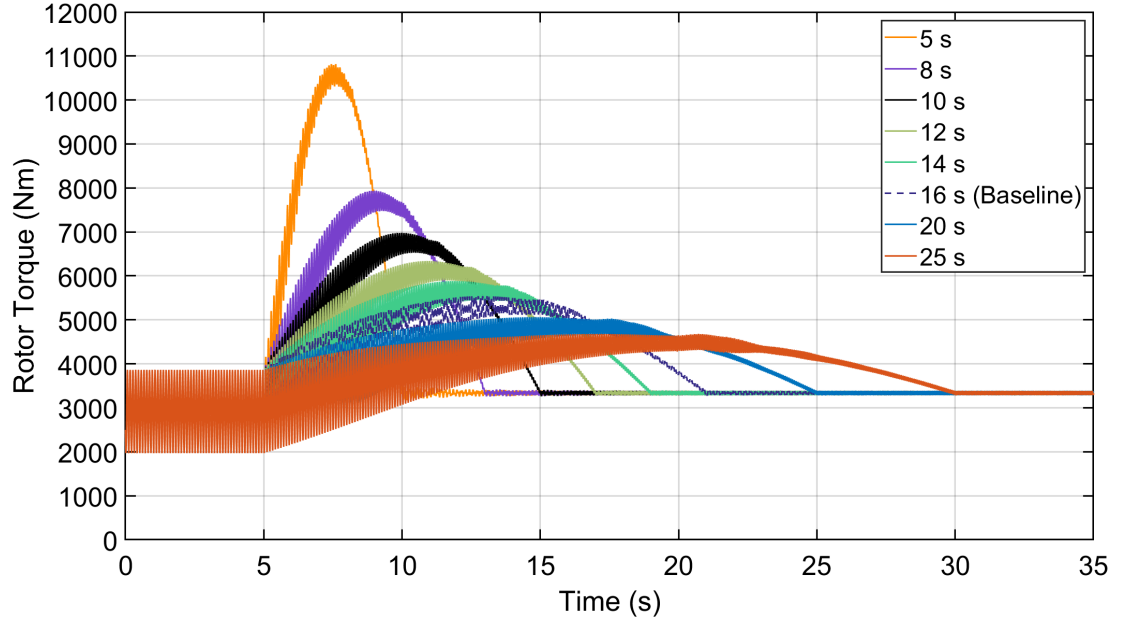


Figure 5.29: Time history of rotor torque ($\mu_N = 0.2$; $150 \rightarrow 230$ RPM)

5.1.5 $\mu_N = 0.1$, $230 \rightarrow 130$ RPM

The rotor speed and acceleration curves for high-to-low speed transition at $\mu_N = 0.1$ are shown in Figures 5.30 and 5.31, respectively. The baseline transition time is at 20 seconds. One might have noticed that 13 seconds transition time case has been inserted into our existing cases, the reason for which will become obvious in the later portion of this section.

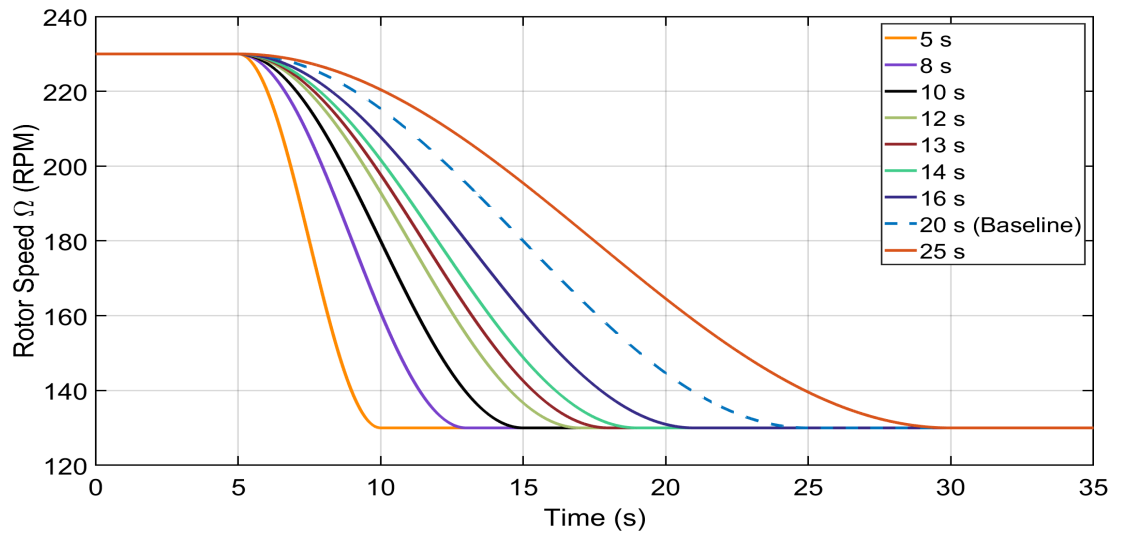


Figure 5.30: Rotor speed transition time cases ($\mu_N = 0.1$; $230 \rightarrow 130$ RPM)

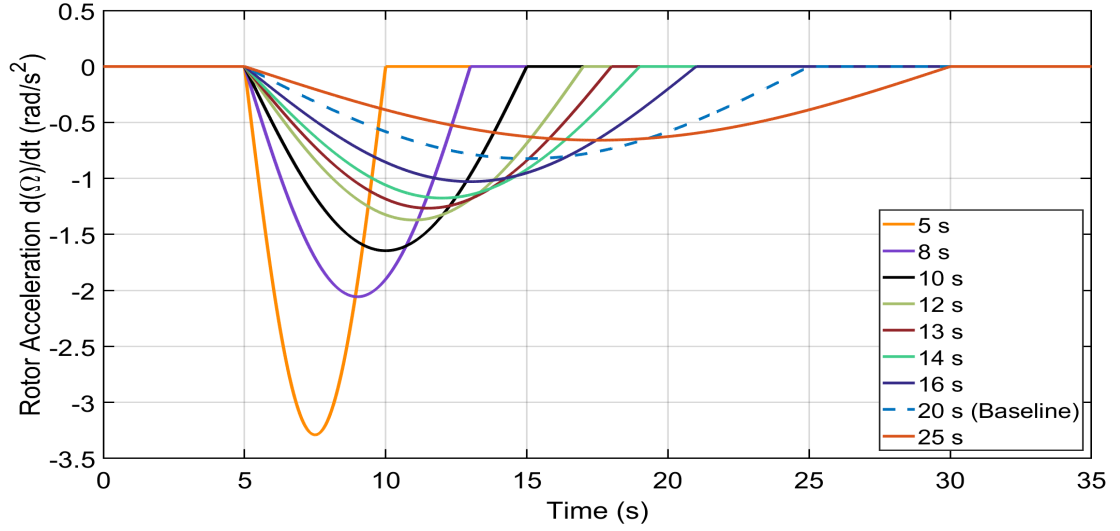


Figure 5.31: Rotor speed transition time cases ($\mu_N = 0.1$; $230 \rightarrow 130$ RPM)

The lag moment responses are shown in Figure 5.32. This transition has two resonance crossings, one at $2/\text{rev}$ and the other at $3/\text{rev}$. The $3/\text{rev}$ resonance has significantly higher amplitude than the $2/\text{rev}$ resonance. Hence, reducing the $3/\text{rev}$ resonance amplitude is of greater importance. Reducing the $3/\text{rev}$ crossing amplitude also reduces the $2/\text{rev}$ crossing amplitude as seen in Figure 5.32. The variation of $3/\text{rev}$ peak amplitude with transition time is shown in 5.33.

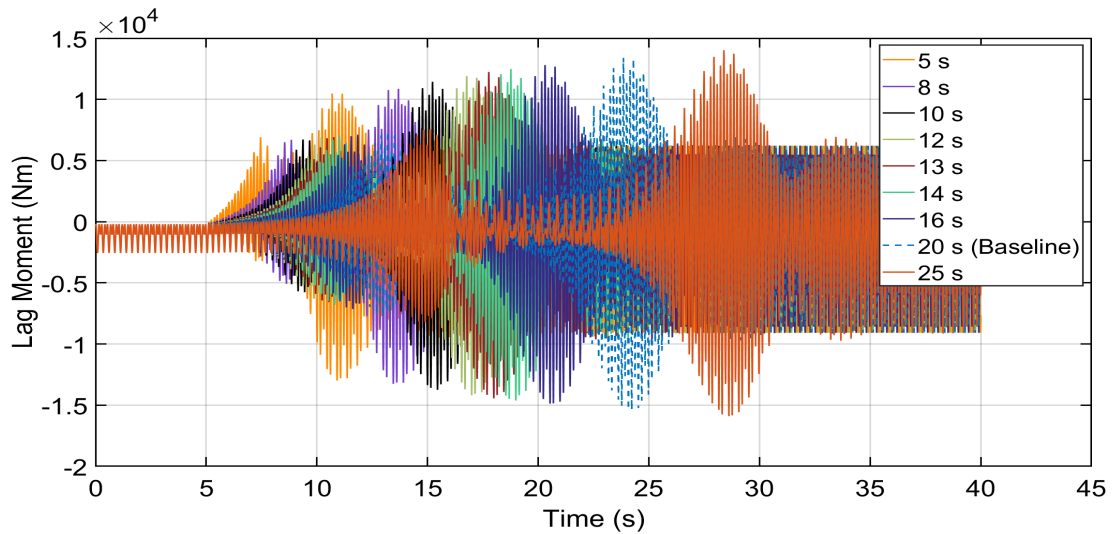


Figure 5.32: Time history of lag moment at blade root ($\mu_N = 0.1$; $230 \rightarrow 130$ RPM)

The torque behavior is shown in Figure 5.34. It can be seen that below 13 seconds

transition time the torques enter the negative region. The torque is just above the zero line for 13 s case, Figure 5.35. Hence, a 7.3% reduction in peak amplitude from the baseline can be achieved for lag moment, Figure 5.33.

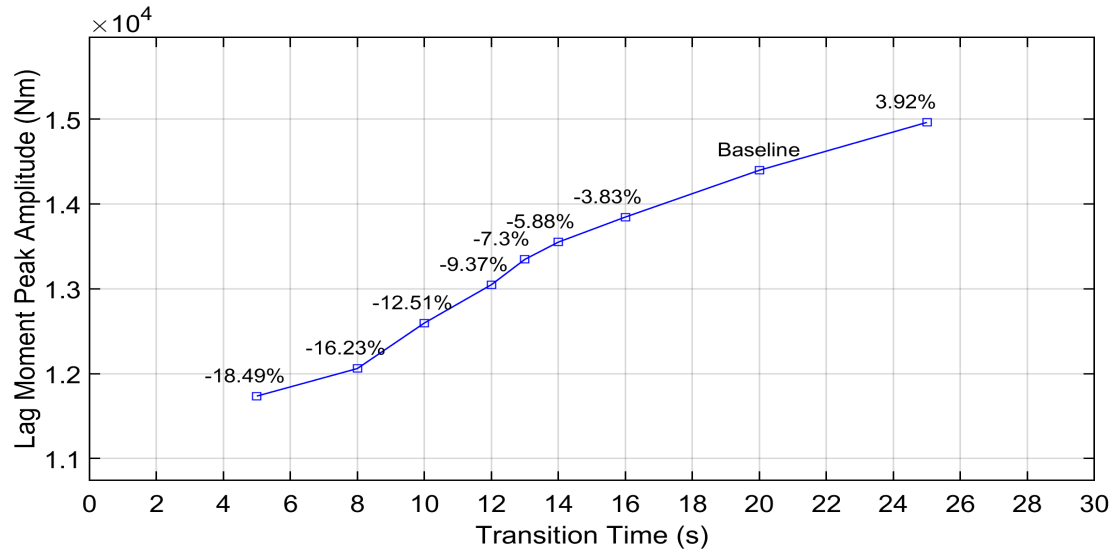


Figure 5.33: Lag moment's peak amplitude at 3/rev resonance ($\mu_N = 0.1$; 230 \rightarrow 130 RPM)

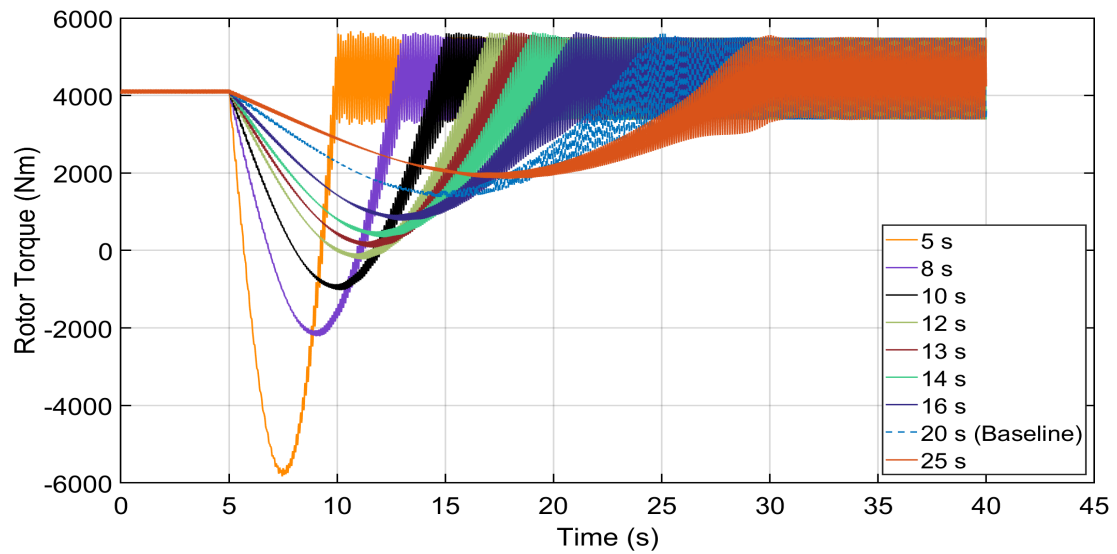


Figure 5.34: Time history of rotor torque ($\mu_N = 0.1$; 230 \rightarrow 130 RPM)

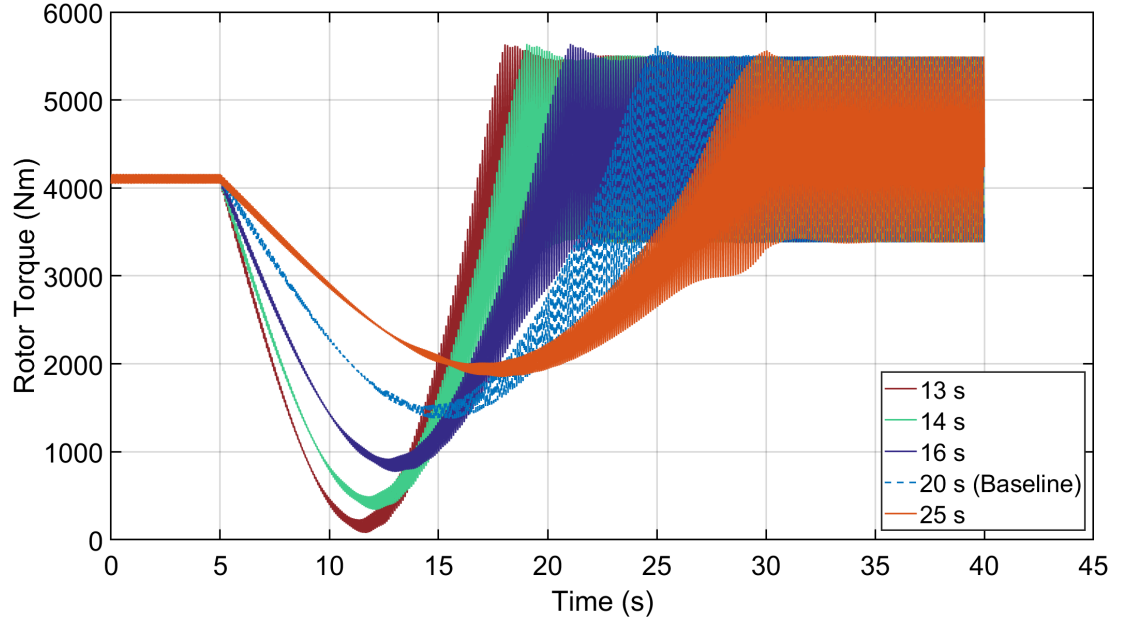


Figure 5.35: Time history of rotor torque from and above 13 s transition time ($\mu_N = 0.1$; 230 \rightarrow 130 RPM)

5.1.6 $\mu_N = 0.1$, 130 \rightarrow 230 RPM

The rotor speed curves for low-to-high speed transition are shown in Figure 5.36 and acceleration curves are shown in Figure 5.37.

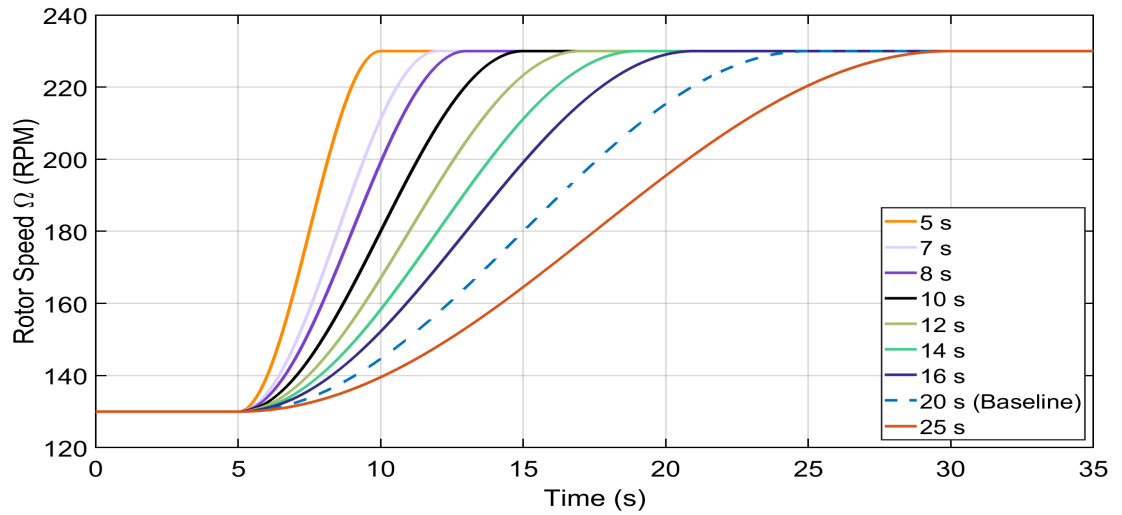


Figure 5.36: Rotor speed transition time cases ($\mu_N = 0.1$; 230 \rightarrow 130 RPM)

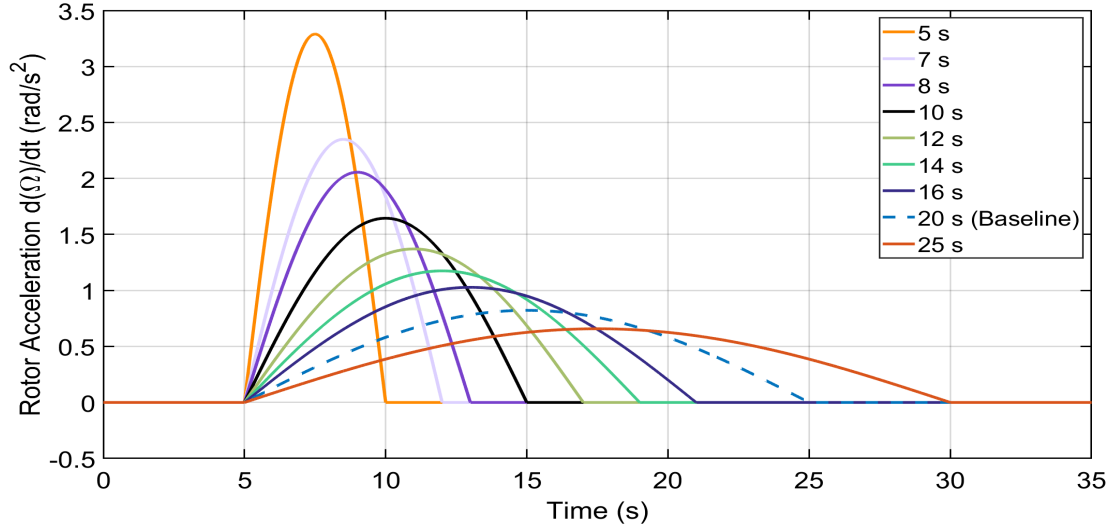


Figure 5.37: Rotor speed transition time cases ($\mu_N = 0.1$; $230 \rightarrow 130$ RPM)

The lag moment responses and the corresponding 3/rev peak amplitudes are given in Figures 5.38 and 5.39, respectively. The first resonance corresponds to 3/rev crossing as the rotor goes from lower-to-higher speed. The rotor torque for these transitions is given in Figure 5.40. The torque for the 7 seconds transition is just below the maximum assumed limit. Reducing the transition time any further increases the torque beyond 1.1×10^4 Nm. Therefore, 20.73% reduction in lag moment peak amplitude can be achieved for 7 s transition according to Figure 5.39.

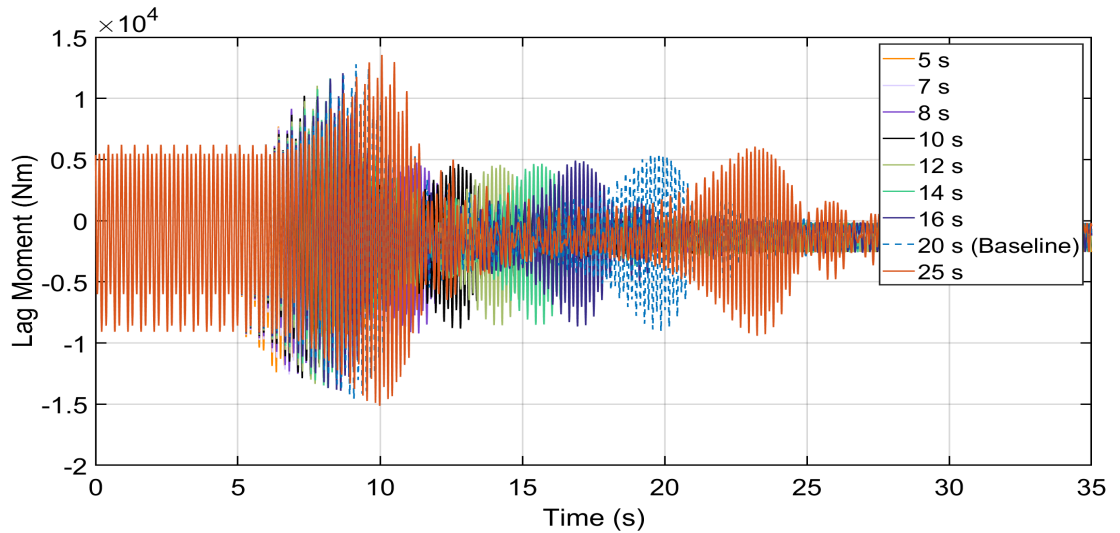


Figure 5.38: Time history of lag moment at blade root ($\mu_N = 0.1$; $130 \rightarrow 230$ RPM)

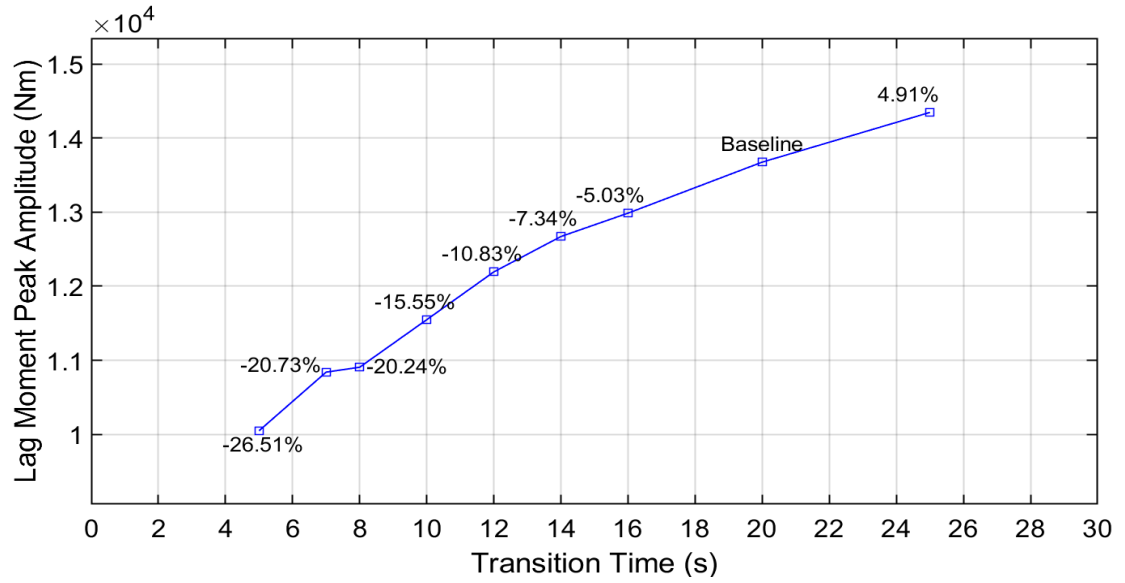


Figure 5.39: Lag moment's peak amplitude variation with transition time ($\mu_N = 0.1$; 130 \rightarrow 230 RPM)

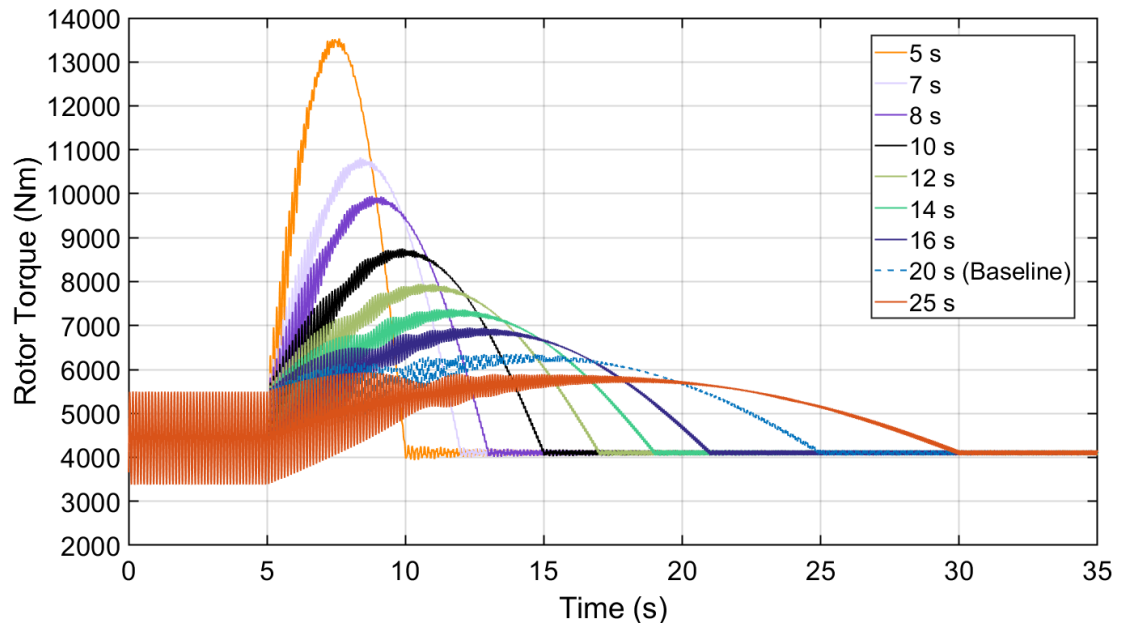


Figure 5.40: Time history of rotor torque ($\mu_N = 0.1$; 130 \rightarrow 230 RPM)

5.1.7 Transition Time: Summary

The results of the transition time impact on resonances are given in Tables 5.1 and 5.2.

Table 5.1: Transition time impact on high-to-low speed transition.

μ_N	Transition (RPM)	Ideal transition time (s)	Lag moment peak amplitude reduction
0.3	230 \rightarrow 180	8	5.55%
0.2	230 \rightarrow 150	14	3.50%
0.1	230 \rightarrow 130 (Second Resonance)	13	7.30%

Table 5.2: Transition time impact on low-to-high speed transition.

μ_N	Transition (RPM)	Ideal transition time (s)	Lag moment peak amplitude reduction
0.3	180 \rightarrow 230	4	21.50%
0.2	150 \rightarrow 230	5	27.92%
0.1	130 \rightarrow 230 (First Resonance)	7	20.73%

5.2 Structural Damping Impact

The rotor loads are affected by the amount of damping. Hence, another parameter that can be varied is the structural damping of the blade. It was shown theoretically that up to $\sim 7\%$ lag damping can be attained by embedding carbon nanotubes (CNTs) into composite blades that are stiff in-plane [161]. The current lag damping of our blade is at 1%. It is increased to 3%, 5% and 7% to study the impact on resonance loads. The corresponding baseline transition time is used for each μ_N case.

5.2.1 $\mu_N = 0.3, 230 \rightarrow 180$ RPM

The baseline transition time for $\mu_N = 0.3$ is 10 s as shown in Figures 4.22 and 4.36. The lag moment response as a function of structural damping is shown in Figure 5.41. It can be seen that increasing the damping ratio, ζ , from 1% to 3% has a significant impact on the resonance amplitude. Peak amplitude as a function of ζ is shown in Figure 5.42. The peak amplitude drops by 47.5% from the baseline for $\zeta = 3\%$. On further increase in damping, the peak amplitude drops by 65% and 73% for $\zeta = 5\%$ and $\zeta = 7\%$, respectively. It can be seen that the difference in drop percentage reduces as ζ increases. The amplitude difference between 3% and 5% ζ is 17.3% and between 5% and 7% ζ is only 8%.

The rotor torque response is compared in Figure 5.43, As the damping increases, the additional vibration that arises due to resonance almost disappears. The response is already smooth at $\zeta = 3\%$. Beyond 3%, the amplitude of oscillations decrease further the valley region.

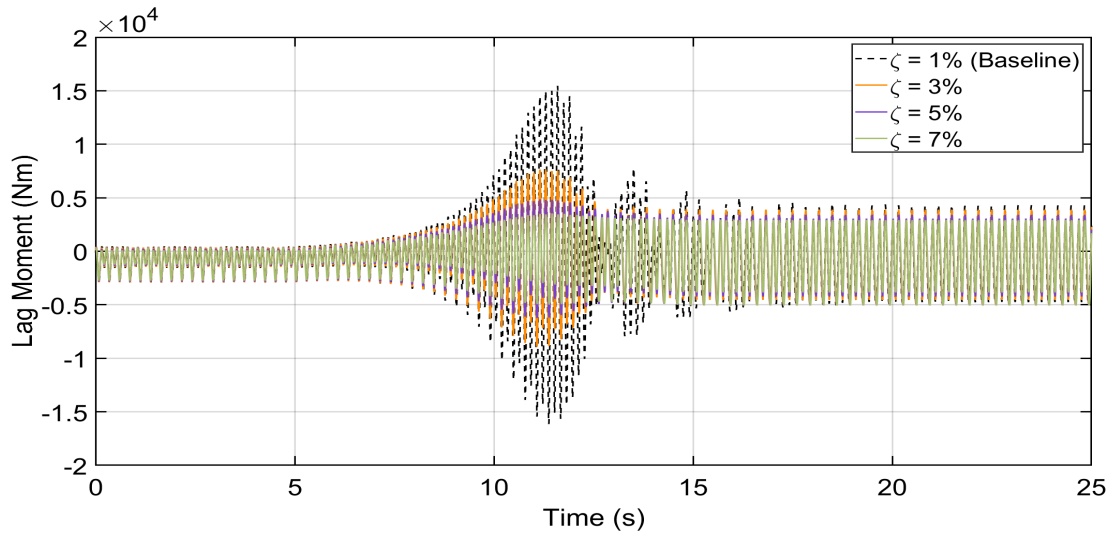


Figure 5.41: Effect of structural damping on lag moment ($\mu_N = 0.3; 230 \rightarrow 180$ RPM)

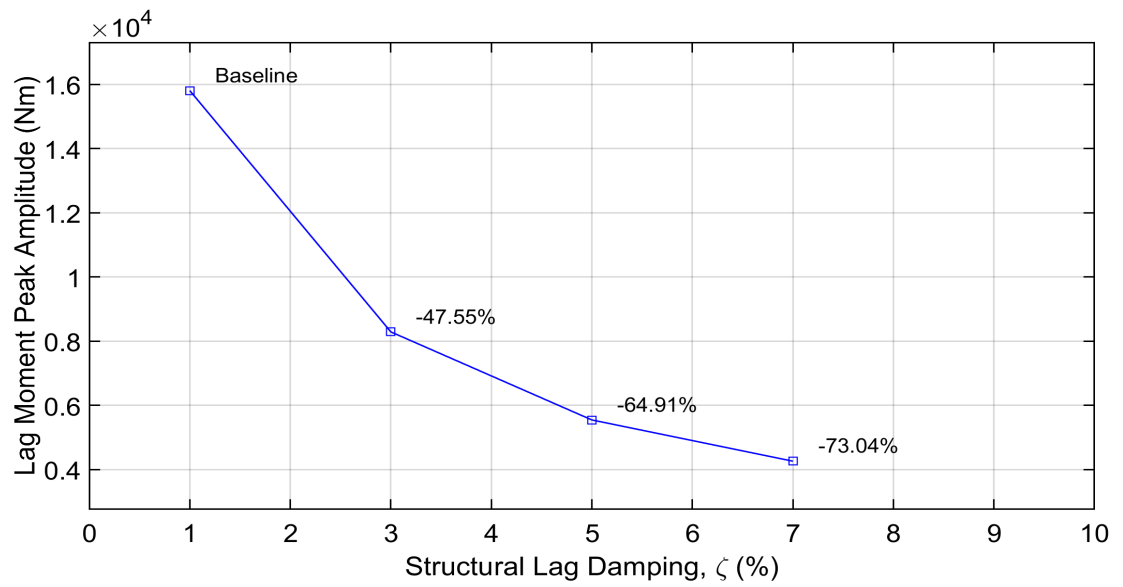


Figure 5.42: Structural damping impact on lag moment peak amplitude ($\mu_N = 0.3$; 230 \rightarrow 180 RPM)

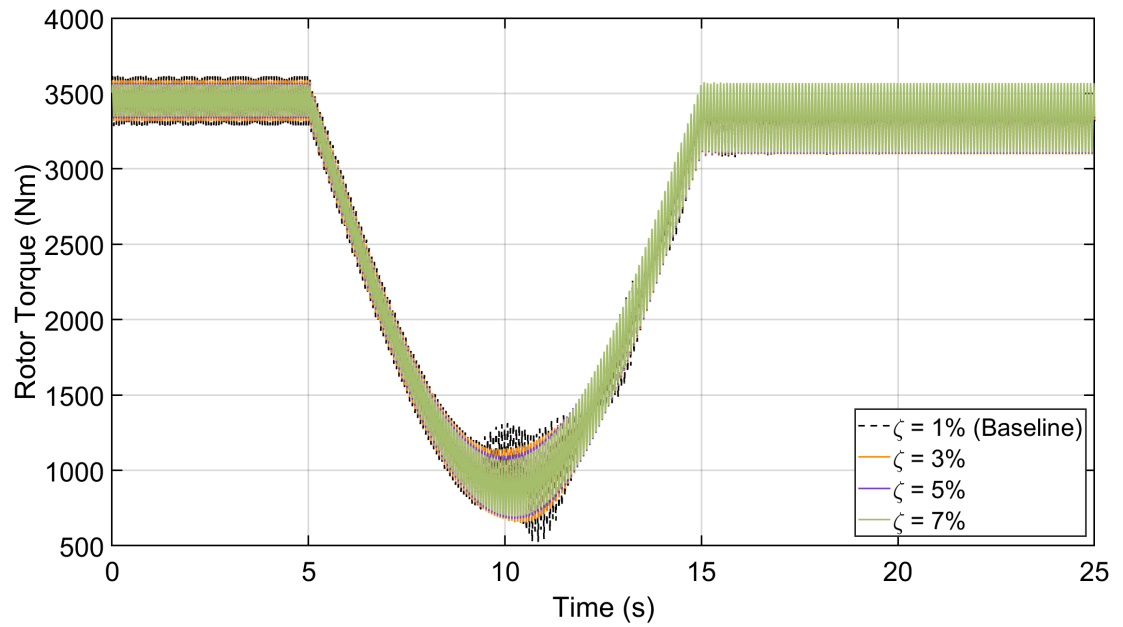


Figure 5.43: Effect of structural damping on rotor torque ($\mu_N = 0.3$; 230 \rightarrow 180 RPM)

5.2.2 $\mu_N = 0.3, 180 \rightarrow 230$ RPM

The lag moment response for the low-to-high speed transition is shown in Figure 5.44. The decrease in peak amplitude shows a similar trend as the previous case. The peak amplitude reduces by 44% at $\zeta = 3\%$ and by 70% at $\zeta = 7\%$, shown in Figure 5.45.

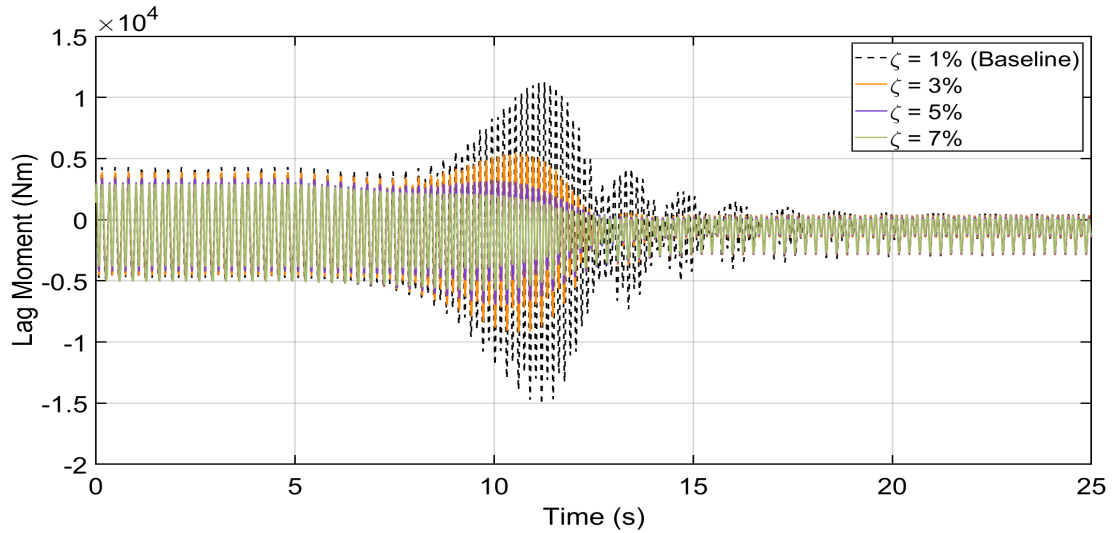


Figure 5.44: Effect of structural damping on lag moment ($\mu_N = 0.3; 180 \rightarrow 230$ RPM)

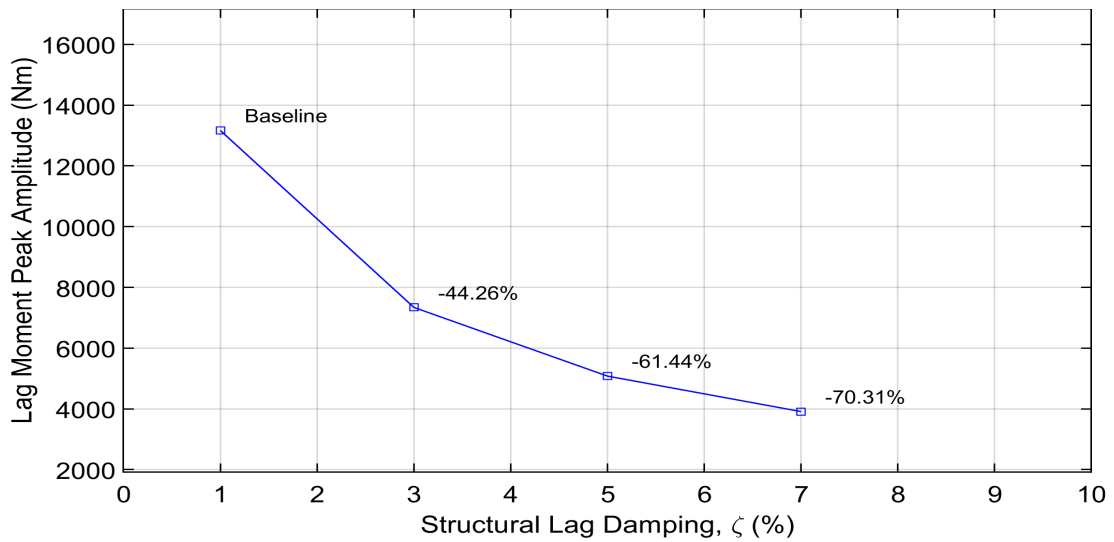


Figure 5.45: Structural damping impact on lag moment peak amplitude ($\mu_N = 0.3; 180 \rightarrow 230$ RPM)

The rotor torque is shown in Figure 5.46. The amplitude increase due to resonance almost disappears. The peak value of rotor torque shows only a small change from the

baseline value due to damping increase, Figure 5.47.

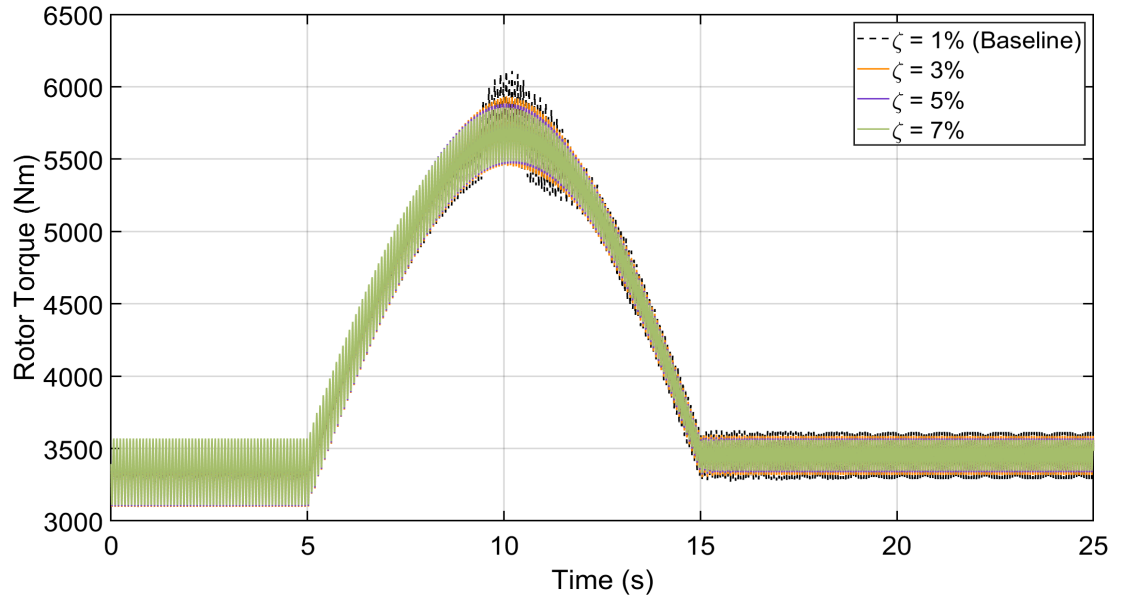


Figure 5.46: Effect of structural damping on rotor torque ($\mu_N = 0.3$; $180 \rightarrow 230$ RPM)

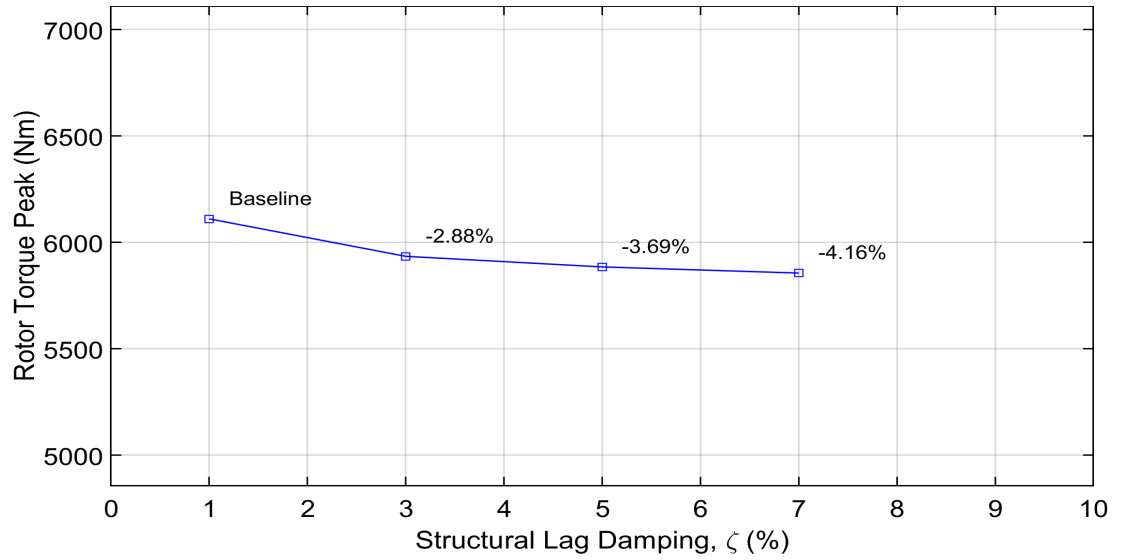


Figure 5.47: Rotor torque peak value ($\mu_N = 0.3$; $180 \rightarrow 230$ RPM)

5.2.3 $\mu_N = 0.2$, $230 \rightarrow 150$ RPM

Baseline transition time for this μ_N case is 16 s. The lag moment response for the high-to-low speed transition is shown in Figure 5.48. The peak amplitude reduction due to increase

of damping is shown in Figure 5.49. The amplitude decrease from $\zeta = 1\%$ to $\zeta = 7\%$ follows a trend similar to $\mu_N = 0.3$ case, Figure 5.42. The drop percentages in both the high-to-low speed transition is matching very closely. The rotor torque response is shown in Figure 5.50. The torque amplitudes do not change significantly with damping.

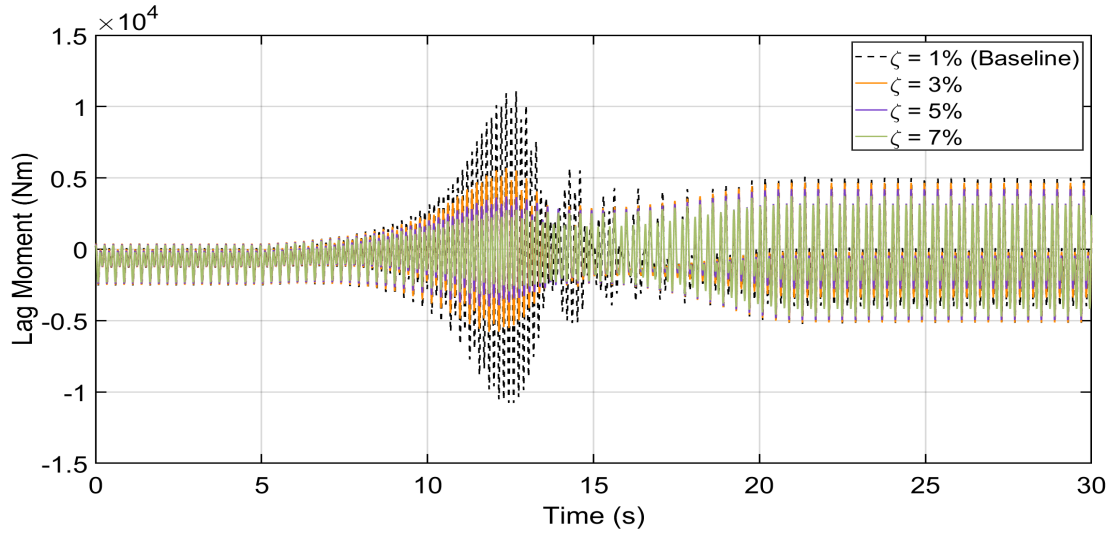


Figure 5.48: Effect of structural damping on lag moment ($\mu_N = 0.2$; 230 \rightarrow 150 RPM)

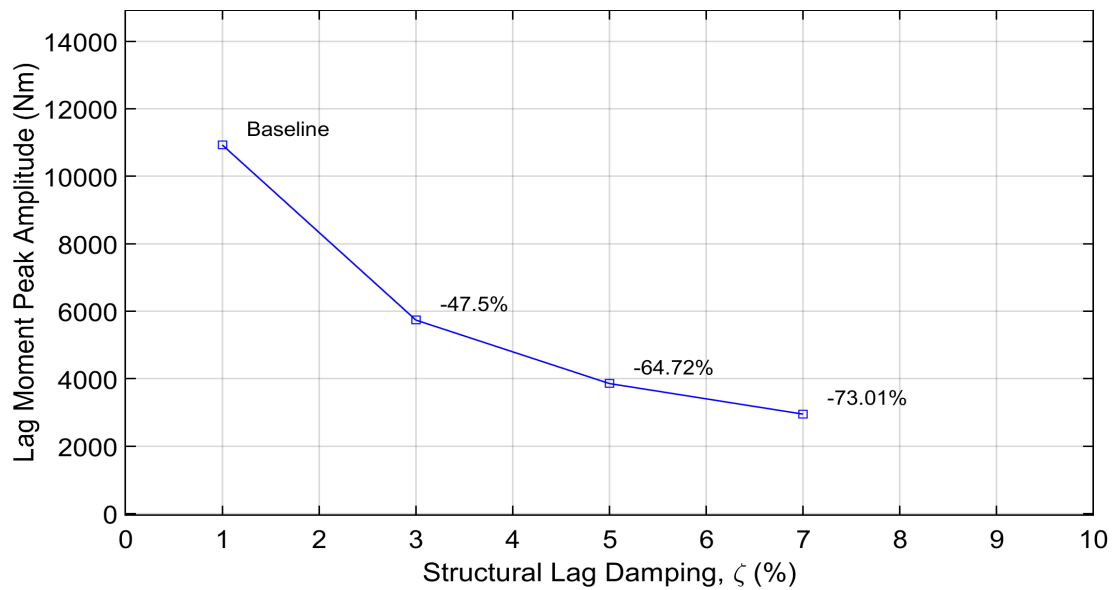


Figure 5.49: Structural damping impact on lag moment peak amplitude ($\mu_N = 0.2$; 230 \rightarrow 150 RPM)

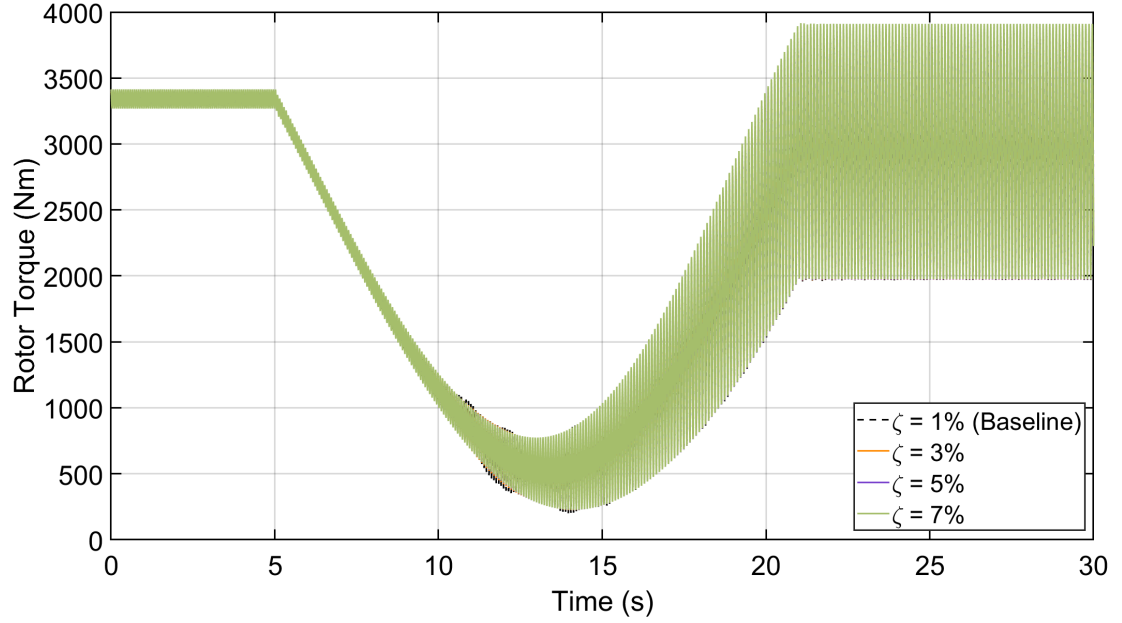


Figure 5.50: Effect of structural damping on rotor torque ($\mu_N = 0.2$; 230 \rightarrow 150 RPM)

5.2.4 $\mu_N = 0.2$, 150 \rightarrow 230 RPM

The lag moment response for the low-to-high speed transition is shown in Figure 5.51. The amplitude reduction due to damping increase is shown in Figure 5.52.

The amplitude decrease shows a very close trend to the previous case, Figure 5.49. The rotor torque response is shown in Figure 5.50.

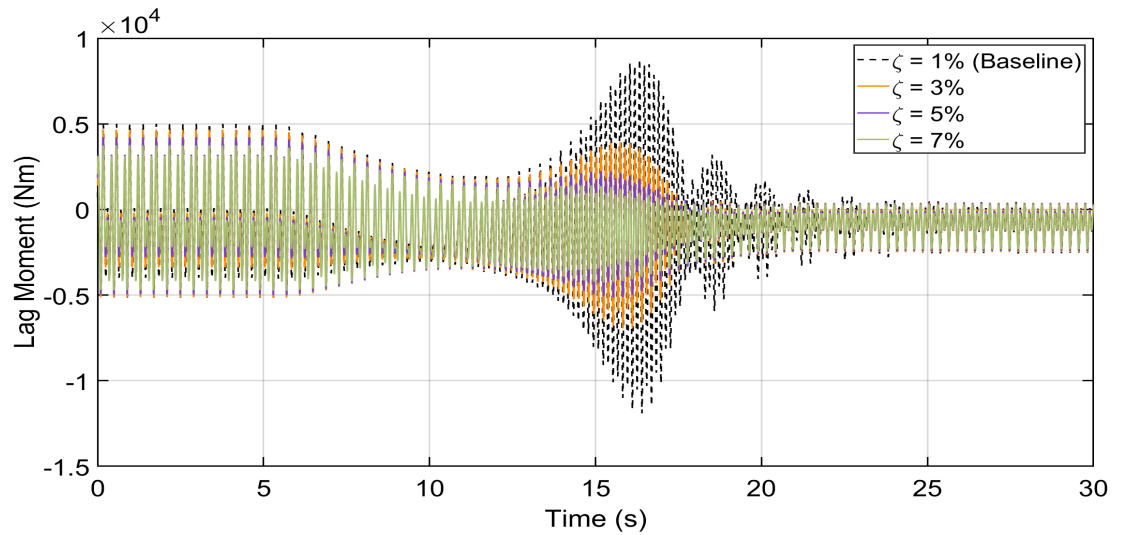


Figure 5.51: Effect of structural damping on lag moment ($\mu_N = 0.2$; 150 \rightarrow 230 RPM)

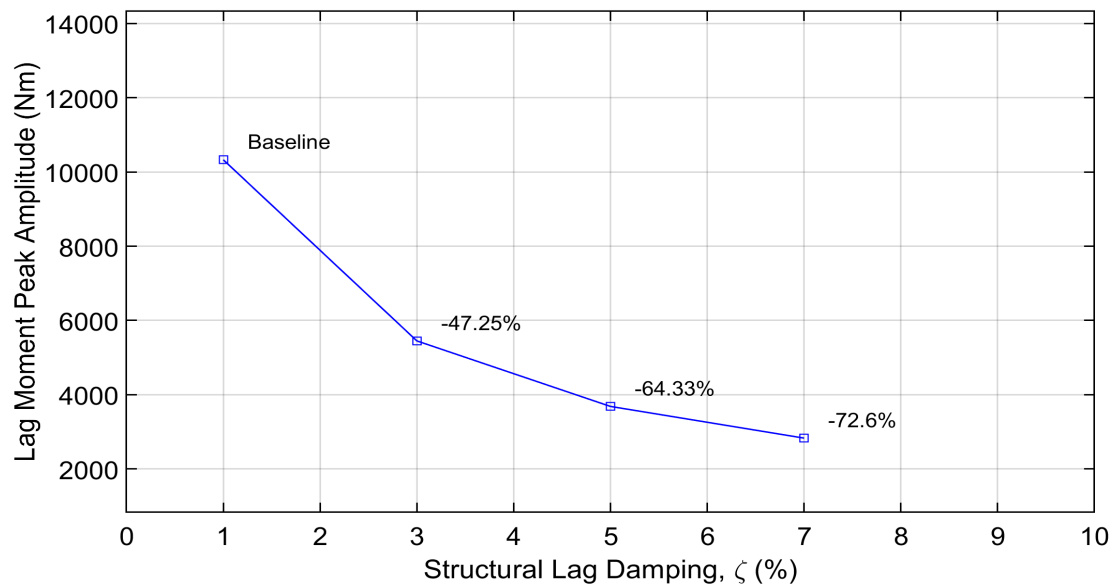


Figure 5.52: Structural damping impact on lag moment peak amplitude ($\mu_N = 0.2$; 150 \rightarrow 230 RPM)

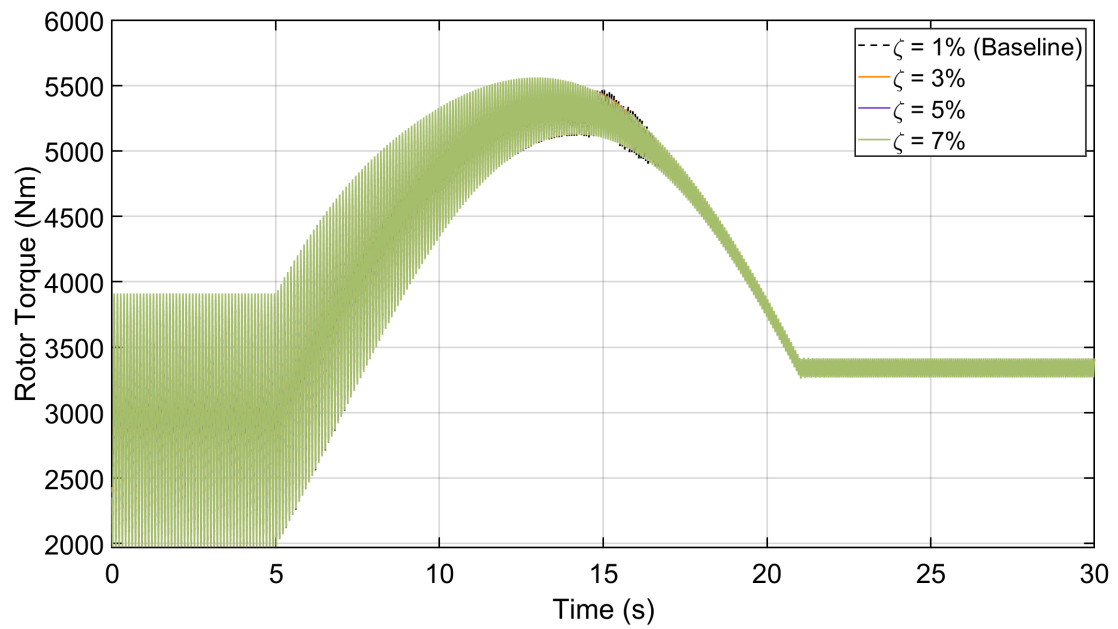


Figure 5.53: Effect of structural damping on rotor torque ($\mu_N = 0.2$; 230 \rightarrow 150 RPM)

5.2.5 $\mu_N = 0.1, 230 \rightarrow 130$ RPM

Baseline transition time for $\mu_N = 0.1$ case is 20 s. The lag moment for the high-to-low speed transition is shown in Figure 5.54. Since there are two resonances, the amplitude reduction of the first resonance is shown in Figure 5.55 and the second resonance is shown in Figure 5.56. It can be seen that the amplitude decrease of the first and second resonances are proportional to each other. The rotor torque response is shown in Figure 5.57.

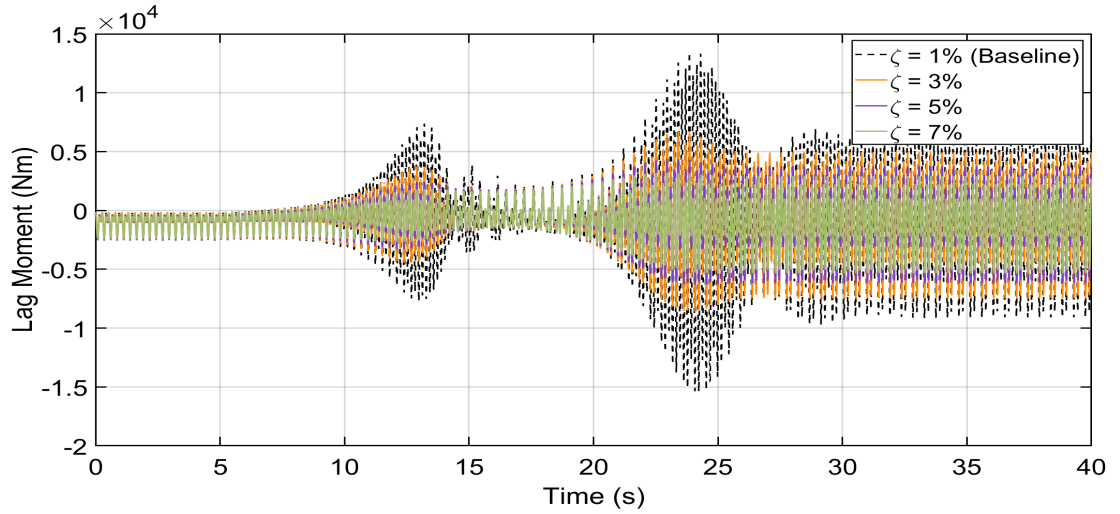


Figure 5.54: Effect of structural damping on lag moment ($\mu_N = 0.1$; 230 \rightarrow 130 RPM)

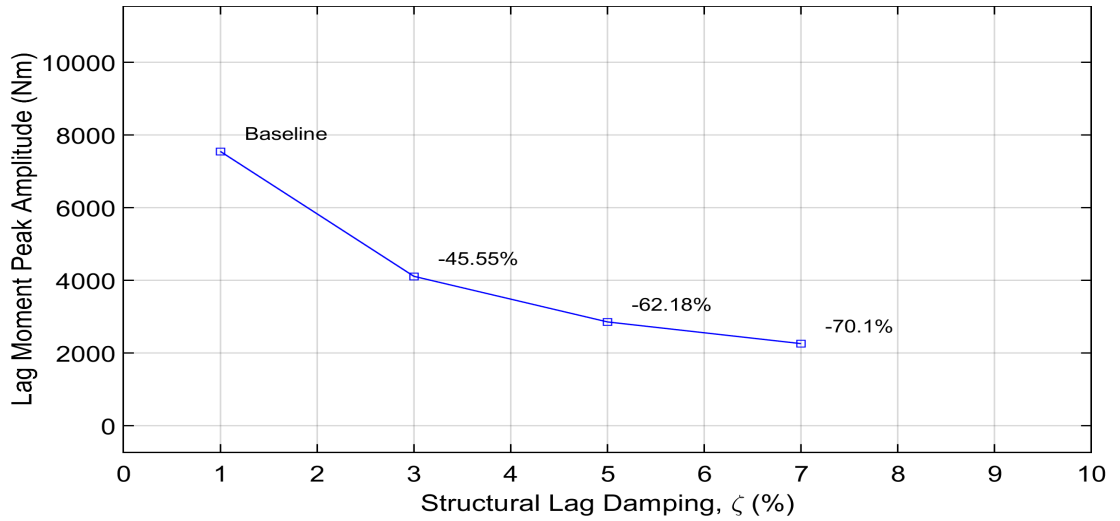


Figure 5.55: Structural damping impact on first resonance amplitude ($\mu_N = 0.1$; 230 \rightarrow 130 RPM)

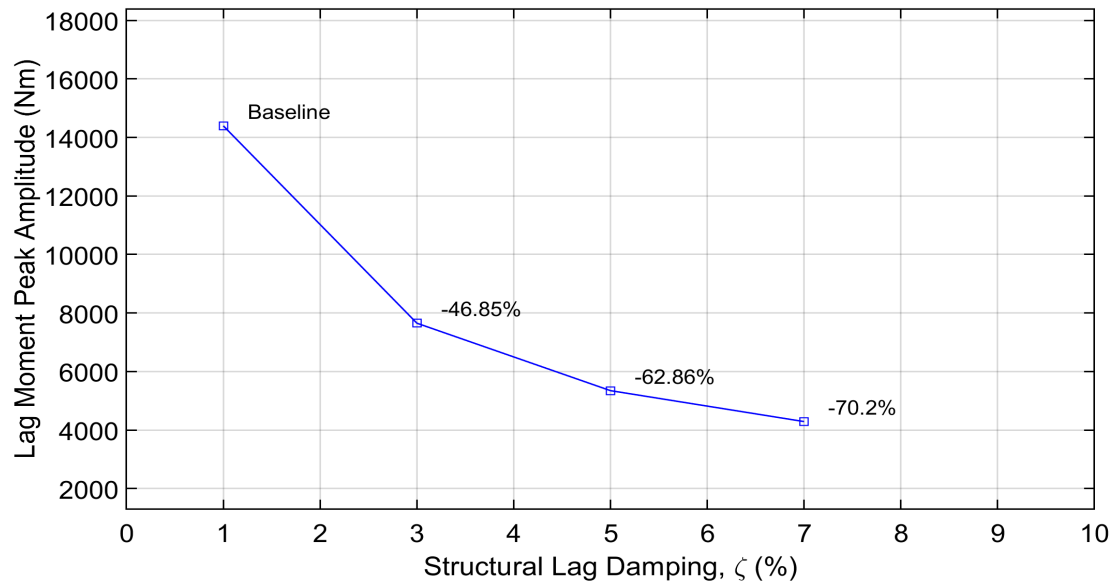


Figure 5.56: Structural damping impact on second resonance amplitude ($\mu_N = 0.1$; 230 \rightarrow 130 RPM)

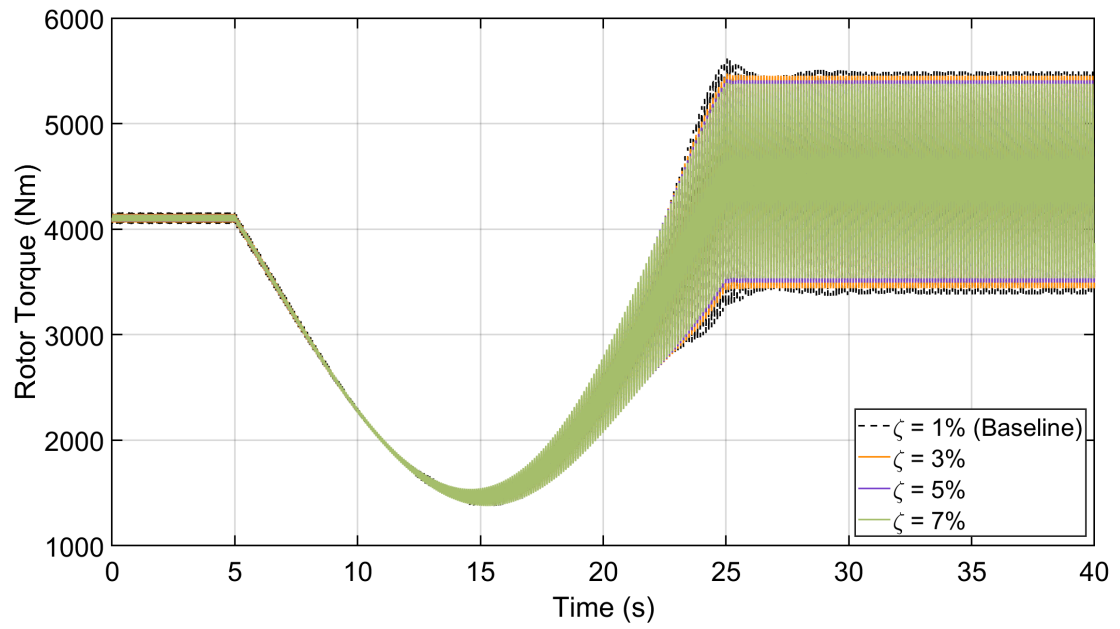


Figure 5.57: Effect of structural damping on rotor torque ($\mu_N = 0.2$; 230 \rightarrow 150 RPM)

5.2.6 $\mu_N = 0.1, 130 \rightarrow 230$ RPM

The lag moment response for the low-to-high speed transition is shown in Figure 5.58. The resonances switch places for this transition.

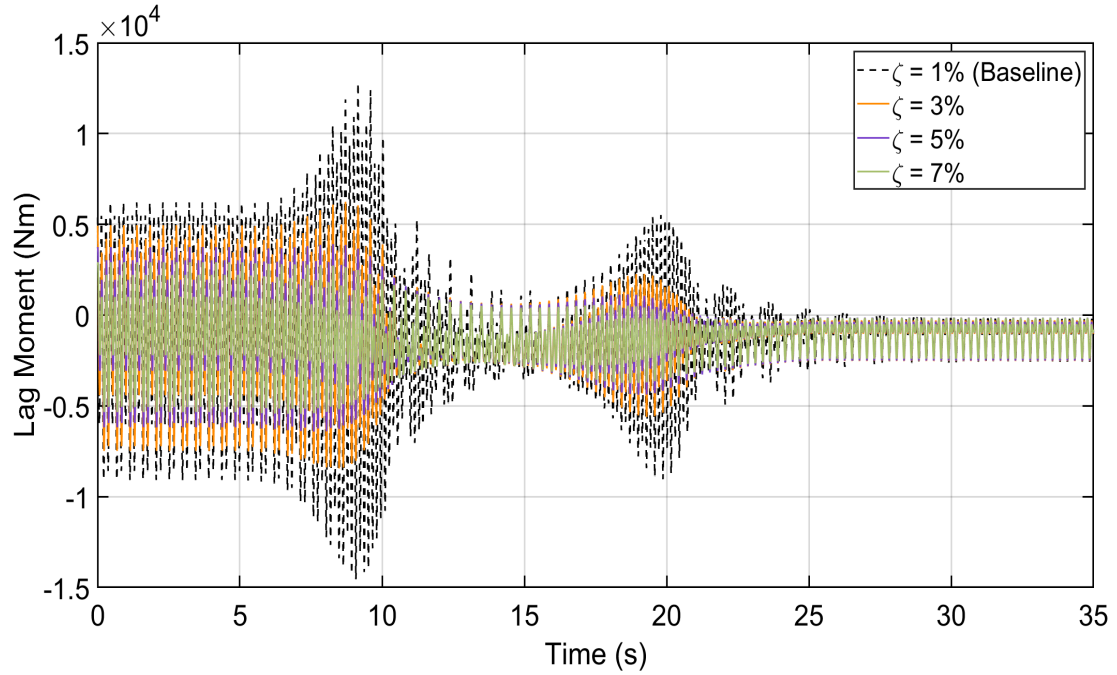


Figure 5.58: Effect of structural damping on lag moment ($\mu_N = 0.1$; $130 \rightarrow 230$ RPM)

The amplitude reduction of the first and second resonances are shown in Figures 5.59 and 5.60, respectively. It can be seen that the amplitude decrease trend is similar to the previous case. The rotor torque response is shown in Figure 5.61. The peak value of rotor torque during transition is hardly affected by lag damping as shown in Figure 5.62.

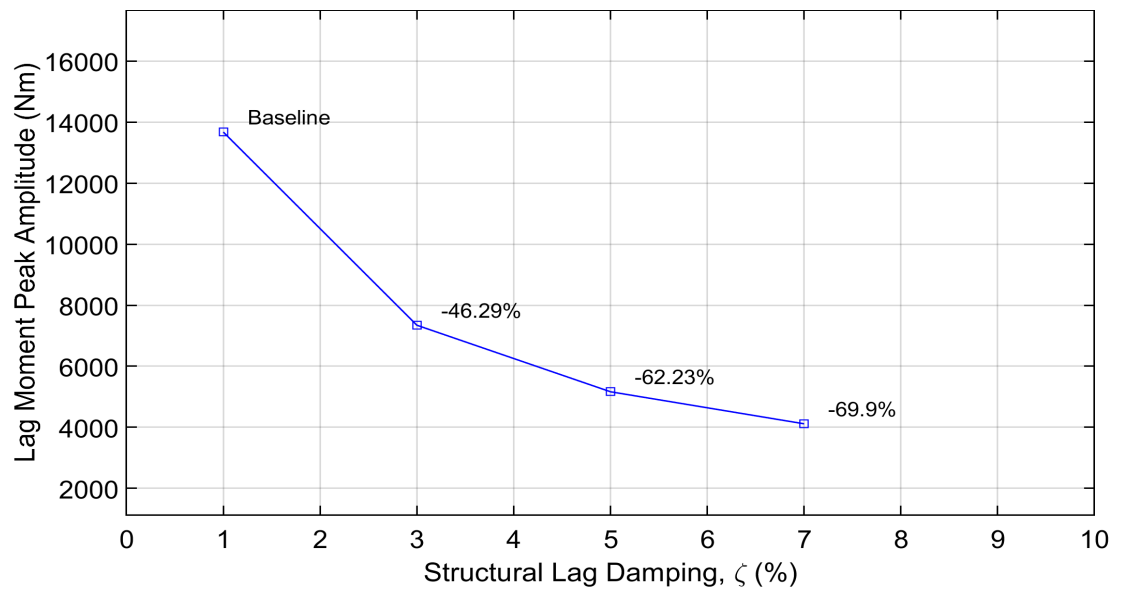


Figure 5.59: Structural damping impact on first resonance amplitude ($\mu_N = 0.1$; 130 \rightarrow 230 RPM)

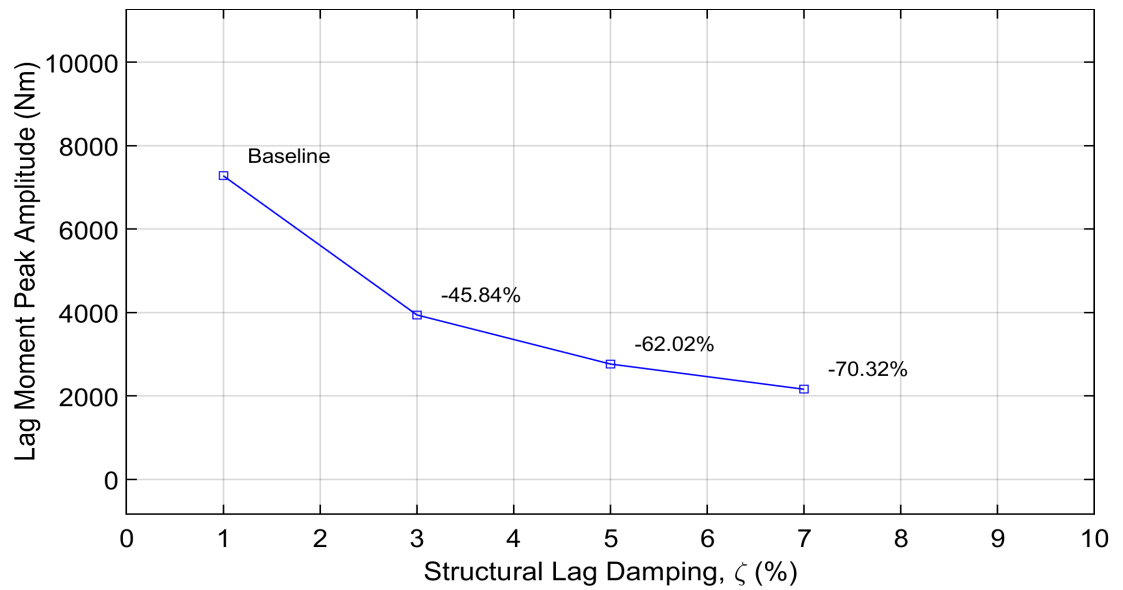


Figure 5.60: Structural damping impact on second resonance amplitude ($\mu_N = 0.1$; 130 \rightarrow 230 RPM)

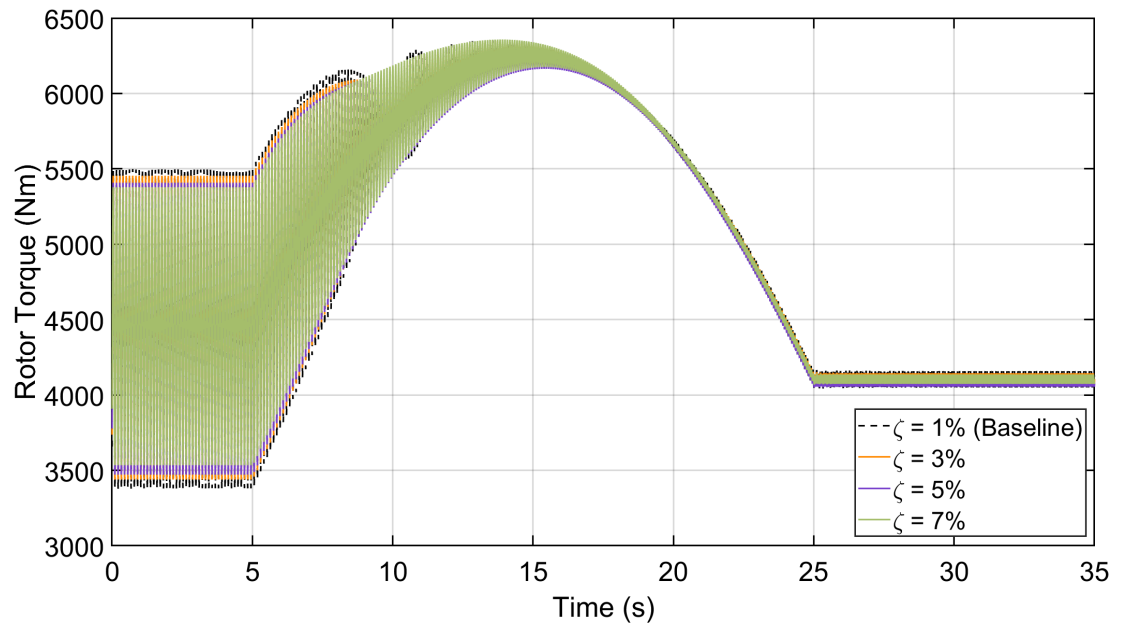


Figure 5.61: Effect of structural damping on rotor torque ($\mu_N = 0.1$; 130 \rightarrow 230 RPM)

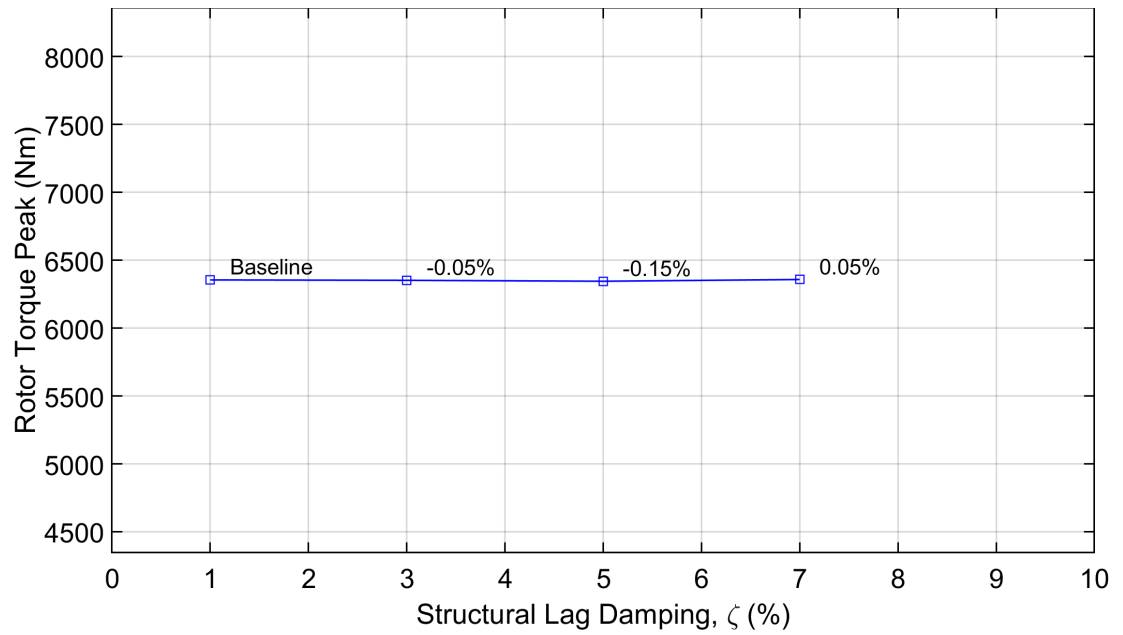


Figure 5.62: Rotor torque peak value ($\mu_N = 0.1$; 130 \rightarrow 230 RPM)

5.2.7 Structural Lag Damping (ζ): Summary

The results of the lag damping impact on resonances are given in Tables 5.3 and 5.4.

Table 5.3: ζ impact on high-to-low speed transition.

μ_N	Transition (RPM)	Lag moment amplitude reduction		
		$\zeta = 3\%$	$\zeta = 5\%$	$\zeta = 7\%$
0.3	230 \rightarrow 180	47.55%	64.91%	73.04%
0.2	230 \rightarrow 150	47.50%	64.72%	73.01%
0.1	230 \rightarrow 130 (Second Resonance)	46.85%	62.86%	70.20%

Table 5.4: ζ impact on low-to-high speed transition.

μ_N	Transition (RPM)	Lag moment amplitude reduction		
		$\zeta = 3\%$	$\zeta = 5\%$	$\zeta = 7\%$
0.3	180 \rightarrow 230	44.26%	61.44%	70.31%
0.2	150 \rightarrow 230	47.25%	64.33%	72.60%
0.1	130 \rightarrow 230 (First Resonance)	45.84%	62.02%	70.32%

5.3 Rotor Blade Stiffness Impact

In our transition studies, it was noticed that the higher frequency resonance crossings had no noticeable impact on the blade response, such as the second-flap crossing 5/rev or the first-torsion crossing 7/rev. Therefore, increasing the lag crossing from 2/rev to higher frequency crossings could reduce the resonance loads. This can be achieved by increasing the lag stiffness of the blade. In [162], Carter includes a composite spar at the blade root to increase the lag wise stiffness of a variable speed rotor blade. Here, we will only be increasing the stiffness property of our blade model without changing the mass. This makes

it easier to compare with the baseline rotor case. Two new stiffness cases will be analyzed, one that changes the 2/rev lag crossing to 3/rev crossing and the other from 2/rev to 4/rev crossing, for $\mu_N = 0.3$ case. The new lag stiffnesses are given in Table 5.5 and are named as Case 1 and Case 2. The fan plot for these two cases are shown in Figures 5.63 and 5.64. The other blade properties are unchanged. The upper bound of the stiffness was determined based on literature. The Mars helicopter [163] has a 4/rev lag crossing close to the rotor operating speed. This crossing was the highest found in literature. X2 and XH-59A have only 2/rev lag crossing close to the rotor operating speed [2].

Table 5.5: Lag stiffness for higher crossings ($\mu_N = 0.3$).

Lag crossing between 180 and 230 RPM	EI_{Lag} (Nm ²)
2/rev (Baseline)	1.864×10^6
3/rev (Case 1)	4.308×10^6
4/rev (Case 2)	7.735×10^6

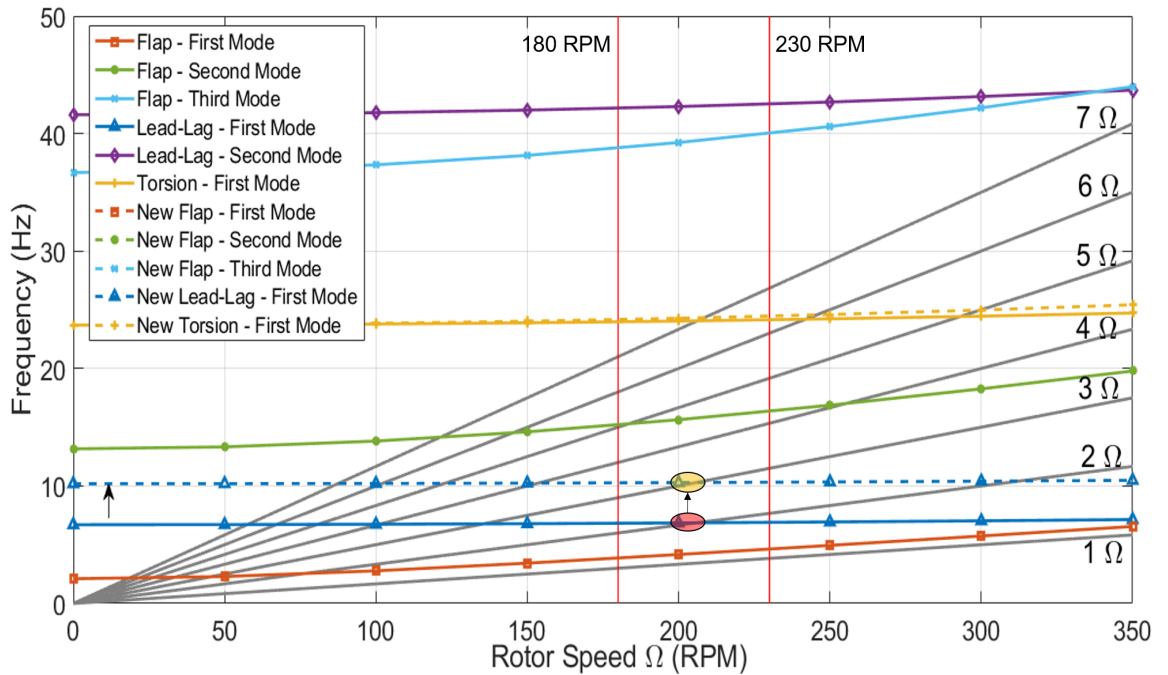


Figure 5.63: Fan plot: Baseline Vs Case 1 ($\mu_N = 0.3$)

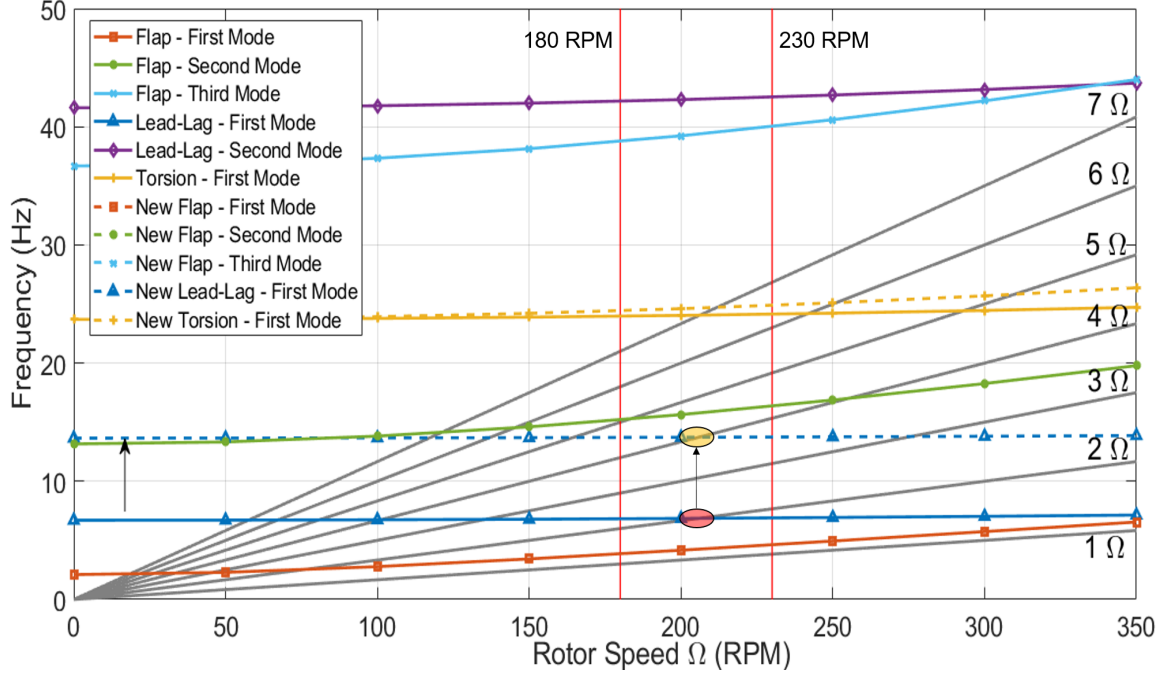


Figure 5.64: Fan plot: Baseline Vs Case 2 ($\mu_N = 0.3$)

Baseline transition time is maintained for all the cases in this section.

5.3.1 $\mu_N = 0.3$, 230 \rightarrow 180 RPM

The lag moment response for all the lag stiffness cases is shown in Figure 5.65. It can be seen that the amplitude is significantly reduced for 4/rev crossing. The peak amplitude plot, 5.66, shows that the resonance amplitude is reduced by 75% for 4/rev crossing. The FFT of the lag moment response shows that the dominating frequencies are 2/rev, 3/rev and 4/rev for the corresponding crossing cases, 5.67.

However, the rotor torque response reveals a different story as shown in Figure 5.68. The steady state amplitude of the torque increases with increase in lag stiffness. The amplitude increase during resonance is shown in Figure 5.69. A tremendous increase is observed for 4/rev crossing, 729%. It was seen previously that a four-bladed rotor transfers 4/rev loads to the hub. Having a 4/rev lag resonance has transferred significant loads to the rotor hub causing the rotor torque to increase immensely. The FFT of the resonance region shows the dominance of the 4/rev frequency, Figure 5.70. Even though the 4/rev crossing

reduces the lag moment, it increases the loads on the transmission system. Hence, it may not be advantageous to increase the stiffness to such high degree. The 3/rev crossing, which provides a 26% reduction in lag moment peak amplitude, would be a better compromise.

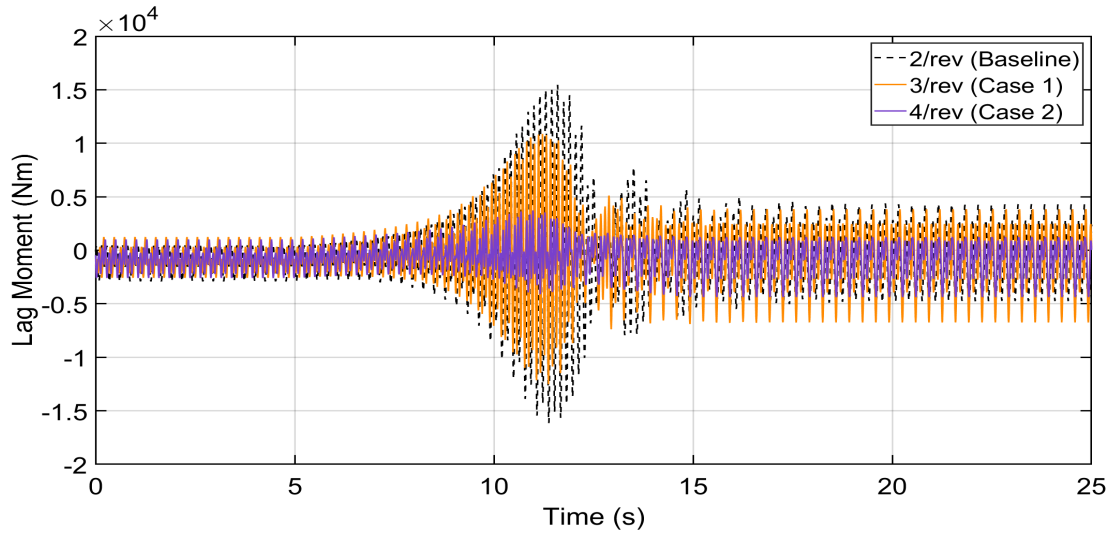


Figure 5.65: Effect of lag stiffness on lag moment ($\mu_N = 0.3$; 230 \rightarrow 180 RPM)

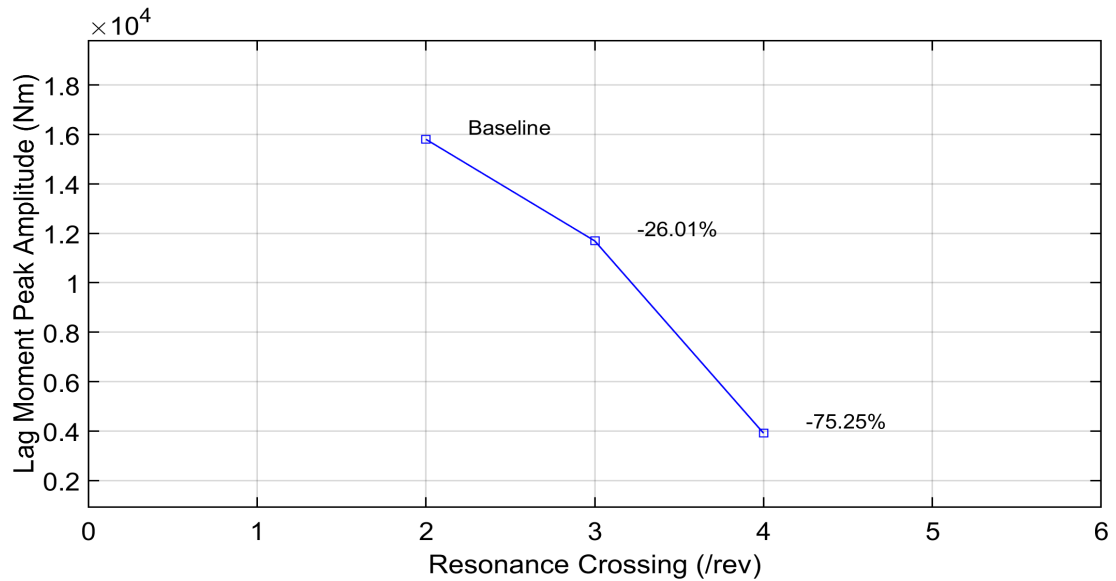


Figure 5.66: Resonance amplitude variation with lag crossing ($\mu_N = 0.3$; 230 \rightarrow 180 RPM)

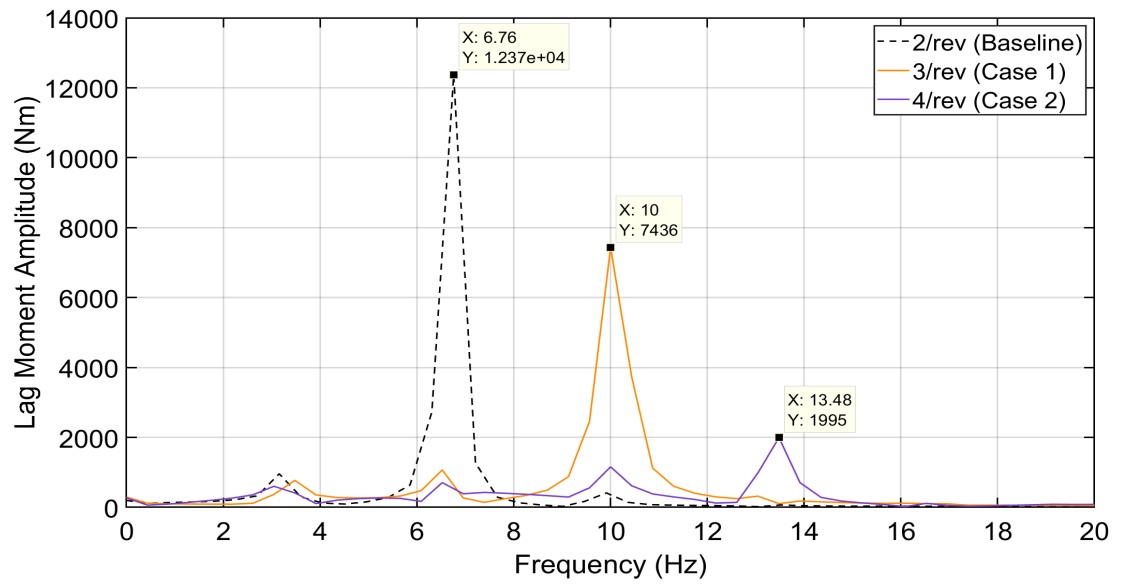


Figure 5.67: FFT on lag moment resonance amplitude ($\mu_N = 0.3$; 230 \rightarrow 180 RPM)

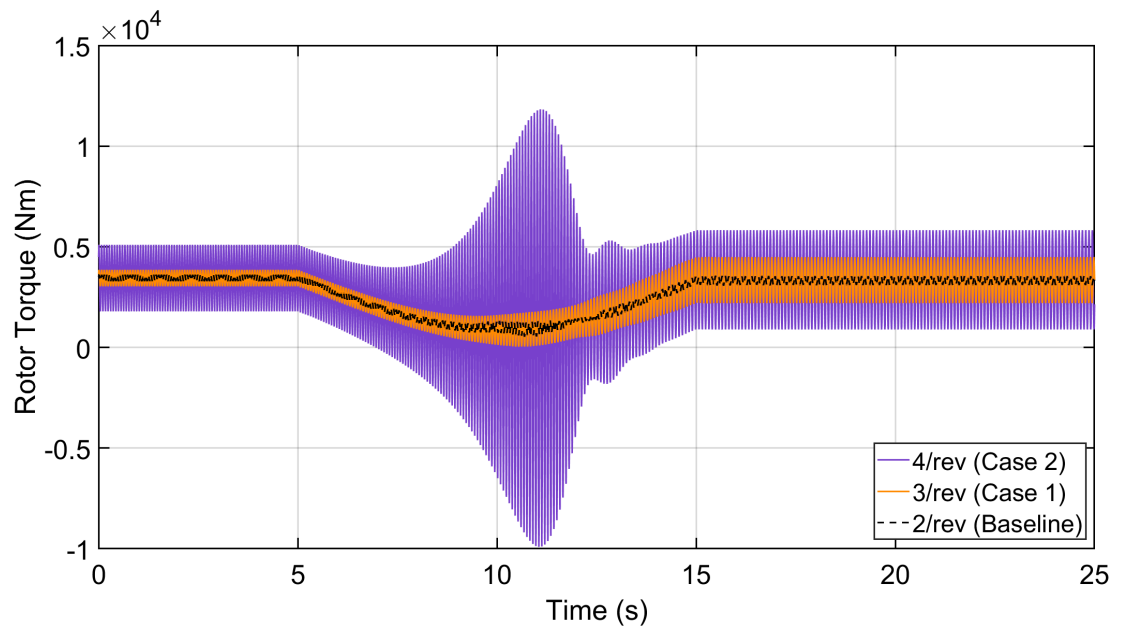


Figure 5.68: Effect of lag stiffness on rotor torque ($\mu_N = 0.3$; 230 \rightarrow 180 RPM)

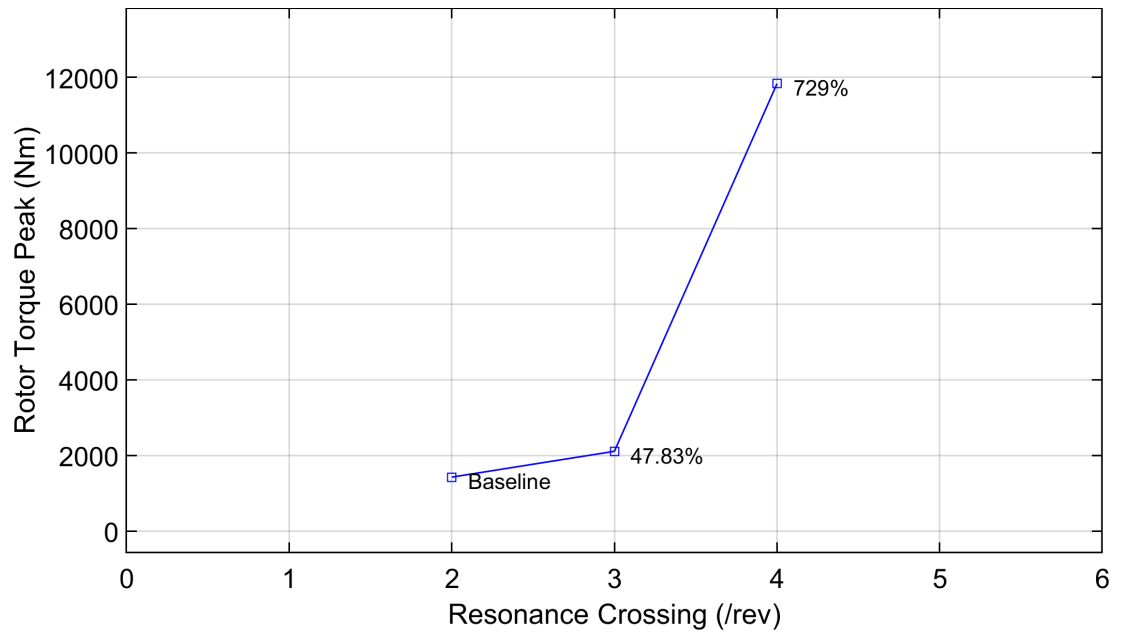


Figure 5.69: Rotor torque peak value during resonance ($\mu_N = 0.3$; 230 \rightarrow 180 RPM)

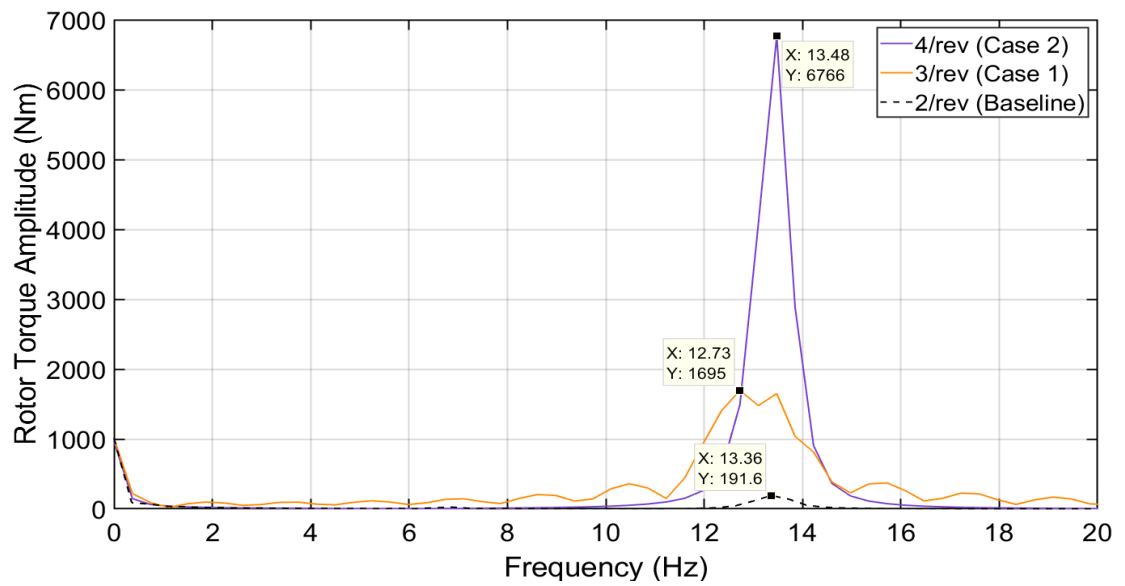


Figure 5.70: FFT on rotor torque resonance amplitude ($\mu_N = 0.3$; 230 \rightarrow 180 RPM)

5.3.2 $\mu_N = 0.3, 180 \rightarrow 230$ RPM

The lag moment response for the reverse transition is shown in Figure 5.71.

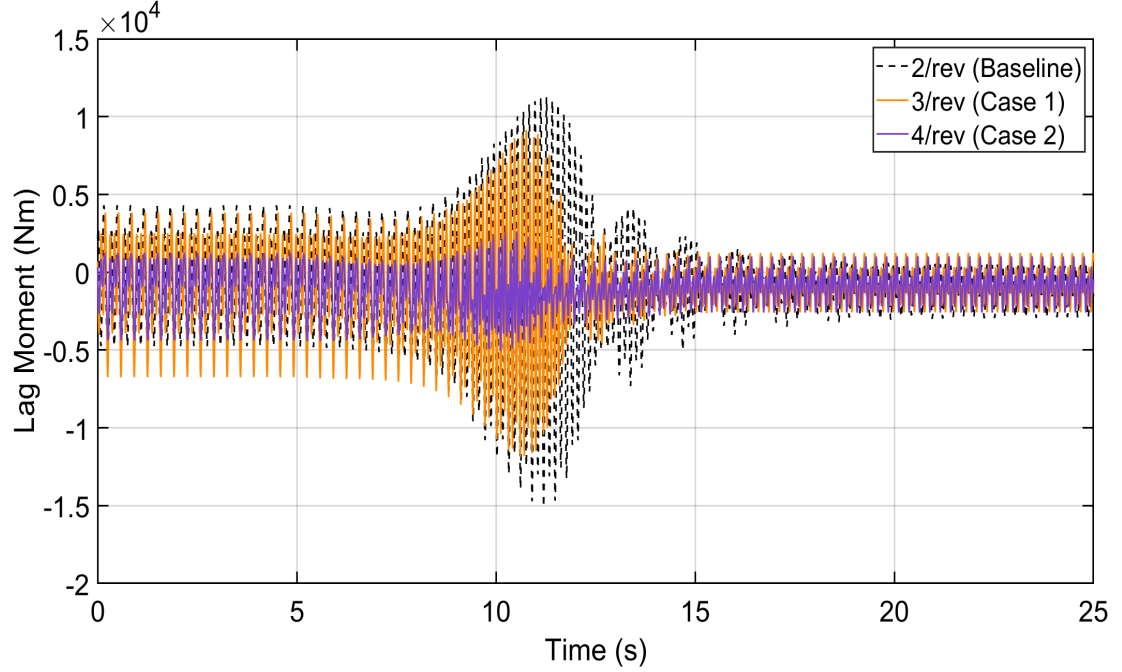


Figure 5.71: Effect of lag stiffness on lag moment ($\mu_N = 0.3$; $180 \rightarrow 230$ RPM)

The peak amplitude plot shows a 20% drop for 3/rev crossing and a 71% reduction for 4/rev crossing, Figure 5.72. The rotor torque exhibits a similar behavior as the previous case. The torque amplitude increases significantly during the 4/rev crossing, Figure 5.73. The peak torque during the 3/rev crossing increases only by 5% from the baseline, Figure 5.74. During the 4/rev crossing, it increases by 171.5%, which is above the maximum limit we assumed previously.

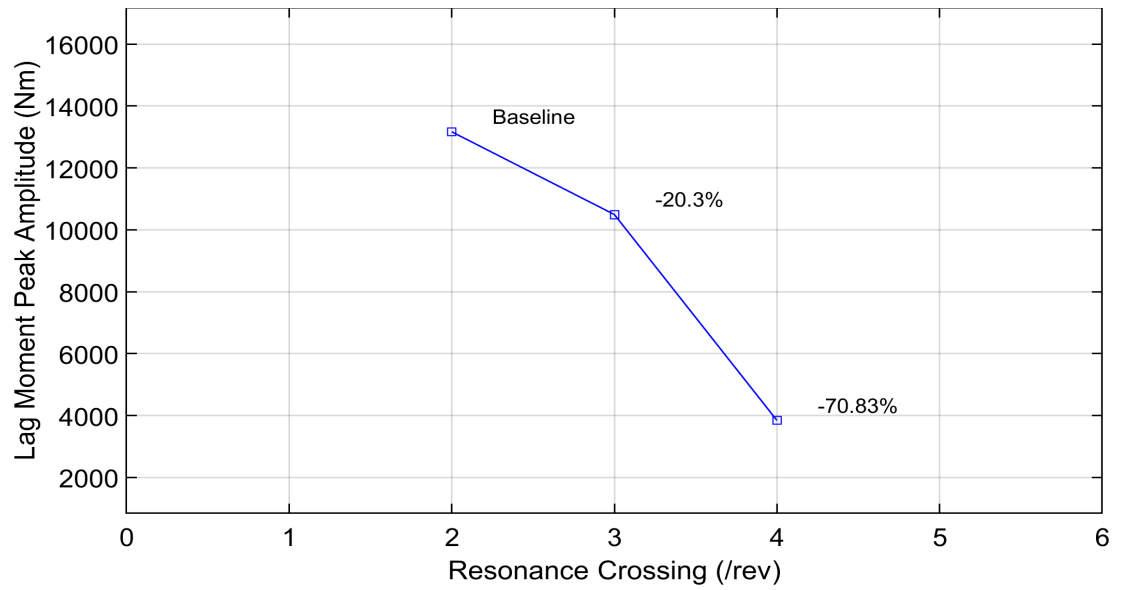


Figure 5.72: Resonance amplitude variation with lag crossing ($\mu_N = 0.3$; 180 \rightarrow 230 RPM)

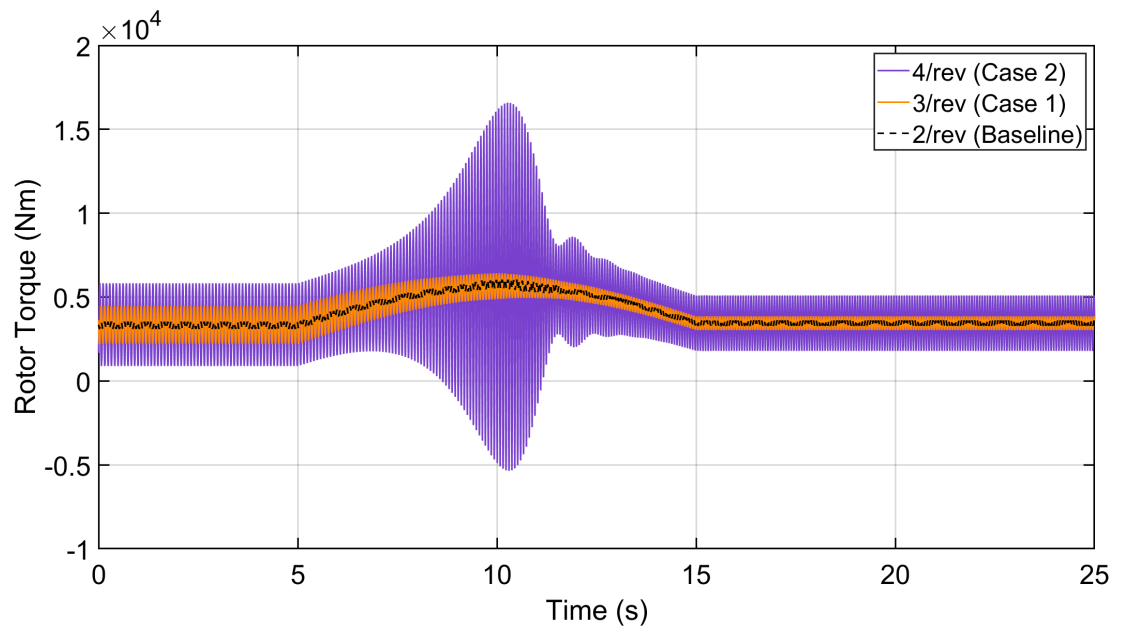


Figure 5.73: Effect of lag stiffness on rotor torque ($\mu_N = 0.3$; 180 \rightarrow 230 RPM)

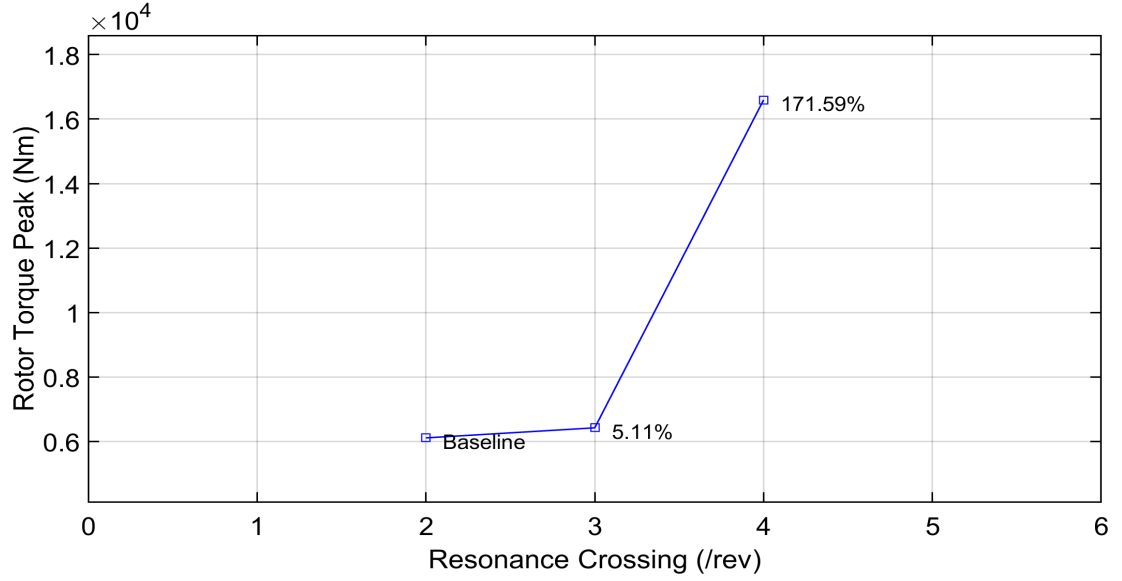


Figure 5.74: Rotor torque peak value during resonance ($\mu_N = 0.3$; 180 → 230 RPM)

5.3.3 $\mu_N = 0.2$, 230 → 150 RPM

The resonance points for the new stiffness values at $\mu_N = 0.2$ are shown in Figures 5.75 and 5.76. It can be seen that an additional 4/rev lag resonance point comes into play for Case 1 and a 5/rev resonance point for Case 2.

The lag moment response is shown in Figure 5.77. The baseline case has only one resonance crossing, whereas Case 1 and 2 have two crossings during this transition. The peak amplitudes for the first transition is shown in Figure 5.78. The drop percentage varies from 20% for 3/rev crossing to 65% for 4/rev crossing. The peak amplitudes for the second crossing are shown in Figure 5.79. Compared to the steady state value of the baseline, the Case 1 4/rev crossing has 102% higher amplitude. This is almost as high as the first 2/rev crossing. The 5/rev crossing has 3.5% lower amplitude than the baseline.

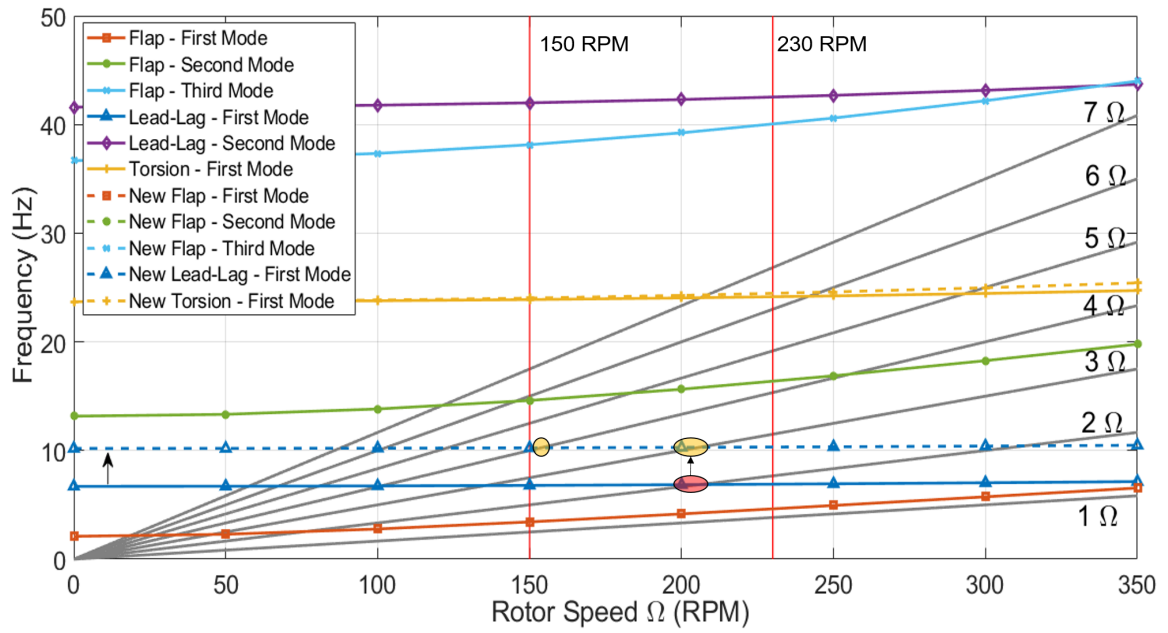


Figure 5.75: Fan plot: Baseline vs. Case 1 ($\mu_N = 0.2$)

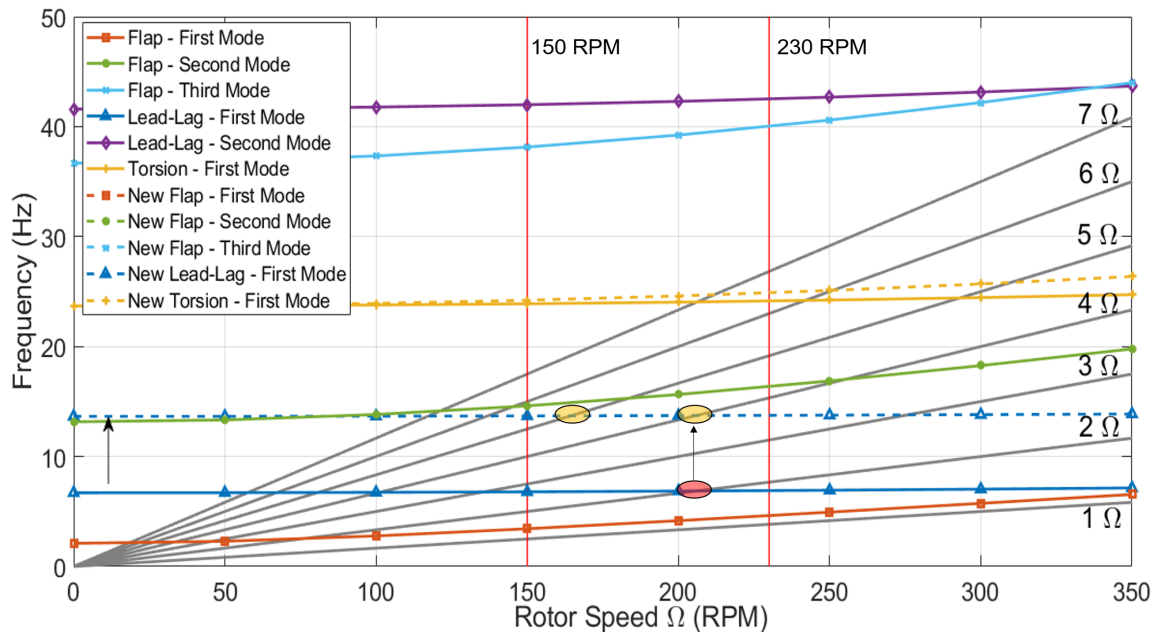


Figure 5.76: Fan plot: Baseline vs. Case 2 ($\mu_N = 0.2$)

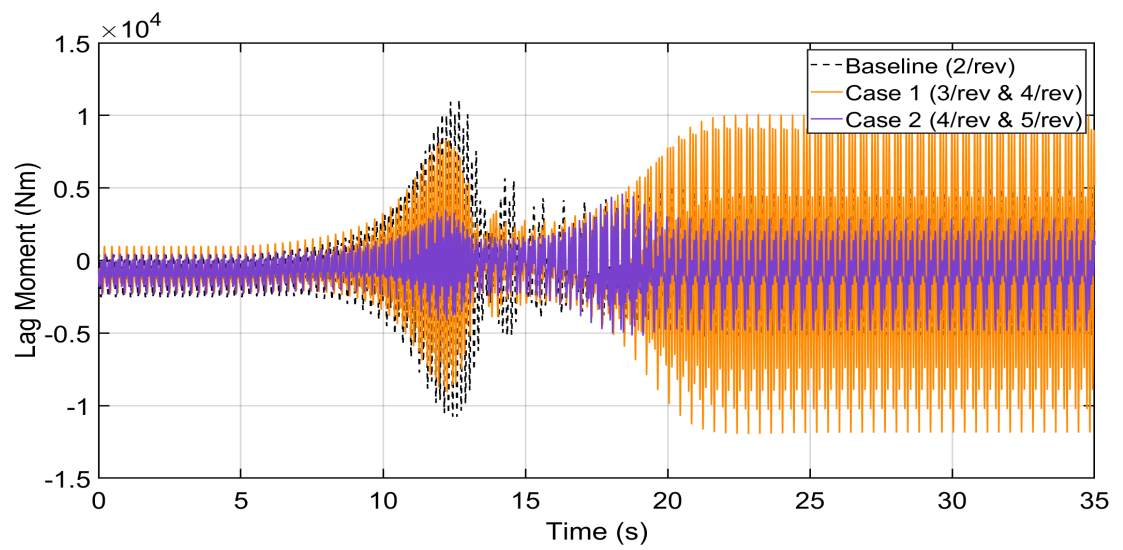


Figure 5.77: Effect of lag stiffness on lag moment ($\mu_N = 0.2$; 230 \rightarrow 150 RPM)

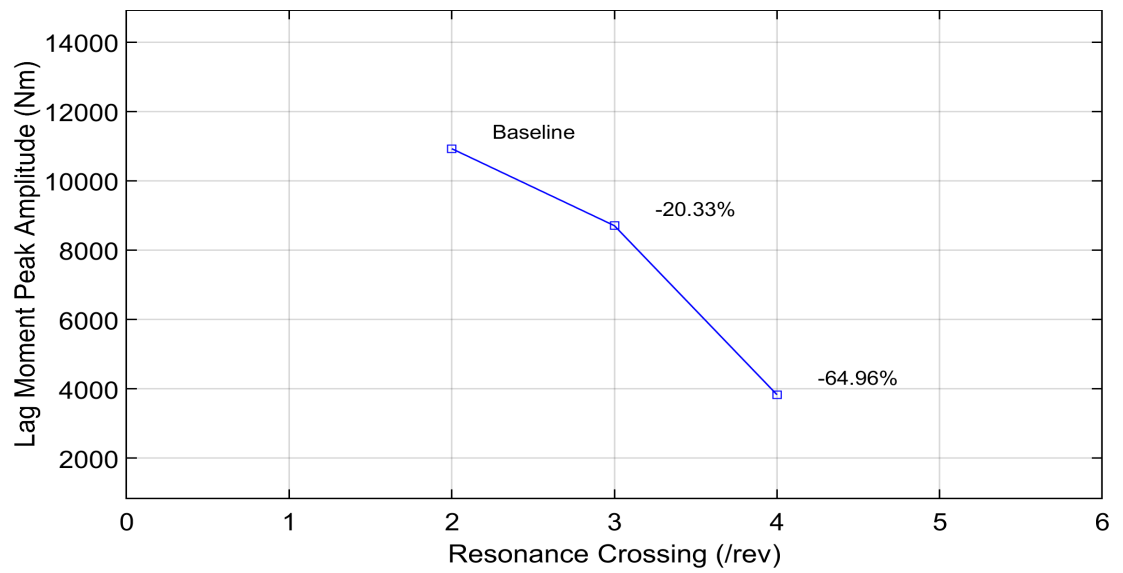


Figure 5.78: Resonance amplitude during first crossing ($\mu_N = 0.2$; 230 \rightarrow 150 RPM)

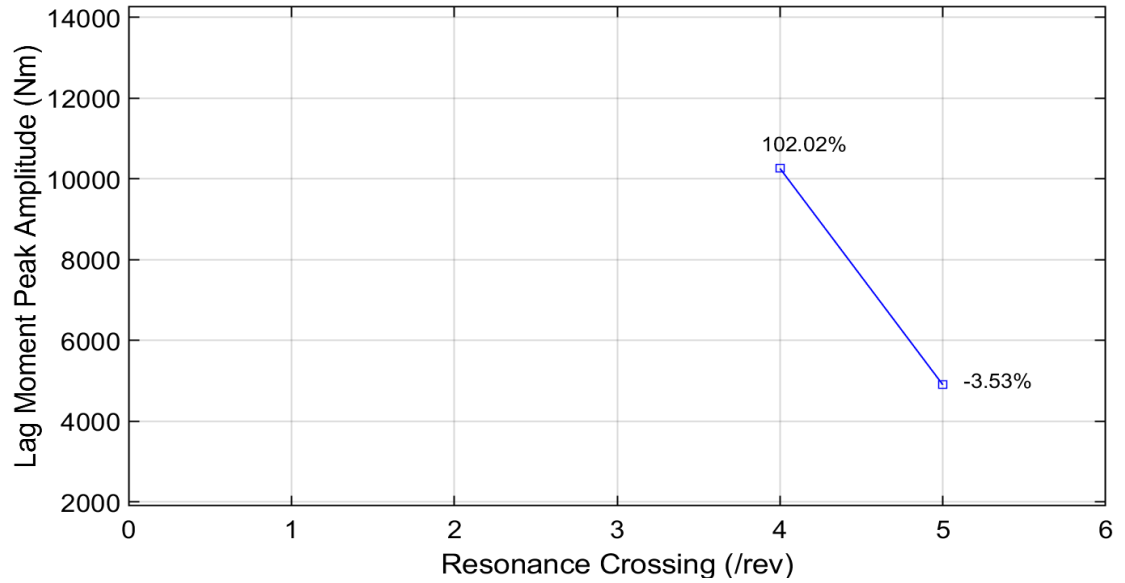


Figure 5.79: Resonance amplitude during second crossing ($\mu_N = 0.2$; 230 \rightarrow 150 RPM)

The rotor torque response for both the crossings is shown in Figure 5.80. The torque increase during the 4/rev crossing of Case 1 is three times the torque increase during the 4/rev crossing of Case 2. This is because the 4/rev crossing of Case 1 occurs at a lower rotor speed. Lower rotor speeds tend to have higher amplitude oscillations in the torque response. During these crossings, the torque crosses the maximum limit on both the ends. Hence, neither Case 2 nor Case 1 lag stiffnesses are desirable for this transition. The baseline rotor has a better response. If we were to use the Case 1 lag stiffness, the rotor shouldn't cross the 4/rev resonance. The speed change should be limited to 160 RPM.

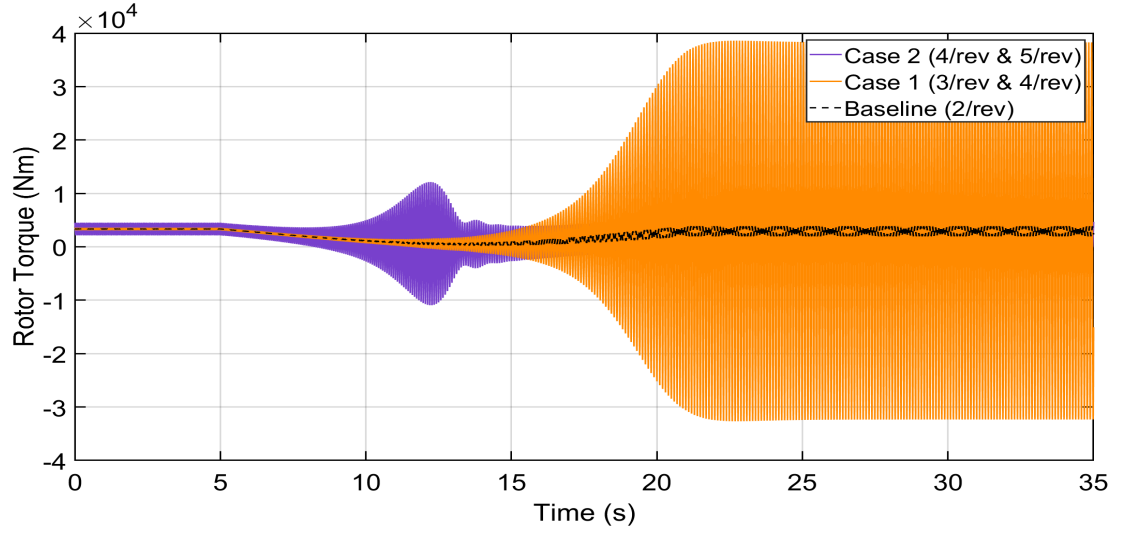


Figure 5.80: Effect of lag stiffness on rotor torque ($\mu_N = 0.2$; 230 \rightarrow 150 RPM)

5.3.4 $\mu_N = 0.2$, 150 \rightarrow 230 RPM

The reverse transition of the previous case is discussed in this section. The lag moment response is shown in Figure 5.81. The steady state response of Case 1 has a high magnitude at the beginning as the rotor is operating very close to 4/rev crossing. The rotor torque response is shown in Figure 5.82. It can be seen that both Case 1 and Case 2 cross the torque limits at both ends. Hence, neither of these cases are ideal for this transition.

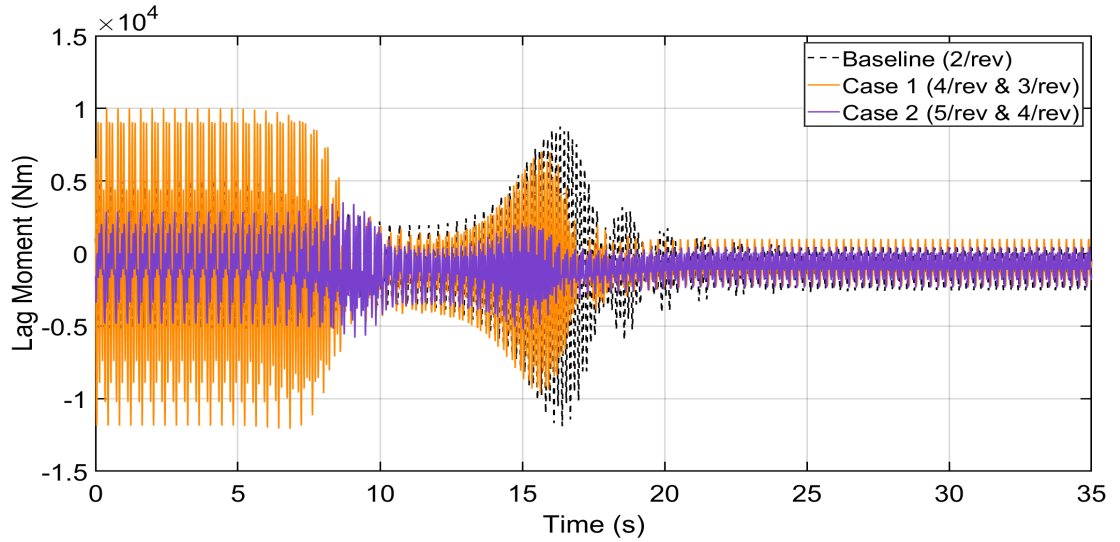


Figure 5.81: Effect of lag stiffness on lag moment ($\mu_N = 0.2$; 150 \rightarrow 230 RPM)

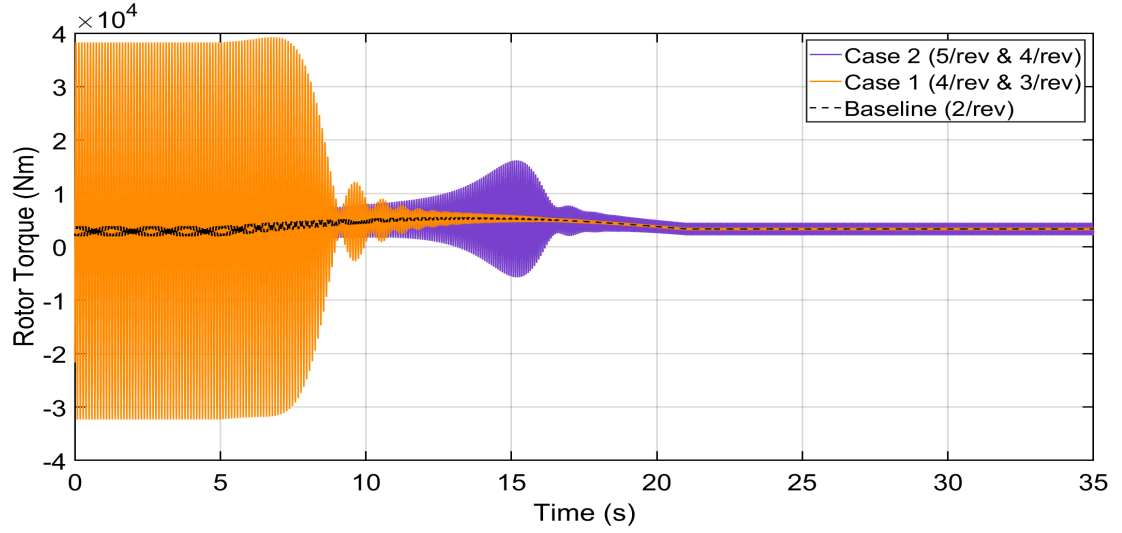


Figure 5.82: Effect of lag stiffness on rotor torque ($\mu_N = 0.2$; $150 \rightarrow 230$ RPM)

5.3.5 $\mu_N = 0.1$, $230 \rightarrow 130$ RPM

The resonance points at $\mu_N = 0.1$ are shown in Figures 5.83 and 5.84. It can be seen that Case 1 has the same two resonance points as the previous case. The 6/rev lag resonance point is in the operating regime for Case 2, in addition to 4/rev and 5/rev resonance points.

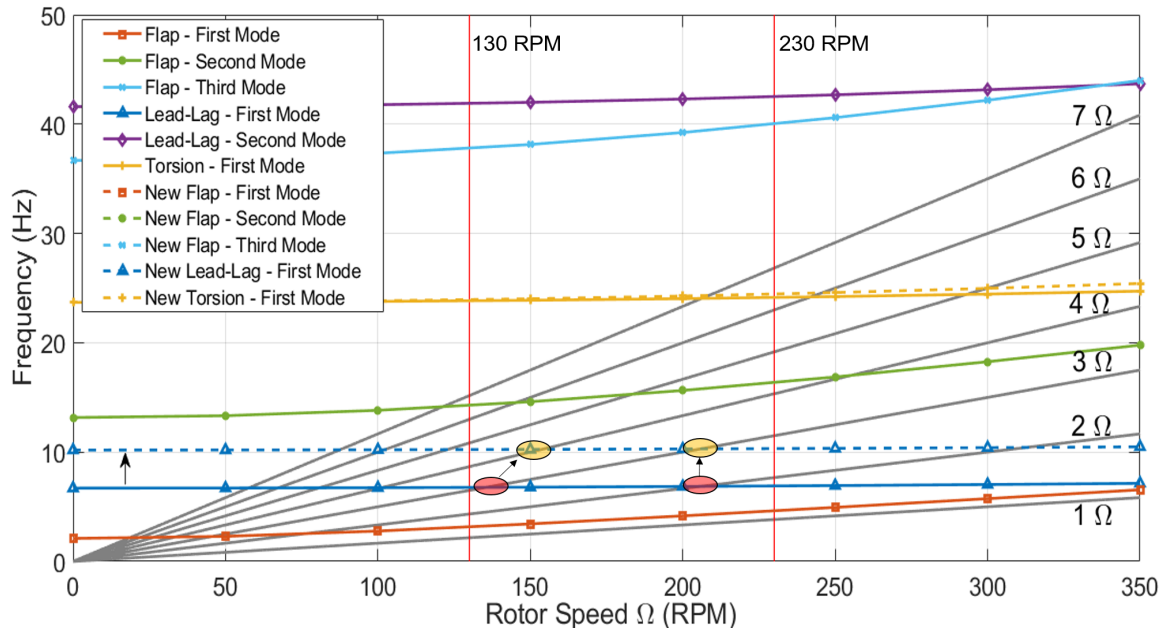


Figure 5.83: Fan plot: Baseline vs. Case 1 ($\mu_N = 0.1$)

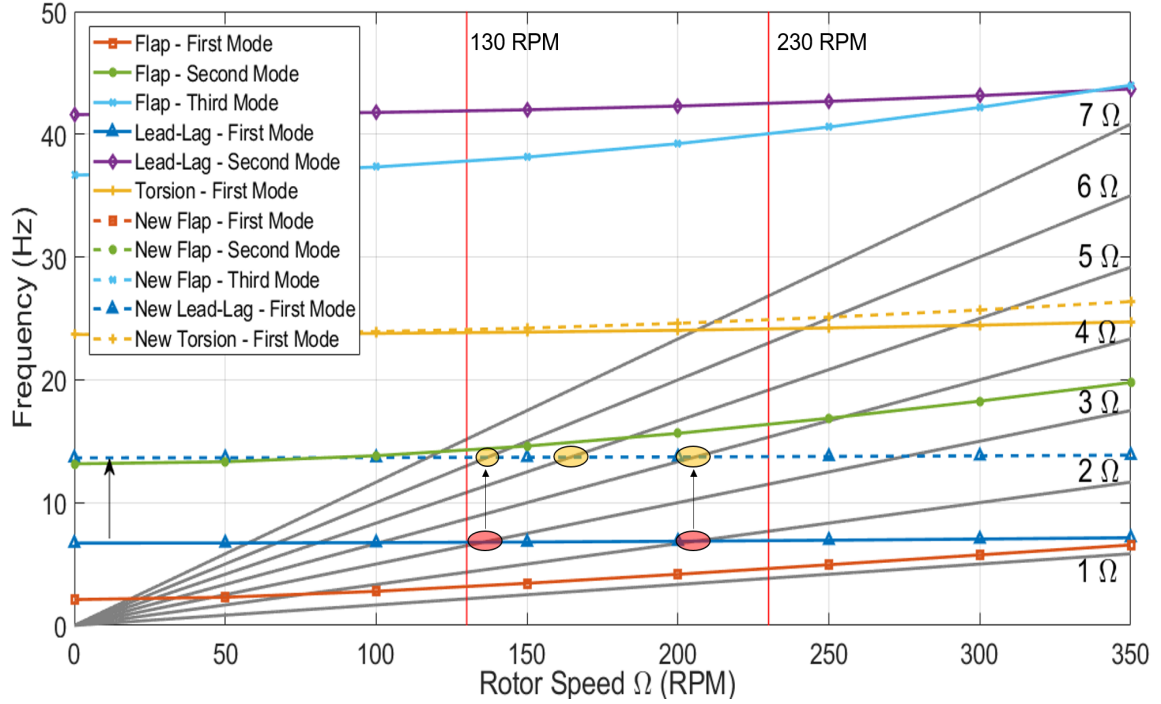


Figure 5.84: Fan plot: Baseline vs. Case 2 ($\mu_N = 0.1$)

The lag moment response is shown in Figure 5.85. The baseline case has two resonance crossings, 2/rev and 3/rev. The 3/rev resonance is of primary importance in this transition due to its higher amplitude. As the stiffness is increased to Case 1 or Case 2, the large second resonance bump is replaced by smaller bumps as shown in 5.85. The 6/rev crossing has no noticeable impact on the blade response. The peak amplitudes for the first and second resonances are shown in Figures 5.86 and 5.87, respectively. For the second resonance, 75% reduction in peak amplitude was obtained by using Case 1 stiffness. But looking at the torque response, Figure 5.88, it can be seen that the torque crosses the previously decided limits for Case 1. The torque response for Case 2 is moderate compared to Case 1 and doesn't cross the positive limit. However, it crosses the negative region, which is not desirable. Also, previous cases have shown that Case 2 crosses the positive limit.

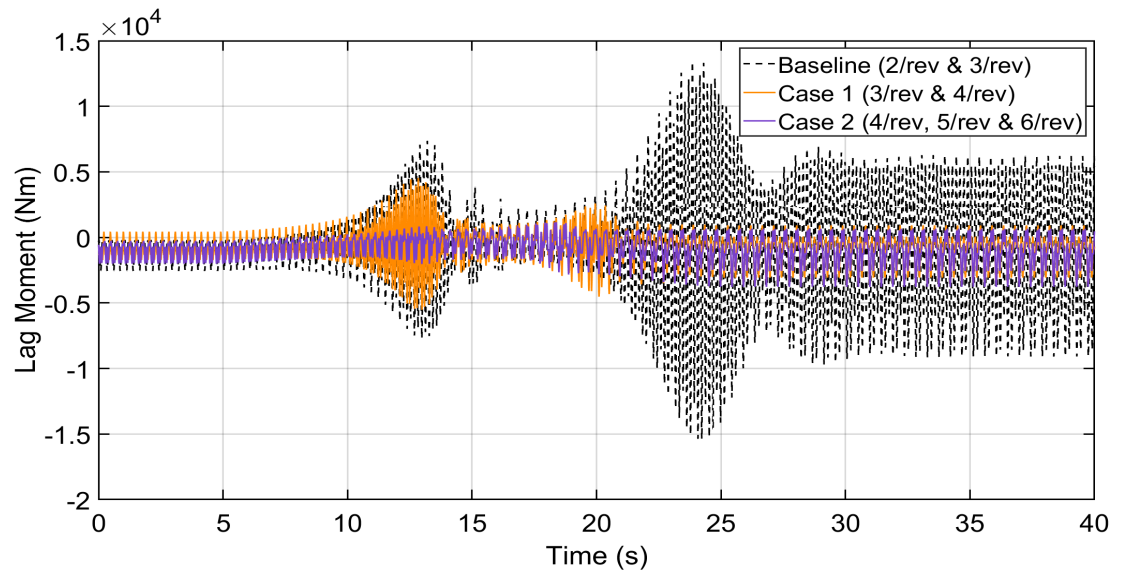


Figure 5.85: Effect of lag stiffness on lag moment ($\mu_N = 0.1$; 230 \rightarrow 130 RPM)

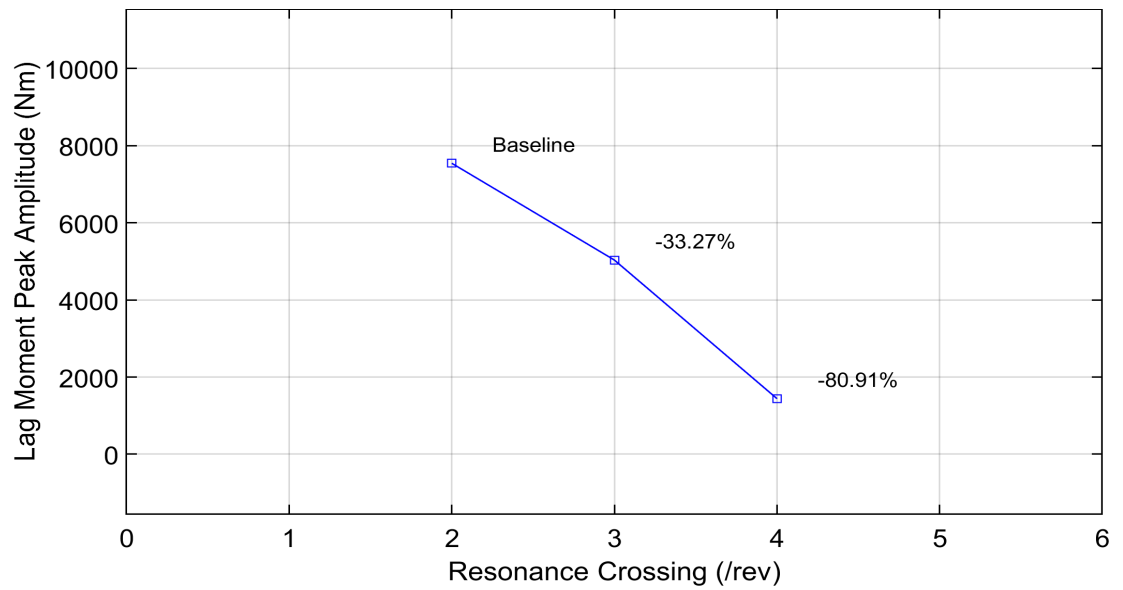


Figure 5.86: Resonance amplitude during first crossing ($\mu_N = 0.1$; 230 \rightarrow 130 RPM)

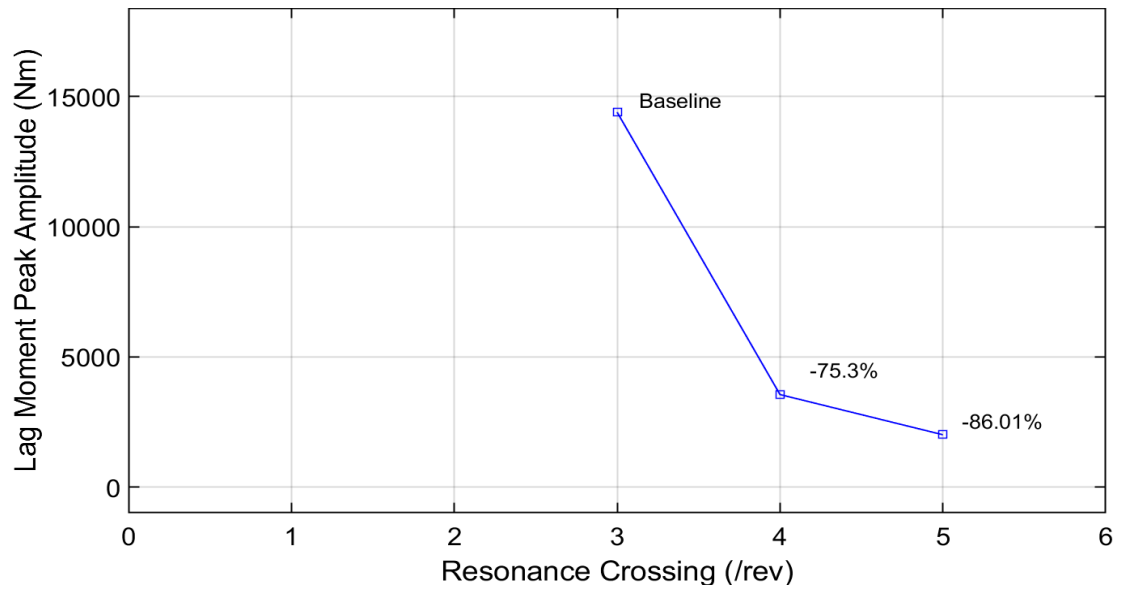


Figure 5.87: Resonance amplitude during second crossing ($\mu_N = 0.1$; 230 \rightarrow 130 RPM)

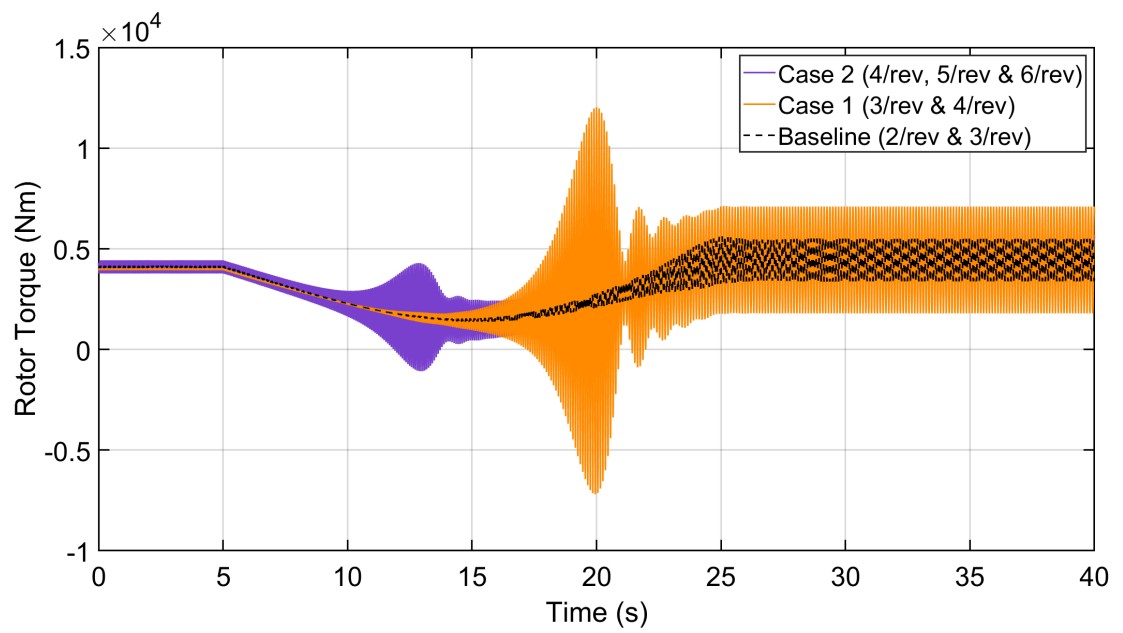


Figure 5.88: Effect of lag stiffness on rotor torque ($\mu_N = 0.1$; 230 \rightarrow 130 RPM)

5.3.6 $\mu_N = 0.1, 130 \rightarrow 230$ RPM

The lag moment response is shown in Figure 5.89. The amplitude reduction due to stiffness increase has a trend similar to the previous case, Figures 5.90 and 5.91.

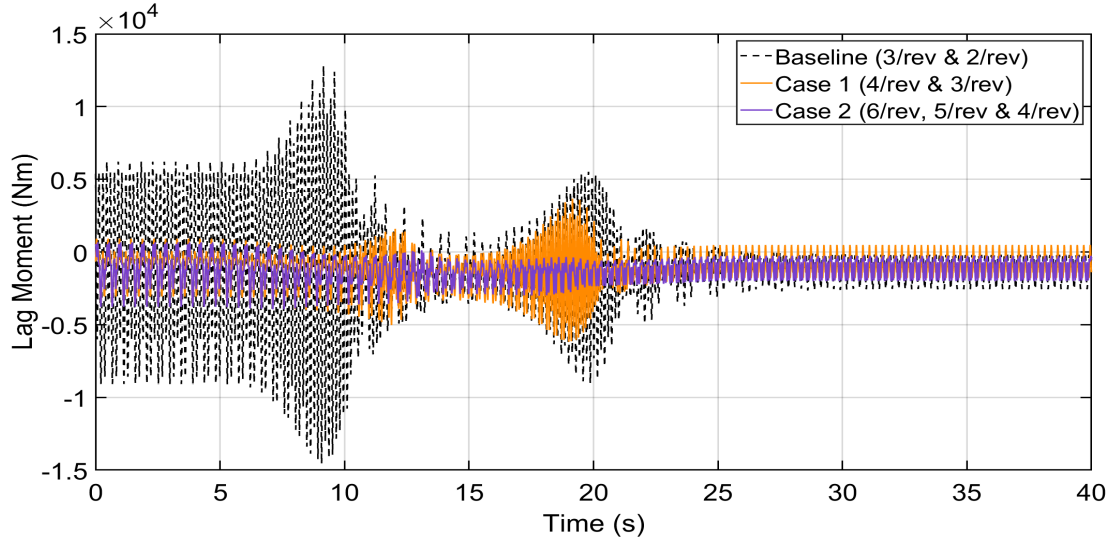


Figure 5.89: Effect of lag stiffness on lag moment ($\mu_N = 0.1$; $130 \rightarrow 230$ RPM)

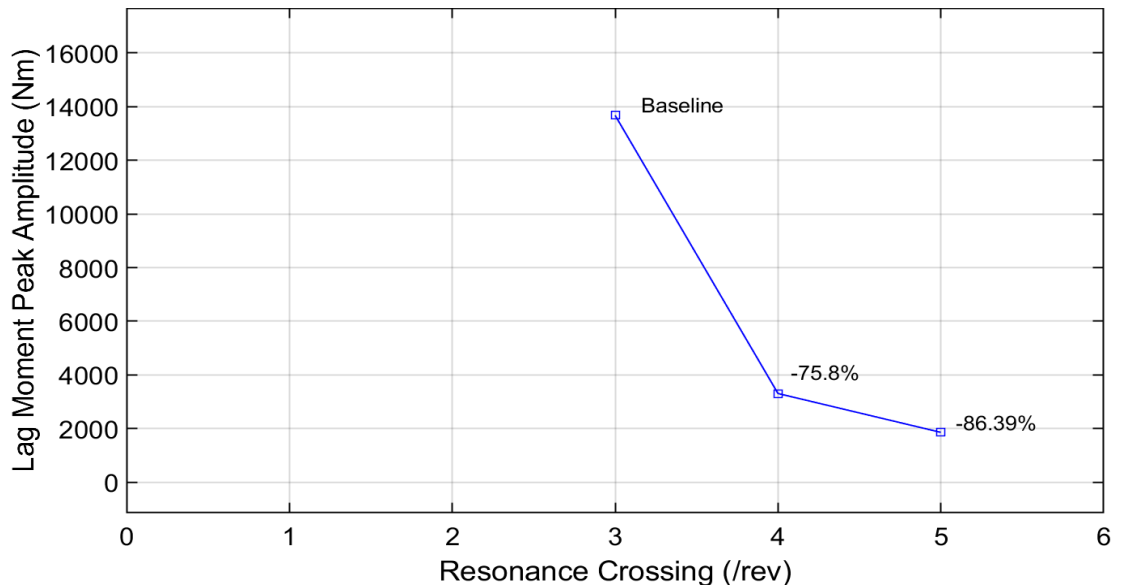


Figure 5.90: Resonance amplitude during first crossing ($\mu_N = 0.1$; $130 \rightarrow 230$ RPM)

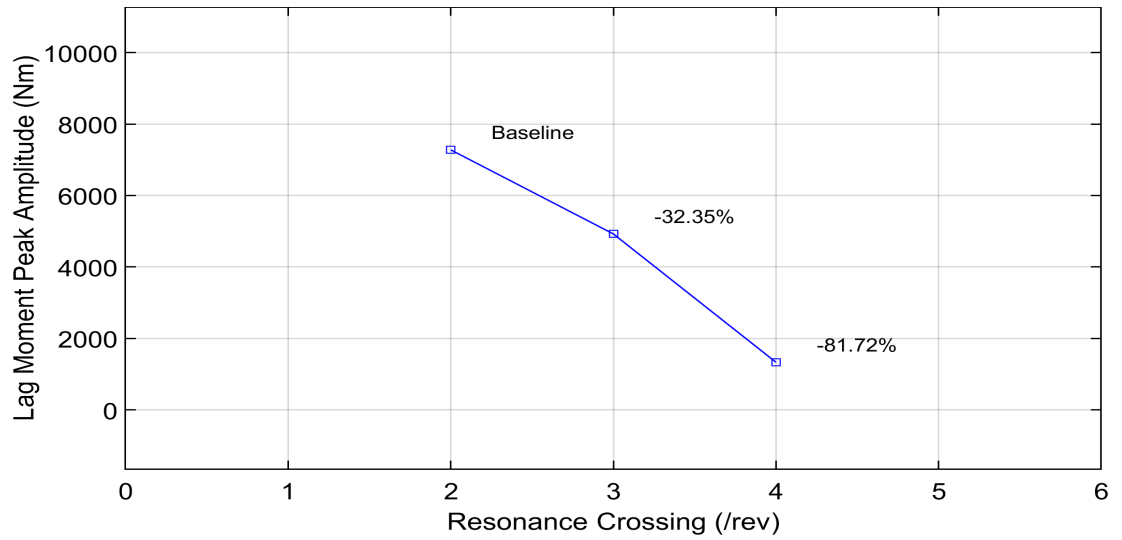


Figure 5.91: Resonance amplitude during second crossing ($\mu_N = 0.1$; 130 \rightarrow 230 RPM)

The rotor torque response is shown in Figure 5.92. Once again, Case 1 torque crosses the maximum limits during the 4/rev crossing. Interestingly, Case 2 torque does not cross the limits during this transition. The amplitude increase during this 4/rev crossing is only 35% more than the baseline amplitude. Hence, this is the only acceptable transition scenario for Case 2 stiffness in terms of torque.

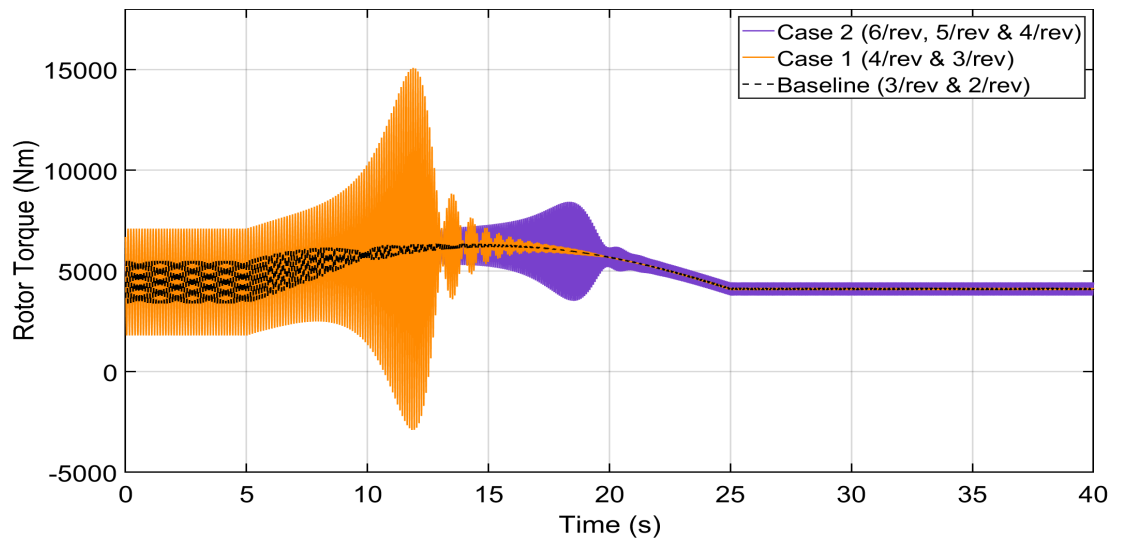


Figure 5.92: Effect of lag stiffness on rotor torque ($\mu_N = 0.1$; 130 \rightarrow 230 RPM)

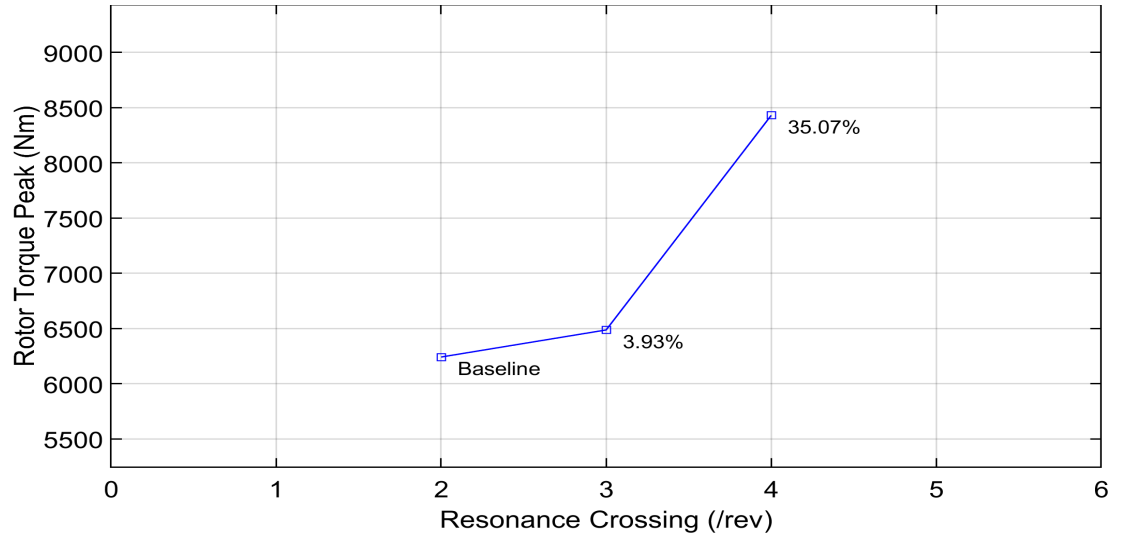


Figure 5.93: Rotor torque peak value during resonance ($\mu_N = 0.1$; 130 \rightarrow 230 RPM)

5.3.7 Impact of Lag Stiffness (EI_{Lag}): Summary

The results of the lag stiffness impact on resonances are given in Tables 5.6 and 5.7.

Table 5.6: EI_{Lag} impact on high-to-low speed transition.

μ_N	Transition (RPM)	Case 1		Case 2	
		Lag moment amplitude	Torque within bounds?	Lag moment amplitude	Torque within bounds?
0.3	230 \rightarrow 180	-26.01%	Yes	-75.25%	No
0.2	230 \rightarrow 150 (First Resonance)	-20.33%	No	-64.96%	No
0.2	230 \rightarrow 150 (Second Resonance)	+102.02%	No	-3.53%	No
0.1	230 \rightarrow 130 (First Resonance)	-33.27%	Yes	-80.91%	No
0.1	230 \rightarrow 130 (Second Resonance)	-75.3%	No	-86.01%	Yes

Therefore, increasing the lag stiffness reduces the lag moment amplitude during resonance for most of the cases. However, the torque response goes out of limits for most of them. If my dissertation is a democracy and torque bounds are my constituents, the lag stiffness increase as a candidate is defeated by 11 'No' votes to 9 'Yes' votes. Either the lag

Table 5.7: EI_{Lag} impact on low-to-high speed transition.

μ_N	Transition (RPM)	Case 1		Case 2	
		Lag moment amplitude	Torque within bounds?	Lag moment amplitude	Torque within bounds?
0.3	180 \rightarrow 230	-20.30%	Yes	-70.83%	No
0.2	150 \rightarrow 230 (First Resonance)	+123.67%	No	+35.86%	Yes
0.2	150 \rightarrow 230 (Second Resonance)	-19.38%	Yes	-64.44%	No
0.1	130 \rightarrow 230 (First Resonance)	-75.8%	No	-86.39%	Yes
0.1	130 \rightarrow 230 (Second Resonance)	-32.35%	Yes	-81.72%	Yes

stiffness has to be increased beyond Case 2 to have 5/rev crossing instead of 4/rev crossing or the stiffness has to remain the same. Even with a stiffness higher than Case 2, the steady state torque could be an issue as the amplitude keeps increasing with increased stiffness. Increasing the lag stiffness beyond the second flap frequency is no easy task, it has to be 6.5 times the current lag stiffness to avoid any resonance issues. Hence, keeping the original stiffness and tweaking ζ and transition time seems more reasonable.

5.4 Combination Impact: Transition time (t_T) and ζ

In this section, the combined effects of structural damping and transition time, t_T , are studied. The structural lag damping ratio is increased to 7%, as it produced the best results, and ideal transition times from Tables 5.1 and 5.2 are used. The results are discussed in the following sections.

5.4.1 $\mu_N = 0.3, 230 \rightarrow 180$ RPM

The baseline parameters for $\mu_N = 0.3$ are $\zeta = 1\%$ and $t_T = 10$ s. For the new case, $\zeta = 7\%$ and $t_T = 8$ s, Table 5.1. The lag moment comparison is given in Figure 5.94. The peak amplitude is reduced by 73% as shown in Figure 5.95. This is almost the same as the reduction obtained using the baseline transition time as described in Table 5.3. In

this case, there is no additional reduction obtained by reducing the transition time. Since we are comparing the peak amplitudes during resonance, the reduction will never be 100% as there will always be loads that are independent of resonance. Hence, there is a natural upper bound on the amplitude reduction that can be achieved. The rotor torque response is shown in Figure 5.96. The torque dips further down because of the lower t_T and the resonance bump disappears.

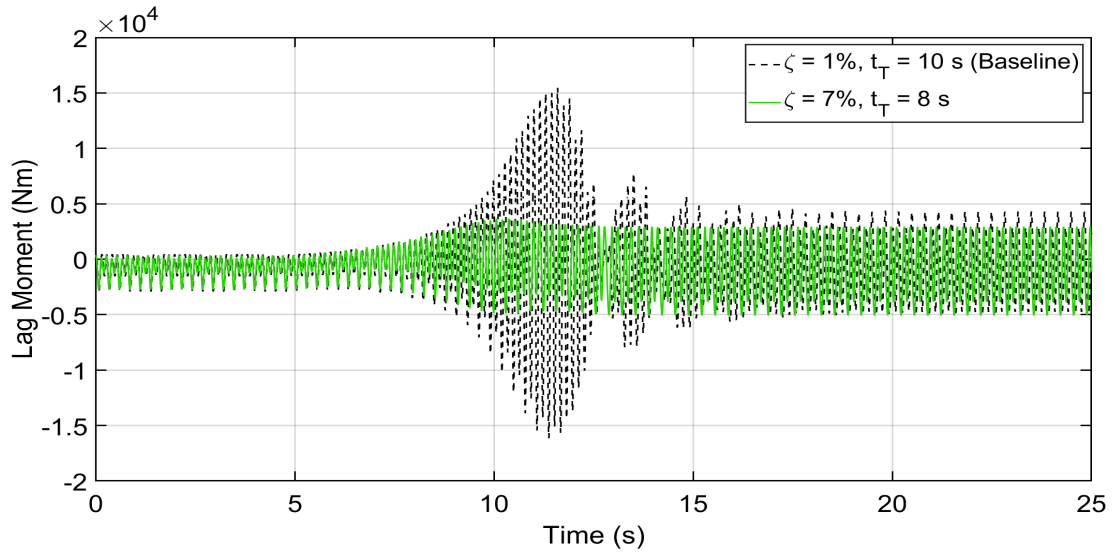


Figure 5.94: Effect of ζ and t_T on lag moment ($\mu_N = 0.3$; $230 \rightarrow 180$ RPM)

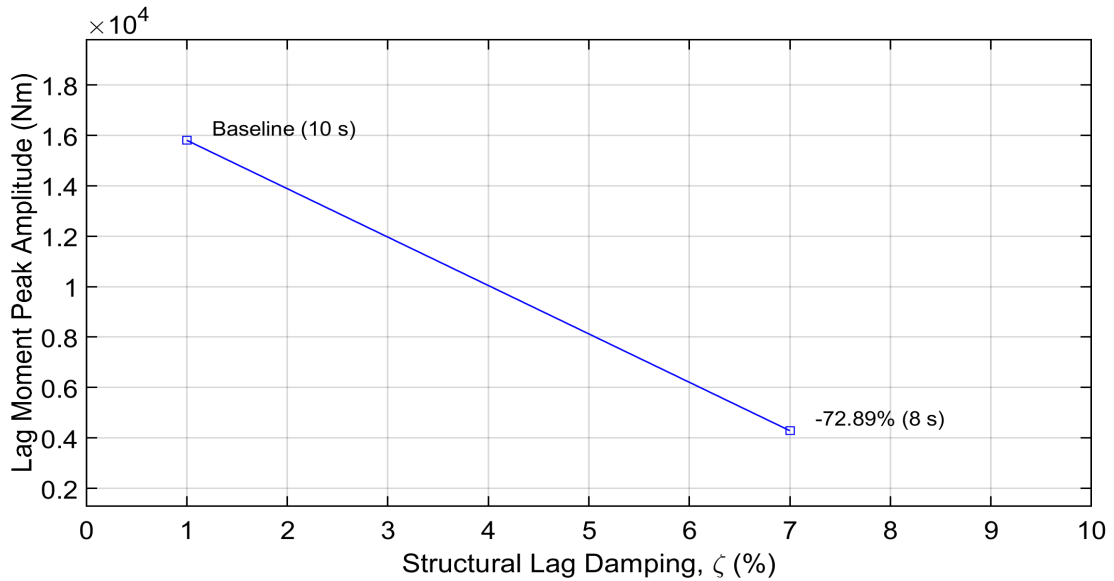


Figure 5.95: Resonance amplitude variation with ζ and t_T ($\mu_N = 0.3$; $230 \rightarrow 180$ RPM)

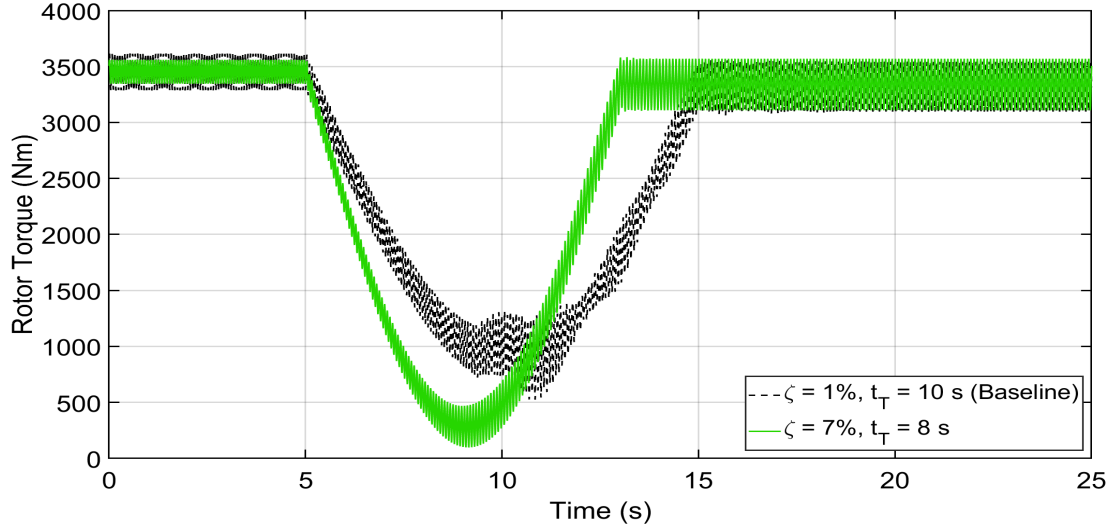


Figure 5.96: Effect of ζ and t_T on rotor torque ($\mu_N = 0.3$; 230 \rightarrow 180 RPM)

5.4.2 $\mu_N = 0.3$, 180 \rightarrow 230 RPM

The ideal transition time for this low-to-high speed scenario is $t_T = 4$ s, Table 5.2. The lag moment results are given in Figure 5.97.

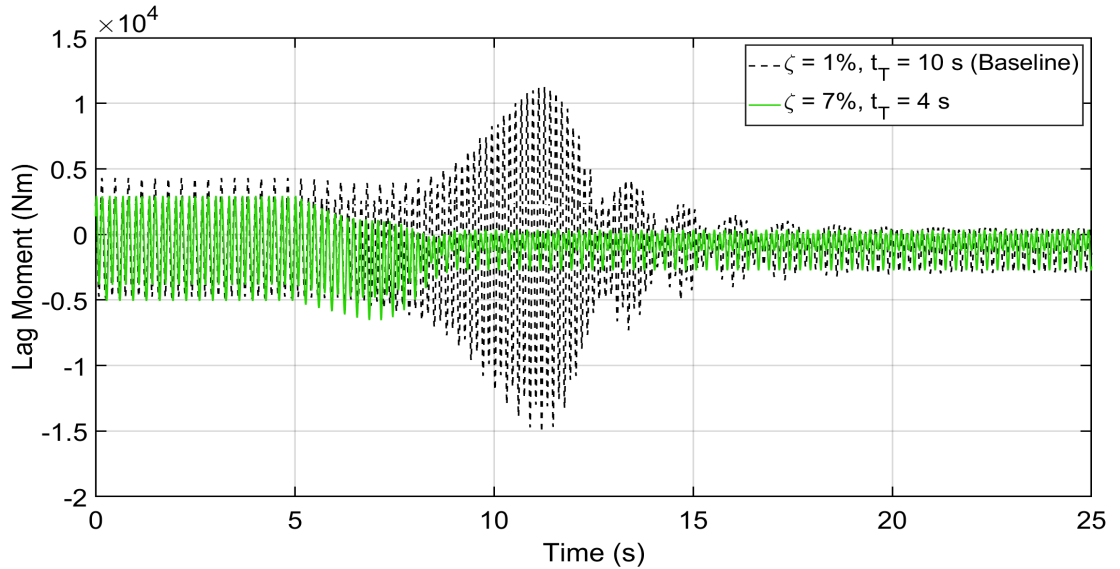


Figure 5.97: Effect of ζ and t_T on lag moment ($\mu_N = 0.3$; 180 \rightarrow 230 RPM)

The peak amplitude is reduced by 71% as shown in Figure 5.98, which is slightly more than the reduction obtained using baseline transition time, Table 5.4. The difference is only 0.65%. It appears that the transition time is not providing any significant additional

reduction to the amplitude that is already reduced by ζ increase. The torque, however, increases in amplitude due to shorter transition time as shown in Figure 5.99. The new peak is about 54% higher than the baseline, Figure 5.100.

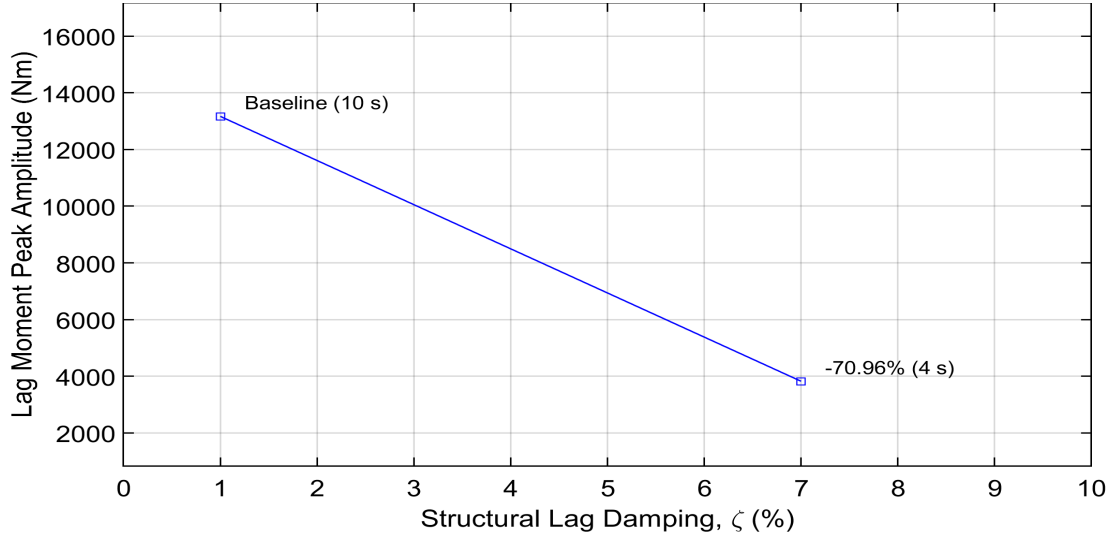


Figure 5.98: Resonance amplitude variation with ζ and t_T ($\mu_N = 0.3$; 180 \rightarrow 230 RPM)

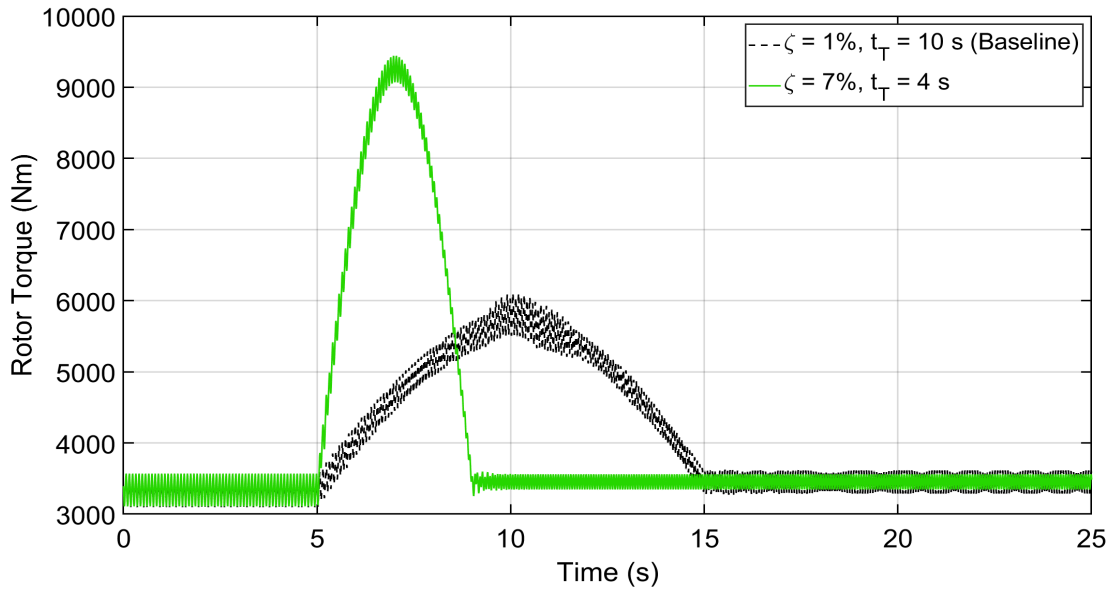


Figure 5.99: Effect of ζ and t_T on rotor torque ($\mu_N = 0.3$; 180 \rightarrow 230 RPM)

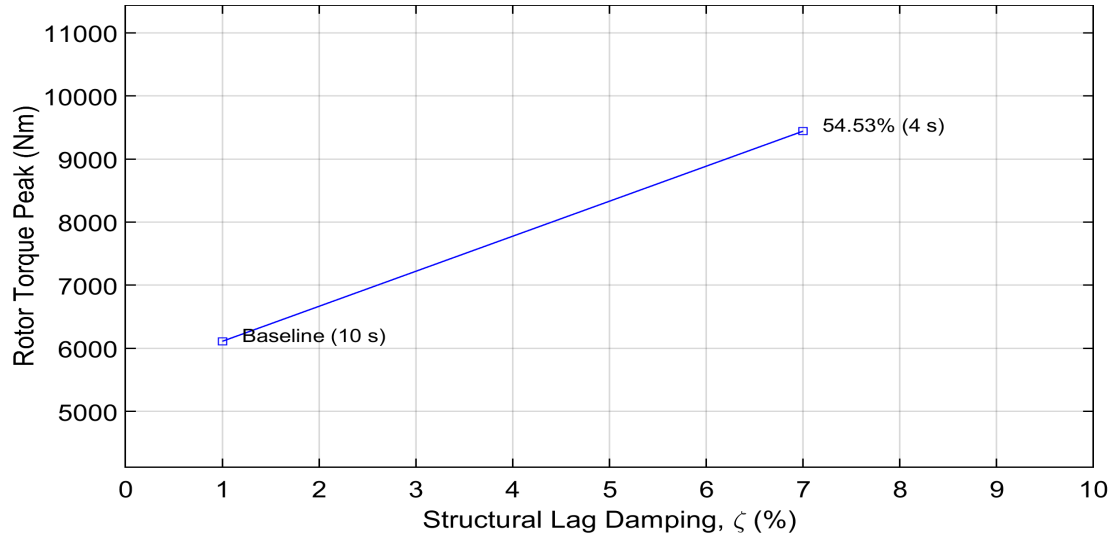


Figure 5.100: Rotor torque peak value during resonance ($\mu_N = 0.3$; 180 \rightarrow 230 RPM)

5.4.3 $\mu_N = 0.2$, 230 \rightarrow 150 RPM

The baseline transition time for $\mu_N = 0.2$ is 16 s. The ideal transition time for the current case is 14 s, Table 5.1. The lag moment response is given in Figure 5.101. The peak amplitude is reduced by 73% as shown in Figure 5.102. This is the same as the reduction shown in Table 5.3 for the baseline time. The rotor torque response is shown in Figure 5.103.

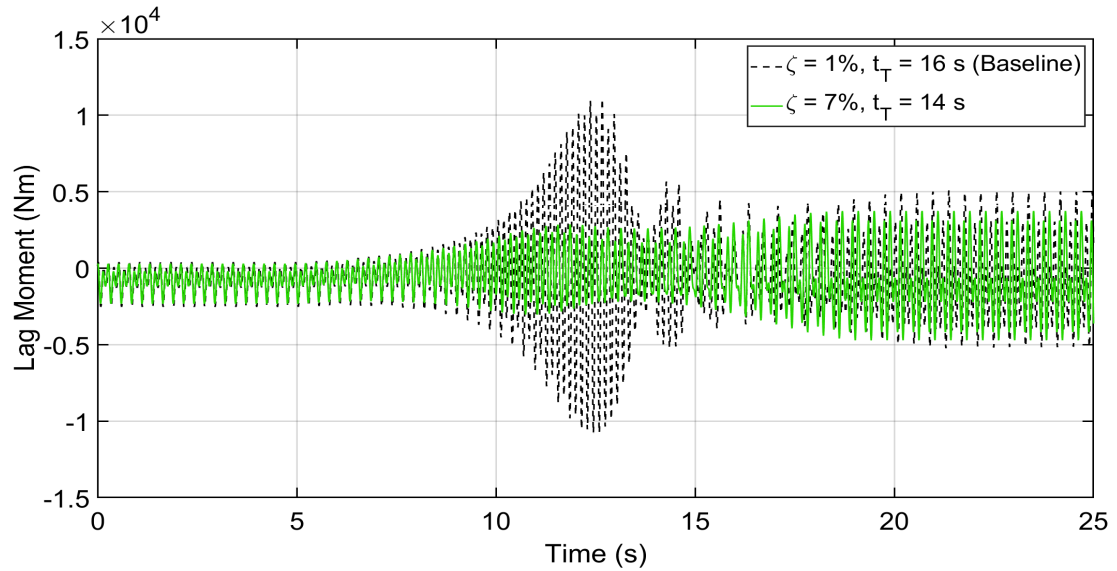


Figure 5.101: Effect of ζ and t_T on lag moment ($\mu_N = 0.2$; 230 \rightarrow 150 RPM)

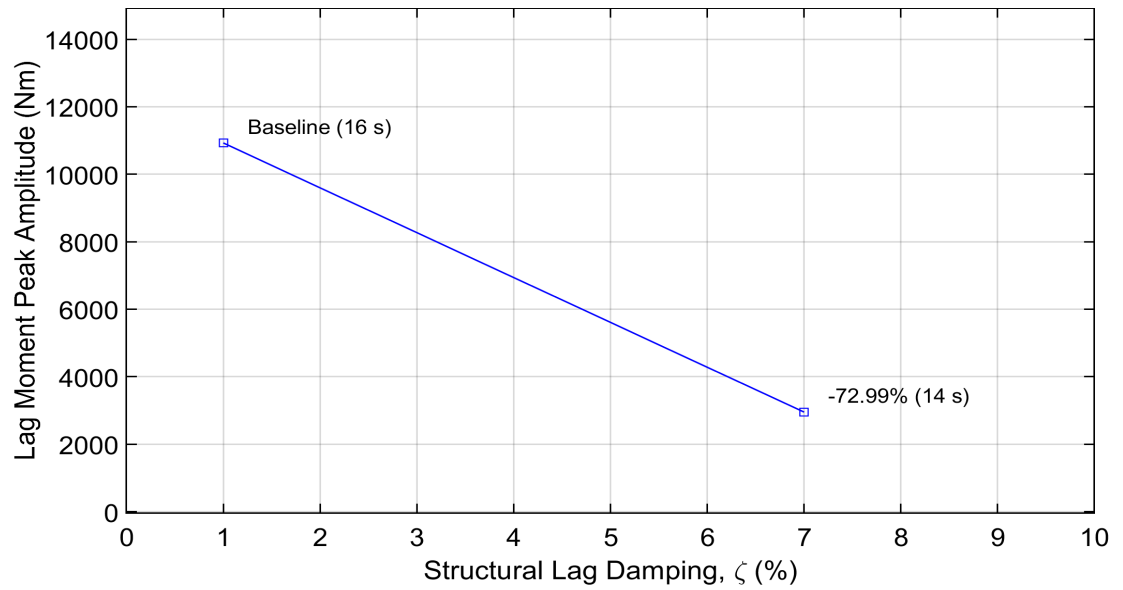


Figure 5.102: Resonance amplitude variation with ζ and t_T ($\mu_N = 0.2$; 230 \rightarrow 150 RPM)

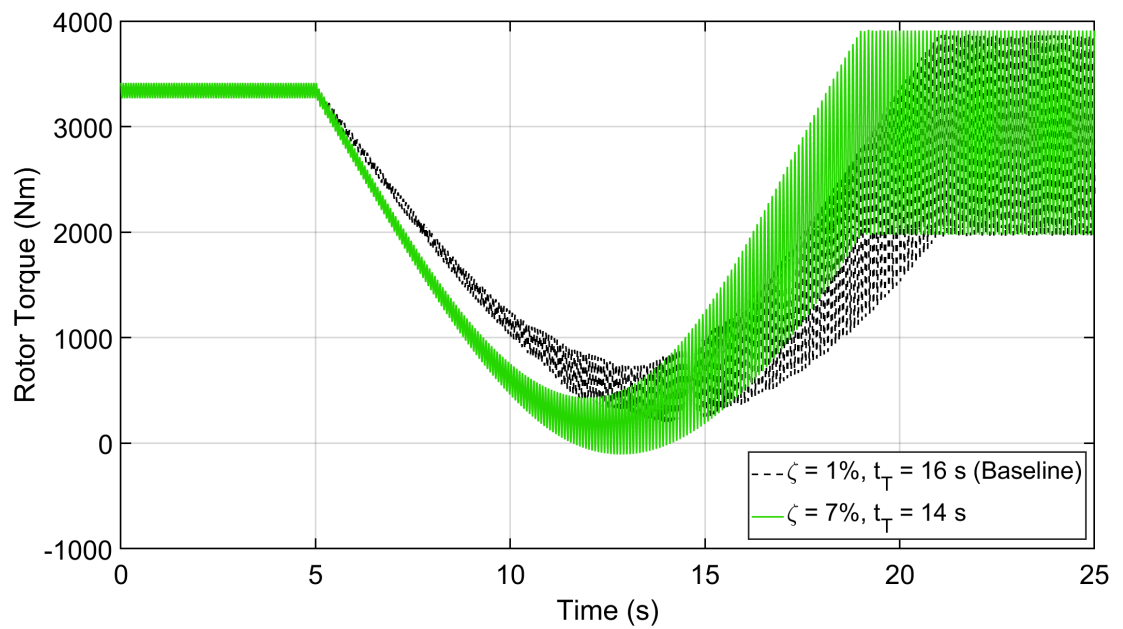


Figure 5.103: Effect of ζ and t_T on rotor torque ($\mu_N = 0.2$; 230 \rightarrow 150 RPM)

5.4.4 $\mu_N = 0.2, 150 \rightarrow 230$ RPM

The ideal transition time for this speed change scenario is 5 s, Table 5.2. The lag moment results are given in Figure 5.104. The peak amplitude is reduced by 74% as shown in Figure 5.105, which is 1.18% more than the reduction shown in Table 5.4. The torque increase is shown in Figure 5.106. The new peak is 95.42% higher than the baseline, Figure 5.107

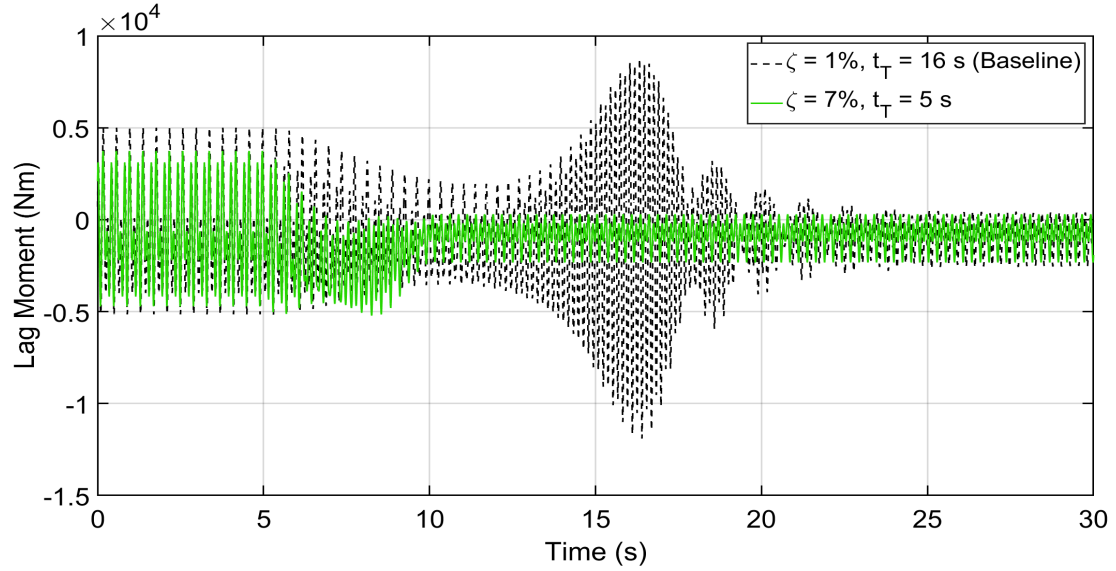


Figure 5.104: Effect of ζ and t_T on lag moment ($\mu_N = 0.2$; 150 \rightarrow 230 RPM)

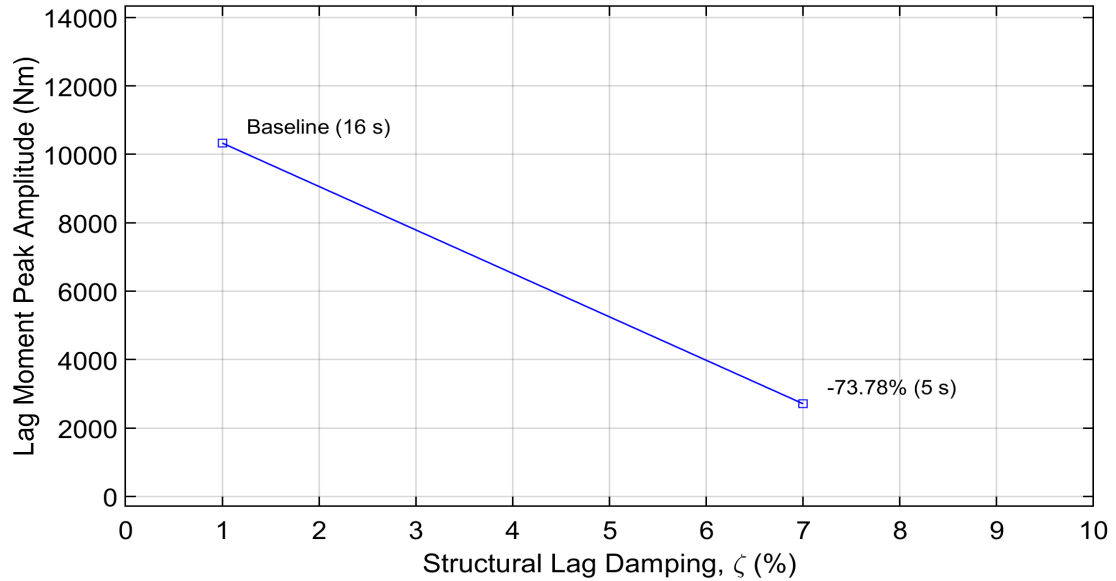


Figure 5.105: Resonance amplitude variation with ζ and t_T ($\mu_N = 0.2$; 150 \rightarrow 230 RPM)

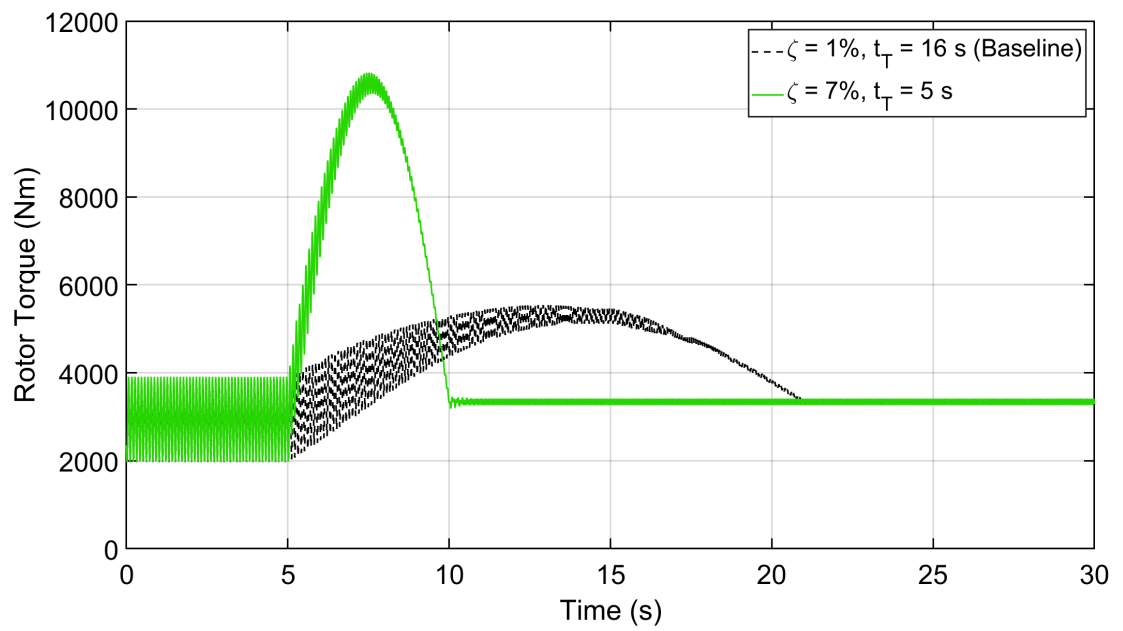


Figure 5.106: Effect of ζ and t_T on rotor torque ($\mu_N = 0.2$; 150 \rightarrow 230 RPM)

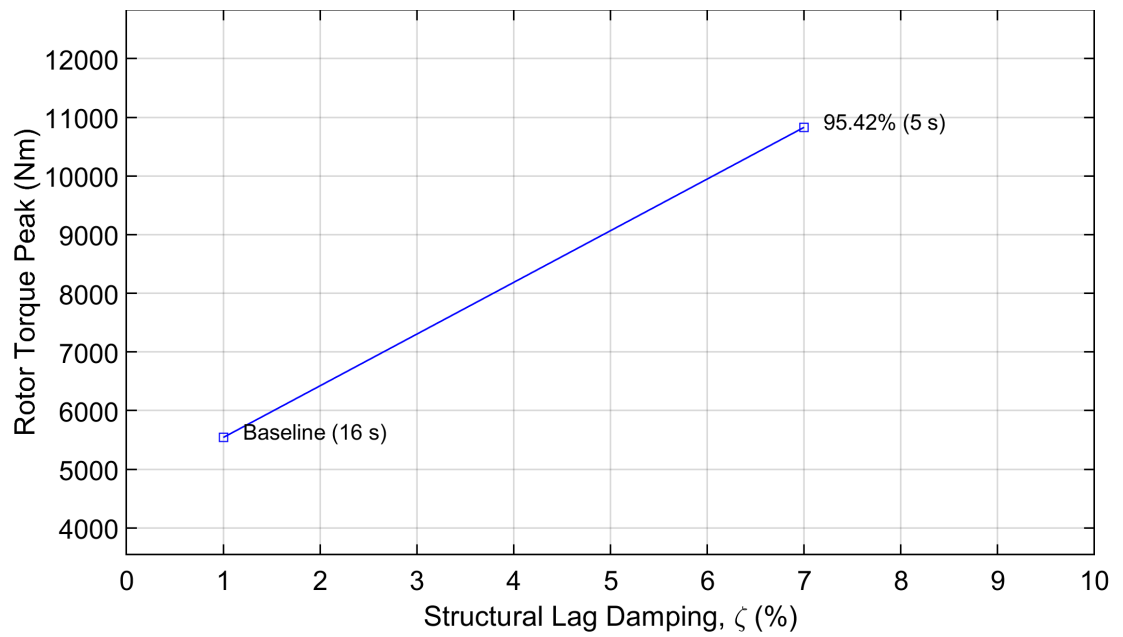


Figure 5.107: Rotor torque peak value during resonance ($\mu_N = 0.2$; 150 \rightarrow 230 RPM)

5.4.5 $\mu_N = 0.1, 230 \rightarrow 130$ RPM

The baseline transition time for the current case is 20 s and the ideal transition time is 13 s, Table 5.1. The lag moment response is shown in Figure 5.108. The second resonance has a higher magnitude as discussed previously. The peak amplitude of the second resonance is reduced by 70% as shown in Figure 5.109, almost the same as the Table 5.3 value. The rotor torque response is shown in Figure 5.110.

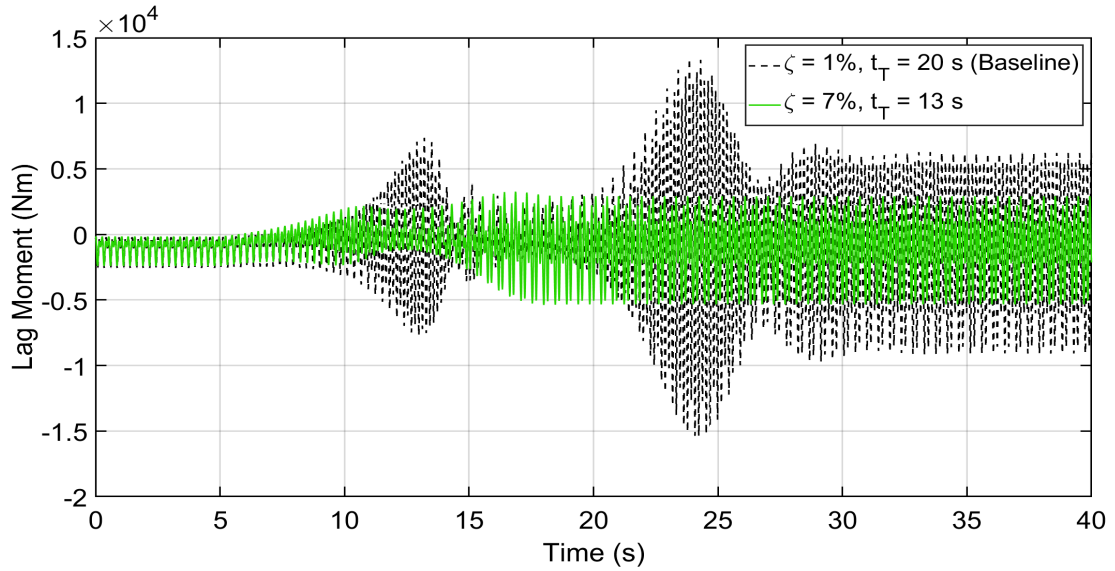


Figure 5.108: Effect of ζ and t_T on lag moment ($\mu_N = 0.1$; 230 \rightarrow 130 RPM)

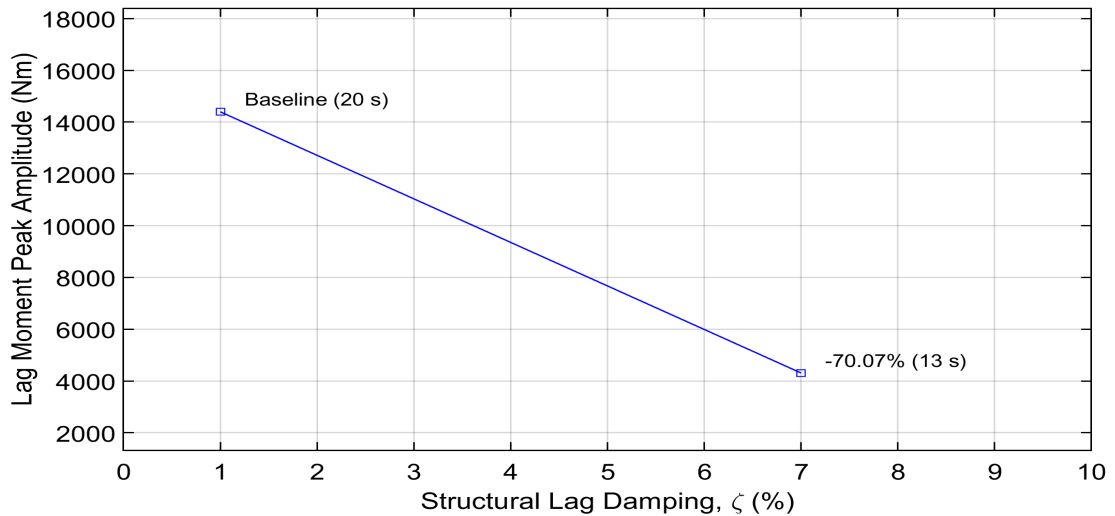


Figure 5.109: Resonance amplitude variation with ζ and t_T ($\mu_N = 0.1$; 230 \rightarrow 130 RPM)

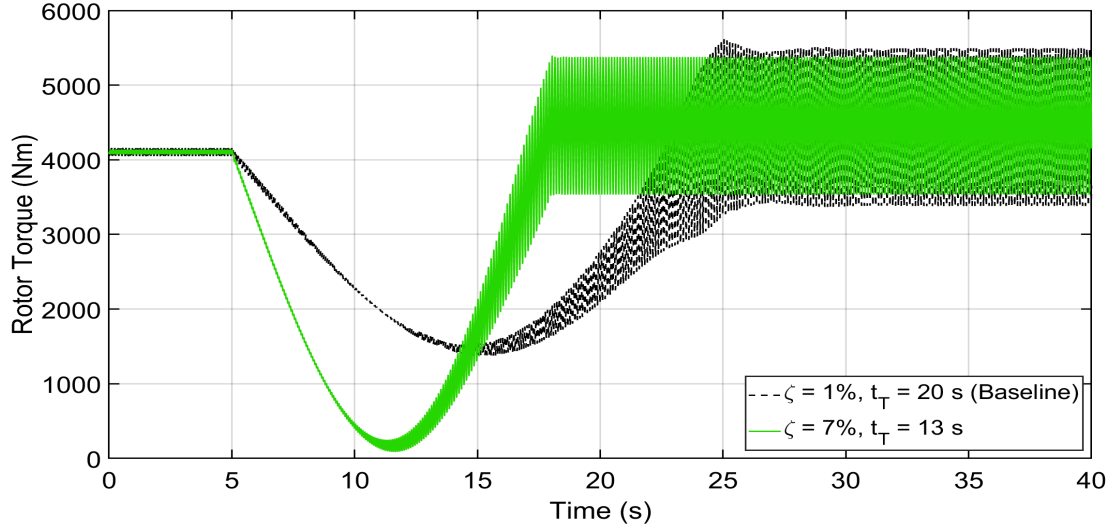


Figure 5.110: Effect of ζ and t_T on rotor torque ($\mu_N = 0.1$; 230 \rightarrow 130 RPM)

5.4.6 $\mu_N = 0.1$, 130 \rightarrow 230 RPM

The ideal transition time for this case is 7 s, Table 5.2. The lag moment results are given in Figure 5.111. The peak amplitude of the dominant first resonance is reduced by 70% as shown in Figure 5.112. The torque increases as shown in Figure 5.113. The new peak is about 70% higher than the baseline, Figure 5.114.

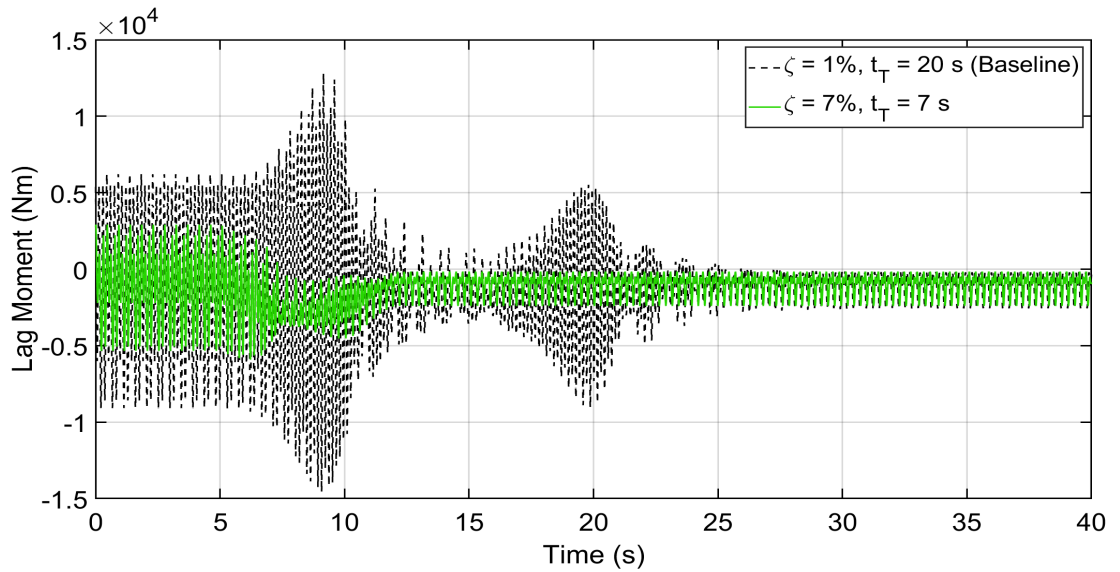


Figure 5.111: Effect of ζ and t_T on lag moment ($\mu_N = 0.1$; 130 \rightarrow 230 RPM)

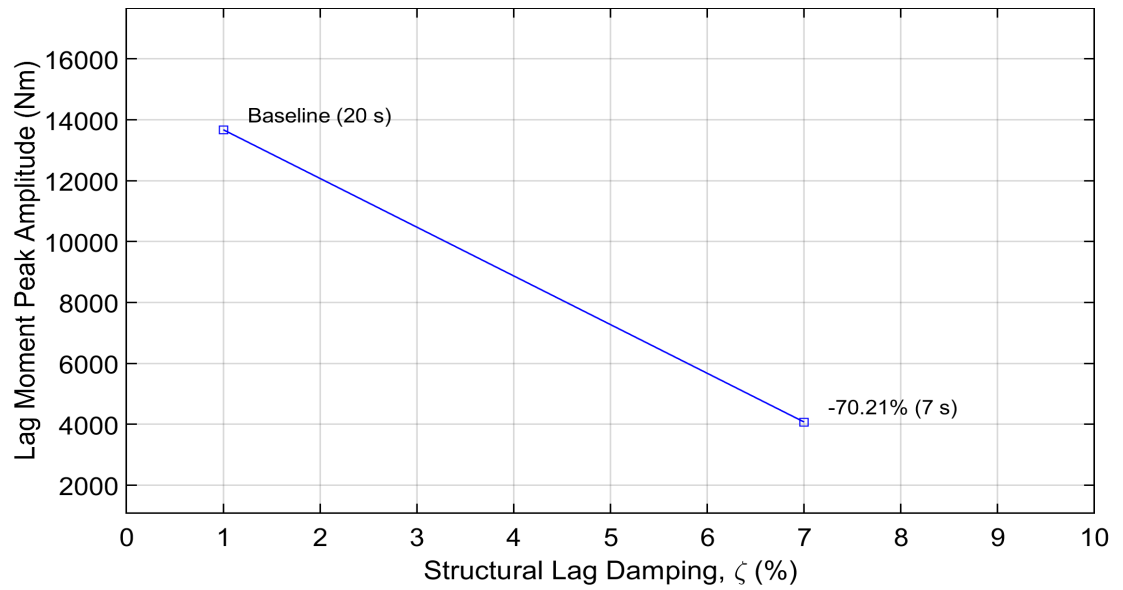


Figure 5.112: Resonance amplitude variation with ζ and t_T ($\mu_N = 0.1$; 130 \rightarrow 230 RPM)

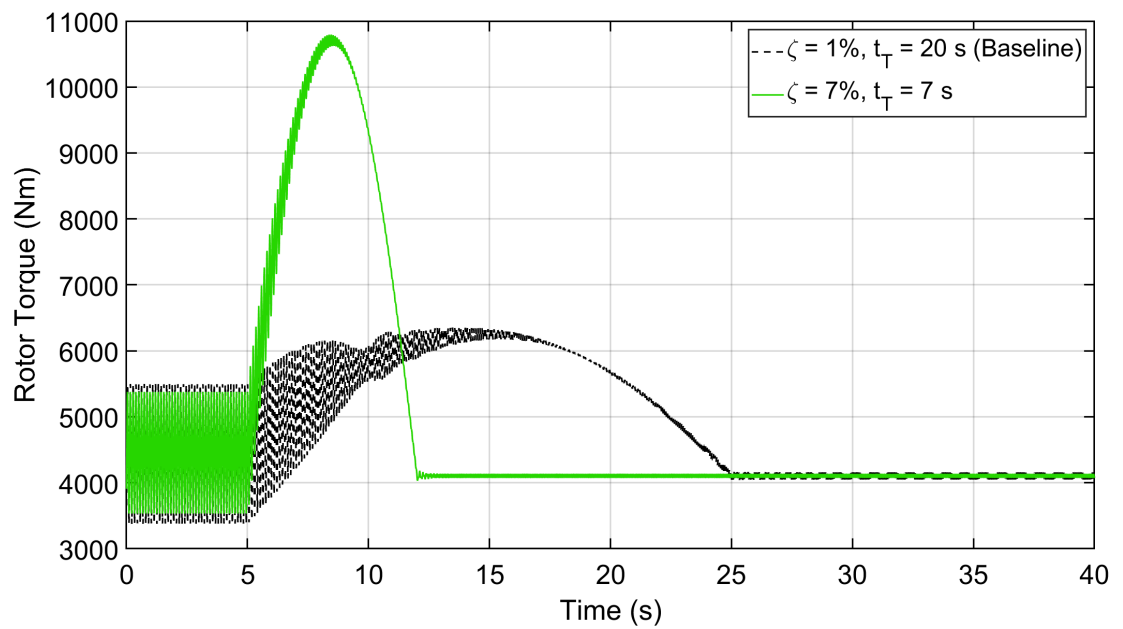


Figure 5.113: Effect of ζ and t_T on rotor torque ($\mu_N = 0.1$; 130 \rightarrow 230 RPM)

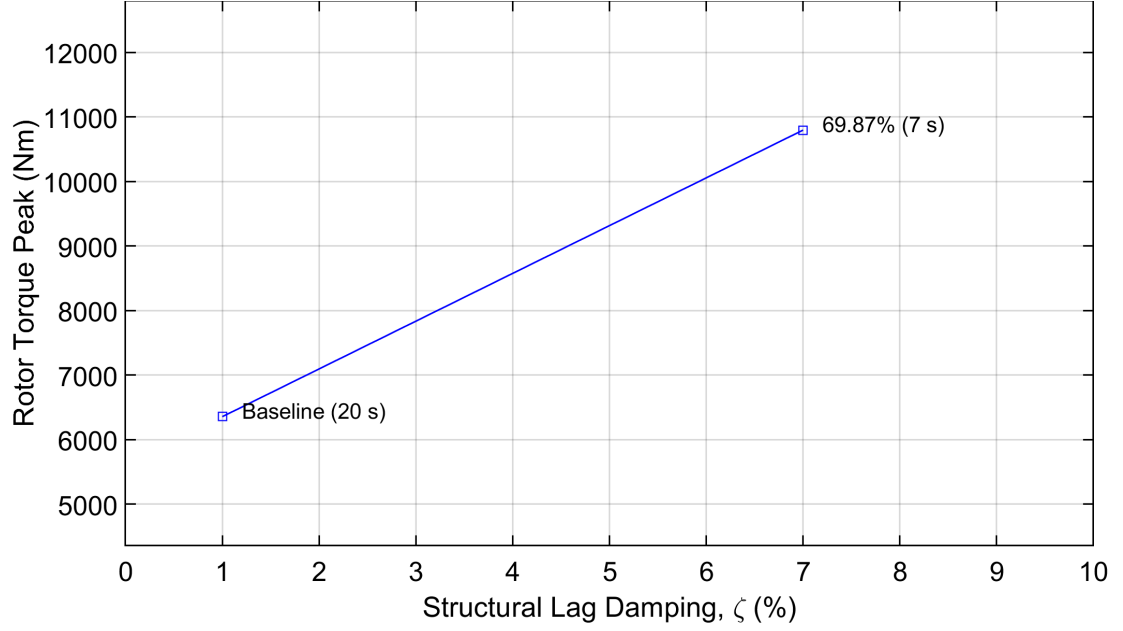


Figure 5.114: Rotor torque peak value during resonance ($\mu_N = 0.1$; 130 \rightarrow 230 RPM)

5.4.7 Combined Impact (ζ & t_T): Summary

The impact of the lag damping and transition time combination on resonances are given in Tables 5.8 and 5.9. The results from previous sections are also given here for comparison.

Table 5.8: ζ and t_T impact on high-to-low speed transition.

μ_N	Transition (RPM)	Lag moment amplitude reduction		
		$\zeta = 7\%$ alone	Ideal t_T alone	$\zeta = 7\%$ & Ideal t_T combined
0.3	230 \rightarrow 180	73.04%	5.55%	72.89%
0.2	230 \rightarrow 150	73.01%	3.50%	72.99%
0.1	230 \rightarrow 130 (Second Resonance)	70.20%	7.30%	70.07%

Combining the high damping cases with ideal transition times has the same effect as increasing the ζ alone. Therefore, increasing the structural damping using CNTs is an

Table 5.9: ζ and t_T impact on low-to-high speed transition.

μ_N	Transition (RPM)	Lag moment amplitude reduction		
		$\zeta = 7\%$ alone	Ideal t_T alone	$\zeta = 7\%$ & Ideal t_T combined
0.3	180 \rightarrow 230	70.31%	21.50%	70.96%
0.2	150 \rightarrow 230	72.60%	27.92%	73.78%
0.1	130 \rightarrow 230 (First Resonance)	70.32%	20.73%	70.21%

effective way to reduce resonance loads. Following the baseline transition times also means that the sharp rotor torque increase during quick transitions can be avoided.

CHAPTER 6

ANTI-RESONANCE SYSTEM (ARS)

In this chapter, a new blade concept is introduced. Let us assume that there is a sliding mass inside the blade that can travel along the length of the blade. The mass moves on a rail, which runs along the length and deforms with the blade. A schematic of this system is shown in Figure 6.1, by cutting a top section of the blade. Let us assume that the mass can be moved to the desired location using a mechanical control system, without going into the details, for the sake of simplicity. By changing the location of the mass along the length, the mass moment of inertia of the blade about the vertical axis is altered. Changing the mass moment of inertia of the blade changes the natural frequency of the blade. Varying the natural frequency, in turn, changes the resonance crossings. Hence, the new blade can actively change the location of its resonance points. This moving mass system inside the blade will be referred to as the Anti-Resonance System (ARS) and the new blade will be called as the ARS blade. If the mass and location of the moving mass are carefully selected, it is possible to move the resonance point out of the rotor operating range.

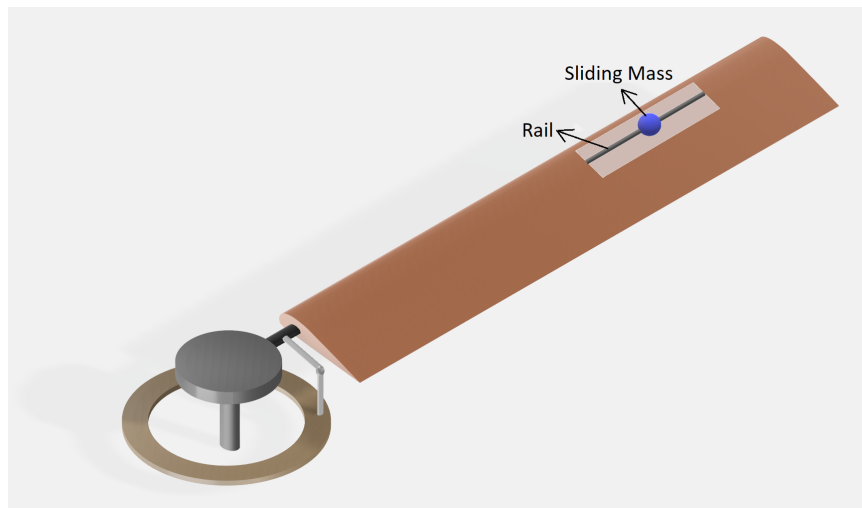


Figure 6.1: Schematic of a hingeless blade with sliding mass.

It should be mentioned here that a concentrated mass was used in [164] to change the

twist angle of a rotating blade, which is different from what is attempted in the present work.

The moving mass is modeled as a point mass in DYMORE, Figure 6.2, and the sliding motion is defined using the prismatic joint definition. The stiffness of the rail is assumed to be small compared to the blade and hence, neglected. The mass is assumed to be located on the beam's reference line. The mass properties of the ARS blade are selected such that the first lag frequency remains close to the baseline blade as shown in Figure 6.3. These properties are given in Table 6.1. The total mass of the blade is maintained the same, which makes it easier to compare with the previous results.

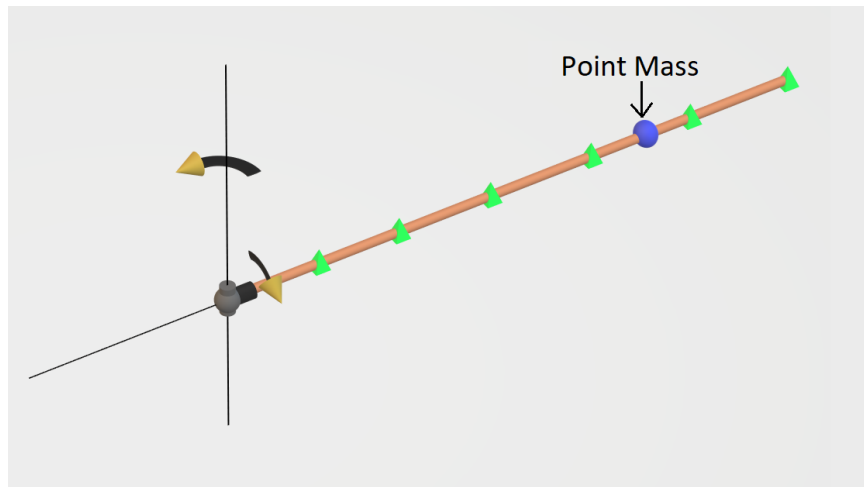


Figure 6.2: Blade model in DYMORE with sliding point mass.

Table 6.1: Mass properties: Baseline vs. ARS Blade.

Blade Property	Baseline Blade	ARS Baseline Blade
Sliding mass, m_s (kg)	0	15
Location of sliding mass, x_m (m)	-	4.16
Mass/length (kg/m)	10	7.5
Total mass (kg)	60	60

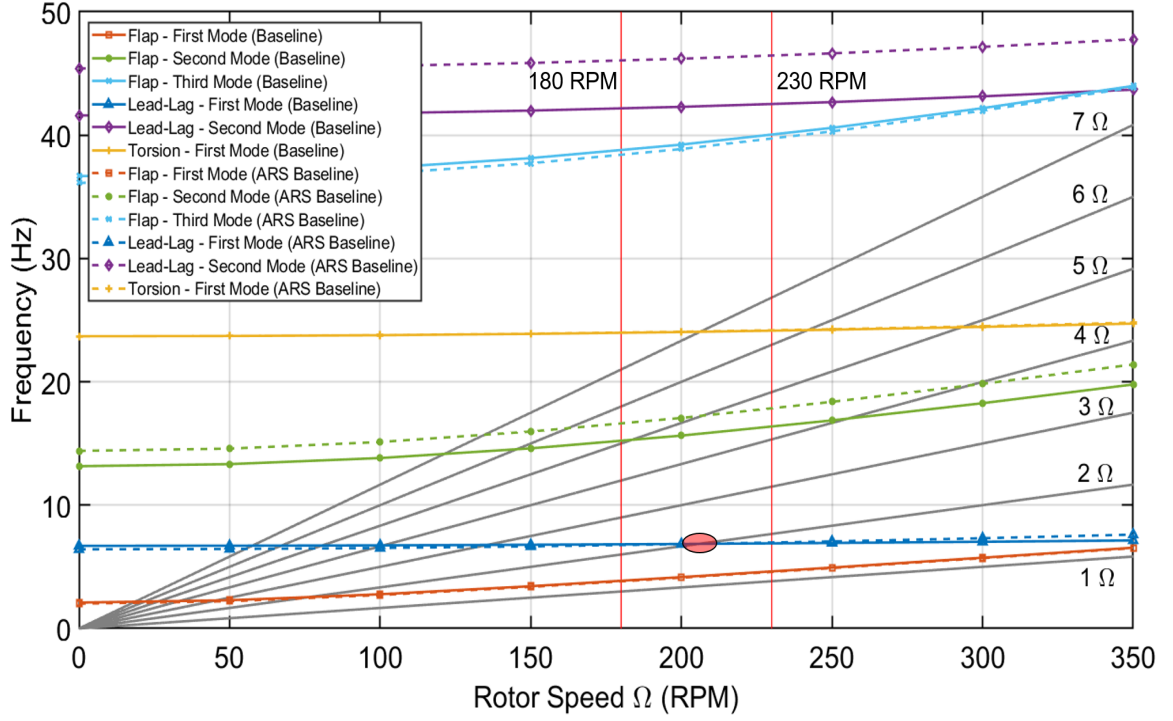


Figure 6.3: Fan plot: Baseline vs ARS Baseline ($\mu_N = 0.3$)

6.1 $\mu_N = 0.3, 230 \rightarrow 180$ RPM

The baseline location of the sliding mass is given in Table 6.1. As the rotor speed is changed from 230 to 180 RPM in 10 s, the sliding mass is moved from 4.16 m to 5.90 m, towards the tip. This displacement occurs in a smooth manner as shown in Figure 6.4 to avoid any sharp changes to the rotor torque. As the mass is moved towards the tip, the natural frequency decreases. Therefore, the 2/rev lag resonance point located inside the rotor operating range is moved out of range as shown in the fan plot, Figure 6.5.

The lag moment response is shown in Figure 6.6. It can be seen that the ARS blade has no significant amplitude increase during this transition due to the absence of 2/rev resonance point. In comparison, the amplitude is decreased by almost 83% from the baseline blade as shown in Figure 6.7, which is more than what was achieved using 7% lag damping.

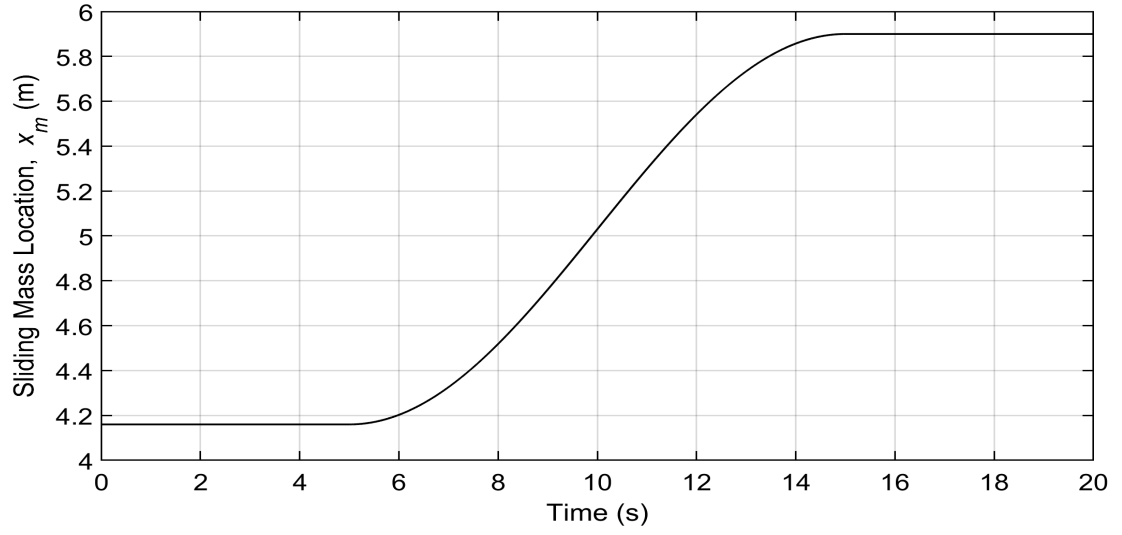


Figure 6.4: Location of sliding mass with time ($\mu_N = 0.3$; $230 \rightarrow 180$ RPM)

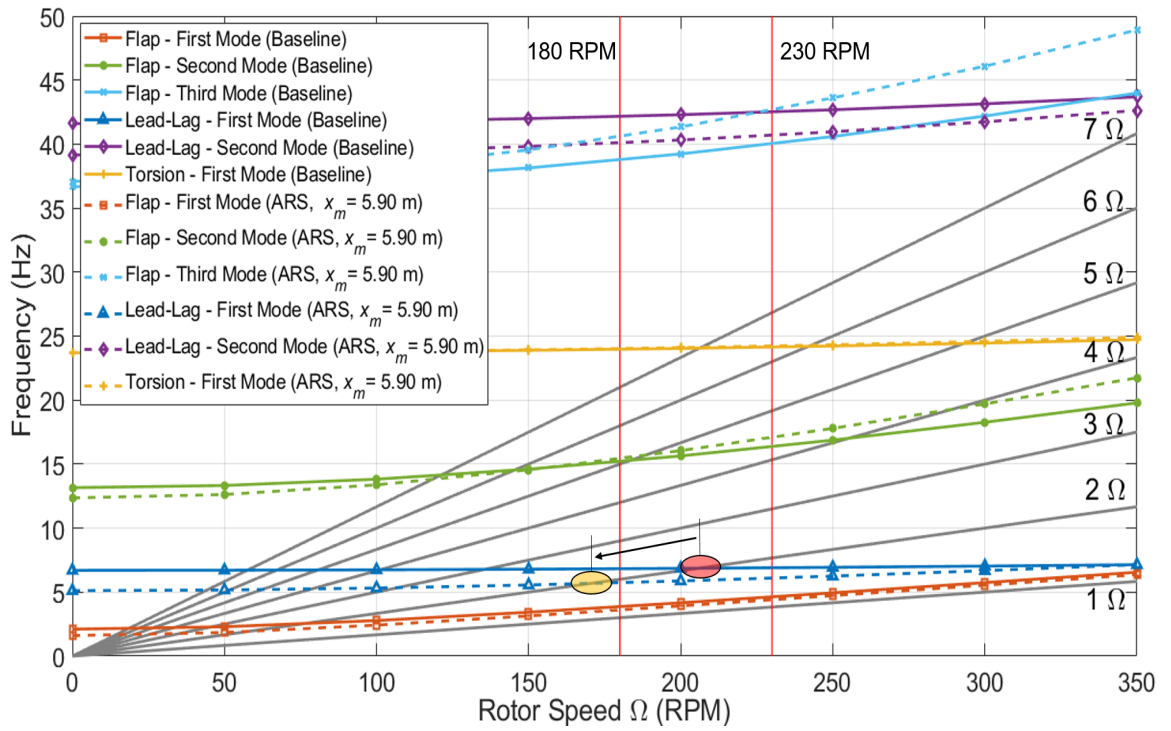


Figure 6.5: Fan plot: Baseline vs. ARS with mass at tip ($\mu_N = 0.3$)

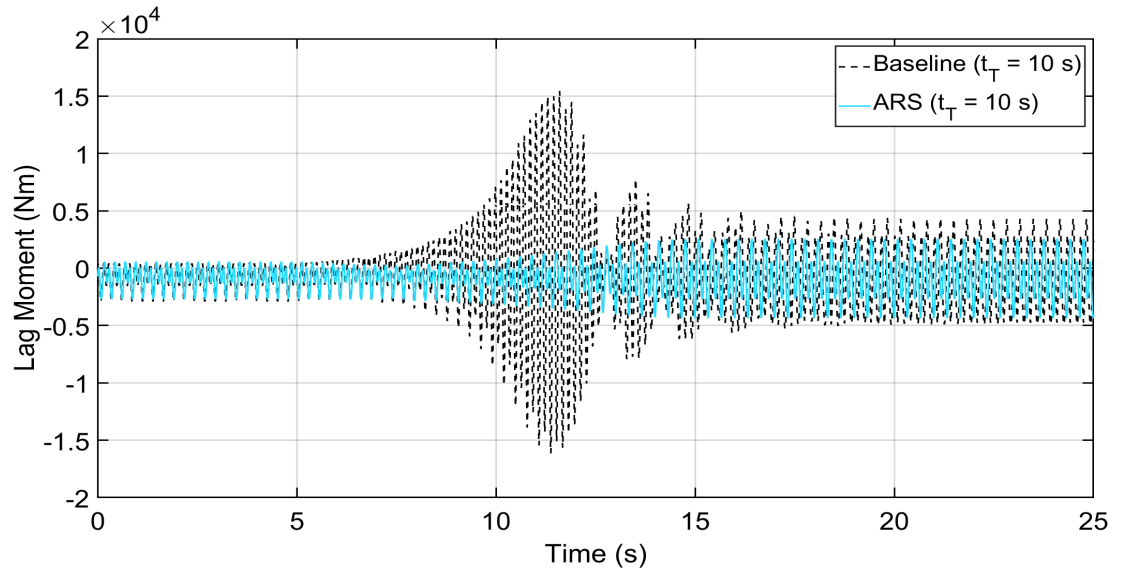


Figure 6.6: Lag moment: Baseline vs. ARS ($\mu_N = 0.3$; $230 \rightarrow 180$ RPM)

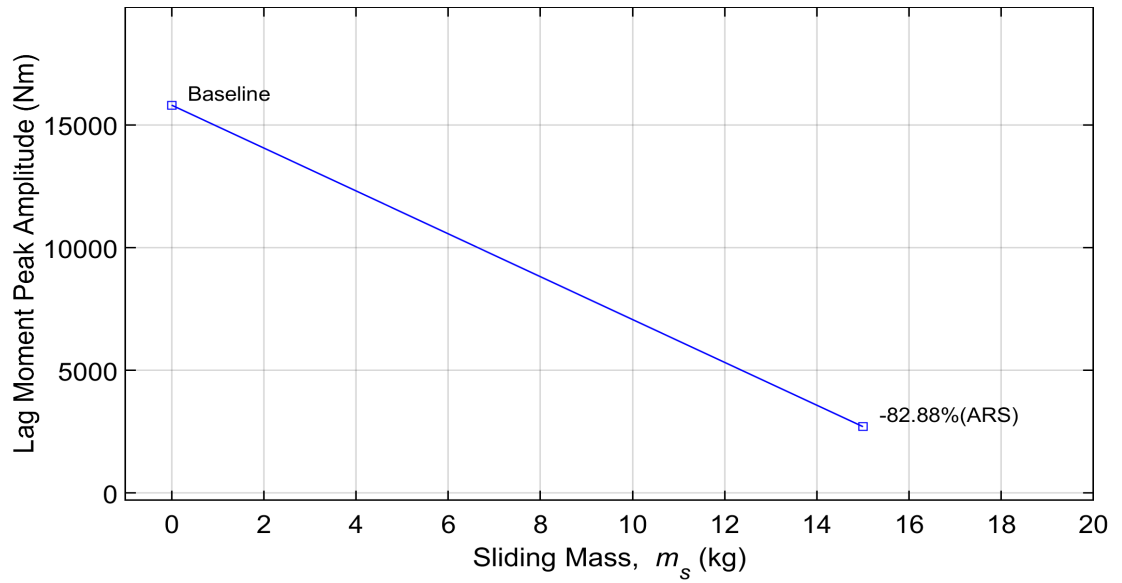


Figure 6.7: Peak amplitude: Baseline vs. ARS ($\mu_N = 0.3$; $230 \rightarrow 180$ RPM)

The rotor torque has a peculiar behavior compared to the previous cases. As the mass is moved towards the tip, the rotor has a natural tendency to slow down due to conservation of angular momentum. Hence, the torque need not dip significantly as in the baseline case. In fact, the torque is required to increase slightly during this transition to prevent the rotor from slowing down too fast, Figure 6.8.

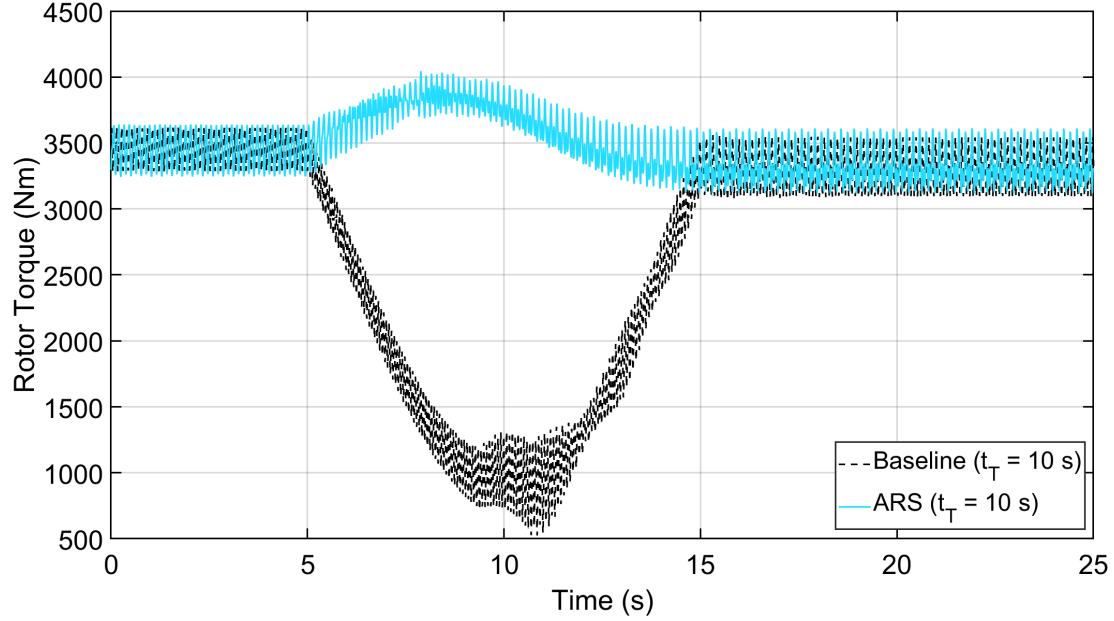


Figure 6.8: Rotor torque: Baseline vs. ARS ($\mu_N = 0.3$; 230 \rightarrow 180 RPM)

6.2 $\mu_N = 0.3$, 180 \rightarrow 230 RPM

For the reverse transition, the mass is moved back to its previous location as shown in Figure 6.9. The resonance point is located behind the rotor operating speed at 180 RPM, Figure 6.10. The mass location with time is defined such that the 2/rev lag resonance always stays behind the rotor operating speed during the low-to-high speed transition.

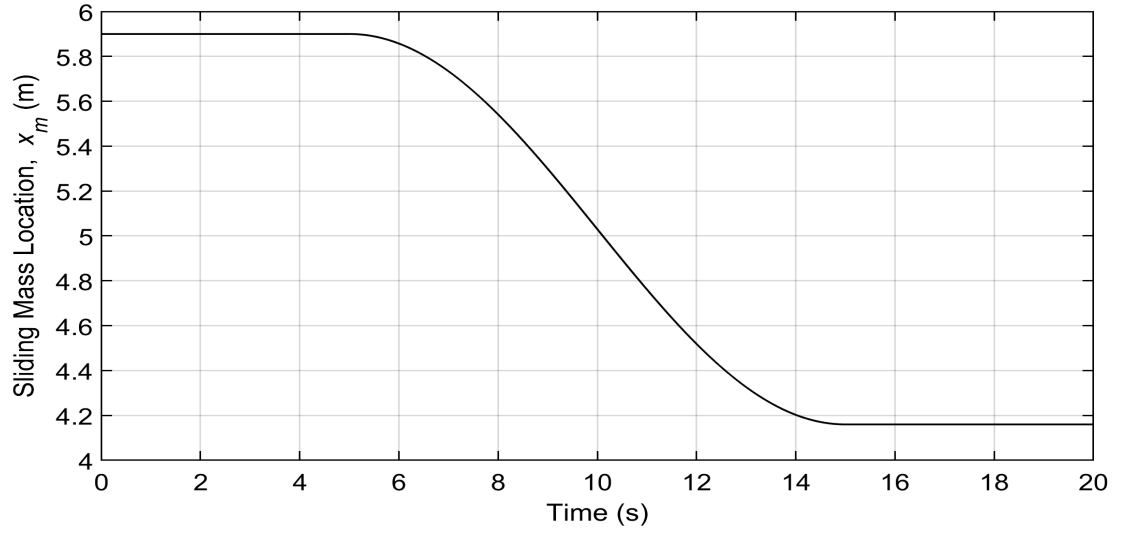


Figure 6.9: Location of sliding mass with time ($\mu_N = 0.3$; $180 \rightarrow 230$ RPM)

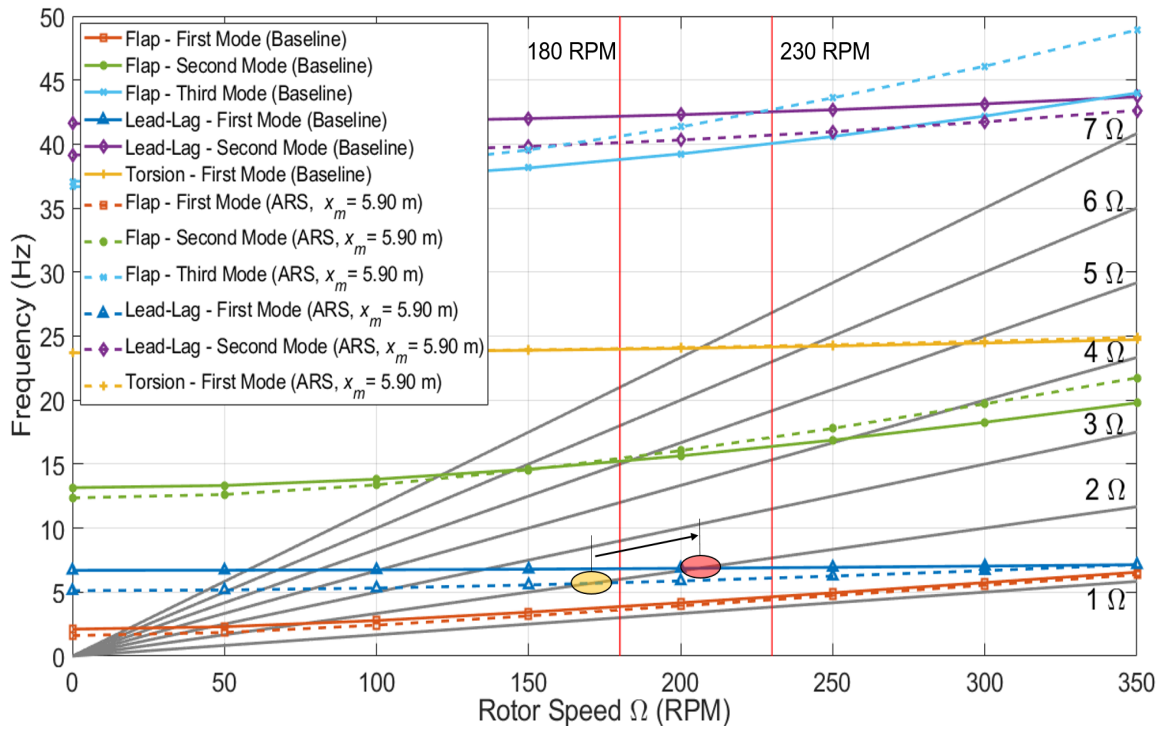


Figure 6.10: Fan plot: Baseline vs. ARS with mass at tip ($\mu_N = 0.3$)

The lag moment comparison is shown in Figure 6.11. Once again, the ARS blade shows no significant amplitude increase. The amplitude is decreased by almost 86% from the baseline blade as shown in Figure 6.12.

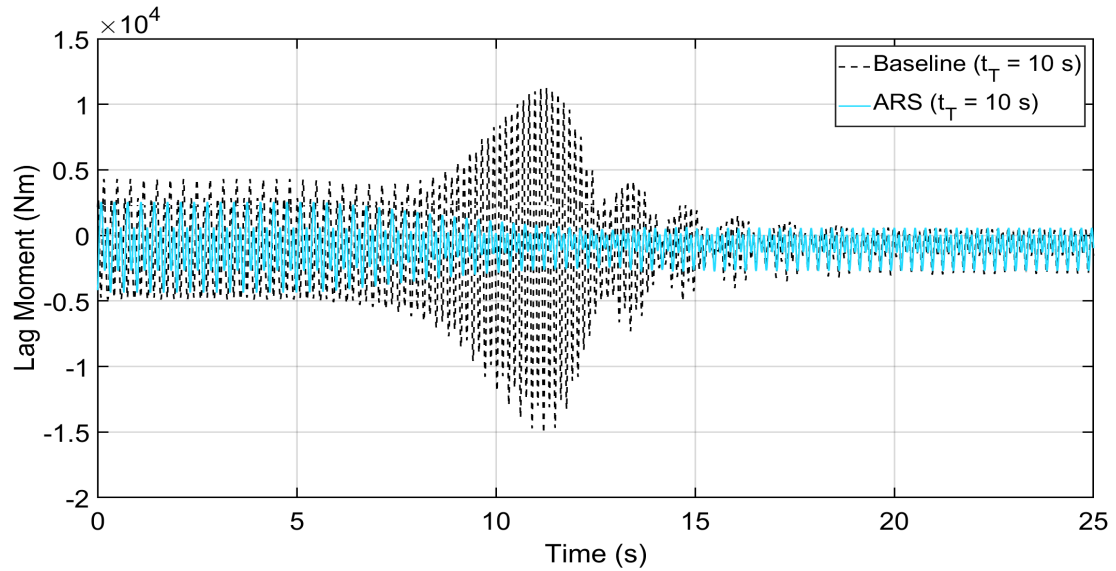


Figure 6.11: Lag moment: Baseline vs. ARS ($\mu_N = 0.3$; 230 \rightarrow 180 RPM)

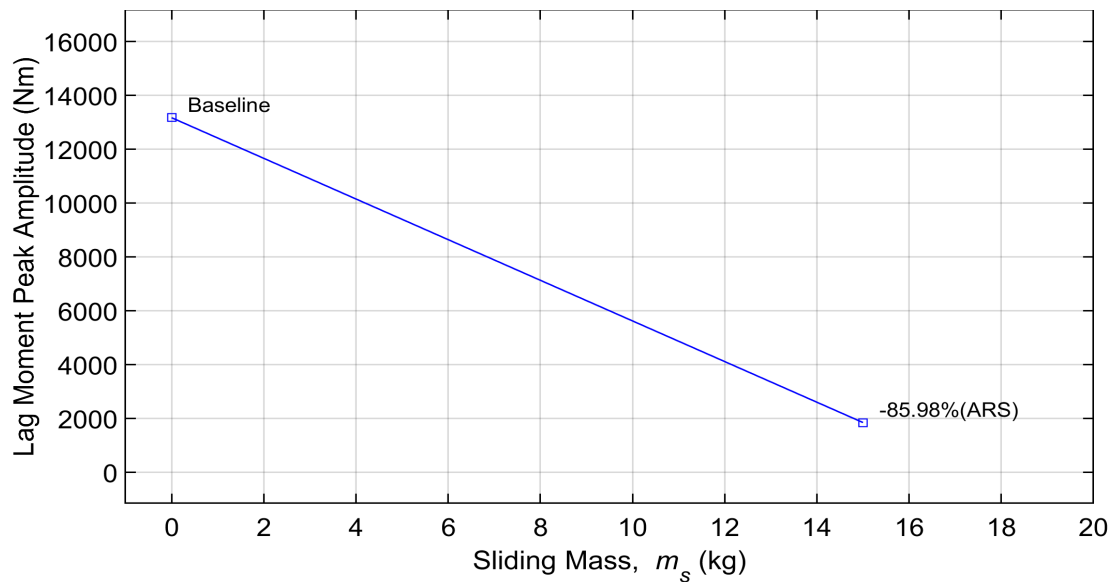


Figure 6.12: Peak amplitude: Baseline vs. ARS ($\mu_N = 0.3$; 230 \rightarrow 180 RPM)

The rotor torque response is shown in Figure 6.13. In this case, as the mass is moved towards the center, the rotor has a natural tendency to speed up. As can be seen from Figure

6.13, the torque is in fact required to decrease slightly during this transition to prevent the rotor from speeding up too fast. Hence, using the ARS system, the lag resonance is completely removed from the transition range and the torque increase required is also decreased significantly.

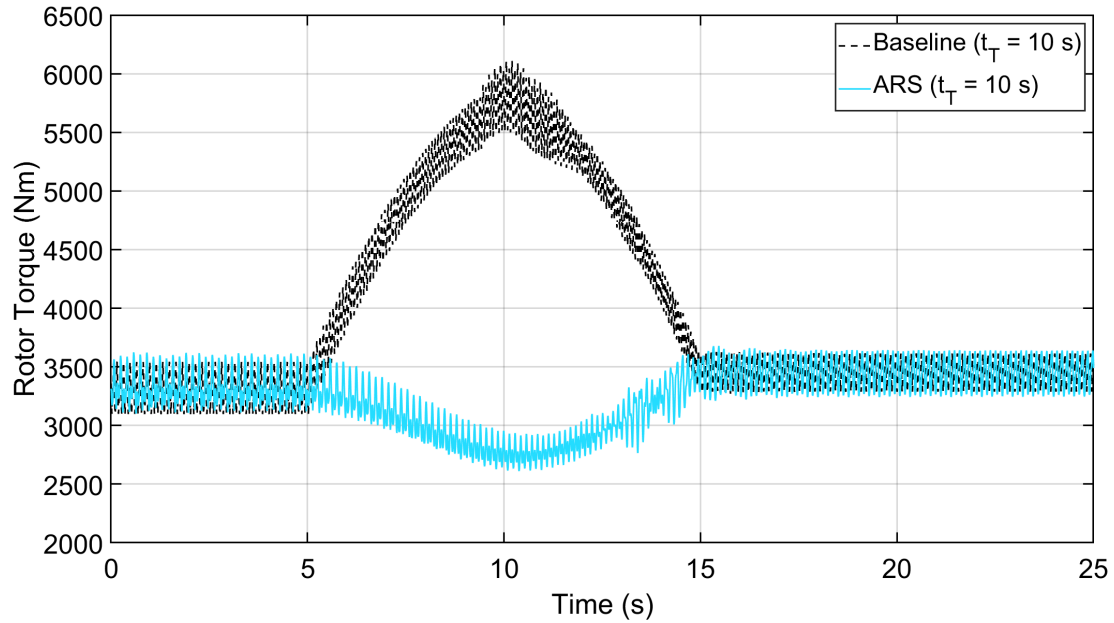


Figure 6.13: Rotor torque: Baseline vs. ARS ($\mu_N = 0.3$; $230 \rightarrow 180$ RPM)

6.3 $\mu_N = 0.2$, $230 \rightarrow 150$ RPM

At this lower forward speed, the range of rotor speed change is wider. Therefore, with the existing parameters of the ARS system it is not possible to move the 2/rev crossing below 150 RPM, as shown in Figure 6.14.

The rotor needs to travel through the resonance as the speed is changed from 230 RPM to 150 RPM. The location of the sliding mass remains constant at the baseline location as shown in Figure 6.15.

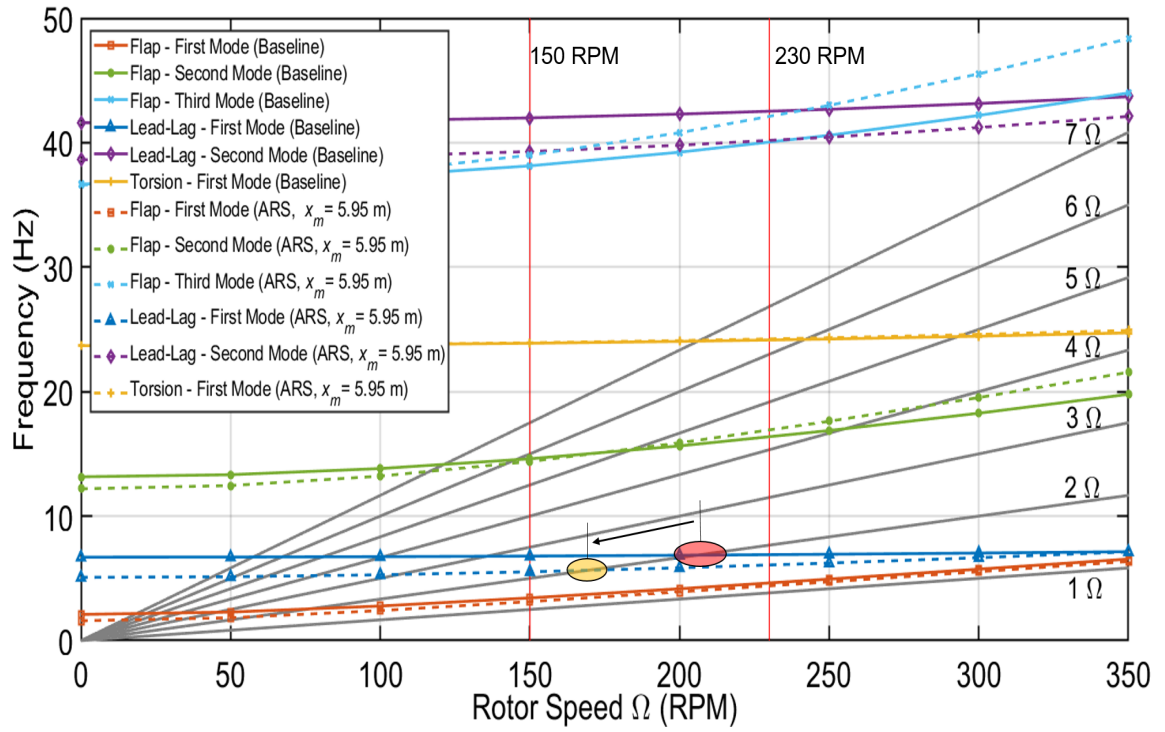


Figure 6.14: Fan plot: Baseline vs. ARS with mass at tip ($\mu_N = 0.2$)

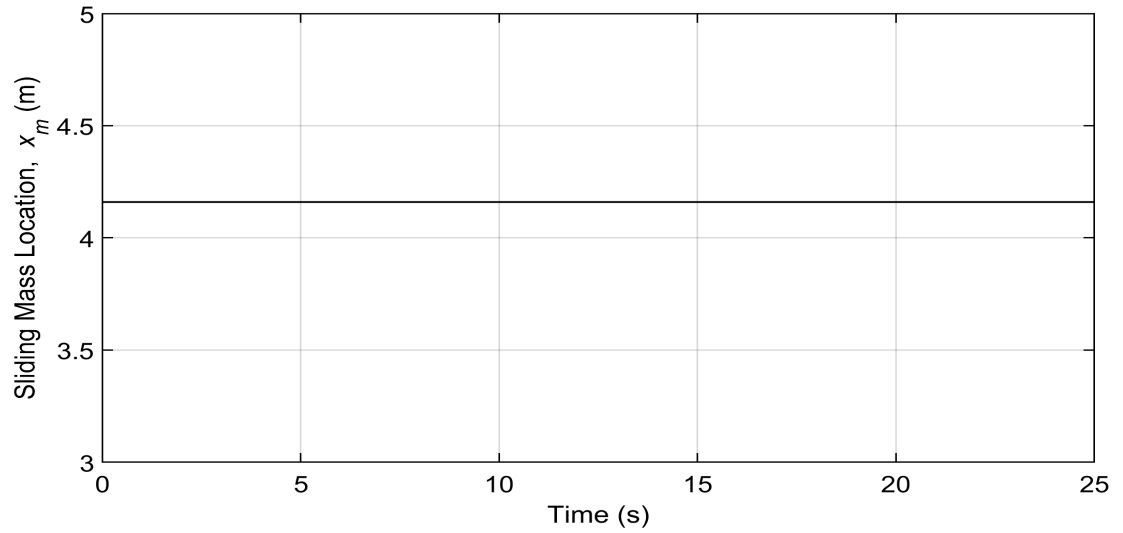


Figure 6.15: Location of sliding mass with time ($\mu_N = 0.2$; 230 \rightarrow 150 RPM)

The lag moment response is shown in Figure 6.16. The rotor torque response is shown in Figure 6.17. It can be seen that the ARS blade has a greater amplitude increase during resonance. This is because of the presence of concentrated masses. The deformation of the blade depends on its azimuth location. As each blade has a different deformation at any instance, the presence of concentrated masses is causing the dissimilarity of the rotor to increase. This dissimilarity is causing an increase in resonance loads. Such a resonance response can also be seen in [18]. The rotor torque exceeds the acceptable limit.

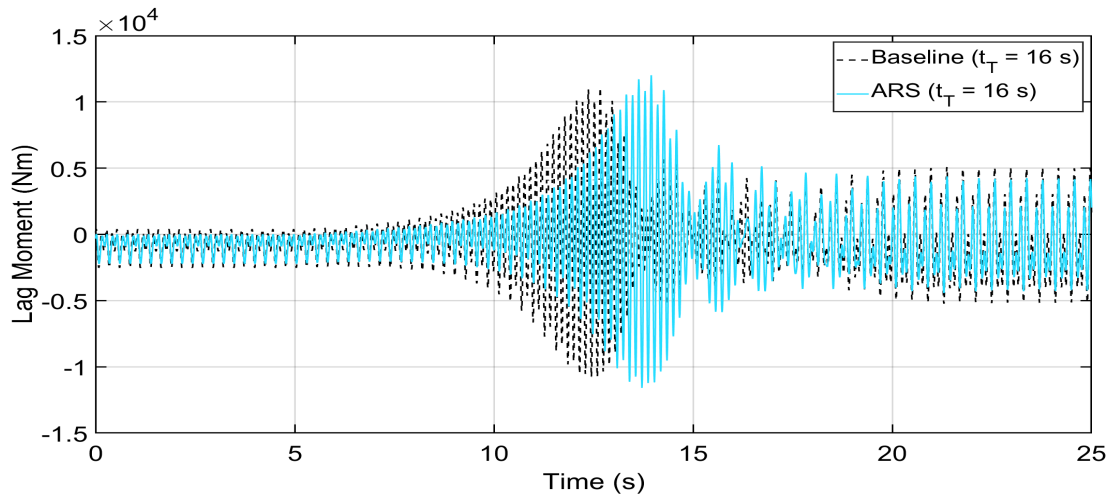


Figure 6.16: Lag moment through resonance: Baseline vs. ARS ($\mu_N = 0.2$; 230 \rightarrow 150 RPM)

In order to reduce the torque amplitude during resonance, the lag damping of the rotor is increased from 1% to 3%. The transition time is changed from 16 s to 25 s. The fan plot with 3% lag damping is shown in Figure 6.18, the frequency doesn't change significantly due to increased damping.

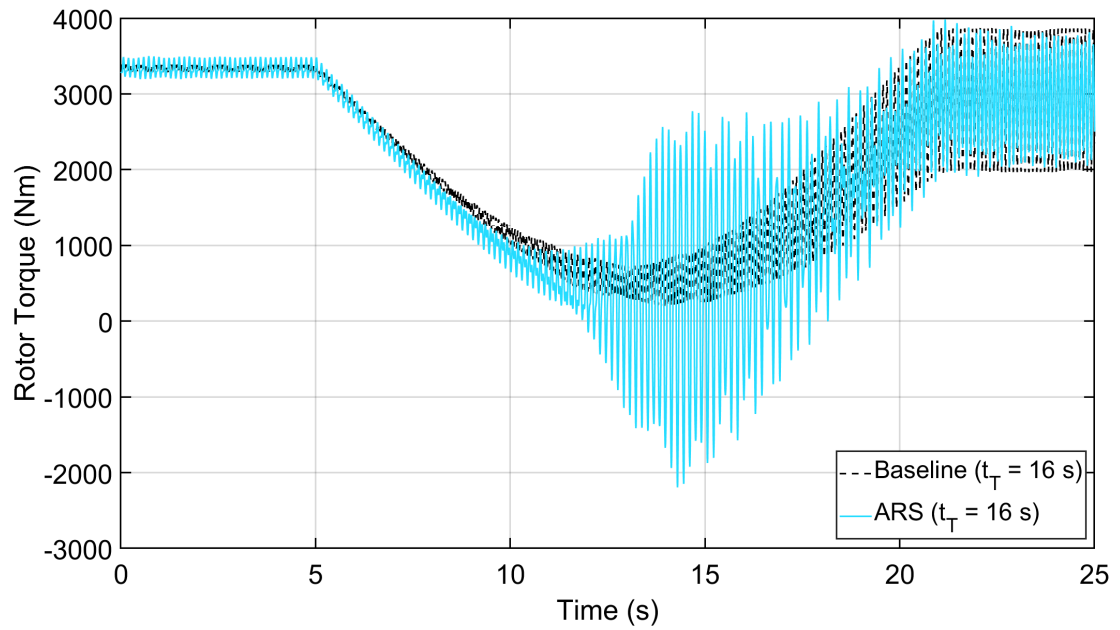


Figure 6.17: Rotor torque through resonance: Baseline vs. ARS ($\mu_N = 0.2$; $230 \rightarrow 150$ RPM)

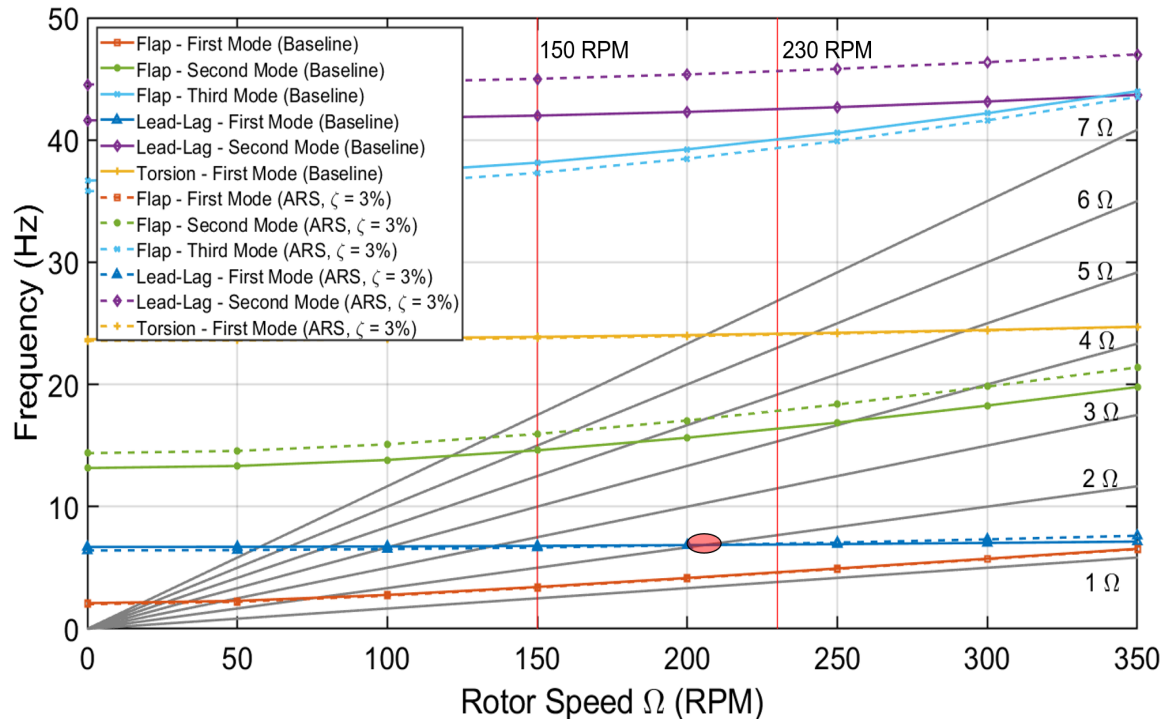


Figure 6.18: Fan plot: Baseline vs. ARS with 3% lag damping ($\mu_N = 0.2$)

The results of the increased damping case is shown below. The lag response is shown in Figure 6.19. The amplitude during resonance is decreased by 36% from the baseline due to increased damping, Figure 6.20. The rotor torque is within the acceptable limits as shown in Figure 6.21.

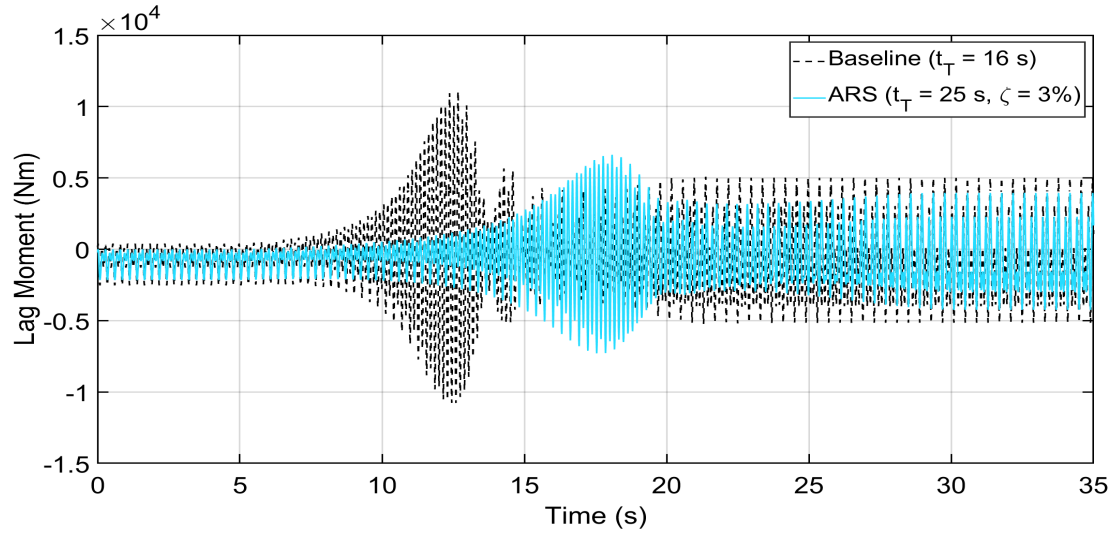


Figure 6.19: Lag moment through resonance: Baseline vs. ARS with 3% lag damping ($\mu_N = 0.2$; 230 \rightarrow 150 RPM)

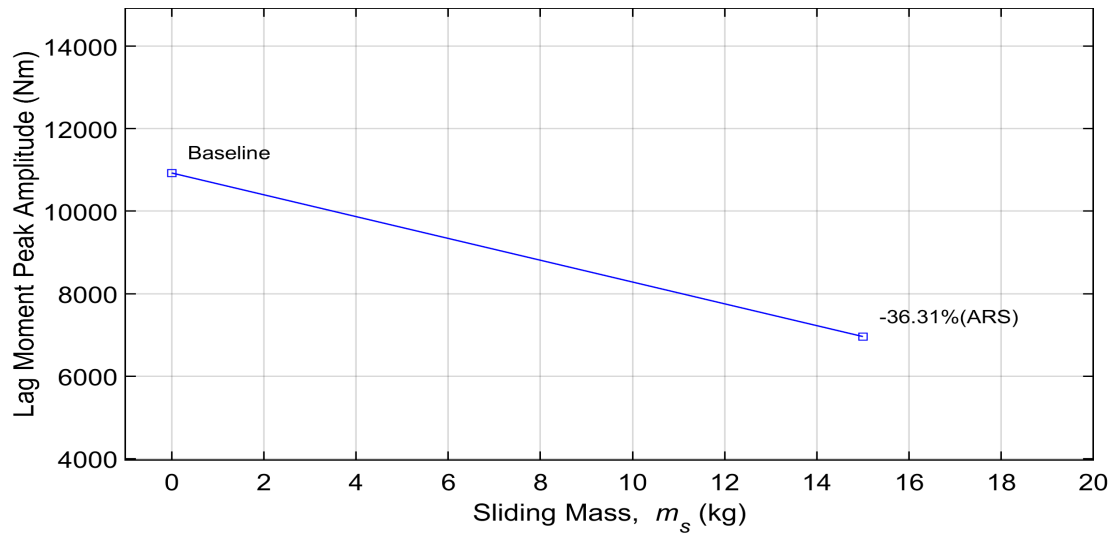


Figure 6.20: Peak amplitude through resonance: Baseline vs. ARS with 3% lag damping ($\mu_N = 0.2$; 230 \rightarrow 150 RPM)

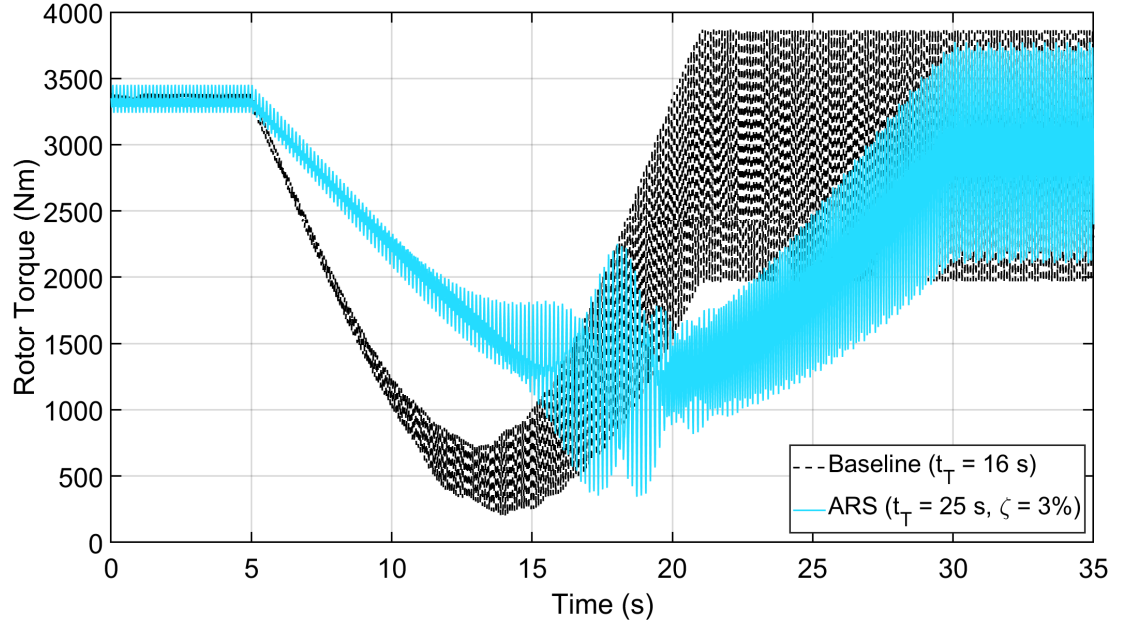


Figure 6.21: Rotor torque through resonance: Baseline vs. ARS with 3% lag damping ($\mu_N = 0.2$; 230 \rightarrow 150 RPM)

6.4 $\mu_N = 0.2$, 150 \rightarrow 230 RPM

However, as the rotor speed is changed from lower to higher RPM, it is possible to move the resonance point up and beyond the nominal rotor speed. The sliding mass needs to be moved inwards to increase the natural frequency. By moving the mass from the baseline location to the root, the natural frequency is moved up as shown in Figure 6.22. The mass location for this transition is shown in Figure 6.23.

The lag moment response is shown in Figure 6.24. It can be seen that the ARS blade has no significant amplitude increase during this transition due to the absence of 2/rev resonance point. In comparison, the amplitude is decreased by 76% from the baseline blade as shown in Figure 6.25.

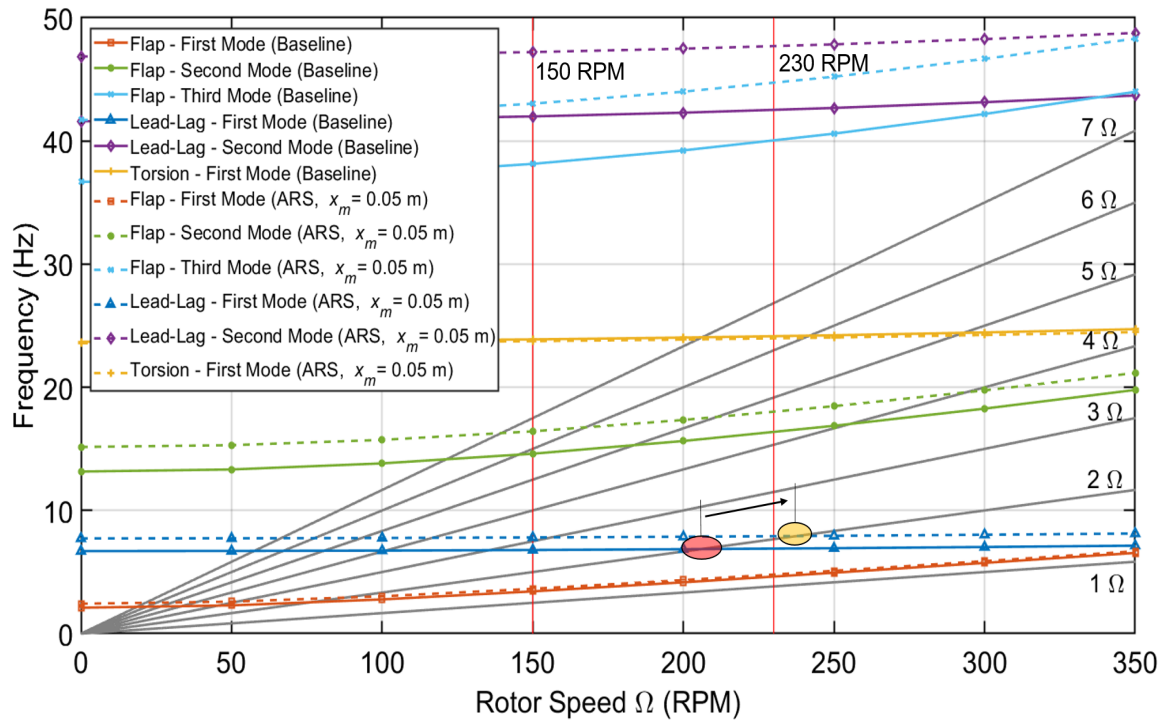


Figure 6.22: Fan plot: Baseline vs. ARS with mass at root ($\mu_N = 0.2$, $\zeta = 3\%$)

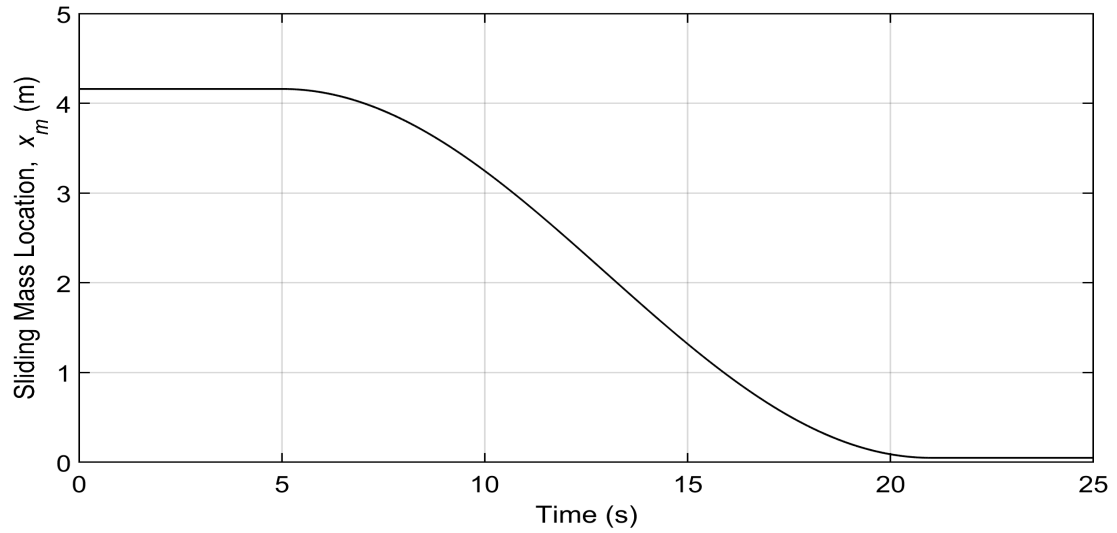


Figure 6.23: Location of sliding mass with time ($\mu_N = 0.2$; 150 \rightarrow 230 RPM)

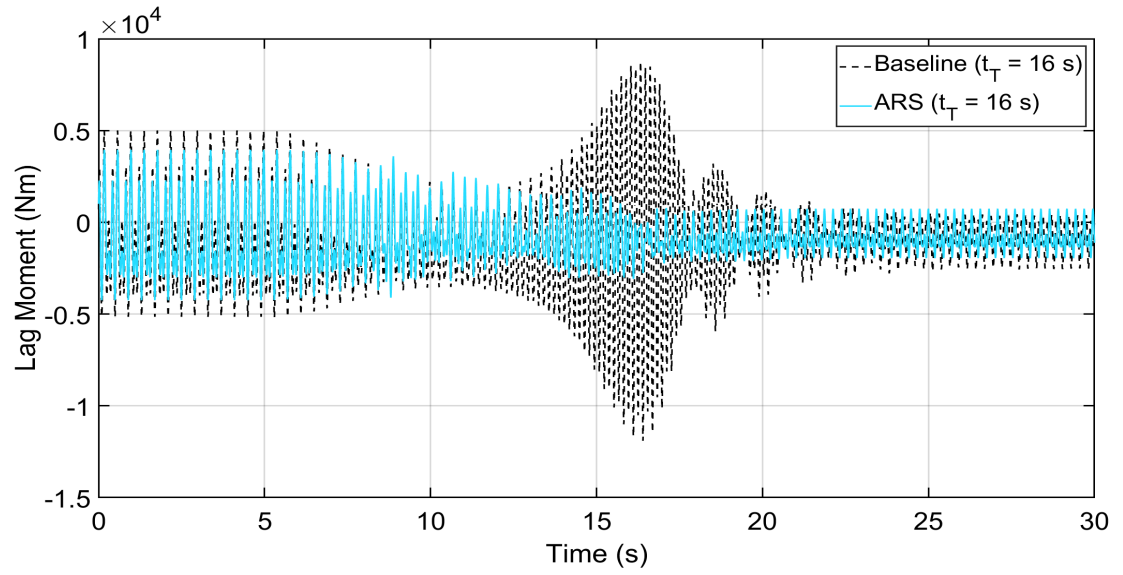


Figure 6.24: Lag moment: Baseline vs. ARS ($\mu_N = 0.2$; $230 \rightarrow 150$ RPM; $\zeta = 3\%$)

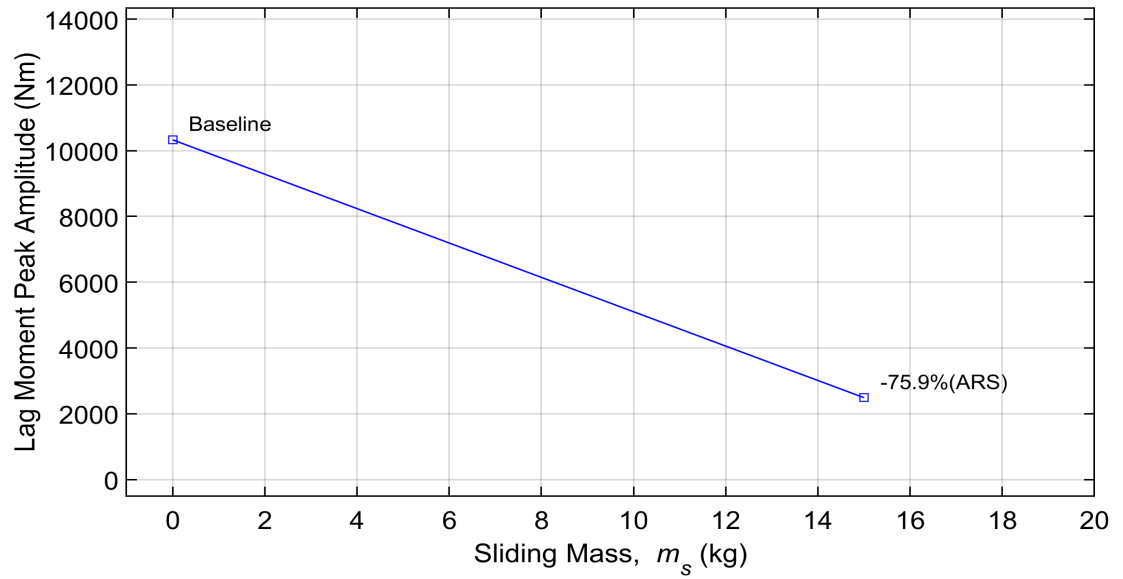


Figure 6.25: Peak amplitude: Baseline vs. ARS ($\mu_N = 0.2$; $230 \rightarrow 150$ RPM; $\zeta = 3\%$)

The rotor torque response is shown in Figure 6.26. As the mass is moved towards the root, the rotor has a natural tendency to speed up. Initially, the torque decreases slightly as seen in Figure 6.26 to prevent the rotor from speeding up too fast. The torque increases later during the transition and approaches the baseline response. The torque response is not as smooth as the baseline case.

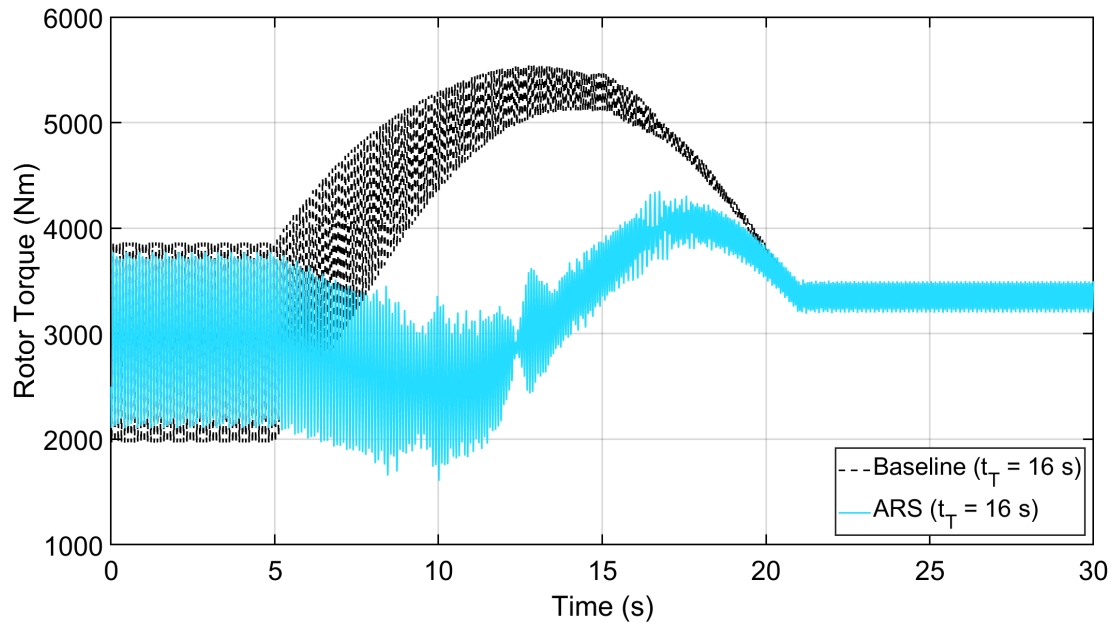


Figure 6.26: Rotor torque: Baseline vs. ARS ($\mu_N = 0.2$; $150 \rightarrow 230$ RPM; $\zeta = 3\%$)

6.5 $\mu_N = 0.2$, $230 \rightarrow 150$ RPM (Resonance Outside)

During the previous transition, the 2/rev resonance is moved beyond the nominal rotor speed. Therefore, the rotor speed can be reduced to 150 RPM without going through a resonance region. Even though a 3/rev resonance point is located close to 150 RPM, it can be moved out of range by bringing the mass back to the baseline location as shown in Figure 6.27. The mass location for this transition is shown in Figure 6.28. The mass is kept at the root until 210 RPM and begun to move below this rotor speed. This is done to prevent the 2/rev resonance point from reaching the operating speed at anytime during the transition. The rotor speed is shown in Figure 6.29.

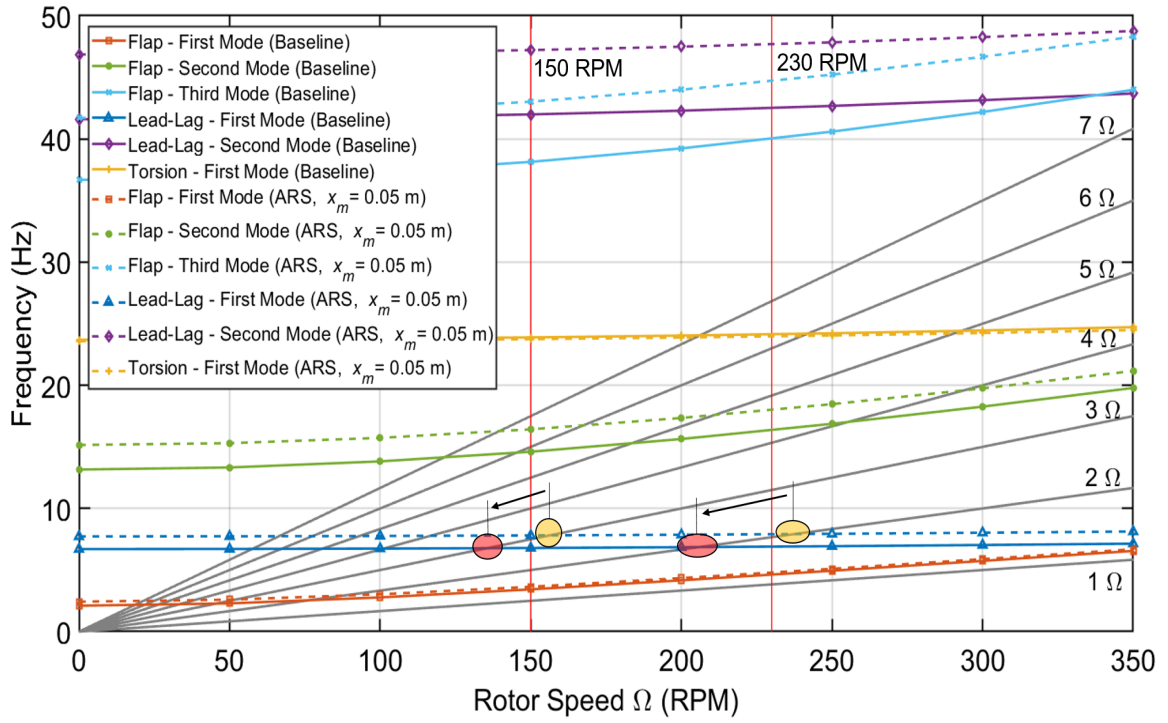


Figure 6.27: Fan plot: Baseline vs. ARS with mass back to baseline ($\mu_N = 0.2$, $\zeta = 3\%$)

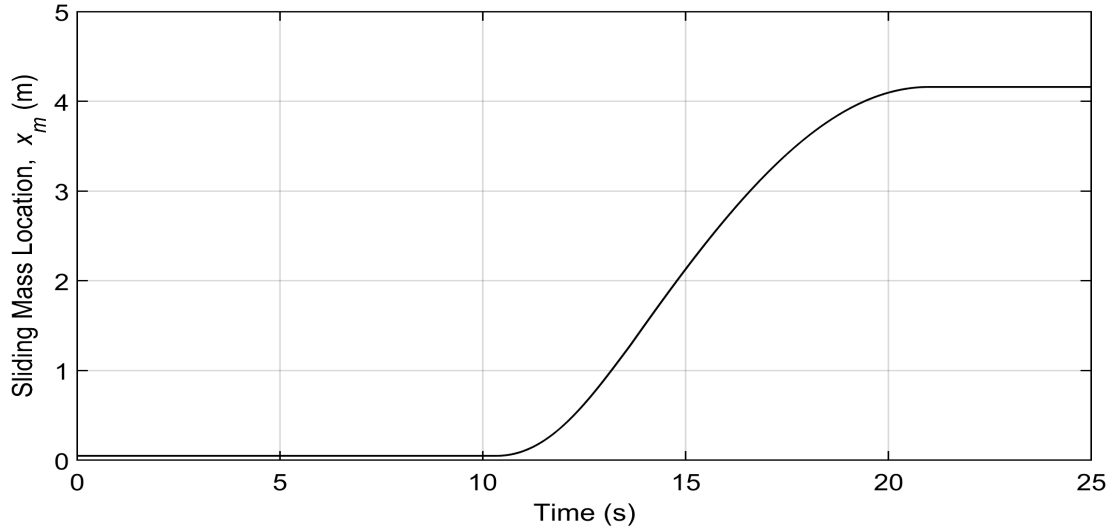


Figure 6.28: Location of sliding mass with time ($\mu_N = 0.2$; 230 \rightarrow 150 RPM)

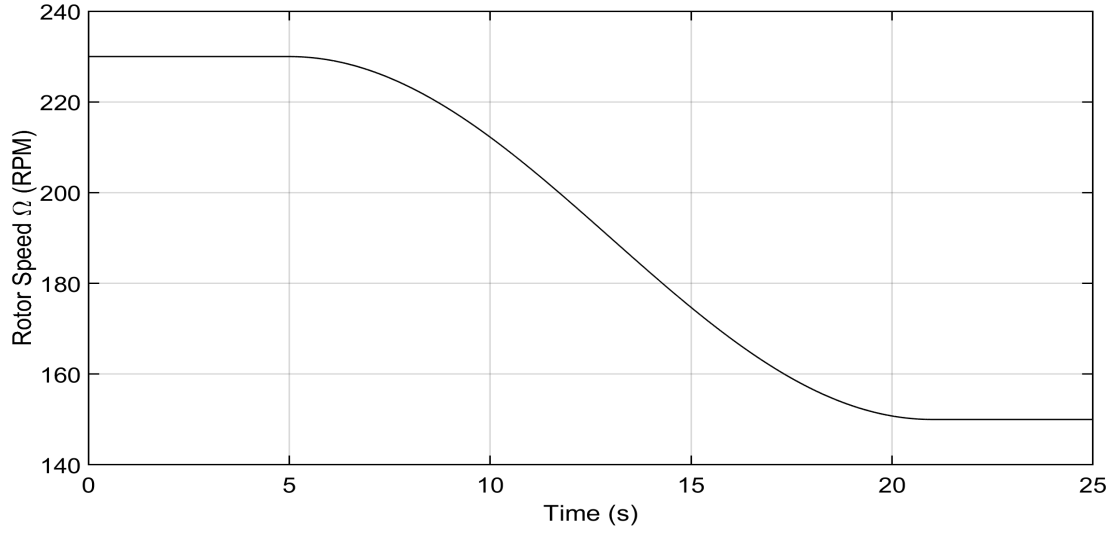


Figure 6.29: Rotor speed change from 230 to 150 RPM (16 s)

The lag moment response is shown in Figure 6.30. It can be seen that the ARS blade doesn't have a significant amplitude increase during this transition. In comparison, the amplitude is decreased by 75% from the baseline blade as shown in Figure 6.31.

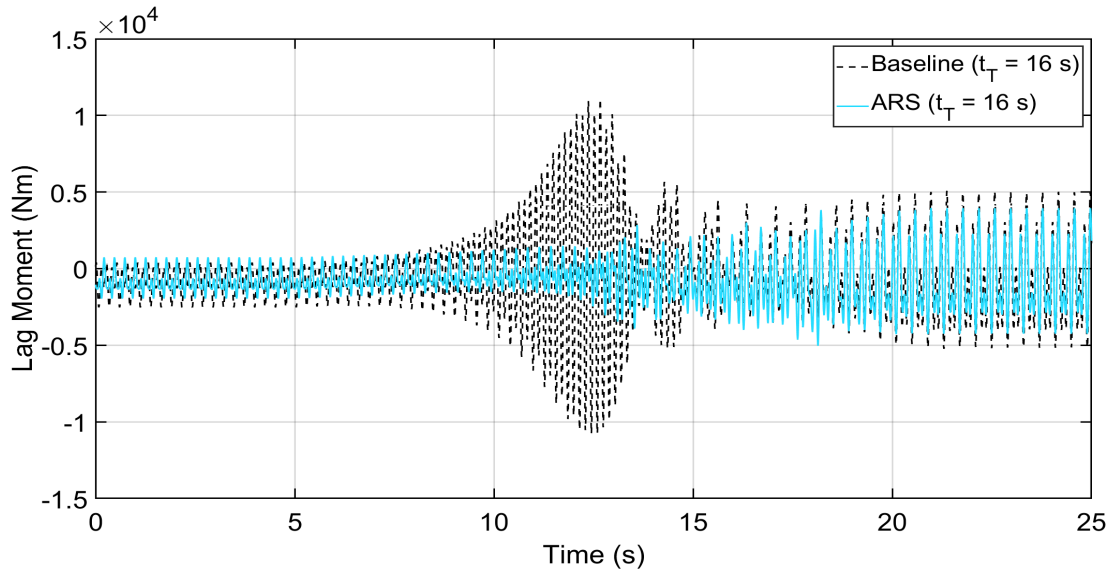


Figure 6.30: Lag moment: Baseline vs. ARS ($\mu_N = 0.2$; $230 \rightarrow 150$ RPM; $\zeta = 3\%$)

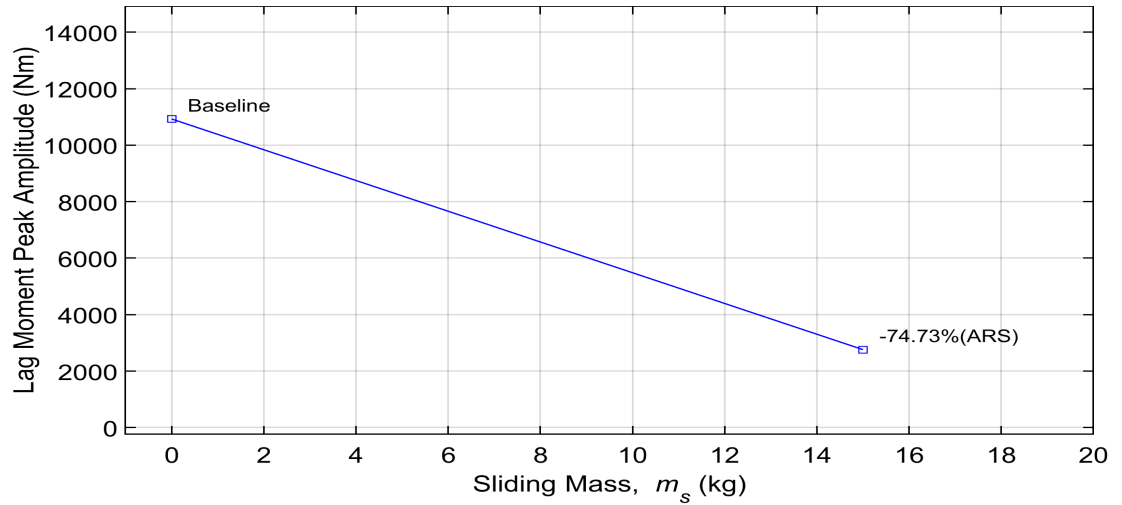


Figure 6.31: Peak amplitude: Baseline vs. ARS ($\mu_N = 0.2$; $230 \rightarrow 150$ RPM; $\zeta = 3\%$)

The rotor torque response is shown in Figure 6.32. The torque reduces initially as the mass is kept at a fixed location on the blade. As the mass starts moving outwards, the torque increases before dropping to the steady state. Once again, the torque response is not smooth as the baseline case due to the movement of the mass along the radial direction.

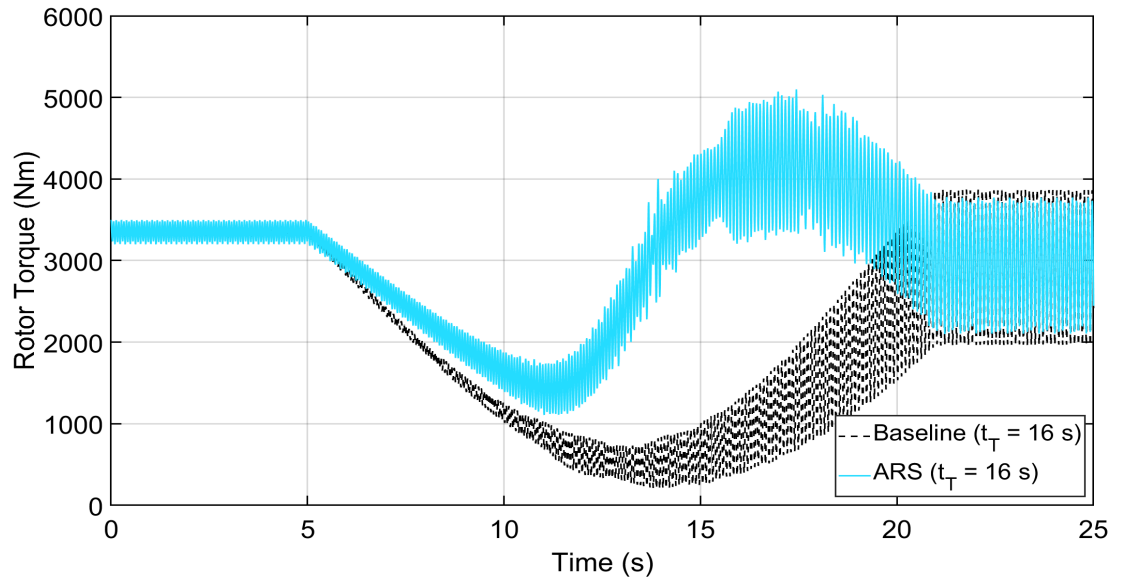


Figure 6.32: Rotor torque: Baseline vs. ARS ($\mu_N = 0.2$; $230 \rightarrow 150$ RPM; $\zeta = 3\%$)

Therefore, the ARS blade needs to pass through the resonance only once at this forward speed. The subsequent transitions can take place by pushing the resonance regions out of the operating zone.

6.6 $\mu_N = 0.1, 230 \rightarrow 130$ RPM

The transition range at $\mu_N = 0.1$ is shown in Figure 6.33. It can be seen that there are two resonance points inside the transition range. Like mentioned in the previous case, it is not possible to move the 2/rev resonance out of range if it is initially located within the transition bounds. However, the 3/rev resonance can be moved below 150 RPM by moving the mass towards the tip, after the 2/rev resonance is crossed.

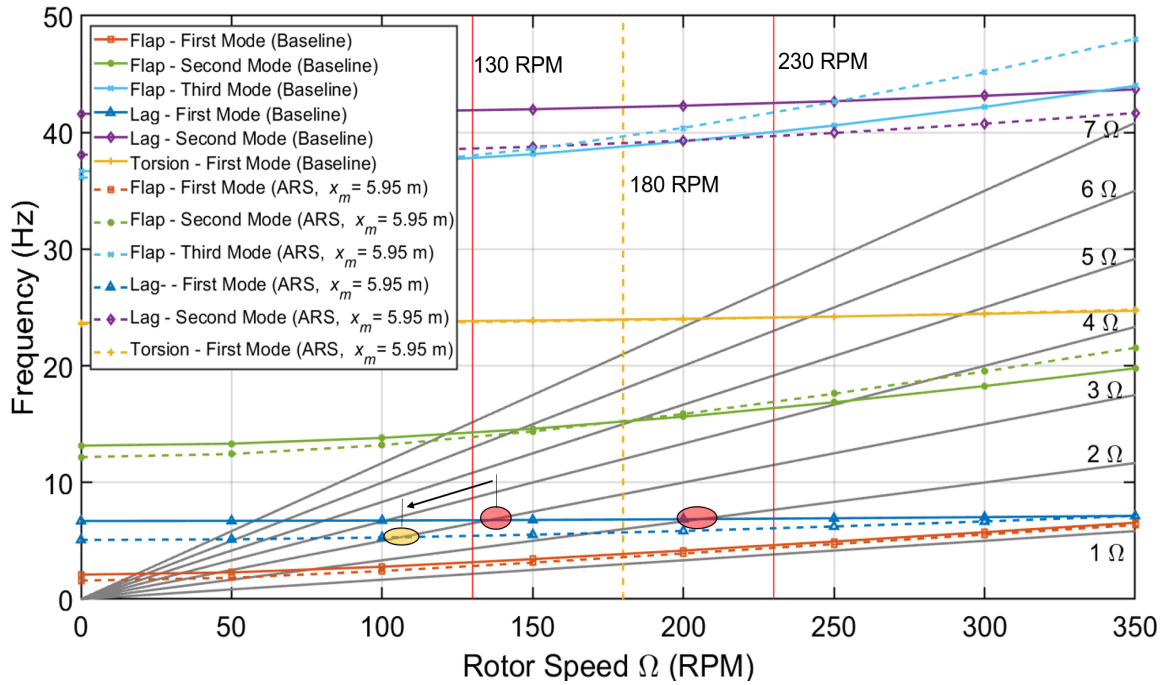


Figure 6.33: Fan plot: Baseline vs. ARS with mass at tip ($\mu_N = 0.1, \zeta = 3\%$)

The sliding mass is kept at the baseline location until 180 RPM and moved towards the tip as shown in Figure 6.34. The rotor speed change is shown in Figure 6.35.

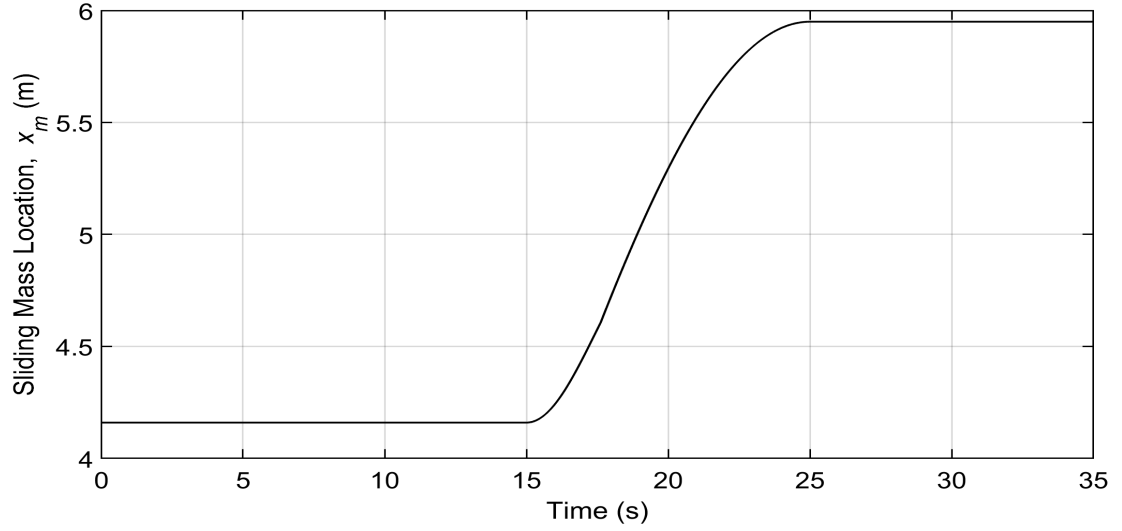


Figure 6.34: Location of sliding mass with time ($\mu_N = 0.1$; 230 \rightarrow 130 RPM)

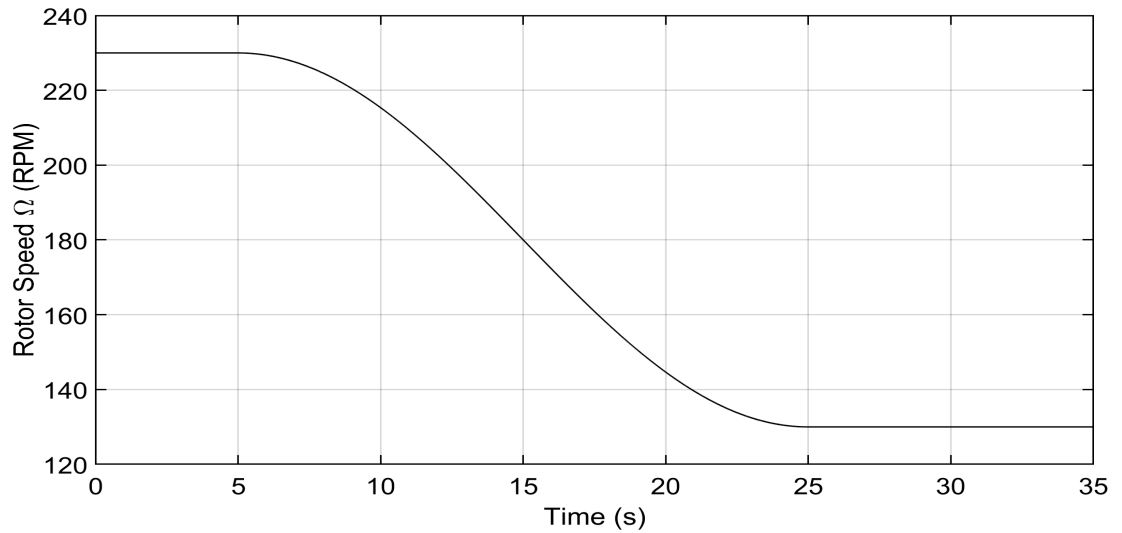


Figure 6.35: Rotor speed change from 230 to 130 RPM (20 s)

The lag moment response as the rotor passes through the 2/rev crossing but skips the 3/rev crossing is shown in Figure 6.36. The ARS blade has only one resonance bump and the second bump completely disappears. The amplitude in the second resonance region is decreased by 80% from the baseline blade as shown in Figure 6.37.

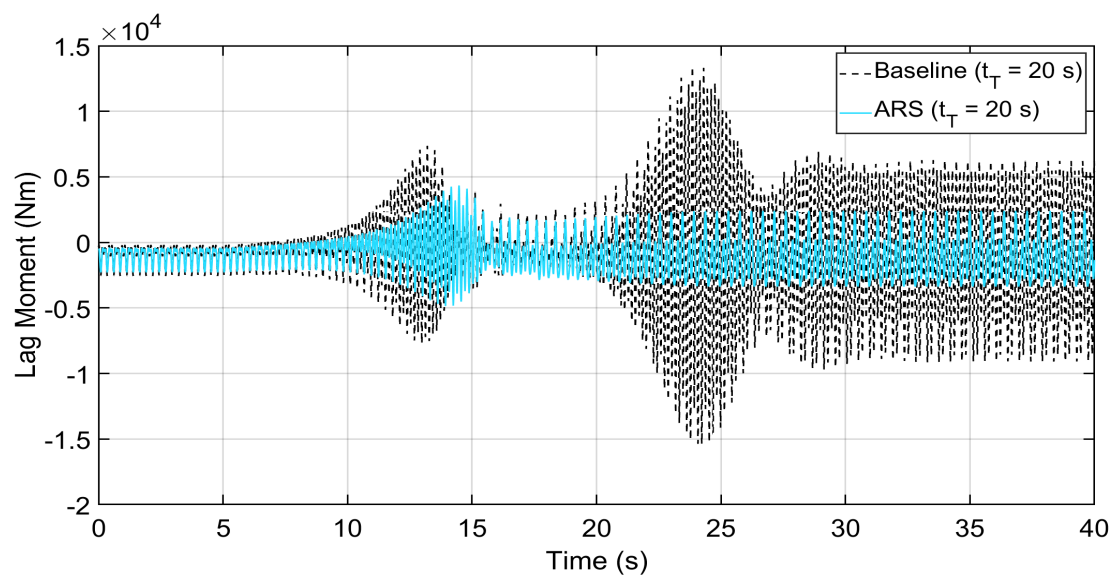


Figure 6.36: Lag moment: Baseline vs. ARS ($\mu_N = 0.1$; $230 \rightarrow 130$ RPM; $\zeta = 3\%$)

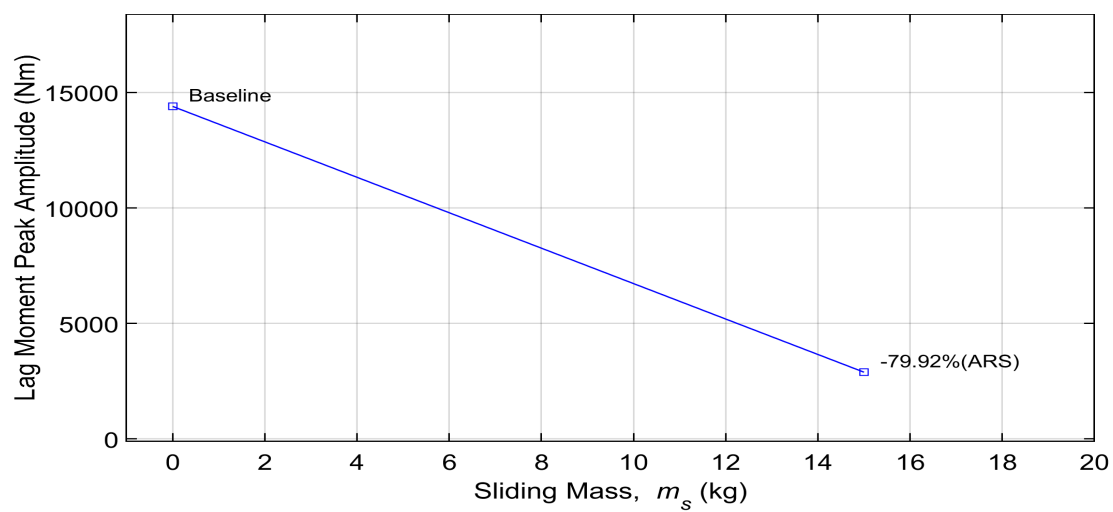


Figure 6.37: Second resonance amplitude: Baseline vs. ARS ($\mu_N = 0.1$; $230 \rightarrow 130$ RPM; $\zeta = 3\%$)

The rotor torque response is shown in Figure 6.38. The first resonance has a noticeable impact on torque but not a significant increase in amplitude. As the mass starts to move towards the tip, the torque needs to increase to prevent the rotor from slowing down too fast. The steady state value of the torque is significantly lower compared to the baseline case as the resonance is moved away from the rotor operating speed.

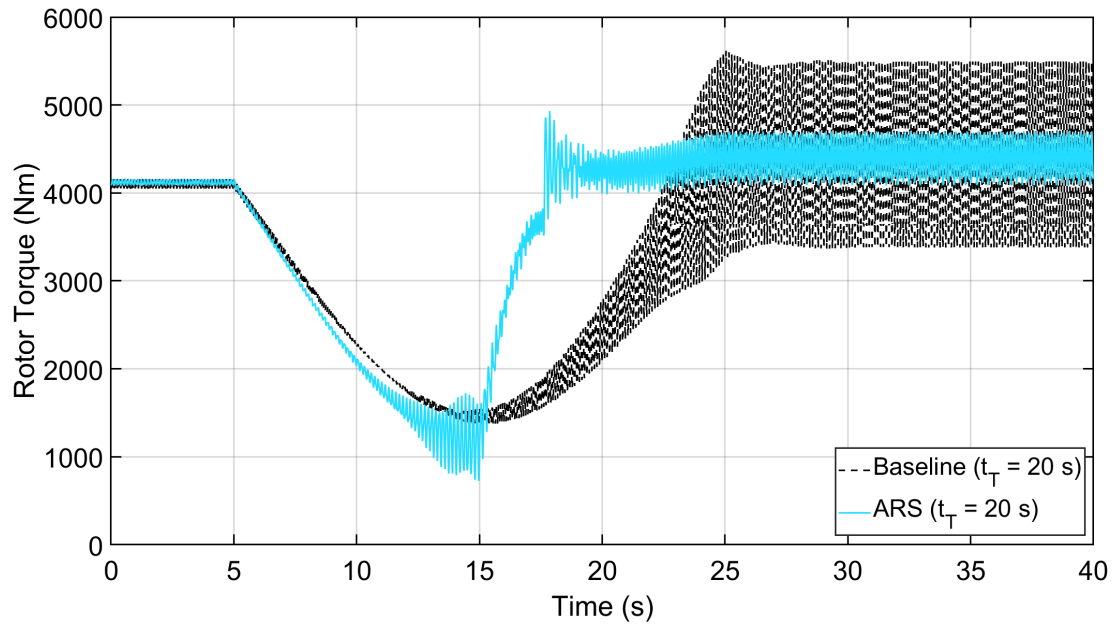


Figure 6.38: Rotor torque: Baseline vs. ARS ($\mu_N = 0.1$; $230 \rightarrow 130$ RPM; $\zeta = 3\%$)

6.7 $\mu_N = 0.1$, $130 \rightarrow 230$ RPM

At the end of the previous transition, the $2/\text{rev}$ resonance stays inside the transition region and the $3/\text{rev}$ resonance is moved out. During the reverse transition, the $2/\text{rev}$ resonance can be moved out as well by moving the mass close to the root of the blade. The movement of the resonance points is shown in Figure 6.39.

The sliding mass is moved continuously during this transition as shown in Figure 6.40. The rotor speed change is shown in Figure 6.41.

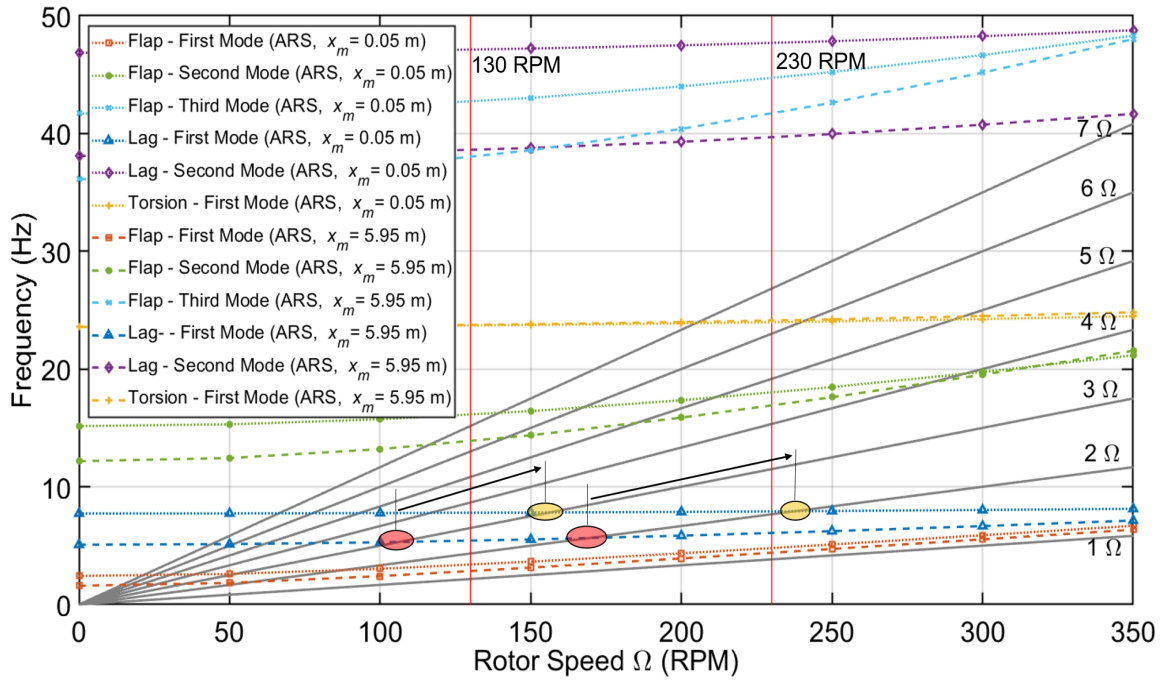


Figure 6.39: Fan plot: ARS with mass at root vs. mass at tip ($\mu_N = 0.1$, $\zeta = 3\%$)

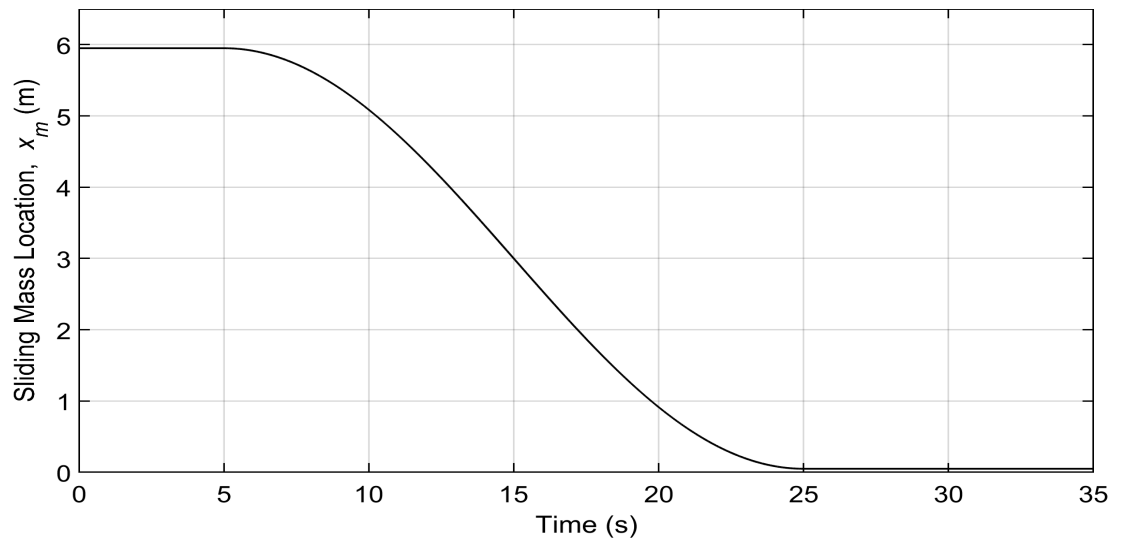


Figure 6.40: Location of sliding mass with time ($\mu_N = 0.1$; 130 \rightarrow 230 RPM)

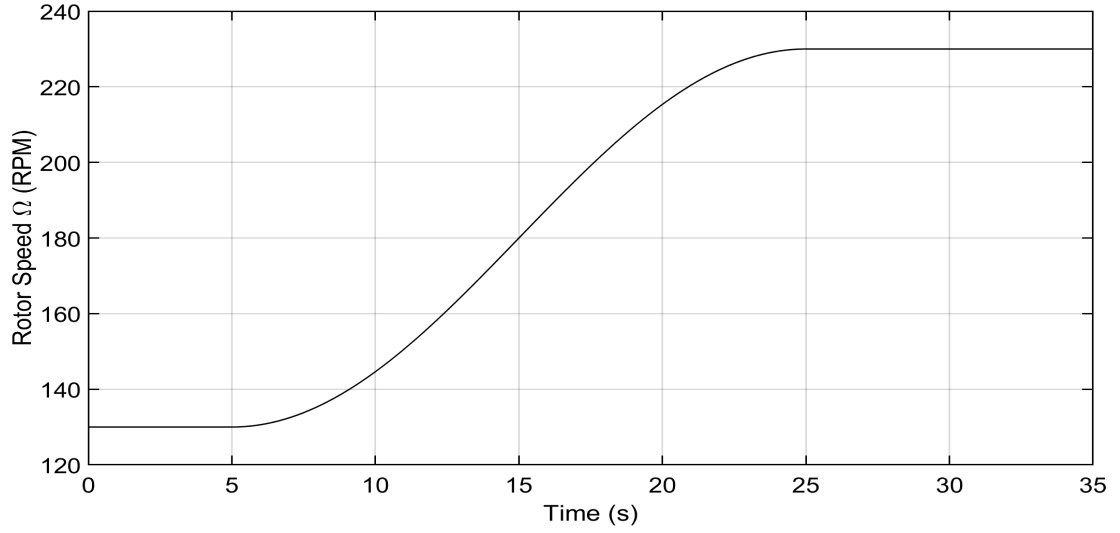


Figure 6.41: Rotor speed change from 130 to 230 RPM (20 s)

The lag moment response as the rotor travels from lower to higher speed is shown in Figure 6.42. The ARS blade has no resonance bumps. The amplitude in the first resonance region is decreased by 80% and in the second resonance region by 76% from the baseline, Figures 6.43 and 6.44.

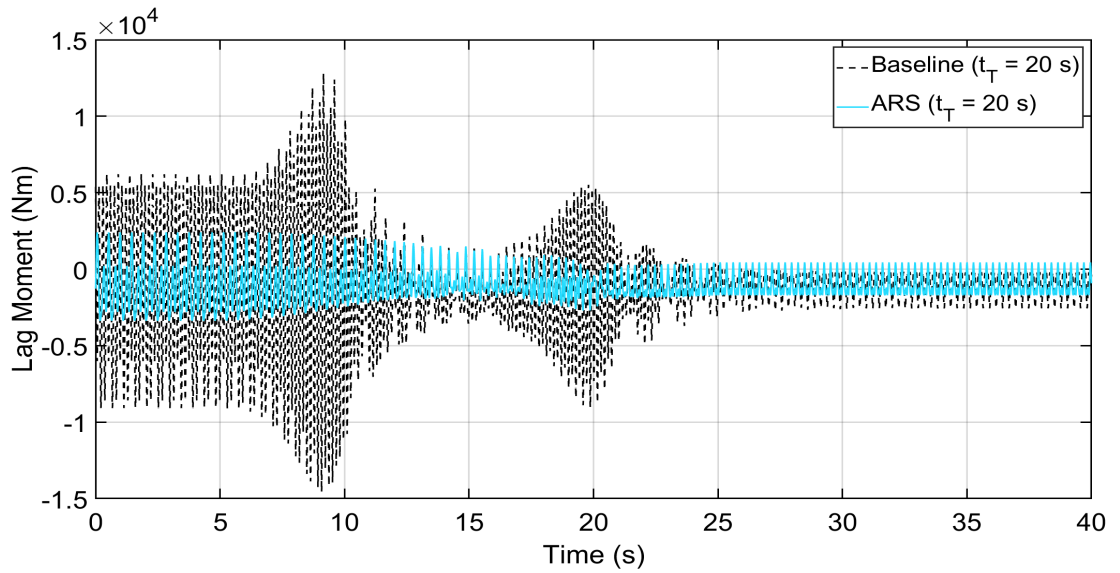


Figure 6.42: Lag moment: Baseline vs. ARS ($\mu_N = 0.1$; 130 \rightarrow 230 RPM; $\zeta = 3\%$)

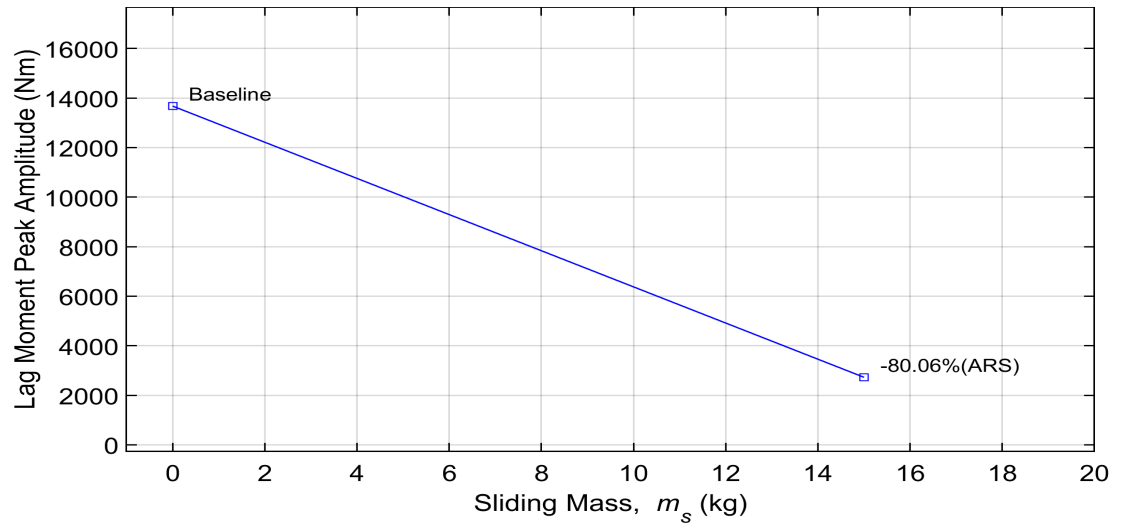


Figure 6.43: First resonance amplitude: Baseline vs. ARS ($\mu_N = 0.1$; 130 \rightarrow 230 RPM; $\zeta = 3\%$)

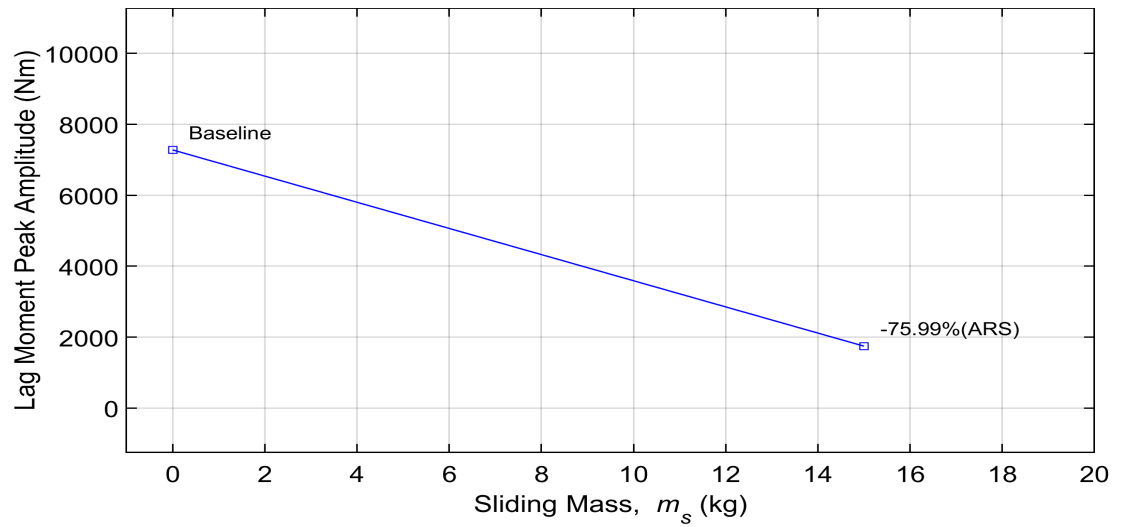


Figure 6.44: Second resonance amplitude: Baseline vs. ARS ($\mu_N = 0.1$; 130 \rightarrow 230 RPM; $\zeta = 3\%$)

The rotor torque response is shown in Figure 6.45. The torque needs to be reduced initially as the mass is moved inwards, which alone can make the rotor to speed up. The torque needs to increase during the later half of the transition to speed up the rotor. No significant amplitude increase is noted in the torque response.

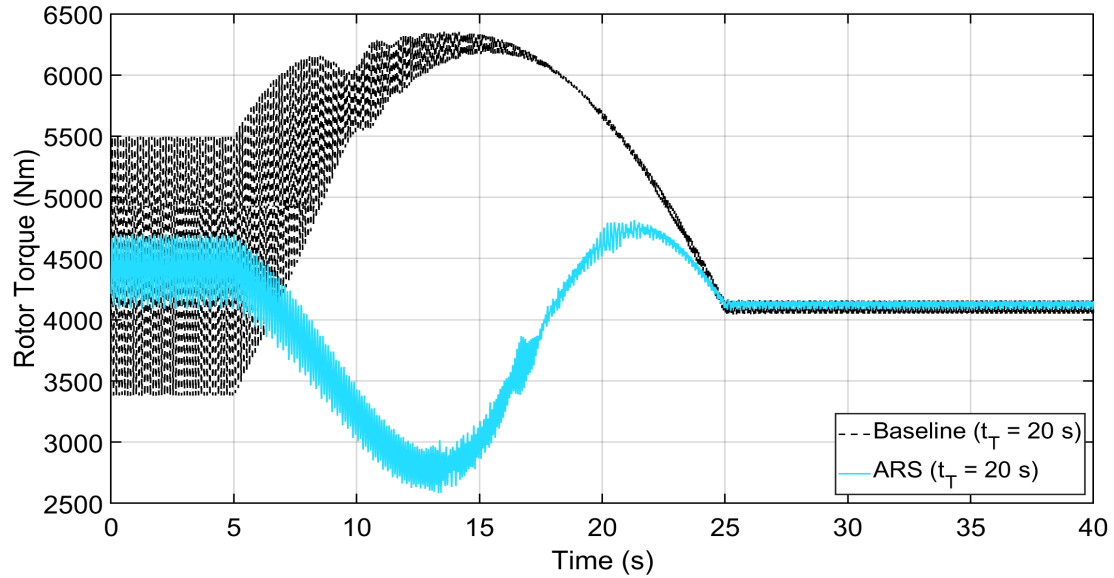


Figure 6.45: Rotor torque: Baseline vs. ARS ($\mu_N = 0.1$; $130 \rightarrow 230$ RPM; $\zeta = 3\%$)

6.8 $\mu_N = 0.1$, $230 \rightarrow 130$ RPM (Resonance Outside)

Once the $2/\text{rev}$ resonance is moved out, the high to low speed transition can take place without passing through a resonance point. The resonance movements are shown in Figure 6.46. The sliding mass is moved continuously but in the reverse direction, Figure 6.47. The rotor speed change follows the same path as in Figure 6.35.

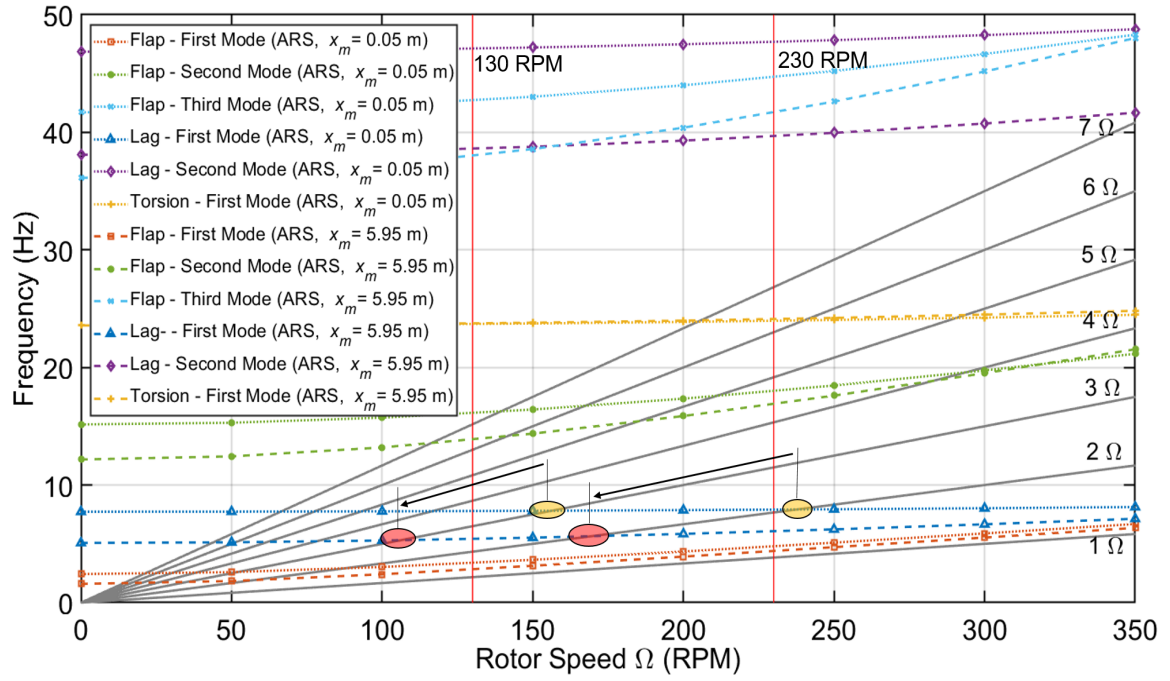


Figure 6.46: Fan plot: ARS resonance points movement ($\mu_N = 0.1$, $230 \rightarrow 130$ RPM, $\zeta = 3\%$)

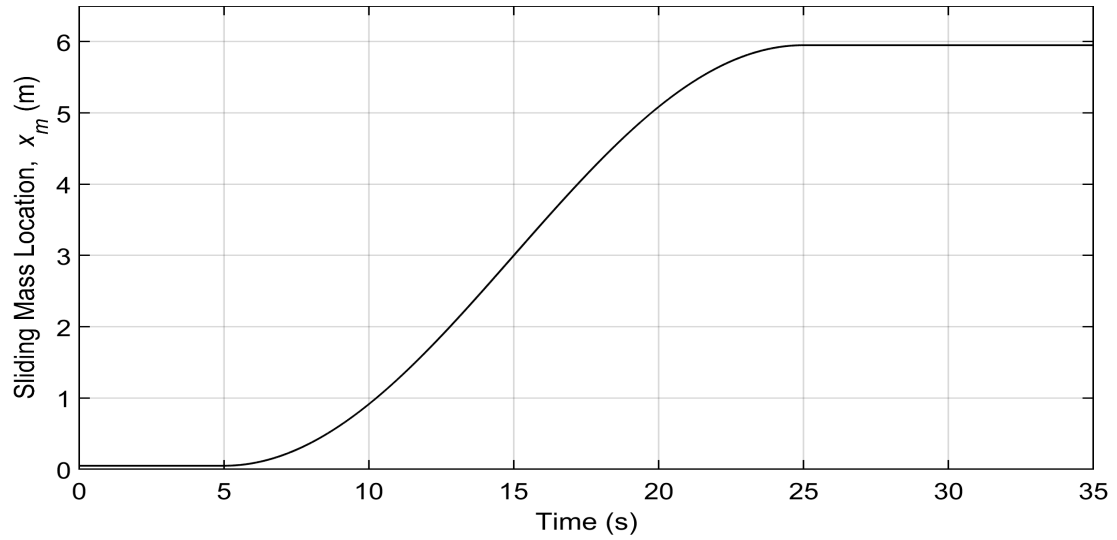


Figure 6.47: Location of sliding mass with time ($\mu_N = 0.1$; $230 \rightarrow 130$ RPM)

The lag moment response for the high to low speed transition with continuous mass movement is shown in Figure 6.48. There is no significant amplitude increase in the resonance regions for the ARS blade. The rotor torque response is shown in Figure 6.49.

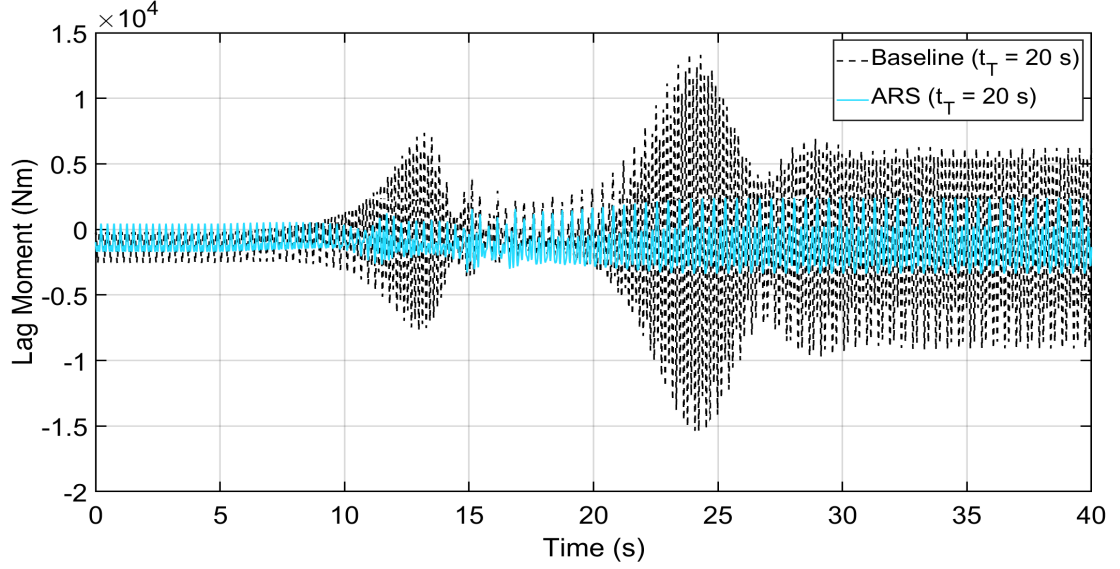


Figure 6.48: Lag moment: Baseline vs. ARS ($\mu_N = 0.1$; $230 \rightarrow 130$ RPM; $\zeta = 3\%$)

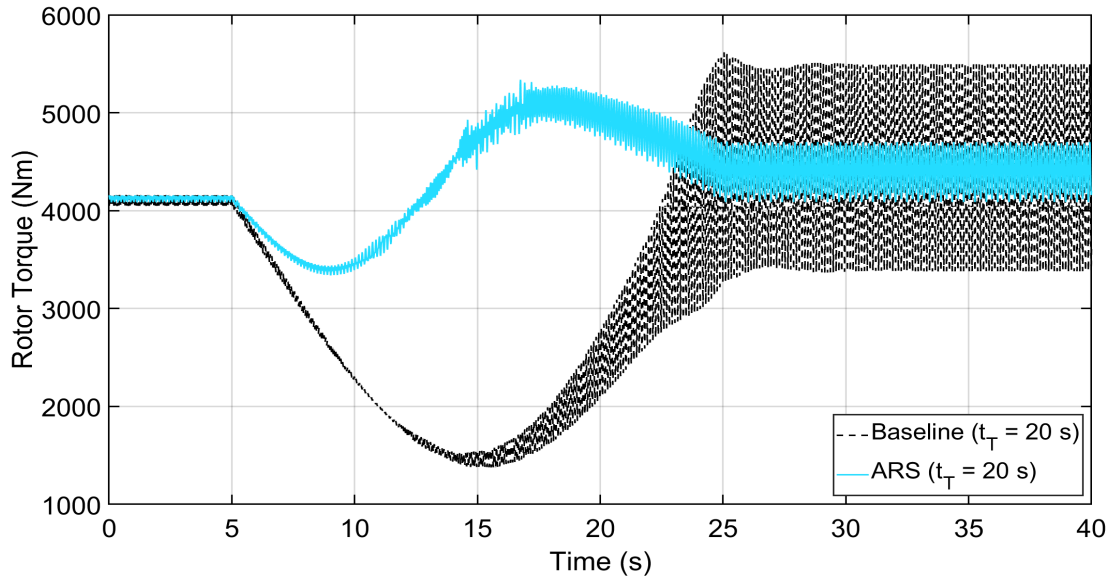


Figure 6.49: Rotor torque: Baseline vs. ARS ($\mu_N = 0.1$; $230 \rightarrow 130$ RPM; $\zeta = 3\%$)

Hence, the ARS system is capable of avoiding resonance regions during rotor speed transition. It works best for $\mu_N = 0.3$ case. The torque needed for 0.2 and 0.1 nominal advance ratios can be a little challenging to provide, but the load benefits are highly

noteworthy. For some of the cases, the transition times can be stretched without any lag moment penalties as no resonance is involved. This means that the transition can occur as slowly as needed.

CHAPTER 7

CONCLUSIONS, CONTRIBUTIONS AND FUTURE WORK

7.1 Conclusions

Power advantages and resonance crossings of a variable speed rotor is analyzed using an enhanced rotor model. The model incorporates geometrically exact beam theory to predict the blade response and Peters et al unsteady aerodynamics model for obtaining the aerodynamic loads. The rotor model was built in Dymore and incorporates a finite state inflow model and dynamic stall effects. Some important observations and conclusions are as follows,

- Power saving characteristics of a variable speed rotor stems from the variation of profile drag and induced drag with the rotor speed change. Reducing the rotor speed reduces the profile drag but increases the induced drag for most of the Ω range. As the rotor speed is reduced, the pitch angles increase to provide the same load condition. Changing the speed of a rotor improves its performance characteristics. Reducing the rotor speed from 230 to 150 RPM at $\mu_N = 0.2$ led to a maximum power saving of 41.47%.
- Important resonance crossing points for a given μ_N can be identified from the fan plot based on power studies. The range of allowable speed change reduces with increase of μ_N , and so does the number of important resonance points. During a resonance crossing, the forces acting on the blade root increase significantly.
- The lower frequency 2/rev lag crossing dominates the blade response for $\mu_N = 0.3$ and 0.2 transitions. The higher frequency crossings, such as the 5/rev flap and 7/rev torsion, do not have a noticeable impact on the blade response. The increase in moment amplitude during a resonance is a strong function of the cyclic pitch angles

during the resonance crossing.

- For $\mu_N = 0.1$, the 3/rev lag crossing causes a greater increase in amplitude than the 2/rev lag crossing. Once again, the higher frequency 5/rev, 6/rev and 7/rev crossings do not contribute significantly to the resonance response.
- The magnitude increase during the low-to-high rotor speed transition was found to be slightly different from the high-to-low rotor speed transition in most of the cases.
- For the baseline blade, the rotor torque follows the rotor acceleration trend. The torque has an \cup shape for high-to-low speed transitions and a \cap shape for low-to-high speed transitions. The rotor torque's resonance behavior is dominated by the 4/rev frequency for a four bladed system.
- For transitions during hover, the resonance crossings were found to have no impact on the blade response, even when perturbations were introduced into the system in the form of gusts.
- Load reduction studies were carried out by varying the transition time, structural damping, and lag stiffness of the blade. The longer the rotor takes to traverse a resonance region, greater were the resonance loads. Hence, the quickest transitions had the least lag moment increase during resonance. However, there were torque limitations on how quickly a rotor can pass through resonance. For the high to low speed transition, the rotor torque dips into the reverse torque region if the transition happens too quickly. For the low to high speed transition, the torque exceeds the maximum assumed limit for quick transitions. Therefore, the low-to-high speed transitions had a greater window for transition time reduction than the high-to-low speed transitions. The ideal transition times for the high-to-low speed cases varied from 8 to 14 seconds, whereas the ideal transition times were between 4 and 7 seconds for the low-to-high speed scenarios. The maximum amplitude reduction that was achieved by changing the transition time was only 28%.

- Increasing the structural damping was a very effective way of reducing the resonance loads. Increasing the lag damping from 1% to 3%, reduced the resonance loads by 40 – 50%. On further increasing the lag damping to 7%, by assuming that the blades have embedded carbon nanotubes, slightly over 70% load reduction was achieved for all the cases. This a significant result on the load reduction front of variable speed rotors.
- The lag stiffness of the rotor blade was increased to move the lag resonance crossing from 2/rev to 3/rev, and 4/rev. Even though the lag moment during resonance was reduced for most of the cases, the torque response deteriorated due to 4/rev crossings. The amplitude of the steady state torque response also increased with increase in stiffness. The torque response crossed the limitations for majority of the transitions. Hence, it was decided not to increase the lag stiffness of the blade to Case 1 or Case 2 value.
- A detailed combination study was performed by combining the ideal transition times with 7% lag damping. Combining ideal t_T with ζ showed that the load reduction remained close to 70%, which was already achieved by changing the ζ to 7%. Hence, the ideal transition time was not providing any additional reduction to the resonance loads in this scenario. Therefore, the higher torque peak that is required for some of the ideal transition times can be avoided.
- A novel blade design with a moving mass system was conceptualized and modeled in Dymore to analyze its dynamic behavior. The moving mass system was called as the Anti-Resonance System (ARS). The ARS system was able to effectively move the resonance points out of the rotor operating range. At $\mu_N = 0.3$, the ARS system not only eliminated the load increase due to resonance but also reduced the torque change needed during transition. For $\mu_N = 0.2$ and 0.1, the rotor had to pass through the resonance region at least once before the ARS system was able to move the

resonance points out of the operating zone. The lag damping was increased to 3% to reduce the loads during 2/rev crossing at $\mu_N = 0.2$. Significant load benefits were obtained using a moving mass system that could move the resonance points in and out of the operating range.

Hence, the range of rotor speed change depends on the flight condition, whereas the response of the blade depends on the flight conditions, blade parameters, and the resonance crossing. It is important to take these different behaviors into account while designing a VSR helicopter. This study provides a broad set of resonance response results that could be useful for future research on VSR technology.

7.2 Contributions

The contributions of this study are mentioned below,

- An enhanced rotor model with state of the art beam theory and an unsteady aerodynamics model was built in Dymore to analyze the rotor dynamics of a variable speed rotor.
- A frame work was provided to identify the important resonance crossing points based on power studies.
- Resonance studies were carried out for a wide range of advance ratios and in both the transition directions to characterize the blade response during various resonance crossings..
- Load reduction studies were carried out by changing the transition times, structural damping, and lag stiffness of the blade. The analysis performed here expanded the work carried out in [18] and has a more detailed combination studies.
- A novel blade design with a moving mass system was conceptualized to eliminate the presence of resonance points within the rotor operating range.

7.3 Future work

In this study, we were able to analyze some of the important aspects of a variable speed rotor with respect to the resonances. This work can be expanded to broaden its scope and analysis capabilities. Some of the suggestions are given below,

- The modeling was only limited to a hingeless rotor system with no root offset or pitch link components. Other mechanical components can be added to make it a more realistic rotor model.
- A model of a transmission system that allows unlimited speed change, like a continuously variable transmission (CVT), can be combined with the rotor model to analyze the coupled system.
- Stability of the rotor can be studied at various operating conditions by performing stability analysis using Floquet theory.
- The effect of airfoil properties on the resonance response needs to be studied as the amplitude increase during the resonance is a function of the pitch angles. Using an airfoil that can lead to lower cyclic pitch angles in forward flight could be an effective way to reduce resonance loads.
- The effect of lower rotor speed and higher pitch angles on the maneuverability of the aircraft can be studied from a flight dynamics perspective.
- In this study, the resonance analysis was only limited to sea level conditions. Studying the resonance crossing behaviors at different altitudes will also be of importance in understanding variable speed rotors.
- In the present study, the response of the blade during resonance is compared between two different beam theories in the validation section. Other beam theories, such as the elastica theory, could be used to study the blade response during resonance.

- In the last chapter, only one sliding mass was used to modify the location of resonances. Having a distributed set of smaller sliding masses along the length of the blade could expand the capabilities of the ARS. Such a system needs to be modeled and analyzed.
- The power needed by the mechanical control system to move the sliding mass also needs to be taken into account for the rotor power studies of an ARS blade.

REFERENCES

- [1] Ruddell, A. J. et al, "XH-59A ABC Technology Demonstrator Altitude Expansion and Operational Tests," Applied Technology Laboratory, U. S. Army Research and Technology Laboratories, Tech. Rep. USAAVRADCOM TR 81-D-35, Dec. 1981.
- [2] R. Blackwell and T. Millot, "Dynamics Design Characteristics of the Sikorsky X2 TechnologyTM Demonstrator Aircraft," *American Helicopter Society, 64th Annual Forum*, 2008.
- [3] F. P. Lentine, W. P. Groth, and T. H. Oglesby, "Research in Maneuverability of the XH-51A Compound Helicopter," U. S. Army Aviation Materiel Laboratories, Tech. Rep. USAAVLABS TR 68-23, Jun. 1968.
- [4] W. H. Barlow, W. C. McCluskey, and H. W. Ferris, "OH-6A Phase II Quiet Helicopter Program," U. S. Army Air Mobility Research and Development Laboratory, Tech. Rep. USAAMRDL TR 72-29, Sep. 1972.
- [5] A. E. Kareem, "Optimum Speed Rotor," pat. WO 99/42360, 1999.
- [6] J. Carter and J. R. Lewis, "Beyond Clean Sky: CarterCopter Slowed Rotor / Compound Exceeds Efficiency and Emission Goals," *41st European Rotorcraft Forum*, 2015.
- [7] J. Carter, "The Next Generation Cartercopter (NXCC): Transformational Technology for a Paradigm Shift in VTOL Aviation," *American Helicopter Society, 59th Annual Forum*, May 2003.
- [8] R. W. Prouty, "Should We Consider Variable Rotor Speeds?" *Vertiflite*, vol. 50, no. 4, pp. 24–27, 2004.
- [9] R. W. Prouty, *Helicopter Aerodynamics*. Phillips Business Information, Inc., 1985.
- [10] J. Steiner, F. Gandhi, and Y. Yoshizaki, "An Investigation of Variable Rotor RPM on Performance and Trim," *American Helicopter Society, 64th Annual Forum*, 2008.
- [11] J. Steiner, "An Investigation of Performance Benefits and Trim Requirements of a Variable Speed Helicopter Rotor," Master's thesis, The Pennsylvania State University, University Park, PA, 2008.

- [12] M. Mistry and F. Gandhi, "Helicopter Performance Improvement with Variable Rotor Radius and RPM," *Journal of American Helicopter Society*, vol. 59, no. 042010, 2014.
- [13] A. Linden, W. Bausch, D. Beck, M. D'Onofrio, R. Flemming, E. Hibyan, R. Johnson, R. J. Murrill, and D. Unsworth, "Variable Diameter Rotor Study," Air Force Flight Dynamics Laboratory, Air Force Systems Command, Wright-Patterson Air Force Base, OH, Tech. Rep. AFFDL-TR-71-170, Jan. 1972.
- [14] T. Prabhakar, F. Gandhi, J. Steiner, and D. McLaughlin, "A Centrifugal Force Actuated Variable Span Morphing Helicopter Rotor," *American Helicopter Society, 63rd Annual Forum Proceedings*, May 2007.
- [15] T. Prabhakar, "A Centrifugal Force Actuated Morphing Rotor," Master's thesis, The Pennsylvania State University, University Park, PA, 2007.
- [16] R. Ormiston, "Further Investigations of Helicopter Rotor Induced Power," *American Helicopter Society, 61st Annual Forum Proceedings*, 2005.
- [17] J. DiOttavio and D. Friedmann, "Operational Benefits of an Optimal, Widely Variable Speed Rotor," *American Helicopter Society, 66th Annual Forum*, May 2010.
- [18] D. Han and E. C. Smith, "Lagwise dynamic analysis of a variable speed rotor," *Aerospace Science and Technology*, vol. 54, pp. 164–173, 2013.
- [19] D. H. Hodges and E. H. Dowell, "Non-linear equations of motion for the elastic bending and torsion of twisted non-uniform blades," NASA, Tech. Rep. TN D-7818, Dec. 1974.
- [20] A. H. Nayfeh and D. T. Mook, *Nonlinear Oscillations*. Wiley-Interscience, 1979.
- [21] D. Han, J. Wang, E. C. Smith, and G. A. Lesieutre, "Transient Loads Control of a Variable Speed Rotor During Lagwise Resonance Crossing," *AIAA*, vol. 51, no. 1, 2013.
- [22] D. Han and E. C. Smith, "Lagwise Loads Analysis of a Rotor Blade with an Embedded Chordwise Absorber," *Journal of Aircraft*, vol. 46, no. 4, 2009.
- [23] H. A. DeSmidt, E. C. Smith, R. C. Bill, and K. Wang, "Comprehensive Modeling and Analysis of Rotorcraft Variable Speed Propulsion System With Coupled Engine/Transmission/Rotor Dynamics," NASA, Tech. Rep. NASA/CR—2013-216502, 2013.

- [24] D. Han and G. N. Barakos, "Variable Speed Tail Rotors for Helicopters with Variable Speed Main Rotors," *The Aeronautical Journal*, vol. 121 (1238), pp. 433–448, Apr. 2017.
- [25] B. Berry and I. Chopra, "Wind tunnel testing for performance and vibratory loads of a variable-speed mach-scale rotor," *American Helicopter Society, 67th Annual Forum*, May 2011.
- [26] G. Bowen-Davies and I. Chopra, "Aeromechanics of a Variable-Speed Rotor," *American Helicopter Society, 67th Annual Forum*, May 2011.
- [27] A. Datta, H. Yeo, and T. Norman, "Experimental Investigation and Fundamental Understanding of a Slowed UH-60A Rotor at High Advance Ratios," *American Helicopter Society, 67th Annual Forum*, May 2011.
- [28] D. Han, V. Patrikakis, and G. N. Barakos, "Helicopter performance improvement by variable rotor speed and variable blade twist," *Aerospace Science and Technology*, vol. 29, pp. 277–286, 2016.
- [29] D. Han, "Pitch link loads reduction of variable speed rotors by variable tuning frequency fluidlastic isolators," *Chinese Journal of Aeronautics*, vol. 28(5), pp. 1408–1415, 2015.
- [30] O. A. Bauchau and J. I. Craig, *Structural Analysis*. Springer, 2009.
- [31] L. Meirovitch, *Fundamentals of Vibrations*. McGraw Hill, 2001.
- [32] S. P. Timoshenko, "On the correction for shear of the differential equation for transverse vibrations of prismatic bars," *The London, Edinburgh, and Dublin Philosophical Magazine and Journal of Science*, vol. 41, pp. 744–746, Apr. 1921.
- [33] S. P. Timoshenko, "On the transverse vibrations of bars of uniform cross-section," *The London, Edinburgh, and Dublin Philosophical Magazine and Journal of Science*, vol. 43, pp. 125–131, Apr. 1922.
- [34] S. M. Han, H. Benaroya, and T. Wei, "Dynamics of Transversely Vibrating Beams Using Four Engineering Theories," *Journal of Sound and Vibration*, vol. 225(5), pp. 935–988, 1999.
- [35] A. E. H. Love, *A Treatise on the Mathematical Theory of Elasticity*. New York: Dover, 1944.
- [36] J. C. Houbolt and G. W. Brooks, "Differential Equations of Motion for Combined Flapwise Bending, Chordwise Bending, and Torsion of Twisted Nonuniform Ro-

- tor Blades,” National Advisory Committee for Aeronautics, Tech. Rep. 3905, Feb. 1957.
- [37] R. A. Ormiston and D. H. Hodges, “Linear Flap-Lag Dynamics of Hingeless Rotor Blades in Hover,” *Journal of American Helicopter Society*, vol. 17, no. 2, pp. 2–14, Apr. 1972.
 - [38] H. B. Huber, “Effect of Torsion-Flap-Lag Coupling on Hingeless Rotor Stability,” *American Helicopter Society, 29th Annual Forum*, May 1973.
 - [39] D. H. Hodges and R. A. Ormiston, “Non-linear Equations for Bending of Rotating Beams With Application to Linear Flap-Lag Stability of Hingeless Rotors,” NASA, Tech. Rep. TM X-2770, May 1973.
 - [40] P. Friedmann and P. Tong, “Dynamic Nonlinear Elastic Stability of Helicopter Rotor Blades in Hover and in Forward Flight,” NASA, Tech. Rep. CR-114485, May 1972.
 - [41] D. H. Hodges, “Nonlinear Bending and Torsion Equations for Rotating Beams With Application to Linear Stability of Hingeless Rotors,” PhD thesis, Stanford University, Department of Aeronautics and Astronautics, Dec. 1972.
 - [42] A. Rosen and P. P. Friedmann, “Nonlinear Equations of Equilibrium for Elastic Helicopter or Wind Turbine Blades Undergoing Moderate Deflection,” NASA, Tech. Rep. CR-159478, Oct. 1978.
 - [43] P. Friedmann, “Influence of Structural Damping, Preconing, Offsets and Large Deflections on the Flap-Lag-Torsional Stability of a Cantilevered Rotor Blade,” *AIAA*, 1977.
 - [44] R. G. Kvaternik and K. R. V. Kaza, “Nonlinear Curvature Expressions For Combined Flapwise Bending, Chordwise Bending, Torsion And Extension Of Twisted Rotor Blades,” NASA, Tech. Rep. TM X-73997, Dec. 1976.
 - [45] K. R. V. Kaza, “Nonlinear Aeroelastic Equations of Motion of Twisted, Nonuniform, Flexible Horizontal-Axis Wind Turbine Blades,” NASA, Tech. Rep. CR-159502, Jul. 1980.
 - [46] D. H. Hodges and R. A. Ormiston, “Stability of Elastic Bending and Torsion of Uniform Cantilevered Rotor Blades in Hover,” *AIAA*, no. 73-405, 1973.
 - [47] D. H. Hodges and R. A. Ormiston, “Stability Of Elastic Bending And Torsion Of Uniform Cantilever Rotor Blades In Hover With Variable Structural Coupling,” NASA, Tech. Rep. TN D-8192, Apr. 1976.

- [48] J. Shamie and P. Friedmann, "Aeroelastic Stability of Complete Rotors with Application to a Teetering Rotor in Forward Flight," *Journal of Sound and Vibration*, vol. 53, no. 4, pp. 559–584, 1977.
- [49] L. W. Rehfield and A. R. Atilgan, "A Structural Model for Composite Rotor Blades and Lifting Surfaces," NASA, Tech. Rep. N87-26989, Sep. 1987.
- [50] L. W. Rehfield and A. R. Atilgan, "Analysis, Design and Elastic Tailoring of Composite Rotor Blades," NASA, Tech. Rep., Sep. 1987.
- [51] R. V. Hodges, M. W. Nixon, and L. W. Rehfield, "Comparison of Composite Rotor Blade Models: A Coupled-Beam Analysis and an MSC/NASTRAN Finite-Element Model," NASA, Tech. Rep. TM-89024, Sep. 1987.
- [52] M. W. Nixon, "Extension-Twist Coupling of Composite Circular Tubes and Application to Tilt Rotor Blade Design," *AIAA*, no. 87-0772, pp. 295–303, 1987.
- [53] V. L. Berdichevskii, "On the Energy of an Elastic Rod," *Journal of Applied Mathematics and Mechanics*, vol. 45, pp. 518–529, 1981.
- [54] R. Worndle, "Calculation of the Cross Section Properties and the Shear Stresses of Composite Rotor Blades," *Vertica*, vol. 6, pp. 111–129, 1982.
- [55] J. B. Kosmatka and P. P. Friedmann, "Structural Dynamic Modeling of Advanced Composite Propellers by the Finite Element Method," *AIAA*, no. 87-0740, 1987.
- [56] J. B. Kosmatka and P. P. Friedmann, "Vibration Analysis of Composite Turbopropellers Using a Nonlinear Beam-Type Finite Element Approach," *AIAA*, vol. 27, no. 11, pp. 1606–1614, 1989.
- [57] V. Giavotto, M. Borri, P. Mantegazza, G. Ghiringhelli, V. Carmaschi, G. C. Maffioli, and F. Mussi, "Anisotropic Beam Theory and Applications," *Computers & Structures*, vol. 16, no. 1-4, pp. 403–413, 1983.
- [58] O. A. Bauchau, "A Beam Theory for Anisotropic Materials," *Journal of Applied Mechanics*, vol. 107, 1985.
- [59] O. A. Bauchau, B. S. Coffenberry, and L. W. Rehfield, "Composite Box Beam Analysis: Theory and Experiments," *Journal of Reinforced Plastics and Composites*, vol. 6, pp. 25–35, 1987.
- [60] A. D. Stemple and S. W. Lee, "Finite-Element Model for Composite Beams with Arbitrary Cross-Sectional Warping," *AIAA*, vol. 26, no. 12, pp. 1512–1520, 1988.

- [61] A. D. Stemple and S. W. Lee, "Large Deflection Static and Dynamic Finite Element Analysis of Composite Beams with Arbitrary Cross-Sectional Warping," *AIAA*, no. 89-1363-CP, 1989.
- [62] C. H. Hong and I. Chopra, "Aeroelastic Stability Analysis of a Composite Rotor Blade," *Journal of the American Helicopter Society*, vol. 30, no. 2, pp. 57–67, 1985.
- [63] C. H. Hong and I. Chopra, "Aeroelastic Stability of a Composite Bearingless Rotor Blade," *Journal of the American Helicopter Society*, vol. 31, no. 4, pp. 29–35, 1986.
- [64] E. C. Smith and I. Chopra, "Formulation and Evaluation of an Analytical Model for Composite Box-Beams," *AIAA*, no. 0962-CP, 1990.
- [65] E. C. Smith and I. Chopra, "Aeroelastic Response, Loads, and Stability of a Composite Rotor in Forward Flight," *AIAA*, vol. 31, no. 7, pp. 1265–1273, 1993.
- [66] B. Panda and I. Chopra, "Dynamics of Composite Rotor Blades in Forward Flight," *Vertica*, vol. 11, no. 1/2, pp. 187–209, 1987.
- [67] O. Song and L. Librescu, "Free Vibration of Anisotropic Composite Thin-Walled Beams of Closed Cross-Section Contour," *Journal of Sound and Vibration*, vol. 167, pp. 129–147, 1993.
- [68] W. B. Stephens, D. H. Hodges, J. H. Avila, and R. Kung, "Stability of Nonuniform Rotor Blades in Hover Using a Mixed Formulation," *Sixth European Rotorcraft and Powered Lift Aircraft Forum*, no. 13, 1980.
- [69] D. H. Hodges, "Nonlinear Equations of Dynamics of Pretwisted Beams Undergoing Small Strains and Large Rotations," NASA, Tech. Rep. 2470, May 1985.
- [70] E. H. Dowell, J. Traybar, and D. H. Hodges, "An Experimental Theoretical Correlation Study of Non-linear Bending and Torsion Deformations of a Cantilever Beam," *Journal of Sound and Vibrations*, vol. 50, pp. 533–544, 1977.
- [71] A. Rosen and P. P. Friedmann, "The Nonlinear Behavior of Elastic Slender Straight Beams Undergoing Small Strains and Moderate Rotations," *Journal of Applied Mechanics*, vol. 46, pp. 161–168, 1979.
- [72] D. H. Hodges, R. A. Ormiston, and D. A. Peters, "On the Nonlinear Deformation Geometry of Euler-Bernoulli Beams," NASA, Tech. Rep. TP 1566, Apr. 1980.
- [73] J. C. Simo and L. Vu-Quoc, "A Three-Dimensional Finite-Strain Rod Model. Part II: Computational Aspects," *Computer Methods in Applied Mechanics and Engineering*, vol. 58, pp. 79–116, 1986.

- [74] J. C. Simo, "A Finite Strain Beam Formulation. The Three-Dimensional Dynamic Problem. Part I," *Computer Methods in Applied Mechanics and Engineering*, vol. 49, pp. 55–70, 1985.
- [75] M. Borri and T. Merlini, "A Large Displacement Formulation for Anisotropic Beam Analysis," *Meccania*, vol. 21, pp. 30–37, 1986.
- [76] M. Borri, G. L. Ghiringhelli, and T. Merlini, "Linear analysis of naturally curved and twisted anisotropic beams," *Composites Engineering*, vol. 2, pp. 433–456, 1992.
- [77] O. A. Bauchau and C. H. Hong, "Finite Element Approach to Rotor Blade Modeling," *Journal of the American Helicopter Society*, vol. 32, no. 1, pp. 60–67, Jan. 1987.
- [78] O. A. Bauchau and C. H. Hong, "Large Displacement Analysis of Naturally Curved and Twisted Composite Beams," *AIAA*, vol. 25, no. 11, pp. 1469–1475, Nov. 1987.
- [79] O. A. Bauchau and C. H. Hong, "Nonlinear Composite Beam Theory," *Journal of Applied Mechanics*, vol. 55, pp. 156–163, Mar. 1988.
- [80] P. Minguet and J. Dugundji, "Experiments and Analysis for Composite Blades Under Large Deflections: Part 1 - Static Behavior," *AIAA*, vol. 28, no. 9, pp. 1573–1579, 1990.
- [81] P. Minguet and J. Dugundji, "Experiments and Analysis for Composite Blades Under Large Deflections: Part 2 - Dynamic Behavior," *AIAA*, vol. 28, no. 9, pp. 1580–1588, 1990.
- [82] P. F. Pai and A. H. Nayfeh, "A Nonlinear Composite Beam Theory," *Nonlinear Dynamics*, vol. 3, pp. 273–303, 1992.
- [83] D. A. Danielson and D. H. Hodges, "Nonlinear Beam Kinematics by Decomposition of the Rotation Tensor," *Journal of Applied Mechanics*, vol. 54, no. 2, pp. 258–262, 1987.
- [84] D. A. Danielson and D. H. Hodges, "A Beam Theory for Large Global Rotation, Moderate Local Rotation, and Small Strains," *Journal of Applied Mechanics*, vol. 55, pp. 179–184, 1988.
- [85] D. H. Hodges, "Mixed Variational Formulation Based on Exact Intrinsic Equations for Dynamics of Moving Beams," *International Journal of Solids and Structures*, vol. 26, no. 11, pp. 1253–1273, 1990.

- [86] M. V. Fulton and D. H. Hodges, "Aeroelastic Stability of Composite Hingeless Rotor Blades in Hover-Part II: Results," *Mathematical and Computer Modelling*, vol. 18, no. 3/4, pp. 19–35, 1993.
- [87] A. R. Atilgan, D. H. Hodges, and M. V. Fulton, "Nonlinear Deformation of Composite Beams: Unification of Cross-Sectional and Elastic Analyses," *Applied Mechanics Reviews*, vol. 44, Nov. 1991.
- [88] A. R. Atilgan and D. H. Hodges, "Unified Nonlinear Analysis for Nonhomogeneous Anisotropic Beams with Closed Cross Sections," *AIAA*, vol. 29, pp. 1990–1999, Nov. 1991.
- [89] D. H. Hodges, A. R. Atilgan, C. E. S. Cesnik, and M. V. Fulton, "On a Simplified Strain Energy Function for Geometrically Nonlinear Behaviour of Anisotropic Beams," *Composites Engineering*, vol. 2, pp. 513–526, 1992.
- [90] C. E. S. Cesnik and D. H. Hodges, "Variational–Asymptotical Analysis of Initially Twisted and Curved Composite Beams," *International Journal for Engineering Analysis and Design*, vol. 1, pp. 177–187, 1994.
- [91] C. E. S. Cesnik and D. H. Hodges, "Stiffness Constants for Composite Beams Including Large Initial Twist and Curvature Effects," *Applied Mechanics Reviews*, vol. 48, S61–S67, 1995.
- [92] C. E. S. Cesnik, D. H. Hodges, and V. G. Sutyrin, "Cross-Sectional Analysis of Composite Beams Including Large Initial Twist and Curvature Effects," *AIAA*, vol. 34, no. 9, pp. 1913–1920, 1996.
- [93] C. E. S. Cesnik and D. H. Hodges, "VABS: A new concept for composite rotor blade cross-sectional modeling," *Journal of the American Helicopter Society*, vol. 42, pp. 27–38, 1997.
- [94] D. H. Hodges, X. Shang, and C. E. S. Cesnik, "Finite Element Solution of Nonlinear Intrinsic Equations for Curved Composite Beams," *Journal of American Helicopter Society*, vol. 41, no. 4, pp. 313–321, 1996.
- [95] C. E. S. Cesnik, D. H. Hodges, B. Popescu, and D. Harursampath, "Composite beam cross-sectional modeling including obliqueness and trapeze effects," *AIAA*, no. A9626938, pp. 1384–1397, 1996.
- [96] B. Popescu and D. H. Hodges, "Asymptotic Treatment of the Trapeze Effect in Finite Element Cross-Sectional Analysis of Composite Beams," *International Journal of Non-Linear Mechanics*, vol. 34, pp. 709–721, 1999.

- [97] V. V. Volovoi, D. H. Hodges, V. L. Berdichevsky, and V. Sutyrin, “Asymptotic Theory for Static Behavior of Elastic Anisotropic I-Beams,” *International Journal of Solids and Structures*, vol. 36, pp. 1017–1043, 1999.
- [98] W. Yu, D. H. Hodges, V. V. Volovoi, and C. E. S. Cesnik, “On Timoshenko-like Modeling of Initially Curved and Twisted Composite Beams,” *International Journal of Solids and Structures*, vol. 39, pp. 5101–5121, 2002.
- [99] W. Yu, D. H. Hodges, V. V. Volovoi, and E. D. Fuchs, “A Generalized Vlasov Theory for Composite Beams,” *Thin-Walled Structures*, vol. 43, pp. 1493–1511, 2005.
- [100] J. Loughlan and M. Ata, “The Behaviour of Open and Closed Section Carbon Fibre Composite Beams Subjected to Constrained Torsion,” *Composite Structures*, vol. 38, pp. 631–647, 1997.
- [101] J. C. Massa and E. J. Barbero, “A Strength of Materials Formulation for Thin Walled Composite Beams with Torsion,” *Journal of Composite Materials*, vol. 32, pp. 1560–1594, 1998.
- [102] E. R. Johnson, V. V. Vasiliev, and D. V. Vasiliev, “Anisotropic Thin-Walled Beams with Closed Cross-Sectional Contours,” *AIAA*, vol. 39, pp. 2389–2393, 2001.
- [103] S. N. Jung, V. T. Nagaraj, and I. Chopra, “Refined Structural Model for Thin and Thick-Walled Composite Rotor Blades,” *AIAA*, vol. 39, pp. 2389–2393, 2002.
- [104] O. A. Bauchau and N. K. Kang, “A Multibody Formulation for Helicopter Structural Dynamic Analysis,” *Journal of American Helicopter Society*, vol. 38, pp. 3–14, 1993.
- [105] O. A. Bauchau, “DYMORE User’s Manual,” Dymore Solutions, Tech. Rep., 2020, URL: <http://www.dymoresolutions.com/UsersManual.html>.
- [106] O. A. Bauchau, “Computational Schemes for Flexible, Nonlinear MultiBody Systems,” *Multibody System Dynamics*, vol. 2, pp. 169–225, 1998.
- [107] O. A. Bauchau and C. L. Bottasso, “On the Design of Energy Preserving and Decaying Schemes for Flexible, Non-Linear Multi-Body Systems,” *Computer Methods in Applied Mechanics and Engineering*, vol. 169, pp. 61–79, 1999.
- [108] E. Carrera and G. Giunta, “Refined Beam Theories Based on a Unified Formulation,” *International Journal of Applied Mechanics*, vol. 2, no. 1, pp. 117–143, 2010.

- [109] E. Carrera and M. Petrolo, “On the Effectiveness of Higher-Order Terms in Refined Beam Theories,” *Journal of Applied Mechanics*, vol. 78, 2010, Article 021013.
- [110] E. Carrera, A. Pagani, and M. Petrolo, “Classical, Refined, and Component-Wise Analysis of Reinforced-Shell Wing Structures,” *AIAA*, vol. 51, no. 5, pp. 1255–1286, 2013.
- [111] W. Yu and M. Blair, “GEBT: A general-purpose nonlinear analysis tool for composite beams,” *Composite Structures*, vol. 94, no. 9, pp. 2677–2689, 2012.
- [112] W. Yu, D. H. Hodges, and J. C. Ho, “Variational asymptotic beam sectional analysis – An updated version,” *International Journal of Engineering Science*, vol. 59, pp. 40–64, 2012.
- [113] M. Gupta, “Enhancements in Analysis of Beam-Like Structures using Asymptotic Methods,” PhD thesis, Georgia Institute of Technology, May 2019.
- [114] O. A. Bauchau and S. Han, “Three-Dimensional Beam Theory for Flexible Multibody Dynamics,” *Journal of Computational and Nonlinear Dynamics*, vol. 9, no. 4, 2014, Article 041011.
- [115] S. Han and O. A. Bauchau, “Nonlinear three-dimensional beam theory for flexible multibody dynamics,” *Multibody System Dynamics*, vol. 34, no. 3, pp. 211–242, 2015.
- [116] O. A. Bauchau, *Flexible Multibody Dynamics*. Springer, 2011.
- [117] O. A. Bauchau and D. H. Hodges, “Analysis of Nonlinear Multibody Systems with Elastic Couplings,” *Multibody System Dynamics*, vol. 3, pp. 163–188, 1999.
- [118] M. J. Patil and D. H. Hodges, “Flight Dynamics of Highly Flexible Flying Wings,” *Journal of Aircraft*, vol. 43, no. 6, pp. 1790–1799, 2006.
- [119] C. Chang, D. H. Hodges, and M. J. Patil, “Flight Dynamics of Highly Flexible Flying Aircraft,” *Journal of Aircraft*, vol. 45, no. 2, pp. 538–545, 2008.
- [120] M. J. Patil, D. H. Hodges, and C. E. S. Cesnik, “Nonlinear Aeroelasticity and Flight Dynamics of High-Altitude Long-Endurance Aircraft,” *Journal of Aircraft*, vol. 38, no. 1, pp. 88–94, 2001.
- [121] H. S. Hoseini, “A joined 3D/1D finite element method for aeroservoelastic analysis of damaged HALE aircraft wings,” PhD thesis, Georgia Institute of Technology, May 2018.

- [122] H. S. Hoseini and D. H. Hodges, “Aeroelastic Stability Analysis of Damaged High-Aspect-Ratio Composite Wings,” *Journal of Aircraft*, vol. 56, no. 5, pp. 1794–1808, 2019.
- [123] P. P. Friedmann, “Recent Developments in Rotary-Wing Aeroelasticity,” *Journal of Aircraft*, vol. 14, no. 11, pp. 1027–1041, Nov. 1977.
- [124] D. H. Hodges, “Review of Composite Rotor Blade Modeling,” *AIAA*, vol. 28, no. 3, pp. 561–565, Mar. 1990.
- [125] K. A. Yuan and P. P. Friedmann, “Aeroelasticity and Structural Optimization of Composite Helicopter Rotor Blades with Swept Tips,” NASA, Tech. Rep. CR-4665, May 1995.
- [126] D. H. Hodges, *Nonlinear Composite Beam Theory*. Reston, Virginia: AIAA, 2006.
- [127] W. Johnson, *Helicopter Theory*. Princeton University Press, 1980.
- [128] J. G. Leishman, *Principles of Helicopter Aerodynamics*. Cambridge University Press, 2006.
- [129] J. M. Greenberg, “Airfoil in Sinusoidal Motion in a Pulsating Stream,” NACA, Tech. Rep. TN 1326, 1947.
- [130] R. G. Loewy, “A Two-Dimensional Approximation to the Unsteady Aerodynamics of Rotary-Wings,” *Journal of Aeronautical Sciences*, vol. 24, no. 2, Feb. 1957.
- [131] K. W. Shipman and E. R. Wood, “A Two-Dimensional Theory for Rotor Blade Flutter in Forward Flight,” *Journal of Aircraft*, vol. 8, no. 12, pp. 1008–1015, Dec. 1971.
- [132] J. W. Edward, “Unsteady Aerodynamic Modeling and Active Aeroelastic Control,” NASA, Tech. Rep. CR-148019, Feb. 1977.
- [133] M. A. H. Dinyavari and P. P. Friedmann, “Unsteady Aerodynamics in the Time and Frequency Domains for Finite Time Arbitrary Motion of Rotary Wings in Hover and Forward Flight,” *AIAA*, no. 84-0988, 1984.
- [134] M. A. H. Dinyavari and P. P. Friedmann, “Application of Time-Domain Unsteady Aerodynamics to Rotary-Wing Aeroelasticity,” *AIAA*, vol. 24, pp. 1424–1432, Sep. 1986.
- [135] D. A. Peters, “Hingeless rotor frequency response with unsteady inflow,” NASA, Tech. Rep. NASA-SP-352, 1974.

- [136] G. H. Goankar and D. A. Peters, "Use of Multiblade Coordinates for Helicopter Flap-Lag Stability with Dynamic Inflow," *Journal of Aircraft*, vol. 17, no. 2, pp. 112–118, 1980.
- [137] D. A. Peters and G. H. Goankar, "Theoretical Flap-Lag Damping with Various Dynamic Inflow Models," *Journal of the American Helicopter Society*, vol. 25, no. 3, pp. 29–36, 1980.
- [138] D. M. Pitt and D. A. Peters, "Theoretical Prediction of Dynamic Inflow Derivatives," *Vertica*, vol. 5, no. 1, pp. 21–34, 1981.
- [139] D. A. Peters, S. Karunamoorthy, and W. Cao, "Finite State Induced Flow Models Part I: Two Dimensional Thin Airfoil," *Journal of Aircraft*, vol. 32, no. 2, pp. 313–322, 1995.
- [140] D. A. Peters and C. J. He, "Finite State Induced Flow Models Part II: Three Dimensional Rotor Disk," *Journal of Aircraft*, vol. 32, no. 2, pp. 323–333, 1995.
- [141] R. Dat, "Development of Basic Methods Needed to Predict Helicopter Aeroelastic Behavior," *Vertica*, vol. 8, no. 3, pp. 209–228, 1984.
- [142] C. T. Tran and D. Petot, "Semi-Empirical Model for the Dynamic Stall of Airfoils in View of the Application to the Calculation of the Responses of a Helicopter Blade in Forward Flight," *Vertica*, vol. 5, no. 1, pp. 35–53, 1981.
- [143] K. W. McAlister, O. Lambert, and D. Petot, "Application of the ONERA Model of Dynamic Stall," NASA, Tech. Rep. TP 2399, 1984.
- [144] J. P. Rogers, "Application of an Analytical Stall Model to Time History and Eigenvalue Analysis of Rotor Blades," *Journal of the American Helicopter Society*, vol. 29, no. 1, pp. 25–33, 1984.
- [145] D. A. Peters, "Toward a Unified Lift Model for use in Rotor Blade Stability Analysis," *Journal of the American Helicopter Society*, vol. 30, no. 3, pp. 32–42, 1985.
- [146] T. S. Beddoes, "A Synthesis of Unsteady Aerodynamic Effects Including Stall Hysteresis," *Vertica*, vol. 1, no. 2, pp. 113–123, 1976.
- [147] T. S. Beddoes, "Representation of Airfoil Behavior," *Vertica*, vol. 7, no. 2, pp. 183–197, 1983.
- [148] J. G. Leishman, "Two-Dimensional Model for Airfoil Unsteady Drag Below Stall," *Journal of Aircraft*, vol. 25, no. 7, pp. 665–666, 1988.

- [149] J. G. Leishman, “Modelling Sweep Effects on Dynamic Stall,” *Journal of the American Helicopter Society*, vol. 34, no. 3, pp. 18–29, 1989.
- [150] J. G. Leishman and T. S. Beddoes, “A Generalized Model for Unsteady Aerodynamic Behavior and Dynamic Stall Using Indicial Method,” *Journal of the American Helicopter Society*, vol. 34, no. 3, pp. 3–17, 1989.
- [151] P. P. Friedmann, “Rotary-Wing Aeroelasticity with Application to VTOL Vehicles,” *AIAA*, no. AIAA-90-1115-CP, 1990.
- [152] P. P. Friedmann and D. H. Hodges, “Rotary Wing Aeroelasticity-A Historical Perspective,” *Journal of Aircraft*, vol. 40, no. 6, pp. 1019–1046, Dec. 2003.
- [153] D. A. Peters and D. Barwey, “A General Theory of Rotorcraft Trim,” *Mathematical Problems in Engineering*, vol. 2, no. 1, Jan. 1996.
- [154] P. P. Friedmann and J. Shamie, “Aeroelastic Stability of Trimmed Helicopter Blades in Forward Flight,” *Vertica*, vol. 1, no. 3, pp. 189–211, 1977.
- [155] P. P. Friedmann, K. Yuan, T. A. Millott, and C. Venkatesan, “Correlation Studies for Hingeless Rotors in Forward Flight,” *AIAA*, no. 94-1722, 1994.
- [156] D. A. Peters and J. A. Morillo, “Harmonic Balance Approach for Rotorcraft with both Unsteady and Unknown Rotor Speed,” *AIAA*, no. 97-1095, 1997.
- [157] D. A. Peters, B. S. Kim, and H. Chen, “Calculation of Trim Settings for a Helicopter Rotor by an Optimized Automatic Controller,” *Journal of Guidance*, vol. 7, no. 1, 1984.
- [158] D. A. Peters and B. S. Kim, “Control Settings for a Trimmed, Stalled Rotor by an Automatic Feedback System,” *AIAA*, no. 81-0617, 1981.
- [159] D. A. Peters and S. Li, “A Combined Periodic-Shooting, Auto-Pilot Technique for Rotorcraft Analysis,” *Computational Mechanics Conference Paper*, pp. 654–659, 1995.
- [160] G. A. Miste and E. Benini, “Variable-Speed Rotor Helicopters: Performance Comparison Between Continuously Variable and Fixed-Ratio Transmissions,” *Journal of Aircraft*, vol. 53, no. 5, pp. 1189–1200, Oct. 2016.
- [161] K. Prakash, E. C. Smith, and C. E. Bakis, “Structural Damping Model for Composite Rotorcraft Blades with Carbon Nanotube Interlayers,” *AIAA Journal*, vol. 59, no. 5, pp. 1539–1547, May 2021.
- [162] J. W. Carter, “EXTREME MU ROTOR,” pat. US 2004/0042901 A1, 2004.

- [163] D. Escobar, I. Chopra, and A. Datta, “High-Fidelity Aeromechanical Analysis of Coaxial Mars Helicopter,” *Journal of Aircraft*, vol. 58, no. 3, pp. 609–623, Jun. 2021.
- [164] M. R. Amoozgar, A. D. Shaw, J. Zhang, and M. I. Friswell, “Composite Blade Twist Modification by Using a Moving Mass and Stiffness Tailoring,” *AIAA Journal*, vol. 57, no. 10, pp. 4218–4224, Oct. 2019.